REFERENCE

Characterisation and properties of alkali activated pozzolanic materials

Georgeta Simona Bordeian

A thesis submitted in partial fulfilment of the requirements of
Sheffield Hallam University
for the degree of Doctor of Philosophy.

November 2000

Abstract

Many of the waste materials produced from modern heavy industries are pozzalans, which develop cementitious properties when finely divided in the presence of free lime. This property allows a potential industrial use for this waste as a cement replacement material in concrete. An example of such a waste material is blast furnace slag from the smelting of iron and steel. The US produces 26 million tons of blast furnace slag annually. Most of the slag is slowly cooled in air and it makes a poor pozzolan. Only 1.6 million tons of the slag is available in the granulated form, which is suitable as a cementitious and pozzolanic admixture. Most European countries are well endowed with coal-fired power stations and this produces fly and bottom ash, flue gas desulphurisation (FGD) gypsum. However, less than 25% of the total ash from power stations has found an industrial use mainly in cement and concrete industry. This creates a massive waste-disposal problem. Disposal of unused fly ash in open tips and ponds, for example, creates pollution problems since the drainage of effluents from the ash in the deposit ponds threaten water supplies by polluting the ground water with traces of toxic chemicals.

Recent research has concentrated on the alkali activation of waste pozzolanic materials, especially ground blast furnace slag. This thesis has investigated the alkali activation of low calcium fly ashes. These form very poor pozzolans and the alkali activation of the fly ash offers the opportunity for the large scale use of fly ash. Water glass was selected as a suitable activator for the fly ash. A comprehensive series of tests have been carried out to gain information on the effect of different parameters, such as proportion and composition of the constituent materials, curing conditions and casting methods, in developing high performance construction materials. Laboratory investigations were carried out to determine the following characteristics of alkali activated materials:

- density, water absorption, apparent porosity and coefficient of saturation,
- drying shrinkage,
- compressive creep,
- compressive, flexural and tensile splitting strength,
- dynamic modulus of elasticity,
- accelerated weathering (freeze-thaw cycle) resistance,
- fire resistance (temperatures up to 600°C),
- microstructure, macrostructure and investigation of hydration phases by SEM, EDAX, Digital-mapping and X-ray diffraction.

The influence of key parameters e.g. slag content, curing method, water/binder ratio and water glass hardener content on the mechanical properties were determined. Optimisation of the alkali-activation of fly ash materials was achieved by blending this with other pozzolans such as silica fume and slags. Mechanical properties were further improved by using moulding pressures and by thermal treatment. The use of short fibre reinforcements was investigated to overcome microcracking, volumetric deformation and creep in the materials. The free shrinkage and creep of the materials agree with the model developed by Mangat and Azari for fibre reinforced Portland cement composites. Other additives were also investigated to improve workability, frost and water resistance and physical properties of the alkali activated materials. The fundamental relationships between chemical composition, hydration phases,

microstructure and engineering properties (strength, durability and stability) of alkali activated materials were investigated. It is clear that strength development is a function of the hydration products developed and these are affected by the mix composition and the curing temperature. The current work found parameters such as the Si/Al ratio, the Ca/Si ratio and the Na_2O content to be important. These chemical parameters decide the principal phases in the hydration products formed in alkali activated materials, between calcium silicate hydrate (C-S-H) and zeolite of the form (R_2O n Al_2O_3 x SiO_2 r H_2O).

Overall the thesis shows the great potential of alkali activated materials to produce high strength construction materials. Limitation in the shrinkage of the materials can be overcome by the use of fibre reinforcement. At the end of the thesis limitations and suggestions for further work are made.

ACKNOWLEDGEMENT

The author wishes foremost to express her sincere appreciation to her supervisor, Prof. P.S. Mangat for his guidance, valuable suggestions and encouragement throughout the preparation of this work. The also acknowledges the contribution of Mr Cliff Ellis and Dr Jamal Khatib for their help and guidance during this research project.

The author would also like to thank the members of staff of the School of Environment and Development, in particular, Geoff Harwood, Bob Skelton, Steve Herington and Simon Outwhite for their help.

The author gratefully acknowledges the help of Paul Slingsby and Cheryl Shaw for the use of the scanning electron microscope and X-ray difractometer in the Material Research Institute.

Thanks go to; Mike Connell of Appleby Group Ltd for his valuable advice and the supply of ggbs, Ash Resources Ltd for supplying the pfa and Elkem Materials Company for their supply of silica fume. Thanks also go to; Hepworth Minerals Chemicals Ltd for supplying the high silica sand, Crossfield Ltd for their supply of sodium silicate solution and Wilfred Smith Ltd for their supply of hardener. Thank go to Cem-FIL Ltd for supplying the glass fibres.

The author wishes to express her sincere gratitude to Gifford and Partners, in particular, J. P. Hartley and R. Smith for their understanding during the last two months before completion of this work.

Finally the author is particularly grateful to her husband whose consistent encouragement and love have been a tremendous impetus to the completion of this work.

TABLE OF CONTENTS

LIST OF TABLES

LIST OF FIGURES

DX243271

"To develop a thought into a finished visible entity is as stupendous a marvel as is the transformation of a seed into a tree."

Karl Terzaghi

1 Introduction

1.1 BACKGROUND

Large quantities of pozzolanic waste materials are produced world wide by:

- the burning of coal in power stations, in the form of fly ash and bottom ash,
- the iron and steel industry, in the form of blast furnace slag,
- the burning of flue gas, in the form of silica fume,
- the burning of high sulphur-content coal in power stations, in the form of flue gas desulphurisation (FGD) gypsum.

This is now becoming a serious disposal problem. The introduction of tighter European Community (EC) directives on disposal of waste materials makes the problem even more urgent. These waste materials have the potential for use in the construction industry but the amounts used at present are small in comparison with the vast amounts available. Disposal of unused fly ash in open tips and ponds, for example, creates pollution problems since the drainage of effluents from the ponds threatens water supplies by polluting the ground water with traces of toxic chemicals.

The US produces 26 million tons of blast furnace slag annually. Most of the slag is slowly cooled in air and it makes a poor pozzolan. Therefore, it is only suitable for use as an aggregate in concrete or for subbase construction. Only 1.6 million tons of the slag is available in the granulated form which is a suitable cementitious and pozzolanic admixture. FGD gypsum produced by the desulphurisation of flue gases has not been widely used in industry and ends up in disposal sites. This is due to the availability of alternative gypsum (calcium sulphate) from natural sources and other industrial by-products.

Most countries are well endowed with coal-fired power stations, which regularly produce large quantities of fly ash. A great proportion of energy production in the world is through the burning of solid fuels, see Figure 1.1.

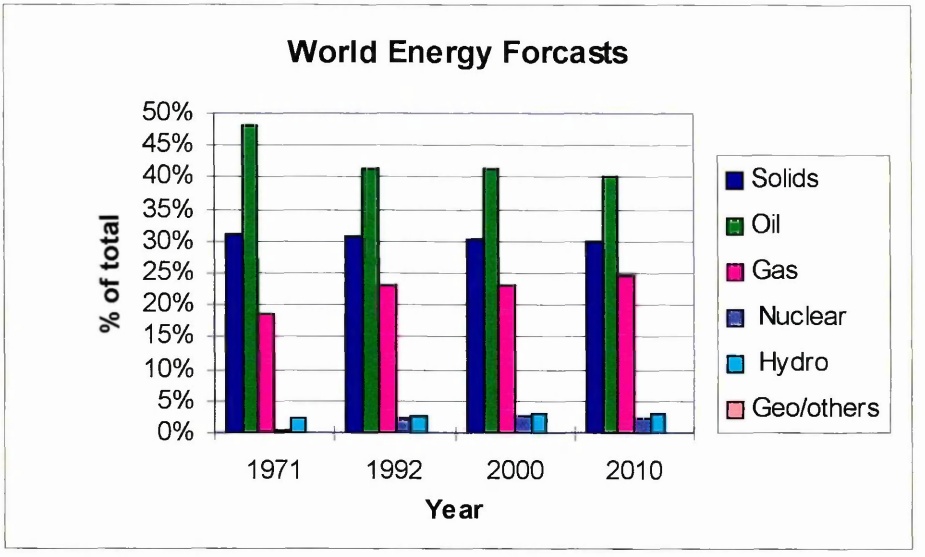

Figure1.1 World Energy Forecasts

Less than 25% of the total ash from power stations has found an industrial use mainly in cement and concrete industry. This creates a massive waste-disposal problem. The properties that make fly ash useful in industrial applications (e.g. in concrete) are: it is a fine particulate lightweight powder, it combines with free lime, it has predominately rounded particles, and it takes up water. As a consequence, this waste material has a strong potential for economic utilisation. The use of fly ash for blending hydraulic cements in concrete industry has been established in many countries. Fly ash has also been used in applications as diverse as soil stabilisation, road construction, asphalt filling, refractories, paints, insulation and fire resistant materials. In recent years, the lightest fraction of particles, which can be floated out of pfa has been used as lightweight filler in plastics and foams. However, the quantities of fly ash used in these applications are too small to make any significant impact in utilising the large quantities available.

The construction industry continues to use traditional materials. After aluminium and steel, Portland cement is the most energy-intensive material to manufacture. Growing environmental concerns and the need to use less energy-intensive products, means that efforts are now being made to find alternatives to Portland cement based materials. Future research into the pozzolanic waste materials offers the potential of their large scale utilisation in a safe, environmentally friendly manner.

1.2 SCOPE OF RESEARCH

New processes and technologies have been developed to produce building materials using large proportions of fly and pond ashes, blast furnace slag and silica fume. These can be activated by lime with or without FGD gypsum or by alkali activators such as sodium silicate solutions, alkaline hydroxides or alkaline sulphates. However, there are many basic problems which need to be solved for a full understanding of the behaviour of alkali activated materials.

Fly ash has largely been used as a cement replacement material in concrete. More recent research has concentrated on the alkali activation of waste pozzolanic materials, especially ground blast furnace slag. Because of the chemical and mineralogical similarities of fly ashes and ground granulated blast furnace slags, the findings of studies on alkali-activated slags are to a considerable extent applicable to alkali-activated fly ashes. Previous work on alkali-activated materials has produced high strength materials using alkali activated slag mixes. It has revealed that the physical and chemical composition of the constituent materials is very important in obtaining the desired strength. The contribution of different chemical elements of the final hydration products as well as the contribution of the different phases of the hydration products to strength is of critical importance for the development of optimal compositions. Research in this area is required.

A successful outcome of the present research will have a great impact on the utilisation of industrial waste materials (e.g. fly ash) and, therefore, it will provide an important environmental achievement. A spin-off of this research is likely to be the greater use of fly ash in traditional hydraulic cement and concrete construction areas. This research has great potential to create a new industry for construction materials. It promises to bring small industrial enterprises to areas where coal burning power stations are located. Owing to the vast quantities of fly ashes stockpiled and being produced, together with monetary and environmental costs associated with its disposal, there is considerable urgency for such research.

1.3 SCOPE OF PRESENT INVESTIGATION

A comprehensive series of tests have been carried out to gain information on the effect of different parameters, such as mix proportions and composition of the component materials, curing conditions and casting methods, in developing high performance construction materials. This will provide a better understanding of the behaviour of alkali activated materials and suggest suitable applications for them.

Laboratory investigations were carried out to determine the following characteristics of alkali activated materials:

- density, water absorption, apparent porosity and coefficient of saturation;
- drying shrinkage;
- compressive creep
- compressive, flexural and tensile splitting strength;
- dynamic modulus of elasticity;
- accelerated weathering (freeze-thaw cycle) resistance;
- fire resistance (temperatures up to 700°C);
- microstructure, macrostructure and investigation of hydration phases by SEM, EDAX, Digital-mapping and X-ray diffraction.

One of the problems of alkali activated slags and fly ash mortars is their tendency to develop very extensive microcracking. Although alkali-activation is a very efficient way of activating slags, this type of material has a shrinkage three times larger than the corresponding OPC mortar. Research is required to develop methods of reducing microcracking and volumetric deformation and its negative effects. This was carried out by:

- identifying suitable curing conditions;
- using reinforcement by short steel and glass fibres.

Optimisation of the alkali-activation of fly ash materials was achieved by mixing other pozzolans such as silica fume and slags with it. Mechanical properties were further improved by using moulding pressures and by thermal treatment. The use of short fibre reinforcements was investigated to overcome microcracking and volumetric

deformation. Other additives were investigated to improve workability, frost and water resistance and physical properties.

The results show that the strength of alkali activated pozzolanic materials is a function of the porosity and resulting hydration products developed in the mix. The mix composition and curing temperature affects these properties. The chemical parameters found to be important are the Si/Al ratio, the Ca/Si ratio and the Na_2O content. These chemical parameters determine the principal phase in the hydration products, between calcium silicate hydrate (C-S-H) and zeolite (R_2O n Al_2O_3 x SiO_2 r H_2O). Curing temperature alters the value of x in the zeolite structure, producing different forms of zeolite phases. Previous researchers in literature have identified the presence of calcium silicate hydrate (C-S-H) phases and zeolite (R_2O n Al_2O_3 x SiO_2 r H_2O) phases in the hydration products. But the contribution of each phase to the strength of the matrix has not been investigated. Research is required to investigate the fundamental relationship between chemical composition, microstructure and properties (strength, durability and porosity) of alkali activated materials. This research investigates the phases produced using X-ray diffraction, electron microscopy and EDAX analysis and then relates these to the modulus of rupture and porosity of alkali activated fly ash materials.

1.4 THESIS LAYOUT

The thesis is divided into nine chapters. An introduction to the thesis is given in Chapter I.

Chapter II is a comprehensive literature review covering the characterisation of pozzolanic by-product (waste) materials such as fly ash, ground granulated blast furnace slag and silica fume (microsilica). The alkali activation of pozzolanic materials is reviewed on the basis of the current state of the art knowledge.

Chapter III provides a detailed description (chemical, physical and mineralogical) of the constituent materials used in the present investigation. Details of the experimental programme and testing methods together with a brief description of the constituent materials are also given at the beginning of Chapters IV, V, VI, VII and VIII.

Chapter IV investigates the parameters which influence the performance of alkali activated materials, such as chemical composition of fly ashes, pressure compaction, curing conditions, fineness of sand, addition of ggbs and PC clinker, addition of water glass hardener, and silica modulus of water glass. A detailed discussion of the results is presented

Chapter V investigates the shrinkage and creep properties of alkali activated materials and fibre reinforced alkali activated materials. Shrinkage of the materials under high and low humidity curing is determined. The compression creep is determined at a stress/strength of 0.3. The delayed elastic and flow components of creep are determined to give a fundamental understanding of the creep mechanism of alkali activated materials. A detailed discussion of the results is presented. Theoretical and semi-empirical derivations are made to determine the free shrinkage and creep properties of alkali activated fibre reinforced composites. These relationships can be used to design optimal composition.

Chapter VI presents the mechanical properties of alkali activated materials and fibre reinforced alkali activated materials such as: compressive strength, modulus of rupture, tensile splitting strength and dynamic modulus of elasticity. The influence of key parameters of the mixes, e.g. slag content, curing method, water/binder ratio and water glass hardener content on the mechanical properties are determined. The study comprises of experimental investigations and theoretical analysis for the modulus of rupture of fibre reinforced materials.

Chapter VII deals with the physical properties alkali activated materials, such as density, water absorption, porosity and permeability. It also investigates durability of alkali activated materials exposed to freeze-thaw cycles and high temperatures simulating exposure to fire. The influence of key parameters such as: curing method,

water/binder ratio and water glass hardener content on the physical properties and durability properties is determined. The residual compressive strength after exposure to high temperature (600°C) and freeze-thaw cycling is also determined.

Chapter VIII presents the investigations of macro and microstructure of alkali activated materials. The fundamental relationships between chemical composition, hydration phases, microstructure and engineering properties (strength and durability) of alkali activated material is investigated. SEM, EDAX, Feature analysis, Digital mapping and X-ray diffraction methods are used.

Conclusions and recommendations for further work are given in Chapter IX. Previous research publications and sources of information referred to in this thesis are presented at the end of the thesis.

"Although nature commences with reason and ends in experience it is necessary for us to do the opposite, that is to commence with experience and from this to proceed to investigate the reason."

Leonardo da Vinci

2 Literature Review

2.1 INTRODUCTION

In the modern power plants during combustion of powdered coal, volatile matter and carbon are burned off. However, most of the mineral impurities deposited in coal during its formation, such as clays, shale, quartz and feldspar are generally fused and remain in suspension in the flue gas[1]. The fused matter is injected or blown into the boiler furnace at high speed and is burnt at a temperature of around 1500°C. The temperature is quickly lowered to a point where the fused matter solidifies to spherical particles. Most of this mineral matter flies out with the flue gas stream and hence is called "fly ash". Modern practice is to remove the fly ash from the flue gas stream by mechanical separators, electrostatic precipitators or by bag filters. Figure 2.1 shows schematically the approximate amounts of total solid waste in a coal-fired electric generating plant where coal is used as fuel, containing 10% total ashes and 1% sulphur.

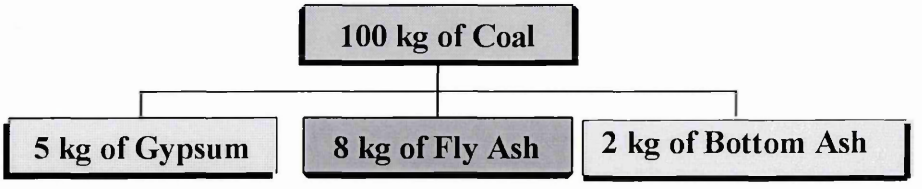

Figure 2.1 Amounts of total solid waste for 100 kg of coal

Fly ash production in the UK amounts to approximately $10x10^6$ tons a year from the burning of coal in thermal power stations. This means that the disposal of this waste material is a problem. Not just because of the quantity, but also because of the toxic compounds within the waste which can contaminate land and ground water. New EC directives have led to tighter controls and the demand for more effective encasement of this material[2].

Research into the use of standardised fly ash[3] and computational packages to predict the mineralogy of fly ash by thermodynamics and kinetic constraints for quality assurance and disposal assessment indicate the serious pollution problems fly ash poses world wide.

As with all waste materials the emphasis on disposal has now changed to identifying potential uses and developing a long-term solution to the hazard of fly ash. The main use for fly ash is as a cement replacement material and was first used in 1937 in the Hungry Horse Dam in Montana[4] Since then quantities of fly ash used in concrete mixes have grown steadily. However, despite over four decades of use as mineral admixture in cement and concrete, soil stabilisation, road construction and asphalt filling, less than 25% of the total production is used as shown in Figures 2.2 and 2.3[5].

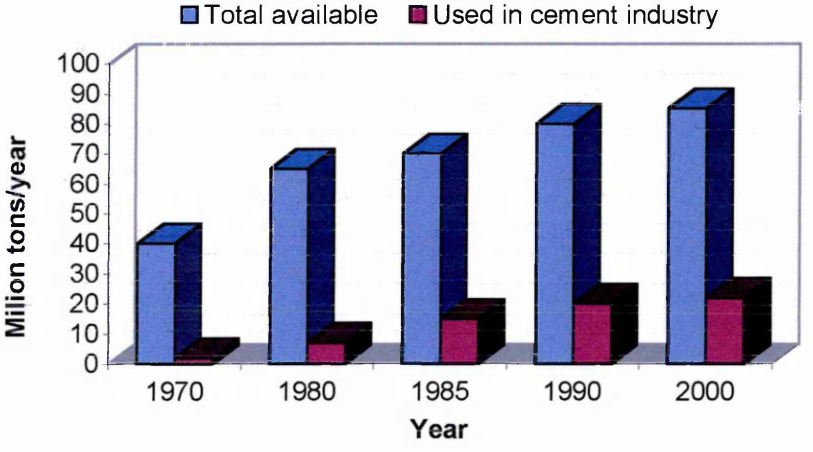

Figure 2.2 Available and Utilized fly-ash in USA

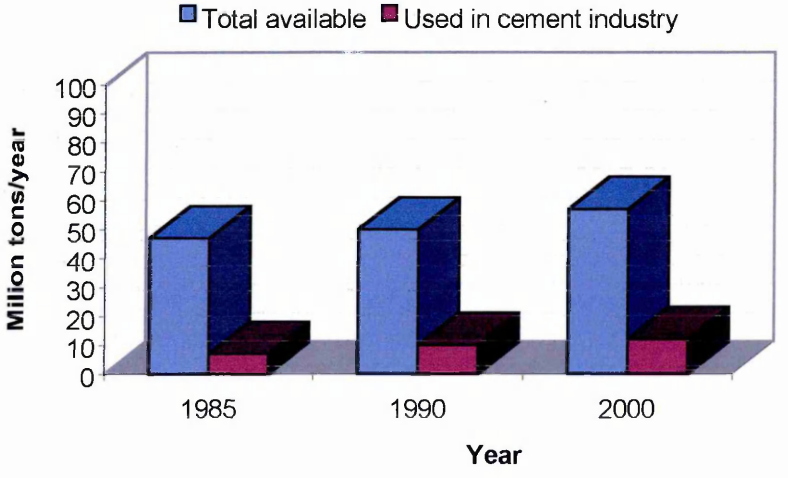

Figure 2.3 Available and Utilized fly ash in Western Europe

Fly ash can be used as a cement replacement material because of its pozzolanic properties. Low calcium fly ashes, which are used in this investigation, do not contain enough calcium to be self-activating. They need more calcium from an external source in order to develop their full cementitious potential. The activation of fly ashes is normally carried out with lime, directly with lime powder or indirectly with ordinary Portland cement, or with gypsum all of which provide the external source for Ca. According to ASTM C 595[6] a pozzolan is defined as "a siliceous or siliceous and aluminous material which in itself possesses little or no cementitious value but which will, in finely divided form and in the presence of moisture, chemically react with calcium hydroxide at ordinary temperature to form compounds possessing cementitious properties". It is clear from the above definition of pozzolans, that the Portland cement minerals are not the only possible source of formation of cementitious materials. Significant efforts have been put into research and development of different pozzolanic materials and a large number of publications are available on the subject of alkali activated materials.

The activation of fly ash by alkaline compounds to create a cementitious material using high volumes of fly ash as reactive filler, is the basis of this study. In this study only low-calcium fly ashes from the UK have been used. These fly ashes, due to the high proportion of silica and aluminium consist principally of aluminosilicate glass. According to Mehta[1], Hubbart et al examined fly ashes from 26 UK sources. They were all found to be low in calcium oxide (less than 55% analytical CaO) and all contained, mullite ($Al_6Si_2O_{13}$), 9-43%, quartz, 1-9%, hematite (Fe_2O_3), 3-11%, magnetite (Fe_3O_4), 2-9%, unburned carbon (C), 1-12% and concentration of amorphous silicates ranging from 29-74%.

2.2 NATURE OF POZZOLANIC MATERIALS

2.2.1 Nature of Fly Ash (pfa)

General review papers[1,3] provide information on the work carried out into the mineralogical composition of fly ash. The studies indicate that fly ashes reflect the differences of the mineral contents of the different types of coal that produce them. A typical composition of the major compounds can be seen in Table 2.1[2]. The classification of fly ashes in current international standards (ASTM C618) is based on the mineral composition, that is, the $SiO_2 + Al_2O_3 + Fe_2O_3$ content[7]. Class C fly ash contains a minimum of 50% ($SiO_2 + Al_2O_3 + Fe_2O_3$) and class F a minimum of 70%. However, the classification of fly ashes in terms of the lime content has also been found to be important in estimating their pozzolanic activity[5]. Fly ashes with a low content of CaO (class F) have only pozzolanic properties whereas those with a high content of CaO (class C) also have some cementitious properties. In class C there are fly ashes with a high CaO content, normally up to 35% by weight, and in class F there are fly ashes with a low CaO, up to 5% by weight.

Table 2.1 Typical Composition of Fly Ash[2]

Compound	Content [%]
SiO_2	49 – 53
Al_2O_3	25 – 29
Fe_2O_3	8 – 11
CaO	1.8 - 5.3 (class F) -35(class C)
MgO	1.3 - 2.2
K_2O	2.2 - 3.7
Na_2O	0.7 - 1.5
TiO	1.0 - 2.0
SO_3	0.3 - 1.7

Contrary to the definition of pozzolannic activity[1] not all siliceous and aluminous materials are active. Crystalline minerals, for instance silica as quartz, alumina as corundum (Al_2O_3), and aluminosilicates such as sillimanite (Al_2SiO_5) and mullite

($Al_6Si_2O_{13}$) do not react with lime solutions. It is only when the siliceous and aluminous minerals are present in a noncrystalline form and as small particles, that they can hydrate at a slow rate in an alkaline solution to furnish silica and alumina for reaction with lime which leads to the formation of cementitious products at room temperature[1]. The non-crystalline glassy alumino silicates are the major component of fly ashes, sometimes 90% or even more. Differences in the type of solid phase, glass or crystalline, accounts for the difference in the pozzolanic activity of class C and class F fly ash.

Class F fly ash, owing to the high proportion of silica and alumina, consist principally of aluminosilicate glass. In the furnace very large spheres of molten glass may not get cooled rapidly and uniformly, thus crystallisation of aluminosilicates takes place in the interior of the glassy sphere. This partial devitrification of glass would account for the presence of crystalline aluminosilicates, which are relatively nonreactive.

The situation in class C fly ashes is more complicated[1] than the low calcium class F fly ash, however, no work is available to quantify these differences. It seems that the reason for high activity of high-calcium fly ashes may partially lie in the chemical composition of the glass, which is different than the glass in low-calcium fly ashes[1]. The principal crystalline mineral in the class C fly ash tends to be tricalcium aluminate C_3A, which is the most reactive mineral present in Portland cement, and free lime. Together these probably account for the cementitious behaviour and better pozzolanic activity of the class C fly ash.

2.2.2 Nature of ground granulated blast furnace slag (ggbs)

A number of pozzolans are available from wastes of industrial processes. It appears that the behaviour and the composition of the glassy phase of class C fly ash is very similar to blast furnace slag[1]. This is another waste material consisting mainly of silicate glass containing calcium, magnesium, aluminium and silica. Owing to high

proportion of calcium, magnesium, aluminium and silica, ggbs consists mainly of calcium aluminosilicate glasses. The chemical composition of the glass in ggbs corresponds to melilite phase, which is a solid solution phase between gehlenite ($Ca_2Al_2SiO_7$) and akermanite ($Ca_2MgSi_2O_7$). In addition to these, diopsite ($CaMgSi_2O_6$) and merwinite ($Ca_3Mg(SiO_4)_2$) have also been detected in devitrified particles of slag[1]. The progressive hydration of slag admixture in cement enhances later age strengths. They produce further compaction of the cement paste with gel formation and pore filling and the suppression of $Ca(OH)_2$ formation.

2.2.3 Nature of silica fume (microsilica)

Another pozzolan commonly used in blended cements is silica fume. This is a fine powder, almost pure amorphous silica, and is characterised by its prompt pozzolanic activity[8]. Condensed silica fume, sometimes known as microsilica or volatilized silica, is produced by electric arc furnaces as a by-product of the production of metallic silicon of ferrosilicon alloys[1]. In the reduction of quartz to silicon at temperatures up to 2000°C, a gaseous SiO_2 is produced. It is transported to lower temperatures where it oxidises on coming in contact with air and condenses in the form of spheres consisting of noncrystaline silica. This material, which is extremely fine, is removed by filtering the outgoing gases in a bag filter. Silica fume consists mainly of noncrystaline silica with a very high surface area which makes it highly pozzolanic. Silica fume has been used in the development of high-strength, low permeability concrete.

In addition to their pozzolanic activity in concrete, it is beginning to be recognised that two to three of the mineral admixtures, such as fly ash, slag and silica fume, together are complementary and almost synergistic[8]. Silica fume is the fastest reacting pozzolanic material; because of this its effect becomes evident in increasing the early strength of the material. Rapid matrix densification and the refinement of the paste-aggregate interface occur early with silica fume. Fly ash and slag, being less reactive pozzolanic materials influence the microstructure of the material at a later stage. The

progressive hydration of fly ash and slag admixtures enhances later age strengths. Fly ash and slags produce further compaction of the paste and cause pore filling and suppression of $Ca(OH)_2$ formation. Therefore, in order to obtain maximum short and long term performance from the use of industrial by-products in concrete, binary or ternary combinations may be necessary.

2.3 QUALITY COEFFICIENT OF A POZZOLANIC MATERIAL

There are a number of classification procedures that can be used to draw comparisons between different pozzolanic materials. The 'acidity' of the pozzolan[9] can be calculated with equation (2.1), this is basically the ratio of siliceous and aluminous material to free lime:

Acidity of a pozzolan = $(SiO_2 + Al_2O_3 + Fe_2O_3)/(CaO + MgO)$ Equation 2.1

Using this classification procedure, ordinary Portland cement would have an acidity of approximately 0.5, slag of 1 and fly ash of about 15. Malolepszy used different equations in order to identify the type of slag[10]. M_b, the basicity ratio and M_a, the acidity ratio were calculated using the following formulae:

M_b = (CaO [%] + MgO [%])/(Al2O3 [%] + SiO2 [%]) Equation 2.2

M_a= (CaO [%] + MgO [%]+Al2O3 [%])/(MnO [%]+ SiO2 [%]) Equation 2.3

Another classification technique[11] for pozzolanic materials is using the quality coefficient 'K' which can be determined using equation (2.4).

K= $(CaO+ MgO + Al_2O_3)/ (SiO_2+ MnO + TiO)$ Equation 2.4

For ground granulated blast furnace slag 'K' falls in the range 1.65 - 1.85. The effectiveness of 'K' classification procedure could be due to the Siliceous/Alumina ratio, which has been shown to be important in the formation of certain zeolites in the hydration process[12].

Many formulae have been proposed to estimate the slag qualities[9.12]. It is accepted[13] that the following are the main factors in determining the hydraulic activity of a slag: chemical composition, glass content, specific surface area and type of alkali activator. Because of the complexity and interdependence of these factors, it has been shown that strength testing is still the most satisfactory method of estimating the slag quality. Caijun and Robert[14] investigated the alkali activation of ground pelletized blast furnace slag by NaOH, Na_2CO_3 and Na_2SiO_3 following the method for quality control and evaluation of hydraulic activity of ground slag by activation with alkali described in ASTM C1073-91[15]. The samples were mixed with 5M NaOH solution (or equivalent) and cured for 24 hours at 50°C. The mix proportions of slag/ sand/ NaOH solution were 24/ 65/ 11. From all activators investigated[14] (NaOH, Na_2CO_3 and Na_2SiO_3), Na_2SiO_3 produced the highest strength for both slag finesses 400 m^2/kg or 600 m^2/kg as seen in Table 2.2. Sodium silicate activated slag mortar has a higher strength than OPC type III mortar at early and later ages.

Table 2.2 Compressive Strength of alkali activated mortars and Portland cement mortar cured for 24 hours at 50°C[14]

	Compressive Strength [N/mm^2]	
Activator type	**Slag ***	**Slag****
OPC type III	42	-
NaOH	10	10
Na_2CO_3	32	35
Na_2SiO_3	50	63

Specific surface area of slag* was 400 [m^2/kg]

Specific surface area of slag** was 600 [m^2/kg]

From their investigations they concluded that in order to improve the sensitivity of the quality control test (ASTM C1073-91[15]), the alkali activators should be selected by activator-optimisation testing[14]. NaOH, Na_2CO_3 and Na_2SiO_3 should be tested at the same time and the most effective one should be selected as the activator for the quality control testing.

2.4 ALKALINE ACTIVATION

The pozzolanic reaction in some respects is similar to the hydration mechanism in Portland cement[1]. In addition to the factors affecting the strength of a normal Portland cement mortar, the nature and dosage of the activator play a key role in the strength development of alkali activated materials. Studies of the hydration mechanism of alkali activated materials often run into difficulties because of the complexities of the alkali solutions and the factors determining the hydraulic activity of the pozzolanic materials.

2.4.1 Portland Cement

The first form of alkaline activation employed for fly ash was ordinary Portland cement. Here fly ash was used as a cement replacement material. This was first employed in the Hungry Horse Dam in Montana[2] in 1948. Portland cement has proved to be a good activator for fly ash. Cement with 25 to 50% fly ash addition has been found to improve the quality of the concrete[2]. Concrete containing fly ash, because of its fine particles, shows an increase in the rate of hydration[1] and therefore high early age strength.

Only after 91 days any increase in strength of blended cement mortar could be attributed to the pozzolanic activity of the fly ash because of its slower rate of activation. Nasser and Marzouk[16] found that concrete containing fly ash exposed to high temperatures in the range 121° C to 149° C exhibited an increase in strength. This was put down to the formation of tobermorite gel, a product of the reaction of lime and fly ash at high temperatures. At higher temperatures then 149° C, the strength gain was lost because of the transformation of tobermorite to crystallised alpha dicalcium silicates, which has poor binding qualities.

Concrete containing fly ash has a finer pore structure with smaller void size than ordinary Portland cement[1]. This accounts for its low permeability and, therefore, high resistance to chlorides ingress or carbonation. The alumina content of fly ash also provides the concrete with higher sulphate resistance. In addition fly ash also reduces the heat of hydration and lowers expansion caused by the alkali silica reaction[17]. The addition of fly ash will also increase the drying shrinkage leading to cracking problems and will greatly influence the modulus of elasticity and creep performance.

2.4.2 Alkaline Hydroxide

Many researchers[18, 19, 20, 21] have investigated the performance of alkaline hydroxide as activators for materials containing ggbs. Wang et al[19, 20] and Mesto and Kajaus[21] investigated the effectiveness of various alkaline hydroxides, as activators, on compressive strength showing NaOH to be effective but less than Na_2CO_3 and water glass. Malolepszy[22] tested the strength of different slags using various activators and found that NaOH is a suitable activator for slags rich in $(CaO)_2Al_2O_3SiO_2$. Isozaki et al[18] used NaOH to activate blast furnace slag and found that the optimum amount of NaOH activator is of the order of 7.5-10% by weight of slag. The compressive strength of NaOH activated blast furnace slag increases with fineness of slag. There appeared to be no formation of calcium hydroxide in the hydration of slag, the morphology of the hydrate was homogeneous and the paste structure was dense when compared with OPC. The flow curves of NaOH activated slag paste are of the pseudoplastic type and thixotropic in nature. Sodium lignosulfonate proved to be a suitable superplasticiser for this mix whereas formaldehyde condensates of β-naphthalene sodium sulfonate was not.

Andersson and Gram[23] developed an alkali activated slag mortar. Granulated blast furnace slag was used as a base material and NaOH, Na_2CO_3 and water glass were used as activators. The flexural and compressive strength, modulus of elasticity, porosity, shrinkage and crack sensitivity were fully investigated. NaOH whilst being a

good activator and catalyst for the hydration process produced specimens with lower strength than water glass and Na_2CO_3. The conclusion was that the difference in strength was due to differing anions in the activator. These findings were confirmed in the work of Wang et al[19] and Mesto[21]. However, the mechanism by which the anions affect the activators is not fully understood.

Parameswaran[24] used in their investigations Indian slag with CaO content between 30-35%, Al_2O_3 content 20-24% and MgO of 7-9%. The mixture was 1:2 slag and sand activated by NaOH, Na_2CO_3 and Na_2SiO_3 and cured at ambient temperature. Their results[24], summarised in Figure 2.4, show that NaOH was the best activator. These findings are contrary to the results produced by Bin[25]. He found that the compressive strength of Na_2SiO_3 activated slag is higher than the strength of NaOH activated slag mortars at both early and late age.

Bijen and Waltje[26] used experimental model of Smith and Osborne[27] to investigate the durability of cements consisting of 60% ggbs and 40% fly ash activated by 7% sodium hydroxide solution and water glass (concentration of 7M). NaOH proved to be the best activator for the fly ash slag mixes, water glass showing no activation effect on such mixes. Intensive efflorescence was observed after one week for alkali activated slag-fly ash mortars whereas for the reference Portland cement mortar, efflorescence appears only after four months[26].

Other researchers[28] found similar results concluding that NaOH was the best activator for both slag and slag plus fly ash alkali activated cements. The optimum dosage of NaOH was 3-5% and the optimum fineness of slag and slag-fly ash blends was 4000-5000 cm^2/g (Blaine). Activated slag and its blends with fly ash and other pozzolanic materials have strengths at 7 and 28 days similar with those of ordinary Portland cement as seen in Table 2.3.

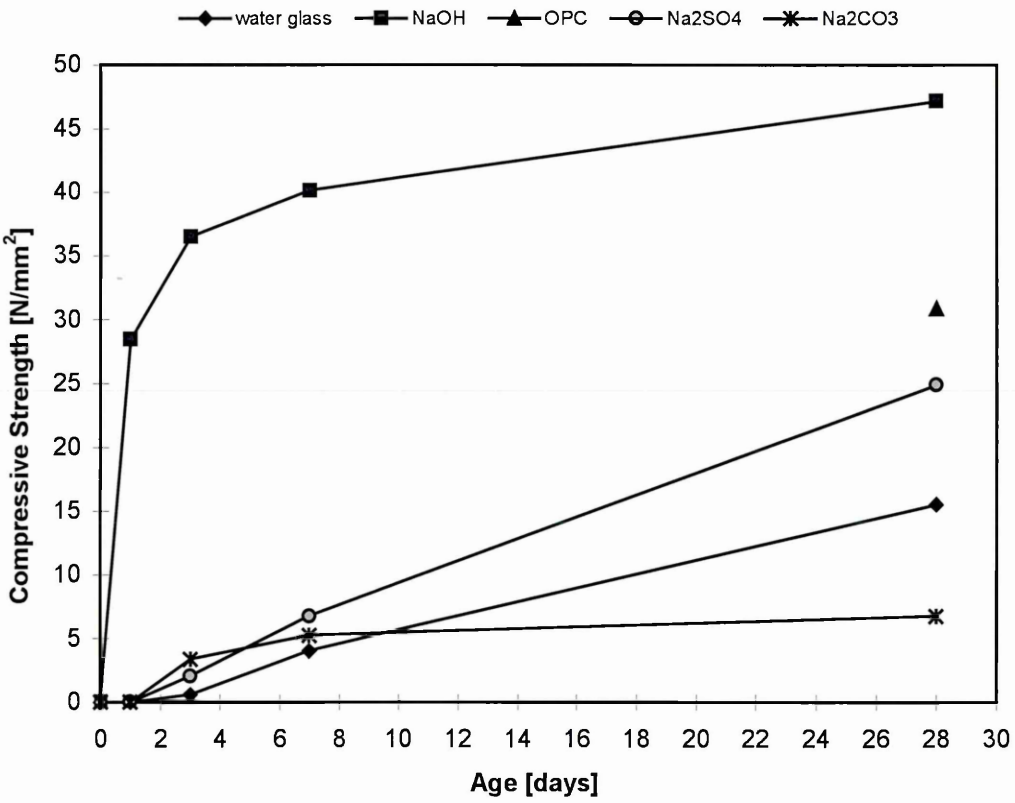

Figure 2.4 Compressive Strength of ordinary Portland cement mortar and alkali activated materials[24]

Table 2.3 Compressive strength of alkali activated mortars[28]

Type of slag	Type of activator	Dosage of activator [%]	Compressive Strength [MPa]	
			7 days	28 days
synthetic slag	NaOH	1	*1	*1
synthetic slag	NaOH	3	26.5	33.6
synthetic slag	NaOH	5	41.4	49.4
synthetic slag : fly ash 1:1	NaOH	1	*2	*2
synthetic slag : fly ash 1:1	NaOH	3	25.9	30.4
synthetic slag : fly ash 1:1	Na_2OnSiO_2	5	8.9	15.1
synthetic slag : fly ash 1:1	Na_2CO_3	3	-	4.7
synthetic slag : fly ash 1:1	Na_2CO_3	5	-	6.9
synthetic slag : fly ash 1:1	$Ca(OH)_2$	5	3.1	12.7
LCFC alloy slag	Na_2OnSiO_2	10	0	0
blast furnace slag	Na_2OnSiO_2	10	0	0
blast furnace slag	Na_2CO_3	5	0	0
blast furnace slag	kiln dust	20	5.3	9.0

Note *1 disintegrated during demoulding, *2 crumbled after demoulding

Alkali slag-fly ash cements activated by NaOH carbonate much faster than the reference mortars made only with slag or ordinary Portland cement because of the extensive microcraking of the hardened paste which enhances the penetration of the carbonation frontier and reduces strength. The carbonation of alkali activated slag-fly ash cements is followed by a substantial reduction in compressive and flexural strength[26].

2.4.3 Lime

Even though it provides a high Ca content, lime was not as effective at activating slag as sodium hydroxide. NaOH proved to be capable of activating high levels of slag or fly ash. However, other authors have found lime a useful addition to ground granulated blast-furnace slag concrete[29, 30]. Here water glass was the activator and hydrated lime slurry was used as a retarder. This allowed the attainment of much higher compressive strengths both at early age and after 28 days[29].

The use of lime as an activator is an obvious choice with a long history of use in cement and brick making. Dube and Palit[31, 32] detail a study into the production of bricks using pond ash and fly ash as a filler and lime as the alkali activator. Chemical composition of the fly ash used in their investigations is presented in Table 2.4.

Table 2.4 Chemical composition of fly ash[31, 32]

ELEMENTS	Fly Ash [%]	Pond Ash [%]
Silica (SiO_2)	60.11	58.62
Alumina (Al_2O_3)	26.55	25.01
Iron oxide (Fe_2O_3)	5.84	5.12
Calcium oxide (CaO)	4.83	4.06
Magnesium oxide (MgO)	1.25	1.20
Loss on Ignition	0.45	5.57
Density (kg/m^3)	1095	853
Surface area [cm^2/g]	6120	2680
$\frac{CaO + MgO + Al_2O_3}{SiO_2}$	**0.542**	**0.516**

The various attempts made to utilise fly ash in making bricks and blocks used five different technologies:

1. natural curing;
2. warm water curing;
3. cement process (water curing)
4. autoclaving at low & high steam pressure and low pressure moulding with high water content (40%) and with vibration;
5. autoclaving at low and high steam pressure and high pressure moulding with very low water content.

The study found that for the best results, the mix proportions should be; fly ash/ sand/ lime, in the ratio of 72/ 20/ 08. The moulding pressure should be 240 kg/cm^2; the steam pressure should be 10 kg/cm^2 and the autoclaving duration should be 6 hours. The full range of mechanical and physical properties of the fly ash based bricks are:

- compressive strength: 13.73 N/mm^2
- flexural strength: 2.59 N/mm^2
- bulk density: 1663 kg/m^3
- abrasion resistance: 51.4% (loss)
- linear drying shrinkage: 0.012%
- water absorption: 13.1%

Lenz et al[33] used brown coal fly ash, which is high in CaO and MgO. They investigated the use of the brown coal fly ash as a substitute for fine white lime, which is the most common feedstock material beside quartz sand, for the production of bricks. Malhotra and Tehri[30] used blast furnace slag, activated with lime and mixed with sand to produce slag sand lime bricks. The bricks were pressed into moulds at low pressure and cured at 95% humidity and 27° C for 28 days then dried at 70° C for 24 hours. This technology produced a good quality brick at lower energy costs than normal methods, very similar to the work of Dube and Palit[31, 32].

2.4.4 Sodium Carbonate

Mesto and Kajaus[21] reported sodium carbonate (Na_2CO_3) as being a poor activator, but Andersson found that the addition of Na_2CO_3 to granulated blast furnace slag in the range of 3-11% by weight of slag caused an increase in flexural and compressive strength[23]. Because of the lower solubility of sodium carbonate it is generally best added as a solid. Anderson also found that the higher the alumina content the higher the compressive strength when granulated blast furnace slag is activated by sodium carbonate[23]. Reducing the water binder ratio also had a favourable effect on compressive strength. Wang also confirmed that Na_2CO_3 is a good activator, but found it to be poorer than water glass[19]. Malolepszy tested the strength of different slags using various activators and found that Na_2CO_3 is a suitable activator for slags rich in $(CaO)_2MgOSiO_2$.

2.4.5 Sulphate Activation: calcium sulphate, alkaline sulphate

Calcium Sulphate in form of either gypsum or anhydrite has been widely used to produce super sulphated cements[34]. Sulphate activation depends on two factors:

1. the availability of alumina to form sulphoaluminates
2. the solubility of the sulphates

Activation by sulphates requires an alkaline medium, normally $Ca(OH)_2$. However there is an optimum dosage of $Ca(OH)_2$, an excess hinders the formation of some of the hydration products responsible for strength loss and leaves the concrete vulnerable to carbonation.

Sodium sulphate is believed to react with $Ca(OH)_2$ in the following way,

$Ca(OH)_2+Na_2SO_4+2H_2O \leftrightarrow 2NaOH + CaSO_4\ 2H_2O$ Equation 2.5

This means that activation by a combination of gypsum and sodium hydroxide produces a higher pH than that of $Ca(OH)_2$ alone[35]. Addition of Na_2SO_4 produces dramatic increases in early age strength but has been found to cause efflorescence[35].

2.4.6 Water Glass

Sodium silicates are soluble in water if the sodium content is high and result in an alkaline solution (water glass) containing ions such as $[SiO(OH)_3]^-$ and $[SiO_2(OH)_2]^-$. If the sodium content is low then large polymeric ions are present and the product formed is insoluble in water. Water glass is usually expressed in terms of its silica modulus that is the molar ratio of SiO_2/Na_2O[36]. Soluble silicates are essentially combinations of alkali metal oxide and silica with water. The general formula for the soluble silicates of Na, K and Li is $mSiO_2\ M_2O$, where m can be Na, K or Li and m is the molar ratio defines the number of moles of silica per mole of alkali metal oxide (moles of SiO_2/moles of M_2O). However, the ratio can also be expressed on a mass basis.

Soluble silicate solutions contain mixtures of silicate anions, ranging from monomeric and dimeric through to high molecular weight polymers containing a larger number of Si atoms[37] as shown in Figure 2.5. The polymer distribution determines the properties of the silicates and is mainly dependent on the molar ratio and solution concentration. It is believed that an equilibrium situation develops for any given solution composition and that a rapid re-arrangement of polymer species occurs if the solution is diluted or if extra alkali is added. There is evidence that equilibrium is more quickly reached for lower molar ratio solutions.

The versatility of these products stems largely from the modification of their properties by varying the molar ratio and the physical form in which the product is supplied e.g. liquid, powder or granules. The reaction mechanisms in such a complex system are almost impossible to define. However, research has provided insights into important areas of these reactions. The hydroxide ions from the activator break down the glassy structure of the slag or fly ash by breaking the Si-O and Al-O bonds producing =Si-OH and =Al-OH[12, 38, 39].

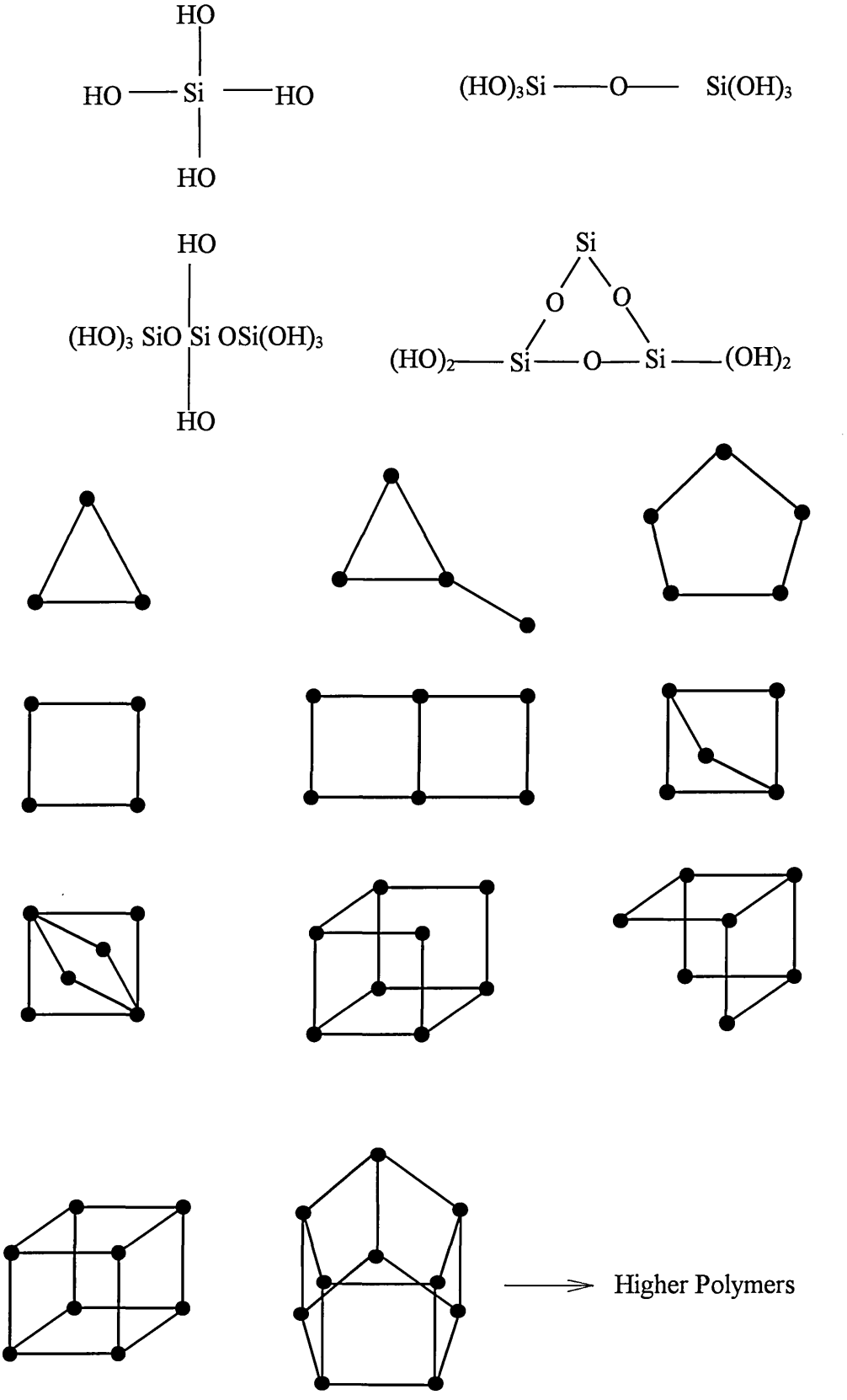

Figure 2.5 Polysilicate species identified in sodium silicate solutions [37].

The alkaline metal ions also act as a catalyst dispersing the coagulant into solution. Hydrates of alumino silicates form cations, which are incorporated to form zeolites. These alumino silicates (zeolites) have the general formula $R_2O{\cdot}Al_2O_3xSiO_2$.

The value of x and, therefore, the amount and type of zeolite formed varies with the curing temperature[12, 38, 39]. Various authors have studied the effect of curing temperature on mechanical properties[12, 38]. However, it has not been shown how different types of zeolites affect the mechanical properties and durability of the material.

The pore solution pH for alkali-activated materials is above 14 due to the presence of sodium hydroxide. However, Na concentration decreases with time indicating the consumption of Na in the hydration process[38, 40]. This probably occurs during the formation of low lime calcium silicate hydrate (C-S-H). Calcium ions are replaced by Mg, this is because $Ca(OH)_2$ has a low solubility in highly alkaline activated fly ash, but no crystalline ettringite or $Ca(OH)_2$ is seen in the hydration products[18]. Si ions are replaced by a combination of Al and Na ions to balance the charge. It is likely, however, that the type of crystalline products and hydration products found will be dependent on the activator used[53], e.g. activators such as Portland cement or gypsum with larger quantities of $Ca(OH)_2$ are likely to result in the presence of ettringite and crystalline $Ca(OH)_2$.

Water glass has shown itself to be the most effective activator in comparison with other activators such as NaOH and Na_2CO_3 and has been studied by many authors[11, 19 - 21, 23, 39]. However, studies of the hydration mechanism of slags activated with water glass run into problems because of the complicated nature of the water glass solution in which SiO_2 exists in various forms[11, 19, 20]. This leads to complex amorphous hydrates whose degree of polymerisation and crystallinity are difficult to control. Na_2SiO_3 produces much higher strengths than NaOH because of the higher

polymer content of Na_2SiO_3 activated cements[11, 19, 20]. This implies that the silicates in the water glass are important in producing the silica gel, which binds the particles. The type of silicate is also important as the solid sodium silicates[11, 19, 20] and the solid sodium metasilicates (hydrous water glass)[19, 20] have produced very low strengths under normal curing. Anhydrous sodium water glass (without crystallised water) has produced higher strengths compared with hydrous water glass[11].

As the silica gel makes a significant contribution to strength, there is an obvious interaction between the silica modulus and the Na_2O content of the mix. If the Na_2O content is kept constant, the alkali activation effect will be the same. The higher the silica modulus, the more the contribution from silica gel and hence the higher the strength, within a certain range. However, if the water glass content is kept constant then the higher the silica modulus the lower is the Na_2O content. This means a smaller alkali activation effect but a greater amount of silica gel[19, 20, 39]. The implication of this is that there is a variable optimum modulus[41] depending on the slag, its fineness and its curing conditions.

Research shows that the optimum water glass modulus for slags is 0.75-1.25 for acid slag, 0.9-1.3 for neutral slag and 1.0-1.5 for basic slag when the amount of water glass solid is kept constant. However, increasing the silica modulus increases setting time and workability of the mix[23, 40]. Setting time also decreases with increasing Na_2O content. This leads to best results being obtained with a water glass of modulus in the range 1-1.5 and a Na_2O content in the range 3-11% by weight of slag.

2.4.7 Mixed Activation

Many of the common activators used are in reality mixed activators such as gypsum, Portland cement and sodium sulphate as shown above. However, Mesto[21] reported that many activators resulted in better levels of activation when mixed rather than used individually e.g. phosphogypsum and NaOH, fly ash + NaOH (with slag), NaOH + Na_2CO_3.

Another example of a mixed activator is the F Admixture[21, 42]. A mixture of lignosulphates, sodium carbonate, sodium hydroxide and ground blast furnace slag was used to produce F-cement. This had a higher strength at all ages than ordinary Portland cement, but suffered from microcracking and sensitivity to salt weathering. Durability tests revealed it to be dense and impermeable with excellent frost and corrosion resistance[42].

2.4.8 Dosage of Alkali

Dosage of alkali is dependent of the activator and the type of slag or fly ash used. Isozaki et al found that for NaOH the addition was in the range 1-10 %, by weight of slag, but other reports showed that dosages within the range 3-11% had little effect on strength[14]. The reason for this is that an Na_2O content of between 2-8%, by weight of slag is required for activation[19, 20]. Beyond these levels there is little gain in strength and a higher alkaline content will causes efflorescence and brittleness. Buenfeld et al[39] have summarised the results for different activators (Table 2.5) from authors such as Wang[19, 20] and Mesto[21].

Table 2.5 Optimum Dosage and Degree of Activation[39]

Activator	Activation Degree	Optimum Dosage as % of Slag Weight	Scope
ROH R is Na or K	Good	3-10% R_2O equivalent	Added as Solution Suitable for acidic slags or with acidic additions e.g. s fume
Na_2CO_3	Moderate	2-7% Na_2O equivalent	Preferably added as a solid its low solubility. Gives hi strengths with slags of hig alumina content
$NaOH + Na_2CO_3$	Very Good	2-2.75% NaOH+ 1-3% Na_2CO_3 or 3% Na_2O equivalent	
F-Admixture	Very Good	Total alkali content of 3.75 - 4.00% Na_2O equivalent as 1-3% NaOH + 1-2% Na_2CO_3 + 1-4% sodium lignosulphonate + 0.02% sodium gluconate + 0.02% tributyl phosphate	suitable water/binder ratio = 0.34-0.36 Microcracks are generally ob in F-Cement
$R_2O(1\text{-}2)SiO_2$ in solution known as water glass. Where R is Na or K	Very Good	2 - 8% Na_2O equivalent	Potassium silicates are expe Workability of mixes is p
R_2SO_4 + any activator	Very Good	SO_3 content < 3%	Gives higher early age stre
$Ca(OH)_2$	Moderate	10%	
Phospho-gypsum + NaOH	Good	10%	Slow setting
OPC + NaOH	Good		Not better than NaOH
Ash of sulphite + NaOH	Moderate		slow setting
Gypsum + P=OPC	Good	Slag : 85%, Gypsum: 15% and OPC: 5%	Friable surface probably d carbonation

2.5 ADMIXTURES

Many authors have discussed the use of admixtures to alleviate some of the poor properties of alkali-activated materials. Superplasticisers such as sulfonated naphthalene formaldehyde condensate have been used to improve the poor workability of mixes and to reduce water content to maintain high strengths[18, 42]. Acid silica fume has been found to suppress efflorescence[39] and to improve workability.

Air entrainment agents, because of their dense microstructure, can improve freeze thaw resistance and improve workability[43] but higher dosages than when used with OPC are required. Polymers such as siloxanes have been used to reduce the water absorption[44]. Complex aluminium polyphosphates[45], which improve the water resistance and flexibility of inorganic paints based on water glass, may be suitable for use when water glass is used as an activator.

Reactive powder concretes use certain principles in their development similar to those in the current work[46]. Reactive powder concrete uses cement with silica fume, quartz powder, a polynaphthalene superplasticiser to improve workability and short steel fibres to reduce the brittleness[46]. Depending on the composition and the curing conditions, the compressive strength can vary from 200 N/mm^2, when cured in hot water at 90°C for three days to 800 N/mm^2 when dry heated at 400°C. Such high strengths were achieved by;

- improving the homogeneity of the mix by eliminating coarse aggregates
- improving the packing of the granular matrix by carefully selecting the grain size of component materials
- improving the microstructure by heat treatment that changes the nature of hydration products
- improving compaction by pressure moulding
- improving the ductility of the material through the use of short steel fibres

Pressure compaction produces stronger test samples for fly ash alkali-activated materials[44]. Pressure compaction[47] has been used before with concrete and results in increased strength especially when using low water cement ratios. Here layers of unhydrated paste are surrounded by thin layers of hydrated paste and the pressure compaction consolidates the mix.

2.6 EFFECT OF TYPE AND FINENESS OF FLY ASH AND SLAG

It is known that the fineness of slag improves strength and decreases the setting time regardless of the type of activator[10, 23, 41, 48]. Cajun et al used water glass to activate phosphorous slag[41]. The experimental results showed that the silica modulus of water glass had a great effect on strength of the cement as did the fineness of the slag. It was also found that there was a critical fineness of slag above which strength was not affected and that increasing the water slag ratio had a detrimental effect on strength. However, Anderson found that both compressive strength and flexural strength increased with slag fineness, but this did not apply to water glass activated slag[23]. Malolepszy and Deja[10] found that finer slags reduced the problem of micro cracking. Berube et al[48] found that finer fly ashes helped suppress alkali silica reaction expansion. Fineness of slag was a key factor affecting strength of alkali activated slag cement[39].

Wang[19, 20] investigated different types of slags, their hydraulic activity and fineness, and found the optimum blaine fineness to be in the range 400-550 m^2/kg. In another investigation, the optimum fineness of slag was found to be 400 m^2/kg, higher fineness increased water demand[38]. This seems to confirm that the optimum fineness of slag is around 400 m^2/kg. However, grinding the slag to achieve this fineness was found to be less effective than sieving out oversized particles. This could be due to greater

proportion of inactive crystalline material in the larger particles. Parameswaran[24] also investigated the activation of slag -fly ash blends of a 3/ 2 ratio. The compressive strength obtained from slag (fineness of 600 m^2/kg) fly ash mortars is equivalent to the strength obtained from slag (fineness 400 m^2/kg) mixes.

2.7 EFFECT OF CURING

As with fineness of slag, curing has been found to be a key parameter affecting the strength of alkali activated cements. Steam curing has been found to generate high compressive and flexural strength at early age[10]. Increase in strength immediately after steam curing was limited and in some cases flexural strength decreased. Malolepszy used NaOH and Na_2CO_3 to activate blast furnace slag to produce mortars, which were cured in different ways[10]. The samples were tested for compressive and flexural strength and freeze-thaw resistance. Variations in curing did not significantly affect the compressive strength, but the flexural strength showed large variations. This was explained by the formation of micro cracks due to volumetric changes of the hydration product, caused by the ease in which it lost and absorbed water. Using finer slag was found to reduce the problem.

Talling[40] investigated the effect of curing conditions on the strength of water glass activated slags and found that optimum activator choice and curing temperature were important. The aluminosilicate (silica binding gel) hydration products are found to be zeolites of the general formula $R_2O.Al_3O_3.xSiO_3$. The 'x' value was found to be 2 for normal curing and between 2 and 3 for short term steam curing and 4 for long term steam curing. The compressive strength of the activated slags was found to increase with steam curing. Higher strengths developed with longer curing times and higher curing temperature up to 80°C.

Compressive strength development continues after steam curing and the initial strength of 10 N/mm^2 after curing appeared to act as an activation level beyond which strength increase was rapid even when stored at 20°C. A one day strength of 40 N/mm^2 meant that there was no need for post curing and the strength continued to develop in open air. The optimum Na_2O addition to the slag mixes was found to be between 3 and 5% and activator choice and dosage was critical on early age strength development[23].

Caijun et al[49] investigated the strength development, pore structure and hydration products of alkali activated blast furnace slag cements (ABSC) and phosphorus slag cements (APSC) cured at 150°C for 15 days using ordinary Portland cement as control. They found that the APSC and ABSC mortars show a slight increase in strength after one day whereas Portland cement mortar showed a maximum strength at 1 day then decreased greatly as seen in Figure 2.6. At the age of 15 days, the strength of the PC paste is only half of the strength at age 1 day. They concluded that the alkali slag mortars are more stable at high temperature than the Portland cement mortars.

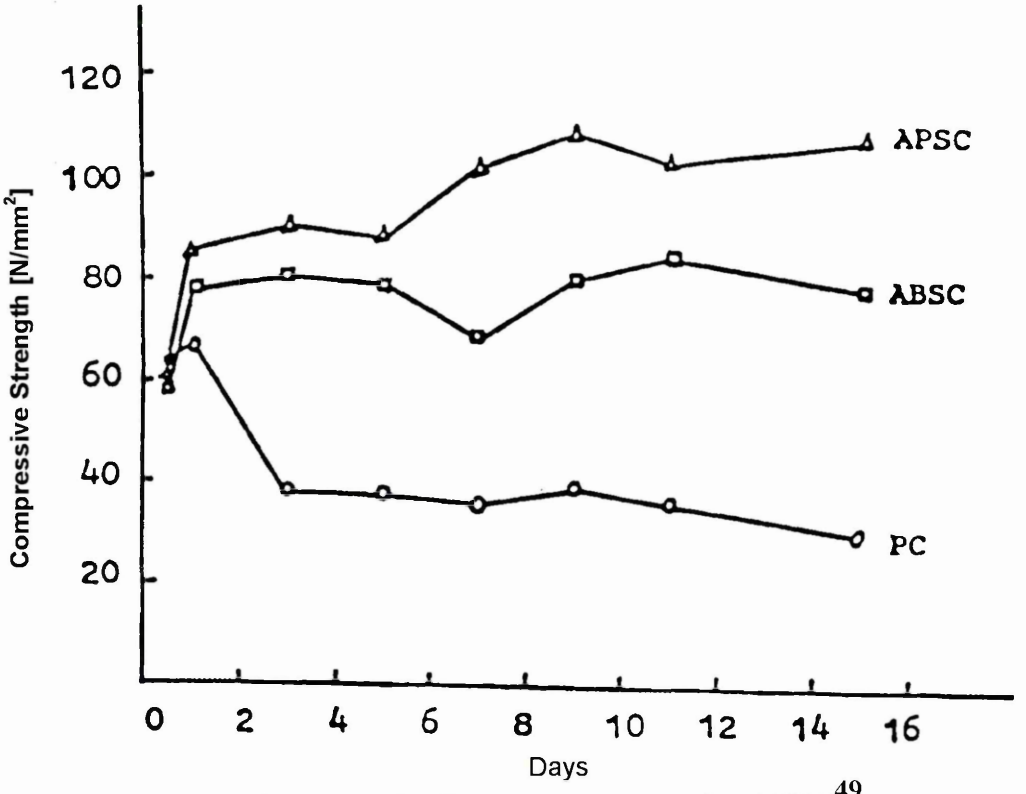

Figure 2.6 Compressive Strength of cement pastes cured at 150°C[49]

2.8 HYDRATION PRODUCTS IN BLENDED CEMENTS

The hydration products in blended cements have been covered by a large number of authors. The initial work was related to the study of cement pastes[50]. The hypothesis that C-S-H formed in calcium silicate and cement pastes has a layered structure was proposed in 1952, based on x-ray diffraction evidence. Various studies have found the structure to contain either tobermorite ($C_5S_6H_9$) or jennite ($C_9S_6H_{11}$) and in some cases, both have been found. However in practice the C-S-H of cement pastes differs greatly from either of these crystalline phases because it is almost totally amorphous. The Ca/Si ratio of CSH in cement paste is 1.75, which is higher than jennite or tobermorite. The C-S-H formed in calcium silicate and cement paste with mineral additions (fly ash, slag and silica fume) is similar in nanostructure to that formed in their absence, but the typical Ca/Si ratio is lower, between 1.4 to 1.6 and even as low as 1.0 to 1.2 in pastes made with high proportion of microsilica or alkali activated slag. The lower Ca/Si ratio has been found to increase the proportion of tobemorite like phases. It is also believed that the extent to which Al can substitute Si in the C-S-H increases with decreasing Ca/Si ratio.

In the fifties, hydraulic binding properties of the compounds of Li, Na, K, Rb, Cs, were discovered and in 1980's mixed hydraulic binding systems were put into practice in the construction industry[51, 52]. The slag-alkaline cements produced are ground granulated products of metallurgical and electrothermophosphorus slags, which are activated by solutions of alkali metal compounds. The hydration products of the slag-alkaline cements have been found to be mainly silicic acid, low-basic calcium hydrosilicates of C-S-H (B) type. These have been identified from x-ray diffraction work with major lines from d=3.07, 2.71, 2.11, 1.82 Å. Other products detected in alkali activated slag cements were alkaline hydroaluminosilicates of different types such as;

- Hydronephelite ($R_2OAl_2O_3 \cdot 2SiO_2 \cdot nH_2O$), with major lines from d=6.28, 3.66, 3.28, 2.80, 2.08 Å,
- Natrolite type ($R_2OAl_2O_3 \cdot 3SiO_2 \cdot nH_2O$), with major lines at d=6.7, 4.10, 3.17, 2.82 Å,

- Analcite type ($R_2OAl_2O_3 \cdot 4SiO_2 \cdot nH_2O$), with major lines at d=5.60, 3.45, 2.94, 2.09 Å,
- Paragonite and muscovite type ($R_2OAl_2O_3 \cdot 6SiO_2 \cdot nH_2O$) with major lines at d=4.39, 3.18, 2.52 Å.

Apart from these, gismondite type ($CaOAl_2O_3 \cdot 2SiO_2 \cdot nH_2O$), hydrogranates and mixed sodium-calcic and potasium-calcic hydroaluminosilicates are found. Hydration products containing no free lime such as hydroaluminates, hydrosulphoaliminates and high basicity calcium hydrosilicates which are characteristic of Portland cement mixtures were also found. This illustrates the complex varied nature of the hydration products found in cementitious materials.

Data from scanning electron-microscopy analysis shows the initial phases appearing at the boundary of interaction of slag grain and alkaline solution. Their appearance is fibrous because of the high pH and low lime concentration in the mix. Secondary phases are formed (crystallised) in the pores of the cement body. These can be zeolite like phases, which have high adhesive properties. They develop strong crystallisation contacts with calcium hydrosilicates and have a high sorbability which causes the gradual lowering of porosity of the material. The slag-alkaline cements[51, 52] produce strengths ranging from 40 to 118 N/mm^2. The durability of these cements is better than the sulphate-resistant cements and strength is higher than the alumina cements.

The essential goal of research into slag cements is to create binder, which would exclude from the hydration products the highly basic components such as C_3A, C_3S, and C_4A. The hydration products of these components have no essential effect on the synthesis of the cement stone strength (C_3AH_6 and $Ca(OH)_2$) or on enhancing its reaction capacity (C_3AH_6, C_4AH_{13}, C_2SH_2 and $Ca(OH)_2$). These binders are caustic alkalis, and will ensure the hydration of the aluminosilicates of the cement.

The hydration products of fly ash in blended cements have also been extensively investigated. Speras et al[53] used two computational packages, F*A*C*T and MTDATA in the prediction of the mineralogy of the ash and the distribution of elements between ash and emissions. Pore water extracted from borehole of the sample demonstrates significant leaching of elements and was thought to be more associated with the glassy phase. The use of fly ash in blended cements is reviewed noting the enhanced properties attainable comparable with conventional Portland cement mixes[53]. The main conclusion was that in considering the pozzolanic reaction of PFA in concrete it is possible to ignore the crystalline phases such as quartz and mullite and concentrate on the reactivity of the cenosheres comprising siliceous amorphous material.

Atkins et al[54] developed a thermodynamic model called CEMCHEM for blended cements based on a simplified chemical description of OPC and PFA which assumes that if the alkali and iron contents are low they can be ignored The system can then be treated as though it was formed from CaO-Al_2O_3-MgO-SiO_2-SO_3-H_2O[55]. The model calculates the equilibrium phase distribution at 25°C based on a proportion of the CaO-Al_2O_3-MgO-SiO_2-SO_3-H_2O whose phase relations have been determined from results of compatibility experiments. It is assumed that all the Mg combines with Al and OH to form the hydrotalcite like phase [$Mg_4Al_2O_7.10H_2O$]. Other solids considered are Portlandite, ettringite, gehlenide hydrate, calcium silicate hydrogel a non-crystalline solid of variable Ca/Si ratio (0.85-1.7) and a silica substituted hydrogarnet phase[55].

Three levels of replacement of OPC by PFA may be distinguished and taken as representative of important practical circumstances[53]. At 5% replacement level, the phase assemblage is affected only slightly. There is a significant decrease in the level of Portlandite (calcium hydroxide) because of its participation in the pozzolanic reaction, which results in an increase in the amount of C-S-H gel phase. Both of these changes may result in benefits in the long term strength and durability of the concrete and the incorporating of 5% PFA seems to be a desirable development.

When 25% of OPC is replaced by PFA, the equilibrium phase assemblage is markedly different. Calcium hydroxide content is now reduced, which allows gehlenite hydrate (strallingite) C_2ASH_8 to form in the low calcium fly ash blends. In the case of high calcium fly ashes, equivalent concentration of gehlenite hydrate (strallingite) C_2ASH_8 is achieved at higher replacement levels. C-S-H gel is the major phase in these blended cements; in cement blended with low calcium fly ash it is present in greater amounts than in unblended cements.

The other phase present in greater quantities than in OPC pastes is the hydrogarnet solid solution. The composition of this phase (hydrogarnet solid solution) along with the chemistry of the initial system determines that the relative amounts of hydrogarnet and gehlenite hydrate present. Glasser and Jappy have concluded that hydrogarnet may became a prominent component of OPC- PFA (low calcium) blended pastes and that hydrogarnet so formed will tend to contain silicon in solid solution[56]. As more silicon and perhaps iron enter the hydrogarnet phase, its density will increase, which may lead to changes in the macrostructure of the cement. The solid solution in the hydrogarnet not only makes it difficult to be precise about the amount of this phase present, but also affects the calculations of the amount of gehlenite hydrate. However, the thermodynamic calculations show much greater amounts of both phases than are present in the absence of PFA or other replacements materials.

Although the implications of incorporating more than 50% PFA in cement cannot be evaluated using the program because of the development of zeolite phases, it is certain that the chemical composition of the system will undergo further major changes. These require careful consideration of their influence on the properties of the cementitious material[53]. The possibility of creating zeolites from alkali activated fly ash is of considerable commercial interest. Due to their uniform molecular pore size and large surface area, zeolites are very useful materials with a large range of applications such as molecular sieves, absorbents and catalysts.

Zeolites are silicates frameworks which include both naturally occurring minerals and synthetic materials. Because of the presence of Al^{3+} and Si^{4+} sites, exchangeable cations such as Na^+ K^+ Ca^+ and Mg^{2+} are incorporated into the structure to compensate charge. The zeolite framework is rigid and very open, consisting of channels, which are able to accommodate both cations and water molecules[57].

In general an alkaline aqueous medium is required to synthesise zeolites. Some of the reaction variables include temperature, composition, pressure, pre-treatment of reactant, low-temperature ageing of reaction mixture, pH of the mixture, seeding and time. Judith L LaRosa et al[57] synthesised Na-P type of zeolites and zeolites Y from class F fly ash. Chemical composition of the constituent materials is presented in Table 2.6. Sodium hydroxide (NaOH) was used as activator. Room temperature and thermal curing was adopted. Na-P type of zeolites, zeolites Y and chabazite were developed in cement pastes blended with fly ash activated by NaOH. They were cured for 2 days at room temperature and then for 6 days at temperatures ranging from room temperature to 90°C[57].

Table 2.6 Chemical composition of component materials[57]

Component	Na_2O equiv.	CaO	Al_2O_3	SiO_2	H_2O	Fe_2O_3	MgO	SO_3
Fly Ash	3.71	3.6	26	53.2	-	8	2	2
PC	1	63	6	20	-	3	0.5	2
2.8m NaOH	7.98	-	-	-	92.02	-	-	-
5.0m NaOH	13.42	-	-	-	86.58	-	-	-
Distilled Water	-	-	-	-	100	-	-	-
Silica Fume	2.97	0.7	1.5	85.8	-	3	2	-

They concluded that although some zeolites can coexist with C-H-S, this required the system to be high in Al/Si ratio and sufficiently low in Ca/Si ratio. The following type of zeolites were detected in alkali activated fly ash materials:

- Zeolites Na-P $Na_3Al_3{\cdot}Si_5O_{16}{\cdot}6H_2O$
- Zeolites Y $Na_{2.06}Al_2{\cdot}Si_{3.}O_8O_{11.62}{\cdot}8H_2O$
- Chabazite $Ca_2Al_4Si_8O_{24}{\cdot}12H_2O$
- Bayerite $Al(OH)_3$

Wei-Heng Shih et al[12] attempted to convert fly ash chemically into zeolites. It was shown that fly ash can be converted into two types of zeolites, P and Y faujasite, by varying the temperature conditions. Faujasite Y was formed at 38°C after 3 days. When the temperature was increased to 80°C faujasite did not form but instead zeolite P was formed after several days and if the temperature was further increased to 100°C, zeolite P was formed after several hours (33h). The relative ease in producing zeolite P is consistent with the fact that zeolite P is a more stable phase than faujasite Y. Seeding of faujasite was also studied in which faujasite seeds were added to the fly ash mixtures. It was found that the final yield of faujasite did not increase significantly, although the rate of formation increased[12].

It was found that the amount of zeolites P was increased by addition of quartz. This enhancement indicates that the form of silicon oxide may play a role in the formation of zeolites P. In order to investigate how different types of silicon oxide influence the formation of zeolites P the quartz was replaced with amorphous silica[12]. It was found that the amount of zeolites P formed was in between that with quartz and without quartz. Furthermore when the fly ash was activated only by NaOH, the yield of zeolites P was similar to that when sodium silicate was used. Therefore, it can be concluded that the crystalline form of silicon oxide is favoured over the amorphous form and the molecular (colloidal) form was least favoured. A model study revealed that it was the Si/Al ratio in solution which controlled the zeolite phase formed and increasing the Si/Al ratio favoured the formation of zeolite P over the faujasite Y.

Akira Yoshida used ground volcanic glass "Shirasu", which is similar in composition to fly ash. The "Shirasu" fly ash was used to form faujasite type zeolites. The yield of faujasite was affected by ageing at ambient temperatures, the particle size of the volcanic glass and reaction time[58]. After heating at 90°C for 24-72 hours, the yield of faujasite-type zeolite decreased and species zeolite P (phillipsite and analcime) formed in that order. From the analysis of component concentration in the liquid phase and the nature of the solid phase, it was concluded that the formation of the faujasite might be disturbed by the K^+ ions and the formation of a rigid amorphous solid.

Other authors have investigated the hydration products of high volume fly ash cements in order to explain on the high strengths obtained. Xu and Sarkar[59] investigated the hydration products and their development in the high volume fly ash cements containing 60% of class F fly ash by weight of binder. The cement used in the experimental work contained very low amounts of C_3A and alkalies. At very early age all the fly ash particle are covered by a fibrous C-S-H gel and 1-2μm small spaces between particles are formed which are the reason for the low strength at this age. At seven days the spaces between the fly ash particles are filled by the C-S-H gel as well as needle like crystals 0.1-0.4μm in width and 5μm in length. They found that the hydration products are not purely C-S-H, Ca/Si is much lower and Al/Si is much higher than C-S-H in pure cement (e.g. Ca/Si/Al/K = 35.2/44.1/20.4/40.2) and the potassium is mainly generated due to alkali dissolution from fly ash. At 28 days the structure is much denser and the hydration products are well developed but some inter-particulate gaps are still to be filled by the growing hydrates. Compared with the hydration products of an ordinary Portland cement there is more gel formation in the fly ash pastes, this gel is a major contributory factor in high strength as well as the filling action that fly ash particles have in fly ash -cement systems.

The high strength of high volume fly ash cements and the potential presence of zeolites suggested to some authors that the two may be related. The brittle nature of ordinary Portland cement requires an additional reinforcing phase to be incorporating into the mixture. For example aggregates and rebars (steel, alkali-resistant glass, and organic polymers) serve as reinforcement in concrete. As an alternative to these types of composites there is another type, a so-called self-generating composites in which the reinforcing phase develops within the matrix during curing. Zeolite phases may serve in this capacity since they readily precipitate in samples containing fly ash and an alkali solution[57].

Cheng et al[60] used in their investigations a water glass with a silica modulus (n) of 2.85, which was altered by NaOH addition at n=1.5 to activate ggbs. From their investigations it can be concluded that the principal hydration products formed are C-S-H and possible zeolite like phase[60].

The compressive strength is maximum for an addition of 5% alkali activator of the total pozzolanic materials as shown in Table 2.7.

Table 2.7 Compressive strength (σ_c) of alkali activated mortars[60]

Batch Code	Slag	WG	Na_2O	$Ca(OH)_2$	NaOH	σ_c [N/mm^2] 7days	σ_c [N/mm^2] 28 days
A	100	0	0	0	5.00	7.2	14.8
B	94.3	5.7	2.3	0	4.72	1.3	27.2
C	92.6	5.6	2.2	1.9	4.73	29.1	40.1
D	88.9	11.1	4.4	0	4.45	42.7	54.4
E	85.8	10.7	4.3	3.4	4.46	52.3	68.1

Naiqian et al[61] investigated the effect of natural zeolite as well as mineral admixtures such as fly ash, slag and silica fume on preventing the expansion caused by alkali-aggregate reaction. Natural zeolites can produce a better inhibiting effect on the alkali reaction than slag, as good as fly ash but not as good as silica fume. The results showed that the expansion can be further reduced by increasing the fineness of natural zeolite (up to 1000 m^2/kg) or by previous heat treatment of the zeolites additive.

Yan Fu et al.[62] investigated the use of zeolite as additives in high alumina cement. This is intended to prevent the conversion of hexagonal calcium aluminate hydrates (CAH_{10} or C_2AH_8) to cubic hydrogarnet under certain environmental conditions. It was found that when zeolites were added no hydrogranate was detected and strallingite were preferentially formed in high alumina cement mixes.

The role played by fly ash in a cementitious system may be more complex than assumed. Gruntzec et al[63] showed that fly ash retards C_3S hydration (even if is difficult to specify the necessary concentration for its formation), suggesting that this effect was due to fly ash particles in solution functioning as calcium sinks (the fly ash particles tie up part of Ca^{2+}). Fly ash particles adhering to the clinker surface might occupy dissolution sites, so that they retard hydration.

Zeolite type phases have been identified by Qullinn et al[64] in OPC/fly ash (60:40) mixes activated with high sulphate and carbonate bearing ground waters. These mixes were sealed in PTFE bottles and kept at temperatures of 5°C, 20°C, 50°C and 90°C for a period up to 360 days. Thomsonite like phase was found in all mixes cured at 90°C after 180 and 360 days but it was also found in smaller quantities at 50°C[64]. A different zeolite-like phase, similar to phillipsite, was formed in mixes activated with deionised water after 180 days at 90°C and 50°C. Neither of these two zeolite phases was found in mixes cured at 5°C and 20°C[64]. From the non zeolitic phases, CSH, hydrotalcite and a silica substituted hydogranet were identified. Ettringite and small quantities of strallingite were present in mixes cured at 50°C.

Ettringite ($C_6AS_3H_{32}$) formation in Portland cement concrete can be responsible for both positive and negative effects, in unrestrained hardened concrete can cause cracking by development of tensile stresses which are frequently high enough to overcome the tensile stress of concrete. On the other hand, ettringite formation under restraint can be utilised to develop compressive stresses of either low magnitude in shrinkage compensating concrete or of high magnitude in self stressing concrete.

Mehta[65] proposes new hypotheses on the mechanism of expansion associated with ettringite formation which is based on experimental evidence. In the presence of lime the nature of ettringite formed is colloidal and not long lath-like crystals[65]. For colloidal ettrigite to cause expansion it must be in contact with an outside source of water. Their high specific surface area combined with a negative net charge is probably responsible for attracting a large number of water molecules. These will surround the ettringite crystals and cause interparticle repulsion producing an overall expansion of the system without any change in the crystal lattice of ettringite. This mechanism explains why expansion and cracking associated with ettringite formation is more common in Portland cement concrete rather then in supersulphated, high alumina and pozzolanic and slag cements which contain little or no $Ca(OH)_2$ after hydration. It also explains why Portland cement concrete failures owing to sulphate attack are generally found in areas where concrete is exposed to wet environments, for example concrete in sewage pipes, mine cribbing, foundations and sulphate soils

and seawater structures[65]. Lafuma[66] suggested that the aluminates are relatively insoluble in the presence of calcium hydroxide and that the solid conversion of calcium aluminates to ettringite could cause expansion. Talero[67] investigated the analogies, differences and semiquantitative relations with their respective origins between the ettringite formed in Portland cement and ettringite formed in pozzolanic cements. He concluded from XRD and SEM results that ettringite formed in pozzolanic cements may be of similar type but smaller in size than the ettringite formed from the C_3A in Portland cement[67]. The rate of formation of ettingite in pozzolanic cements is greater than ettringite formed in Portland cement.

Evidence for the formation of zeolites has not been found by all authors. Richardson et al[68] used nine ggbs/OPC blends (0% to 100% ggbs addition). They expected to find the Mg/Ca and Al/Ca ratios resulting from some level of combination of precipitate and C-S-H in the analysed volume.

The results of microanalysis by EPMA and TEM confirmed their hypothesis; all the data fell on a single trend line which could be described by following equation:

$$\frac{Al}{Ca} = a + b\left(\frac{Mg}{Ca}\right)$$

Equation 2.6

where, a, represents the Al/Ca ratio of a single phase C-S-H gel and, b, the Al/Mg ratio of the Mg, Al rich precipitate[68].

The composition of the C-S-H in all parts of the microstructure was substantially identical. The mean Ca/Si ratios decreased with the increasing of slag addition in the mix, for example, for a slag addition of 0%, 50% and 100% (alkali activated) slag the values at 14 months were 1.70 ± 0.12, 1.55 ± 0.12 and 1.18 ± 0.06, respectively. The mean value of the inner product from the clinker and of the outer product increased with the slag content, values for the outer product being 0.09 ± 0.01 and 0.19 ± 0.06 for the mixes with 0% and 100% slag, respectively. The amount of trivalent ion, Al or Fe, which can be incorporated in the structure of C-S-H gel, increases as the ratio of the C-S-H increases. The relationship between Si/Ca and R/Ca is approximately linear and can be represented by following equation:

$$\frac{Si}{Ca} = 0.444 + 2.25\frac{(R)}{Ca}$$ Equation 2.7

where, R, is mainly Al with the addition of minor amounts of Fe.

In order to investigate the microstructural development during the alkaline activation of slag pastes, Shao-Dong Wang et al used different techniques including XRD, DTA, BSE of polished samples in the SEM coupled with EDAX and SEM of fracture surfaces. These studies indicate that the products form by a dissolution and precipitation mechanism during the early stages of reaction, but at later stages the reaction may continue by a solid state mechanism[19, 20]. Regardless of the activator used, the main hydration product is calcium silicate hydrate with a low Ca/Si ratio and different degrees of crystallinity. A crystalline phase of hydrotalcite type $Mg_6Al_6CO_3(OH)_{16}.4H_2O$ is formed in slag activated paste with either NaOH or water glass. A crystalline phase of monosulphate Afm type $(CaO)_4Al_2O_3SO_3 .12H_2O$ is also formed in slag activated with NaOH pastes. No hydrates of zeolites group or mica group were formed in slag activated paste with either NaOH or water glass solution cured at 20+_2°C up to 15 months or at 80 °C for 14 days[19, 20].

In a normal alkali activated slag system, the formation of zeolites phase is highly improbable because the Ca content in slag is often high enough to consume all Si forming C-S-H. As expected from the chemical composition of the overall hydration products formed in AAS, $Ca(OH)_2$ may form if the slag has a high Ca/Si ratio. However, it is unlikely that $Ca(OH)_2$ will coexist with C-S-H, at a Ca/Si ratio of only 1. In the long term; a further reaction is expected to increase the Ca/Si ratio of the C-S-H or to form monosulphate Afm type $(CaO)_4Al_2O_3SO_3{\cdot}12H_2O$[19, 20]. There appears to be no convincing evidence for the existence of aluminate hydrates type $(C, M)_4AH_{13}$ solid solution as postulated by some investigators[51-53, 57-63].

The effect of pH, type, valence and radius of the activator cation on the hydration products and microstructure of the ground granulated iron blast furnace slag was investigated[69]. A variety of techniques were employed in the research including thermogravimetry and derivative thermogravimetry, x-ray diffractometry, scanning

electron microscopy and energy dispersive X-ray microanalysis. The slag was activated by alkali-metal hydroxides of Li, Na and K (12.34<pH<14.71) and alkaline-earth hydroxides of Ca, Sr and Ba (12.47<pH<13.53) using a water to slag ratio of 0.4 and curing from 1 day to 26 months. Reactivity of the slag was found to be more dependent on the pH of the activators than on the curing time. The hydration products identified were mainly varieties of calcium silicate hydrate (C-S-H), aluminate hydrates $(C,M)_4AH_{13}$ and minor amount of $Ca(OH)_2$ and stallingite-gehlenite hydrate C_2ASH_8. The effect of charge or ionic radius of the activators cation was found to be insignificant[69, 70].

Kutti[71] investigated the hydration products of a blast furnace slag with $CaO/ SiO_2/ Al_2O_3$ = 40.3/ 37.1/ 9.6 activated by 8% NaOH. From the SEM results they concluded that the hydration products of alkali activated materials consist of two main phases. One of them is a type of C-S-H gel, which has similarities, but a much lower CaO/SiO_2 than hydrated Portland cement or hydrated slag cement. The other one is a gel rich in silica. This gel is formed principally during the very early stage of hydration. The compound is voluminous, continuous, and contains a surplus of water[35]. The water is not chemically combined and is easily evaporated. On drying the silica gel shrinks substantially causing cracking within the gel. This phase governs the shrinkage properties, the permeability and the flexural strength of the alkali activated mortars.

2.9 KINETICS OF THE HYDRATION OF ALKALI ACTIVATED MATERIALS

Stade[72] has investigated the mechanism of alkali (MOH) incorporated within the inner layer of the C-S-H and proposed following three mechanisms:

1. neutralisation of acidic Si-OH groups by (Na/K)OH

$$C\text{-}S\text{-}H + M^+ \rightarrow M\text{-}C\text{-}S\text{-}H \qquad \text{Equation 2.8}$$

2. ion exchange, of Na/K for Ca

$$C\text{-}S\text{-}H + M^{+} \rightarrow M\text{-}C\text{-}S\text{-}H + Ca^{2+} \qquad \text{Equation 2.9}$$

3. clevage of Si-O-Si bonds by (Na/K)O with attachments of Na/K to Si

$$Si\text{-}O\text{-}Si + 2M^{+} \rightarrow 2SiOM \qquad \text{Equation 2.10}$$

The first mechanism (2.8) will be more suitable for a mix with a low CaO/SiO_2 ratio. The second mechanism (2.9) will increase with an increase in CaO/SiO_2 ratio. Because of the complexity of the alkali reaction it is suitable to assume that multiple mechanisms may operate at one time to take up alkaline cations[71].

Huanhai et al[73] investigated the kinetics of the hydration of the alkali activated slag mortars. In their investigations they used a blast furnace slag with a surface area of 600 m^2/kg and a chemical composition $CaO/ SiO_2/ Al_2O_3/ MgO$ of 40.29/ 33.65/ 10.65/ 10.35. Similar to OPC the hydration process can be classified into five stages: induction, acceleration, deceleration and decay but the mechanisms that govern these stages are different from those of PC mortars. The calorimetric curve of alkali activated mortars consists of two thermal peaks, one representing the reaction of silicate ions from the water glass with the Ca ions from slag producing C-S-H whereas the second peak is related to the reaction of the silicate and aluminate ions from the water glass with metal ions (Ca, Na and Mg) from the degraded slag forming secondary C-S-H and other phases. The main factor of the hydration of AAS is the pH value of the solution, and the silicate concentration only affects the early hydration. They concluded that the pH of the solution is the main factor influencing the hydration rate while the silicate concentration only affects the early hydration and has little effect at later stage, which is contrary to other researchers results[73].

Belitsky et al[74]. found that the disintegration of the slag carcass occurs owing to cation exchange reaction between Ca ions of slag and Na ions of sodium silicate solution The rate of hydration of slag, especially in the first stage, was affected by the silica content of the sodium silicate solution but the alkalinity of the water glass did not influence much the initial hydration reaction of the slag[74]. In their experimental

programme Belitsky et al[74] used a slag with a composition CaO/ SiO_2/ Al_2O_3/ MgO = 42.4/ 34.1/ 13.7/ 6.1 and fineness of 400 m^2/kg and 0.321 kg of water glass (silica modulus between 1, 1.5 and 2) per 1 kg of slag.

Even though the hydration process of alkali activated cements consists of different stages and it is heterogeneous, it is possible to apply the concept of activation energy of a chemical reaction in order to explain the character of hydration of alkali activated cements and other cements[75]. Using Arrhenius relation :

$$\frac{K_1}{K_2} = e^{\frac{E'(T_1 - T_2)}{RT_1T_2}}$$

Equation 2.11

The apparent activation energy, E', can be determined from the calorimetric curves at two temperatures T1 and T2. However, it is not possible to obtain the ratio of hydration rate (K_1/K_2) constant. The apparent activation energy 53.63 kJ/mole, which was calculated using Arrhenius equation[73] (2.11), is higher then the value of 50 kJ/mole found by Regroud[75] for alkali activated materials with 80 % slag addition and of 49.1 kJ/mole found by Wu for 50 % slag addition[76]. Huanhai et al concluded that the alkali activated cements can benefit from thermal activation owing to the fact that they exhibit high activation energy[73].

Kondo et al[77] reported that the mechanism of slag activation and hydration with different activators is different. While lime and gypsum are considered reactants NaOH is considered a catalyst. Other researchers[28] doubt that the role of NaOH in the alkali reaction is that of a simple catalyst because of very high strengths obtained at one day in slag or slag and fly ash alkali cements compared with ordinary Portland cements as well as strength improvement with increased dosage of NaOH. They[28] consider that NaOH takes part in the alkali reaction in the same way as lime and gypsum but because of its strong cationic influence acts relatively strongly producing high strengths at very early age.

2.10 POROSITY – STRENGTH RELATION

Strength in general is a function of the pore structure and type of hydration products formed in the hardened cementitious material. The pore structure is the principal factor controlling the strength and takes into consideration the pore size distribution their volume and morphology[78].

Uchikawa et al[78] investigated the structural factors controlling the strength of the hydrate, focusing on the policondensation degree of silicate anion as a structural factor. In their experimental work they used three different types of mortars (white cement - W, white cement + 50% slag - WSL and white cement + 10% silica fume - WSF as well as ordinary Portland cement - OPC) cured in different conditions (water curing at 20°C, steam curing and autoclave curing). The water /cement ratio was maintained constant for all mortar mixes at 0.65. They found that for the water cured mortars the policondensation degrees of silicate anions in C-S-H are in the same level and closely correlated to strength. In steam and autoclave curing the mortars containing silicate anions of high polycondensation develop higher strength per unit pore volume greater than 20 nanometers diameter. In the water and steam cured mortars there is no difference in the types of hydration phases formed and the differences in the Ca/Si ratio are small although well grown type II C-S-H are observed in steam cured mortar. In autoclave cured mortars with slag and silica fume addition Ca/Si ratio is reduced considerably and in these mortars tobemorite and hydrogarnet are observed[78]. The higher strength per unit volume of total pore (Table 2.8) of autoclave cured mortar and silica fume blended white cement cured in water are mainly attributed to the increase in the fine pores on which the stress is poorly concentrated. The lower strength per unit volume of >20nm (Table 2.8) of silica fume blended cement mortar cured under high temperature is attributed to the low degree of polycondensation of the silicate anion. The low cohesive energy of the hydrate product is caused by an increase in the crystallinity and the formation of different kind of hydration phases. They concluded that there is an increase in strength of the hydrate itself, with the increase of temperature and age, by the increase in highly

polycondensed silicate anions of C-S-H compensates for the decrease in cohesive energy caused by the increase in crystallinity and the formation of different types of hydrates[78].

Table 2.8 Compressive strength (σ_c) of slag and silica fume blended mortars[78]

Batch Code	Curing Conditions	σ_c/pore vol.>20nm	σ_c /total pore vol
WSL	autoclave	6.15	1.65
WSF	autoclave	3.92	1.26
OPC	steam	3.68	2.10
WSF	water	3.26	1.42
WSL	steam	3.08	1.41
W	autoclave	3.07	1.53
W	steam	2.96	1.81
W	water	2.45	1.60
WSF	steam	2.28	1.14
WSL	water	1.93	1.43

Alkali phosphorous slag cements and alkali blast furnace slag cement mortars exhibit lower porosity, larger specific surface area and higher frequency of smaller pores with increasing curing time, whereas Portland cement mortars show an opposite trend[49].

Caijun[79] investigated the strength, pore structure development and water permeability of alkali activated blast furnace slag with $SiO_2/Al_2O_3/CaO$ of 35.33/9.94/34.65) activated by NaOH, Na_2CO_3 and Na_2SiO_3.Samples were cured in a fog room at 23°C. The conclusion of this study[79] was that Na_2SiO_3 is the most effective activator and gave a compressive strength of 62 N/mm^2 at 28 days, higher than the Type III Portland cement mortar at 41 N/mm^2. The porosity of the 3 days old Na_2SiO_3 mortars was lower than the porosity of the Portland Cement mortars at 90 days and the NaOH mortars have the highest porosity and the coarsest pore structure. The pore size distribution was different, PC mortars have a continuous distribution over the measured pore size range from 500Å to 12000Å while Na_2SiO_3 mortars contained only pores smaller then 100 Å and greater than 2000Å. Strength is in general a

function of the pore structure and distribution and the amount and type of different hydration products formed in the hardened cementitious material[79].

Other researchers have concluded that for alkali activated slag materials, pore distribution, volume and morphology of pores is the main factor controlling strength. Cajun attributed the difference in strength between different alkali activated slag materials to difference in the pore structure of the hardened materials and not to the hydration product formed because the main hydration product is always the same regardless of the alkali activator used even if the minor product varies with the activator[79]. The water permeability results (Figure 2.7) follow the same trend as pore structure , the Na_2SiO_3 mortars have the lowest Darcy coefficient (permeability coefficient) while PC mortars showed the highest at seven days[79]. The most common relationships between porosity and compressive strength of Portland cement pastes are as follows[79]:

- Balshin's equation

  $\sigma = \sigma_o (1 - P)^A$ Equation 2.12

- Ryshkevich's equation

  $\sigma = \sigma_o \exp^{(-B P)}$ Equation 2.13

- Schindller's equation

  $\sigma = D \ln (P_o / P)$ Equation 2.14

- Hasselmann's equation

  $\sigma = \sigma_o (1 - C P)$ Equation 2.15

where:

P-porosity:

P_o-porosity at zero strength:

σ_o-compressive strength at zero porosity:

σ-compressive strength at porosity P:

A, B, C, D-experimental constants.

Ryshkevitch's equation (2.13) is more suitable for low porosity materials and Schindller's equation (2.14) is suitable for high porosity systems[79]. Robert and Older

have investigated a series of cement pastes with different w/c ratios at different ages, and concluded that the existing relationship between strength and porosity can be expressed with sufficient accuracy but Hasselmann's equation (2.15) yields slightly more accurate results than others[80].

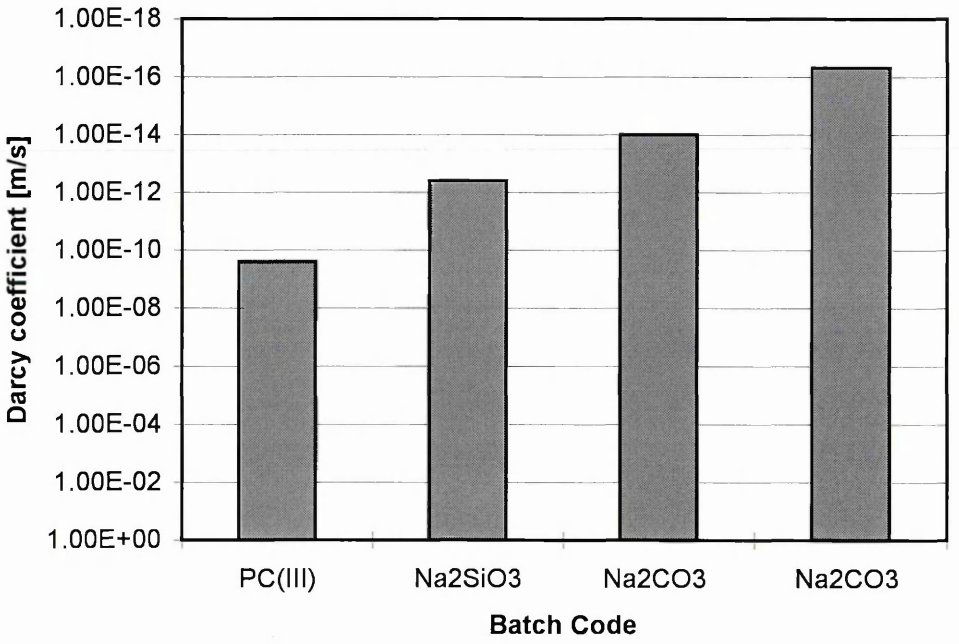

Figure 2.7 Water permeability of alkali activated slag and Portland cement mortars

2.11 SHRINKAGE

Withdrawal of water from drying concrete stored in unsaturated air causes drying shrinkage. The change in volume of drying concrete is not equal to the volume of water removed. The loss of free water, which takes place initially, causes little or no shrinkage. As drying is continued, adsorbed water is removed and the change in volume of the unrestrained hydrated cement paste at early ages is equal approximately with the loss of water layer one molecule thick from the surface of all gel particles. Since the thickness of a water molecule is about 1% of the gel particle size, a linear change in the dimensions of cement paste on complete drying will be expected to be in the order of 10000×10^{-6}, values up to 4000×10^{-6} have actually been observed[34].

The influence of the gel particle size on drying is shown by the low shrinkage of the much more coarse-grained natural building stones and by the high shrinkage of the fine grain shale. Also high pressure steam-cured cement paste shrinks 5 to 10 times less than a similar paste cured in normal conditions[81]. It is also possible that shrinkage or a part of it is related to the removal of intercrystalline water[80].

Drying takes place at the surface of a specimen, therefore, the magnitude of shrinkage varies considerably with the size and shape of the specimen. This is a function of the surface/volume ratio[82]. Many investigations have indicated an influence of the dimensions of a specimen on shrinkage[83]. The observed shrinkage decreases with an increase in the size of the specimen as seen in Figure 2.8. It has been argued that theoretically the final value of shrinkage is independent of the size of the concrete element, but for the realistic periods of time it must be accepted that the shrinkage is smaller in larger specimens[84, 85].

The constituent components of a material greatly affect its shrinkage. Lea[34] studied the effect of aggregate/cement ratio and water/cement ratio on the shrinkage of mortar and concrete. The results presented in Table 2.9 show that increasing the aggregate /cement ratio decreases the shrinkage of the mortar and concrete. However, increasing the water/cement ratio raised the shrinkage[34].

Table 2.9 Drying shrinkage of mortars and concrete[34] (12.5 cm cube) exposed for 6 months in air at 21°C and 50%RH

Aggregate/cement	**water/cement ratio**			
Ratio	**0.4**	**0.5**	**0.6**	**0.7**
3	800	1200	-	-
4	550	850	1050	-
5	400	600	750	850
6	300	400	550	650
7	200	300	400	500

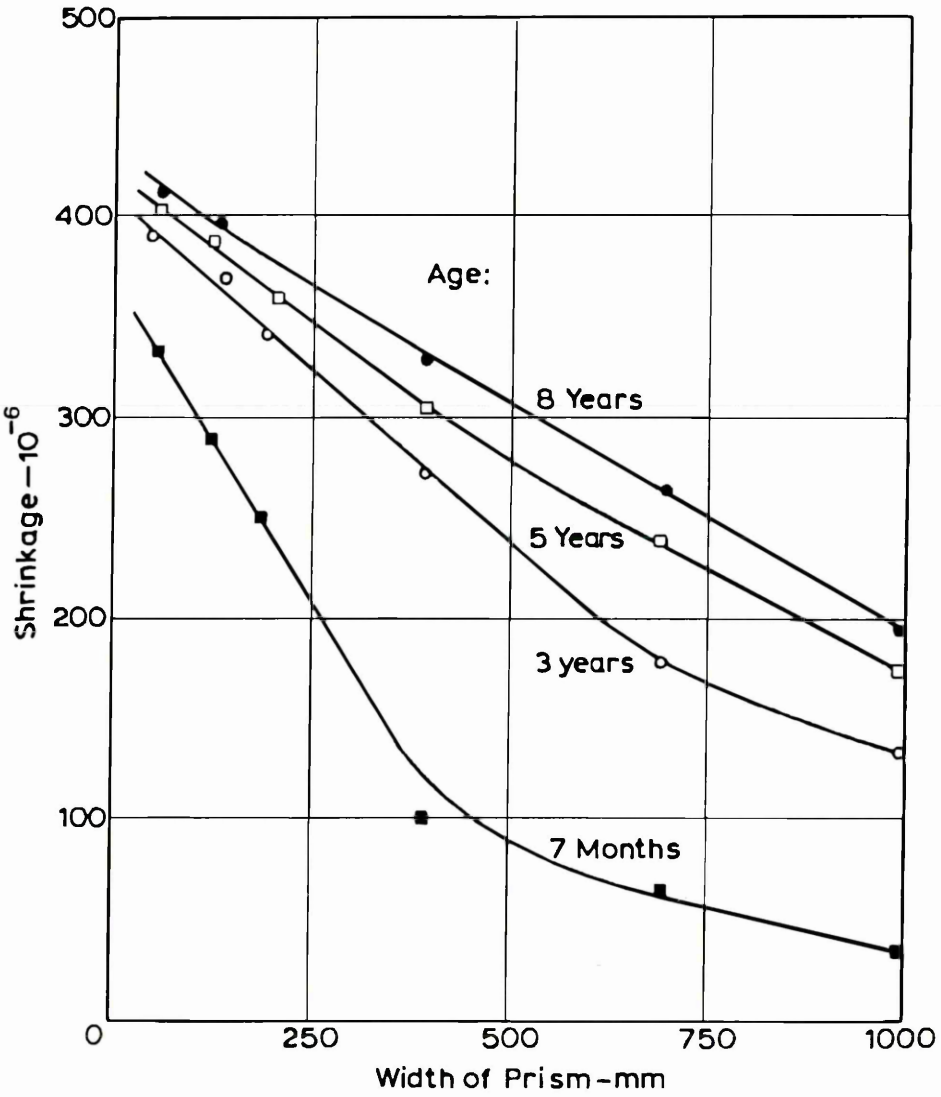

Figure 2.8 Relation between axial shrinkage and width of concrete prisms of square cross-section and length/width ratio of 4 (drying allowed at all surfaces)

Increasing the fineness of cement raises the rate of strength development, but decreases the ability of the restrained material to deform by creep and adjust itself to shrinkage stress without cracking[34].

Additions of mineral admixtures such as fly ash and ggbs to the mix increases shrinkage. Specifically at a constant water/ cement ratio, a higher proportion of fly ash or ggbs in the blended cements increases the shrinkage between 20% to 60% for very high contents of ggbs[80]. Silica fume also increases the long term shrinkage.

The curing conditions and the rate of drying can have an effect on the magnitude of shrinkage of the material. Rapid drying does not allow a relief of stress by creep and may lead to more pronounced cracking. A higher extensibility of the material is desirable because it permits the material to withstand higher volume changes. Shrinkage cracks can appear if the material attains rigidity too rapidly and cannot accommodate the changes in volume[80]. However, neither wind or forced convection have an effect on the rate of drying of hardened concrete because the moisture conductivity in concrete is so low that only a very small rate of evaporation is possible, and it has been proved experimentally that the rate cannot be increased by movement of air[86].

Several researchers have shown that alkali activated mortars have higher shrinkage than ordinary Portland cement mortars and are afflicted with microcraks[87, 88, 89]. High level of microcraking decreases the flexural strength and makes them more sensitive to gases and water penetration.

Byfors et al[87] found that there is a good correlation between the flexural strength and frequency of cracks. Other researchers[88] found high levels of microcraking even in moist cured samples and concluded that the formation of microcraks is not exclusively a result of drying. Vesikari[89] suggested that the original formation of cracks must take place during the hydration process, caused by early shrinkage.

Andersson et al developed an alkali activated slag mortar[23]. The binder used was ground granulated blast furnace slag with a chemical composition presented in Table 2.10 and the sand was fine sand with particle size between 0-2mm. NaOH, Na_2CO_3, water glass and Portland cement were used as activators. The water/binder ratio varied as listed in Table 2.11, the water within the alkali activator was not included in the water: binder ratio. The flexural and compressive strength, modulus of elasticity, porosity, shrinkage and crack sensitivity were fully investigated. Shrinkage was measured in mortar prisms 40x 40x 160 mm manufactured with alkali activated slag and with ordinary Portland Cement[23]. Shrinkage measurements were started after 1-3

days in case of air curing and after 8 hours in the case of steam curing. The shrinkage which takes place before that, has not been studied. The results refer to the final shrinkage after 231 days and constitute a mean value of at least two tests.

The shrinkage of the alkali activated slag mortars which were cured at ambient temperature, 20°C and 80% RH, was found to be considerably higher (up to three times) than that of corresponding reference ordinary Portland cement mortar. Increasing the silica modulus of the water glass raises the free shrinkage of the alkali activated mortars. Water glass with a higher silica modulus (n=3.35) gives the highest shrinkage followed by the water glass with lower silica modulus (n=0.9) and Na_2CO_3 activator (Table 2.11).

The lowest shrinkage of the alkali activated slag mortars was obtained using NaOH as activator but it is still greater than that of reference Portland cement mortar. In the case of steam curing, shrinkage of the alkali activated mortars is in most cases less than that of reference Portland cement mortar[23] (Table 2.11).

Table 2.10 Chemical composition of the slag[23]

Elements	Content [%]
Silica (SiO_2)	35
Aluminia (Al_2O_3)	10
Iron oxide (FeO)	0.5
Magnesia (MgO)	12
Calcium oxide (CaO)	38
Sulphide (S^{2-})	1.2
Potassium oxide (K_2O)	0.8
$Na_2O_e = 0.658 * K_2O + Na_2O$	0.526
Manganese (MnO)	0.8
$\frac{CaO + MgO + Al_2O_3}{SiO_2}$	1.714

Table 2.11 Shrinkage of alkali activated mortars and reference Portland cement mortar[23]

Activator Type	Activator [%]of the slag weight	Water/Binder ratio	Shrinkage at 231 days [o/oo]			
			Air Cured* (20°C, 80%RH)	Air Cured** (20°C, 80%RH)	Steam Cured** (up to 80°C)	Steam Cured*** (up to 80°C)
NaOH	3.0	0.43	-	-	0.63	-
NaOH	5.0	0.37	-	-	0.61	-
NaOH	5.0	0.43	0.62	0.93	0.67	0.64
NaOH	7.0	0.43	-	-	0.61	-
Na_2CO_3	3.0	0.43	-	-	0.62	-
Na_2CO_3	5.0	0.37	-	-	0.35	-
Na_2CO_3	5.0	0.43	0.62	1.11	0.45	0.28
Na_2CO_3	7.0	0.43	-	-	0.34	-
WG, n=3.35	4.0	0.43	-	-	2.72	-
WG, n=3.35	6.0	0.37	-	-	1.24	-
WG, n=3.35	6.0	0.43	-	2.29	1.76	-
WG, n=3.35	8.0	0.43	-	-	0.70	-
WG, n=1.80	4.0	0.43	-	-	0.59	-
WG, n=1.80	6.0	0.37	-	-	0.84	-
WG, n=1.80	6.0	0.43	-	1.33	0.35	-
WG, n=1.80	8.0	0.43	-	-	0.30	-
WG, n=0.90	4.0	0.43	-	-	0.79	-
WG, n=0.90	6.0	0.37	-	-	0.29	-
WG, n=0.90	6.0	0.43	-	1.44	0.42	0.48
WG, n=0.90	8.0	0.43	-	-	0.33	-
Portland Cem.		0.50		0.68	0.48	

Note: **PC** reference ordinary Portland cement mortar (1:3 sand to cement ratio), * specific surface area of the slag was **350 [m^2/kg],** ** specific surface area of the slag was **530 [m^2/kg],** *** specific surface area of the slag was **670 [m^2/kg]**

Malolepszy et al[10] used prisms with dimensions of 25mmx 25mmx 120mm. The binder used was ground granulated blast furnace slag with a chemical composition presented in Table 2.12 and a fine sand with particle size between 0-2mm. The mix proportion of alkali activated mortar was 1:3 sand to binder ratio with exception of specimens ii and vii (Table 2.13) which had a sand/binder ratio of 1:3.86. The water/ binder ratio used was 0.42 for the alkali activated slag mortars and 0.5 for the reference Portland cement mortar. The water within the alkali activator was included in the water/ binder ratio.

Table 2.12 Chemical composition of the slag[10]

Elements	Content[1] [%]	Content[2] [%]	Content[3][%]
Silica (SiO_2)	38.4	34.7	34.9
Aluminia (Al_2O_3)	7.3	10.0	10.1
Iron oxide (FeO)	1.4	0.37	0.32
Magnesia (MgO)	6.7	12.2	12.3
Calcium oxide (CaO)	42.5	37.4	37.4
Sulphide (S^{2-})	2.7	1.19	1.19
Manganese (MnO)	0.7	1.05	1.05
Glassy content	78.9	98.6	98.2
$\frac{CaO + MgO + Al_2O_3}{SiO_2}$	1.471	1.718	1.713

Note:

[1] Slag with Mb/Ma=1.08/1.45

[2] Slag with Mb/Ma=1.11/1.67

[3] Slag with Mb/Ma=1.10/1.66

Note: Ma and Mb are the acidity ratio and the basicity ratio respectively (detailed in section 2.3)

After 24 hours initial curing, the mortar prisms were immersed in water at 20°C then subjected to alternative cycles of curing in water and standard temperature of 20°C and 65% relative humidity. Slag mortars activated by Na_2CO_3 (batches i and vi, see Table 2.13) give the smallest shrinkage, but still higher than the reference ordinary Portland cement mortar. In the case of steam cured mortars shrinkage decreases in the alkali activated slag mortars[10] (Table 2.13).

Table2.13 Shrinkage of alkali activated mortars and reference Portland cement mortar[10]

No.	Activator type	Specific surface [m^2/kg]	Activator [%]of the slag weight	Mb/Ma	Initial 24 h curing	Shrinkage Strain at different ages [microstrain]						
						7 days	14 days	15 days	21 days	22 days	28 days	90 days
i	Na_2CO_3	360	15	1.08/1.45	up to 85°C*	100	700	200	0	300	1000	4700
ii	$NaSiO_3$	360	15	1.08/1.45	up to 85°C*	300	1000	800	600	1000	2100	7800
iii	$NaSiO_3$	360	15	1.08/1.45	20°C and 95%RH	1200	2400	1700	1500	2100	5700	9200
iv	$NaSiO_3$	350	15	1.11/1.67	up to 85°C*	700	1800	1400	1200	2400	4000	6200
v	$NaSiO_3$	350	15	1.11/1.67	20°C and 95%RH	800	1800	1400	1200	2000	3400	8100
vi	Na_2CO_3	500	15	1.10/1.66	up to 85°C*	400	600	800	200	500	3400	8100
vii	$NaSiO_3$	500	15	1.10/1.66	20°C and 95%RH	1400	2300	1800	1500	2900	5200	9400
viii	$NaSiO_3$	500	15	1.10/1.66	20°C and 95%RH	1000	2200	1700	1200	2400	6100	8400
Ref Pc					20°C and 95%RH	100	500	100	100	800	2700	4100

Note: *Thermal cycle curing as shown in the following temperature vs. time diagram

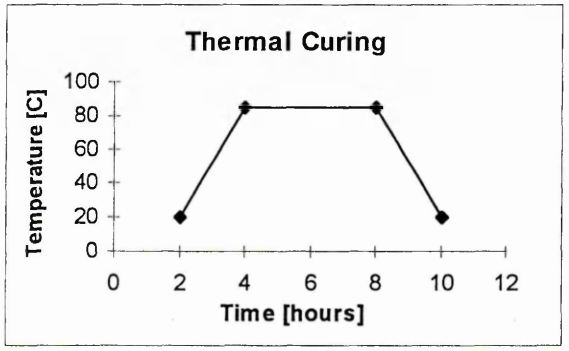

Other researchers[90] measured drying shrinkage of lime-slag mortars (Table 2.14) after a curing period of seven days in lime water. Shrinkage tests were performed over a period of 224 days of air drying at 23 ± 1.7°C and 50 ± 4 % relative humidity[90].

Table 2.14 Specimen composition[90]

No	w/b	slag	Wg	lime	water	aggregate
1	0.48	11%	5%	1%	3%	80%
2	0.48	11%	5%	1%	3%	80%
3	0.39	18%	7%	1%	6%	68%
4	0.38	18%	7%	1%	6%	69%
5	0.33	18%	6%	1%	6%	69%

Table 2.15 Shrinkage (microstrain)[90]

No	7 days	14 days	28 days	56 days	112 days	224 days
1	284	380	511	674	746	986
2	305	404	525	645	738	940
3	298	408	557	646	791	929
4	203	305	397	500	589	745
5	245	319	440	525	663	844

Drying shrinkage strains in lime-slag mortars were higher than those observed in Portland cement concrete or in Portland cement concrete incorporating various amounts of slag with the equivalent water-binder ratio and workability[90] (Table 2.15).

2.12 CREEP

Compressive creep is the slow continuous deformation which occurs in cementitious materials when subjected to a sustained stress in compression[91]. Compressive creep has three components as shown in Figure 2.9:

1. instantaneous recoverable creep, time dependent recoverable and irrecoverable creep, defined by Illston[91] as elastic creep

2. delayed elastic creep

3. flow creep

The instantaneous elastic strain occurs in concrete specimens immediately upon application of the load, at t_1. The concrete specimens maintained under constant compressive load between t_1 and t_2 exhibit a creep strain, which includes the delayed elastic component. If the sustained compressive load is removed at t_2, the strain decreases immediately by an amount equal to the elastic strain at the given age, generally lower than the elastic strain at the age of loading. This immediate recovery is followed by a gradual decrease in strain, over a period of time, called creep recovery, which is also evident as delayed creep. The delayed elastic component of creep is determined as follows:

(Creep strain + Instantaneous Elastic strain) - (Elastic Recovery + Flow Creep) 2.16

The recovery of creep is not complete, and creep is not simply a reversible phenomenon. An unsustained application of load results in permanent strain called flow creep. Creep strain is determined as the sum of flow and delay elastic creep components.

Creep coefficient ϕ is the ratio between creep strain and instantaneous elastic strain. A high creep coefficient will result in a low effective elastic modulus which will reduce the load bearing effectiveness of the material:

$E_{r(eff)} = E_r/(1+\phi)$ Equation 2.17

Where:

E_r is the instantaneous elastic modulus of the material,

$E_{r(eff)}$ is the effective elastic modulus of the material.

On the other hand, it will allow significant stress relaxation, which may prevent cracking in a material when high tensile stresses are induced due to restrained shrinkage

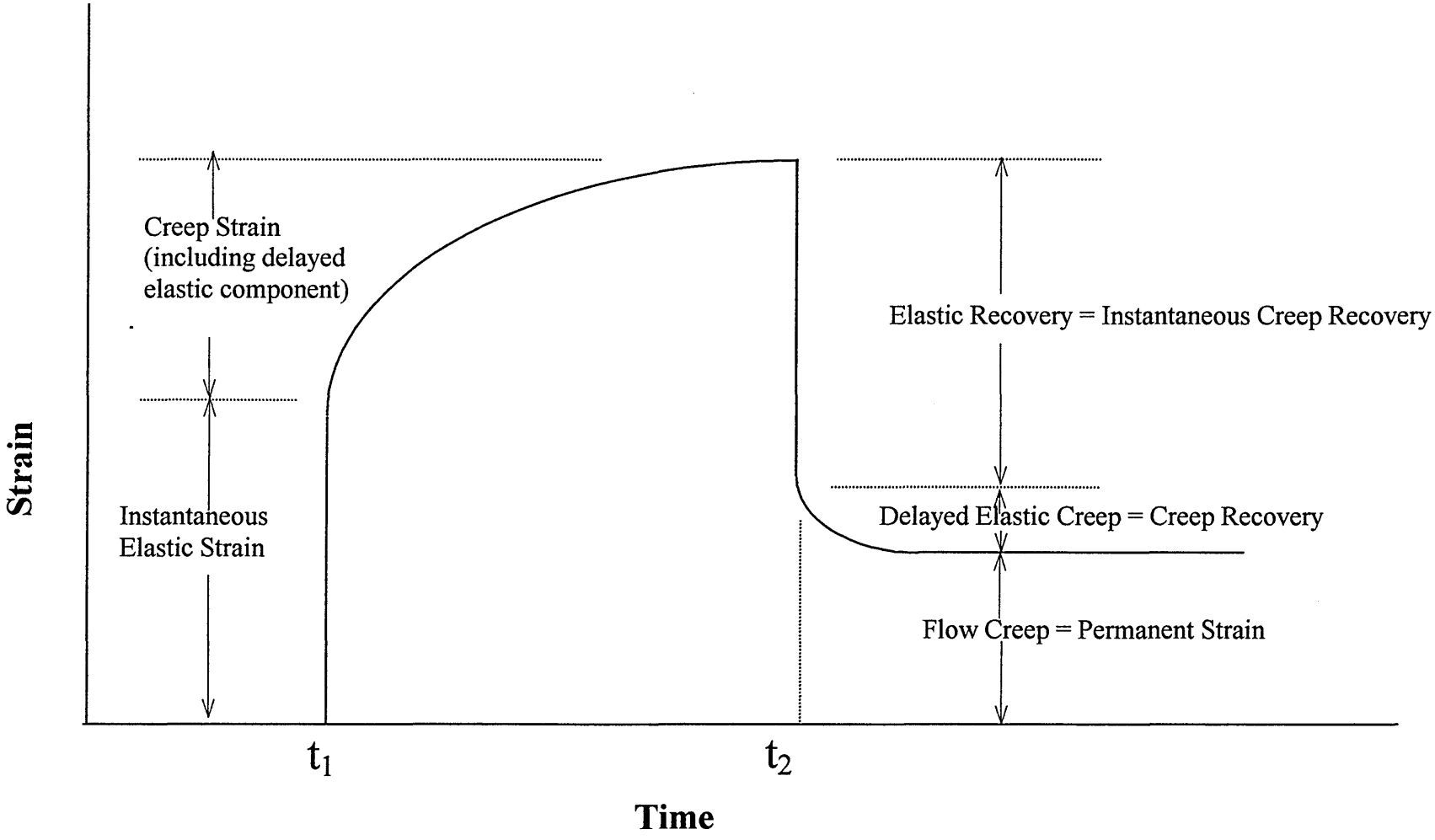

Figure 2.9 Components of compressive creep in concrete[91]

Table 2.16 summarises the creep coefficients as investigated by Emberson and Mays[92], for repair materials and control concrete subjected to a sustained compressive stress over a period of 16 months. The gross creep coefficients for materials A, B, D-I range from 1.2 to 4.0.The range of creep coefficients of materials tested in the current project reported in this thesis ranged from 1.14 to 3.03.

Table 2.16 Compressive Creep Strain Results (Emberson and Mays)[92]

Repair Material	Shrinkage [μstrain] 1-16months	Creep [μstrain] 1-16 months	Creep Coefficient	Stress Strength
A	0	720	1.4	0.14
B	10	1370	3.3	0.10
C	100	4110	7.6	0.14
D	200	230	0.9	0.13
E	420	1600	2.8	0.17
F	320	10	0.1	0.13
G	440	400	1.1	0.12
H	280	960	3.1	0.13
I	210	580	2.2	0.09
concrete			2.2	1.5

Creep recovery of concrete specimens loaded in compression has been studied by Brooks and Neville[93]. They used in their investigation bobbin shaped concrete specimens with dimensions presented in Figure 2.10. The mix proportions of cement /sand /aggregates was 1/ 2/ 4 and the water /cement ratio was 0.5.

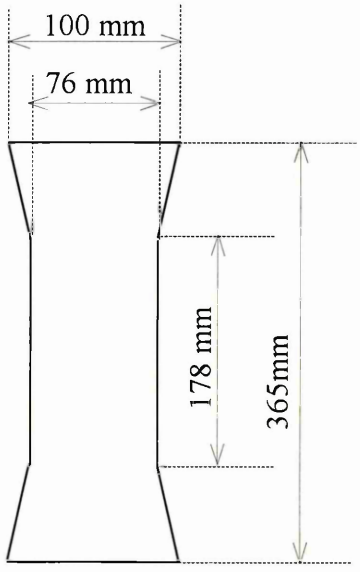

Figure 2.10 Dimensions of the bobbin shaped concrete specimen[93]

Initially concrete specimens were cured in water for 28 days at 22 ± 2°C. Creep was determined at age 28 and 56 days for a period of 28 days when specimens were unloaded and allowed to recover. The final values of creep recovery are given in Table 2.17.

Table 2.17 Creep recovery[93]

Storage	Creep recovery 10^{-6} per N/mm^2	% of final creep
water	6.2	40
water then air	8.0	16.3

Illston[94] investigated the creep recovery using cylinders with 305 mm length and 12 mm diameter cured in water. The results from his investigations are presented in Table 2.18. The rate of occurrence of delayed elastic strain diminishes with the age of concrete and it can be linked with the corresponding rate of flow as seen in Table 2.18.

Nasser and Al-Manaseer[95] investigated the effect of high temperature on the shrinkage and creep of unsealed and sealed concrete containing 50% lignite fly ash and 50% type I OPC, water/binder ratio of 0.6 and aggregate/binder ratio of 7. The concrete specimens (cylinders 75 mm diameter and 225 mm height) were water cured for 28 days and then tested at six different temperatures between 21° and 232°C under three stress levels 5.2, 8.3 and 10.3 N/mm^2. Both creep of sealed and unsealed concrete specimens were measured for a period off 112 days, while creep recovery was recorded over a period of 28 days. They found that the shape of the shrinkage and creep curves were similar at both normal and elevated temperatures. Shrinkage and creep of unsealed fly ash concrete specimens follows the same trends as those of plain concrete, decreasing with an increase in temperature from 21° to 177°C and increasing with a further rise in the temperature. This was opposite to the shrinkage and creep of sealed specimens, which increased with a rise in temperature from 21 to 71°C and then decreased with further rise in temperature[95].

Table 2.18 Flow and delayed strain (Illston)[94]

Age at loading	Flow creep 10^{-6} per N/mm^2	Delayed Creep 10^{-6} perN/mm^2
10	13.31	5.4
24	5.17	3.65
52	2.76	2.83
108	2.14	3.93

Mazourk[96] investigated the creep of high strength concrete (70 N/mm^2) and normal concrete (40 N/mm^2) subjected to stresses of 25, 50 and 75% of their 28 day strength for a period of 12 months. The test specimens were exposed to three temperature conditions 20°C, 0°C and -10°C for a period of 91 days. In their experimental work they used mixes with a cement content of 50 kg/m^3 and 12% replacement of cement by type F fly ash and 6% replacement by silica fume. A very low water/binder ratio of 0.27 was used. The results show that creep strains of high strength concrete are smaller then those for normal strength concrete at corresponding strength-stress ratios. The relation of creep to stress-strength ratio at 20°C was found to be linear for both grades of concrete. Tests revealed that low temperature has a minor effect on creep strains regardless of the strength of concrete. The creep mechanism of high strength and normal concrete at ambient temperature can be explained by the diffusion of adsorbed moisture while at low temperatures both the gel formation and adsorbed moisture diffusion can cause a large change in the energy of the system causing a slight increase in creep[96].

Brooks et al[97] investigated the influence of 50 and 75% replacement of cement by slag on the early compressive and flexural creep together with that of temperature. They found that an increase in temperature during creep testing does cause additional transitional thermal creep and, for the same maturity, the creep strain of concrete with slag addition is less than that of normal cement concrete. For a given strength, the influence of cement replacement by slag slightly decreases the compressive creep strain at loading but increasing the level of replacement from 50 to 75% has no effect. The general compressive creep strain versus cube strength relationship is similar with that for aged concrete cured at normal temperature.

For both types of concrete with or without slag, tensile creep is higher than compressive creep.

Investigations of tensile and compressive creep of mortars reinforced with 5.0% (by weight) glass fibres show a significant reduction in creep strains. Fibre addition had a greater influence on controlling compressive creep than tensile creep[97].

Neville et al[98] studied the effect of aggregates on creep of concrete. They concluded that there are no major differences in creep behaviour between concrete made with normal weight aggregates and light-weight aggregates. The most important factors which affect creep were found to be the type (see Figure 2.11) and modulus of elasticity of the aggregates (see Figure 2.12). Both factors contribute to resisting the creep of cement paste. Increasing the water/ cement ratio lowers strength and increases creep.

The effect of fibre reinforcement on creep of mortar and concrete is due to the additional restraint provided. Fibres can be considered as additional aggregates of special shape which bond with the cement paste matrix and restrain its creep. The influencing factors on creep behaviour are, therefore, the modulus of elasticity, the quantity and shape of the fibres.[99, 100].

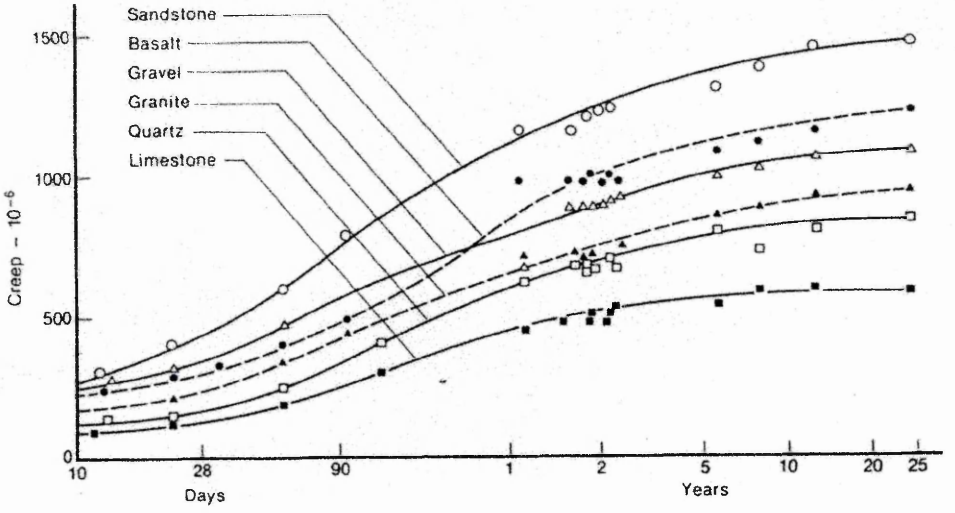

Figure 2.11 Creep of concretes made with different aggregates

Note: aggregate /cement ratio = 5.67, w/c = 0.59 and applied stress = 5.5N/mm^2

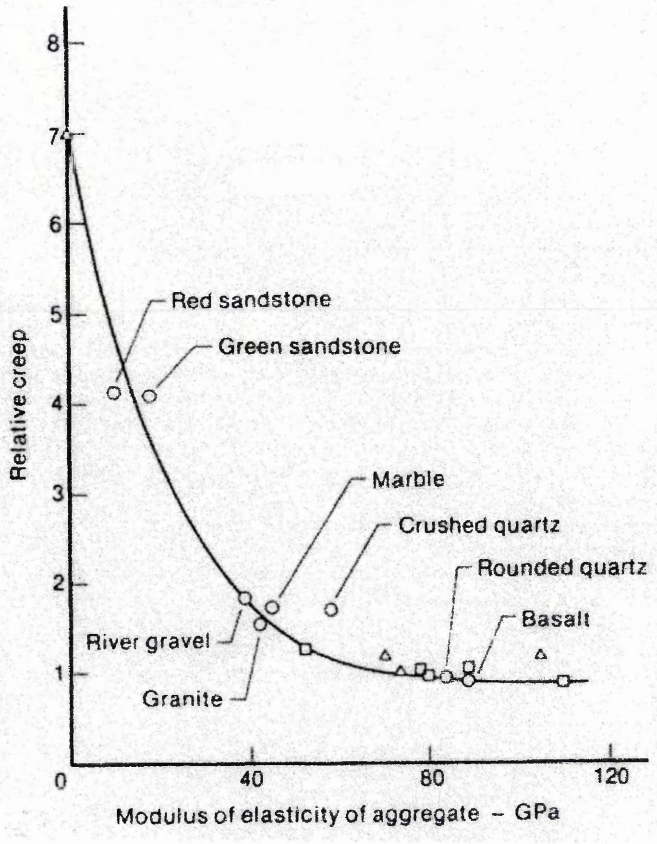

Figure 2.12 Effect of modulus of elasticity on relative creep of concrete (equal to 1 for an aggregate with a modulus of 69 GPa)

2.13 DURABILITY

Durability can be defined as the ability of the concrete to resist attack from the environment in which is placed. The nature of the attack can take two basic forms:

Physical
- Abrasion
- Impact
- Ice Growth
- High Temperatures
- Permeation/Diffusion

Chemical
- Sulphates
- Chlorides
- Acids

2.13.1 Chemical Attack

The alkali activated slag cements have been shown to have dense microstructures[38] with small pore sizes, 18°A, measured using mercury intrusion porosimetry. This dense structure with fine pore size makes the slag activated cements relatively impermeable to most forms of chemical attack to which Portland cements are more susceptible. F cement was more resistant to NaCl and $MgCl_2$ solutions and salt weathering than ordinary Portland cement[89]. This resistance should allow the alkali activated slags to give steel reinforcement superior levels of protection against corrosion than ordinary Portland cement.

Diabind[42] is a hydraulic binder composed of blast furnace slag, fly ash, sodium metasilicate and a small amount of ordinary Portland cement clinker. The binder is produced by ENCI of the Netherlands and patented in the USA and most of Europe. The binder is used to produce an acid resistant concrete for sewer and industrial applications. The binder uses slags and fly ashes of a high fineness, and sodium metasilicate as the alkali activator.

2.13.2 Temperature effect in cementitious materials

Laboratory testing of cementitious materials is often performed at ambient temperature, so most of the data about the properties of materials is based on the behaviour of these materials at this temperature[81]. The actual applied range of temperature is considerably wider, with a lot of construction taking place in countries with a very hot climate or in very cold regions. Materials can also be used at elevated temperatures or exposed to fire situations. Knowledge of the temperature effect on the properties of construction materials is of great importance.

2.13.2.1 Frost action

Water cooled from 20°C to 4°C, at atmospheric pressure, expands[101] by 0.06%. Water heated from 4°C to 40°C expands[101] by 0.4%. The changes in density of various water phases and ice can be seen in Figure 2.13. The conditions shown in Figure 2.14 may be reasonably expected to exist in nature. Free water freezes at 0°C at 1 atmosphere pressure causing an instantaneous expansion[95] from a density of 1000 to 916.5 kg/m^3. The pressure produced during confined freezing increases by 118.43 atm for each degree Celsius decrease in temperature.

Frozen water expands by approximately 1/10 of its original volume[101]. Heavy rain followed by a severe frost of a great number of freezing & thawing cycles can lead to great damage in building blocks. As the water in the capillary pores expands there is a 9% increase in volume. If water freezes within a confined space, considerable pressures can be evolved. When there is no room for the ice to expand (i.e. the pores are full of water) the expansive forces will cause disruption of the pores by breaking the capillary wall as shown in Figure 2.14. The water contained within the pores contains dissolved salts in varying concentrations, which means that all the water will not freeze at the same time. These differences in ionic concentrations lead to the creation of osmotic pressures.

Since an expansion of 10% occurs on freezing, it could reasonably be expected that damage by frost should not occur unless 90% or more of the available open pore space in the material was filled with water. The ratio between the capacity of the material to absorb water naturally and capacity of material to hold water after vacuum saturation is measured by the saturation coefficient. The maximum saturation coefficient possible is 1. Theoretically a material having a saturation coefficient of 0.9 or less should be immune to frost damage, however, a lower figure between 0.7 and 0.8 is taken as an upper limit for the saturation coefficient[102].

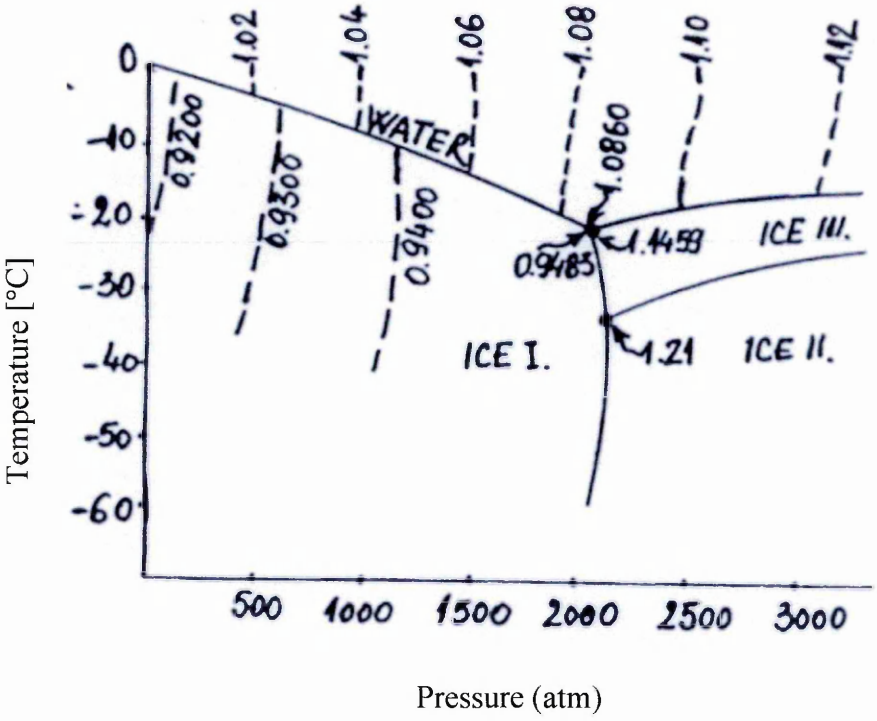

Figure 2.13 Pressure Temperature Diagram of the water and ice phases

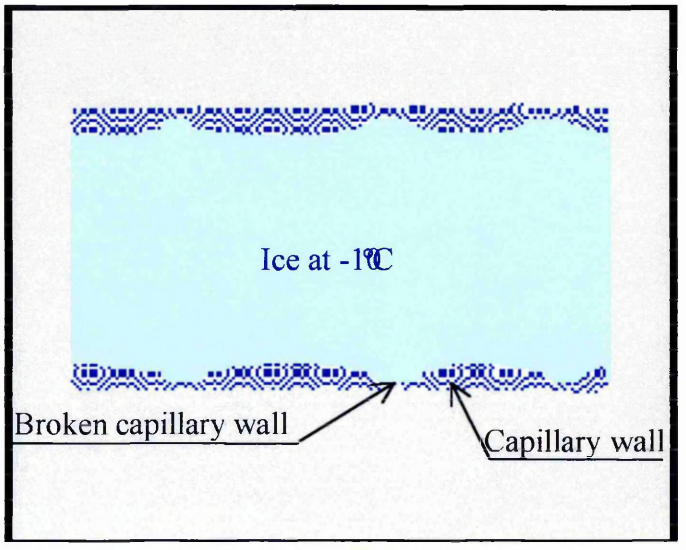

Figure 2.14 Capillary pore damaged by the ice expansion

Dunn and Hudec[103] found that the grain size, porosity and permeability were important in determining the frost durability of a material in laboratory experiments.

Confusion still exists around the exact temperature at which the pore water freezes. Winkler[104] claims that all water freezes below -22°C. Other researchers[103] argue that some water in the pore system remains unfrozen even at very low temperatures of -40°C[103]. This phenomenon is attributed to the presence of ordered water. Cold differential thermal analysis was used to calculate the freezing curves generated by ice formation in frost sensitive and frost resistant rocks. It was found that less than 50% of the total available water was frozen at -20°C in three of the frost resistant rocks whereas freezing in the frost sensitive rocks occurs between -2°C and -7°C and no further freezing was detected after this point. The phenomena of unfreezable water has been attributed to the presence of ordered water in microcapilliaries of bordering clay minerals by polar attraction[103]. Another factor which can play a key role in the above mechanism is the critical pore diameter. It has been found that rocks with a pore diameter greater than 5 microns are less susceptible to frost damage because of the ability of water to drain during freezing preventing the build- up of hydraulic pressure or ice expansion in confined pores. However, water in the micropores is unfreezable and is in an ordered state[104].

The freezing process which affects materials generally occurs over extended periods of time, some operating over many hundreds of years. Because of this, the process needs to be accelerated in a laboratory environment[102]. Modern technology has made it possible to accurately control the ambient temperature and water supply to the test specimens. The increased use of such technology means that durability studies can be produced in a matter of weeks rather than years. However, a question still remains of how this accelerated test relates to the real performance and other testing procedures. The American test for resistance of concrete to rapid freezing and thawing, defined in ASTM C666-92[105], uses pre-cast concrete prisms or cylinders which satisfy the dimensions; 76 mm<(w,d,D)<127 mm and 279 mm<L<406mm

where, w is the with of the specimen, d is the depth of the specimen, D is the diameter of the specimen and L is the length of the specimen.

This test[105] investigates the resistance of concrete to rapid freezing and thawing in the laboratory by two different procedures.

- *Procedure A*: Rapid freezing and thawing in water. Here the samples are completely surrounded by water (1 mm<water depth<3mm) at all times while the specimen is being subjected to freeze thaw cycles.

- *Procedure B*: Rapid freezing in air and thawing in water, samples are completely surrounded by air during the freezing component of the cycle and by water during the thawing component.

The nominal cycle for both procedures[105] consists of alternately lowering the temperature from + 4.4 °C to -17.8 °C and raising it from-17.8 to +4.4 °C in a period of time between 2 and 5 hours. Temperature in the centre of the specimen remains at -17.8 ± 1.7°C at the end of cooling period and 4.4 ± 1.7°C at the end of thawing period. At the beginning of the test and then after each cycle the fundamental transverse frequency and the length of the specimen are recorded. The test is continued until 300 cycles are completed or until the relative dynamic modulus reaches 60% of the initial modulus or if there is an expansion greater then 0.1 %.

At the end of the testing period the durability factor is calculated using the following equation:

$$DF = \frac{PN}{M}$$ Equation 2.18

Where

DF is the durability factor

P is relative dynamic modulus at N cycles [%]

N is the number of cycles at which P reaches the specified minimum value for discontinuity of the test

M is specified number of cycles at which the exposure is to be terminated

$$P = \left(\frac{n}{n_o}\right) \cdot 100 \qquad \text{Equation 2.19}$$

n is the fundamental transverse frequency at 0 cycles of freezing and thawing

n_o is the fundamental transverse frequency after N cycles of freezing and thawing

The British standard BS 5075: Part 2, 1982[106] uses 75 mm x 75 mm x 305 mm prisms for freeze-thaw testing. The normal freezing and thawing cycle of 24 hours consists of 16 to 17 hours of freezing at -15 ± 3 °C followed by 7 to 8 hours of thawing at 20 ± 2°C. After the completion of 50 cycles the specimens are placed in a tank, which contains water at 20 ± 1 °C, till the temperature of the specimens reaches 20 ± 1 °C. At the beginning of the test and then at the end of the test the length of the specimens is recorded. At the end of the 50 cycles of freezing and thawing the relative length change is calculated using following equation

$$Length\ change = \frac{l_{50} - l_o}{L_o} \qquad \text{Equation 2.20}$$

where

l_{50} is the wet invar rod measurement after 50 cycles of freezing and thawing

l_0 is the initial wet invar rod measurement

L_0 is the initial length measurement

The British Ceramic Association[107] set out a standard for a freezing test for brickwork. Freeze-thaw damage is noted for the degradation of the brick in terms of spooling and cracking and extensive efflorescence due to salt crystallisation. The authors[107] noted that although there were indirect means of testing based upon the physical properties of the material practical experience with long-term exposure and accelerated weathering testing were preferred means of assessing the durability of the bricks. It was also observed that the freeze-thaw durability of the bricks is not always necessarily a function of the physical properties of the material.

The literature about the resistance of alkali activated slag and fly ash cements to freeze-thaw cycling is confused. According to Talling and Brandster[38] the fine pore

structure and more concentrated pore solution leads to 10 times greater freeze thaw resistance than Portland cement [38]. Work by Bowser et al and Gifford & Gillot[108, 109] using activated slags, fly ash and silica fume concrete showed that they performed worse than control ordinary Portland cement mixes. Kukko and Mannonen[35] found that the dense impermeable F-concrete showed greatly increased frost resistance.

The poor durability performances displayed by alkali-activated slags, seen by some authors is probably due to overdosing of activator i.e. the Na_2O content was too high. A good example of this is Freidin and Erell[44] who investigated bricks made of coal fly ash and slag cured at ambient temperature. Pressed test specimens of a mixture of coal ash, slag and water glass were made and cured in the open air. The conclusion was that the material solidified with a water stable silica gel binder and produced a compressive strength between 2- 20 N/mm^2. The bricks, however, suffered from large water uptake up to 40% due to the high absorbing capacity of the fly ash. These results showed that the durability of activated slags and fly ash cement is suspect, however, the authors did not control the Na_2O content or silica modulus of the water glass activator[44]. If the Na_2O content is too high, unreacted alkali causes efflorescence during curing and weakens the sample, as does using a water glass with silica modulus greater than two. This means that the cementitious material was weaker and the microstructure not as dense as that produced by better experimental control of previous researchers. However, slag mortars are susceptible to microcracking[23] which could remove any advantages of the dense microstructure and small pore size.

Durability performance of alkali activated slag and fly ash depends on the likelihood of alkali-silica reaction. With the total Na_2O content of 3% or higher, alkali-silica reaction is possible and the samples exhibited a 0.05% expansion level which is considered safe[11, 19, 20]. However if only 3% water glass is used then expansion increases to 0.1 - 0.15 % which are excessive levels. Silica fume additions can be used to control this expansion but problems could occur if siliceous aggregates or quartz additions are used.

Douglas et al[29] investigated the durability of concrete activated by sodium silicate solution. The silica modulus of water glass (2.85) was adjusted to 1.47 by NaOH addition. The mix proportions are summarised in Table 2.19. Prisms with dimensions of 76 mm x 102 mm x 390 mm were used for freeze - thaw testing. Freezing and thawing cycling was performed in an automatic unit, which performed six cycles per day.

Table 2.19 Mix proportions[29]

Batch Code	Slag	Water Glass	Lime	Water	Aggregate fine	Aggregate coarse	Air entrainment
1	10.0%	4.8%	1.1%	5.9%	31.3%	39.8%	10.8%
2	10.0%	4.8%	0.9%	5.8%	31.4%	39.9%	10.8%
3	10.7%	4.2%	0.9%	6.1%	32.5%	41.4%	7.5%
4	10.3%	3.9%	0.7%	5.8%	33.8%	43.0%	5.4%
5	10.1%	3.3%	0.6%	5.6%	34.5%	43.8%	4.5%

The specimens were subjected to a total of 500 freezing-thawing cycles in 2000 hours. The nominal freezing-thawing cycle of this test consisted of alternatively lowering the temperature of specimens from 4.4°C±1.7 to -17.8°C± 1.7 and raising it from -17.8°C± 1.7 to 4.4°C±1.7. The specimens were moist cured for 14 days prior to exposure to the freezing-thawing cycling. The results from their investigations are summarised in Table 2.20 which show that increasing the slag content and reducing the aggregate content has a detrimental effect on the freeze - thaw resistance of the material. As the water binder ratio was reduced the samples suffered greater weight loss and length changes.

Table 2.20 Residual dynamic modulus, weight loss and length change of alkali activated mortars[29]

No	Air content	σ_c [N/mm^2]	σ_f [N/mm^2]	Relative dynamic modulus [%]	Residual σ_f [%]	Pulse velocity [%]	Weight loss [%]	Length change [%]
1	6.2	39.8	6.1	103.7	62	-1.04	-3.70	0.033
2	5.2	41.7	6.8	106.9	63	0.79	-0.99	0.039
3	7.3	34.6	5.56	97.2	58	-3.57	-2.67	0.066
4	7.2	37.7	5.46	99.9	67	-8.13	-2.86	0.089
5	5.7	37.6	5.76	49.6	32	-28.96	-2.63	0.181*

*freeze-thaw tests were terminated after 300 cycles

2.13.2.2 Fire Resistance

Changes in the strength of cementitious materials subjected to high temperature are due to a series of complex physical and chemical phenomenon. An increase in temperature will lead to loss of free moisture. This will be followed by loss of the physically absorbed water and finally loss of the chemically combined water of the hydration products. The loss of chemically bound water will cause progressive loss of strength. The differential movement caused by the expansion of the aggregates will cause micro-cracking leading to further strength loss in the material[110].

There are several methods used to assess the residual capacity of building materials: penetration resistance test, ultrasonic pulse velocity, colour analysis. These methods are able to determine the changes in physical properties and quality of materials to give an indirect indication of the degree of fire damage. The damage effect can also be assessed by determining the strength loss due to the fire to give the residual capacity of the concrete[111]. In his study Mohamedbhai[111] used 100mm cubes to asses the effect of high temperatures in the range of 200-800°C (heating rate of 1°C per 10 seconds). He studied the influence of duration of exposure at maximum temperature and conditions of cooling on the pulse velocity and compressive strength of the concrete. He found that these parameters influence the performance of concrete heated to the lower range of temperature (up to 600°C), but the effect is less pronounced at high temperatures. The strength loss occurs within two hours of exposure to maximum temperature. Pulse velocity measurement seems to give a better correlation of the level of the temperature at which the concrete has been exposed rather than the residual compressive strength of the concrete.

Other researchers[79] concluded that temperatures up to 70°C have a limited effect on the compressive strength and modulus of elasticity of the material. However, specimens exposed to temperatures between 120°-150°C exhibit an increase in the compressive strength but the modulus of elasticity is smaller than the corresponding value at 21°C. This is contrary to the behaviour of Portland cement concrete at the

same range of temperature as the strength and the modulus elasticity are adversely affected by the increase in temperature, see Table 2.21.

Table 2.21 Residual compressive strength[79]

Exposure time [days]	Compressive Strength [N/mm^2]	21 °C [%]	70 °C [%]	120 °C [%]	150 °C [%]	177 °C [%]	232 °C [%]
3	21.66	84	85	86	99	73	82
7	27.21	106	98	107	104	89	73
14	23.84	93	86	111	107	92	61
28	25.75	100	93	133	144	81	55
56	25.91	101	92	152	140	74	50
91	30.23	117	97	148	142	64	42
180	30.23	117	115	145	130	53	27

The increase in strength was attributed to the formation of tobemorite which is 2-3 times stronger than tobemorite gel. At temperatures in the range 177° to 232°C, both the compressive strength and modulus of elasticity were reduced by 60% and 65% respectively. The deterioration in the mechanical properties is due to the transformation of the tobemorite into crystalline alpha dicalcium silicate which has poor binding qualities.

The long term effect that fire will have on the mechanical properties of alkali activated materials has not been widely reported but some authors[112] have studied the effect of sustained high temperatures on concrete made with OPC and slag (c/slag = 10/3) and OPC and fly ash (cement/fly ash = 10/1.85). Malhotra et al[112] investigated the changes in the mechanical properties of concrete after long term exposure (1, 4 or 8 months) to sustained temperatures ranging from 75° to 600°C at a heating or cooling rate of 20°C per hour. The water/ binder ratio of the mixes tested was 0.45. The addition of fly ash in the concrete did not improve the mechanical properties after exposure to high temperatures, regardless of the exposure temperature and water /binder ratio (Table 2.22).

Riley[113] used cylindrical cores from existing structures which were subjected to temperatures in excess of 800°C for a period of two hours. Longitudinal thin sections were taken and examined to determine the association of certain features induced in the concrete by heat exposure from specific temperature regimes. This is schematically represented in Figure 2.15.

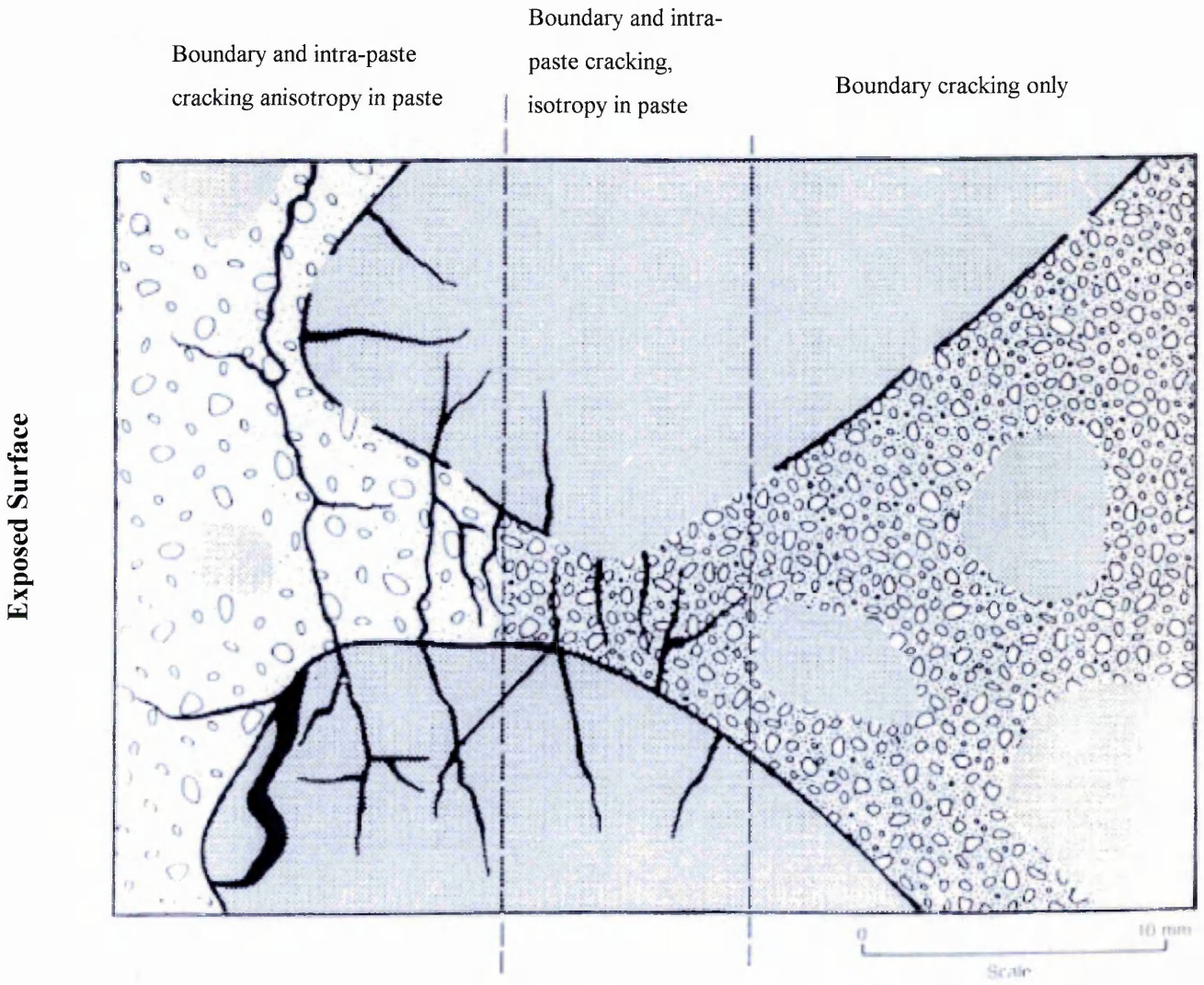

Figure 2.15 Schematic representation of temperature-related features in fire damaged flint aggregate concrete[113]

Table 2.22 Compressive σ_c and flexural σ_f strength before and after exposure to high temperatures[112]

Type of mix	Exposure Temp	Mist cured 28 days		Lab environment 112 days		Heat exposed 1 month		Heat exposed 4 months		Heat exposed 8 months	
		σ_c [MPa]	σ_f [MPa]	σ_c [MPa]	σ_f [MPa]	σ_c [MPa]	σ_f [MPa]	σ_c [MPa]	σ_f [MPa]	σ_c [MPa]	σ_f [M
OPC	75	49.2	4.36	61.9	5.38	59.8	4.78	59.5	5.08	60.4	5.0
	150	50.6	4.37	62.5	5.56	53.7	4.64	-	-	-	-
	300	50.6	4.37	60.1	5.39	39.1	3.98	36.4	3.90	-	-
	450	48.7	4.68	56.7	4.97	27.9	3.08	27.9	2.95	-	-
	600	50.4	4.76	61.5	5.18	14.2	1.99	-	-	-	-
OPC+Slag	75	49.9	4.70	60.1	4.96	62.8	5.01	65.3	4.87	65.0	4.7
	150	52.6	5.03	63.5	4.83	54.6	4.56	-	-	-	-
	300	52.6	5.03	60.5	5.35	40.9	3.70	36.7	3.56	-	-
	450	49.6	4.85	61.2	5.14	27.1	3.01	26.3	2.77	-	-
	600	54.4	4.52	63.5	5.18	12.5	1.51		-	-	-
OPC+Fly	75	45.6	4.37	60.6	5.19	57.0	4.70	57.6	4.90	59.1	4.9
ash	150	44.6	4.34	60.8	4.90	51.9	4.05	-	-	-	-
	300	46.0	4.37	60.1	5.08	37.9	3.60	37.7	3.66	33.7	3.1
	450	44.7	4.62	60.4	5.12	24.7	2.85	24.8	2.78	-	-
	600	45.4	4.24	60.3	4.93	20.2	2.57	-	-	-	-

2.14 FIBRE REINFORCED COMPOSITES

Plain concrete as a structural material is brittle and has a low tensile strength. In order to overcome its brittleness concrete is reinforced. Steel is traditionally used in the form of round or deformed bars to reinforce concrete. In a reinforced concrete member, tension is taken first by concrete and then transferred to steel when microcraks are initiated in tensile zone. In addition to structural concrete, mass concrete is used in massive structures, such as dams, where density and compressive strength are primarily relevant. However, there are also applications which do not require strength and weight alone but also require a good durability and resistance to abrasion, fatigue and impact etc. Concrete by itself is not capable of satisfying these requirements but the addition of short fibres has a favourable effect on its performance. The use of fibres to reinforce concrete has been well investigated[114, 115, 116, 117]. The strengthening effect is dependent on the concrete matrix, fibre material and the fibre characteristics such as aspect ratio and shape. The different fibre types employed include steel, polyester, polypropylene and glass. Romualdi and Mandel[118] used steel fibres of 0.25 to 1.0 mm diameter and up to 4% by volume. The dynamic tensile strength increased by 5 to 10 times compared with plain concrete and the flexural strength by 2.5 times. The use of other types of fibres produced similar results, showing great improvements to tensile and flexural properties.

Considerable work has been carried out on the use of steel fibres to reinforce concrete or Portland cement mortar, with a significant amount of work available on the theoretical analysis of the strengthening mechanisms [114 - 116]. The use of these fibres in alkali activated slag and fly ash mortars has not been investigated, opening up the potential for original research which can make a significant contribution to this area.

Patel et al[119] investigated the effect of steel, polypropylene and polyester fibres on the properties of the composite materials. Steel fibres, 0.4 mm diameter and 25 mm long (aspect ratio of 62.5), were used by volume 1.0, 1.5 and 2.0%. The results showed that 1.5% addition of steel fibres produced the maximum improvement in the mechanical properties e.g. shear strength by 115%, impact strength 90%, split tensile strength 45%, compressive strength 31%, flexural strength by 20% and modulus of elasticity by 4%.

Besides steel, polypropylene and polyester fibres, alkali resistant glass fibres have been successfully used for more than 25 years[99, 100, 120, 121, 122]. The great potential for a glass fibre reinforced cement material was recognised in the early days of reinforced plastics. Unfortunately, conventional borosilicate glass fibres made from E-glass were rapidly attacked and destroyed in the highly alkaline environment present in cement and concrete systems[121]. Cem-FIL fibres are manufactured from a specially formulated glass composition with a critical region of the Na_2O-CaO-ZrO_2-SiO_2 system. Cem -FIL fibres were specifically developed to overcome the problem of chemical attack produced by the very high alkalinity of the hydration products of ordinary Portland cement[120, 121]. There is a wide range of alkali resistant glass fibres available. Two distinctive types have been investigated. Integral chopped strand consisting of 100x14μm filaments bounded together. These fibres are designed to be resistant to the breakdown of the fibre bundle during concrete mixing. Water dispersible fibres consisting of strands of 20μm filaments bounded together in bundle are allowed to disperse into individual filaments on contact with moisture and during mixing[120, 121]. These two types of fibres are totally different. The integral fibres allow much higher addition without having a negative effect on the workability. The water dispersible fibres allow better dispersion of the fibres throughout the concrete but because of their higher surface area they can be added only at lower volumes.

An illustration of the expulsion of coarse aggregate by high fibre concentration is presented in Figure 2.16.

a) No fibre added, coarse particles can pack with the finer ones

b) Low levels of fibre addition, individual fibre bundle can fit between coarse particles and coarse particle can reposition slightly

c) High levels of fibre addition, high concentration of fibres between the particles leads to clumping and resistance to packing even under vibration. Fine particle can accommodate repositioning but some of the coarse particle cannot and tend to be expelled near the surface.

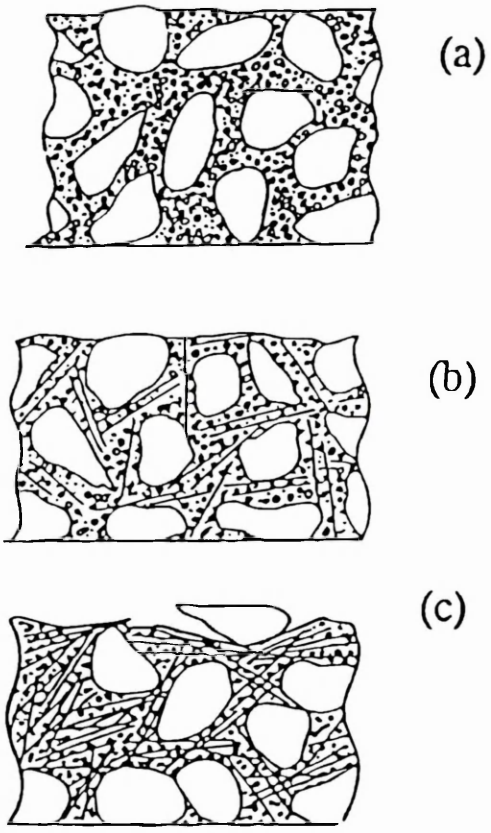

Figure 2.16 Illustration of the expulsion of coarse aggregate by high fibre concentration

Results show that the integral glass fibre strands can be added to normal concrete at 10 kg/m^3 with the benefits of increasing the impact resistance and resistance to cracking caused by restrained shrinkage. Increasing the integral fibre content to 2% by volume increases the bending strength[120, 121] by 50%.

Other researchers[123] have used steel fibres with an aspect ratio of 46.9 (64μm diameter and 3mm length) at volume fractions 1.3, 2.6 and 5.1% and glass fibres[124] added to the mix as percentage by weight of 0.25 to 1%. The results showed considerable increases in the fatigue resistance, toughness and flexural strength while the improvement in compressive strength and modulus of elasticity was moderate. The workability and compactibility of the fresh composite material were not significantly affected by the fibre addition. The effect of fibre reinforcement in mortar and concrete is due to additional restraint provided by the special shape of fibres through interfacial bond.

Other researchers[99, 100] have studied the influence of glass fibres on the shrinkage and creep of mortar and concrete. They concluded from their investigations that the factors which influence creep are the modulus of elasticity, the quantity and possibly the shape of the fibre, their combined effect being more apparent in mortar mixes than in concrete mixes.

"It takes less time to do a thing right than it does to explain why you did it wrong."

Henry Wadsworth Longfellow

3 Details of Constituent Materials

3.1 PULVERISED FUEL ASH (pfa)

During combustion of powdered coal in modern power plants the volatile matter and carbon are burned off but most of the mineral impurities deposited in coal during its formation, such as clays, shale, quartz and feldspar are generally fused and remain in suspension in the flue gas[1]. Injected or blown into the boiler furnace at high speed, it is burnt at a temperature of around 1500°C. The fused matter is quickly cooled to a temperature where it solidifies as spherical particles. Most of this solidified mineral matter flies out with the flue gas stream and hence is called "fly ash". In modern practice fly ash is removed from the flue gas stream by mechanical separators, electrostatic precipitators or by bag filters. In this study only low-calcium UK fly ashes have been used. These fly ashes, due to a high proportion of silica and aluminium, consist principally of aluminosilicate glass. pfa particles are predominantly spherical with a small proportion of irregular shaped particles which are mainly unburnt coal. Agglomeration of spheres may also occur. By limiting the residue material retained on the 45μm sieve to a maximum 12.5%, as specified in BS 3892: Part 1[125], the quantity of larger particles which contain mainly unburned carbon is kept low. Coal pulverisation ensures that at least 80% of it will pass a 75μm sieve.

According to Mehta[2], Hubbart et al examined fly ashes from 26 UK sources. They were all found to be low in calcium oxide (CaO) and contained mullite (9-43%), quartz (1-9%), hematite (3-11%), magnetite (2-9%), unburnt carbon (1-12%) and amorphous silicates (29-74%).

The main pozzolanic material used in this study was fly ash supplied by the Ash Resources Ltd from their power plant at Ratcliffe, Nottingham. Two other sources of fly ash were used fly ash from Ferrybridge power plant, fly ash from West Burton power plant

The grading curve for fly ash from Ratcliffe power plant is given in Figure 3.1. It represents a typical example of grading of fly ashes used in this research.

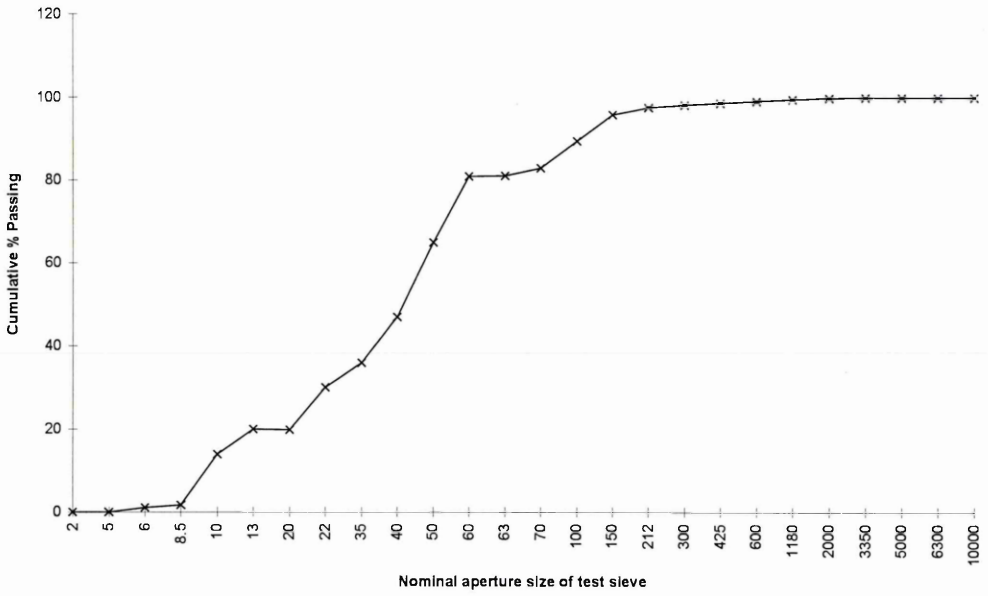

Figure 3.1 Grading Curve for Ratcliffe fly ash

The bulk density of loose pfa is usual between 1.1 to 1.2 mg/m^3. The density of fully compacted material will be 1.5 mg/m^3. Chemical analysis of pfa was performed by x-ray Fluorescence Method TSD/C in accordance with BS3892 Part 1, 1997[125]. The results for each of the three fly ashes are presented in Table 3.1.

Table 3.1 Chemical composition of the fly ashes (Supplier: Ash Resources Ltd).

	Content [%]		
Element	**FERRYBRIDGE**	**WESTBURTON**	**RATCLIFFE**
Silicon dioxide (SiO_2)	49.9	50.9	47.4
Aluminium oxide (AlO_3)	24.2	25.2	25.6
Iron oxide (Fe_2O_3)	11.7	8.9	10.4
Magnesium oxide (MgO)	1.65	1.4	1.7
Calcium oxide (CaO)	1.50	1.6	3.3
Sulphate (SO_3)	0.79	0.8	1.0
Potassium oxide (K_2O)	3.51	3.6	3.1
Sodium oxide (Na_2O)	1.64	1.6	1.4
$Na_2O_e = 0.658 \cdot K_2O + Na_2O$	3.95	4.00	3.4
Titanium oxide (TiO_2)	0.94	1.0	1.0
Chlorite (Cl)	0.016	0.01	0.01
Loss of Ignition	3.95	4.70	4.54
Specific Gravity [kg/m3]	2328	2300	2290
Sieve Residue Retained 45μm	9.3	na	na
$\frac{CaO+ MgO+ Al_2O_3}{SiO_2}$	**0.548**	**0.554**	**0.645**

3.2 SLAG

Slags from five UK sources were selected for the investigations: Purfleet, Teesside, Llanwern, Scunthorpe and Calumite. Ground granulated blast furnace slag (ggbs) was obtained from Appleby Group Ltd in Scunthorpe. Slag is a by-product from the production of pig iron in a blast furnace. It is shown in literature[1] that the mineralogical characteristics and properties of class C fly ash which contains high proportions of calcium are very similar to blast furnace slag. Owing to high proportion of calcium, magnesium, aluminium and silica ggbs consist mainly of calcium aluminosilicate glasses. The chemical composition of glass in ggbs corresponds to the melilite phase which is a solid solution phase between gehlenite and akermanite. In addition diopside and merwinite have also been detected in the devitrified particles of slag. It is beginning to be recognised that the addition of two or three admixtures (fly ash, silica fume, slag) in concrete is complementary and almost synergistic[8]. The progressive hydration of slag enhances later age strengths. Slag produces further compaction of the paste with gel formation and pore filling and the suppression of $Ca(OH)_2$ formation.

Chemical analysis[126] have been carried out using methods which have been calibrated against the requirements of BS EN 196-2 1995[127] for Purfleet, Lanwern, Scunthorpe and Teesside slag. The average results are presented in Table 3.2. Calumite slag samples were analysed by the methods detailed in the Appleby Calumite ISO 9002 quality manual and the Calumite procedure manual. The grading curve for a typical calumite slag is given in Figure 3.2

Table 3.2 Chemical composition of slags (Supplier: Appleby Group Ltd).

	Content [%]				
Element	**Purfleet**	**Teesside**	**Llanwern**	**Scunthorpe**	**Calumite**
Silicon dioxide (SiO_2)	35.02	35.67	34.97	35.57	35.08
Aluminium oxide (AlO_3)	11.47	13.47	11.15	13.06	12.94
Iron oxide (Fe_2O_3)	0.72	0.55	0.46	0.66	0.25
Magnesium oxide (MgO)	8.80	7.45	7.84	9.30	8.25
Calcium oxide (CaO)	42.34	40.90	42.73	39.18	40.08
Sulphate (SO_3)	0.13	0.05	0.30	0.2	0.05
Sulphide (S^{2-})	1.00	0.91	0.94	0.43	0.80
Potassium oxide (K_2O)	0.19	0.26	0.39	0.53	0.42
Sodium oxide (Na_2O)	0.26	0.19	0.21	0.31	0.24
$Na_2O_e = 0.658 * K_2O + Na_2O$	0.39	0.36	0.47	0.66	0.52
Titanium oxide (TiO_2)	0.57	0.69	0.53	0.71	0.58
Chlorite (Cl)	0.00	0.013	0.02	0.02	0.02
Manganese Oxide (MnO)	0.23	0.27	0.52	0.48	0.33
Manganese Oxide (Mn_2O_3)	0.26	-	0.58	-	-
Loss of Ignition	0.51	0.48	0.60	1.27	
Insoluble Residue	0.13	0.14	0.07	0.78	
Specific Surface Area [kg/m^2]	**464**[kg/m^2]	**466**[kg/m^2]	**450**[kg/m^2]	**436**[kg/m^2]	see Figure 3.2
$\frac{CaO+ MgO+ Al_2O_3}{SiO_2}$	**1.788**	**1.733**	**1.765**	**1.730**	**1.746**

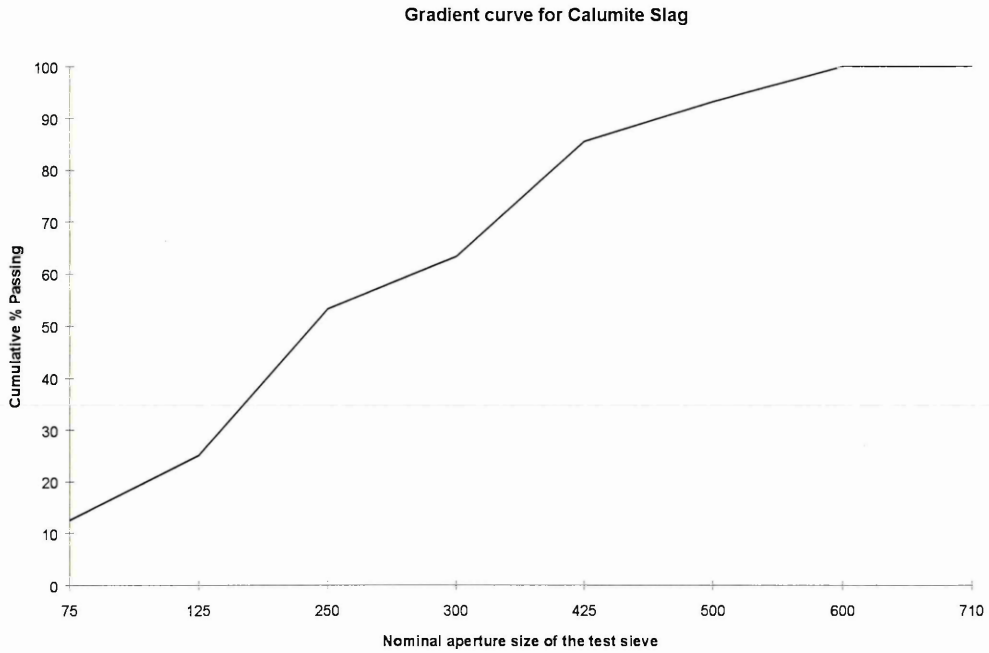

Figure 3.2 Grading curve for Calumite slag

3.3 CONDENSED SILICA FUME (MICROSILICA)

Condensed silica fume, sometimes known as microsilica or volatilised silica, is produced by electric arc furnaces as a by-product of the production of metallic silicon of ferrosilicon alloys[1]. In the reduction of quartz to silicon at temperatures up to 2000°C, a gaseous SiO_2 is produced. It is transported to lower temperatures where it oxidises on coming in contact with air and condenses in the form of spheres consisting of noncrystaline silica. The material, which is extremely fine, is removed by filtering the outgoing gases in a bag filter. Silica fume consists mainly of noncrystaline silica with a very high surface area which makes it highly pozzolanic. Silica fume has been used extensively in the development of high-strength, low permeability cast-in place concrete. Previous work with alkali activated slag materials, detailed in the literature review, found that the addition of silica fume enhanced the early age strength, enabled the rapid matrix densification and the refinement of the paste-aggregate interface. It was decided to investigate whether the addition of silica fume would produce the same effects on the microstructure for alkali activated fly ash materials.

Microsilica was provided by Elkem Materials Company. Its chemical composition is presented in Table 3.3.

Table 3.3 Chemical composition of silica fume (Supplier: Elkem Materials Company).

Element	Content [%]
Silicon dioxide (SiO_2) amorphous	85 to 98
Iron oxide (Fe_2O_3)	max. 3.0
Aluminium oxide (Al_2O_3)	max.1.5
Calcium oxide (CaO)	max.0.7
Magnesium oxide (MgO)	max.2.0
Sodium oxide Na_2O)	max.1.0
Potassium oxide (K_2O)	max.3.0
$Na_2O_e = 0.658 \cdot K_2O + Na_2O$	max 2.97
Carbon (C)	max.3.0
$\frac{CaO + MgO + Al_2O_3}{SiO_2}$	**0.0494 to 0.0428**

The physical properties of silica fume are as follows:

- Melting Point (°C) 1550 to 1570
- Solubility (water) Insoluble / Slightly soluble
- Solubility (organic solvents) Insoluble / Slightly soluble
- Specific Gravity (water =1) 2.2 to 2.3
- Bulk Density (kg/m3) 150 to 700
- Specific Surface (m^2/g) 15 to 30
- Particle Size (μm) ≈ 0.5

3.4 GROUND PORTLAND CEMENT CLINKER

Portland cement clinker is a hydraulic material which consists of alite $(CaO)_3 \cdot SiO_2$ (65% by mass) and belite $(CaO)_2 \cdot SiO_2$ (14%), calcium aluminate, $CaO \cdot Al_2O_3$ (11%), $(CaO)_4 \cdot Al_2O_3 \cdot Fe_2O_3$ (6.5%) and the remainder containing aluminium oxide, $Al_2 O_3$, iron oxide, $Fe_2 O_3$and other oxides[34]. Ground Portland cement clinker, as an additive in alkali activated materials, is different from Portland cement because the latter contains gypsum which neutralises the alkali compound reactions. It was found

from literature that mixes of ground granulated blast furnace slag activated by water glass and ground Portland cement clinker as an additive (up to 1 %) produced a very high strength[42]. However, mixes containing higher amounts of ground Portland cement clinker exhibited lower flexural and compressive strengths.

In this investigation the effect of 1% addition of ground Portland cement clinker to alkali activated fly ash materials was determined. Chemical analysis of the clinker were performed by the x-ray Fluorescence Method TSD/C in accordance with BS EN 196-2 1995[127]. The results are presented in Table 3.4.

Table 3.4 Chemical Composition of ground Portland cement clinker (Supplier: Castle Cement Ltd).

Element	Content [%]
Silicon dioxide (SiO_2) amorphous	21.35
Aluminium oxide (Al_2O_3)	5.16
Iron oxide (Fe_2O_3)	2.82
Magnesium oxide (MgO)	2.40
Calcium oxide (CaO)	64.88
Sulphate (SO_3)	1.58
Potassium oxide (K_2O)	0.73
Sodium oxide (Na_2O)	0.30
$Na_2O_e = 0.658 \cdot K_2O + Na_2O$	0.78
Specific Surface Area [m^2/kg]	490
$\frac{CaO + MgO + Al_2O_3}{SiO_2}$	**3.393**

3.5 SAND

In the preliminary work on the exploratory mixes, medium grain sand from Belmoor quarry was used. Grain size composition was made in house and the grading curve is presented in Figure 3.3. Tarmac Quarry Products Ltd supplied the sand. Its chemical composition is presented in Table 3.5.

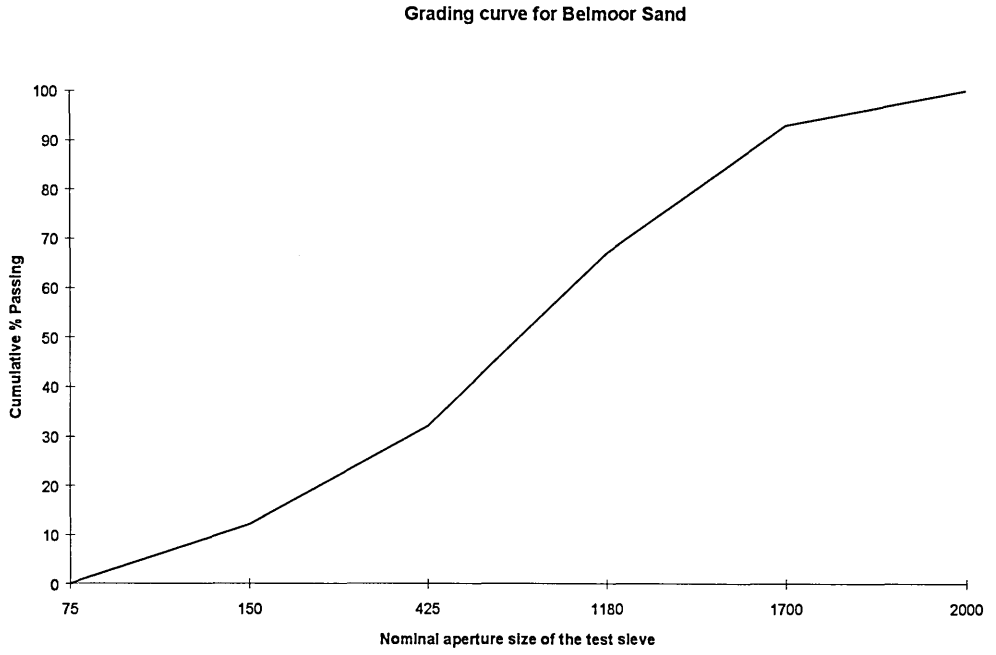

Figure 3.3 Grading curve for Belmoor sand

Table 3.5 Chemical composition of Belmoor sand (Supplier: Tarmac Quarry Products Ltd).

ELEMENTS	Content [%]
Silicon dioxide (SiO_2)	93.6
Aluminium oxide (Al_2O_3)	3.2
Iron oxide (Fe_2O_3)	0.9
Magnesium oxide (MgO)	0.2
Calcium oxide (CaO)	0.3
Sulphate (SO_3)	0.01
Potassium oxide (K_2O)	1.0
Sodium oxide (Na_2O)	0.1
$Na_2O_e = 0.658 \cdot K_2O + Na_2O$	0.76
Chlorite(Cl)	<0.01
Loss of Ignition	0.7
Bulk Density (kg/m3)	1765 to 1620
$\frac{CaO + MgO + Al_2O_3}{SiO_2}$	**0.04**

Five different washed and graded high silica fine sands were used to investigate the influence of fineness on mechanical and physical properties of the resulting composites, Chelford 80, Chelford 95, Redhill 110, Congleton 80 and Congleton HST 95. The sand was delivered by Hepworth Minerals and Chemicals Ltd with the chemical composition presented in Table 3.6.

Table 3.6 Chemical composition of silica sands (Supplier: Hepworth Minerals and Chemicals Ltd).

	Content [%]				
Element	**CO 80**	**CO 95**	**CH 80**	**CH 95**	**RD 110**
Silica (SiO_2)	95.13	94.5	95.2	95	98.8
Aluminium oxide (Al_2O_3)	2.34	2.96	2.42	2.64	0.21
Iron oxide (Fe_2O_3)	0.24	0.28	0.19	0.23	0.09
Sodium oxide (Na_2O)	nil	nil	nil	nil	nil
Potassium oxide (K_2O)	1.61	1.83	1.52	1.61	0.03
$Na_2O_e = 0.658 \cdot K_2O + Na_2O$	1.059	1.204	1.00	1.059	0.02
L.O.I.	0.25	0.41	0.29	0.37	0.14
Clay content	0.1 to 0.3	0.2 to 0.4	0.1 to 0.3	0.3 to 0.4	na
Grain shape	Rounded	Semirounded	Rounded	Semirounded	Angular
Loose Bulk density [kg/m^3]	1450	1420	1450	1430	1350
Average grain size [μm]	175	130	165	145	120

Grain size composition of the above 5 sands was determined by sieve analysis in accordance with BS 112: part 101, 1984 and is shown in Figure 3.4

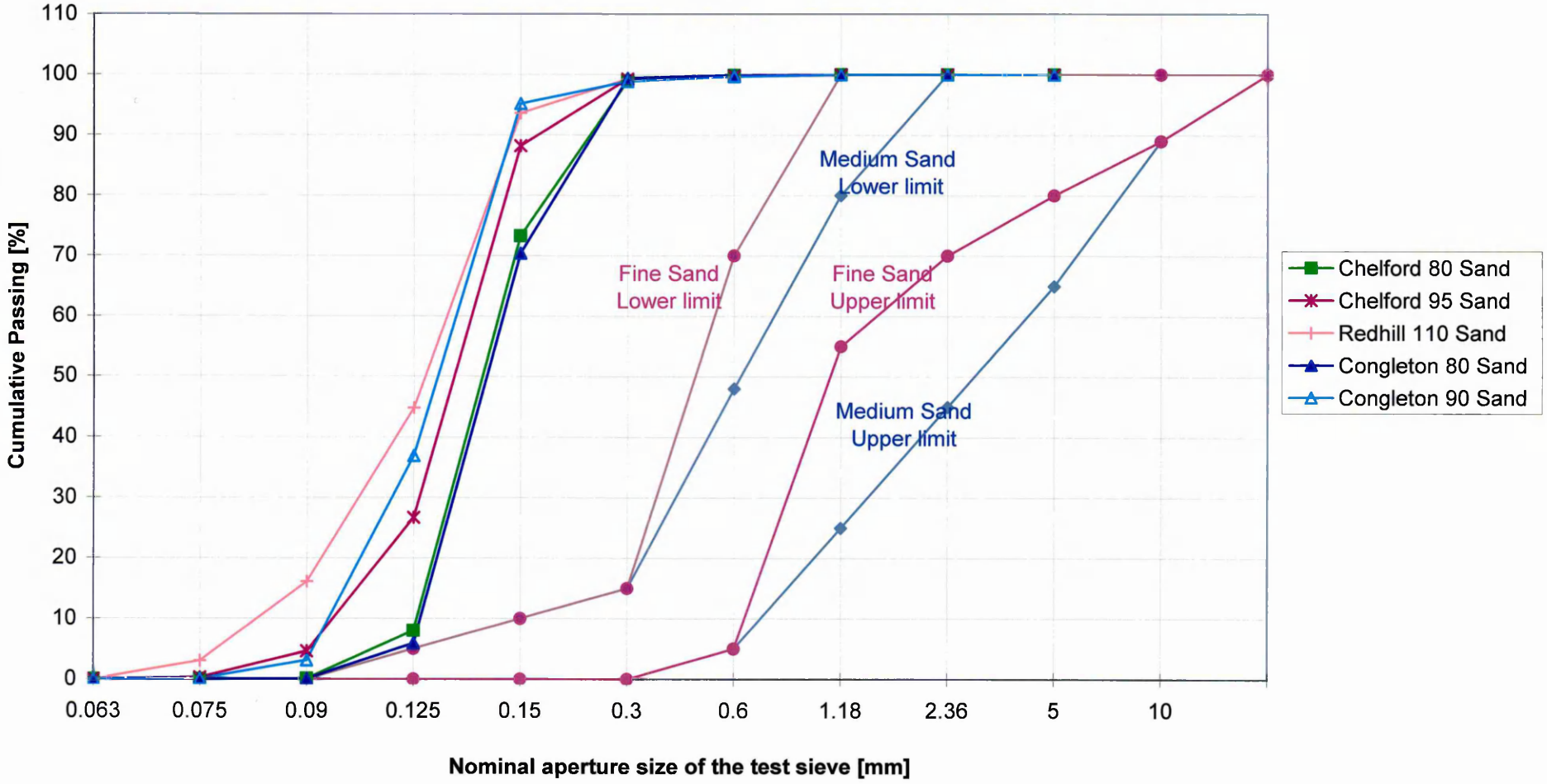

Figure 3.4 Grading curves for fine high silica sands and BSI Grading Curves for fine and medium sand (BS 812: Part 101, 1984)[128]

3.6 WATER GLASS

Soluble silicates are essentially combinations of alkali metal oxides and silica with water. The general formula for the soluble silicates of Na, K and Li is $xSiO_2 : M_2O$ where:

M is Na, K or Li

x is the molar ratio which defines the number of moles of silica per mole of the alkali metal oxide (moles of SiO_2/moles of M_2O). However this ratio can also be expressed on a mass basis.

Silicate glasses contain thetraedral SiO_4 which are common to many other forms of silica, crystalline silicates and glasses. The silicate tetrahedra may be monomers or polymerised with up to four other tetrahedra sharing oxygen atoms to form Si-O-Si bridges, sometime termed as siloxane bond[37]. The overall structure in the glass is a random arrangement of the SiO_4 molecules with cations spaced in the interstices.
Soluble silicate solutions contain mixtures of silicate anions, ranging from monomeric and dimeric trough to high molecular weight polymers containing a larger number of Si atoms.

The polymer distribution determines the applicational properties of the silicates and is mainly dependent on the molar ratio and solution concentration. It is believed that an equilibrium situation develops for any given solution composition and that a rapid re-arrangement of polymer species occurs if the solution is diluted or if extra alkali is added[37]. There is evidence that equilibrium is more quickly reached for lower molar ratio solutions. The versatility of these products stems largely from the modification of their properties made possible by varying the molar ratio and the physical form in which the product is supplied e.g. liquid, powder or granules[37].
From literature[14, 24, 39, 42], water glass has shown itself to be the most effective activator for slag in comparison with other activators. Limited research with fly ash also shows effective activation by water glass[44]. In this investigation water glass was selected as the main activator for fly ash.

Water glass with a mean molar ratio (silica modulus, n = SiO_2/Na_2O) of 2.06 was used. Its chemical composition is shown in Table 3.7.

Table 3.7 Chemical Composition of water glass (Supplier: Crossfield Ltd)

Constituent Elements	Content [%]
Silicon dioxide (SiO_2)	30.55
Sodium oxide (Na_2O)	15.27
Water (H_2O)	54.18

The literature indicates that the sodium silicate solutions with silica modulus $n \leq 1$ will give the best results for slag activation[19,20] with respect to mechanical properties. It was decided to investigate whether this is also true for fly ash activation.

Sodium silicate solutions with silica modulus $n \leq 1$ are not commercially available. Therefore, a water glass with mean molar ratio (silica modulus) of 1.65 was modified by the addition of 12.5 molar concentration NaOH (technical grade) to produce water glass with silica modulus of 0.5, 0.7, 0.8, 0.9, 1, 1.1 (see Table 3.8). This was undertaken less than 24 hours before mixing with fly ash in order to avoid the use of an unstable solution with a gel-like precipitation.

Commercially available water glass CRYSTAL 0501 was used. Its silica modulus ,n equals 1.65.

100g of CRYSTAL 0501 yields the following element content:

Na_2O =17.98 g and SiO_2 = 28.75 g

Na_2O reacts with water to produce NaOH as follows:

$Na_2O + H_2O \leftrightarrow 2\ NaOH$

The proportion of Na_2O to NaOH in the above reaction is 1:2

Therefore, the addition of 2 mols of NaOH is the equivalent of adding 1mol of Na_2O.

Hence, 500g NaOH + 1000 ml H_2O yields 12.5 molar NaOH solution

The values given in Table 3.8 are for 100g of Crystal 0501 sodium silicate solution

Table 3.8 NaOH content for modification of silica modulus of CRYSTAL 0501 water glass

$n = SiO_2/ Na_2O$ (molar)	Total Na_2O (g)	Na_2O added (g)	Na_2O added (molar)	2 NaOH (molar)	Vol. 12.5 NaOH (ml)
0.5	59.2	41.22	0.66	1.32	106
0.7	42.3	24.3	0.39	0.78	62
0.8	37	19	0.31	0.62	50
0.9	32.9	14.9	0.24	0.48	38
1	29.6	11.6	0.19	0.38	30
1.1	26.9	8.9	0.14	0.28	22
1.2	24.7	6.7	0.11	0.22	17.5
1.3	22.8	4.8	0.08	0.16	12.8
1.4	21.15	3.2	0.05	0.1	8
1.5	19.74	1.8	0.03	0.06	4.8

3.7 WATER GLASS HARDENERS

The water glass hardeners were all of the aluminium phosphate type. They are currently used as hardeners in water glass based paints[45] in order to improve flexibility and water absorption properties. Their beneficial effect with the alkali activated materials, especially with regard to curing and water absorption properties is investigated. Three water glass hardeners of the aluminium phosphate type produced by Wilfred Smith Ltd. Corporation, were selected for investigation:

1. K-Bond # 80 - Aluminium Thriophosphate Compound,
2. K-Bond # 90 - Aluminium Methaophosphate Compound,
3. K-Bond # 200 - Aluminium Orthophosphate Compound.

The properties of the hardeners are given in Table 3.9.The hardener was added as percentage by weight of the sodium silicate solution (water glass). It was made into slurry with water before adding it to the mix as this aided its dispersion.

Table 3.9 Physical properties of water glass hardeners (Supplier: Wilfred Smith Ltd)

General Properties	KB#80	KB#90	KB#200
Appearance	Fine white powder	Fine white powder	Fine white powder
Acidity [meq/g]	4.3 ± 0.5	1.2 ± 0.5	1.2 ± 0.5
Moisture [%]	max 1.5	max 1.5	0.3
Solubility in water [%]	max 3.0	max 3.0	0.4
pH	2.5 ± 0.5	3.2 ± 0.5	5.3 ± 0.5
Sieve residue > 44 micron [%]	1.0	max 1.0	0.2

3.8 FIBRE REINFORCEMENT

In order to evaluate their influence on the mechanical properties and brittleness of the alkali activated materials, two types of fibres were selected for the research:

a) Stainless steel fibres of straight shape and undeformed, smooth surface. The fibres were of length 7mm and diameter 0.15 mm. The aspect ratio (length/diameter) was 46.67. The specific gravity and Young's modulus of elasticity were 7.8 kg/m3 and 215.3 GPa, respectively.

b) Melt extract steel fibres of non-uniform surface. The fibres were of length 12 mm and equivalent diameter 0.5 mm. The aspect ratio was 24. The specific gravity and Young's modulus of elasticity of the fibres were 7.8 kg/m3 and 215.3 GPa, respectively.

c) Alkali resistant integral chopped strand glass fibres (Cem-FIL 62/2) consisting of 100 filaments bound together. These fibres were designed to be resistant to the breakdown of the filaments during mixing. The individual filaments were of length 12 mm and diameter 14μm. The aspect ratio of the fibre strand was 36.5. The physical properties of the glass fibres are presented in Table 3.10.

Table 3.10 Properties of glass fibres (Supplier: by Cem-FIL Ltd).

Property	Unit
Virgin Filament Tensile Strength	3500 N/mm^2
Young's Modulus of Elasticity	72 GPa
Specific Gravity	2.68 kg/m3
Strain at breaking point	2.4 %
Water uptake	< 0.1%
Softening Temperature	860 °C
Fire	Incombustible

"We are too much accustomed to attribute to a single cause that which is the product of several and the majority of our controversies come from that."

Justus van Liebig

4 Parameters which influence the performance of alkali activated fly ash materials

4.1 INTRODUCTION

UK industry annually produces about 4 million tonnes of wastes which present a disposal hazard, whether toxic, acidic, combustible, caustic or irritant, although much of this will contain 1% or less of hazardous components[39]. Around 80% of these waste materials are landfilled, that is deposited in or on the ground without any pre-treatment. However, it is increasingly recognised that landfilled sites are a potential source of ground water contamination affecting the drinking water supplied to the population[39]. Once the contamination of the groundwater has occurred it is rarely possible to rehabilitate the resource.

One of these industrial waste materials is fly ash. Fly ash has largely been used as a cement replacement material in concrete. Despite over four decades of using fly ash, less than 25% of the total production is used and the remainder is disposed of as a waste material. Low calcium fly ashes, which are used in this investigation, do not contain enough calcium to be self activating. They need more calcium from an external source in order to develop their full cementitious potential. The activation of fly ashes is normally carried out with lime, either directly with lime powder or indirectly with ordinary Portland cement or with gypsum, all of which provide the external source of Ca.

Since fly ash has a high glassy content, it reacts very slowly with water but it can be activated chemically. Fly ash has the potential to produce a strong cementitious material when activated by alkali solutions owing to its high alumino-siliceous content. Most of the research on alkali activation in recent years has been foccused on the use of ground blast furnace slag. Because of chemical and mineralogical similarities of fly ashes and slags, the findings of studies on alkali-activated slags should also be applicable to alkali-activated fly ashes. Applying the principles of alkali activation to fly ash materials and taking into account the differences and similarities in chemical composition and physical properties of slag and fly ash will allow the development of alkali activated fly ash binders.

4.2 OBJECTIVES

When processing a material it is very important to understand the fundamental relationship between the processing factors and the properties of the resulting materials. One of the main problems with alkali activated materials is that strength development is difficult to control compared with ordinary Portland cement concrete. The strength is sensitive to the chemical composition of pozzolanic materials, the alkali component which activates them and the composition of any additives used. Most of the available data in literature[10-14,22,23,44,51-52] relate to strength measurements of alkali activated slag and fly ash cements under different conditions and some reports are contradictory.

This investigation was conducted in order to gain a more fundamental understanding of the factors affecting the performance of the alkali activated fly ash materials such as;

- chemical composition of the constituent pozzolanic materials (fly ash, slag, microsilica),
- proportion of the constituent materials,
- type and fineness of sand,
- moulding conditions,
- curing conditions,
- use of sodium silicate solution (alkali) activators,
- dosage of alkali activator,
- use of sodium silicate hardeners.

There is a great interdependence between the factors which affect the performance of alkali activated materials, and the effect of changing more than one is usually not additive.

4.3 EXPERIMENTAL PROGRAMME

4.3.1 Constituent Materials

The constituent materials used for the investigations presented in this chapter are detailed in Chapter III (Experimental Programme) and are also summarised in the following section.

The main pozzolanic material used was **pulverised fuel ash** (pfa). In this study only low-calcium fly ashes from three UK power plants (Ferrybridge, West Burton and Ratcliffe) were used. Their chemical composition (by weight) is given in Table 4.1.

Table 4.1 Chemical composition of selected fly ashes

	Content [%]		
Element	**FERRYBRIDGE**	**WESTBURTON**	**RATCLIFFE**
Silicon dioxide (SiO_2)	49.9	50.9	47.4
Aluminium oxide (Al_2O_3)	24.2	25.2	25.6
Iron oxide (Fe_2O_3)	11.7	8.9	10.4
Magnesium oxide (MgO)	1.65	1.4	1.7
Calcium oxide (CaO)	1.50	1.6	3.3
Sulphate (SO_3)	0.79	0.8	1.0
Potassium oxide (K_2O)	3.51	3.6	3.1
Sodium oxide (Na_2O)	1.64	1.6	1.4
$Na_2O_e = 0.658 \cdot K_2O + Na_2O$	3.95	4.00	3.4
Titanium oxide (TiO_2)	0.94	1.0	1.0
Chlorite (Cl)	0.016	0.01	0.01
Loss of Ignition	3.95	4.70	4.54
Specific Gravity [kg/m3]	2328	2300	2290
Sieve Residue Retained 45μm	9.3	na	na
$\frac{CaO + MgO + Al_2O_3}{SiO_2}$	**0.548**	**0.554**	**0.645**

Ground granulated blast furnace slag from five UK power plants (Purfleet, Teesside, Llanwern, Scunthorpe and Calumite were selected and their chemical composition (by weight) and particle size analysis are presented in Table 4.2.

Table 4.2 Chemical Composition of selected ggbs

	Content [%]				
Element	**Purfleet**	**Teesside**	**Llanwern**	**Scunthorpe**	**Calumite**
Silicon dioxide (SiO_2)	35.02	35.67	34.97	35.57	35.08
Aluminium oxide (Al_2O_3)	11.47	13.47	11.15	13.06	12.94
Iron oxide (Fe_2O_3)	0.72	0.55	0.46	0.66	0.25
Magnesium oxide (MgO)	8.80	7.45	7.84	9.30	8.25
Calcium oxide (CaO)	42.34	40.90	42.73	39.18	40.08
Sulphate (SO_3)	0.13	0.05	0.30	0.2	0.05
Sulphide (S^{2-})	1.00	0.91	0.94	0.43	0.80
Potassium oxide (K_2O)	0.19	0.26	0.39	0.53	0.42
Sodium oxide (Na_2O)	0.26	0.19	0.21	0.31	0.24
$Na_2O_e = 0.658 \cdot K_2O + Na_2O$	0.39	0.36	0.47	0.66	0.52
Titanium oxide (TiO_2)	0.57	0.69	0.53	0.71	0.58
Chlorite (Cl)	0.00	0.013	0.02	0.02	0.02
Manganese Oxide (MnO)	0.23	0.27	0.52	0.48	0.33
Manganese Oxide (Mn_2O_3)	0.26	-	0.58	-	-
Loss of Ignition	0.51	0.48	0.60	1.27	
Insoluble Residue	0.13	0.14	0.07	0.78	
Specific Surface Area [kg/m^2]	**464**[kg/m^2]	**466**[kg/m^2]	**450**[kg/m^2]	**436**[kg/m^2]	see Figure 3.2
$\frac{CaO + MgO + Al_2O_3}{SiO_2}$	**1.788**	**1.733**	**1.765**	**1.730**	**1.746**

Microsilica was a dry densified silica fume with the chemical composition (by weight) given in Table 4.3.

Table 4.3 Chemical composition of silica fume

Element	Content [%]
Silicon dioxide (SiO_2) amorphous	85 to 98
Iron oxide (Fe_2O_3)	max. 3.0
Aluminium oxide (Al_2O_3)	max.1.5
Calcium oxide (CaO)	max.0.7
Magnesium oxide (MgO)	max.2.0
Sodium oxide Na_2O)	max.1.0
Potassium oxide (K_2O)	max.3.0
$Na_2O_e = 0.658 \cdot K_2O + Na_2O$	max 2.97
Carbon (C)	max.3.0
$\frac{CaO + MgO + Al_2O_3}{SiO_2}$	**0.0494 to 0.0428**

Portland cement clinker had the chemical composition (by weight) given in Table 4.4.

Table 4.4 Chemical Composition of ground Portland cement clinker

Element	Content [%]
Silicon dioxide (SiO_2) amorphous	21.35
Aluminium oxide (Al_2O_3)	5.16
Iron oxide (Fe_2O_3)	2.82
Magnesium oxide (MgO)	2.40
Calcium oxide (CaO)	64.88
Sulphate SO_3	1.58
Potassium oxide (K_2O)	0.73
Sodium oxide (Na_2O)	0.30
$Na_2O_e = 0.658 \cdot K_2O + Na_2O$	0.78
$\frac{CaO + MgO + Al_2O_3}{SiO_2}$	**3.393**

Two categories of **sand** were used. The first category was a medium grain sand from Belmoore obtained from Tarmac Quarry Products Ltd., with the chemical composition presented in Table 4.5.

Table 4.5 Chemical composition of Belmoor sand

ELEMENTS	Content [%]
Silicon dioxide (SiO_2)	93.6
Aluminium oxide (Al_2O_3)	3.2
Iron oxide (Fe_2O_3)	0.9
Magnesium oxide (MgO)	0.2
Calcium oxide (CaO)	0.3
Sulphate (SO_3)	0.01
Potassium oxide (K_2O)	1.0
Sodium oxide (Na_2O)	0.1
$Na_2O_e = 0.658 \cdot K_2O + Na_2O$	0.76
Chlorite (Cl)	<0.01
Loss of Ignition	0.7
Bulk Density (kg/m^3)	1765 to 1620
$\frac{CaO+ MgO+ Al_2O_3}{SiO_2}$	**0.04**

Washed and graded high silica sands from Chelford quarry (CH 80 and CH 90), Redhill quarry (RD 110) and Congleton quarry (CO 85 and CO 95) formed the second category of sands. Grain size and chemical composition of the five sands is presented in Table 4.6.

Table 4.6 Chemical composition and grain size of high silica sands

Element	CO 80	CO 95	CH 80	CH 95	RD 110
Silicon dioxide (SiO_2)	95.13	94.5	95.2	95	98.8
Aluminium oxide (Al_2O_3)	2.34	2.96	2.42	2.64	0.21
Iron oxide (Fe_2O_3)	0.24	0.28	0.19	0.23	0.09
Sodium oxide (Na_2O)	nil	nil	nil	nil	nil
Potassium oxide (K_2O)	1.61	1.83	1.52	1.61	0.03
$Na_2O_e = 0.658 \cdot K_2O + Na_2O$	1.059	1.204	1.00	1.059	0.02
L.O.I.	0.25	0.41	0.29	0.37	0.14
Average grain size [μm]	175	130	165	145	120
Bulk density [kg/m^3]	1450	1420	1450	1430	1350

Sodium silicate solution (water glass) with a mean molar ratio (silica modulus) SiO_2: NaO_2 =2.05 was selected as the major activator throughout this project. Its chemical composition is presented in Table 4.7.

Table 4.7 Chemical Composition of water glass

Constituent Elements	Content [%]
Silicon dioxide (SiO_2)	30.55
Sodium oxide (Na_2O)	15.27
Water (H_2O)	54.18

Water glass hardener: Aluminium phosphate compounds, commercial chemical products K-Bond, were selected as water glass hardener in order to accelerate the curing process of alkali activated materials at ambient temperatures. The chemical composition of these compounds was kept confidential by the manufacturer. Three water glass hardeners produced by Tayaca Corporation were selected for the present investigation. Their physical properties are presented in Table 4.8.

1. K-Bond # 80 - Aluminium Thriphosphate Compound, $AlH_2P_3O_{10}\ 2H_2O$
2. K-Bond # 90 - Aluminium Methaphosphate Compound,
3. K-Bond # 200 - Aluminium Orthophosphate Compound.

Table 4.8 Physical properties of water glass hardeners

General Properties	KB#80	KB#90	KB#200
Appearance	Fine white powder	Fine white powder	Fine white powder
Acidity [meq/g]	4.3 ± 0.5	1.2 ± 0.5	1.2 ± 0.5
Moisture [%]	max 1.5	max 1.5	0.3
Solubility in water [%]	max 3.0	max 3.0	0.4
pH	2.5 ± 0.5	3.2 ± 0.5	5.3 ± 0.5
Sieve residue > 44 micron [%]	1.0	max 1.0	0.2

4.3.2 Mixing Procedure

Mixing was carried out according to BSI EN 196-1 1994[130] "Testing cement for strength", using a forced action pan Hobart mixer. The mixer consisted of:

- a stainless steel bowl with a capacity of 5 *l* (see Figure 4.1) which can be fixed securely to the mixer frame during mixing. The height of the bowl can be finely adjusted and fixed to provide the required clearance to the blade;
- a stainless steel blade (as shown in Figure 4.1) revolving about its own axis as it is driven in a planetary movement around the axis of the bowl by an electric motor at controlled speed.

The fly ash, silica fume, sand and hardener (in selected mixes), were weighed using a Mettler PL 1200 analytical balance. The sand was mixed with the constituent pozzolanic materials before the addition of the liquid binder. After mixing the dry constituents thoroughly, the liquid constituents (water glass and water) were added and mixed to produce a homogeneous mixture. At this stage, because of high consistency (low workability) of the mix, the speed of the Hobart mixer was increased in order to achieve a uniform mix. The water glass hardener was then added (in selected mixes) and high speed mixing continued to produce a homogeneous mixture. The hardener was made into slurry with water before adding to the mix as this aided its dispersion.

4.3.3 Casting and Curing

Stainless steel moulds were specially manufactured for the prism (10x25x100mm) and cube (50 mm) test specimens. The dimensions, flatness, parallelism and surface smoothness of the moulds were accurate according to BS 308, Part 3[131]. The internal surfaces of the prism and cube moulds were coated with a relief agent (silicone oil) so that it formed an extremely thin layer on the mould faces. The coating was applied to prevent adherence of the material to the mould.

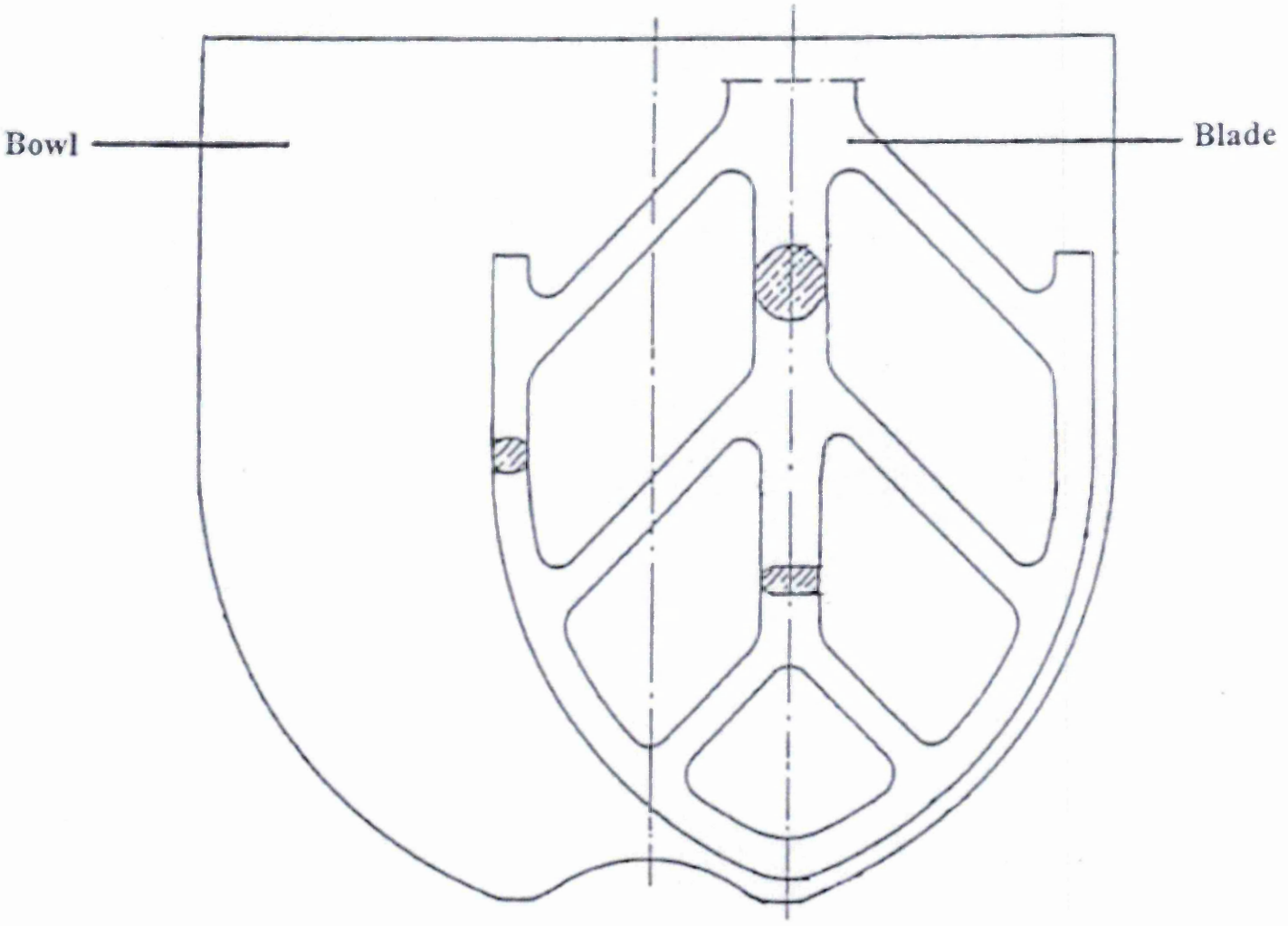

Figure 4.1 Hobart mixing bowl and blade.

After mixing, the fresh material was placed horizontally in one or two layers into the moulds. Compaction of the specimens was carried out by one of the following methods:

i. hand compaction method:

Specimens were cast in two layers, and compacted by applying strokes with a tamping rod (cross-section of 15x15mm) on each layer. The top surface of the specimen was trowelled using a steel float. This method was suitable for plastic mixes with relatively high workability (low consistency).

ii. pressure compaction method:

The mixed (homogenised) material was cast in one layer and compacted by a hydraulic press using a compaction pressure of 10, 20 or 30 N/mm^2. The hydraulic press was a hybrid frame with a 100 kN capacity Schenck loading rig. This method of compaction was necessary for high consistency (very low workability) mixes

Immediately after casting the specimens were cured under one of the following two conditions:

i. 20°C temperature and 65% relative humidity, in a controlled environment room. The specimens developed adequate strength to allow demoulding after seven hours.

ii. high temperature curing in a Forcecraft fan aided oven with a time programmable facility. The specimens were subjected to the curing profile 1, which is detailed in Table 4.9.

Table 4.9 Curing profile 1

Temperature T [°C]	**20.6**	**30**	**40**	**50**	**60**	**70**	**80**	**90**	**100**	**120**
Time t [minutes]	15	15	15	15	15	15	15	15	15	15

It appeared, however, that under the high temperature curing condition (profile 1), the thermal treatment time was too short to remove excess water from the plastic material. As a result, the samples developed a convex surface after curing (the free

surface of specimens within the moulds, which was not restrained by the mould surface). Therefore, the duration of thermal treatment was increased to several hours at the lower temperature ranges to allow the samples to attain sufficient strength to support the internal stresses caused by water loss. This time was strongly dependent on the size of the specimens. The temperature was maintained at each increment until the sample weight was stable (no further loss of H_2O). Any increase or decrease in temperature was carried out at a slow and regular rate. Rapid temperature changes were avoided to prevent extensive fissures in the material. To avoid these problems, curing profile 2 was used which is detailed in Table 4.10.

Table 4.10 Curing profile 2

Temperature T [°C]	**20.6**	**30**	**45**	**60**	**80**	**100**	**120**
Time t [minutes]	15	300	300	300	180	60	60

The specimens were exposed to curing profiles 1 or 2 immediately after casting. They remained in the mould during the whole curing period. After thermal curing (profiles 1 or 2) the specimens were demoulded and stored in the controlled environment room (20°C, 65%RH) until testing.

4.3.4 Details of investigated batches

4.3.4.1 Mix Design

In order to control the Na_2O content of the specimens within the range 2-4% by weight, as suggested in literature[19, 20], the amount of sodium silicate solution used was 10-11% by weight. The pozzolanic material content of the mix (fly ash, microsilica, slag and Portland clinker) was varied from 25 to 39% by weight. The amount of water glass hardener added to the mix was 20% of the sodium silicate content. The amount of sand was up to 65% by weight.

4.3.4.2 Series 1: Influence of chemical composition of fly ash

In order to evaluate the influence of the chemical composition of fly ashes on the mechanical properties of alkali activated materials, fly ashes from three UK coal power plants were used: Ferrybridge, West Burton and Ratcliffe. Batches of specimens were cast using the hand compaction method and subsequently subjected to the thermal curing (profile1) detailed in section 4.3.3. The proportions of the constituent materials used in these batches are presented in Table 4.11.

Table 4.11 Proportions of the constituent materials using different sources of fly ash.

Batch Code	Source of Fly Ash	Fly Ash [w_t %]	Sand [w_t %]	Water Glass [w_t %]
FB	Ferrybridge	20	65	10
WB	West Burton	20	63	12
RT	Ratcliffe	20	65	10

Bach code key:

FB - fly ash from Ferrybridge power plant,

WB - fly ash from West Burton power plant,

RT - fly ash from Ratcliffe power plant.

4.3.4.3 Series 2: Influence of microsilica (silica fume)

Microsilica has been extensively used in the development of high-strength, low permeability concrete[8]. In order to study the effect of microsilica on the properties of alkali activated fly ash materials, five levels of additions were investigated: 0.5%, 1%, 2.5%, 5%, 10% (by weight) as presented in Table 4.12. The total pozzolanic material content of the mix (fly ash and microsilica) was kept constant (25% by weight) varying only the amount of microsilica. Proportions of the constituent materials used in these batches are presented in Table 4.12. Fly ash from Ratcliffe power plant and sand from Belmoore quarry were used. All six batches were cast using the hand compaction method and subsequently subjected to thermal curing (profile1) detailed in section 4.3.3.

Table 4.12 Proportions of the constituent materials

Batch Code	Fly Ash [w_t %]	Microsilca [w_t %]	Sand [w_t %]	Water Glass [w_t %]
M 0	25	0	65	10
M 5	24.5	0.5	65	10
M 10	24	1.0	65	10
M 25	22.5	2.5	65	10
M 50	20	5.0	65	10
M 100	15	10.0	65	10

Bach code key:

M - microsilica

4.3.4.4 Series 3: Influence of compaction method

Pressure compaction [47] has been used before with concrete and results in increased strength especially when using low water /cement ratios. Owing to the fact that the mixes produced in this investigation have low water/binder ratios and high consistency it is appropriate to use the pressure compaction method which is detailed in section 4.3.3. In order to determine the optimum compaction pressure, four different levels were employed: 0 N/mm^2, 10 N/mm^2, 20 N/mm^2 and 30 N/mm^2 as shown in Table 4.13. After casting and compacting all four batches were subjected to thermal curing conditions (profile 1) detailed in section 4.3.3. A constant proportion of the constituent materials was used in these series (Table 4.14). Fly ash from Ratcliffe power plant and sand from Belmoore quarry were used.

Table 4.13 Batches used to study the influence of compacting pressure

Batch Code	Compaction pressure [N/mm^2]
CP 0	0 (hand compaction)
CP 10	10
CP 20	20
CP 30	30

Table 4.14 Proportion of the constituent materials

Batch Code	Fly Ash [w_t %]	Microsilca [w_t %]	Sand [w_t %]	Water Glass [w_t %]
CP 0	20	5	65	10
CP 10	20	5	65	10
CP 20	20	5	65	10
CP 30	20	5	65	10

4.3.4.5 Series 4: Influence of fineness of sand

High silica sands from six quarries were used to study the effect of fineness of sand and silica content on the properties of alkali activated fly ash materials. Their, particle size and shape are presented in Table 4.15. Further details of their grading curves and chemical composition are presented in Chapter III. All six batches were cast and compacted using the pressure compaction method (compaction pressure 20 N/mm^2) and subsequently subjected to the thermal curing (profile 2) detailed in Section 4.3.3. A constant proportion of the constituent materials was used in these series as presented in Table 4.16. Fly ash from Ratcliffe power plant was used.

Table 4.15 Batches used to study the influence of fineness of sand

Batch Code	Source of sand	Average grain size [μm]	Grain shape
BR	Belmoore (coarse sand)	medium	variable
RH110	Redhill 110 (fine sand)	110	Angular
CH 80	Chelford 80 (fine sand)	160	Rounded
CH 95	Chelford 95 (fine sand)	130	Semirounded
CO 80	Congleton 80 (fine sand)	170	Rounded
CO 95	Congleton 95 (fine sand)	145	Semirounded

Bach code key:

BR - sand from Belmoore quarry,

RH - sand from Redhill quarry,

CH8O, CH95 - sand from Chelford quarry,

CO80, CO95 - sand from Congleton quarry.

Table 4.16 Proportion of the constituent materials

Batch Code	Fly Ash [w_t %]	Microsilca [w_t %]	Sand [w_t %]	Water Glass [w_t %]
BR	20	5	65	10
RH110	20	5	65	10
CH 80	20	5	65	10
CH 95	20	5	65	10
CO 80	20	5	65	10
CO 95	20	5	65	10

4.3.4.6 Series 5: Influence of slag

Ground granulated blast furnace slag from five UK steel plants was used. The particle size varied from 436 to 466 m^2/kg (see section 4.3.1). Six batches of mixes were cast and compacted using the pressure compaction method ii (compaction pressure 20 N/mm^2). Thermal curing condition (profile 2) was used. The proportions of the constituent materials used in these batches are given in Table 4.17. Fly ash from Ratcliffe power plant and sand from Congleton quarry (Congleton 80) were used.

Table 4.17 Proportion of the constituent materials

Batch Code	Fly Ash [w_t %]	Microsilca [w_t %]	Slag [w_t %]	Sand [w_t %]	Water Glass [w_t %]
RT	20	5	nil	64	11
Ca	20	5	10	54	11
Sc	20	5	10	54	11
Te	20	5	10	54	11
Ll	20	5	10	54	11
Pu	20	5	10	54	11

Bach code key:

RT - fly ash from Ratcliffe power plant,

Ca - Calumite slag,

Sc - slag from Scunthorpe power plant,

Te - slag from Teesside power plant,

Ll - slag from Llanwern power plant,

Pu - slag from Purfleet power plant,

In order to study the effect of slag content on the properties of alkali activated materials, different proportions were investigated as shown in Table 4.18 The pressure compaction method (compaction pressure 20 N/mm^2) was used. Both the ambient curing condition (20°C and 65% RH) and thermal curing condition (profile 2) described in section 4.3.3 were used for the batches as outlined in Table 4.19.

Table 4.18 Proportion of the constituent materials

Batch Code	Fly ash wt[%]	Silica Fume wt[%]	Slag wt[%]	Sand wt[%]	Water Glass wt[%]
Te A	20	5	10	54	11
TeA1	19	5	15	50	11
TeA2	17	5	17	50	11
TeA3	15	5	15	54	11
Te H	20	5	10	54	11
TeH2	17	5	17	50	11

Bach code key:

A - air curing (20°C and 65% RH),

H - thermally cured (profile 2).

Table 4.19 Curing conditions of batches used to study the influence of slag content

Batch Code	Curing Condition
TeA	20°C and 65% RH
TeA1	20°C and 65% RH
TeA2	20°C and 65% RH
TeA3	20°C and 65% RH
TeH	thermal treatment (profile 2)
TeH2	thermal treatment (profile 2)

4.3.4.7 Series 6: Influence of PC clinker

Ground Portland cement clinker as an additive to alkali activated materials is quite different from Portland cement because the latter contains gypsum which neutralises alkali compounds. This study investigated the effect of 1% addition of clinker on the properties of alkali activated fly ash materials. Four batches of mixes were cast and compacted using the pressure compaction method (compaction pressure 20 N/mm^2).

Both the ambient curing condition (20°C and 65% RH) and thermal curing condition (profile 2) described in section 4.3.3 were used for the batches as outlined Table 4.20. The proportions of the constituent materials used are presented in Table 4.21. Fly ash from Ratcliffe power plant and sand from Congleton quarry (Congleton 80) were used.

Table 4.20 Batches used to study the influence of ground Portland cement clinker

Batch Code	Curing Condition
TeCA1	20°C and 65% RH
TeCA2	20°C and 65% RH
TeCA3	20°C and 65% RH
TeCH2	thermal treatment (profile 2)

Table 4.21 Proportion of the constituent materials

Batch Code	Fly ash wt[%]	Silica Fume wt[%]	Slag wt[%]	Clinker wt [%]	Sand wt[%]	Water Glass wt[%]
TeCA1	19	5	14	1	50	11
TeCA2	16.5	5	16.5	1	50	11
TeCA3	15	5	14	1	54	11
TeCH2	16.5	5	16.5	1	50	11

Bach code key:

A - air curing (20°C and 65% RH),

H - thermally cured (profile 2),

C-Portland cement clinker.

4.3.4.8 Series 7: Influence of water glass hardeners

The aim of series 7 was to determine the effectiveness of air curing (20°C and 65% RH) and thermal curing (profile 2) to produce high performance alkali activated materials. In addition, the effectiveness of hardeners in providing optimum curing by reducing the need for thermal curing was investigated. Aluminium phosphate hardeners, detailed in section 4.3.1, were selected for the investigations. Two categories of mixes were used, with and without slag addition, details of which are given in Table 4.22. For each group of mixes representing a particular slag (or no

slag) one set of specimens was made without hardener to act as a control. The remaining batches of each group contained one of the hardeners: K Bond#80, K Bond#90 and K Bond#200. The hardener was added as percentage by weight of the sodium silicate solution. It was made into a slurry with water before adding it to the mix as this aided its dispersion. All batches used the pressure compaction method (compaction pressure 20 N/mm^2). The curing conditions are given in and detailed in section 4.3.3. The proportions of the constituent materials are given in Table 4.23. Fly ash from Ratcliffe power plant and sand from Congleton quarry (Congleton 80) were used.

Table 4.22 Batches used to study the influence of hardener

Group	Batch Code	Source of ggbs	Type of hardener	Curing Condition
I	**A**	no slag	no hardener	20°C and 65% RH
I	**H**	no slag	no hardener	thermal treatment (profile 2)
I	**B1**	no slag	KB 80	20°C and 65% RH
I	**B2**	no slag	KB 90	20°C and 65% RH
I	**B3**	no slag	KB 200	20°C and 65% RH
II	**SA**	Scunthorpe	no hardener	20°C and 65% RH
II	**SH**	Scunthorpe	no hardener	thermal treatment (profile 2)
II	**SAB1**	Scunthorpe	KB 80	20°C and 65% RH
II	**SAB2**	Scunthorpe	KB 90	20°C and 65% RH
II	**SAB3**	Scunthorpe	KB 200	20°C and 65% RH
II	**SHB3**	Scunthorpe	KB 200	thermal treatment (profile 2)
III	**CtA**	Calumite	no hardener	20°C and 65% RH
III	**CtH**	Calumite	no hardener	thermal treatment (profile 2)
III	**CtAB1**	Calumite	KB 80	20°C and 65% RH
III	**CtAB2**	Calumite	KB 90	20°C and 65% RH
III	**CtAB3**	Calumite	KB 200	20°C and 65% RH
IV	**LA**	Llanwern	no hardener	20°C and 65% RH
IV	**LH**	Llanwern	no hardener	thermal treatment (profile 2)
IV	**LAB1**	Llanwern	KB 80	20°C and 65% RH
IV	**LAB2**	Llanwern	KB 90	20°C and 65% RH
IV	**LAB3**	Llanwern	KB 200	20°C and 65% RH
IV	**LHB3**	Llanwern	KB 200	thermal treatment (profile 2)

Bach code key:

A - air curing (20°C and 65% RH)

H - thermally cured (profile 2),

B - mix containing water glass hardener,

B1 - water glass hardener Aluminium Thriphosphate compound (K-Bond # 80),

B2 - water glass hardener Aluminium Methaphosphate compound (K-Bond # 90),

B3 - water glass hardener Aluminium Orthophosphate compound (K-Bond # 200),

Ct - Calumite slag,

S - slag from Scunthorpe power plant,

L-slag from Llanwern power plant.

Table 4.23 Proportion of the constituent materials

Group	Batch Code	Fly Ash [w_t %]	Slag [w_t %]	Micro silica [w_t %]	Sand [w_t %]	Water Glass [w_t %]	Hardener [w_t %]
I	A	20	-	5	64	11	-
I	H			5	64	11	-
I	B1	20	-	5	61.8	11	2.2
I	B2	20	-	5	61.8	11	2.2
I	B3	20	-	5	61.8	11	2.2
II	SA	20	10	5	54	11	-
II	SH	20	10	5	54	11	-
II	SAB1	20	10	5	51.8	11	2.2
II	SAB2	20	10	5	51.8	11	2.2
II	SAB3	20	10	5	51.8	11	2.2
II	SHB3	20	10	5	51.8	11	2.2
III	CtA	20	10	5	54	11	-
III	CtH	20	10	5	54	11	-
III	CtAB1	20	10	5	51.8	11	2.2
III	CtAB2	20	10	5	51.8	11	2.2
III	CtAB3	20	10	5	51.8	11	2.2
IV	LA	20	10	5	54	11	-
IV	LH	20	10	5	54	11	-
IV	LAB1	20	10	5	51.8	11	2.2
IV	LAB2	20	10	5	51.8	11	2.2
IV	LAB3	20	10	5	51.8	11	2.2
IV	LHB3	20	10	5	51.8	11	2.2

4.3.4.9 Series 8: Influence of silica modulus of water glass

In order to investigate the effect of silica modulus on the properties of alkali activated fly ash materials, sodium silicate solutions (water glass) with different values of silica modulus (n) were used as shown in Table 4.24. The values of n ranged from 0.9 to

2.06, Sodium silicate solutions with silica modulus n ≤ 1 are not commercially available. Therefore, a water glass with a mean molar ratio (silica modulus) SiO_2: NaO_2 = 1.65 was modified by the addition of 12.5 NaOH (technical grade) to produce water glass with silica modulus of 0.5, 0.7, 0.8, 0.9, 1, 1.1 as detailed in Chapter III. A constant proportion of the constituent materials was used in these series (see Table 4.24). Materials used were fly ash from Ratcliffe power plant, ggbs from Purfleet power plant and sand from Congleton quarry (Congleton 80).

All batches were cast using the pressure compaction method (compaction pressure 20 N/mm^2) and subsequently subjected to thermal curing (profile 2) as detailed in section 4.3.3.

Table 4.24 Proportions of the constituent materials and silica modulus of water glass

Batch	Silica modulus	Water Glass wt[%]	Fly ash wt[%]	Slag wt[%]	Silica Fume wt[%]	Sand wt[%]
WG09	0.9	11	17	17	5	50
WG10	1.0	11	17	17	5	50
WG11	1.1	11	17	17	5	50
WG15	1.5	11	17	17	5	50
WG206	2.06	11	17	17	5	50

4.4 TESTING PROGRAMME

4.4.1 Density

Three specimens (prisms 10x25x125 mm) from each mix (batch code) were tested in accordance with BS 1881: Part114[132], to determine the density, ρ, of the hardened material.

$$\rho = \frac{m}{V} \quad [kg/m^3] \qquad \text{Equation 4.1}$$

where:

m is the mass of the specimen in air [kg],

V is the volume of the specimen calculated from its dimensions [m^3],

$V = b \times d \times L$

L is the length of the specimen [mm],

b is the breath of the specimen [mm],

d is the depth of the specimen [mm].

4.4.2 Physical Properties

Density (bulk and apparent solid), water absorption, apparent porosity and coefficient of saturation of the alkali activated fly ash materials were determined. The top pan method was used to calculate the porosity, density (bulk and apparent solid) and percentage water absorption according to BS 3921, 1974[133]. The standard procedure was to first dry the cube specimens (50mm) at age 28-35 days in a fan assisted oven at 103 ± 2°C for 24 hours or until they showed constant mass. The specimens were then taken out of the oven and left to cool in the laboratory environment (20°C, 65% RH). for approximately 12 hours. After cooling to (20°C, 65% RH), the specimens were weighed to give the dry mass, m_D [g], then placed in a vacuum chamber on a wire mesh base. Following this, the specimens were vacuum saturated according to BS 3921[133].

The pump of the vacuum chamber was started at 101 MPa pressure. When the pressure of 5 x 10^{-4} MPa was reached in the vacuum chamber, air-free water was allowed to cover the specimens and the samples were left submerged for a period of 10 minutes according to BS 3921[133].The mass of the saturated samples, m_S [g], was then measured, followed by the buoyed mass of the sample suspended in water, m_B [g]. A weighting balance, Mettler PL 1200, was used which was calibrated every 6 months against accurate standards.

The temperature of the water introduced in the vacuum chamber was recorded in order to make the necessary correction for the true density of water, which is temperature dependent. Table 4.25[134] presents the values for the density of air free water under normal atmospheric pressure (1atm). Linear interpolation is permitted between the values given in Table 4.25[134]. For the present investigations the

temperature of water in tests was 18.5°C, therefore, the corresponding true density, ρ_w, was 998.5025 [kg/m^3].

Table 4.25 Density of air free water [kg/m^3] at 1 atm pressure[134]

Temperature [°C]	Density [kg/m^3]
0	999.84
2	999.94
4	999.97
6	999.94
8	999.85
10	999.7
12	999.5
14	999.25
16	998.94
18	998.6
20	998.21
22	997.77
24	997.29
26	996.79
28	996.24
30	995.65

In order to determine the saturation and sorption coefficients, the test specimens were first dried in a fan assisted oven at 103 ± 2°C and then cooled to 20°C as detailed above. The dry mass of the samples was recorded, m_D [g].

The specimens were subsequently submerged in water for 24 hours under normal atmospheric pressure at 20°C. After 24 hours the samples were removed from the water, wiped with a damp cloth to remove excess water and then weighed in air to give the wet mass after 24 hours of water intake, m_{24}.

Total Volume

Total volume of solids and voids, V_T, is equal to the buoyed mass of the test specimen suspended in water, m_B, after correction for the true density of water, ρ_w.

$$V_T = \frac{m_B}{\rho_W} \quad [\text{cm}^3] \qquad \text{Equation 4.2}$$

Volume of Voids

Total volume of voids in the specimen, V_V, is calculated by subtracting the dry mass of the sample, m_D, (solids plus voids filled with air) from the saturated mass, m_S, (solids plus voids filled with water).

$$V_V = \frac{m_v}{\rho_w} \qquad \text{Equation 4.3}$$

where:

$m_V = m_S - m_D$ [kg]

$$\therefore V_V = \frac{m_S - m_D}{\rho_w} \ [\text{cm}^3] \qquad \text{Equation 4.4}$$

Volume of solids

Volume of solids in the specimen, V_S, is calculated by subtracting the volume of voids, V_V, from the total volume, V_T.

$V_S = V_T - V_V$ [cm^3] Equation 4.5

Bulk Density

Bulk density, ρ_{Bulk}, is the mass of the whole material per unit volume, reflecting the density of the mineralogical content of the material and the amount of pore spaces. It is usually specified as mass per unit volume e.g. g/cm^3 or kg/m^3.

$$\rho_{Bulk} = \frac{m_D}{V_T} \qquad \text{Equation 4.6}$$

Substituting for V_T from equation 4.2 gives:

$$\rho_{Bulk} = \frac{m_D}{m_B / \rho_W} \ [\text{g/cm}^3] \qquad \text{Equation 4.7}$$

Apparent Solid Density

Apparent solid density $\rho_{Apparent\ Solid}$ is the density of the solids in a material, which is due purely to the mineralogical components of the material. It is usually specified as mass per unit volume e.g. g/cm^3 or kg/m^3. However using the vacuum saturation method, the measurement of the volume of the sealed pores is impossible.

Picnometry is the only method which can calculate the true solid density of the material. Therefore, the solid density determined in this investigation is not the true solid density of the material but the apparent solid density.

$$\rho_{Apparent\ Solid} = \frac{m_D}{V_S} \qquad \text{Equation 4.8}$$

Substituti ng for V_s from equation 4.5 gives :

$$\rho_{Apparen\ Solid} = \frac{m_D}{V_T - V_V}\ [\text{g/cm}^3] \qquad \text{Equation 4.9}$$

where:

m_D is the mass of the dry sample [g],

V_S is the total volume of solids [cm^3].

Apparent Porosity

Apparent porosity, p [%], is the amount of voids expressed as a percentage of the total volume V_T and is given by the expression.

$$p\,[\%] = \frac{V_V}{V_T} \cdot 100 \qquad \text{Equation 4.10}$$

Substituting for V_V from equation 4.5 gives :

$$p\,[\%] = \frac{V_T - V_S}{V_T} \cdot 100 \qquad \text{Equation 4.11}$$

The porosity determined in the laboratory by vacuum saturation does not give any indication of the size and spatial distribution of the pores or the volume of sealed pores. Owing to these factors it is called the apparent porosity. The true porosity and pore structure can be determined by mercury intrusion porosimetry or scanning electron microscopy. Porosity has been used as the main parameter in determining the durability of materials in previous studies owing to the fact that it is responsible for the intake and transport of deleterious substances[134].

Water Absorption

Water absorption is the amount of water taken in by the material under normal temperature and pressure. Water absorption of each specimen was calculated as the

increase in mass resulting from submersion, expressed as a percentage of the mass of the dry specimen.

$$w_a = \frac{(m_S - m_D)}{m_D} \times 100 \ [\%] \qquad \text{Equation 4.12}$$

where:

w_a is the water absorption of the specimen [%],

m_S is the mass of the samples submerged in water [g],

m_D is the dry mass of the sample [g].

Coefficient of Saturation

Coefficient of saturation is the ratio of water taken into a material in 24 hours under normal atmospheric pressure at 20°C to the potential total amount which can be absorbed, based on percentage porosity. A ratio of 1 indicates that all the available pore spaces are filled with water under atmospheric pressure.

The coefficient of saturation was determined using the following equation according to BS 3921, 1974[133].

$$C_{saturation} = \frac{(m_{24} - m_D)}{(m_s - m_D)} \ [\%] \qquad \text{Equation 4.13}$$

where:

$C_{saturation}$ is the coefficient of saturation of the specimen [%],

m_{24} is the mass of the sample after 24 hours in water [g],

m_D is the dry mass of the specimen [g].

Coefficient of saturation is purely a measurement of the natural water intake into the material over a given (24 hours) period of time. Traditionally the saturation coefficient has been used by researchers to establish the likely performance of materials.

4.4.3 Modulus of Rupture

The ASTM Standard for Bending Tests[135] stipulates that the dimensions for the test specimen should be as shown in Figure 4.2.

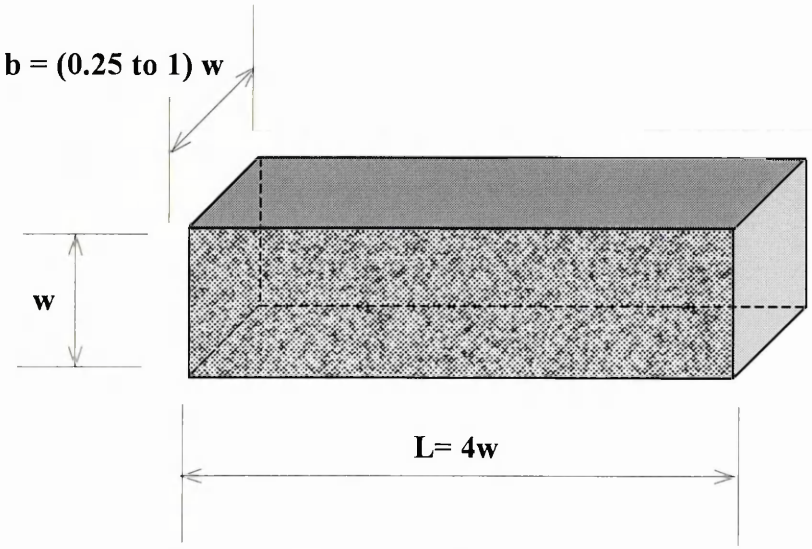

Figure 4.2 Standard dimensions for a bending test specimen[135]

10 mm x 25 mm x 100 mm prism specimens from each mix (batch code) listed in section 4.3.5 were tested in a three point bending test according to BS 1881: Part 118:1983[136], as shown in Figure 4.3. The specimens were placed in the machine centred with the longitudinal axis of the specimens at the right angles to the rollers. The mould filling direction was normal to the direction of loading. Preliminary tests were carried out using a 20kN capacity tensile testing machine manufactured by JJ Lloyd TK450Z. A x-y plotter (manufactured by Bryants Instruments) was connected to the testing machine and was used to record the load - defection chart. For a higher accuracy of the results a computer aided Hounsfield test machine with a 1 kN load cell (model H10KM) was used to determine the modulus of rupture. The load was applied in a displacement-controlled manner at a rate of 10 mm per minute. The results are presented in sections 4.5.5-4.5.8.

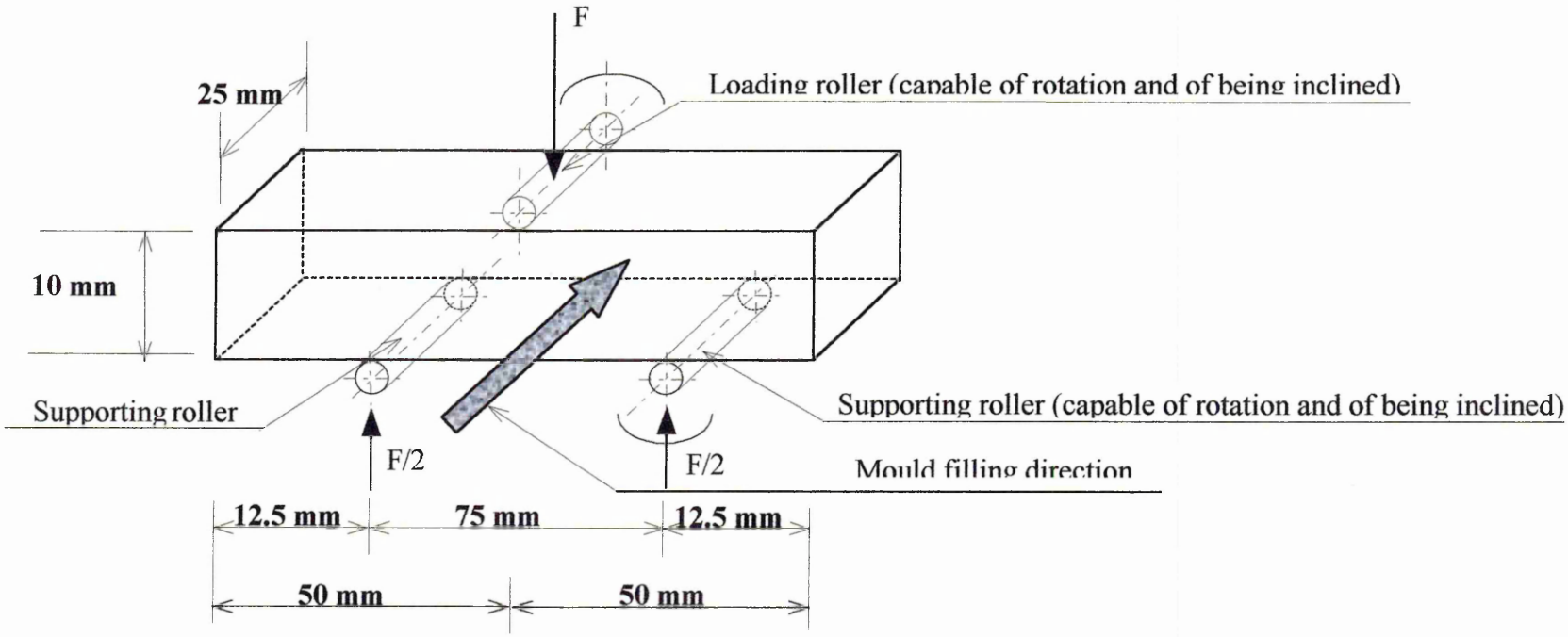

Figure 4.3 Arrangement of loading of test specimen (three point bending)

Four specimens from each batch of material were tested and the average values calculated. The modulus of rupture was calculated using following equation:

$$R_f = \frac{3FL}{2bw^2} \quad [\text{N/mm}^2] \qquad \text{Equation 4.14}$$

where:

F is the maximum transverse load, at which the material fractures [N],

L is the span [mm],

b is the with of the specimen [mm],

w is the thickness of the specimen [mm].

4.4.4 Compression Tests

50x50x50 mm specimens of each mix (batch code) listed in section 4.3.5 were tested in an Avery Dennison Compressive Testing Machine (model 7123-100 kN) in accordance with BS1881: Part 116: 1986[137]. The cubes were immersed in water for 5 minutes prior to testing to overcome the frictional forces between the surface of the test cube and the platen of the testing machine. Each test cube was centred on the lower platen of the compression machine ensuring that the load was applied on two opposite cast faces. The load was applied and increased steadily at a nominal rate of 500N/s according to BS1881: Part 116[137].

Compressive Strength was determined using the following equation:

$$R_c = \frac{F}{A} \quad [\text{N/mm}^2] \qquad \text{Equation 4.15}$$

where:

F is the maximum compressive load, at which the material fractures [N],

A is the cross-sectional area of the specimen [mm^2].

The compressive strength recorded for each type of material was the average of three cube specimens.

4.4.5 Freeze-Thaw Testing

It is impractical to determine the freeze-thaw resistance of a cementitious material by exposing it to natural freeze-thaw cycles, although it is probably the most reliable test method, owing to the fact that the test duration would be too long. Therefore, accelerated freeze-thaw testing is necessary to assess the durability of the material within a reasonable time.

The freeze - thaw test apparatus used in the present investigation consists of a chamber together with the necessary refrigerating and heating equipment and controls as shown in Figure 4.4. It produces continuously and automatically reproducible freeze - thaw cycles within specified temperature ranges. The freeze-thaw chamber is 1.9m x 2.0m x 1.2m high (external dimensions). The outer skin has a 80 mm thick insulation between external (ambient) and internal conditions. An inspection hatch allows access for inspection during temperature cycling, to record damage to the specimens or to transfer specimens to the laboratory for weighing.

Figure 4.4 The freeze-thaw chamber and computer controls

4.4.5.1 Temperature Cycle

The duration of any component part of the freeze - thaw cycle can be altered. The standard[138] BCRA (British Ceramics Research Association) cycle comprises of 132 minutes of freezing at -15°C, 20 minutes of thawing at temperatures up to 25°C followed by 2 minutes of water spray (at 4°C) to replace the water lost by evaporation and 3 minutes of drain[138]. Using this test cycle, it is possible to have a little over nine cycles per day.

In order to allow inspection at regular intervals, the cycle used in this study varied slightly from the BCRA cycle, allowing eight freeze-thaw cycles per day. The duration of the freezing and thawing cycle was 115 minutes and 45 minutes respectively, followed by 10 minutes rain and 10 minutes to allow excess water to drain away. Rain water was chilled to 4°C before being allowed to come in contact with the frozen specimen surfaces in order to prevent thermal shock. The specimens were subjected to a total of 50 freeze-thaw cycles in 150 hours. The nominal freeze-thaw cycle used in this investigation consisted of alternatively lowering the temperature of specimens from +25°C to -15°C and raising it from -15°C up to +25°C. Temperature and humidity were monitored using a Solatron data logger as shown in Figure 4.5. The cycles selected provided complete freezing and thawing of the test specimen due to the small specimen size and moderate freezing ad thawing rates

The salient features of the profile are a steady rate of change of temperature on the freeze down cycle and maintenance of a constant temperature for a pre-set length of time; a steady thaw rate to a pre-set temperature and the maintenance of that temperature. One of the limitations of the equipment used in this investigation is that there is no control over the rate of freezing or thawing. The feedback from the computer controls is related to the final pre-set temperatures, which control the inputs to the system.

Figure 4.5 Temperature and humidity monitoring equipment

4.4.5.2 Testing Technique

The prism test specimens (10x 25x 100 mm) were immersed in water (at 20°C) for 48 hours prior to being subjected freeze-thaw cycles. Omnidirectional freezing was carried out by placing the specimens on a wire tray which was elevated from the metal floor of the chamber to allow drainage and to prevent thermal bridging.

A visual inspection of the specimens was recorded during the test. At the end of the 50 freeze and thaw cycles, the specimens were removed from the chamber and left to dry out at ambient temperature until their mass was constant. Three prisms from each mix (batch code) listed in section 4.3.5 were used to determine the residual modulus of rupture after 50 freeze and thaw cycles. Consequently, the residual modulus of rupture of each batch is an average of three measurements. The residual modulus of rupture was expressed as a percentage of the modulus of rupture of the corresponding prism specimens which were not subjected to freeze-thaw testing.

4.4.6 Choice of test specimens

A great number of parameters were investigated in this study which required a large number of specimens. The primary objective is to determine the relative properties of the different batches of materials and to determine the relative influence of different parameters considered (proportion of constituent materials, curing conditions etc). Consequently the use of relatively small test specimen sizes was considered acceptable and hence 10x25x100 mm prisms and 50mm cubes specimens were used. It is important that the properties are derived from same specimen size in order to exclude the influence of size effect on the results[81].

For each mix (batch code) 3 cubes and 10 prisms were prepared and the sample numbers used for different test are as follows:

Compressive tests:	3 cubes
Modulus of rupture:	4 prisms
Freeze and thaw tests:	6 prisms

4.5 RESULTS AND DISCUSSION

4.5.1 Influence of chemical composition of fly ash

The chemical compositions of the fly ashes, given in Table 4.1 (section 4.3.1) show that all fly ashes used in this study fall into class F of fly ashes i.e. (SiO_2+Al_2O_3+FeO_3) content no less than 70% and CaO content up to 5% conforming to ASTM C618[5]. The CaO content of the investigated fly ashes varied from 1.5% for Ferrybridge fly ash to 3.3% for Ratcliffe fly ash.

The proportion of the fly ash was kept constant in the mixes (20% by weight) but the type of fly ash was varied. All mixes were hand compacted and thermally cured (profile 1) as detailed in section 4.3.3. The detailed description of the mixes considered in this section is presented in Table 4.11, section 4.3.4.

Figure 4.6 shows the modulus of rupture and density of alkali activated materials containing fly ash from different UK power plants. The densities are all within 10% of

each other. However, Ratcliffe fly ash produced the most dense material followed by Ferrybridge fly ash and West Burton fly ash. The alkali activated fly ash from Ratcliffe produced the highest modulus of rupture, followed by the mix with West Burton fly ash. The mix with Ferrybridge fly ash was the weakest. These results follow the same trend when converted to specific strength (strength divided by density) as seen in Table 4.26. Using the chemical composition of fly ashes to try to explain the varying strengths of the fly ash mixes has proved to be difficult. Depending on their source, fly ashes have different contents of Na_2Oe. Na_2Oe is the sum of Na_2O and $0.658K_2O$.The Na_2Oe content of the mixes is shown in Table 4.27. The Na_2Oe content has been shown to be a key factor in the activation of ggbs by sodium silicate solution[11,19,20,24,39]. However, the Na_2Oe content of the alkali activated fly ash materials investigated (Table 4.27) does not correlate well with the modulus of rupture. There appears to be a direct correlation between CaO content of the fly ash and modulus of rupture as shown in Table 4.27. This confirms much of the work in previous literature[2, 53] by showing that the free CaO content governs the modulus of rupture values. However, there is also a correlation with the Al_2O_3 content of the fly ashes and the modulus of rupture, although the variations in Al_2O_3 are small The best measure of the relationship between the modulus of rupture and chemical composition of fly ash is the quality coefficient which is given by the following equation[11] and takes into account more than one chemical element:

$$K= (CaO \times MgO \times Al_2O_3)/(SiO_2 + MnO + TiO) \qquad \text{Equation 4.16}$$

The values of K are listed in Table 4.27. They show a good correlation with the modulus of rupture. Previous work in current literature[7,12,53] suggested a link between the chemical composition of slags and the hydration products formed. The amounts of the different hydration products formed could account for the different strengths of the alkali activated fly ashes. This work suggests that it is both the Al_2O_3/SiO_2 and CaO/SiO_2 ratios of the mix that are important in defining the type and quantities of the hydration products formed. The Al_2O_3/SiO_2 and CaO/SiO_2 ratios are directly related to the quality coefficient K as presented in Table 4.27. The hydration products and their chemical composition are dealt with in detail in Chapter 8.

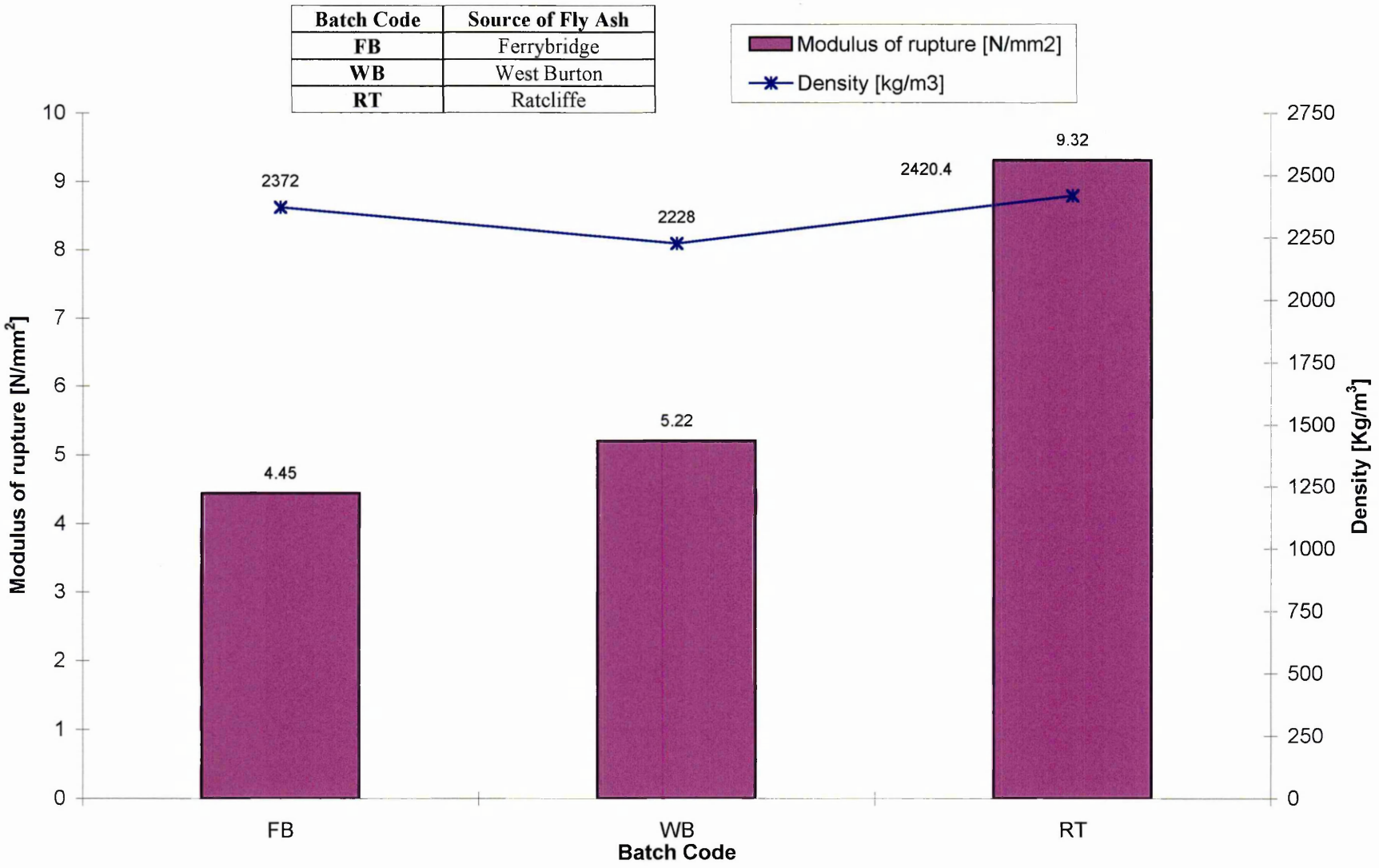

Figure 4.6 Modulus of rupture and density of alkali activated materials with fly ash from different UK sources

Table 4.26 Chemical composition and specific strength of mixes

Batch Code	Na_2O_e wt [%]	Al_2O_3/SiO_2	CaO/SiO_2	CaO/Al_2O_3	Modulus of rupture [N/mm^2]	Specific Strength [N m/kg]
FB	3.014	0.520	0.036	0.070	4.45	1870
WB	3.019	0.528	0.037	0.071	5.22	2340
RT	2.886	0.565	0.068	0.120	9.32	3850

Table 4.27 Chemical composition of fly ashes

Fly ash source	Al_2O_3	CaO	SiO_2	Na_2O_e wt [%]	Quality coef K
FB	24.20	1.50	49.90	3.95	0.548
WB	25.20	1.60	50.90	4.00	0.554
RT	25.60	3.30	47.40	3.40	0.645

4.5.2 Influence of microsilica

Microsilica is one of the most reactive pozzolanic materials because of its high amorphous silica content, 85% to 98 % (see Table 4.3, section 4.3.1) and high specific surface area (15-30 m^2/g). The proportion of the pozzolanic materials (fly ash plus microslica) was kept constant in the mixes (25 % by weight), but the amount of microsilica and fly ash was varied (Table 4.12, section 4.3.4). All six mixes were cast using hand compaction and thermally cured (profile 1).

Figure 4.7 shows the modulus of rupture and density of the alkali activated materials incorporating different amounts of microsilica. Microsilica addition produces higher modulus of rupture for dosage between 2.5% and 5%. For samples with more than 5% microsilica, the strength falls and for those with less than 2.5% microsilica the modulus of rupture is lower than that for material without microsilica, see Figure 4.8. The densities of these materials decrease with increasing microsilica content.

Batch Code	Microsilica [wt%]	Fly ash [wt %]
M0	0	25
M05	0.5	24.5
M10	1.0	24
M25	2.5	22.5
M50	5.0	20
M100	10.0	15

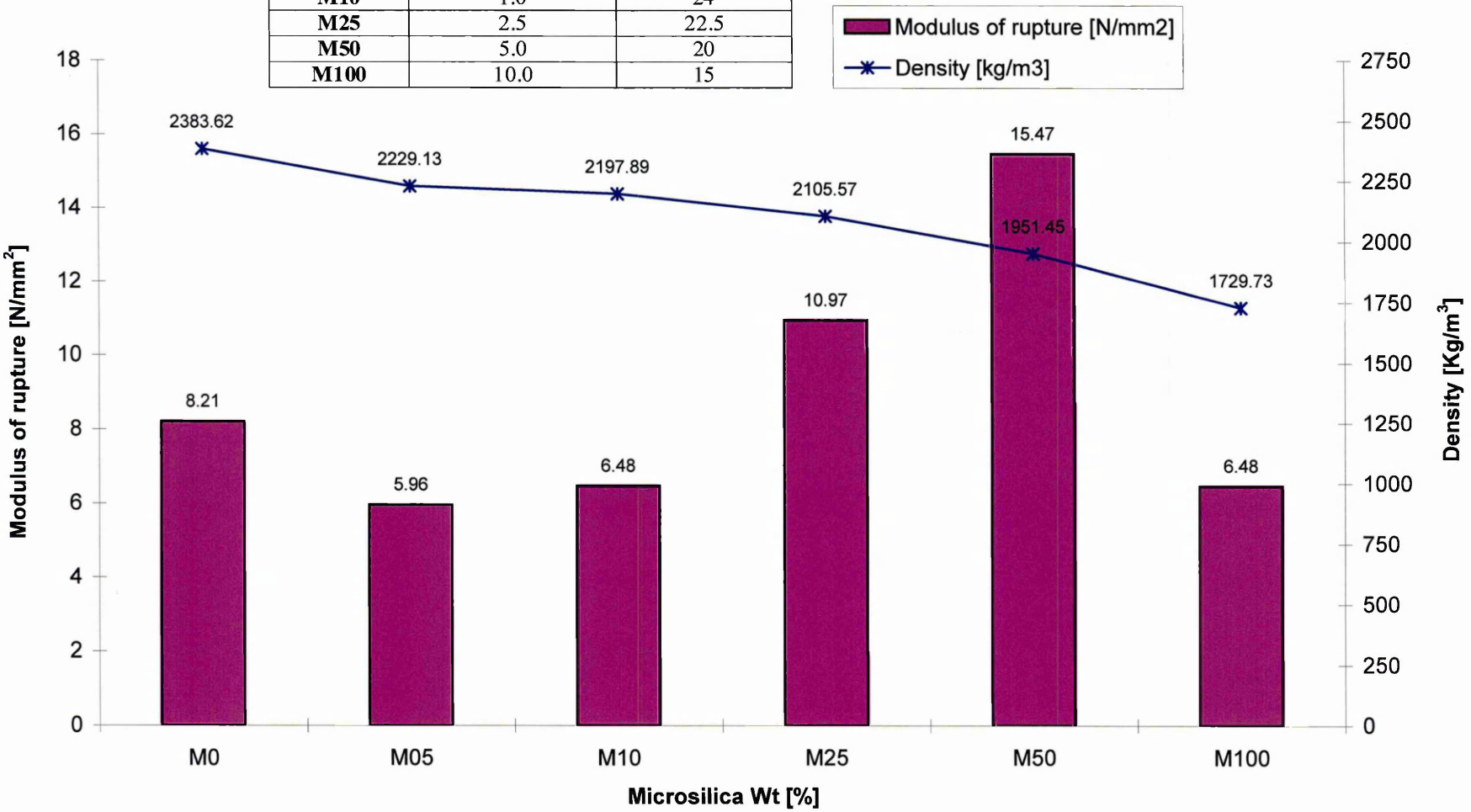

Figure 4.7 Modulus of rupture and density of alkali activated materials with different amounts of microsilica

It was also observed that on addition of microsilica, a convex shape appeared on the face of the specimen which was unrestrained by the mould walls, thereby making its appearance similar to a loaf of bread. This phenomenon will be discussed further in sections 4.5.3 and 4.5.5. The fracture surfaces of the flexural specimens containing silica fume had a more glassy appearance than those without silica fume.

Previous researchers[8, 12] have found that microsilica increases both the early age strength and density of the matrix. This is contrary to the lower densities exhibited by the alkali activated materials containing higher amounts of microsilica. The initial reaction would be the enhanced production of an expansive silica gel[8] since silica fume is known for its prompt pozzolanic reaction. This implies that it produces a more rapid reaction which could be enhanced during curing. An effect of the addition of micro-silica is that it will increase the CaO/Al_2O_3 ratio and lower the CaO/SiO_2 ratio as shown in Table 4.28. The lowering of CaO/SiO_2 determines which types of hydration products form, and results in an increase in the formation of R_2O n Al_2O_3 x SiO_2 n H_2O (zeolites)[12]. The addition of ground granulated blast furnace slag with its higher CaO content may serve to reduce the expansive hydration products by increasing the CaO/SiO_2 ratio. This would allow the production of more of the standard calcium silicate (C-S-H) gel, but the influence on strength is uncertain.

Table 4.28 Chemical composition, density and strength of alkali activated materials containing microsilica

Batch Code	Na_2O_e content wt [%]	CaO/SiO_2	Al_2O_3/SiO_2	CaO/Al_2O_3	Density [Kg/m^3]	Modulus of rupture [N/mm^2]
M 0	2.886	0.068	0.565	0.120	2383.62	8.21
M 5	2.884	0.066	0.550	0.120	2229.13	5.96
M 10	2.881	0.065	0.536	0.121	2197.89	6.48
M 25	2.874	0.060	0.494	0.121	2105.57	10.97
M 50	2.863	0.053	0.430	0.122	1951.45	15.47
M 100	2.839	0.040	0.322	0.125	1729.73	6.48

It is clear from literature[12, 19-21] that a low CaO/SiO_2 ratio will prevent the formation of large amounts of the C-S-H hydration product. A high SiO_2 content and high CaO/Al_2O_3 ratio will encourage the formation of hydration products of the zeolitic form [R_2O n Al_2O_3 x SiO_2 n H_2O]. The formation of these products in preference to the C-S-H gel could be the reason for higher strengths with microsilica addition. Too high dosages of microsilica could result in Na_2O dropping below the level required for optimum activation, Table 4.28. This could account for the peak in modulus of rupture around the 5% microsilica addition. Other researchers[129] have investigated the addition of microsilica to alkali activated materials and reached the same conclusion that the optimum amount is approximately 5% (by weight).

4.5.3 Influence of compaction

Detailed description of mixes (batch codes) considered in this section is given in Tables 4.13 and 4.14 section 4.3.4. The materials were cast using pressure compaction method and thermally cured (profile 2). Figure 4.8 shows the effect of different compaction pressures on modulus of rupture and density of the alkali activated materials. It indicates that as compaction pressure rises above $10N/mm^2$, the modulus of rupture increases. However, the density decreases at very high compaction pressures and the convex surface effect was also observed to increase. Pressure compaction[47] has been used before with concrete and results in increased strength especially when using low water/ cement ratios. The layers of unhydrated cement paste in concrete are surrounded by thin layers of hydrated paste (gel) and the pressure compaction consolidates the mix. In concrete the binding gel occupies twice the volume of the unhydrated material. If a similar effect occurs in the alkali activated materials, compaction would consolidate the mix as well as reducing the amount of unreacted material. This would produce more hydrated fly ash and microsilica, resulting in more expansion and, therefore, lower density. Thermal curing would increase the reaction. The convex shape is caused by the expansion of air bubbles in the paste, the thermal expansion of the air is approximately two orders of magnitude greater than that of the surrounding material.

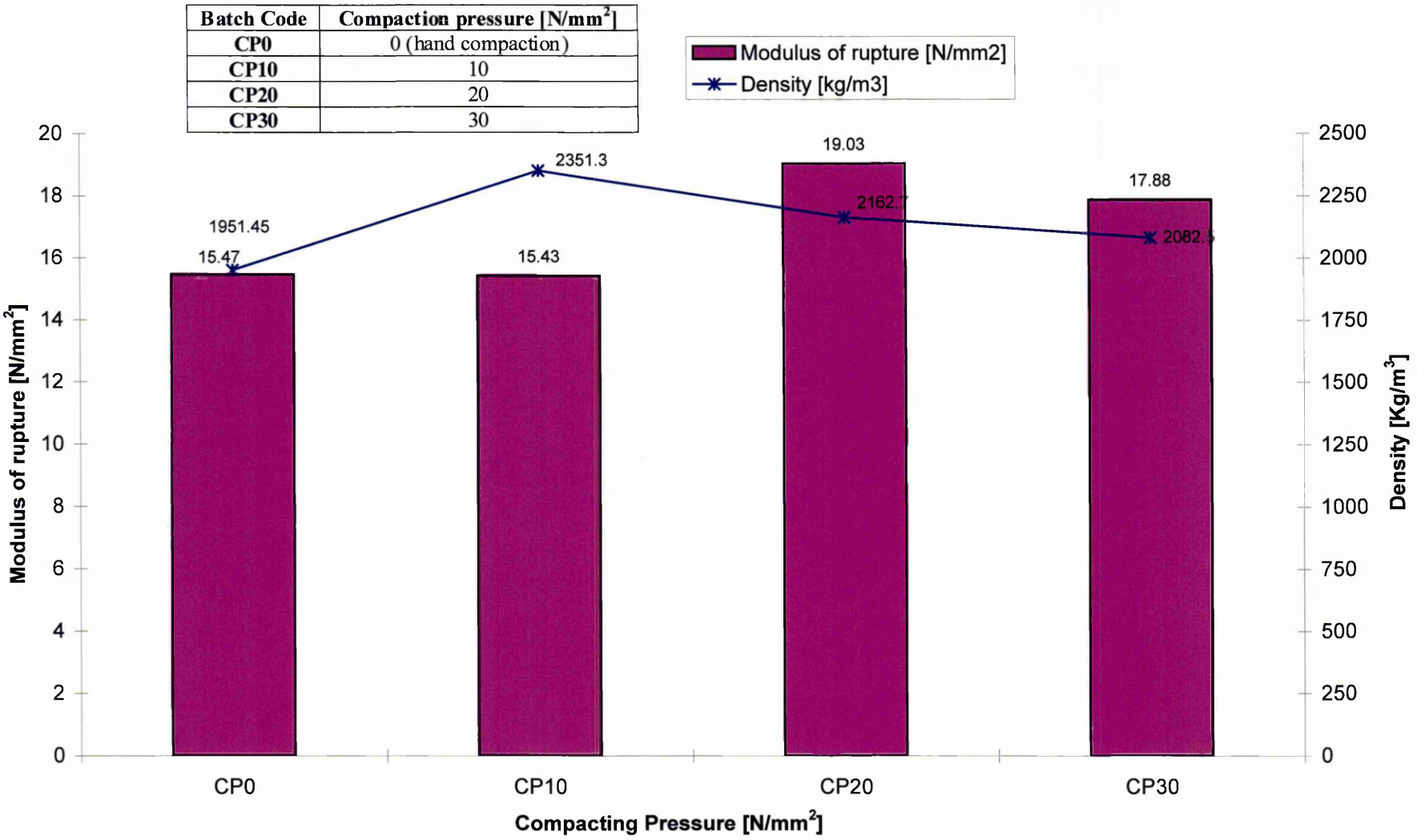

Figure 4.8 Modulus of rupture and density of alkali activated materials compacted using different compacting pressure

The expansion of air bubbles is restrained on both sides by the steel mould so that the air is put under pressure and the only way to escape is top surface. This pressure induces the dome appearance of the specimen, thereby increasing the porosity of the material and decreasing the density. Silica fume also seems to play an important role. The addition of silica fume seems to enhance this dome formation.

4.5.4 Influence of the fineness of sand

All six mixes considered in this section were cast using the pressure compaction method (compaction pressure 20 N/mm^2) and subsequently subjected to the thermal curing (curing profile 2) as detailed in section 4.3.3. The detailed description of mixes (batch codes) is presented in Table 4.16, section 4.3.4. Fly ash from Ratcliffe power plant was used.

Figure 4.9 shows the effect of different sands on the modulus of rupture and density. The type of sand used appears to have little effect on the modulus of rupture of alkali activated materials except for mixes made with sand from Chelford quarry (CH 80). The density of materials produced were all within 10% of each other. The different sands were very similar in chemical composition but varied in size and particle shape. The Chelford CH80 sand, with rounded particle shape and 165 micron average grain size produced the best results. Congleton 80 sand was next and also has rounded particle shape of about 170 microns. The results of the other sand were similar. The other sands have varying particle sizes from 110 microns for Redhill 110 sand, 130 microns for Chelford 95 sand, and 145 microns for Congleton 95 sand. The particle shapes were sub rounded except Redhill sand particles which were angular. The coarse sand Belmoor (BL) produced the lowest modulus of rupture.

There seems to be no apparent reason based on chemical composition for one sand performing better than another except that the mix with Redhill sand which has the lowest Na_2Oe content (Table 4.29) and also the lowest modulus of rupture produced by the fineness of the sands.

Batch Code	Source of sand	Grain size [μm]
BL	Belmoore (coarse sand)	medium
RH110	Redhill 110 (fine sand)	110
CH 80	Chelford 80 (fine sand)	160
CH 95	Chelford 95 (fine sand)	130
CO 80	Chongleton 80 (fine sand)	170
CO 95	Congleton 95 (fine sand)	145

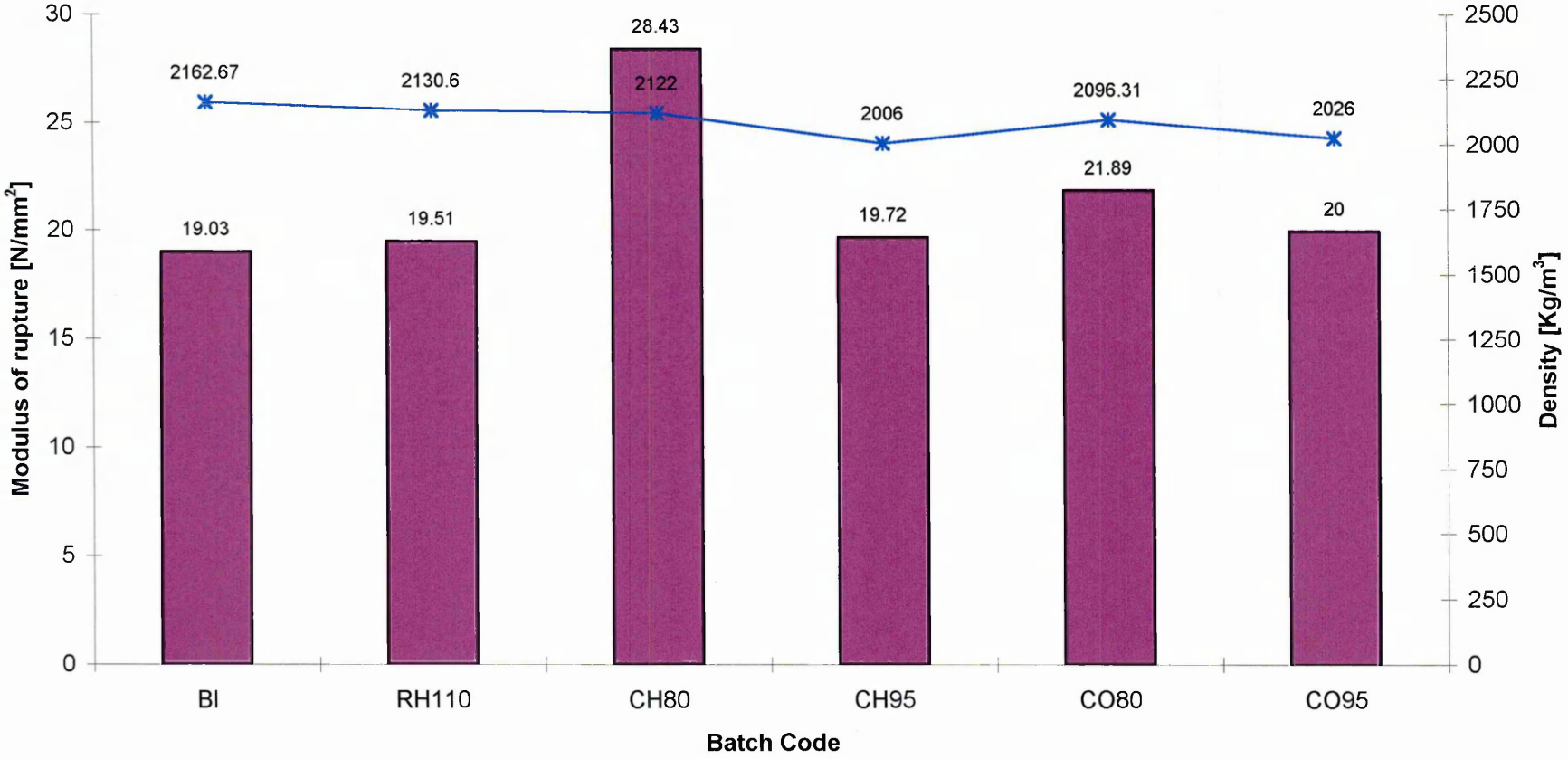

Figure 4.9 Modulus of rupture and density of alkali activated materials with sands from different sources

Table 4.29 Na_2O content of the samples made with high silica fine sands

Batch Code	Na_2O_e
BL	3.008
RH110	2.534
CH80	3.162
CH95	3.199
CO80	3.199
CO95	3.292

More detailed analysis of the sands may reveal differences in the form of the major compounds, such as the form of SiO_2. However, since the sands come from similar geological deposits they are likely to be chemically similar. It does seem that a combination of particle size and shape may play a role, with the rounded particles of Chelford 80 sand and Congleton 80 sand performing slightly better and the finer particles of Chelford 80 sand giving the best performance. It is difficult at this stage to develop a reason beyond the physical differences such as the increased surface area of the Chelford 80 sand.

4.5.5 Influence of slag

The detailed description of mixes considered in this section is presented in Tables Tables 4.17 - 4.19, section 4.3.4. Fly ash from Ratcliffe power plant and Congleton quarry sand (CO 80) were used. All mixes were cast using pressure compaction method.

Ground granulated blast furnace slag has been found to have higher pozzolanic activity than fly ash[10,14, 19, 20]. The pozzolanic reaction is faster and slags have higher quality coefficients K (equation 4.16) than the fly ashes as shown Table 4.30. Five slags were investigated in this study, Calumite (Ca) and Scunthorpe (Sc), Teeside (Te), Llawernn (Ll) and Purfleet (Pu) steel plants. The addition of slag resulted in a higher density and an increase in modulus of rupture and compressive strength, Figures 4.10 and 4.11.

BatchCode	Source of ggbs	Specific surface area [m^2/kg]
RT	no slag	-
Ca	Calumite	see grading curve in chapter III
Sc	Scunthorpe	391
Te	Teesside	466
Ll	Llanwern	450
Pu	Purfleet	464

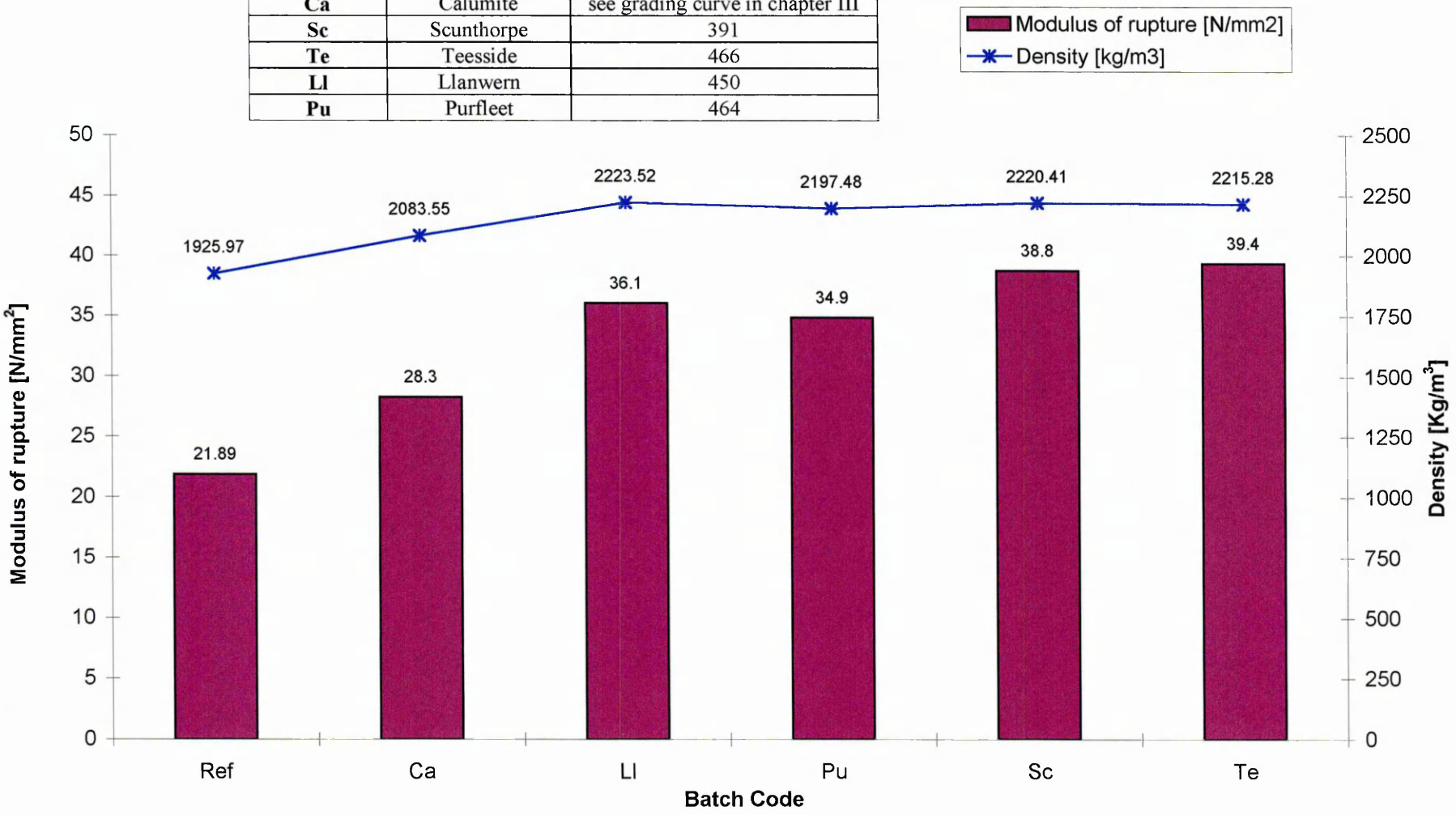

Figure 4.10 Modulus of rupture and density of alkali activated materials with ggbs from different UK sources

Batch Code	Fly ash wt[%]	Slag wt[%]	Curing condition
A (ref)	20	10	20°C and 65% RH
H (ref)	20	10	thermal treatment (profile2)
TeA	19	15	20°C and 65% RH
TeH	17	17	thermal treatment (profile2)

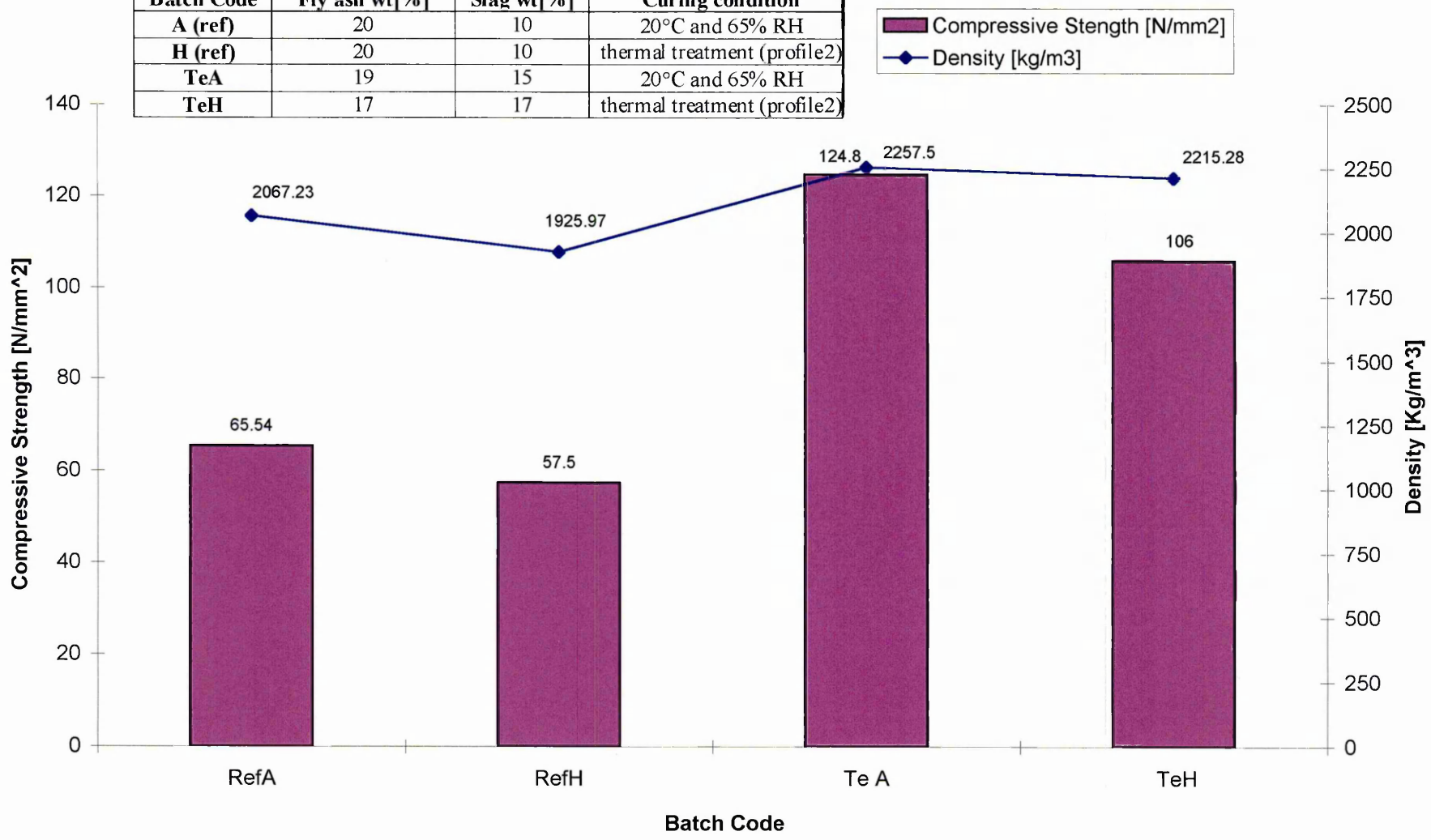

Figure 4.11 Compressive strength and density of alkali acttivated materials with slag addition

The Teeside slag produced the highest modulus of rupture (39.4N/mm^2). Excluding the coarse slag Calumite, the modulus of rupture achieved with the other slags were similar.

The quality coefficient K of ggbs does not correlate with the strengths as it did for fly ashes (see section 4.5.1). Teeside had one of the lowest quality coefficients K =1.733 but exhibited the highest modulus of rupture as shown in Table 4.30. Teeside slag also had amongst the lowest CaO content, 40.90% as shown in Table 4.30. The alkali activated material containing Teeside slag had the lowest Na_2O content. The best correlation between the chemical composition of slags and modulus of rupture appears to be with the Al_2O_3/SiO_2 and CaO/SiO_2 ratios of the slags (see Table 4.30). Scunthorpe and Teeside slags had the highest Al_2O_3/SiO_2 ratios and the lowest CaO/SiO_2 ratios of the finer slags (excluding Calumite). These result in an increase of the zeolite phase in the hydration products. A higher strength of the zeolite phases (R_2O n Al_2O_3 x SiO_2 n H_2O) than the calcium silicate hydrate phase (C-H-S) could account for these slags producing the highest strengths. However, Calumite slag also had similar levels of Al_2O_3/SiO_2 and CaO/SiO_2 to Tesside and Scunthorpe slags but produced the lowest strengths. Calumite is a coarse slag (see grading curve in Chapter III), and fineness has been shown to be very important in strength development. Teeside slag has the highest specific surface area, 466 Kg/m^3, of all five slags investigated and it gives the highest flexural strength. It is probable that a number of competing factors are at play in determining the optimum slag composition.

Table 4.30 Chemical composition of ggbs and strength of alkali activated materials containing slag

Batch Code	K of slag	Al_2O_3/SiO_2 of slag	CaO/SiO_2 of slag	CaO/Al_2O_3 of slag	Na_2O_e of mix wt [%]	Modulus of rupture [N/mm^2]
RT (Ref)	0.654	-	-	-	3.200	21.89
Ca	1.745	0.370	1.142	3.086	3.146	28.3
Sc	1.730	0.370	1.101	2.976	3.160	38.8
Te	1.733	0.380	1.147	3.018	3.130	39.4
Ll	1.765	0.320	1.238	3.869	3.141	36.1
Pu	1.788	0.327	1.209	3.697	3.133	34.9

The difference between slag and fly ash is its higher CaO content. It was postulated in section 4.5.2 that the addition of slag could reduce the amount of curvature on the surface of alkali activated specimens by producing a greater proportion of normal calcium silicate hydrate (C-S-H) gel, assuming the C-S-H gel to have a lower volume than the [R_2O n Al_2O_3 x SiO_2 n H_2O] hydration product of fly ashes. It was found that addition of slag did cure the curvature of the specimen surface. The addition of slag increased the flexural strength by up to 80% (see Figure 4.10) and almost doubled the compressive strength of the material (see Figure 4.11) irrespective of curing conditions used. The cube specimens tested in compression suffered an explosive failure.

Fine slag also improved the physical properties of the alkali activated fly ash materials (see Table 4.31). Water absorption and apparent porosity decreased by approximately 24% and 72% respectively. The coefficient of sorption increased by up to 47%. The reason for the different trends between the saturation coefficient and the apparent porosity results is that pore structure (size, shape and distribution of pores) can be different for each material. The water absorption and apparent porosity test do not give any indication of the size, shape or volume of sealed pores. The shape and size of pores, however, govern the rate at which the pores are filled with water and, therefore, will influence the coefficient of saturation.

Table 4.31 Physical properties of materials containing slag from different sources

Batch Code	Water Absorption	Apparent Porosity	Coeficient of Saturation	Solid Density
RT (Ref.)	12.67	24.40	0.33	2545.49
Ca	9.80	20.42	0.25	2618.27
Sc	6.79	15.08	0.52	2614.46
Te	6.65	14.74	0.48	2598.13
Ll	6.44	14.33	0.43	2595.32
Pu	7.75	17.03	0.51	2648.62

There seems to be an optimum level of slag addition of 10%. Increasing the slag content from 10% to 15% and 17% did not improve the modulus of rupture, whether thermally treated or cured under controlled conditions (20°C, 65%RH) as shown in Figure 4.12.

Batch Code	Fly ash wt[%]	Slag wt[%]	Curing condition
TeA	20	10	20°C and 65% RH
TeA1	19	15	20°C and 65% RH
TeA2	17	17	20°C and 65% RH
TeA3	15	15	20°C and 65% RH
TeH	20	10	thermal treatment (profile2)
TeH2	17	17	thermal treatment (profile2)

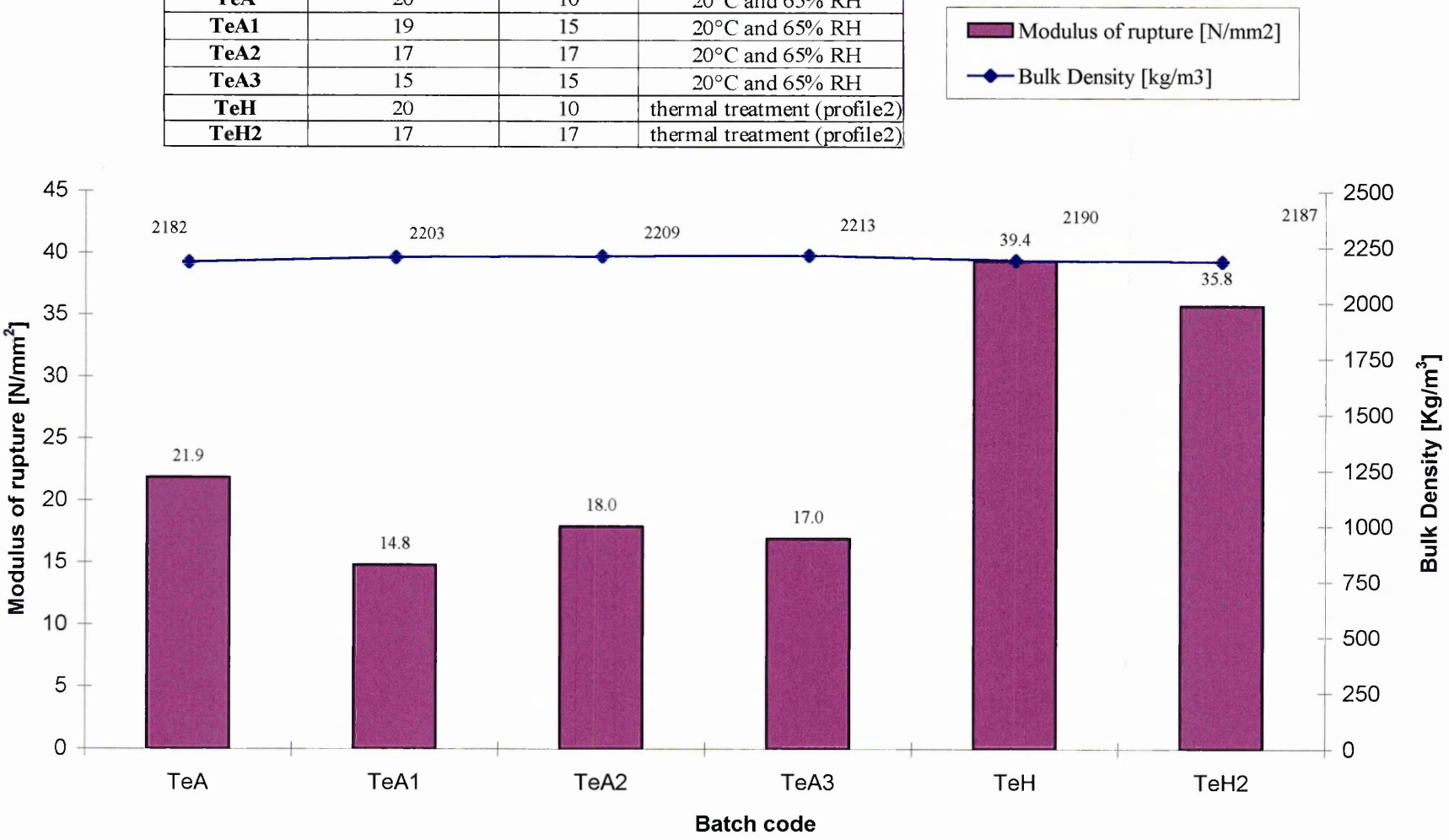

Figure 4.12 Modulus of rupture and density of alkali activated materials with different levels of fly ash and ggbs

4.5.6 Influence of Portland Cement Clinker

The addition of 1% OPC clinker as suggested in literature[10], generally caused a slight decrease in strength, as shown in Figure 4.13. However, the addition of clinker decreases the water absorption and porosity of alkali activated materials, Table 4.32. This could be due to an increase in the CaO level raising the CaO/SiO_2 and CaO/Al_2O_3 ratios (see Table 4.33) so reducing the levels of the [R_2O n Al_2O_3 x SiO_2 n H_2O] (zeolite) hydration product formed. This seems to suggest that maximum strength is achieved with an optimum combination of C-S-H and R_2O n Al_2O_3 x SiO_2 n H_2O hydration products.

Table 4.33 Chemical composition of the samples with slag and clinker addition

Batch	Al_2O_3/SiO_2 Ratio	CaO/SiO_2 Ratio	CaO/Al_2O_3 Ratio	Na_2O_e content wt [%]
Ref A	0.375	0.230	0.613	3.160
Ref H	0.375	0.230	0.613	3.160
TeA1	0.368	0.307	0.834	3.071
TeCA1	0.366	0.320	0.874	3.076
TeA2	0.360	0.345	0.958	3.010
TeCA2	0.357	0.368	1.031	2.999
TeA3	0.356	0.301	0.846	2.976
TeCA3	0.354	0.344	0.972	2.980
TeH2	0.360	0.345	0.958	**3.010**
TeCH2	0.357	0.368	1.031	**2.999**

Batch Code	Fly ash wt[%]	Slag wt[%]	Clinker wt[%]	Curing condition
TeA1	19	15	0	20°C and 65% RH
TeCA1	19	14	1	20°C and 65% RH
TeA2	17	17	0	20°C and 65% RH
TeCA2	16.5	16.5	1	20°C and 65% RH
TeA3	15	15	0	20°C and 65% RH
TeCA3	14.5	14.5	1	20°C and 65% RH
TeH2	17	17	0	thermal treatment (profile2)
TeCH2	16.5	16.5	1	thermal treatment (profile2)

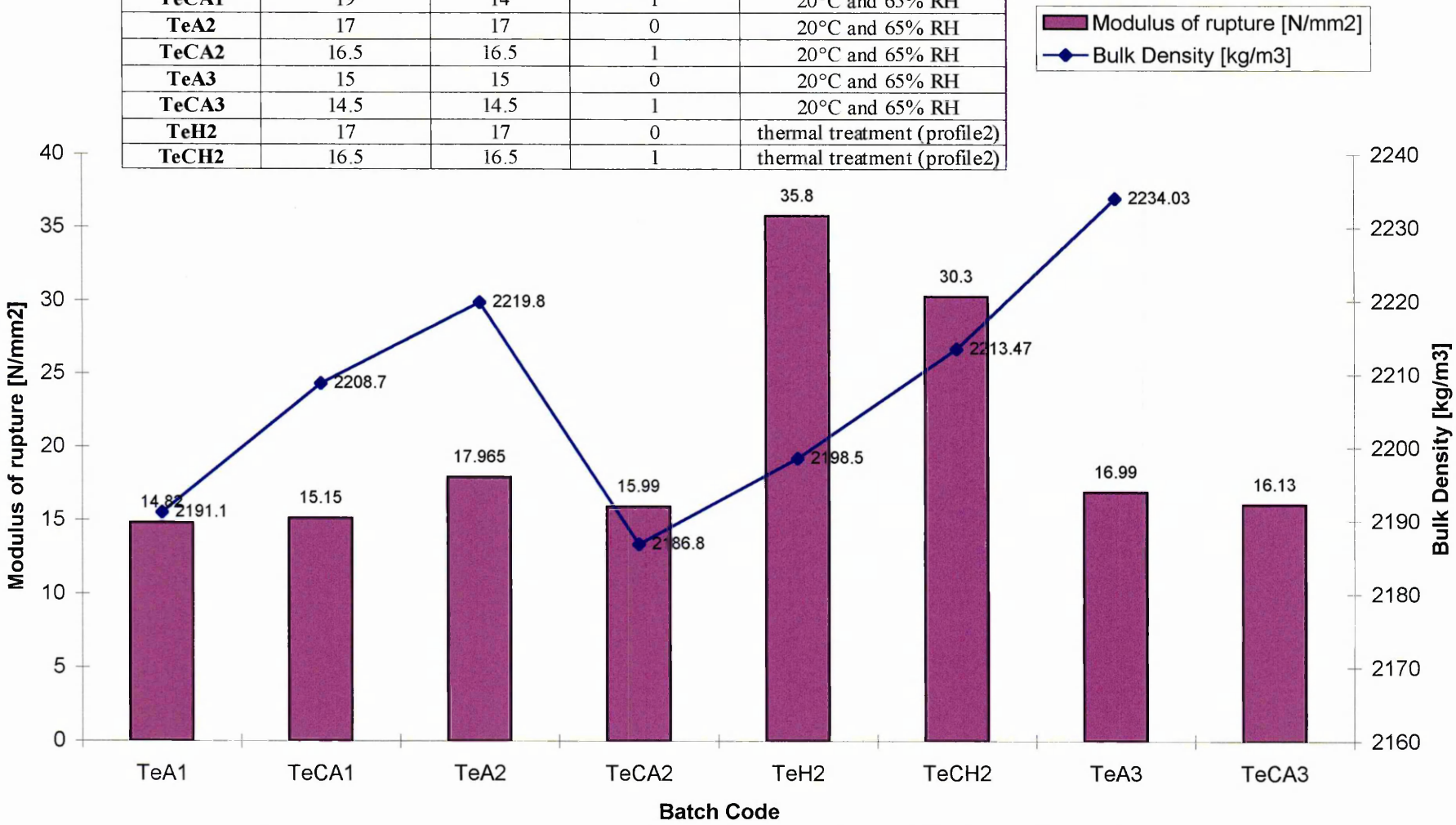

Figure 4.13 Modulus of rupture and density for alkali activated materials with clinker addition

Table 4.32 Physical Properties of materials containing slag and Portland cement clinker

Batch Code	Fly Ash	ggbs	PC Clinker	Curing Conditions	Water Absorption	Apparent Porosity	Coeficient of Saturation	Solid Density
A (Ref)	20	10	nil	20°C and 65% RH	7.71	16.81	0.45	2622.81
H (Ref)	20	10	nil	thermal treatment (profile 2)	8.38	18.33	0.41	2682.94
TeA1	19	15	nil	20°C and 65% RH	7.27	16.04	0.54	2603.38
TeCA1	19	14	1	20°C and 65% RH	7.63	16.70	0.81	2599.32
TeA2	17	17	nil	20°C and 65% RH	7.46	16.44	0.54	2610.56
TeCA2	17	16	1	20°C and 65% RH	6.92	15.39	0.59	2601.61
TeA3	15	15	nil	20°C and 65% RH	6.72	14.87	0.57	2213.47
TeCA3	15	14	1	20°C and 65% RH	6.82	15.22	0.54	2613.92
TeH2	17	16	1	thermal treatment (profile 2)	7.91	17.21	0.55	2609.29
TeCH2	17	16	1	thermal treatment (profile 2)	7.00	15.35	0.62	2591.69

4.5.7 Influence K-Bond hardeners

All mixes considered in this section were cast using the pressure compaction method (compaction pressure 20 N/mm^2) and cured as specified in Table 4.22 and detailed in section 4.3.3. Fly ash from Ratcliffe power plant and sand from Congleton quarry (CO 80) were used. The proportions of the constituent materials are presented in Table 4.23, section 4.3.4. The modulus of rupture data under four sets of curing conditions is considered to asses the effectiveness of the K-bond hardeners. These conditions are as follows:

1. curing under 20°C and 65%RH for 28-31 days and then testing under three point bending
2. following 28-30 days of curing under 20°C and 65%RH the specimens were exposed to 50 cycles of freezing and thawing and subsequently subjected to flexural testing
3. thermally curing up to 120°C for 21 hours and than testing under three point bending
4. following thermal curing up to 120°C, the specimens were exposed to 50 cycles of freezing and thawing and subsequently subjected to flexural testing

4.5.7.1 Specimens without slag (GROUP I)

The addition of water glass hardeners produced no improvement in the modulus of rupture of alkali activated materials tested before the freeze-thaw cycles, Figure 4.14 (compare mixes A, B2 and B3). The addition of water glass hardener KB#80 actually caused a reduction in modulus of from 20.06 N/mm^2 to 9.57 N/mm^2 (control mix A) for material with hardener (batch code B1). Water absorption and apparent porosity of the specimens with each of the KB hardeners (batch code B1, B2 and B3) were lower and coefficients of saturation were higher than those for the control material without hardener addition (batch code A) as shown in Table 4.34.

The densities, both solid and bulk, show no significant changes on the addition of water glass hardeners, see Table 4.34. The apparent porosity of the specimens fell from 20.84% for specimens without hardener (batch code A) to 17.17% for specimens with KB#200 hardener (batch code B3). The same trend can be observed for the water absorption, the addition of KB 200 produced a reduction from 10.08% for material A to 8.08% for material B3.

The influence of hardener becomes more apparent when investigating the freeze-thaw durability of the specimens. Figure 4.14 shows the modulus of rupture of alkali activated fly ash materials with hardener addition before and after exposure to 50 cycles of freezing and thawing. During 50 cycles of freeze - thaw exposure, samples without the addition of hardener (batch code A) disintegrated before the end of the test (see Figure 4.15) and, therefore, yielded a post freeze-thaw modulus of rupture of zero. However, materials with KB#90 and KB#200 hardeners (batch code B2 and B3) survived the freeze-thaw test. With the addition of KB90 hardener, modulus of rupture dropped from 19.46 to 14.05N/mm^2 after 50 freeze-thaw cycles resulting in a residual modulus of rupture of 72%. The corresponding values for the material with KB#200 hardener 19.57 N/mm^2 reducing to 4.45 N/mm^2 after 50 freeze-thaw cycles, see Figure 4.14.

The addition of hardener has improved the microstructure and the freeze-thaw resistance of the specimens without slag addition especially with hardeners KB#90 and KB#200, but has made no improvement to strength.

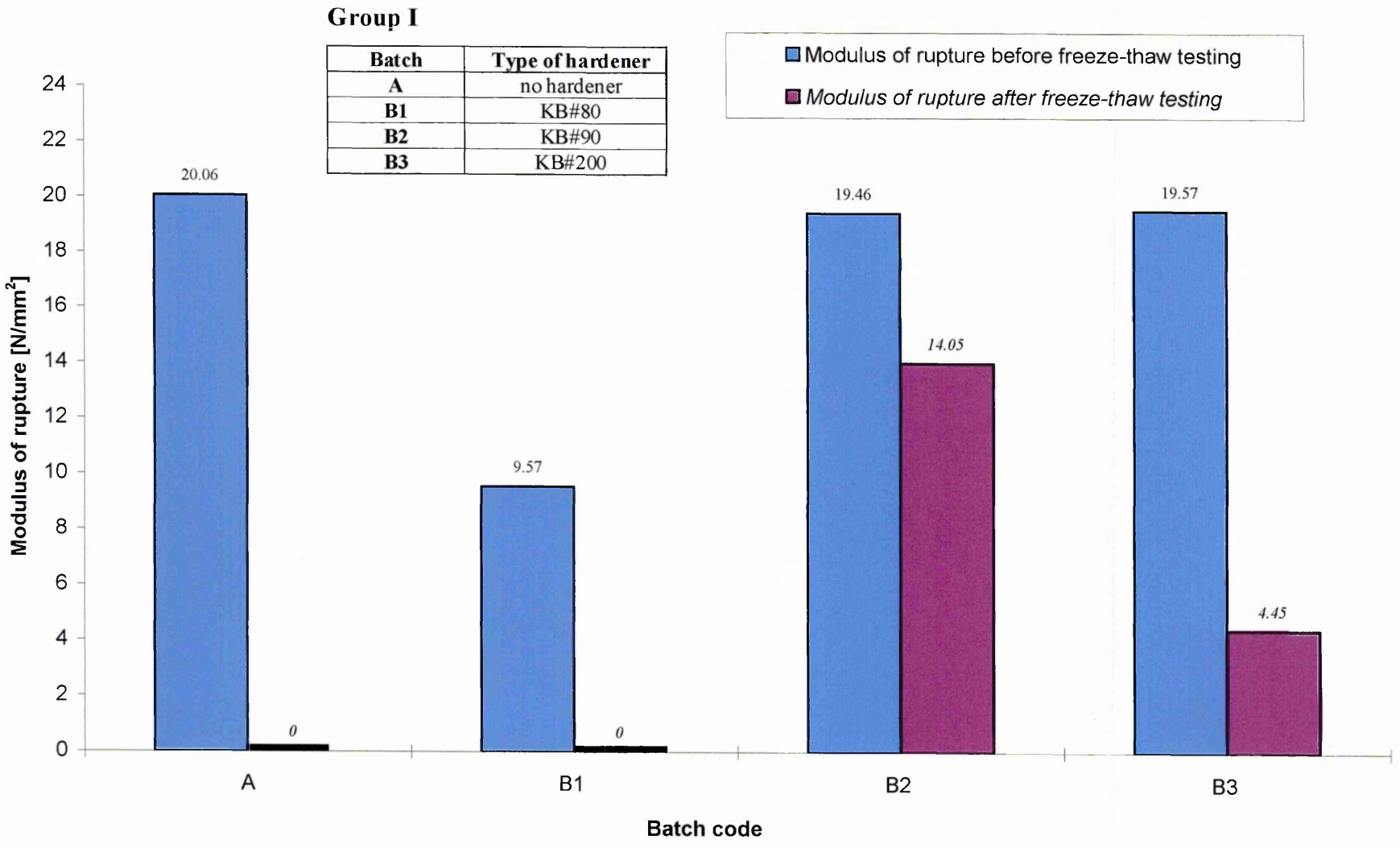

Figure 4.14 Modulus of rupture of alkali activated materials with hardener before and after freeze-thaw exposure

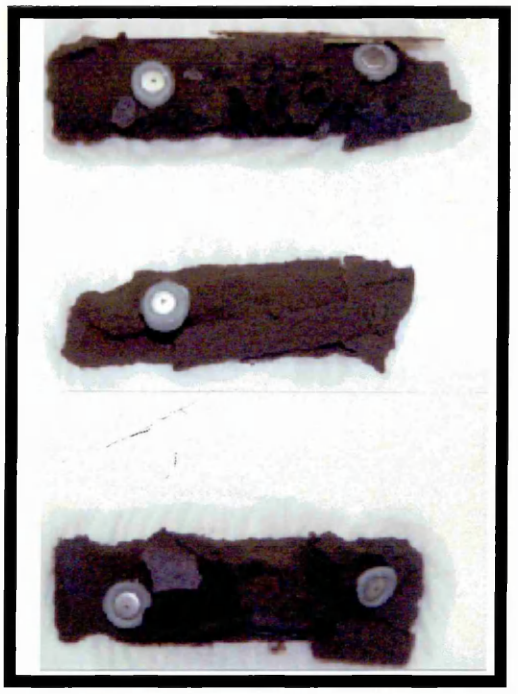

A (No hardener)

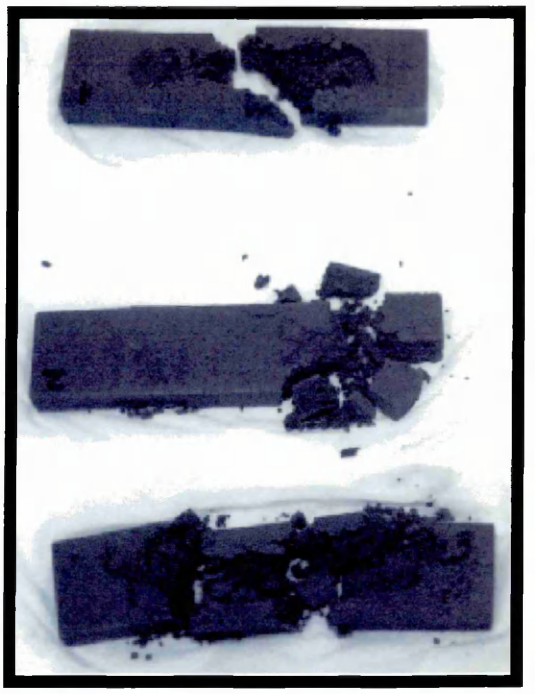

B1 (Hardener: KBond# 80)

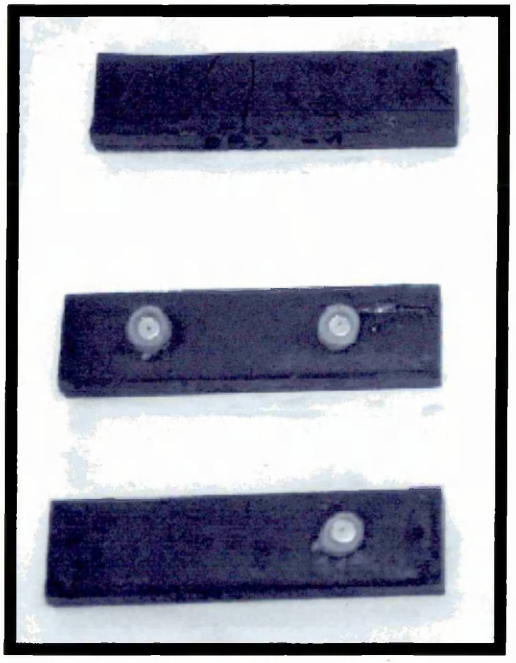

B2 (Hardener: KBond# 90)

B3 (Hardener: KBond# 200)

Figure 4.15 Appearance of samples (group I) after exposure to 50 freeze-thaw cycles.

4.5.7.2 Specimens with Scunthorpe slag (GROUP II)

The physical properties (densities, water absorption, apparent porosity and coefficient of saturation) of alkali activated fly ash materials with Scunthorpe slag and hardener are presented in Table 4.35, Table 4.36. Figure 4.16 shows the modulus of rupture of these materials, before and after exposure to 50 freeze-thaw cycles.

The modulus of rupture (before freeze-thaw testing) of the specimens with hardener KB#90 and KB#200 hardeners (batch code SAB2 and SAB3) is very similar to those without hardener addition (batch code SA1) except for hardener KB#80 (batch code SAB1), which caused a reduction in strength by approximately 50%, Figure 4.16. These tends are similar to those in Figure 4.14 for alkali activated materials without slag addition.

Physical properties were improved by the addition of KB#90 and KB#200 hardeners. For example, the water absorption and apparent porosity of material with KB#200 hardener (batch code SAB3) was approximately 10% lower than the corresponding material without hardener (batch code SA) as shown in Table 4.35. The bulk and solid densities of materials with hardener addition are similar to the control specimens without hardener, as shown in Table 4.34.

Figure 4.16 shows that the residual modulus of rupture after freeze -thaw exposure of specimens with hardeners (batch code SAB1, SAB2 and SAB3) is lower than specimens without hardener (batch code SA1). However, the reductions are much lower than the materials made with no slag addition (Figure 4.14). The appearance of the test specimens after 50 cycles of freezing and thawing is presented in Figure 4.17 and is discussed further in section 4.5.9. A comparison of Figures 4.16 and 4.14 (specimens IA and IISA) shows that the addition of slag improves the freeze-thaw resistance of materials without hardener addition. The addition of hardeners do not make any further improvement in the freeze - thaw resistance, in fact the residual modulus of rupture is reduced to some extent (see Figure 4.16).

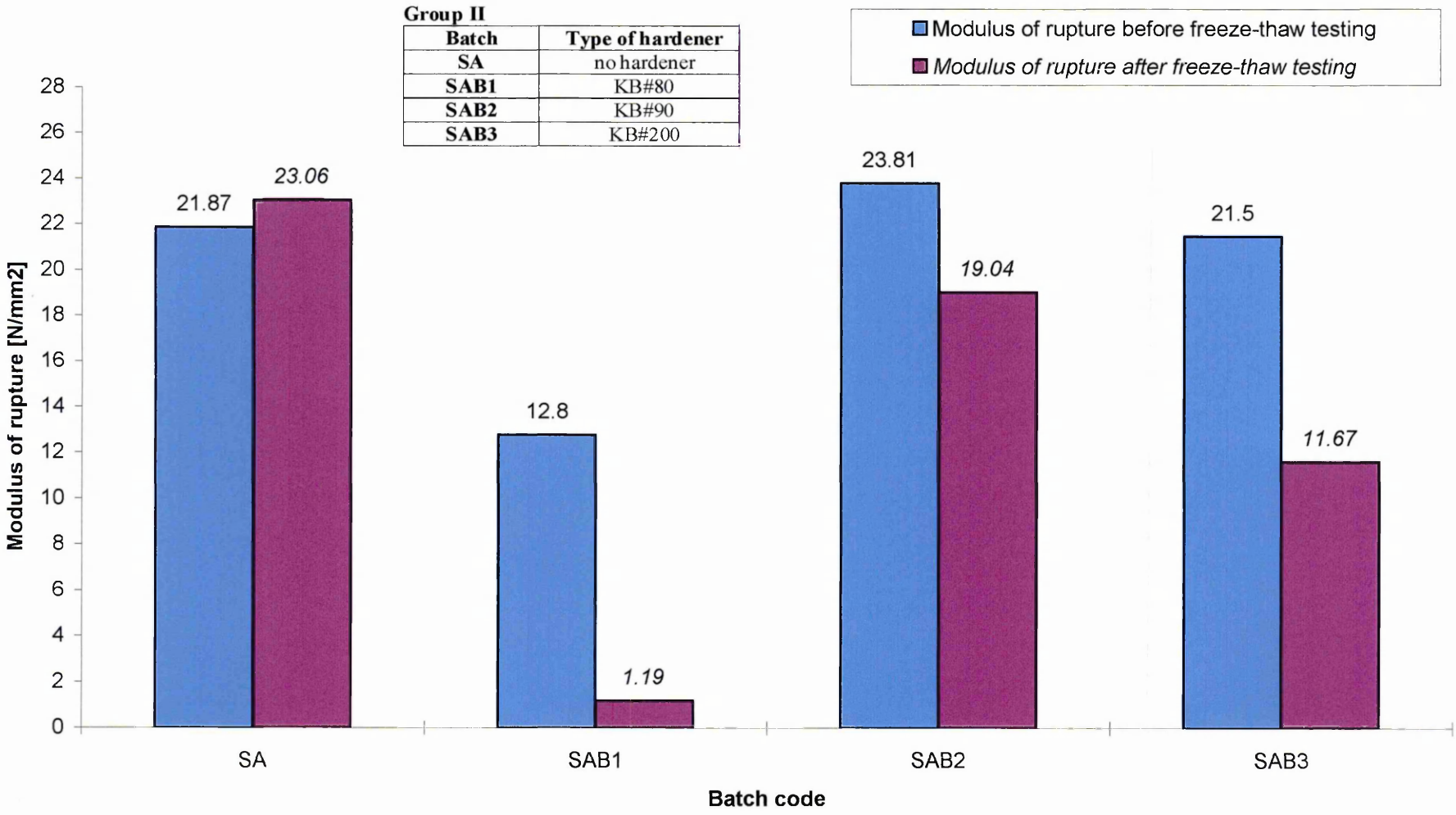

Figure 4.16 Modulus of rupture of alkali activated materials with Scunthorpe slag and hardener before and after freeze-thaw exposure

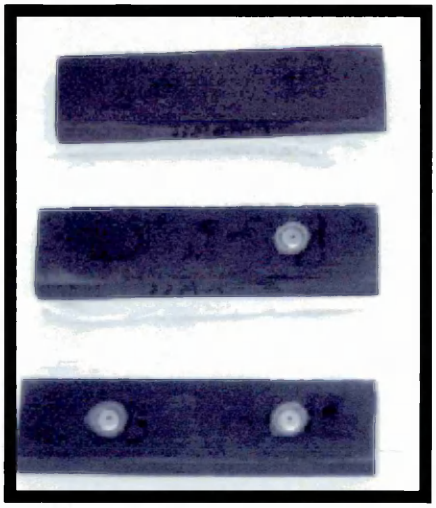

SA

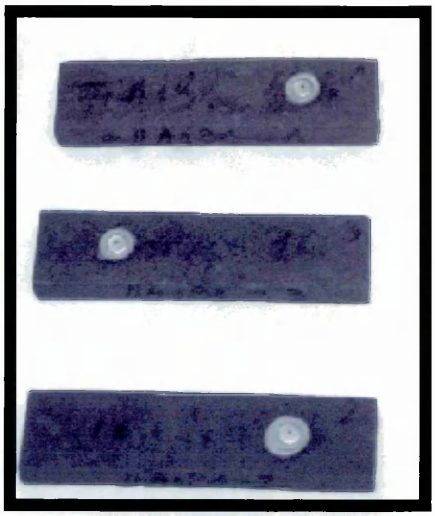

SAB1

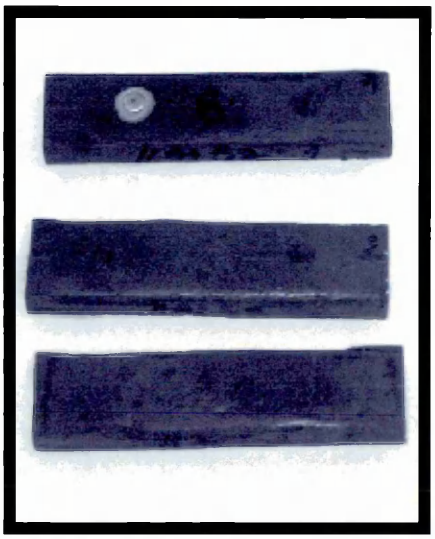

SAB2

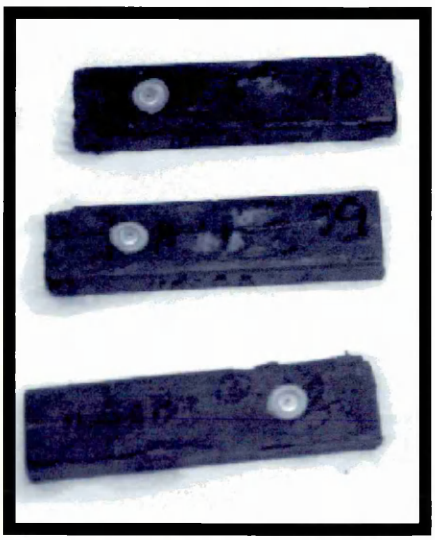

SAB3

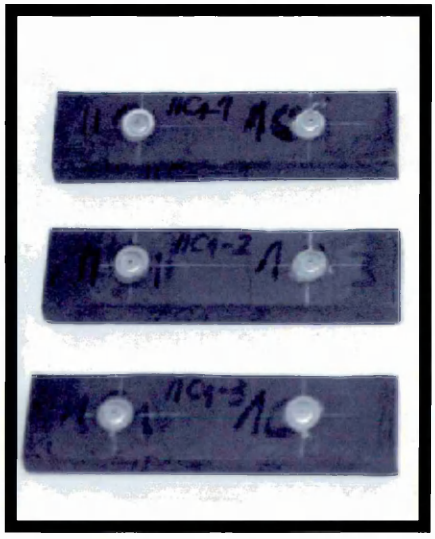

SH

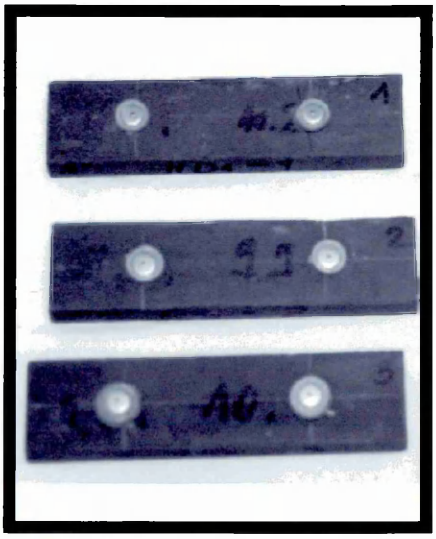

SHB3

Figure 4.17 Appearance of samples containing Scunthorpe slag (group II) after exposure to 50 freeze-thaw cycles.

Table 4.34 Physical properties and Na_2O_e content of materials with hardener and without slag addition (GROUP I)

Batch Code	Hardener type	Na_2O_e content wt [%]	Bulk Density [kg/m^3]	Apparent Solid Density [kg/m^3]	Water Absorption [%]	Apparent Porosity [%]	Coef of Saturation [%]	Residual Modulus of Rupture [%]
A	-	3.20	2067.23	2611.55	10.08	20.84	0.25	0
B1	KB#80	3.176	2060.74	2553.36	9.37	19.29	0.49	0
B2	KB#90	3.176	2072.87	2588.44	9.61	19.92	0.44	72
B3	KB#200	3.176	2136.05	2578.84	8.08	17.17	0.38	23

Table 4.35 Physical properties of the materials containing Scunthorpe slag and hardener addition (GROUP II)

Batch Code	Hardener type	Na_2O content wt [%]	Bulk Density [kg/m^3]	Apparent Solid Density [kg/m^3]	Water Absorption [%]	Apparent Porosity [%]	Coef of Saturation [%]	Residual Modulus of Rupture [%]
SA	-	3.160	2181.86	2622.81	7.71	16.81	0.45	105
SAB1	KB#80	3.136	2122.02	2599.03	8.65	18.35	0.31	9
SAB2	KB#90	3.136	2160.79	2580.66	7.53	16.27	0.40	80
SAB3	KB#200	3.136	2197.35	2589.28	6.89	15.14	0.47	54

4.5.7.3 Specimens with Calumite slag (GROUP III)

The physical properties (densities, water absorption, apparent porosity and coefficient of saturation) of the alkali activated fly ash materials with Calumite slag and hardener addition are presented in Table 4.36. Figure 4.18 shows the modulus of rupture before and after exposure to 50 freeze-thaw cycles.

The hardeners had an insignificant effect on strength before freeze-thaw exposure, except for hardener KB80 which reduced the strength. However, after exposure to 50 freeze - thaw cycles the specimens without hardener were destroyed, while those with hardener survived with a reduced modulus of rupture. The best results were obtained using KB#90 hardener which resulted in a residual modulus of rupture of 44% as shown in Table 4.36. As for the samples with Scunthorpe slag there is no significant difference in the densities of materials with and without hardener. Materials with KB#90 and KB#200 hardeners (batch code CtAB2 and CtAB3), a reduction in water absorption and apparent porosity compared with corresponding materials without hardener (batch code CtA), as shown in Table 4.36. This would suggest a microstructural change through the addition of hardener similar to that achieved with the addition of slag alone. The appearance of the test specimens after 50 freeze - thaw cycles is presented in Figure 4.19 and is discussed further in section 4.5.9.

4.5.7.4 Specimens with Llanwern slag (GROUP IV)

The physical properties (densities, water absorption, apparent porosity and coefficient of saturation) of alkali activated fly ash materials with Llanwern slag and hardener addition are presented in Table 4.37. Figure 4.20 shows the modulus of rupture before and after exposure to 50 freeze - thaw cycles. The appearance of the test specimens after 50 freeze - thaw cycles is presented in Figure 4.21 and is discussed further in section 4.5.9. Materials with Llanwern slag showed similar trends as those with Scunthorpe slag.

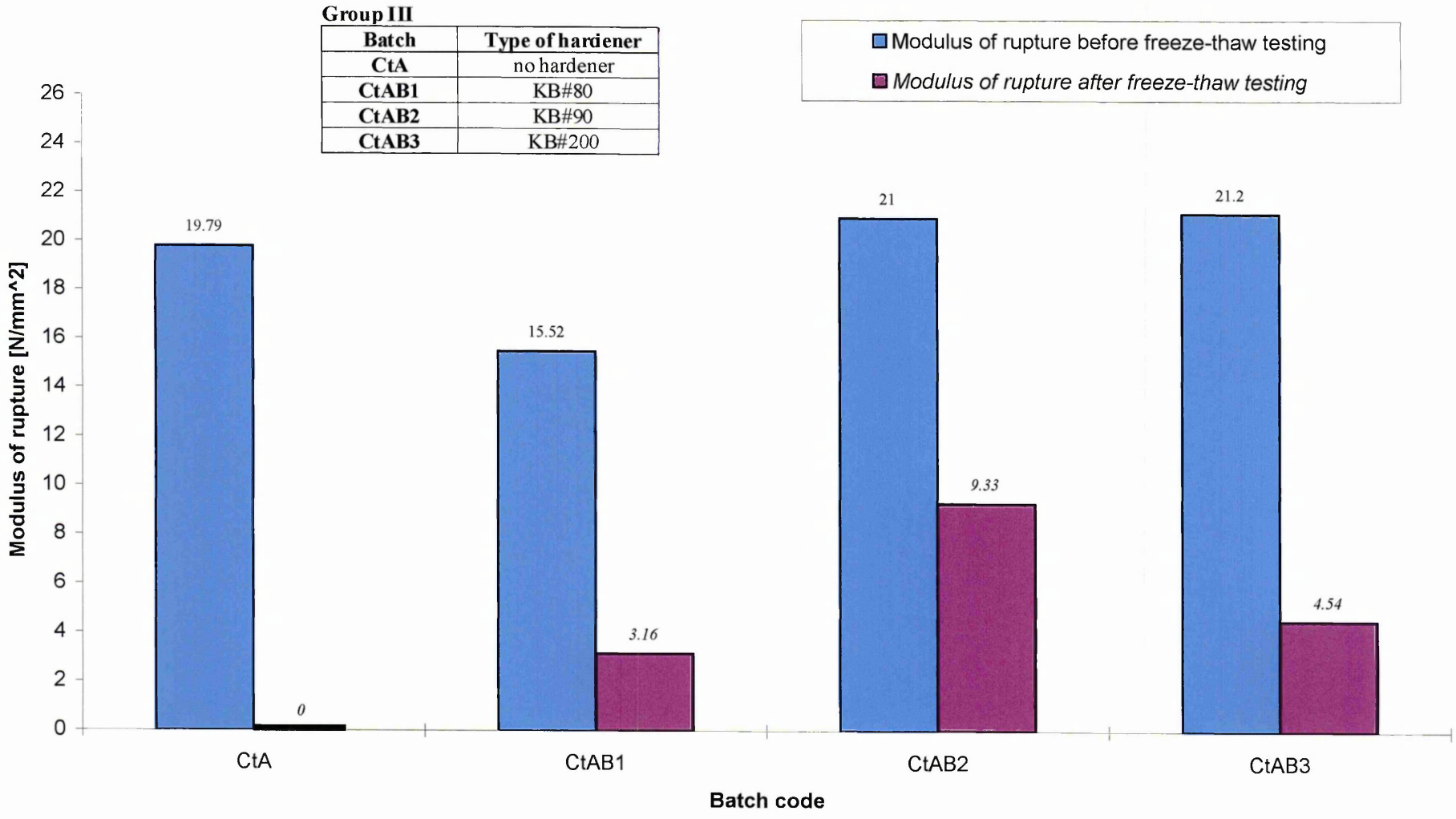

Figure 4.18 Modulus of rupture of alkali activated materials with Calumite slag and hardener before and after freeze-thaw exposure

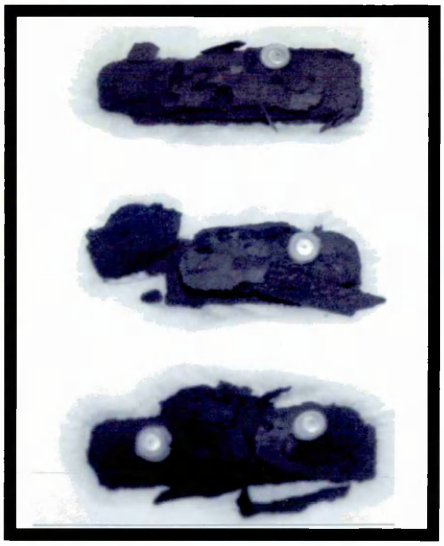

CtA

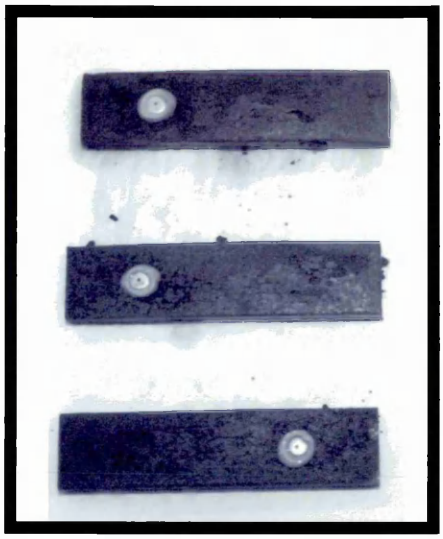

CtAB1

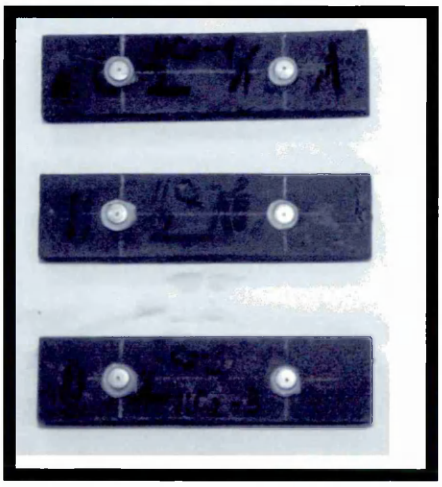

CtAB2

CtAB3

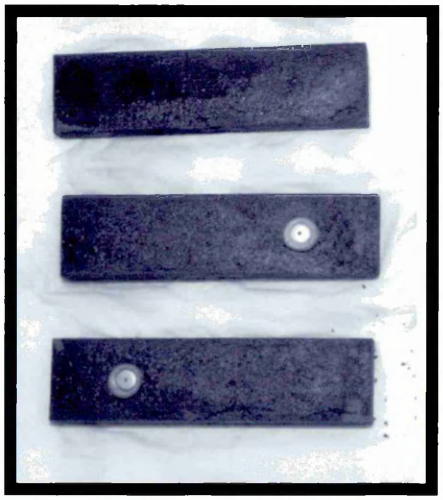

CtH

Figure 4.19 Appearance of samples containing Calumite slag (group III) after exposure to 50 freeze-thaw cycles

Table 4.36 Physical properties and Na_2O_e content of the materials containing Calumite slag and hardener addition (GROUP III)

Batch Code	Hardener type	Na_2O content wt [%]	Bulk Density [Kg/m^3]	Apparent Solid Density [Kg/m^3]	Water Absorption [%]	Apparent Porosity [%]	Coef of Saturation [%]	Residual Modulus of Rupture [%]
CtA	-	3.146	2122.21	2612.82	8.85	18.78	0.24	0
CtAB1	KB#80	3.122	2036.94	2577.08	10.30	20.96	0.38	20
CtAB2	KB#90	3.122	2141.71	2604.31	8.29	17.76	0.50	44
CtAB3	KB#200	3.122	2144.56	2605.29	8.25	17.68	0.43	21

Table 4.37 Physical properties and Na_2O_e content of the materials containing Llanwern slag and hardener addition (GROUP IV)

Batch	Hardener type	Bulk Density [Kg/m^3]	Apparent Solid Density [kg/m^3]	Water Absorption [%]	Apparent Porosity [%]	Coef of Saturation [%]	Na_2O content wt [%]	Residual Modulus of Rupture [%]
LA	-	2181.30	2572.54	6.97	15.21	0.50	3.141	104
LAB1	KB#80	2117.95	2660.52	9.62	20.37	0.34	3.117	31
LAB2	KB#90	2138.34	2553.82	7.61	16.26	0.49	3.117	80
LAB3	KB#200	2164.19	2572.76	7.34	15.88	0.41	3.117	49

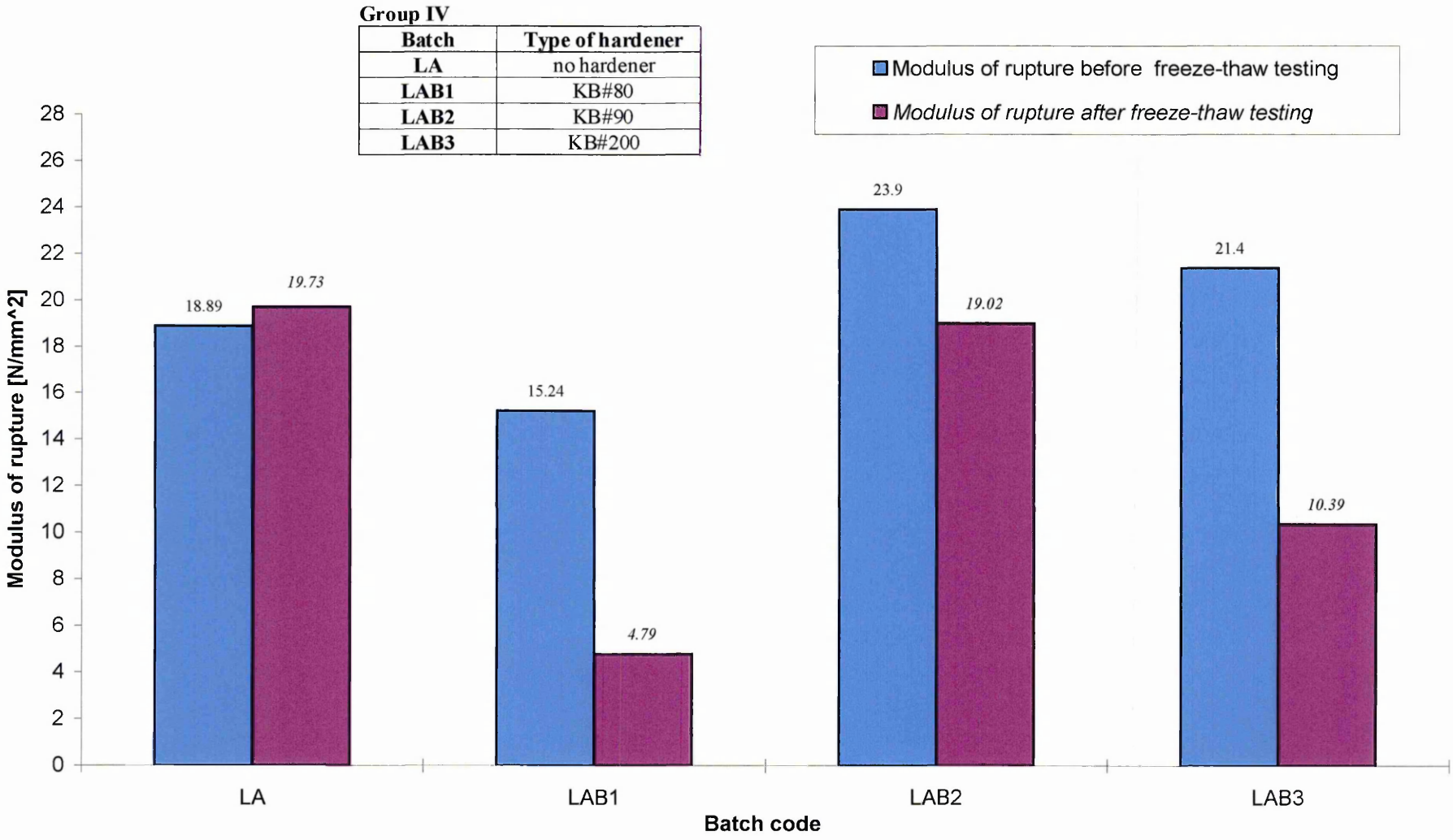

Figure 4.20 Modulus of rupture of alkali activated materials with Llanwern slag and hardener before and after freeze-thaw exposure

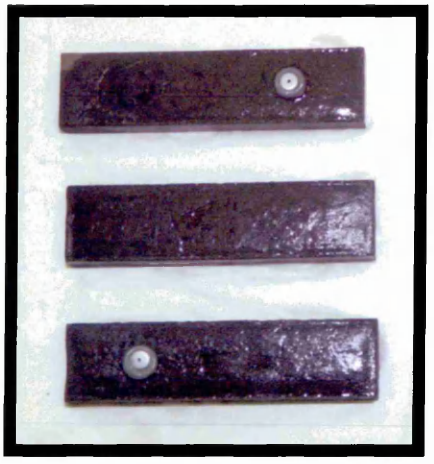

LA

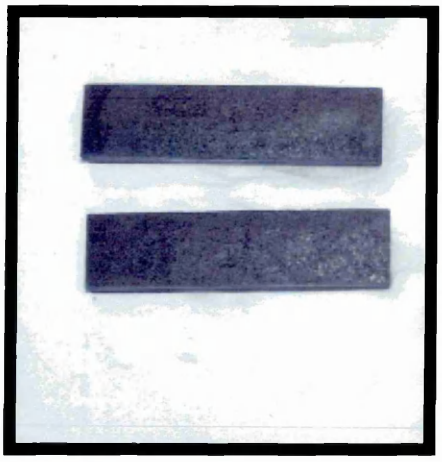

LAB1

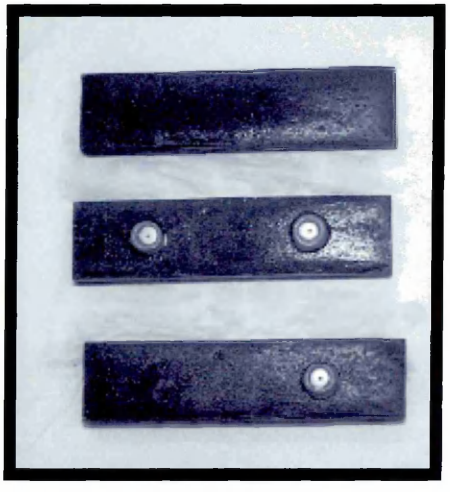

LAB2

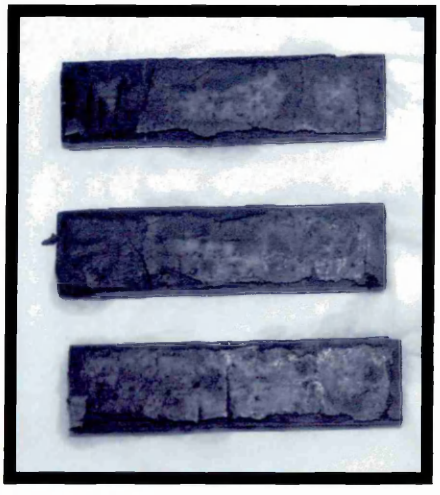

LAB3

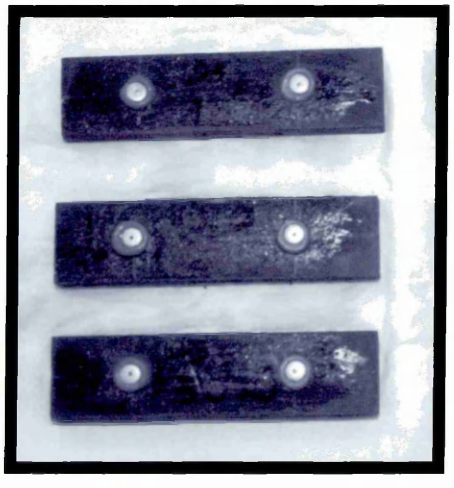

LHB3

Figure 4.21 Appearance of the samples containing Llanwern slag (group IV) after exposure to 50 freeze-thaw cycles.

Hardener addition had a negative effect on the physical properties and freeze - thaw resistance (see Table 4.37 and Figure 4.20).

Modulus of rupture of specimens with hardener (batch code LAB1, LAB2 and LAB3) was slightly higher than that of materials without hardener addition (batch code LA) except for hardener KB#80 which caused a reduction (see Figure 4.20). The bulk and solid densities of materials with hardener addition are slightly less than those of the control specimens without hardener, as shown in Table 4.37. Residual modulus of rupture, after freeze - thaw exposure, shows that the specimens with hardener (batch code LAB1, LAB2 and LAB3) have lower values than those without hardener (batch code LA). Overall the hardeners slightly improved the modulus of rupture of alkali activated materials with Llanwern slag but had a negative effect on their freeze-thaw resistance.

4.5.8 Influence of curing conditions

All mixes considered in this section were cast using the pressure compaction method (compaction pressure 20 N/mm^2) and subsequently subjected to the curing conditions detailed in Table 4.41. Fly ash from Ratcliffe power plant and sand from Congleton quarry (Congleton 80) were used. The proportions of the constituent materials used in these series are presented in Table.4.23, section 4.3.4.

The results presented in Figure 4.22, show that thermal curing increased the modulus of rupture of alkali activated materials. For example a comparison of materials A and H shows an increase from 20.06 N/mm^2 to 21.89 N/mm^2. Similarly, a comparison of materials containing slag (SA and SH) shows an increase from 21.81 N/mm^2 to 38.84 N/mm^2. The increase in the modulus of rupture is greater in the materials containing slag than in those without slag (e.g. compare A, H and SA, SH). The average density for both types of curing was similar, see Table 4.38. The presence of the convex surface of the fee face increased with thermal curing. This suggests that curing at a raised temperature (up to 120°C) increases the rate of any chemical reactions taking place, leading to increased early age strength. This phenomenon was discussed in previous section 4.5.3.

Table 4.38 Physical properties and Na_2O_e content of the materials subjected to ambient thermal curing

Batch Code	Curing Condition	Hardener Type	Bulk Density [kg/m^3]	Apparent Solid Density [kg/m^3]	Water Absorption [%]	Apparent Porosity [%]	Coef of Saturation [%]	Na_2O content wt [%]	Modulus of Rupture [N/mm^2]	Residual Modulus o Rupture [%
A	20°C and 65% RH,	-	2067.23	2611.55	10.08	20.84	0.25	3.20	20.06	0
H	Thermal (profile 2)	-	1925.97	2545.49	12.67	24.40	0.33	3.20	21.89	na
SA	20°C and 65% RH,	-	2181.86	2622.81	7.71	16.81	0.45	3.16	21.84	105%
SH	Thermal (profile 2)	-	2190.49	2682.94	8.38	18.33	0.41	3.16	38.84	22%
SAB3	20°C and 65% RH,	KB#200	2197.35	2589.28	6.89	15.14	0.47	3.136	21.5	54%
SHB3	Thermal (profile 2)	KB#200	2144.6	2591.3	8.04	17.24	0.47	3.136	36.9	101%
CtA	20°C and 65% RH,	-	2122.21	2612.82	8.85	18.78	0.24	3.146	19.79	0%
CtH	Thermal (profile 2)	-	2083.55	2618.27	9.8	20.42	0.25	3.146	28.3	55%
LA	20°C and 65% RH,	-	2181.3	2572.54	6.97	15.21	0.50	3.141	18.89	104%
LH	Thermal (profile 2)	-	2223.52	2595.32	6.44	14.33	0.43	3.141	36.1	na
LAB3	20°C and 65% RH,	KB#200	2164.19	2572.76	7.34	15.88	0.41	3.117	21.4	49%
LHB3	Thermal (profile 2)	KB#200	2107.83	2602.78	9.03	19.01	0.38	3.117	32.3	37%

Group	Batch	Type of hardener	Curing condition
I	A	no hardener	20°C and 65% RH
I	H	no hardener	thermal treatment (profile2)
II	SA1	no hardener	20°C and 65% RH
II	SH1	no hardener	thermal treatment (profile2)
II	SAB3	KB#200	20°C and 65% RH
II	SHB3	KB#200	thermal treatment (profile2)
III	CtA	no hardener	20°C and 65% RH
III	CtH	no hardener	thermal treatment (profile2)
IV	LA	no hardener	20°C and 65% RH
IV	LH	no hardener	thermal treatment (profile2)
IV	LAB3	KB#200	20°C and 65% RH
IV	LHB3	KB#200	thermal treatment (profile2)

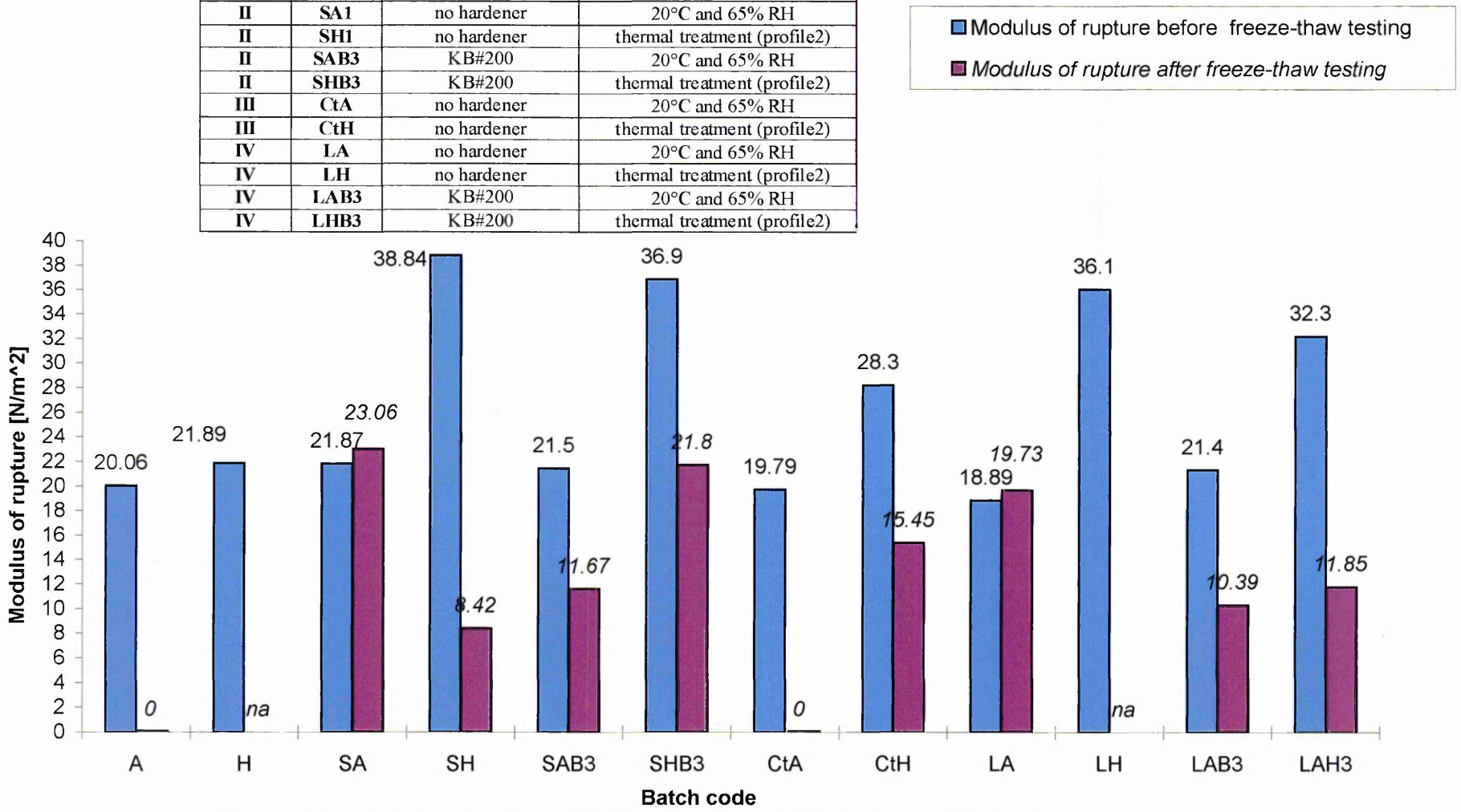

Figure 4.22 Modulus of ruptureof alkali activated materials before and freeze-thaw exposure

Previous research on the hydration products suggests the formation of zeolites of the form [R_2O n Al_2O_3 x SiO_2 r H_2O] with the value of 'x' changing with curing temperature and time, from 2 up to 4 for high temperature and longer time[12, 14, 19, 20]. Shih et al[12] found that two types of zeolites, faujisite and zeolite P were formed. Zeolite P forms at high temperature (80°C - 100°C) whereas faujisite can be obtained at lower temperature (38°C). The quantity of zeolite P will increase with increasing SiO_2/Al_2O_3 ratio. The type of silicate added was found to be important, additions of amorphous silica causing increases in zeolite P formation. Additions of silica fume increased the SiO_2/Al_2O_3 ratio and provided silica in the amorphous state. The investigations on high temperature curing and silica fume addition, in this research, would suggest the formation of zeolites in larger quantities than under normal curing without addition of silica fume. A more rigorous analysis of the microstructure is required to confirm this, but it does provide a possible reason for the change in strength and density.

The average water absorption for the thermally treated specimens increased from 7.97 to 9.06% and apparent porosity from 17.11 to 18.96%, suggesting that durability will be better for samples cured at ambient temperature as shown in Table 4.38. Thermal treatment did appear to result in a greater strength loss after 50 cycles of freezing and thawing compared with specimens cured under ambient conditions (see Figure 4.22 and Table 4.38). For example, the residual modulus of rupture of material with ggbs from Scunthorpe cured under 20C and 65%Rh (batch code SA) was 105% (increasing from 21.87 N/mm^2 to 23.06 N/mm^2) compared with 22% (decreasing from 38.84 N/mm^2 to 8.42 N/mm^2) for the corresponding thermally cured material (batch code SH). This could be due to increased microcracking during thermal curing, making the specimen more susceptible to freeze-thaw damage. The microcracks are caused by the expansion of air bubbles in the paste, the thermal expansion of air is approximately two orders of magnitude greater than that of the surrounding material. The expansion of air bubbles is restrained so that the air is put under pressure and to balance this pressure tensile stresses are induced in the surrounding pozzolanic paste.

These tensile stresses induce very fine cracks, increasing thereby the porosity, water absorption and coefficient of saturation. These disruptive effects of the expansion of air bubbles can be reduced by prolonged curing under ambient conditions prior to heat treatment and by a lower rate of temperature rise[81].The apperance of the test specimens after 50 freeze-thaw cycles is presented in Figures 4.15-4.21.

4.5.9 Influence of silica modulus of water glass

All five mixes considered in this section were cast using a compaction pressure of 20 N/mm^2 and cured thermally (profile 2). The detailed description of mixes (batch codes) considered in this section is presented in Tables 4.27, section 4.3.4. Fly ash from Ratcliffe power plant, ggbs from Purfleet power plant and sand from Congleton quarry (CO 80) were used.

Figure 4.23 shows the modulus of rupture of materials activated with water glass with different silica modulus. Modulus of rupture increases with increasing silica modulus, with the optimum being in excess of 1.5. Current literature[39], mainly on slag based binders, suggests that the silica modulus of water glass is important in strength development and that the optimum modulus is around 1. However, fly ash has a much higher Na_2O and K_2O content than slag and the silica modulus of water glass is determined by the Na_2O content of the mix. Increasing the amount of water glass would also cause brittleness and efflorescence[44]. It seems logical, therefore, that the optimum water glass silica modulus for fly ash activation would be somewhat higher, of the order of 2-2.5%.

The bulk and solid densities were all within 10% of each other as shown in Table 4.39. The modulus of rupture increases with decreasing Na_2O content, with the highest strength achieved with a Na_2O content of 3.494% (see in Table 4.39). An investigation of the other results to find the optimum Na_2O content proves to be inconclusive. Mixes made with Ratcliffe fly ash tended to have the lowest Na_2O content of around 2.886% (Table 4.26), and produced the highest strength.

Batch	Silica modulus
WG0.9	0.9
WG1.0	1.0
WG1.1	1.1
WG1.5	1.5
WG2.06	2.06

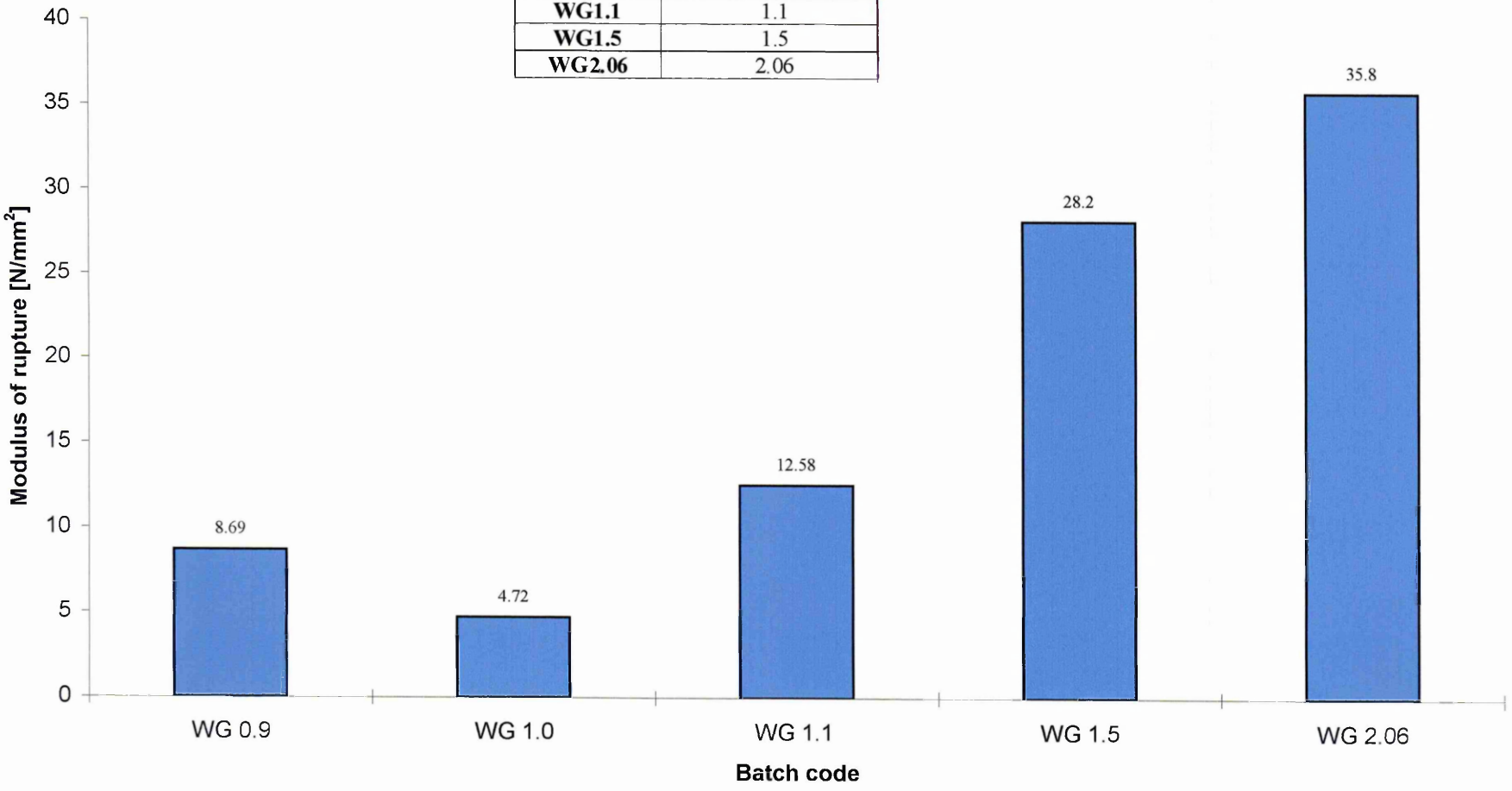

Figure 4.23 Modulus of rupture of materials activated with water glass with different silica modulus

Addition of microsilica tends to bring down the Na_2O content as do the addition of ggbs, but the modulus of rupture results do not accurately follow the trend for Na_2O contents as other factors come in to play such as slag quality and fineness. The present work nevertheless suggests that Na_2O content is very important and a value between 3 - 4% may be the optimum value.

Table 4.39 Physical properties and Na_2O content of materials coontaning water glass of variable silica modulus

Batch Code	Bulk Density [kg/m^3]	Apparent Solid Density [kg/m^3]	Water Absorption [%]	Apparent Porosity [%]	Coefficient of saturation	Na_2O content wt [%]
WG09	2191.3	2604.02	7.23	15.85	0.3	4.994
WG10	2204.93	2603.68	6.95	15.32	0.3	4.581
WG11	2213.65	2600.63	6.72	14.87	0.35	4.284
WG15	2205.99	2597.37	6.83	15.07	0.62	3.494
Wg206	2186.78	2609.29	7.91	17.21	0.55	3.010

The water absorption and apparent porosity do not completely correlate with the silica modulus of the water glass, however, the lowest were for the specimens with n=1.1. The use of a higher modulus water glass offers the opportunity to add more water glass to the mix, while still maintaining a 3% Na_2O level. This could be advantageous by increasing the workability of the mix and therefore the homogeneity.

4.5.10 Further Discussion

The results presented in this chapter show the ability to create high strength materials using alkali activated fly ash mixes. It is revealed that the physical and chemical compositions of the constituent materials are very important in obtaining desired strengths. Clearly strength development is a function of the porosity and hydration products formed and these are affected by the mix composition and curing temperature. The chemical parameters found to be important are the SiO_2/Al_2O_3 ratio, the CaO/ SiO_2 ratio and the Na_2O content. These chemical parameters decide the principal phase in the hydration products formed, between calcium silicate hydrate (C-

H-S) and zeolitic phases [R_2O n Al_2O_3 x SiO_2 r H_2O]. The physical parameters found to have an influence on strength development are pore size and pore distribution.

There are two disintegration patterns that emerged from the visual inspection of the samples after 50 cycles of freezing and thawing. One pattern which was typical for the materials containing hardener KB#80 was crumbling of the sample after exposure to freeze-thaw cycling.
The other pattern characteristic for materials with hardener KB#200 was exfoliation of layers parallel to the direction of casting. Materials with hardener KB#90 seem to have retained their structural integrity showing no real surface damage after exposure to freezing and thawing.

The mechanical and physical properties of alkali activated materials with fly ash slag addition, found in present investigation, are comparable with those obtained by other researchers[129]. For example modulus of rupture ranging from 26.6 to 40.4N/mm^2 and compressive strengths ranging from 63.6 to 124.8 N/mm^2 have been obtained by Malolepszy et all, Bob et all and Durica et all[129].

4.6 CONCLUSIONS

The following conclusions are based on the results of this investigation on alkali activated materials derived from fly ash, microsilica, slag fillers and water glass binder.

1. The physical and chemical composition of fly ash strongly influences the mechanical and physical properties of the alkali activated material.

2. The addition of microsilica has a marked positive effect. The sample with 5% micro silica (by weight) exhibited a modulus of rupture approximately two times larger than the sample without microsilica.

3. Samples with 5% microsilica and no slag addition developed a convex top surface during curing at high temperatures

4. Samples compacted by pressure application give superior mechanical properties than hand compacted ones. Pressure compaction produces a more homogeneous mix than hand compaction, because of the poor workability of mixes.

5. Addition of slag improves mechanical and physical properties of the material. As with fly ash, the physical and chemical composition of slag influences strength development.

6. The addition of slag increased modulus of rupture and compressive strength by approximately 1.8 times.

7. The addition of slag reduced water absorption by 24% and apparent porosity by 72%.

8. The addition of slag improves the freeze thaw resistance of the material. Samples with fine slags, cured at ambient temperature, gave the best overall freeze thaw resistance.

9. The addition of K-Bond hardeners had little effect on flexural strength, but did effect the durability and physical properties of the material

10. Samples without slag or K-Bond hardener did not survive the freeze thaw test. The presence of K-Bond 90 and 200 greatly improved the freeze thaw resistance.

11. The effect of K-Bond 90 and 200 hardeners for mixes which contained slags was less marked. The higher the quality coefficient of the slag the less the effect of the hardeners.

12. K-Bond 80 had a detrimental effect on the mechanical properties and durability both before and after freeze - thaw testing.

13. Thermal curing improves the mechanical properties, but decreases the density and increases the water absorption and apparent porosity. After thermal curing the majority of materials developed a convex surface.

14. Residual modulus of rupture of thermally cured materials was lower than that of materials cured under 20°C and 65% RH.

15. The optimum Na2O content of the mix was found to be of the order of 3%. Fly ashes are naturally higher in Na2O and K2O content than slags, making the optimum silica modulus of the water glass to be around 2 for fly ash activation compared to 1 to 1.5 for slag activation.

16. The silica modulus of water glass influences strength. The advantage of a higher silica modulus is that it allows the addition of more water glass to obtain a constant (3%) Na2O content, which results in a more workable mix.

"Nothing has such powers to broaden the mind as the ability to investigate systematically and truly all that comes under observation"

Marcus Aurelius

5 Shrinkage and Creep Properties of alkali activated materials

5.1 INTRODUCTION

A strain is always associated with any stress applied to a material and vice versa[81]. However, the overall strain in a material may not arise immediately from an applied stress. When a cementitious material is subjected to a sustained load, strain increases with time, this is known as creep. In addition, whether subjected to load or not, cementitious materials undergo shrinkage on drying. The magnitudes of shrinkage and creep strains are of the same order as elastic strain under the working range of stresses. Therefore, in assessing the performance of alkali activated material, as building materials, their shrinkage and creep properties are important.

Alkali activated materials are known to exhibit high free shrinkage compared with Portland cement mortar and concrete[10, 23]. Therefore, free shrinkage has been seen as a detrimental property of alkali activated materials. Fibre reinforcements are likely to provide effective restraint to the free shrinkage of these materials. There are no available data on the free shrinkage of fibre reinforced alkali activated materials.
There is little available data on the creep of alkali activated fly ash materials and alkali activated fibre reinforced materials. Shrinkage and creep tests are, therefore, considered important in extending the current knowledge of alkali activated materials and their fibre reinforced composites.

Factors which effect creep and shrinkage of cementitious materials are similar to those which effect the mechanical properties[81]. These factors are:

- grading of sand and coarse aggregates;
- fineness of binding materials;
- amount of water used;
- duration and method of mixing and temperature and humidity under which it is conducted;
- moulding and compacting methods;
- storing and curing conditions (temperature and relative humidity).

5.2 OBJECTIVES

A comprehensive experimental programme was undertaken to determine the free shrinkage and compressive creep of the alkali activated materials under investigation in this project. The detailed objectives were:

- to determine the influence of water/binder and curing conditions on the free shrinkage and compressive creep of alkali activated materials;

- to determine the influence of fibre reinforcements on the free shrinkage and compressive creep of alkali activated materials;

- to derive a theoretical prediction model for the free shrinkage and compressive creep of steel fibre reinforced alkali activated materials;

- to derive an empirical expression to predict the free shrinkage and compressive creep of steel fibre reinforced alkali activated materials;

- to establish a relationship between the $V_f l/d$ of fibre reinforcement incorporated in alkali activated materials and

a) the free shrinkage,
b) the compressive creep of alkali activated composite materials.

- to establish a relationship between the elastic modulus of fibre reinforcement and

c) the free shrinkage,
d) the compressive creep of alkali activated composite materials.

5.3 EXPERIMENTAL PROGRAMME

5.3.1 Constituent Materials

The constituent materials used for the investigations presented in this chapter are detailed in Chapter III (Experimental Programme) and are also summarised in the following section.

The main pozzolanic material used was **pulverised fuel ash** (pfa) from Ratcliffe power plant. Its chemical composition (by weight) is given in Table 5.1.

Table 5.1 Chemical composition of fly ash from Ratcliffe

Element	Content [%]
Silicon dioxide (SiO_2)	47.4
Aluminium oxide (AlO_3)	25.6
Iron oxide (Fe_2O_3)	10.4
Magnesium oxide (MgO)	1.7
Calcium oxide (CaO)	3.3
Sulphate (SO_3)	1.0
Potassium oxide (K_2O)	3.1
Sodium oxide (Na_2O)	1.4
$Na_2O_e = 0.658 \cdot K_2O + Na_2O$	3.4
Titanium oxide (TiO_2)	1.0
Chlorite (Cl)	0.01
Loss of Ignition	4.54
Density (kg/m^3)	2290
Sieve Residue Retained 45μm	
$\frac{CaO + MgO + Al_2O_3}{SiO_2}$	**0.645**

Ground granulated blast furnace slag from the power plant located in Teesside was used. The chemical composition (by weight) of this slag is given in Table 5.2.

Table 5.2 Chemical composition of ground granulated blast furnace slag from Teesside

Element	Content [%]
Silicon dioxide (SiO_2)	35.67
Aluminium oxide (AlO_3)	13.47
Iron oxide (Fe_2O_3)	0.55
Magnesium oxide (MgO)	7.45
Calcium oxide (CaO)	40.90
Sulphate (SO_3)	0.05
Sulphide (S^{2-})	0.91
Potassium oxide (K_2O)	0.26
Sodium oxide (Na_2O)	0.19
$Na_2O_e = 0.658 \cdot K_2O + Na_2O$	0.36
Titanium oxide (TiO_2)	0.69
Chlorite (Cl)	0.013
Manganese (MnO)	0.27
Loss of Ignition	0.48
Insoluble Residue	0.14
Particle size analysis	**466**[kg/m^2]
$\frac{\underline{CaO+ MgO+ Al_2O_3}}{SiO_2}$	**1.733**

Microsilica (silica fume) used in this investigation was a dry densified silica fume with the chemical composition (by weight) given in Table 5.3.

Table 5.3 Chemical composition of the densified silica fume

Element	Content [%]
Silicon dioxide (SiO_2) amorphous	85 to 98
Iron oxide (Fe_2O_3)	≤ 3.0
Aluminium oxide (Al_2O_3)	≤ 1.5
Calcium oxide (CaO)	≤ 0.7
Magnesium oxide (MgO)	≤ 2.0
Sodium oxide Na_2O)	≤ 1.0
Potassium oxide (K_2O)	≤ 3.0
$Na_2O_e = 0.658 \cdot K_2O + Na_2O$	≤ 2.97
Carbon (C)	≤ 3.0
$\frac{\underline{CaO+ MgO+ Al_2O_3}}{SiO_2}$	**0.0494 to 0.0428**

Washed and graded **high silica fine sand** from Congleton quarry was used as fine aggregate. Its chemical composition (by weight) is given in Table 5.4.

Table 5.4 Chemical composition of silica sand from Congleton quarry

Element	Content [%]
Silicon dioxide (SiO_2)	95.13
Aluminium oxide (Al_2O_3)	2.34
Iron oxide (Fe_2O_3)	0.24
Sodium oxide (Na_2O)	-
Potassium oxide (K_2O)	1.61
$Na_2O_e = 0.658 \cdot K_2O + Na_2O$	1.06
L.O.I.	0.25
Average grain size [μm]	175
Bulk density [kg/m^3]	1450

Sodium silicate solution (water glass) with a mean molar ratio (silica modulus, n) SiO_2/NaO_2 =2.06 was used. Its chemical composition (by weight) is given in Table 5.5.

Table 5.5 Chemical composition of the sodium silicate solution

Element	Content [%]
Silicon dioxide (SiO_2)	30.55
Sodium oxide (Na_2O)	15.27
Water (H_2O)	54.18

Water glass hardener: An aluminium methaphosphate compound, commercial chemical product K-Bond # 90, was selected as water glass hardener in order to accelerate the curing process of alkali activated materials at ambient temperatures.. The general properties of the hardener are given in Table 5.6.

Table 5.6 General properties of the water glass hardener (K-Bond # 90)

Property	Description
Appearance	Fine white powder
Acidity [meq/g]	1.2 ± 0.5
Moisture [%]	≤ 1.5
Solubility in water [%]	≤ 3.0
pH	3.2 ± 0.5
Sieve residue > 44 micron [%]	≤ 1.0

Fibre Reinforcement: Three types of fibres were selected for the investigation.

a) Stainless steel fibres of straight shape and undeformed, smooth surface. The fibres were of length 7mm and diameter 0.15 mm. The aspect ratio (length/diameter) of the fibres was 46.67. The specific gravity and Young's modulus of elasticity were 7.8 kg/m^3 and 215.3 GPa, respectively.

b) Melt extract steel fibres of non-uniform surface. The fibres were of length 12 mm and equivalent diameter 0.5 mm. The aspect ratio of the fibres was 24. The specific gravity and Young's modulus of elasticity of the fibres were 7.8 kg/m^3 and 215.3 GPa, respectively.

c) Alkali resistant integral chopped strand glass fibres (Cem-FIL 62/2) consisting of 100 filaments bound together. These fibres were designed to be resistant to the breakdown of filaments during mixing. The individual filaments were of length 12 mm and diameter 14μm. The aspect ratio of the fibre strand was 36.5. The specific gravity and Young's modulus of elasticity of the fibres were 2.68 kg/m^3 and 72 GPa, respectively.

5.3.2 Mix Composition

The results presented in Chapter IV confirm the ability to create high strength alkali activated materials using high volume of fly ash as reactive filler. They revealed that besides the chemical and physical composition of the constituent materials, mix proportioning is very important in obtaining the optimal properties from the hardened material.

In order to allow a direct comparison with the results of other researchers[10, 23] on pozzolanic materials activated by different alkali activators such as NaOH and Na_2CO_3, the alkali activator proportion was determined in terms of its Na_2O content. Some researchers[57, 58] prefer to define the sodium silicate solution (water glass) in terms of its NaOH concentration. This, however, is equivalent to the Na_2O content of

water glass, which can be determined from the following equation of the chemical reaction between Na_2O and water:

$Na_2O + H_2O \Rightarrow 2NaOH$.

Other researchers[10, 23] have used the silicate modulus, n, which is the ratio between silicon dioxide and sodium oxide (SiO_2 / Na_2O), in order to characterise the concentration of the sodium silicate solution. In the development work on alkali activated materials, presented in Chapter IV, the sodium silicate solution was added as a percentage of the total weight of mix. The optimum amount of Na_2O in the mix was found to be in the range of 3.00- 4.00% (by mix weight). When the mix was redesigned for the investigations presented in chapters V, VI and VII the total Na_2O content of the mix was kept in the same limits (3.00-4.00%) with the value being fixed at 3.3%. The water (54.18%) and solids (45.82%) in the sodium silicate solution were included in the determination of water/binder ratio of the mixes. The hardener was added as a percentage by weight of the sodium silicate solution (water glass).

The proportions (by weight) of solid constituent materials used in the mixes studied in this chapter were:

Fly ash / Slag / Microsilica / Sand = 1/0.5/0.25/3.25

or expressed in percentage by weight;

Fly ash / Slag / Microsilica / Sand =20%/10%/5%/65%,

Total solids = 100%

The type of water glass used was water glass Crystal 112 with the following composition:

SiO_2 = 30.55%

Na_2O = 15.27%

H_2O = 54.18%

and a silica modulus, n = 2.06

The total content of pozzolanic materials (Fly Ash + Slag + Microsilica) of the mix was 35%. The dosage of sodium silicate solution was such that yields of 5% of Na_2O by weight of the total content of pozzolanic material. Since the pozzolanic content of

the mix was 35%, therefore, the Na_2O content of sodium silicate solution was 1.75%. The total Na_2O content of the mix was 3.3. The amount x of water glass Crystal 112 required to yield 1.75% Na_2O is 11.46% which was determined as follows:

100% water glass contains 15.27% Na_2O

x% water glasscontains 1.75% Na_2O

therefore, $x = \frac{100 \cdot 1.75}{15.27} \therefore x = 11.46\%$

Hence, in order to prepare a mix containing 1.75% Na_2O (by weight of the pozzolanic materials) a dosage of 11.46% water glass is required. Therefore, 11.46% of water glass Crystal 112 yields:

3.501% of SiO_2

1.75% of Na_2O

6.20% of H_2O

Mixes with two water/binder ratios were investigated:

- water/binder ratio of 0.20 which produced a stiff mix which was hand compacted.

- water/binder ratio of 0.25 which gave a workable mix which could be compacted by vibration. This mix was also used as a matrix for fibre reinforced composites.

5.3.3 Mixing Procedure

Mixing was carried out according to BSI EN 196-1, 1995[130], using a forced action pan Hobart mixer with a capacity of 15 litres, as described in section 4.3.2 of Chapter IV.

The fly ash, silica fume, hardener, sand and fibre reinforcement (in selected mixes), were weighed using a Mettler PL 1200 analytical balance. The sand was mixed with the constituent pozzolanic materials before the addition of the liquid binder. Fibre reinforcements (when relevant) were then added to the homogenised dry components. After mixing the dry constituents and fibres thoroughly, the liquid

constituents (water glass and water) were added and mixed to produce a homogeneous mixture. At this stage, because of high consistency (low workability) of the mix, the speed of the Hobart mixing machine was increased in order to achieve a uniform mix. The water glass hardener was then added (in selected mixes) and high speed mixing continued to produce a homogeneous mixture. The hardener was made into a slurry with water before adding to the mix as this aided its dispersion.

5.3.4 Casting and Curing Procedure

Stainless steel moulds were specially manufactured for the prism test specimens. The dimensions, flatness, parallelism and surface smoothness of the moulds were accurate according to BS 308, Part 3[131]. The cylindrical and cube moulds were standard cast iron moulds normally used to manufacture concrete specimens. The internal surfaces of the prisms, cube and cylindrical moulds were coated with a relief agent (silicone oil) so that it formed an extremely thin layer on the mould faces. The coating was applied before casting to prevent adherence of the cast material to the mould. After mixing, the fresh material was placed horizontally in two layers into the moulds. Compaction of the specimens was carried out by one of the following methods:

- For the stiff mixes of water /binder ratio of 0.20, each layer was compacted by applying 25 strokes of a tamping rod (cross-section area 25x25 mm and weight 1.75 kg). The top surface of the specimen was trowelled using a steel float (dimensions 115x280 mm).

- For the more workable mixes (water/binder ratio of 0.25), each layer was compacted by vibration using a vibrating table according to BS 1881: Part 108, 1983[139]. Vibration was stopped as soon as the surface of the sample was smooth and had a glazy appearance, which usually took about 10-20 seconds of vibration.

Immediately after casting the specimens were cured under one of the following four conditions:

i. 20°C temperature and 65% relative humidity, in a controlled environment room as shown in Figure 5.1.

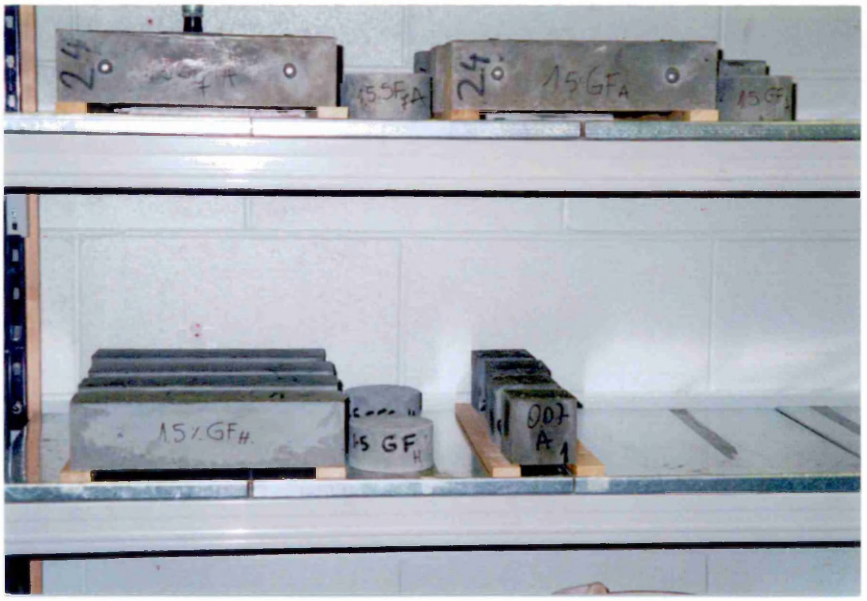

Figure 5.1 Shrinkage and creep specimens cured under 20°C and 65% RH

ii. 20°C temperature and 95% relative humidity, in a mist room, as shown in Figure 5.2.

Figure 5.2 Shrinkage specimens cured under 20°C and 95% RH

iii. 20°C temperature and 95% relative humidity (in a mist room) for the first seven hours after casting while the specimens were still in the moulds. The specimens were then demoulded and stored in a water tank at 18°C, as shown in Figure 5.3. The top surface of the samples, were placed in the mist room, was covered with polythene sheeting to prevent condensation.

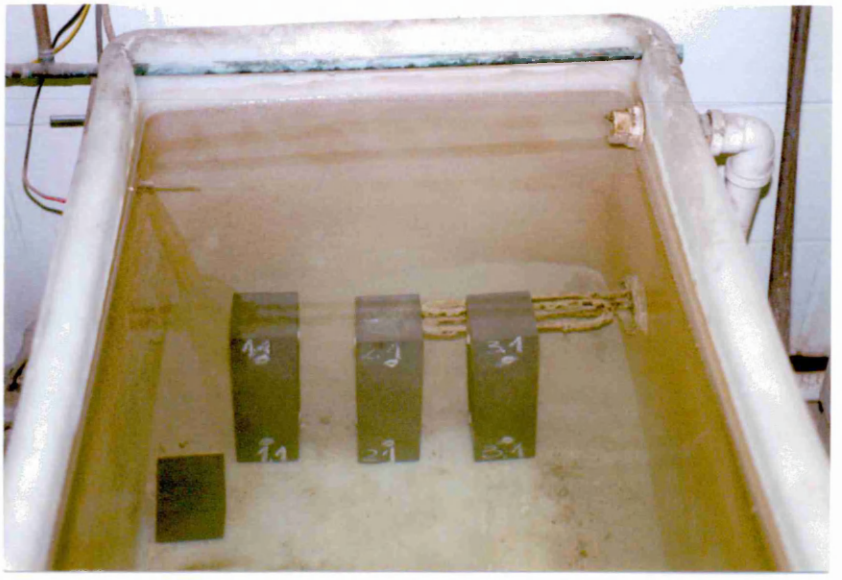

Figure 5.3 Shrinkage specimens cured in water curing at 20°C after 7h curing under 20°C and 65% RH

The specimens developed adequate strength under curing conditions (i to iii), to allow demoulding after seven hours.

iv. high temperature curing in a programmable oven (make: Binder APT Line M115) with class 3.1 overheat controlling thermostat. The overheat thermostat is functionally and electronically independent of the temperature control system.
In the event of system failure, when the pre-set safe temperature is exceeded by 1-3°C, the overheat controlling thermostat takes over the control function of the oven.
The specimens were subjected to a curing temperature programme which is presented in Figure 5.4.

After the samples were placed in the oven, the temperature was raised from 20.6°C to 30°C in 60 minutes and held at 30°C for a further 240 minutes. The temperature was then progressively increased in steps up to 120°C. Finally the temperature was gradually reduced to 20.6°C in 420 minutes (see Figure 5.4). The total duration of the curing period was 1620 minutes (27 hours). The samples were then stored under 20°C and 65% RH.

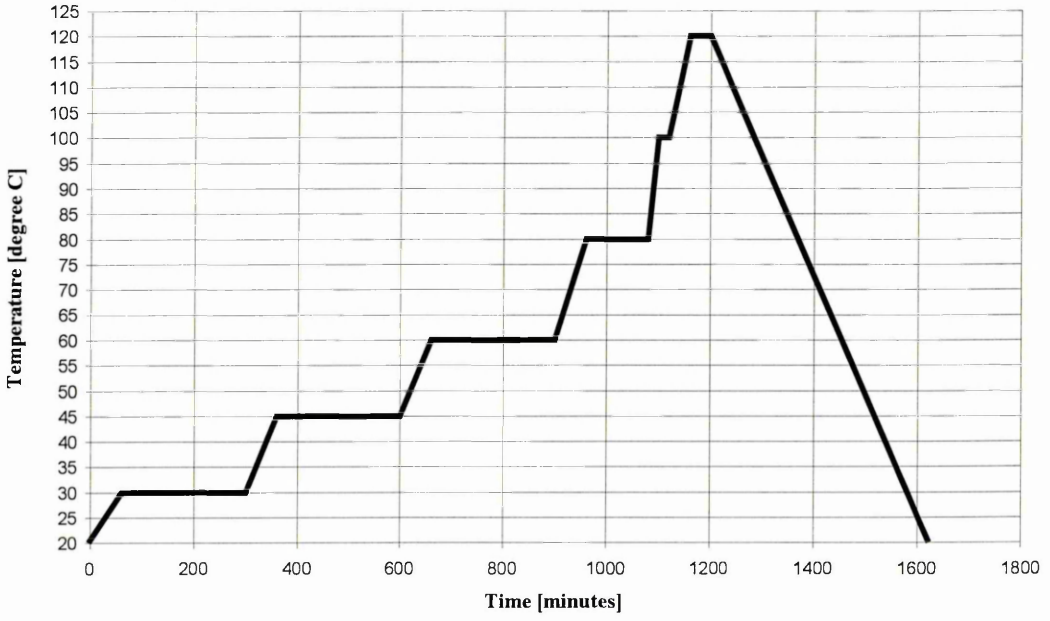

Figure 5.4 Thermal curing profile

The curing sequence was as follows: Immediately after casting, the specimens within the moulds underwent 7 hours of curing under conditions (i), (ii) and (iii) and 27 hours (1620 minutes, see Figure 5.4) for condition (iv). The specimens (within the moulds) were then transferred to the laboratory and demoulded. Following demoulding, Demec points were attached to the specimens at a gauge length of 200 mm using a rapid hardening adhesive (Chemical Metal manufactured by Plastic Padding Ltd.). The location of the Demec points was previously degreased using acetone, cleaned with Emery cloth of grading 160 and dried with a warm air drier to ensure good bond between the specimen surface and the adhesive.

Demec points were attached in accordance with BS 1881 Part 121 - Section 3[140], on all four faces of the specimens as shown in Figure 5.5. These operations were conducted in the laboratory environment (approximately 18°C temperature and 40% relative humidity) and they were completed in approximately 30 minutes. After the Demec points were attached, the specimens were returned to the curing environment (i), (ii) and (iii) for which they had been designated.

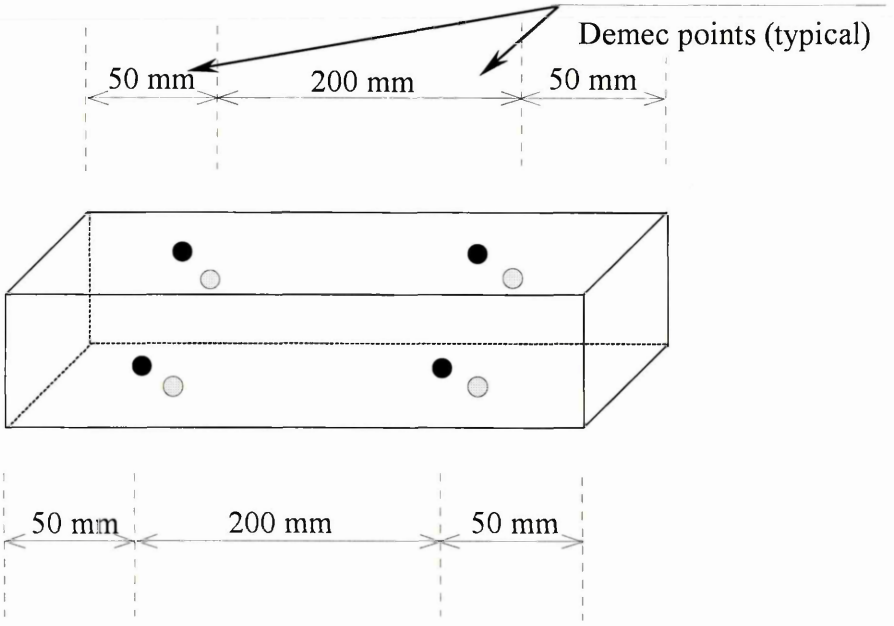

Figure 5.5 Location of Demec points on the test specimen

5.3.5 Details of investigated batches

The composition of all mixes used in the present investigation was fly ash/ggbs/silica fume/sand by weight proportions (%) 20/ 10/ 5/ 65 respectively. Water glass, Crystal 112, was used in proportion of 11.46% by weight of solid constituent materials.

Up to 1.5% hardener was added, as a percentage by weight of the sodium silicate solution (water glass) as detailed in section 5.3.2 of this Chapter.

The water/binder ratio and curing conditions used for the selected materials are shown in Table 5.7 and Table 5.8, respectively.

Table 5.7 Composition of alkali activated fly ash materials

Batch Code	Water/ Binder	Total Water [%]	Hardener [%]	Curing Conditions
A1	0.25	10.28	-	20°C and 65% RH
M1	0.25	10.28	-	20°C and 95% RH
W1	0.25	10.28	-	water curing at 18°C after 7 h
H1	0.25	10.28	-	thermal treatment
KA1	0.25	10.28	1.5	20°C and 65% RH
KM1	0.25	10.28	1.5	20°C and 95% RH
A2	0.20	6.20	-	20°C and 65% RH
M2	0.20	6.20	-	20°C and 95% RH
H2	0.20	6.20	-	thermal treatment
KA2	020	6.20	1.5	20°C and 65% RH
KM2	0.20	6.20	1.5	20°C and 95% RH

Table 5.8 Composition of fibre reinforced alkali activated materials

Batch Code	Water/Binder	Water [%]	Fibres		Curing Conditions
			Type	V_f [%]	
GA1	0.25	10.28	glass	1.5	20°C and 65% RH
GH1	0.25	10.28	glass	1.5	thermal treatment
GA2	0.25	10.28	glass	3.0	20°C and 65% RH
GH2	0.25	10.28	glass	3.0	thermal treatment
SwA1	0.25	10.28	straight steel	1.5	20°C and 65% RH
SA1	0.25	10.28	melt extract	1.5	20°C and 65% RH
SH1	0.25	10.28	melt extract	1.5	thermal treatment
SA2	0.25	10.28	melt extract	3.0	20°C and 65% RH
SH2	0.25	10.28	melt extract	3.0	thermal treatment

5.4 TESTING PROGRAMME

5.4.1 Shrinkage

Three prisms from each mix (batch code) listed in Table 5.7 and 5.8 were used to determine the free shrinkage deformation. The free shrinkage strains were measured according to BS 1881: Part 206, 1986[148] on all four longitudinal faces of three prisms, consequently each shrinkage value presented in this investigation is an

average of 12 readings. Free shrinkage was measured for 40 days during exposure to the three different curing conditions described in Section 5.3.5 of this chapter.
All strain measurements were made with a Demec extensometer over a gauge length of 200 mm. The extensometer is manufactured and calibrated by D. H. Mayes Ltd. The initial datum strain readings were taken immediately after attaching the Demec points, approximately 7 hours after casting. Subsequently, shrinkage strains were monitored at regular intervals, up to 40 days of age. The specimens were transferred from the controlled environments (20°C and 65% RH, 20°C and 95% RH and water curing at 20°C) to the laboratory environment (approximately 18°C and 40% RH) for taking the strain readings. This operation took approximately 10 minutes. Following this the specimens were returned to the controlled environment.

5.4.2 Compressive Creep

Creep tests were carried out according to the recommendations for a standard creep test by Illston and Pomeroy[94]. Two prisms from each mix (batch code) listed in Tables 5.7 and 5.8, were loaded in series in a standard creep rig at the age of 28 days, in a controlled environment room, as shown in Figure 5.6. A temperature of 20°C and a relative humidity of 65% RH were maintained in the control room throughout the test period. Creep measurements were made by means of a Demec extensometer over a gauge length of 200 mm, on all four faces of two prisms. Consequently each compressive creep value presented in this investigation is an average of 8 readings.
Each creep rig consisted of four mild steel plates (300x300x30 mm), 16 nuts and four high yield rolled steel rods of 36 mm diameter as shown in Figure 5.6.

The load in the creep rig was applied by means of a 25 ton capacity Imperial hydraulic jack (manufactured by Taskers-Hydrolite Ltd.) through the top plate. The hydraulic jack was kept in place throughout the testing period (90 days) and the load was topped up regularly using the jack handle to prevent load decrease occurring due to creep relaxation.

Figure 5.6 Creep specimens under load

A ball-joint was incorporated in the creep rig between the two smaller plates (150x150x25 mm), as shown in Figures 5.7 to ensure concentric loading. Before commencing the creep test, a small load (approximately 25% of the load used for creep testing) was applied and strain measured on all faces of the prisms and on the steel rods of the creep frame. This operation was conducted to check that reasonably equal strains were achieved on all rods and on all faces of the specimens which ensured axial loading of the creep specimens.

The test specimens were kept under load for 90 days at a sustained stress level of 0.3 of the ultimate strength of the prism. The specimens were then unloaded and creep recovery measurements were taken for a further period of 30 days.

5.4.3 Choice of test specimens

Preliminary work to develop the alkali activated fly ash materials, reported in Chapter IV, used 10x25x100mm prism and 50mm cube specimens owing to the large number of parameters investigated. These specimen sizes, although suitable for development work on mix composition, are too small to give reliably accurate information on the shrinkage and creep properties of alkali activated materials as small changes in specimen size can produce large differences in these properties[81]. Therefore, specimens of acceptably large dimensions (75mmx 75mmx 300mm prisms, 75mm cubes and 100mm diameter, 200mm height cylinders) were used in the investigations on physical, mechanical, shrinkage and creep properties of alkali activated fly ash materials reported in chapters V, VI and VII. It is important that these properties are derived from common specimen size in order to minimise the influence of size effect on the results.

Twenty specimens were prepared from each mix (batch code) listed in Tables 5.7 and 5.8 according to the procedures outlined in sections 5.3.2-5.3.4. These included eight prisms, eight cubes and four cylinders per mix (batch code). Three prisms were used for each of the following tests: shrinkage and modulus of rupture. The remaining two were used for the compressive creep test. Three cylinders were used for tensile splitting tests and two discs (cut from the remaining cylinder, as described in section 7.4.2) were used for permeability tests. One cube together with the prism halves obtained after flexural testing were used for compression testing. Three cubes were used for the density and pore structure investigation, two cubes were subjected to freeze – thaw cycling and the remaining two cubes were used for the fire resistance tests.

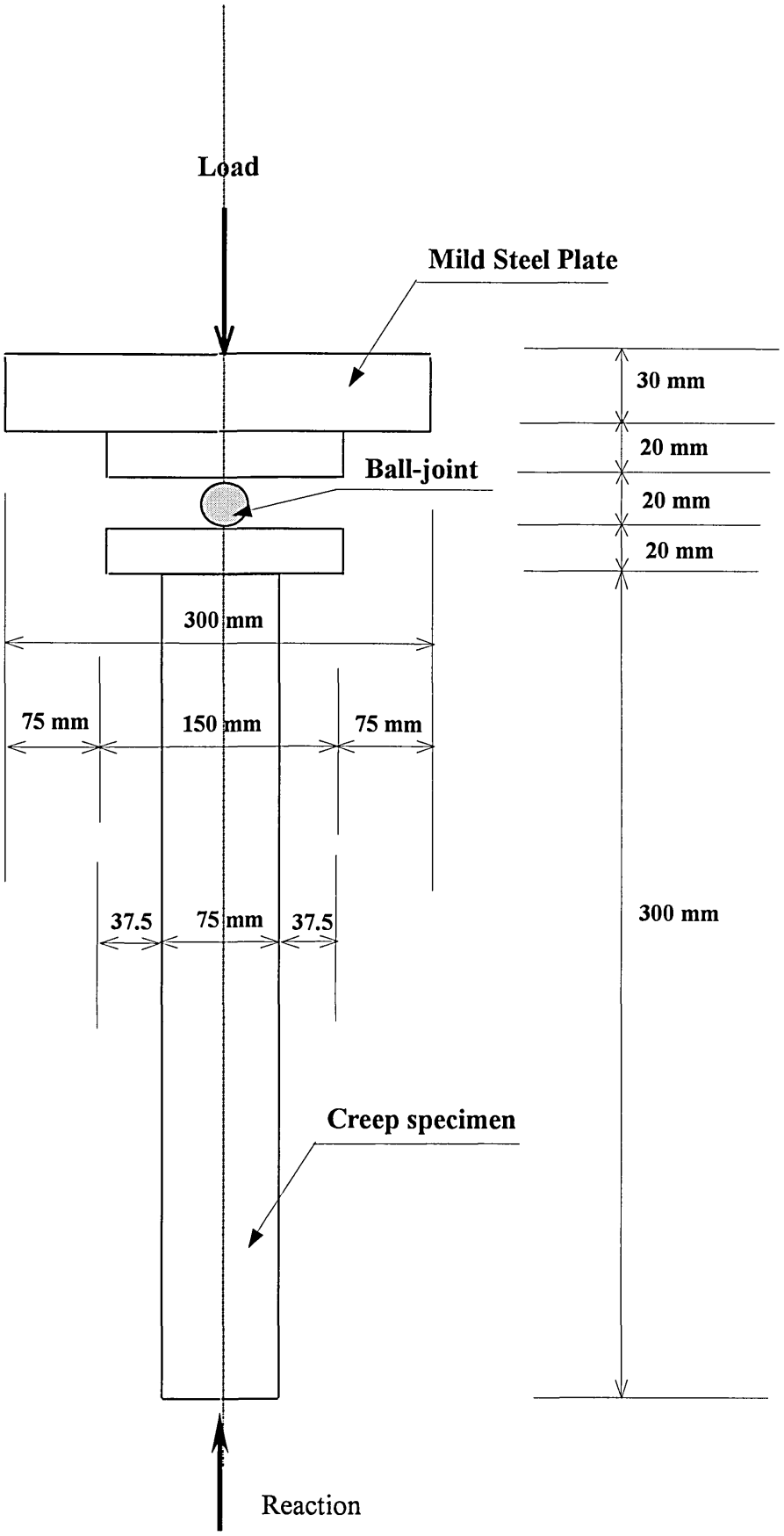

Figure 5.7 Loading of creep specimen

5.5 RESULTS AND DISCUSSION

5.5.1 Free shrinkage of the alkali activated materials

5.5.1.1 Air cured Specimens

The free shrinkage data of the alkali activated materials (listed in Table 5.7) cured under 20°C and 65% relative humidity, condition (i), is shown in Figure 5.8. The exposure conditions of 20°C and 65% RH were maintained throughout the 40 day period of shrinkage monitoring. A summary of the results is also given in Table 5.9. Figure 5.8 shows that materials with a water/ binder ratio of 0.25 (batch code A1 and KA1) exhibit higher free shrinkage (at all ages) than corresponding materials with a lower (0.20) water/binder ratio (batch code A2 and KA2). For example, the material with a water/binder ratio of 0.25 (batch code A1) has a 40 days free shrinkage which is 18% higher than corresponding material with a lower water /binder ratio of 0.20 (batch code A2), as shown in Table 5.9. A comparison of materials with hardener addition (batch code KA1 and KA2), which have a water/ binder ratio of 0.25 and 0.20 respectively, shows that the higher water/binder ratio leads to a slight increase in free shrinkage (Table 5.9).

Table 5.9 Shrinkage of alkali activated materials at 40 days

Batch Code	Curing conditions	Water/Binder	Shrinkage Strain [microstrain]
A1	20°C and 65% RH	0.25	6138
KA1	20°C and 65% RH	0.25	6108
A2	20°C and 65% RH	0.2	5188
KA2	20°C and 65% RH	0.2	6048

The results presented in Table 5.9 and Figure 5.8 show no clear influence of the hardener on the free shrinkage of alkali activated materials cured under 20°C temperature and 65% relative humidity. A comparison of materials A1 and KA1 with a water/ binder ratio of 0.25 shows that the addition of hardener slightly decreases the free shrinkage (at all ages) as shown in Figure 5.8.

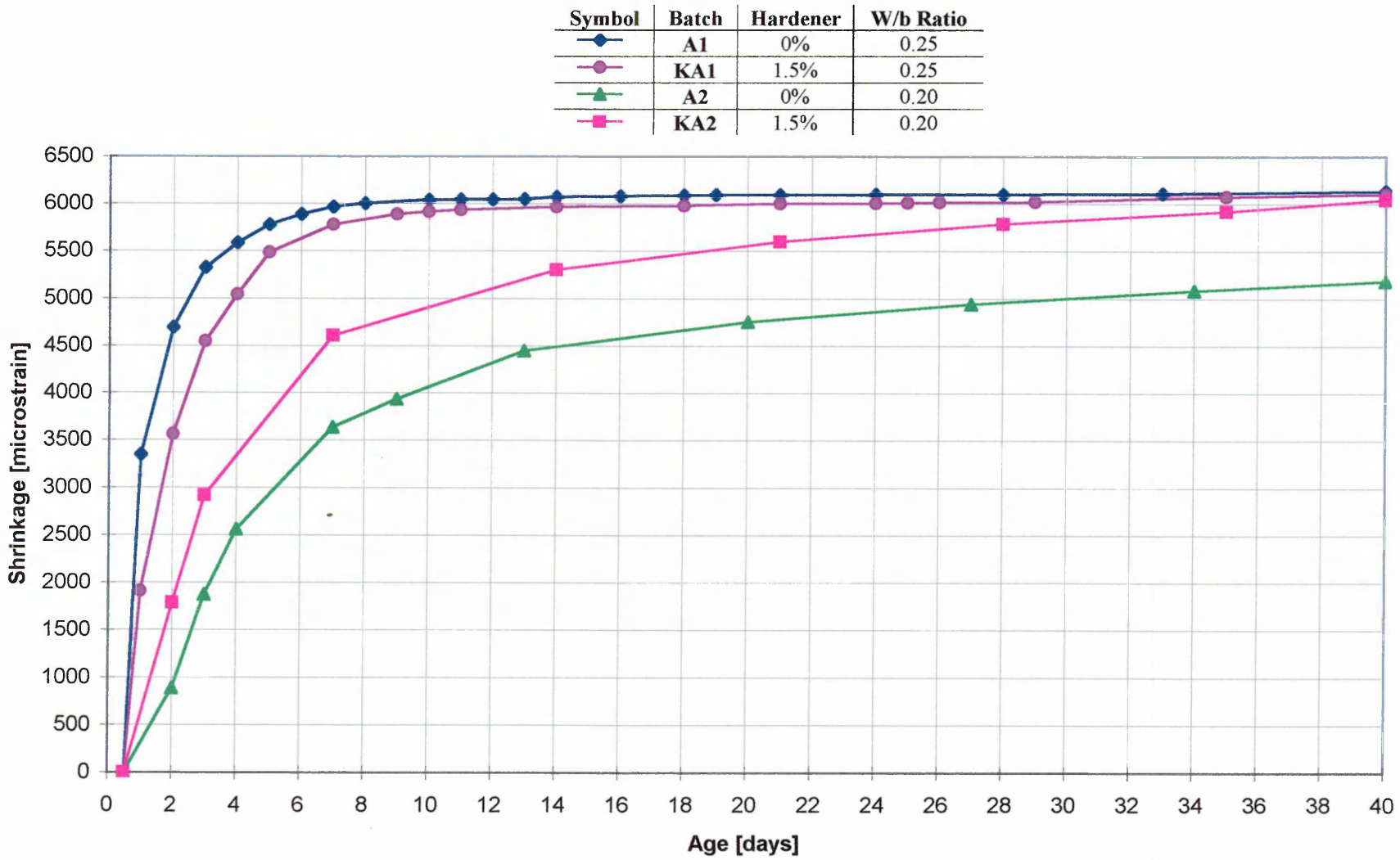

Figure 5.8 Free shrinkage of alkali activated materials cured at 20 °C and 65% RH

For example, at 40 days the free shrinkage of alkali activated material with hardener addition (batch code KA1) is 6108 microstrain compared with 6138 microstrain for the corresponding material without hardener. A comparison of materials A2 and KA2 with a water/binder ratio 0.20, on the other hand, shows that the addition of hardener increases the shrinkage (at all ages) of the alkali activated materials. For example at 40 days the free shrinkage of alkali activated material with hardener addition is 17% higher then that of corresponding material without hardener.

5.5.1.2 Mist cured specimens

The free shrinkage data of the alkali activated materials cured under 20°C and 95% RH, is shown in Figure 5.9. The exposure conditions of 20°C and 95% RH were maintained throughout the 40 day period of shrinkage monitoring. A summary of shrinkage results is also presented in Table 5.10. A comparison of materials with a water/binder ratio of 0.25 and 0.20, batch code M1, KM1 and M2, KM2, respectively, shows that the higher water/ binder ratio leads to much greater free shrinkage at all ages, similar to the case reported above for curing under 20°C and 65% relative humidity (see Figure 5.9). For example, the material with a water/binder ratio of 0.25 (batch code M1) has a 40 days free shrinkage of 75.6 μstrain compared with 42.53 μstrain for the material with a water /binder ratio of 0.2 (batch code M2), as shown in Table 5.9. A comparison of materials with hardener addition (batch code KM1 and KM2), which have a water/ binder ratio of 0.25 and 0.20 respectively, show shrinkage strains of 691.61 and 375.3 μstrain respectively (Table 5.10).

Table 5.10 Shrinkage deformation alkali activated materials at 40 days

Batch Code	Curing conditions	Water/Binder	Shrinkage Strain [microstrain]
M1	20°C and 95% RH	0.25	76
KM1	20°C and 95% RH	0.25	692
M2	20°C and 95% RH,	0.20	43
KM2	20°C and 95% RH	0.20	375

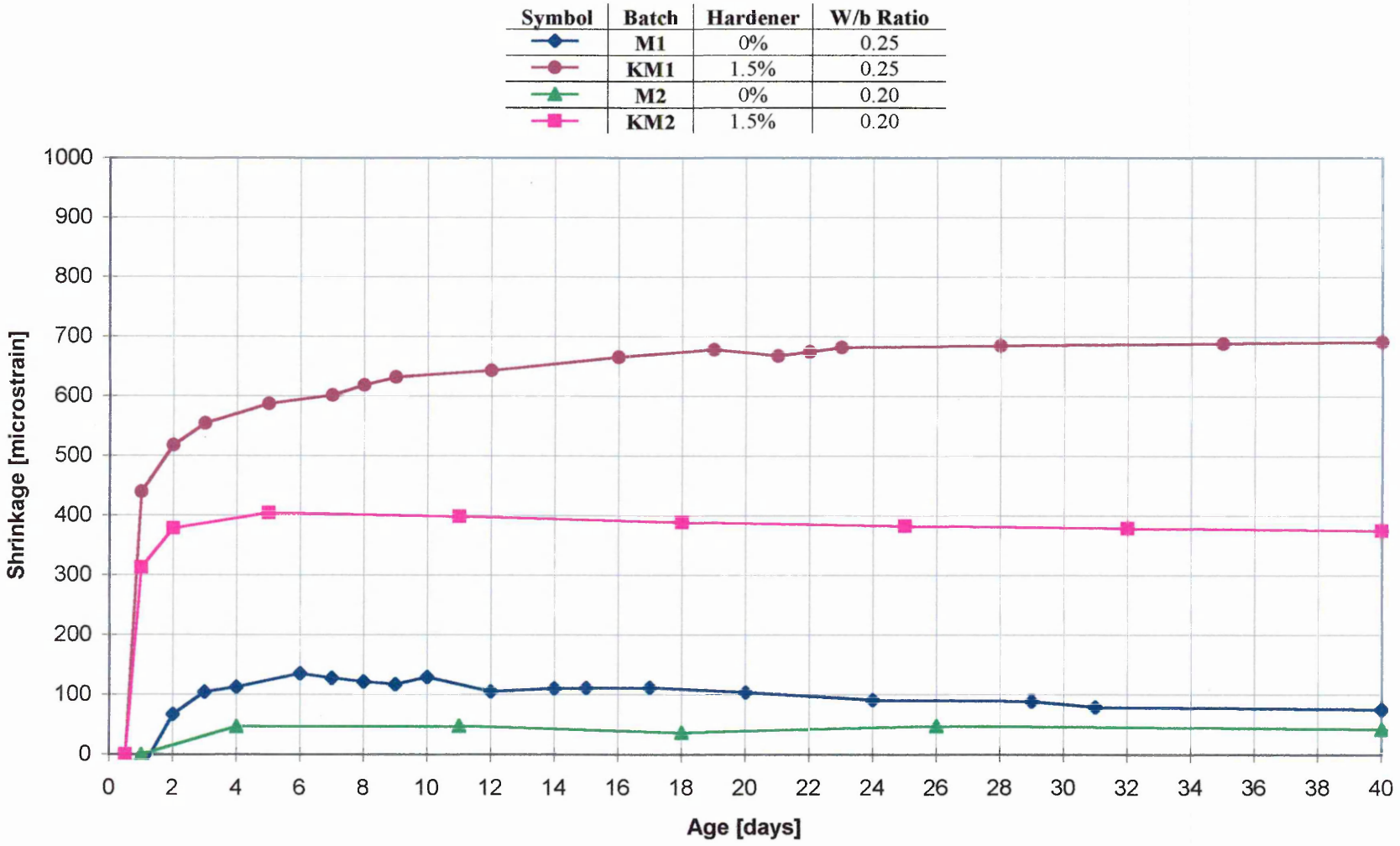

Figure 5.9 Free shrinkage of alkali activated materials cured at 20 °C and 95% RH

The addition of the KB hardener results in an increase of free shrinkage (at all ages) of mist cured alkali activated materials for both water/binder ratios (0.25 and 0.20), as shown in Figure 5.9. This trend is much more pronounced in mist cured materials (Figure 5.9) compared with materials cured under 20°C and 65% RH (Figure 5.9). For example, at water/binder = 0.25 the material with hardener addition (batch code KM1) shows a free shrinkage approximately nine times higher than the corresponding material without hardener (batch code M1).

A comparison of Figures 5.9 and 5.8 shows that all materials cured under 20°C and 95% RH exhibited a much lower free shrinkage (at all ages) than corresponding materials cured under 20°C and 65% RH. For example at water/binder ratio of 0.25 the material cured at 20°C and 65% RH (batch code A1) exhibits a 40 days free shrinkage 82 times higher than the corresponding material cured at 20°C and 95% RH (batch code M1).

An important observation from Figure 5.9 is that at high humidity curing (95%), alkali activated materials are prone to significant shrinkage especially when hardener is added. This is contrary to the behaviour of ordinary Portland cement mortar and concrete.

5.5.1.3 Water cured specimens

The free shrinkage of the alkali activated material with water/binder = 0.25, hardener content 0%, cured in water at 20°C, condition (iii), is given in Figure 5.10. Water curing at 20°C was maintained throughout the 40 day period of shrinkage monitoring. The 40 days shrinkage of the material is 26.15 μstrain. A comparison of Figures 5.8 and 5.10 shows that the free shrinkage of water - cured alkali activated material (w/b=0.25) is negligible compared with the material cured under 20°C and 65% RH. A comparison of Figures 5.9 with 5.10 shows that the free shrinkage of material cured in water at 20°C is of the same order of magnitude as that the matching of corresponding material cured at 20°C and 95% RH.

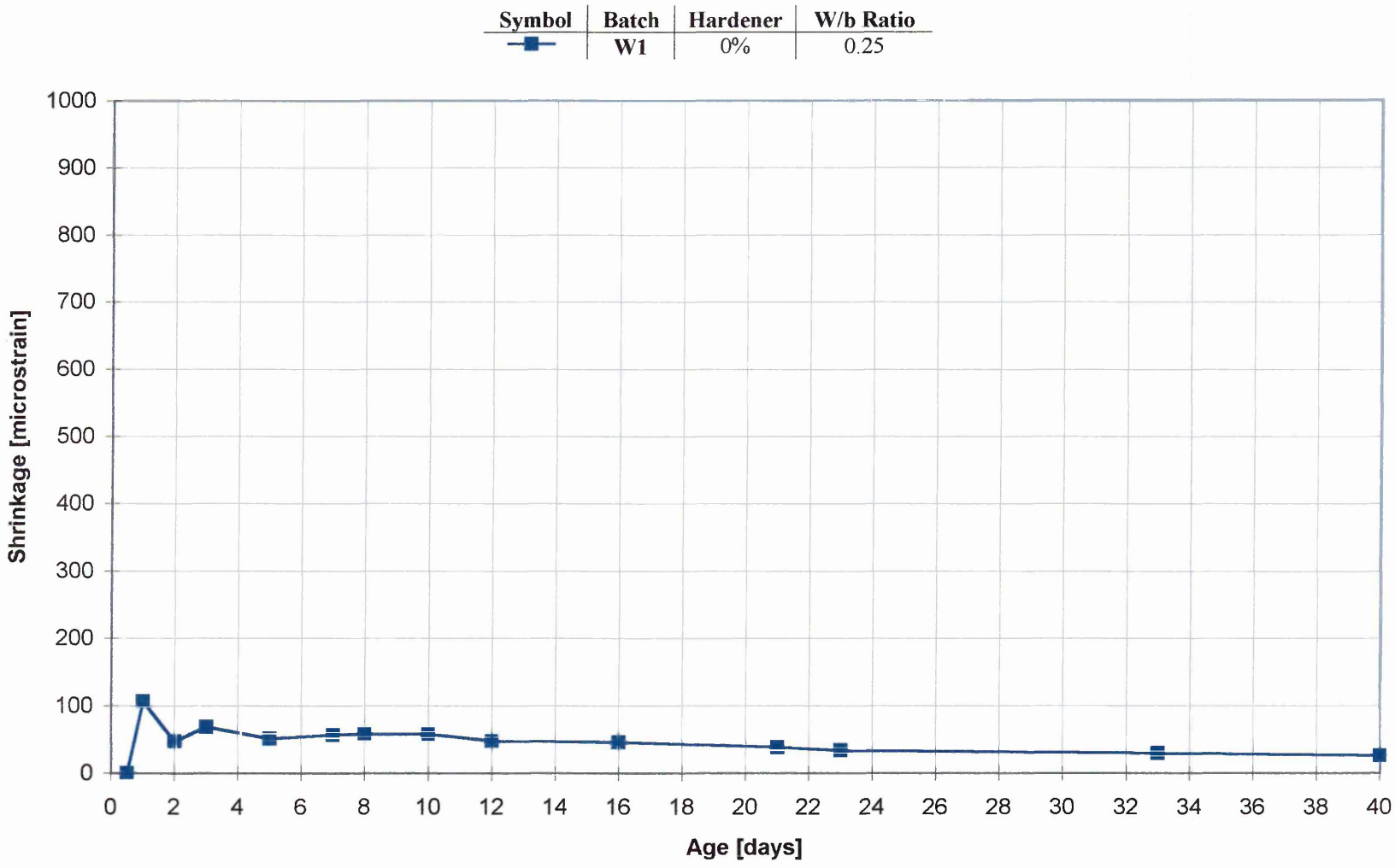

Figure 5.10 Free shrinkage of alkali activated materials cured in water at 20 °C

Again, an important observation is that the alkali activated materials continue to shrink even under water curing whereas cement base materials show significant expansion in similar conditions.

5.5.1.4 Discussion

Free shrinkage in normal concrete and mortar can be restricted by keeping its water/binder ratio and binder (cement) content as low as possible[141]. The results from this investigation confirm that alkali activated materials with a higher water/binder ratio (0.25) exhibit higher free shrinkage than the corresponding materials with a lower water/binder content (0.20) under different curing conditions. Alkali activated materials with a higher water/binder ratio of 0.25 have a lower volume of unhydrated pozzolanic material than materials with lower water/binder of 0.20, as detailed in section 7.4.6 of Chapter 7. Therefore, the layers of hydrated paste surrounding the unhydrated binder grains are thicker at higher water/binder ratios. The unhydrated pozzolanic material restrains the shrinkage of the hydrated material. A greater thickness of the hydrated material surrounding the unhydrated material, which results at higher water/binder ratios, leads to greater shrinkage. At lower water/binder ratios the reduced volume of hydrated paste undergoes greater restraint by the higher volume of the unhydrated material, with consequently lower shrinkage.

Other researchers such as[34, 98, 142, 143] have concluded that the type and quantity of coarse aggregates in a concrete mix and in cementitious repair materials have a great effect on free shrinkage. The aggregate content affects free shrinkage because it determines the amount of cement paste in a mix, which causes shrinkage. In addition, aggregates restrain the shrinkage of the cement paste. The same conclusions were given by O'Flaherty[144] who concluded that cementitious materials with large aggregates and low cement content display the least shrinkage. O'Flaherty found that a normal 1:3 cement mortar with a water/cement ratio of 0.45, cured at 20°C and 65% relative humidity, has a 100 days free shrinkage of 717 microstrain. The 28 days free shrinkage of Portland Cement paste when cured for 7 days at 21°C and then dried was 3000 μstrain[81]. These values are much lower than the values obtained in

the present investigation for the free shrinkage of alkali activated materials. For example, the 40 days free shrinkage of the alkali activated material cured under 20°C and 65%RH is 6138 μstrain. One of the main reasons for this very large difference is the fact that measurement of the free shrinkage of alkali activated materials started at seven hours after casting (adequate strength was developed to allow demoulding) whereas for all the PC mortars shrinkage monitoring started at 24 hours from casting. As a result, the early shrinkage strains are not included in the shrinkage data for PC mortar. Another reason for this difference in the free shrinkage results is the fact that ordinary Portland cement mortar contains zone M sand whereas the alkali activated materials developed in this project have a much finer sand with an average grain size of 175μm as shown in Figure 5.11. Alkali activated materials also have a lower proportion of sand, a pozzolanic materials /sand ratio of approximately 0.5, compared with ordinary Portland cement mortar with cement/sand ratio of 0.3.

Ordinary Portland cement mortars expand when cured in water at 21°C[81]. Alkali activated materials, on the other hand, continue shrinking even when cured in water at 20°C. PC mortar has a ratio of wet cured expansion to dry cured shrinkage (20°C and 65% RH) of 0.6 when shrinkage data after 24 hours from demoulding was used[144], or 0.64 when shrinkage data after 7 hours from demoulding was used. These values indicate significant expansion of wet cured cement mortar whereas alkali activated materials develop significant shrinkage.

Other researchers[34] have investigated the free shrinkage of pozzolanic cement mortars and have found that their expansion in water and shrinkage in air do not differ significantly from ordinary Portland cement mortars. After drying for 28 days, pozzolanic cements mortar (containing opaline breccia or fly ash) showed shrinkage values ranging from 600 to 800 microstrain. These values are comparable with the shrinkage values for ordinary Portland cement mortars. Shrinkage values ranging between 640 to 1150 microstrain have been obtained on mortars made with different pozzolanic materials, wet-cured for 24 hours before exposure to dry conditions[34].
The shrinkage of alkali activated materials has been investigated by other researchers such as Andersson[23] and Malolepszy [10]. Test specimens used by Malolepszy[10] were prisms with dimensions of 25mmx 25mmx 120mm.

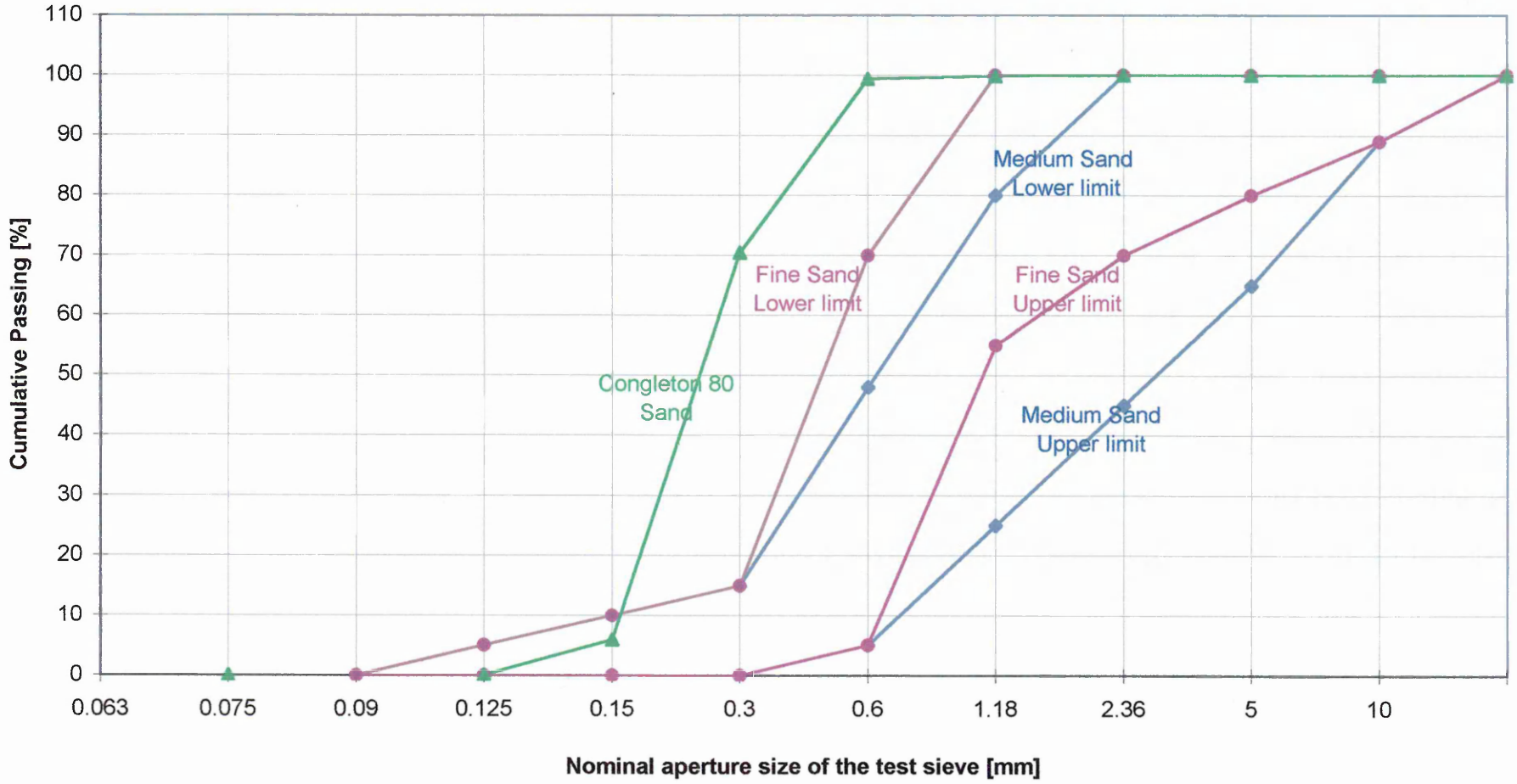

Figure 5.11 Grading curves for fine, medium and Congleton 80 sands

The binder used was ground granulated blast furnace slag and the fine sand was of particle size distribution between 0-2mm. Three types of ground granulated slag were used. Their chemical composition is presented in Table 5.11. The coefficient of quality (K) as well as basicity and acidity ratio (Mb and Ma) are given in Table 5.11. The alkali activator was sodium silicate solution with a silica modulus, n, of 1. The mix proportions of alkali activated mortar used by Malolepszy[10] were 1:3 binder to sand ratio with the exception of specimens 'i' and 'v' (Table 5.13) which have had a ratio of 1:3.86. The alkali activator dosage was 15% by weight of the ground granulated slag. The water/ binder ratio used was 0.42 for the alkali activated slag mortars and 0.5 for the reference Portland cement mortar.

Table 5.11 Chemical composition of slag[10]

Elements	Slag type 1 [%]	Slag type 2 [%]	Slag type 3 [%]
Silicon dioxide (SiO_2)	38.4	34.7	34.9
Aluminium oxide (Al_2O_3)	7.3	10.0	10.1
Iron oxide (FeO)	1.4	0.37	0.32
Magnesia (MgO)	6.7	12.2	12.3
Calcium oxide (CaO)	42.5	37.4	37.4
Sulphide (S^{2-})	2.7	1.19	1.19
Manganese (MnO)	0.7	1.05	1.05
Glassy content	78.9	98.6	98.2
Mb/Ma	**1.08/1.45**	**1.11/1.67**	**1.10/1.66**
Specific surface area [m^2/kg]	**360**	**350**	**500**
$\frac{CaO + MgO + Al_2O_3}{SiO_2}$	**1.471**	**1.718**	**1.713**

Note: Ma and Mb are the acidity ratio and basicity ratio respectively and K is the coefficient of quality (detailed in section 2.3, Chapter 2)

M_b = (CaO [%] + MgO [%])/(Al2O3 [%] + SiO2 [%]) Equation 2.2

M_a= (CaO [%] + MgO [%]+Al2O3 [%])/(MnO [%]+ SiO2 [%]) Equation 2.3

K= (CaO [%] + MgO [%] + Al_2O_3 [%])/ (SiO_2 [%]) Equation 2.4

Two curing conditions were applied for the first 24 hours of curing:

1. 20°C and 95% relative humidity;

2. steam curing, attaining a maximum temperature of 85°C. The temperature was kept constant at 20°C for 2 hours after casting, then progressively increased to 85°C in 2 hours and held at 85°C for a further 4 hours. Finally the temperature was gradually reduced to 20°C in 2 hours. The total curing period was10 hours.

After 24 hours of initial curing in the mould the mortar bars were immersed in water at 20°C and then subjected to alternative cycles of storage in water and air (20°C and 65% RH) as shown in Table 5.12.

Table 5.12 Curing conditions[10]

Age	Curing Conditions
2 to 7 days	water at 20°C
7 to 14 days	air at 20°C and 65% RH
14 to 21 days	water at 20°C
21 to 90 days	air at 20°C and 65% RH

A summary of the experimental details and shrinkage results of alkali activated materials tested by Malolepszy[10] is shown in Table 5.13. The results presented in Table 5.13 show no clear influence of the initial curing conditions on the free shrinkage of alkali activated materials. For example, when slag with Mb/ Ma of 1.08/ 1.45 is used, the steam cured material exhibits a 28 days free shrinkage of 2100 μstrain compared with 5700 μstrain for the same materials cured at 20°C, 95% RH. When slag with Mb/ Ma of 1.11/ 1.67 is used, the steam cured material exhibit a 28 days free shrinkage of 4000 μstrain compared with 3400 μstrain for the material cured at 20°C, 95% RH. A direct comparison of the shrinkage results obtained by Malolepszy and the results from the present investigation of the author is difficult because of the different curing employed by Malolepszy[10].

Table 5.13 Shrinkage data at different ages of alkali activated mortars and reference Portland cement mortar[10]

			Shrinkage Strain [μstrain] at						
Batch No.	**Mb/Ma**	**Initial 24 h curing**	**7 days**	**14 days**	**15 days**	**21 days**	**22 days**	**28 days**	**90 days**
i	1.08/1.45	steam curing (curing 2)	300	1000	800	600	1000	2100	7800
ii	1.08/1.45	20°C and 95%RH (curing 1)	1200	2400	1700	1500	2100	5700	9200
iii	1.11/1.67	steam curing (curing 2)	700	1800	1400	1200	2400	4000	6200
iv	1.11/1.67	20°C and 95%RH (curing 1)	800	1800	1400	1200	2000	3400	8100
v	1.10/1.66	20°C and 95%RH (curing 1)	1400	2300	1800	1500	2900	5200	9400
vi	1.10/1.66	20°C and 95%RH (curing 1)	1000	2200	1700	1200	2400	6100	8400
PC	-	20°C and 95%RH (curing 1)	100	500	100	100	800	2700	4100

Note:

PC represents reference ordinary Portland cement mortar (1:3 sand to cement ratio) Ma and Mb are the acidity ratio and the basicity ratio respectively

Andersson[23] used a 1:3 (binder to sand ratio) alkali activated mortar. Test specimens were prisms with dimensions of 40x40x160 mm. Ground granulated blast furnace slag with a chemical composition given in Table 5.14 and fine sand with particle size between 0-2mm were used as binder and filler, respectively. The alkali activator was sodium silicate solution with a silica modulus, n, of 3.35. Sodium hydroxide was added to the water glass to change the, n, modulus from 3.35 to 0.9 and 1.8. The activator was added as a percentage of the ground granulated slag weight. The water/ binder ratio was includes the proportion of solids and water from the activator.

Table 5.14 Chemical composition of slag[23]

Elements	Content [%]
Silica (SiO_2)	35
Aluminia (Al_2O_3)	10
Iron oxide (FeO)	0.5
Magnesia (MgO)	12
Calcium oxide (CaO)	38
Sulphide (S^{2-})	1.2
Potassium oxide (K_2O)	0.8
$Na_2O_e = 0.658K_2O+Na_2O$	0.526
Manganese (MnO)	0.8
Mb/Ma	**1.11/1.68**
$\frac{CaO + MgO + Al_2O_3}{SiO_2}$	**1.714**

Specimens were cured under two different conditions.

1. 20°C, 80% relative humidity;
2. steam curing consisting of 8 hours of steam at a maximum temperature of 80°C, then stored under 20°C, 80%RH.

Table 5.15 shows the shrinkage data of the alkali activated mortars obtained by Andersson[23]. The free shrinkage of alkali activated slag mortars stored at 20°C, 80% RH is higher than that of the control ordinary Portland cement mortar, regardless of the silica modulus of the water glass. For example, the 35 days shrinkage of the alkali activated slag mortars stored at 20°C, 80% RH ranges from 1015 to 1995 microstrain compared with 603 microstrain for the control ordinary Portland cement mortar. In the case of steam curing, the shrinkage of the alkali activated mortar

containing water glass with a silica modulus, n of 3.35, is more than that of reference Portland cement mortar, regardless of the activator dosage or water/binder ratio. Alkali activated materials containing water glass with silica modulus n of 1.80 and 0.90, exhibit lower shrinkage than ordinary Portland cement mortar for all water glass dosages and water /binder ratios but with the exception of the mixes with 6% water glass and w/b=0.39 and with 4% water glass and w/b of 0.44.

The results presented in Table 5.15 show no clear influence of the water/binder ratio on the free shrinkage of alkali activated materials with 6% water glass. For example, at n=3.35 the material with a w/b of 0.46 exhibits a higher 35 days free shrinkage compared with for the corresponding material with a lower w/b ratio of 0.40. At n = 0.9, on the other hand, materials with a w/b = 0.45 exhibit a lower 35 days free shrinkage of 165 μstrain compared with 239 μstrain for material with a lower w/b ratio of 0.39.

The size and shape of test specimens affect free shrinkage through their influence on the rate of moisture loss[141]. Figure 5.12 presents the relationship between relative shrinkage and volume/surface ratio of a concrete specimen[141]. Figure 5.12 shows that shrinkage varies inversely with the ratio of the volume to surface area of the specimen. Smaller specimens have a smaller volume to surface ratio than larger specimens, which facilitates more rapid drying of the larger test specimens. Malolepszy[10] obtained much higher shrinkage strains than Andersson[23] because the volume/surface ratio of Malolepszy's specimens was 5.67 compared with 8.89 for specimens used by Andersson. The volume/surface ratio of the specimens used in the author's investigation was 16.67.

Applying the volume/surface ratio corrections from Figure 5.12, to the original shrinkage data obtained by Andersson (Table 5.15), the adjusted free shrinkage values are calculated and presented in Table 5.16. These will allow for a direct comparison with the results obtained from the present investigation (Table 5.17).

Table 5.15 Shrinkage data of alkali activated mortars and reference Portland cement mortar[23]

				Shrinkage Strain [μstrain] at age 35/231 days		
Batch No.	**Silica modulus**	**Water glass content [%]**	**Water/Binder ratio**	**Air Cured* (20°C,80%RH)**	**Steam Cured* (up to 80°C)**	**Steam Cured** (up to 80°C)**
1	3.35	4.0	0.45		2483/2720	
2	3.35	6.0	0.40		1311/1240 *(311/240)*[(1)]	
3	3.35	6.0	0.46	1995/2290	1438/1760	
4	3.35	8.0	0.47		400/700	
5	1.80	4.0	0.44		280/590	
6	1.80	6.0	0.39		660/840	
7	1.80	6.0	0.45	1015/1330	85/350	
8	1.80	8.0	0.46		36/300	
9	0.90	4.0	0.44		452/790	
10	0.90	6.0	0.39		239/290	
11	0.90	6.0	0.45	1137/1440	165/420	352/480
12	0.90	8.0	0.46		101/330	
PC	-	-	0.50	603/680	373/480	

Note:

PC represents reference ordinary Portland cement mortar (1:3 sand to cement ratio)

* specific surface of the slag was **530 [m^2/kg]**

** specific surface of the slag was **670 [m^2/kg]**

(1) Anderssonl[23] quotes two contradictory shrinkage values for this mix batch

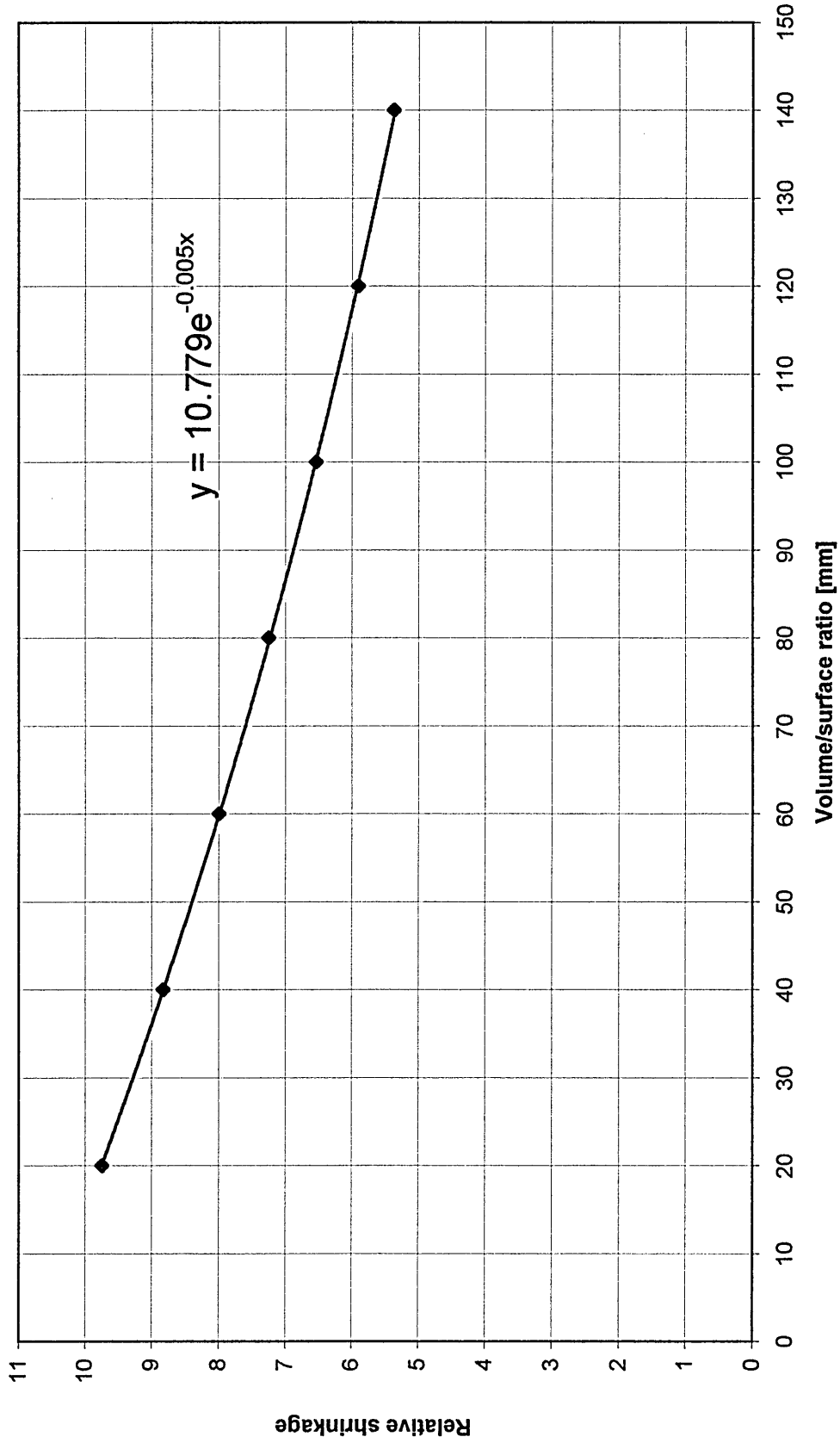

Figure 5.12 Effect of volume/surface ratio on shrinkage[141]

Table 5.16 Shrinkage data of Andersson[23] adjusted to volume /surface area ratio of 16.67

				Shrinkage Strain [μstrain] at age 35/231 days		
Batch No.	**Activator [%]**	**Silica modulus**	**Water/Binder ratio**	**Air Cured* (20°C,80%RH)**	**Steam Cured* (up to 80°C)**	**Steam Cured** (up to 80°C)**
1	4.0	3.35	0.45		2582/2829	
2	6.0	3.35	0.40		1363/1290 *(323/250)*[(1)]	
3	6.0	3.35	0.46	2075/2382	1496/1830	
4	8.0	3.35	0.47		416/728	
5	4.0	1.80	0.44		291/614	
6	6.0	1.80	0.39		686/874	
7	6.0	1.80	0.45	1056/1383	88/364	
8	8.0	1.80	0.46		37/312	
9	4.0	0.90	0.44		470/822	
10	6.0	0.90	0.39		249/302	
11	6.0	0.90	0.45	1182/1498	172/437	366/499
12	8.0	0.90	0.46		105/343	
PC	-	-	0.50	627/707	499/499	

Note:

PC represents reference ordinary Portland cement mortar (1:3 sand to cement ratio)

* specific surface of the slag was **530 [m^2/kg]**

** specific surface of the slag was **670 [m^2/kg]**

(1) Andersson[23] quotes two contradictory shrinkage values for this mix batch

A comparison of the shrinkage of materials cured under 20°C and 95%RH, from the present investigation (Table 5.17), and materials cured under 20°C and 80%RH, from Anderssons's investigations (Table 5.16), shows a big difference in the shrinkage values. For example the 35 days shrinkage of materials cured under 20°C and 95% RH and water/binder ratio of 0.25 (n=2.00) is 77 microstrain, compared with 1056 microstrain for material cured under 20°C, 80% RH with a water/binder of 0.43 (n=1.80). One of the reasons for this difference in the shrinkage results is the change of relative humidity from 80% to 95%. The shrinkage of concrete is greatly affected by the relative humidity of the medium surrounding it during curing and storing[81,98]. The vapour pressure within the cement paste is always less than the saturated vapour pressure and it is logical to expect that there is an intermediate humidity at which the cement paste would be in hygral equilibrium. Figure 5.13 shows the relationship between the relative humidity of curing and the 35 days shrinkage (from both investigations) of alkali activated materials. The clear trend is that free shrinkage increases with decreasing relative humidity of curing.

A regression analysis of the data in Figure 5.13 gives the following relationship:

$\varepsilon_{os} = 5E+26 \cdot RH^{-12.553}$ Equation 5.1

with a coefficient of correlation R^2 of 0.9645.

Where:

ε_{os} is the 35 day free shrinkage of alkali activated materials

RH is the relative humidity of curing

Another reason for the high shrinkage results obtained by Andersson[23] could be the water/ binder ratio. The mixes from the present investigations have a lower water/binder ratio of 0.25 compared with 0.43 from Anderssons's investigations. Increasing the water/ binder ratio is expected to cause greater shrinkage as explained in section 5.5.5.1. However, the results indicate that the most important parameter which governs free shrinkage of alkali activated materials is relative humidity of curing since under 65%RH the material has a much higher shrinkage than under 85%RH even though the water/binder ratio under 65% RH is lower at 0.25 compared with 0.43 at 85%RH.

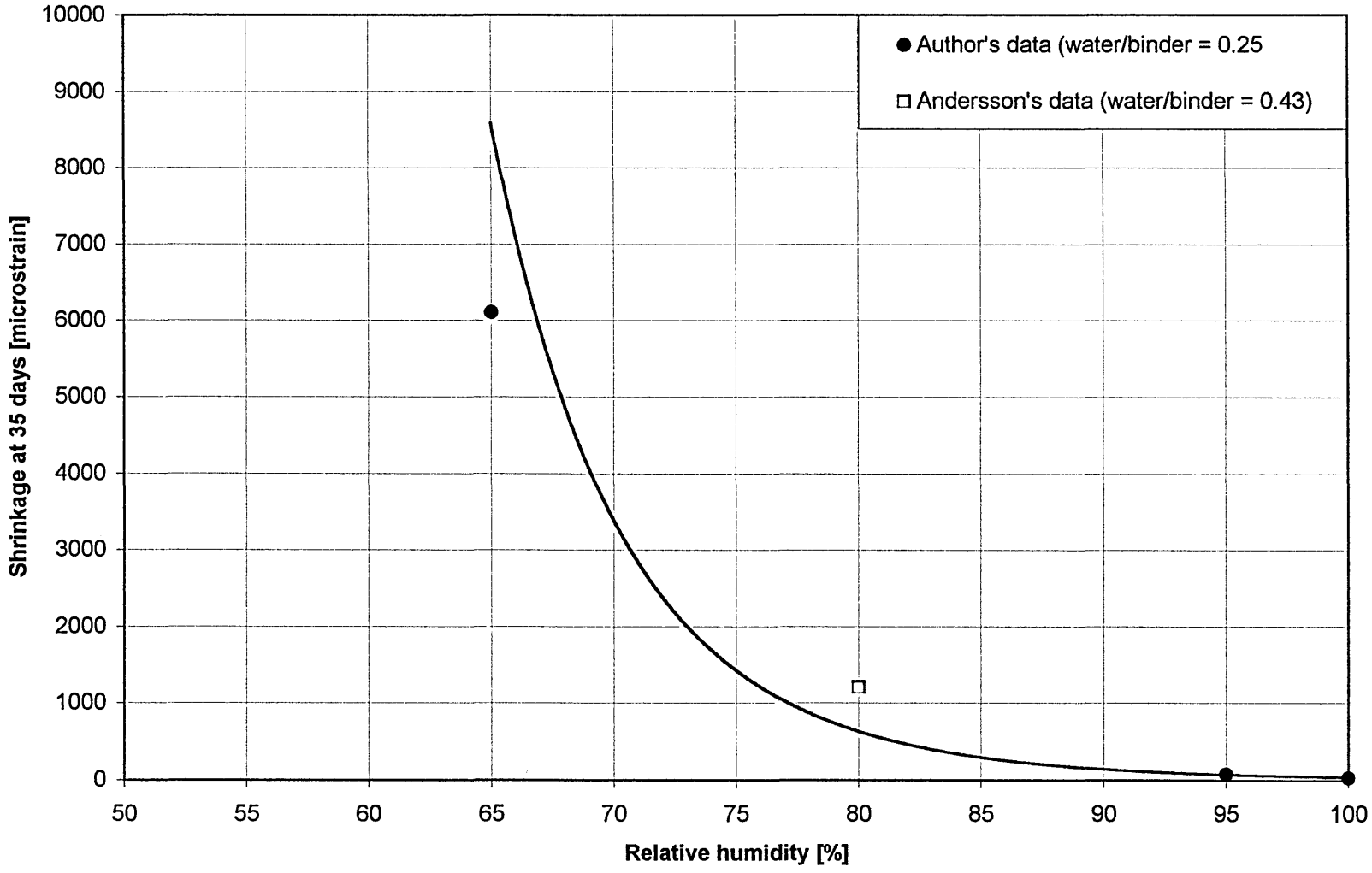

Figure 5.13 Relationship between 35 day shrinkage and relative humidity of curing for alkali activate materials

Table 5.17 35 days Shrinkage of alkali activated materials from the present investigation(volume/ surface area of the test specimens, 16.67)

Batch Code	Curing conditions	Water/Binder	Shrinkage [μstrain]
A1	20°C and 65% RH	0.25	6112
KA1	20°C and 65% RH	0.25	6077
W1	water curing at 20°C	0.25	27
A2	20°C and 65% RH	0.2	5100
KA2	20°C and 65% RH	0.2	5924
M1	20°C and 95% RH	0.25	77
KM1	20°C and 95% RH	0.25	689
M2	20°C and 95% RH	0.20	45
KM2	20°C and 95% RH	0.20	377

5.5.2 Free shrinkage of the fibre reinforced alkali activated materials.

5.5.2.1 Glass fibre

The shrinkage of glass fibre reinforced alkali activated materials cured under 20°C and 65% relative humidity, is presented in Figure 5.14 and summarised in Table 5.18. The exposure conditions of 20°C and 65% RH were maintained throughout the 40 day period of shrinkage monitoring. The glass fibre percentages quoted are by volume of the mix. All mixes in this investigation had a water/binder of 0.25. A detailed description of the mixes used in current investigation is given in section 5.3.5.

Table 5.18 40 days Shrinkage of glass fibre reinforced alkali activated materials

Batch Code	Fibre type	V_f [%]	$V_f l/d$	Shrinkage Strain [μstrain]	% of control
A1 (control)	-	0	0	6138.22	100
GA1	Alkali resistant glass fibres (Cem-FIL 62/2)	1.5	1.06	3880.94	63
GA2	Alkali resistant glass fibres (Cem-FIL 62/2)	3	2.12	2768.63	45

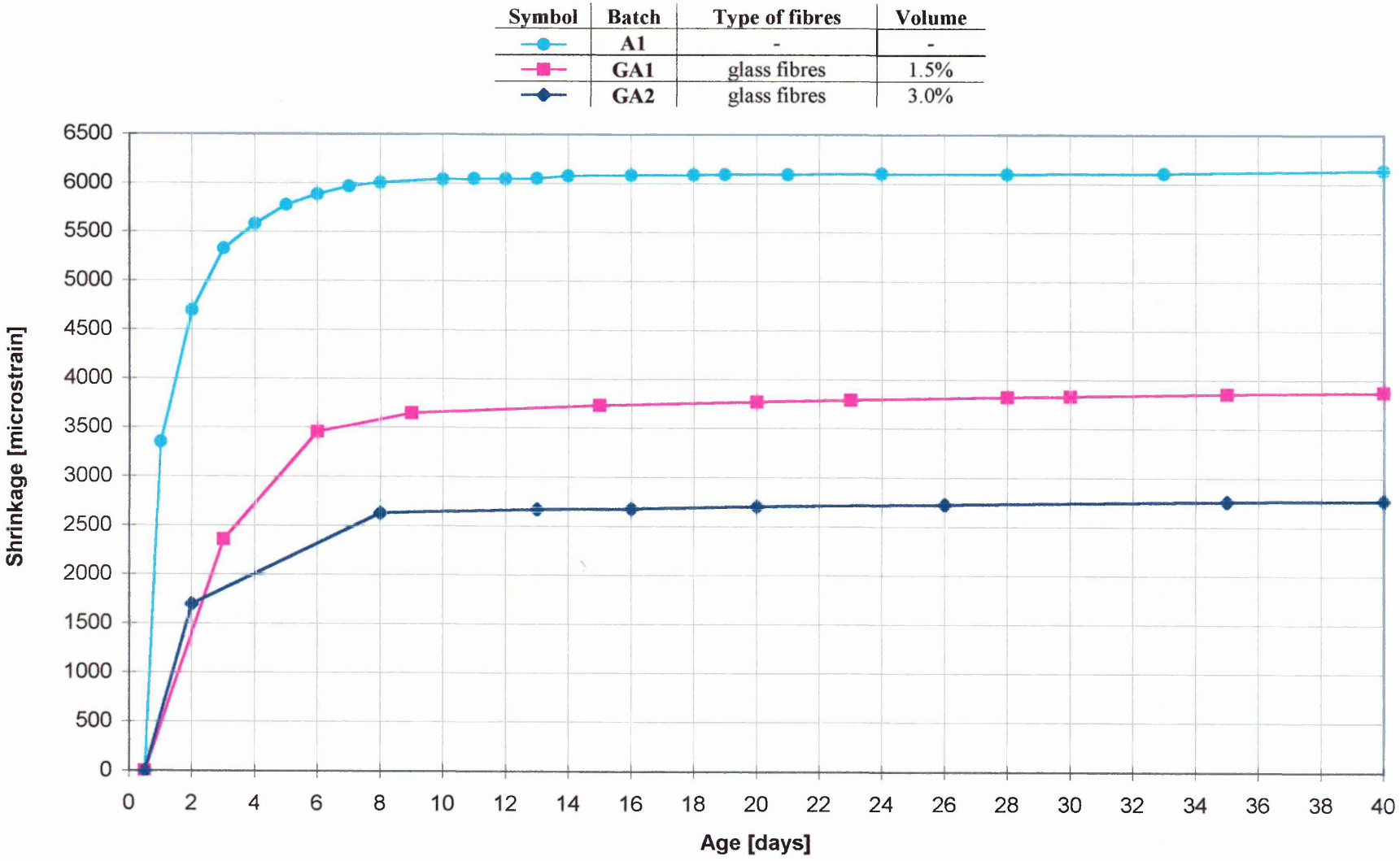

Figure 5.14 Free shrinkage of glass fibre reinforced alkali activated materials cured at 20°C and 65% RH

The results presented in Table 5.18 and Figure 5.14 show that fibre reinforcement provides a considerable restraint to the shrinkage of the matrix and this restraint increases with increasing fibre volume. For example the 40 days shrinkage of materials with 1.5% and 3% volume of glass fibre (batch code GA1 and GA2, respectively) was 63% and 45% of the control matrix, respectively. The data in Table 5.18 indicate that increasing the V_f l/d leads to lower shrinkage. For example, the 40 days shrinkage of materials with V_f l/d=1.06 (batch code GA1) is 3881 μstrain compared with 2769 μstrain for material with V_f l/d=2.12 (batch code GA2).

5.5.2.2 Steel fibre

The shrinkage data of the steel fibre reinforced alkali activated materials cured under 20°C and 65% relative humidity, is presented in Figure 5.15 and summarised in Table 5.19. The steel fibre percentages quoted are all by volume of the mix. All materials have a water/ binder ratio of 0.25.

Table 5.19 40 days Shrinkage of steel fibre reinforced alkali activated materials

Batch Code	Fibre type	V_f [%]	V_fl/d	Shrinkage Strain [μstrain]	% of control specimen
A2 (control)	-	0	0	6138.22	100
SwA1	Stainless steel fibres (straight)	1.5	0.70	4015.33	65
SA1	Melt extract steel fibres	1.5	0.36	4346.83	71
SA2	Melt extract steel fibres	3.0	0.72	3455.92	56

The results presented in Table 5.19 and Figure 5.15 show that steel fibres are effective in reducing the shrinkage of alkali activated materials. The results for steel fibre reinforced materials follow similar trends as the glass fibre reinforced alkali activated materials. For example the 40 day shrinkage of materials with 1.5% volume of steel fibres (batch code SA1) was 71% of the control matrix. The corresponding value for material with 3% volume of steel fibre (batch code SA2) is 56% of the control matrix. The data in Table 5.19 indicate that increasing the V_f l/d leads to lower shrinkage.

Symbol	Batch	Curing	Type of fibres	V_f
	A1	20°C and 65% RH	-	-
	SwA1	20°C and 65% RH	straight steel fibres	1.5%
	SA1	20°C and 65% RH	melt extract fibres	1.5%
	SA2	20°C and 65% RH	melt extract fibres	3.0%

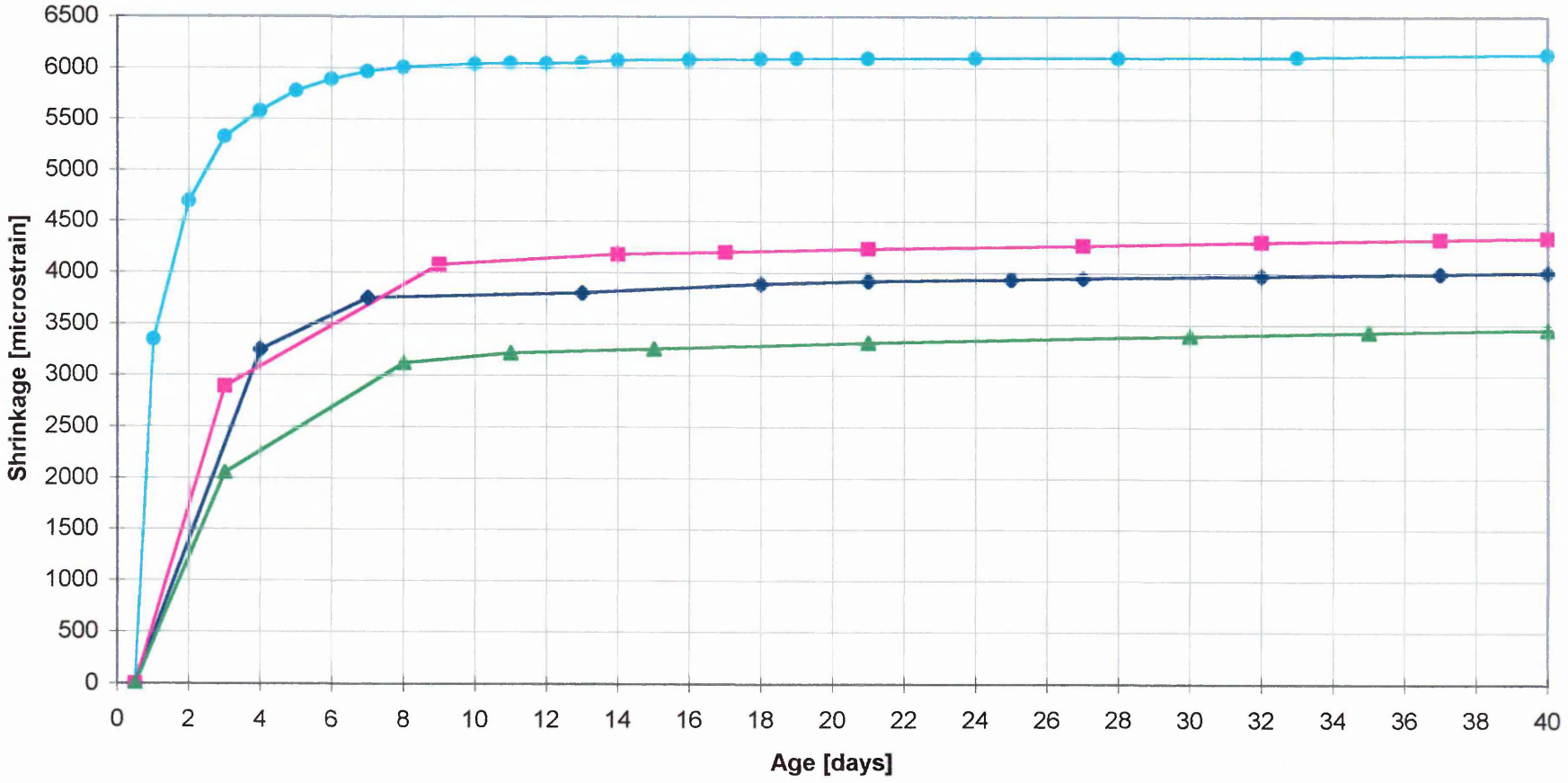

Figure 5.15 Free shrinkage of steel fibre reinforced alkali activated materials at 20°C and 65% RH

For example, the 40 days shrinkage of materials with V_f l/d=0.36 (batch code SA1) is 4347 μstrain compared with 3456 μstrain for material with V_f l/d=0.72 (batch code SA2).

5.5.2.3 Theoretical Prediction of Free Shrinkage

5.5.2.3.1 Free shrinkage theory

A model for the free shrinkage of cement matrices reinforced with randomly orientated fibres of length, *l*, and diameter d is based on the concept that shrinkage in any direction is restrained by an aligned fibre of effective length, l_e, parallel to the direction of shrinkage strain under consideration[114]. This is due to the tendency of the matrix to slide past a fibre during shrinkage, the fibre in turn providing restraint to the sliding action through the fibre-matrix interfacial bond strength, τ[114].

The idealised fibre distribution is shown in Figure 5.16-(a)[114] where the spacing s between the fibres is given by the formula[114]:

$$s^3 + l_e s^2 - B^2\left(H - \frac{l_e}{2}\right)\frac{l}{L} = 0 \qquad \text{Equation 5.2}$$

l_e is the effective length of the random oriented fibres

$l_e = 0.41l$

L is the equvalent length of a continuous fibre which equals :

$$L = \frac{V_f}{A} = \frac{4V_f}{\pi d^2} \qquad \text{Equation 5.3}$$

V_f is the volume of randomly oriented discrete fibres of diameter d

B is the specimen breadth

H is the specimen height

Figure 5.16-(b) [114] represents the shrinkage model which comprises of a single aligned fibre of effective length l_e which is surrounded by a thick cylinder of cement matrix of diameter s.

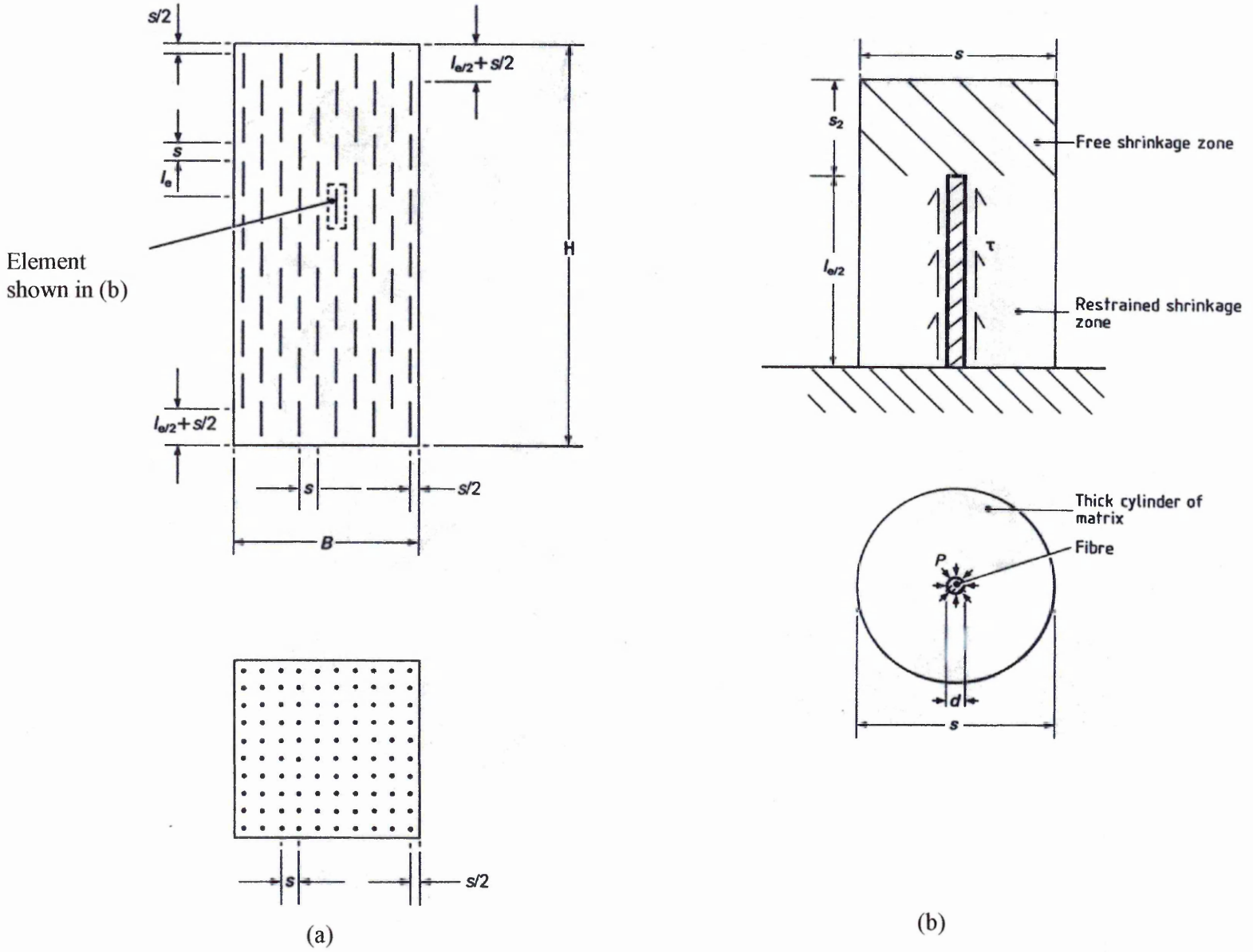

Figure 5.16 (a) Idealised fibre distribution and (b) shrinkage model for fibre reinforced matrices[114]

The shrinkage of the unrestrained cement matrix, $\varepsilon_{os,}$ is restrained by the fibre through interfacial bond to give the following expression for the free shrinkage of the steel fibre reinforced cement matrix, ε_{fs}[114]:

$$\varepsilon_{fs} = \varepsilon_{os} - \frac{0.3362\tau d l^2}{s^2 E\left(0.41l + s\right)} \qquad \text{Equation 5.4}$$

The interfacial bond stress, τ, is a function of the radial pressure, P, exerted by the shrinking matrix at the fibre-matrix interface and the coefficient of friction, μ, and is given by the expression:

$$\tau = \mu \cdot P \qquad \text{Equation 5.5}$$

Applying the classical expression for thick cylinders based on Lame's equations gives the following expression for P[114]

$$P = \frac{\varepsilon_{os}\left(\frac{s}{2} - \frac{d}{2}\right) \cdot E}{\frac{d}{2}\left\{\left[\frac{\left(\frac{s}{2}\right)^2 + \left(\frac{d}{2}\right)^2}{\left(\frac{s}{2}\right)^2 - \left(\frac{d}{2}\right)^2} + \upsilon\right] + \frac{\left(1 - \upsilon_f\right)}{\frac{E_f}{E}}\right\}} \qquad \text{Equation 5.6}$$

Substituting, P, from equation 5.6 into equation 5.5 gives:

$$\frac{\tau}{E} = \frac{\mu\varepsilon_{os}\left(\frac{s}{2} - \frac{d}{2}\right)}{\frac{d}{2}\left\{\left[\frac{\left(\frac{s}{2}\right)^2 + \left(\frac{d}{2}\right)^2}{\left(\frac{s}{2}\right)^2 - \left(\frac{d}{2}\right)^2} + \upsilon\right] + \frac{\left(1 - \upsilon_f\right)}{\frac{E_f}{E}}\right\}} \qquad \text{Equation 5.7}$$

Substituting equation 5.7 in equation 5.4 gives the expression for the shrinkage strain of steel fibre reinforced matrices, ε_{fs}:

$$\varepsilon_{fs} = \varepsilon_{os} - \frac{0.6724 l^2 \mu \varepsilon_{os} \left(\frac{s}{2} - \frac{d}{2}\right)}{s^2 \left\{ \left[\frac{\left(\frac{s}{2}\right)^2 + \left(\frac{d}{2}\right)^2}{\left(\frac{s}{2}\right)^2 - \left(\frac{d}{2}\right)^2} + \upsilon \right] + \frac{(1 - \upsilon_f)}{\frac{E_f}{E}} \right\} (0.41l + s)}$$

Equation 5.8

Where:

l is the length of the randomly orientated fibres,

μ is the coefficient of friction at the fibre - mortar matrix interface. It is a material property of the fibre-matrix interface and a constant value can be assumed for a particular type of fibre and cement matrix,

ε_{os} is the free shrinkage strain of the unrestrained control matrix ,

s is the spacing between fibres,

ν is the Poisson's ratio of unreinforced matrix (0.2),

ν_f is the Poisson's ratio of fibres,

E is the Elastic Modulus of the matrix,

E_f is the Elastic Modulus of fibres,

5.5.2.3.2 Early age coefficient of friction of fibre reinforced alkali activated materials

In order to determine the free shrinkage of the steel fibre reinforced cement matrix, ε_{fs}, from equation 5.8, knowledge of the shrinkage of the control matrix, is required together with a value for the coefficient of friction, μ, fibre dimensions and volume. The value for the coefficient of friction for fibre reinforced alkali activated materials is not available from the current state of knowledge and therefore, it is difficult to check directly the validity of equation 5.8. However, equation 5.8 can be used indirectly to determine, μ, using the experimental data on shrinkage of control and fibre reinforced matrices.

Equation 5.8 is rearranged in terms of, μ, giving:

$$\mu = \frac{(\varepsilon_{os} - \varepsilon_{fs}) \cdot s^2 \cdot (0.41l + s)}{0.6724 l^2 \varepsilon_{os} \left(\frac{s}{2} - \frac{d}{2}\right)} \left\{ \left[\frac{\left(\frac{s}{2}\right)^2 + \left(\frac{d}{2}\right)^2}{\left(\frac{s}{2}\right)^2 - \left(\frac{d}{2}\right)^2} + \upsilon \right] + \frac{(1 - \upsilon_f)}{\frac{E_f}{E}} \right\} \qquad \text{Equation 5.9}$$

The spacing between the fibres was determined using equation 5.2.

For stainless steel straight fibres of d = 0.157mm, l = 7 mm and V_f = 1.5 %,

$s^3 + 2.87\ s^2 - 8.207 = 0$

The acceptable solution of the above cubic equation is, s = 1.39 mm

For melt extract steel fibres of d = 0.5mm, l = 12 mm and V_f = 1.5 %,

$s^3 + 4.92\ s^2 - 155.7915 = 0$

The acceptable solution of the above equation is, s = 4.15 mm

For melt extract steel fibres of d = 0.5mm, l = 12 mm and V_f = 3.0 %,

$s^3 + 4.92\ s^2 - 77.89 = 0$

The acceptable solution of the above equation is, s = 3.12 mm

For alkali resistant glass fibres of d = 0.17mm, l = 12 mm and V_f = 1.5 %

$s^3 + 4.92\ s^2 - 18.01 = 0$

The acceptable solution of the above equation is, s = 1.655 mm

For alkali resistant glass fibres of d = 0.17mm, l = 12 mm and V_f = 3.0 %

$s^3 + 4.92\ s^2 - 9.00 = 0$

The acceptable solution of the above equation is, s =1.212 mm

Substituting the experimental shrinkage data from Figures 5.14, 5.16 and Tables 5.18, 5.19 in equation 5.9 together with material properties E, E_f, ν, ν_f and fibre parameters l, d and s, the coefficients of friction for steel and glass fibres were calculated. The values of, μ, corresponding to the 40 day shrinkage data given in Table 5.18 and 5.19 are listed in Table 5.20.

The values of, μ, obtained for different volumes of steel and glass fibres using the shrinkage data in Figures 5.14 and 5.15 are also plotted against the age of curing in Figure 5.17. Figure 5.17 shows that the age of curing and fibre volume fraction has no significant effect on the values of coefficient of friction beyond the first 5 days after demoulding. The primary parameter which influences the values of, μ, is the type of fibre. Therefore, μ, is considered to be a material property of the matrix-fibre interface, which is governed by the surface texture and shape of fibre and the constituents of the matrix.

Table 5.20 Coefficients of friction for steel and glass fibres reinforced alkali activated materials and Portland cement mortars

Batch Code	ε_{fs} [μstrain]	V_f [%]	d [mm]	l [mm]	s [mm]	μ* (aam)	μ_{es}** (PC)
SwA1	4015.3	1.5	0.15	7	1.389	0.180	na
SA1	4346.8	1.5	0.5	12	4.145	0.328	0.218
SA2	3455.9	3	0.5	12	3.115	0.354	0.275
GA1	3880.9	1.5	0.17	12	1.655	0.135	0.175
GA2	2768.6	3	0.17	12	1.212	0.148	0.150

Note:

ε_{fs} is the 40 day free shrinkage

ε_{os} = 6138.22 [microstrain]

*values determined from the author's data for alkali activated materials (aam).

**values determined by Mangat et al[146] for Portland cement mortar, using early age shrinkage data.

There is no available data on the coefficient of friction of alkali activated materials but other researchers[114, 145, 146] have investigated the coefficient of friction of PC mortar. The values for the coefficient of friction determined by Mangat et al[146] using the early age shrinkage data, μ_{es}, for Portland cement mortar are presented in Table 5.20. The early shrinkage was measured between 4 and 24 hours after mixing. During this period setting and hardening would have occurred and, therefore, this data represents a different phase than either the plastic shrinkage or long term shrinkage.

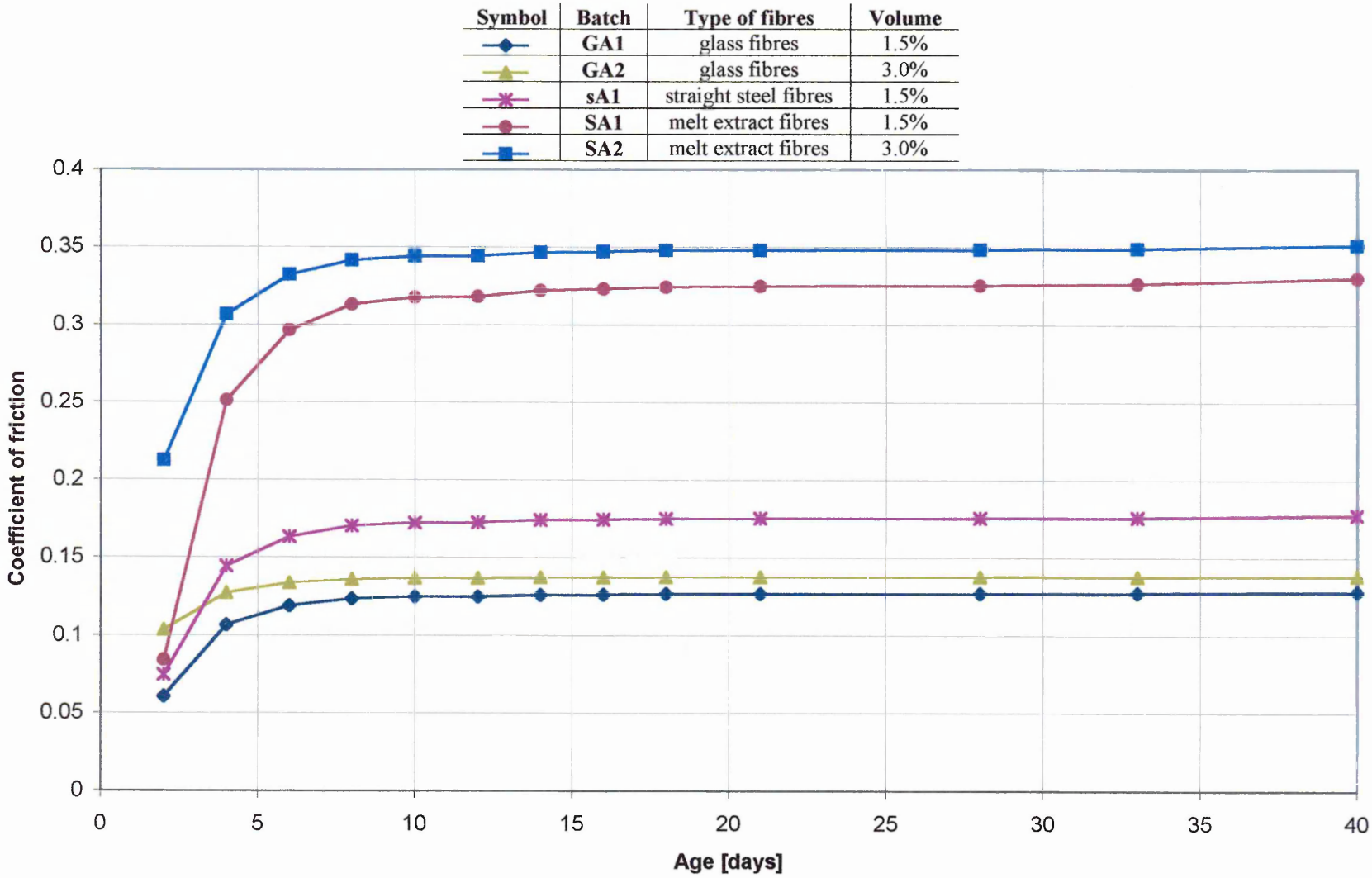

Figure 5.17 Effect of age and fibre volume on coefficient of friction between the fibre and alkali activated matrix

The long term shrinkage data of Portland cement mortars are usually based on measurements taken after 24 hours from casting which excludes the large proportion of shrinkage taking place in the first 24 hours. These long term values of cement mortars are, therefore, not comparable with the shrinkage of alkali activated materials whose the shrinkage measurements commence after 7 hours from casting. The early shrinkage data of Portland cement mortars (4-24 hours) are more relevant for comparison with alkali activated materials.

The average value of, μ, for glass fibres (batches GA1 and GA2) is 0.343 and for melt extract steel fibres (batches SA1 and SA2) is 0.142. The coefficients of friction given in Table 5.20 for fibre reinforced Portland cement mortars are comparable with those obtained in the present investigation for fibre reinforced alkali activated materials. This proves that the theoretical derivations for shrinkage developed for fibre reinforced Portland cement matrices by Mangat et al[114] are also applicable to alkali activated matrices.

5.5.2.4 Discussion

The results from the present investigation show that both glass and steel fibre reinforcement provide a considerable restraining influence to the shrinkage of alkali activated matrices. For example, the free shrinkage of alkali activated material with 1.5% fibre volume is 3880.94 μstrain (glass fibre) and 4346.83 μstrain (steel fibres) compared with 6138.22 for the control matrix.

The relationship between the 40 days free shrinkage and the fibre, V_f l/d, ratio for alkali activated materials cured and stored under 20°C and 65% relative humidity is presented in Figure 5.18. The, V_f l/d, ranged from 0.36 to 2.12. The experimental data of steel and glass fibre reinforced alkali activated materials are considered. The clear trend is that shrinkage decreases with increasing, V_f l/d, ratio for both glass and steel fibres. The, V_f l/d, ratio and shrinkage have a very strong linear and inversely proportional relationship. This is primarily due to the decrease in fibre spacing caused by increasing, V_f l/d, which leads to thinner cylinders of the matrix surrounding each fibre and consequently greater shrinkage restraint and hence lower shrinkage deformation.

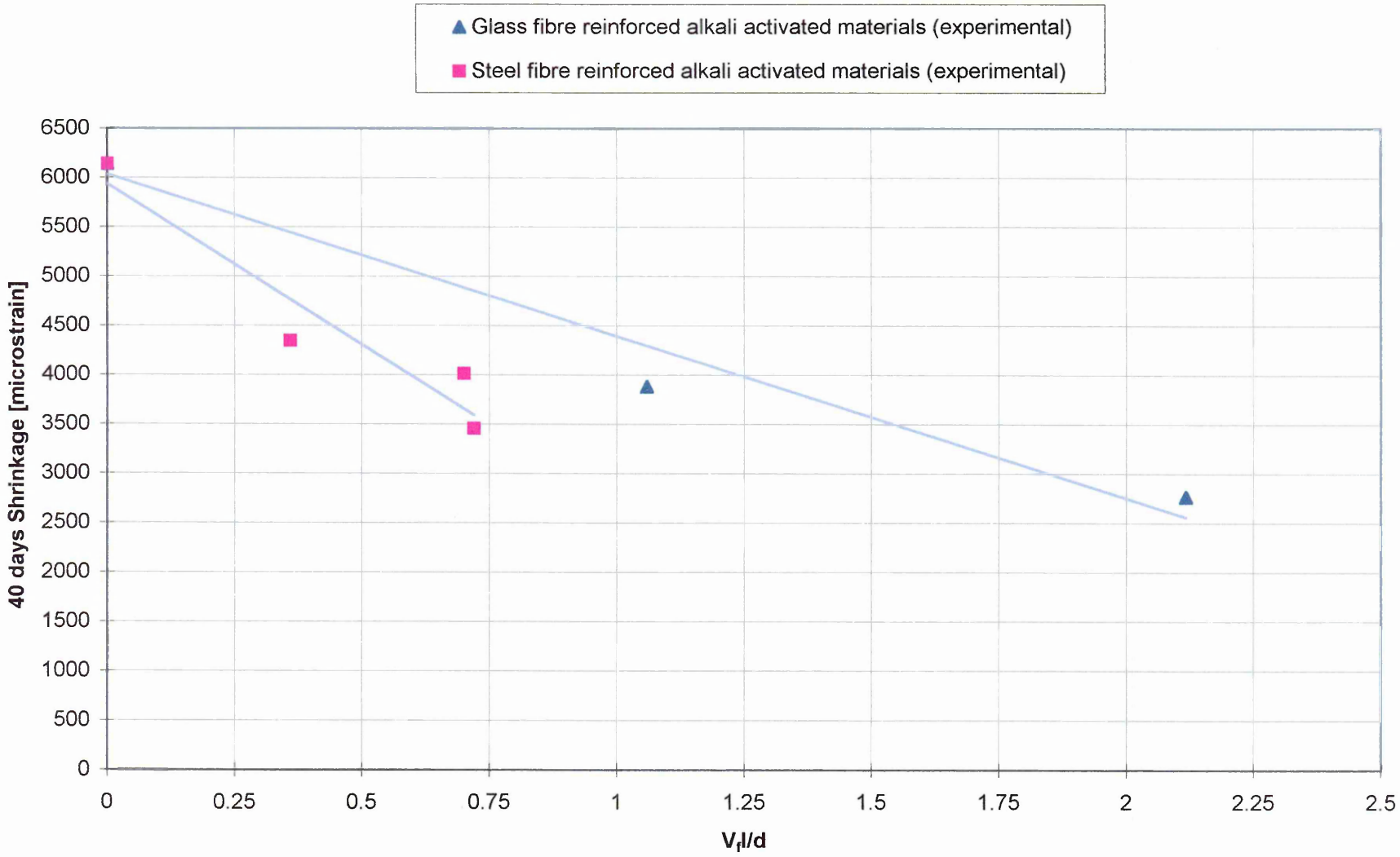

Figure 5.18 Relationship between free shrinkage (40 days) and $V_f l/d$

It is, therefore, evident that, V_f l/d, ratio is of primary importance in controlling the free shrinkage of alkali activated materials.

Other researchers such as Mangat and Azari[114, 146] concluded from their research on Portland cement mortars reinforced with steel fibres that the relationship between free shrinkage and fibre, V_f l/d, ratio is linear and inversely proportional.

The relationship between the 40 days free shrinkage and modulus of elasticity of fibre reinforcement for alkali activated materials cured under 20°C and 65% relative humidity is presented in Figure 5.19. The graph was plotted using the 40 days shrinkage values, determined from Figure 5.18, for selected, V_f l/d ratios of 0.36, 0.70, 0.72 and 1.06. The modulus of elasticity of steel fibres (215.3 GPa) is much higher than that of glass fibre (72 GPa). The relationship between the 40 days free shrinkage and modulus of elasticity of fibre is linear and inversely proportional. The slope of the free shrinkage strain versus modulus of elasticity of fibre graph (Figure 5.19) becomes higher as the, V_f l/d, increases indicating that the reduction in shrinkage due to fibre reinforcements is a function of both E and V_f l/d (also shown by Figure 5.18).

5.5.2.5 Design expression for free shrinkage of fibre reinforced matrices

Figure 5.20 shows the relationship between the, $\varepsilon_{fs}/\varepsilon_{os}$, and the fibre V_f l/d, for fibre reinforced alkali activated materials. Experimental data at different ages are plotted for two groups. The first group combines both glass and plain steel fibres since they show similar coefficients of friction-see Table 5.20 which gives μ values of 0.18, 0.135 and 0.148 for SwA1, GA1 and GA2 respectively. The second group is melt extract steel fibres which have a much greater coefficient of friction (0.328 and 0.354 for SA1 and SA2, see Table 5.20). The data for each group of fibres falls in narrow bands, which have a close correlation with the, V_f l/d, with an average coefficient of correlation R^2 of 0.965.

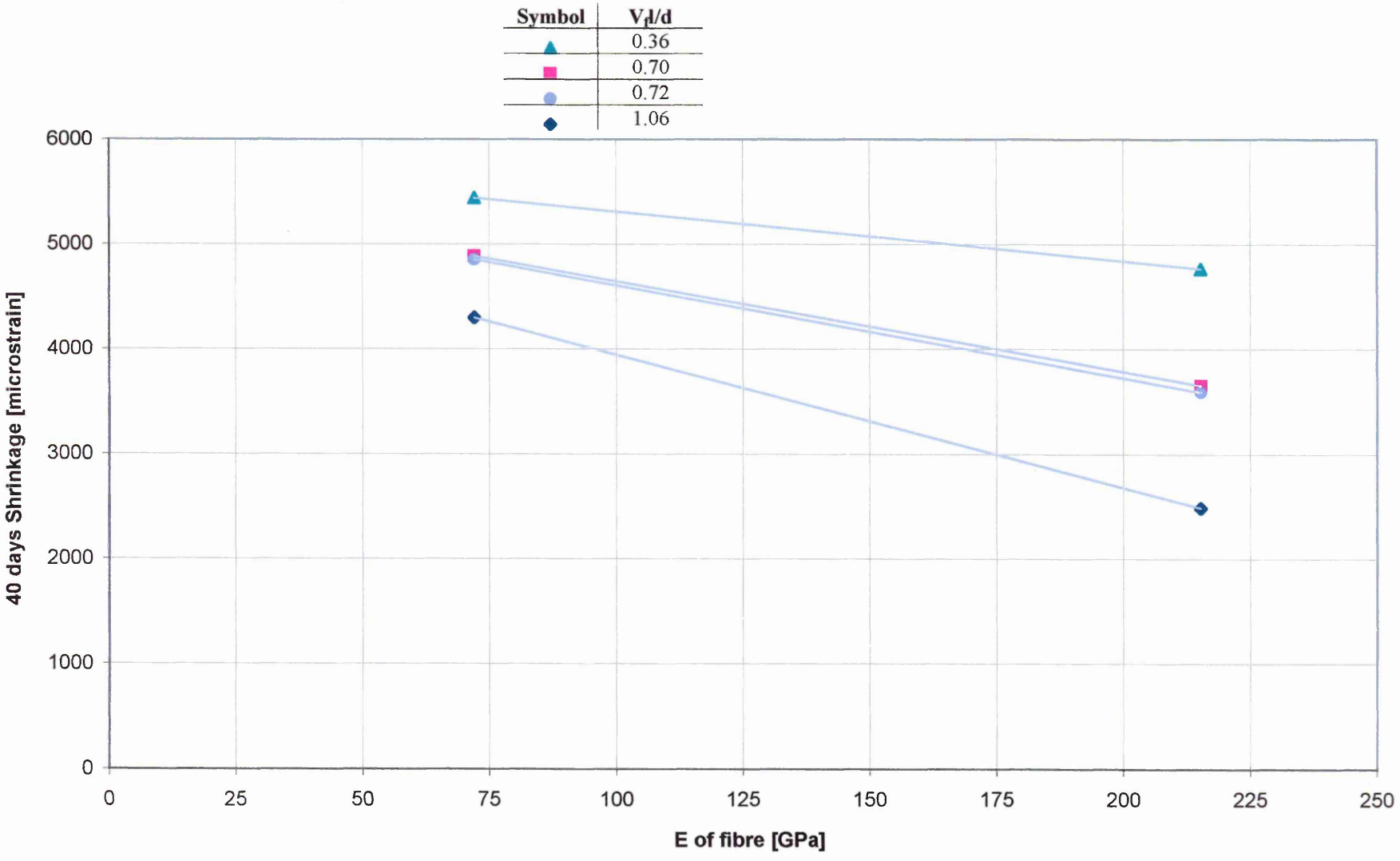

Figure 5.19 Relationship between 40 days free shrinkage and E of fibre reinforcement

Symbol	Age [days]	Type of fibres
○	5	glass fibres/plain steel fibres
◇	20	glass fibres/plain steel fibres
□	70	glass fibres/plain steel fibres
△	90	glass fibres/plain steel fibres
▲	5	melt extract fibres
●	20	melt extract fibres
■	70	melt extract fibres
◆	90	melt extract fibres

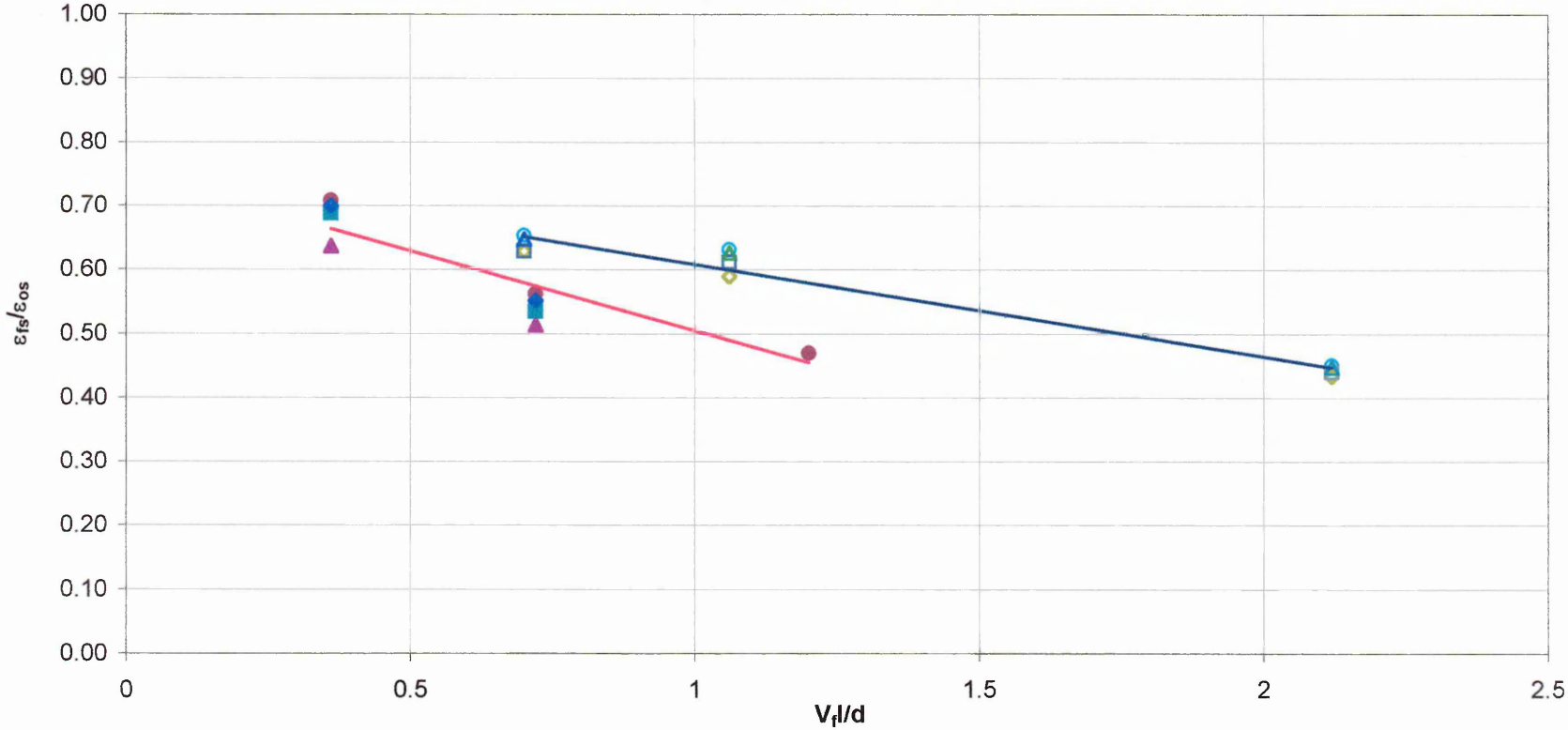

Figure 5.20 Relationship between the $\varepsilon_{fs}/\varepsilon_{os}$ and V_f l/d at different ages of fibre reinforced alkali activated materials

A regression analysis of the data in Figure 5.20 gives the following linear relationship:

$$\frac{\varepsilon_{fs}}{\varepsilon_{os}} = -a \cdot \frac{V_f \cdot l}{d} + b \qquad \text{Equation 5.10}$$

Rearranging equation 5.10 gives :

$$\varepsilon_{fs} = b \cdot \varepsilon_{os} - a \cdot \varepsilon_{os} \cdot \frac{V_f \cdot l}{d} \qquad \text{Equation 5.11}$$

The regression analysis gives the following values for the empirical coefficients a and b for the two groups of fibres glass/plain steel and melt extract.

1. For glass/plain steel fibres:
   the average value of a is 0.145
   and the average value of b is 0.752

2. For melt extract steel fibres:
   the average value of a is 0.311
   and the average value of b is 0.776

Note that the values of empirical coefficient, b are similar for the two groups of fibres. The value of coefficient a is much grater for the melts extract fibres, indicating a greater restraint to the shrinkage provided by this group of fibres. This is due to the greater coefficient of friction, μ, of melt extract fibres.

Thus the shrinkage of fibre reinforced alkali activated materials can be obtained using the equation 5.11 based on the knowledge of shrinkage characteristics of the matrix and details of fibres. Equation 5.11 is valid within the range of the experimental data. It is expected that at very low, V_f l/d ratios, the slope of the linear relationship between $\varepsilon_{fs}/\varepsilon_{os}$ and V_f l/d would increase (coefficient a will increase) to meet the boundary condition of $\varepsilon_{fs}/\varepsilon_{os} = 1$ when V_f l/d = 0.

5.5.3 Compressive Creep of alkali activated materials

Figures 5.21 to 5.25 show the creep curves of the investigated materials. The graphs show the instantaneous elastic strain immediately after loading, the creep stain under sustained stress and the creep recovery after unloading. Tables 5.21 and 5.22 give the batch code of each material (column 1), the 28 day compressive strength (column 2), the instantaneous elastic strain upon loading (column 3), the 90 day creep strain (column 4) and the creep coefficient in column 5. The delayed elastic strain and flow creep, both of which constitute creep recovery, are presented in columns 6 and 8, respectively. The delayed elastic strain is also given as a percentage of the 90 days creep strain in column 7. The ratio between (delayed elastic strain plus flow creep) to the total 90 day creep strain is given in column 9.

5.5.3.1 90 day Creep Strains

Creep testing started at the age of 28 days after the initial curing. Testing was carried out in a controlled environment of 20°C and 65% relative humidity. Two initial curing conditions were employed, 20°C and 65% RH, condition (i) and thermal curing up to 120°C, condition (iv) detailed in section 5.3.4. After initially curing, the specimens were kept in a control environment at 20°C, 65% RH until the creep tests were completed. No creep tests were conducted on thermally cured alkali activated materials with 0% fibre addition.

Compressive creep curves of alkali activated materials initially cured under 20°C and 65% RH and exposed to the same environment during creep testing, are presented in Figure 5.21. The results are also summarised in Table 5.21. A comparison of materials A1 and A2 which have a water/binder ratio of 0.25 and 0.20 respectively shows that water/binder ratio has an insignificant effect on the compressive creep at all ages. For example, the 40 days creep strain of material with w/b=0.25 (batch code A1) is only 6% higher than the corresponding materials with a lower water/binder of 0.20 (batch code A2) while at 90 days the reverse effect is evident.

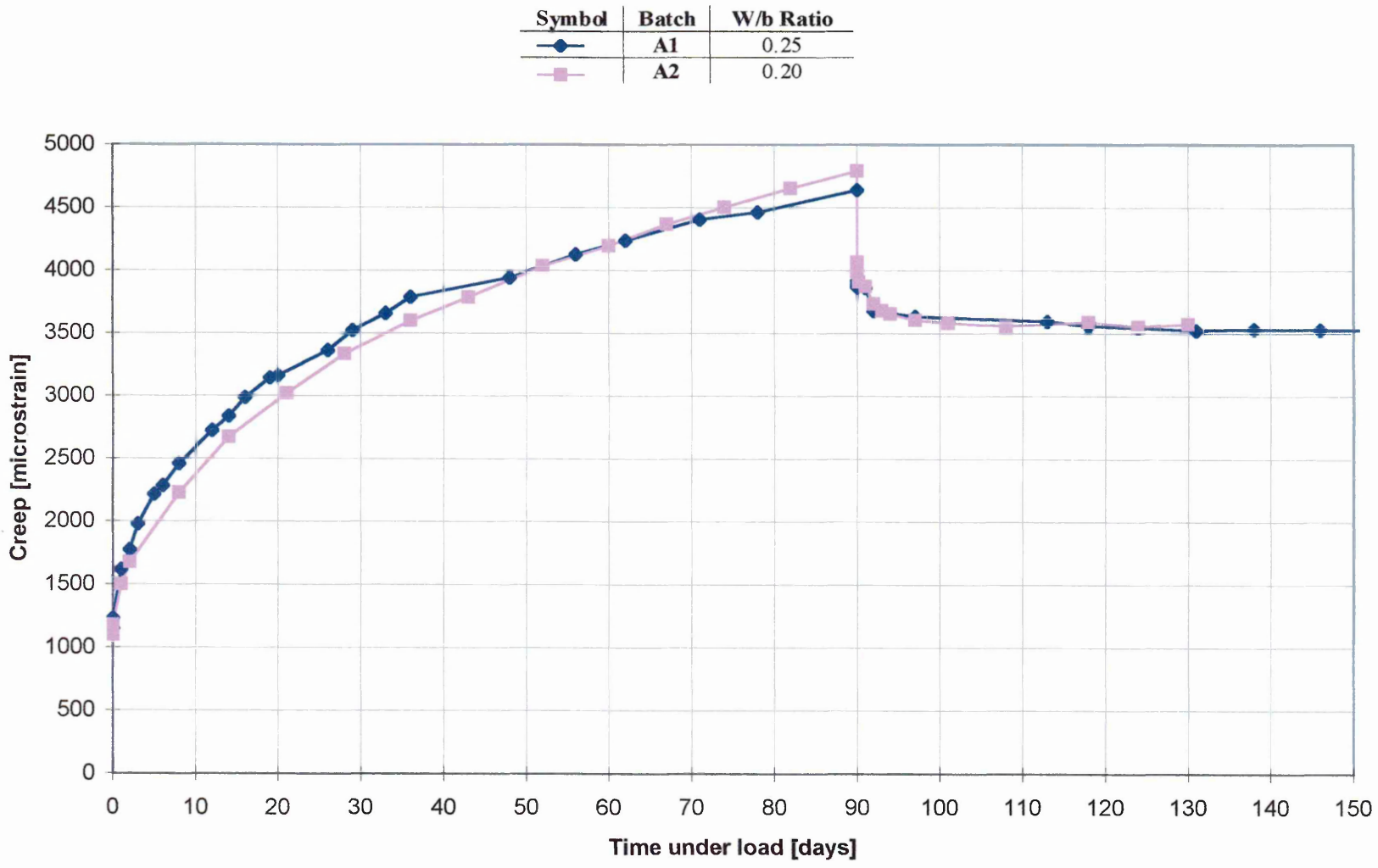

Figure 5.21 Compressive creep of alkali activated materials initially cured under 20°C and 65% RH (stress/strength = 0.3)

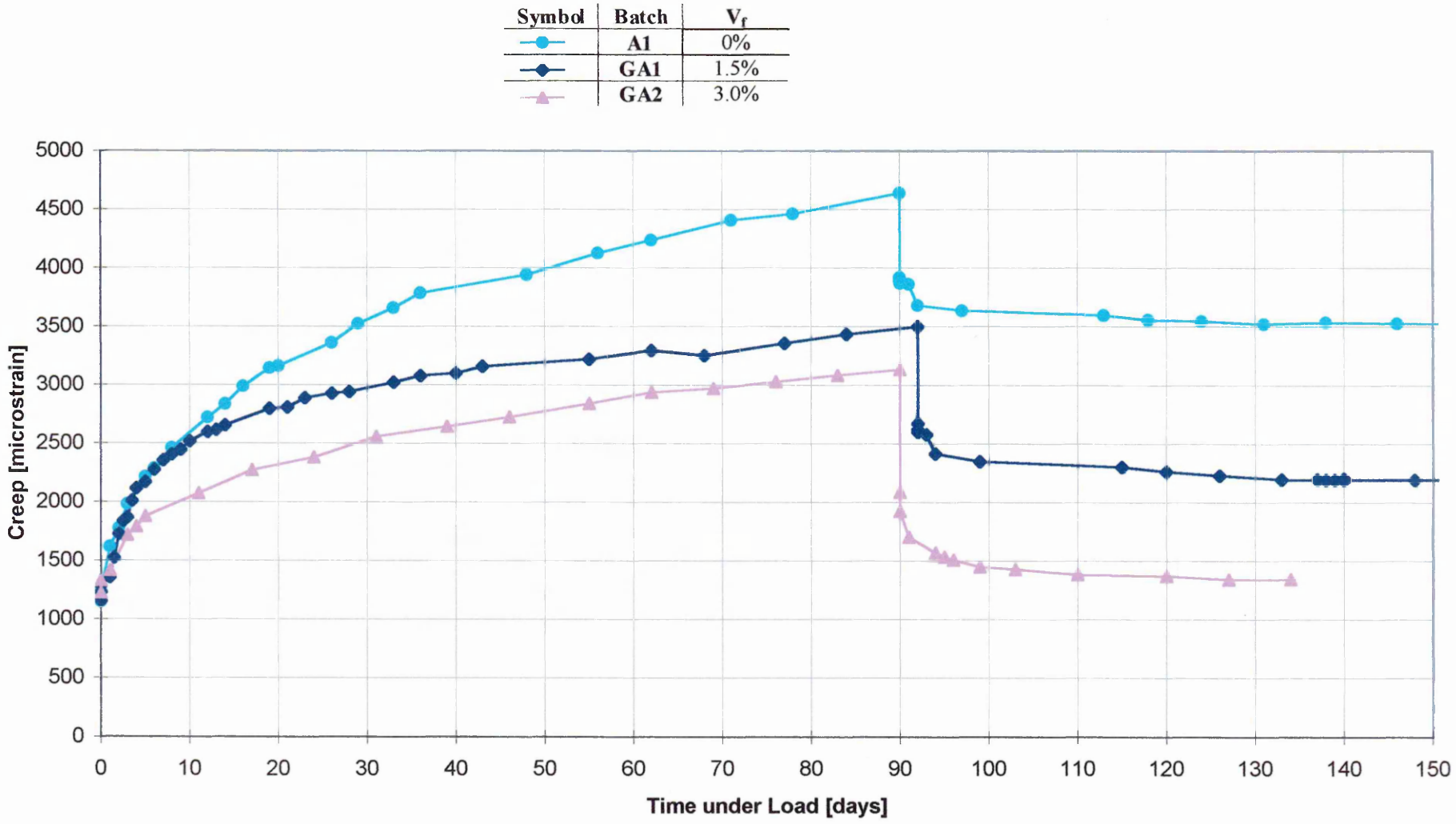

Figure 5.22 Compressive creep of glass fibre reinforced alkali actviated materials initially cured under 20°C and 65%RH (stress/strength = 0.3)

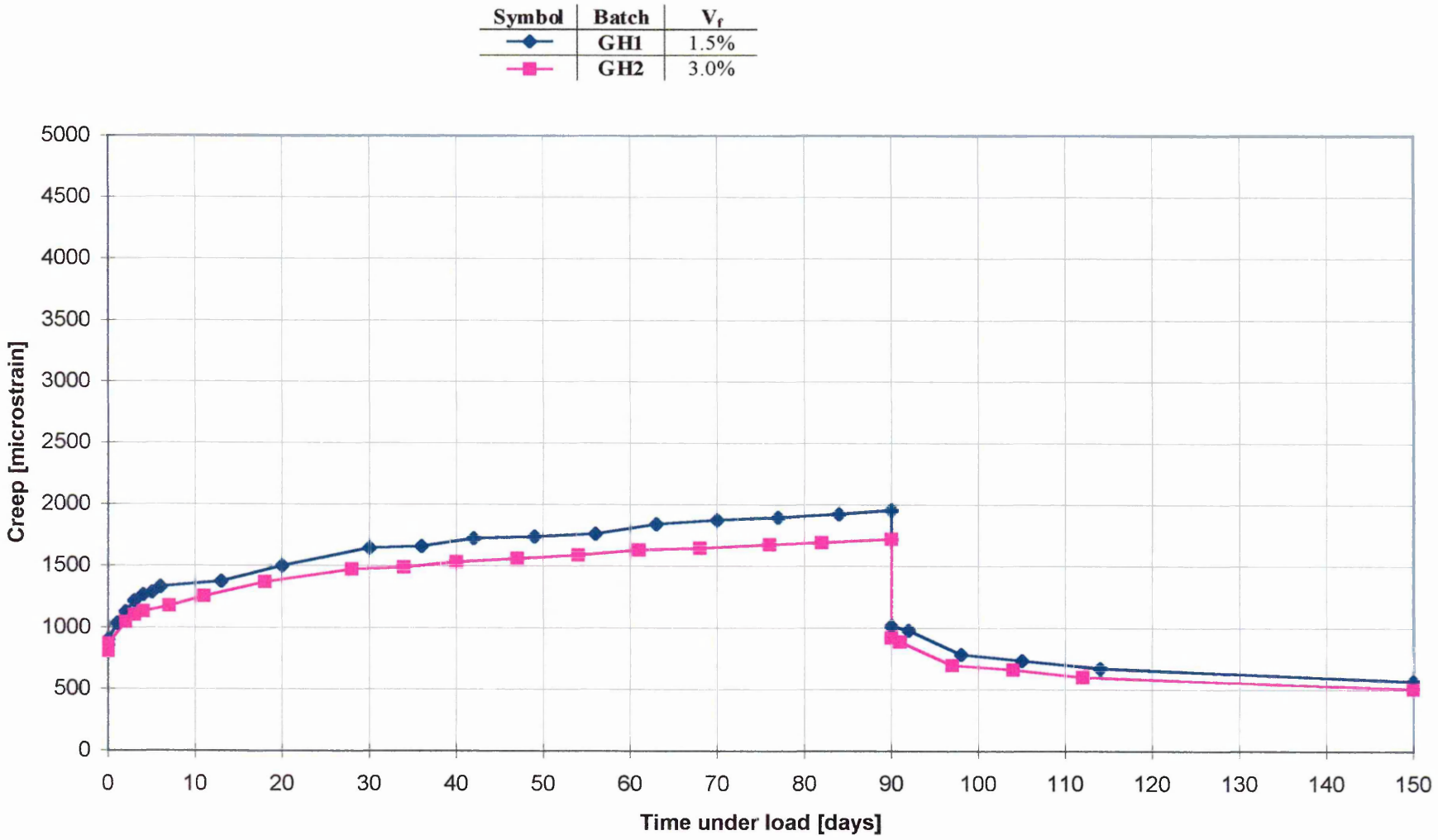

Figure 5.23 Compressive creep of glass fibre reinforced alkali activated materials initially cured thermally (stress/strength = 0.3)

Symbol	Batch	Type of fibres	V_f
	A1	-	0
	SwA1	straight steel fibres	1.5%
	SA1	melt extract fibres	1.5%
	SA2	melt extract fibres	3.0%

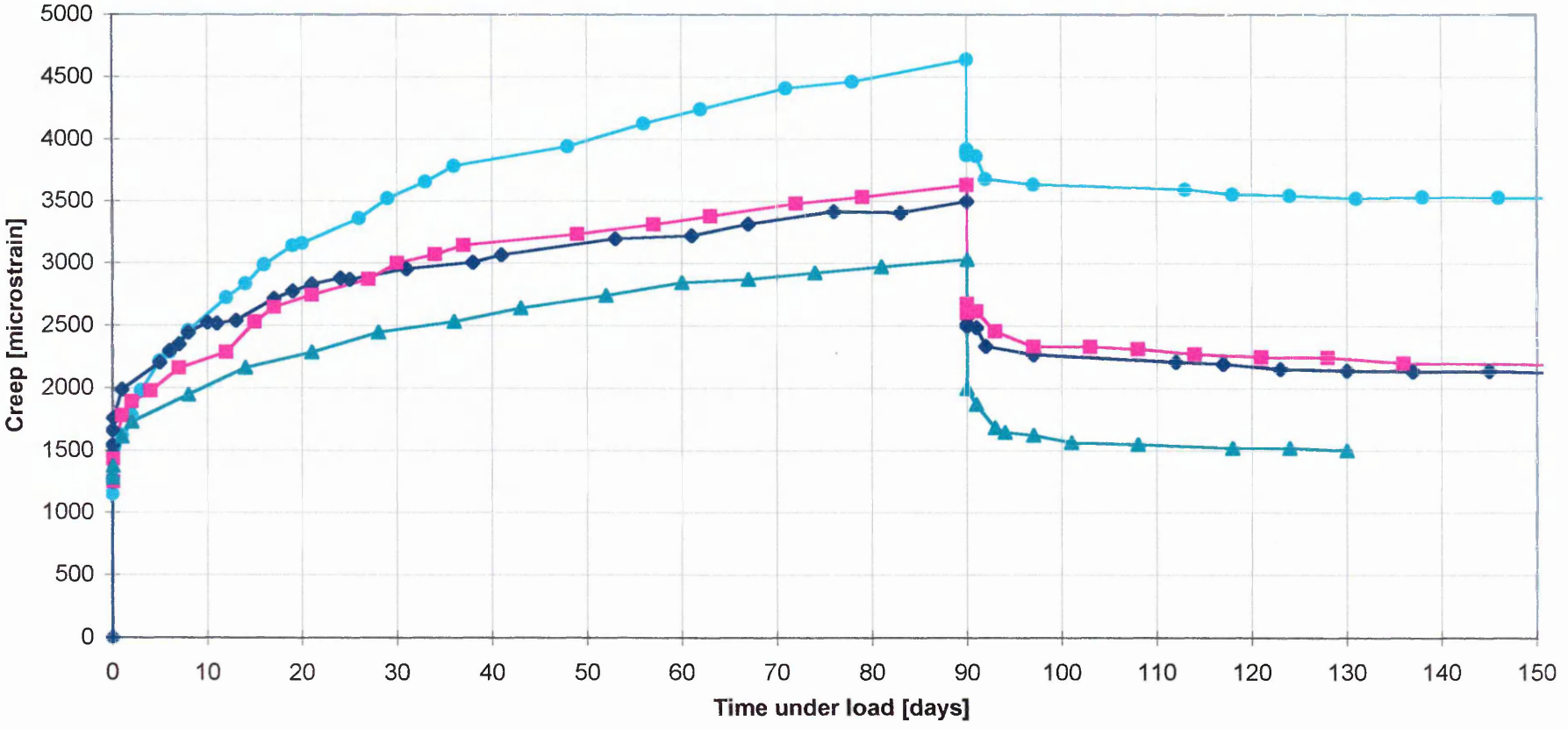

Figure 5.24 Compressive creep of steel fibre reinforced alkali activated materials initially cured under 20°C and 65%RH (stress/strength = 0.30)

Symbol	Batch	Type of fibres	V_f
	SH1	melt extract fibres	1.5%
	SH2	melt extract fibres	3.0%

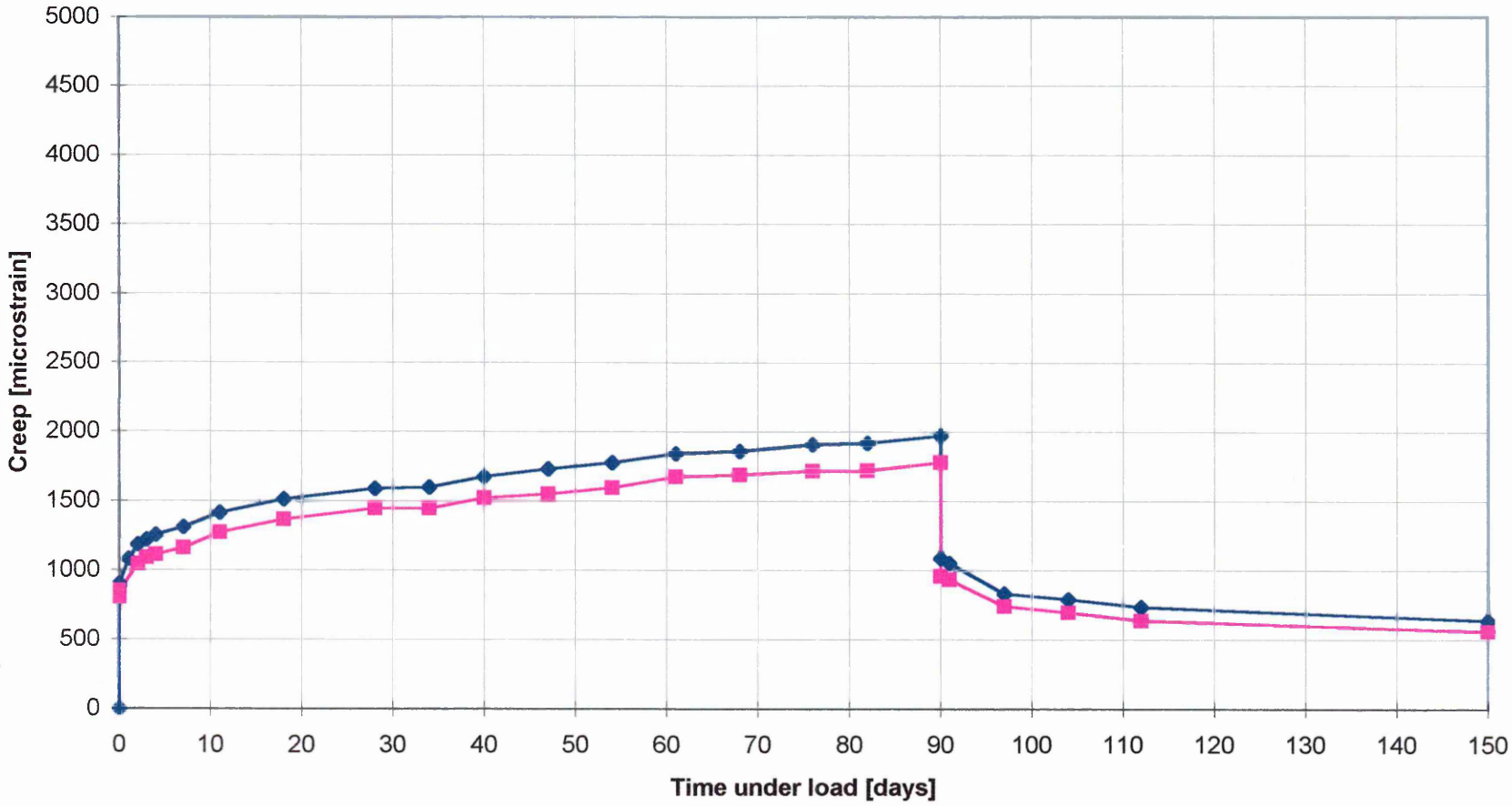

Figure 5.25 Compressive creep strain of steel fibre reinforced alkali activated materials materials initially cured thermally (stress/strength = 0.3)

Table 5.21 Creep data for alkali activated materials and fibre composites initially cured under 20°C and 60%RH

Batch Code	28 days cube strength σ_c	Inst. elastic strain	90 days creep strain	ϕ 90 day creep strain / inst. elast strain	Del elastic Strain	Del elastic Strain	Flow creep	del+flow total	% of Control Material
	[N/mm^2]	[μstrain]	[μstrain]		[μstrain]	[%]	[μstrain]		
1	*2*	*3*	*4*	*5*	*6*	*7*	*8*	*9*	*10*
A2	103.74	1107	3685	3.3	322	9	3553	1.05	-
A1	55.02	1152	3489	3.03	339	10	3524	1.11	-
GA1	59.5	1155	2346	2.03	409	17.4	2194	1.11	67
GA2	58.88	1224	1908	1.56	583	30	1339	1.01	55
SwA1	56.64	1250	2251	1.8	391	17.4	2108	1.11	65
SA1	57.6	1248	2383	1.91	412	17.3	2194	1.09	68
SA2	58.44	1281	1752	1.37	496	28	1502	1.14	50

Table 5.22 Creep data for fibre reinforced alkali activated materials initially thermal cured

Batch Code	28 days cube strength σ_c	Inst. elastic strain	90 days creep strain	ϕ 90 day creep strain / inst. elast strain	Del elastic Strain	Del elastic Strain	Flow creep	del+flow total
	[N/mm^2]	[μstrain]	[μstrain]		[μstrain]	[%]	[μstrain]	
1	*2*	*3*	*4*	*5*	*6*	*7*	*8*	*9*
GH1	68.46	858	1101	1.28	448	40	567	0.92
GH2	62.1	805	919	1.14	415	45	505	1
SH1	75.25	883	1090	1.24	452	41	604	1
SH2	77.18	807	977	1.21	398	41	561	0.98

Compressive creep curves of alkali activated materials reinforced with glass fibres initially cured under 20°C and 65% RH, or by thermal treatment, are given in Figures 5.22 and 5.23, respectively. The corresponding creep curves for steel fibre reinforced alkali activated materials are presented in Figure 5.24 and Figure 5.25. The compressive creep results are also summarised in Tables 5.21 and 5.22.

Figures 5.22 and 5.24 show that fibre reinforcement (glass and steel) is effective in reducing the creep of alkali activated materials initially cured at 20°C and 65% RH. Creep decreases with an increasing fibre volume. For example, the average 90 days creep of materials with 1.5% volume of fibres (batch code GA1 and SA1) was approximately 68% of the control material (batch code A1) compared with a value of 52% for the materials with 3.0% volume of fibres (batch code GA2 and SA2).
Creep of alkali activated materials initially cured at 20°C and 65% RH is influenced similarly by both types of fibre, glass and steel. For example, at 1.5% fibre volume, the 90 day creep of glass fibre reinforced material (batch code GA1) is 2345.9 μstrain compared with 2383.43 μstrain for the corresponding material with steel fibres (batch code SA1).

Initial thermal curing has a big impact on the compressive creep of fibre reinforced alkali activated materials; it greatly decreases the creep compared with corresponding materials initially cured under 20°C and 65% RH. For example the material with 1.5% glass fibres, initially thermal cured (batch code GH1) has a 90 day creep of 1100.61 μstrain compared with 2345.9 μstrain for the corresponding material cured under 20°C and 65% RH (batch code GA1). Similarly the 90 days creep of the thermally cured material with 1.5% steel fibres (batch code SH1) is 1090.46 μstrain compared with 2383.43 μstrain for the material cured under 20°C, 65% RH (batch code SA1), as shown in Tables 5.21 and 5.22.

Creep of initially thermally cured materials decreases with increasing fibre volume but is not affected differently by the type of fibre (glass or steel), as shown by a comparison of Figures 5.23 and 5.25. This follows the same trends as alkali activated materials initially cured at 20°C and 65% RH.

5.5.3.2 Creep Coefficient

Creep coefficient, ϕ, is the ratio between the creep strain and the instantaneous elastic strain upon loading. A higher creep coefficient will result in a low effective, E_{eff}, modulus according to $E_{eff} = E / (1+\phi)$[144] and, therefore, in a decrease in the stiffness of the material after being subjected to a constant compressive stress. E is the instantaneous elastic modulus.

The values for the creep coefficient ϕ are presented in column 5 of Tables 5.21 and 5.22. The material with a water/binder ratio of 0.25 (batch code A1) initially cured under 20°C and 65%RH exhibits slightly lower creep coefficient (3.03) compared with 3.3 for the corresponding material (batch code A2) with a lower w/b of 0.20. In comparison, Portland cement mortar (w/c=0.39) has a creep coefficient of 2.0 which is lower than that of alkali activated materials[144].

The results presented in Tables 5.21 and 5.22 show that the fibre reinforcement provides a considerable reduction to the creep coefficient of the matrix. Creep coefficient decreases with increasing fibre volume for alkali activated materials initially cured at 20°C and 65% RH. For example, the average creep coefficient of the materials with 1.5% volume of fibres (batch code GA1 and SA1) was approximately 65% of the control material (batch code A1) compared with 48% of the control for the materials with 3.0% volume of fibres (batch code GA2 and SA2). The creep coefficient of alkali activated materials, initially cured at 20°C and 65% RH, is influenced similarly by both glass and steel fibres. For example, at 1.5% fibre volume, the creep coefficient of glass fibre reinforced material (batch code GA1) is 2.03 compared with 1.91 for corresponding material with steel fibres (batch code SA1).

Initial thermally cured fibre reinforced alkali activated materials show lower creep coefficients than corresponding materials initially cured under 20°C and 65%RH. For example, the initial thermally cured material with 1.5% volume of glass fibres (batch code GH1) has a creep coefficient of 1.28 compared with 2.03 for corresponding material initially cured under 20°C and 65% RH (batch code GA1). Similarly, the creep coefficient of the initial thermally cured material with 1.5% volume of steel

fibres (batch code SH1) is 1.24 compared with 1.91 for corresponding material initially cured at 20°C and 65%RH (batch code SA1). The creep coefficient of alkali activated materials, initially thermally cured, decreases with the increasing fibre volume and is similarly affected by both types of fibre (glass and steel). This follows the same trends as for alkali activated materials initially cured at 20°C and 65% RH.

5.5.3.3 Creep Recovery

When the sustained compressive load is removed, the strain decreases immediately by an amount equal to the elastic strain at the given age, generally lower than the elastic strain at the age of loading, see Figure 2.10. This immediate recovery is followed by a gradual decrease in strain, over a period of time, called creep recovery[91]. Creep recovery also represents the delayed elastic component of creep. The recovery of creep is not complete since creep is not simply a reversible phenomena. Removal of load results in a residual permanent strain which is equal to the flow component of creep[91] (see Figure 2.9). The delayed elastic component of creep was determined as follows[91]:

Delayed elastic Creep = (Creep Strain + Instantenuous elastic strain) - (Elastic Recovery + Flow Creep)

The delayed elastic strain (creep recovery) and flow creep (residual permanent strain) components are presented in column 6 and 8 respectively of Tables 5.21 and 5.22. The delayed elastic strain is also given as a percentage of the 90 days creep strain in column 7 of Tables 5.21 and 5.22. Alkali activated materials initially cured under 20°C and 65%RH exhibit similar creep recovery (delayed elastic) strains for both water/binder ratios of 0.20 and 0.25 (batch code A1 and A2). The creep recovery of fibre reinforced alkali activated materials increases with increasing fibre volume. For example the average creep recovery of materials with 1.5% volume of fibres (batch code GA1 and SA1) were 1.74 times higher than the control material (batch code A1), column 7, Table 5.21. The corresponding values for the materials with 3% volume of fibres (batch code GA2 and SA2) were 2.9, times higher than the control material (batch code A1).

Alkali activated materials with 1.5% volume of fibres, initially thermally cured show slightly higher creep recovery than corresponding materials initially cured under 20°C and 65%RH (Table 5.21 and 5.22). For example, material with 1.5% volume of glass fibres initially thermally cured (batch code GH1) has a creep recovery of 448 μstrain compared with 409 μstrain for material initially cured under 20°C and 65% RH (batch code GA1). Alkali activated materials with 3 % volume of fibres, initially thermally cured show, on the other hand, lower creep recovery than corresponding materials initially cured under 20°C and 65%RH (Table 5.21 and 5.22). For example, the creep recovery of material initially thermally cured (batch code GH2) is 415 μstrain compared with 582 μstrain material initially cured under 20°C and 65% RH (batch code GA2).

Neville[98] stated that creep recovery of concrete is proportional to the cement paste content of the mix and inversely proportional to the aggregate content. A material which contains coarse aggregates will show less creep recovery than a material which contains finer aggregates. The results from the current investigation show that the alkali activated materials which contain very fine aggregates (average grain size of 175μm) exhibit a low creep recovery (9-10%), contrary to what was predicted by Neville[98]. The same conclusion was given by other researchers[144]. Creep of reference ordinary Portland cement mortar was about 10% when medium grade sand was used as aggregate.

The relationship between fibre volume and the ratio of instantaneous recovery to the initial elastic strain is given in Figure 5.26-(a). The ratios remain constant with increasing fibre volume for both initial curing conditions. The average value of the ratio of instantaneous creep recovery to the initial elastic strain is 0.8 for alkali activated materials initially cured under 20°C and 65%RH, which indicates that the instantaneous recovery is less than the initial elastic creep strain. This is due to the increase in stiffness of the matrix with age while under sustained load. Thermally cured fibre reinforced materials, on the other hand, show an average ratio of 1 which denotes that there are no significant differences between the instantaneous recovery and the initial elastic creep. This indicates no increase in stiffness of the matrix with age while under sustained load.

The relationship between fibre volume and the ratio of creep recovery to the 90 days creep strain is shown in Figure 5.26-(b). The creep recovery 90 days creep ratio ranges between 0.1 to 0.3 for fibre reinforced alkali activated materials initially cured under 20°C and 65%RH and 0.4 to 0.5 for initial thermally cured materials. These values are comparable with the values for Portland cement mortar and concrete given in literature[98], which range between 0.164 and 0.454.

Figure 5.26-(c) shows the influence of fibre reinforcement on the creep recovery (delayed elastic strain). The corresponding relationship for flow creep is presented in Figure 5.26-(d). Best-fit lines have been plotted for each fibre type and initial curing condition. The best-fit lines for materials initially cured under 20°C and 65%RH, indicate that delayed elastic strain (creep recovery) increases markedly with increasing fibre volume. This finding contradicts the assumption of previous researchers[115] on the fibre reinforced Portland cement matrices which shows no fibre restraint to the delayed elastic strain. Flow creep of materials initially cured under 20°C and 65%RH, on the other hand, shows a sharp decrease with fibre volume (see Figure 5.26, d). This agrees with the finding of Mangat[115] on the fibre reinforced Portland cement mortars indicating that fibres provide a restraint to the flow component of creep. Fibre reinforced materials initially thermal cured, on the other hand, show no significant changes in the delayed elastic strain or flow creep with an increase in the fibre volume (see Figure 5.26, c,d).

The total creep of concrete is the sum of flow and delayed elastic components[91] (see Figure 2.9). Tables 5.21 and 5.22 give the ratio of delayed elastic strain plus flow creep strain to the 90 day total creep strain of the alkali activated materials (column 9). The ratio is 1.05 for the material with a water/binder = 0.25 and 1.11 for water/binder = 0.20. The corresponding ratios for the fibre reinforced alkali activated materials ranged between 1.01 and 1.14 for materials initially cured under 20°C and 65% RH and between 0.92 and 1 for materials initial thermally cured. These ratios average approximately unity, within 10% scatter caused by experimental error. These results confirm that, like PC mortar, the creep of alkali activated materials comprises of the delayed elastic and flow components. The results also provide a check on the accuracy of the creep data.

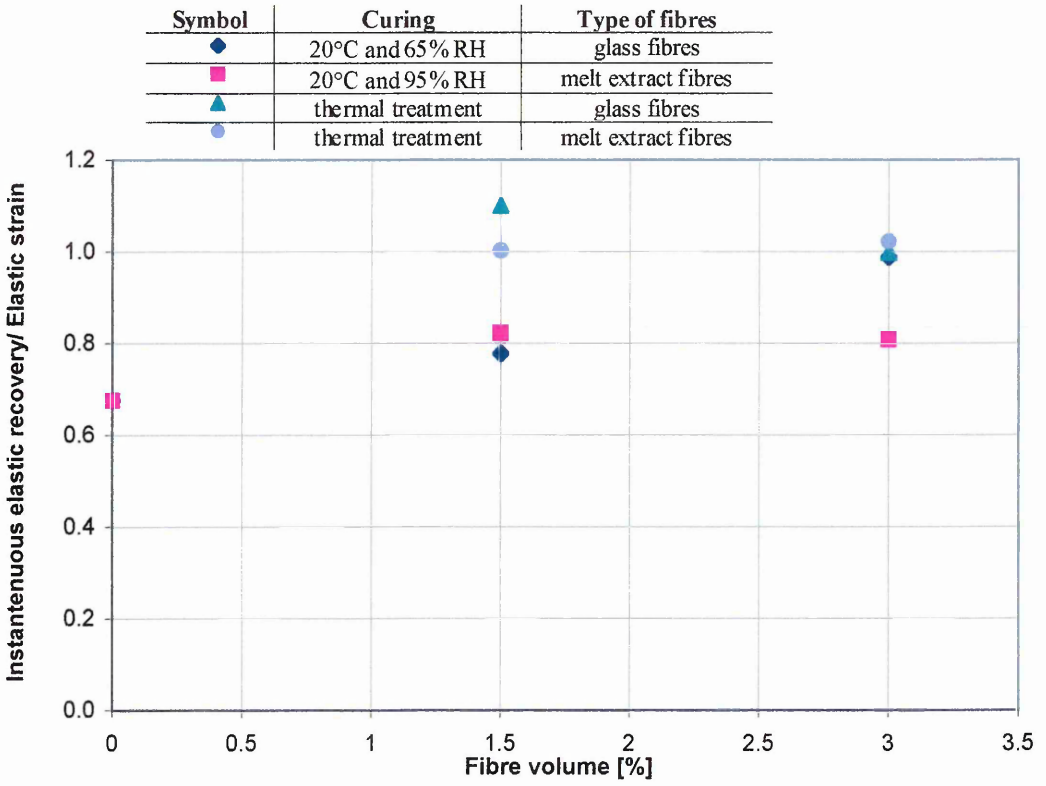

(a)

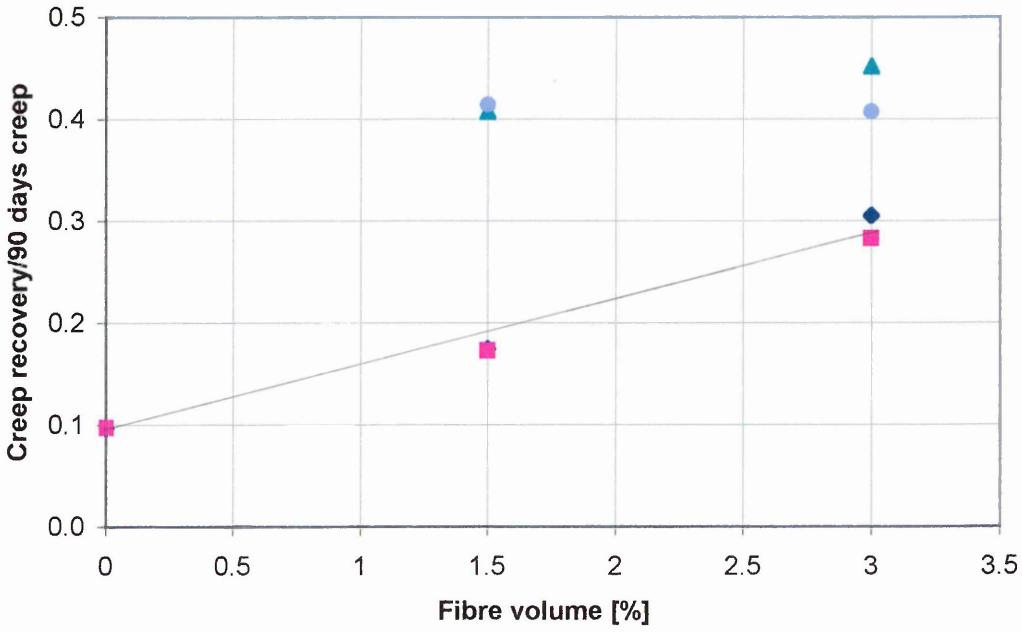

(b)

Figure 5.26 - a and b Influence of fibre reinforcements on the creep recovery of alkali activated materials

Symbol	Curing	Type of fibres
◆	20°C and 65% RH	glass fibres
■	20°C and 95% RH	melt extract fibres
▲	thermal treatment	glass fibres
●	thermal treatment	melt extract fibres

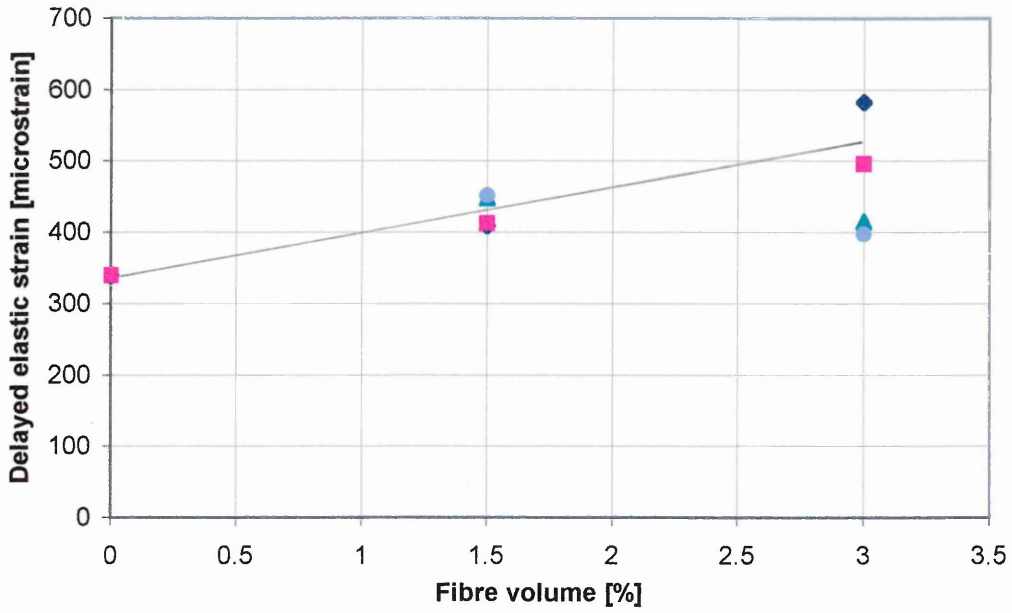

(c)

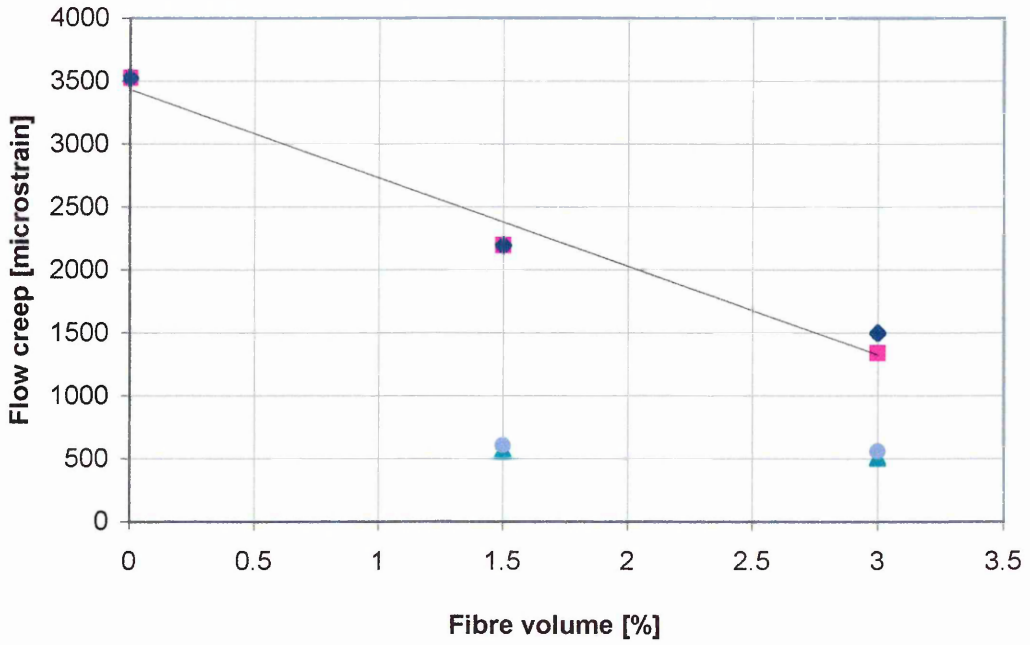

(d)

Figure 5.26 -c and d Influence of fibre reinforcements on the creep recovery of alkali activated materials

5.5.3.4 Theoretical prediction of compressive creep

5.5.3.4.1 Compressive creep theory

The creep model for cement matrices reinforced with randomly orientated short steel fibres of length l is based on the assumption that aligned fibres of length l_e and spacing s resist creep induced in the direction of applied stress.

The idealised distribution of randomly orientated steel fibres in the direction of applied stress is shown in Figure 5.27-(a). The spacing between the fibres s can be calculated from equation 5.2[114] detailed in section 5.5.2.3.

Figure 5.27-(b)[115] represents the compressive creep model. Each fibre is considered to be surrounded by a thick cylinder of cement matrix of diameter s and length (l_e/2+s/2). The flow component of creep of the cement matrix is restrained by the fibre through the interfacial bond stress τ[115]. The creep of steel fibre reinforced cement matrices ε_{fc} is expressed in terms of the creep of the unreinforced control matrix ε_{oc} and the restraint provided by the fibre-matrix interfacial bond against the flow creep of the control matrix, as given in equation (5.12)[115].

$$\varepsilon_{fc} = \varepsilon_{oc} - \frac{0.3362\tau d l^2}{s^2 E(0.41l + s)} \qquad \text{Equation 5.12}$$

The solution for equation (5.12) requires a knowledge of τ/E which is given by the following expression based on Lame's equation for thick cylinders[115]

$$\frac{\tau}{E} = \frac{\alpha\mu(\varepsilon_{os} - \varepsilon_{ol})\left(\frac{s}{2} - \frac{d}{2}\right)}{\frac{d}{2}\left[\frac{\left(\frac{s}{2}\right)^2 + \left(\frac{d}{2}\right)^2}{\left(\frac{s}{2}\right)^2 - \left(\frac{d}{2}\right)^2} + \upsilon\right] + \frac{(1-\upsilon f)}{\frac{E_s}{E}}} \qquad \text{Equation 5.13}$$

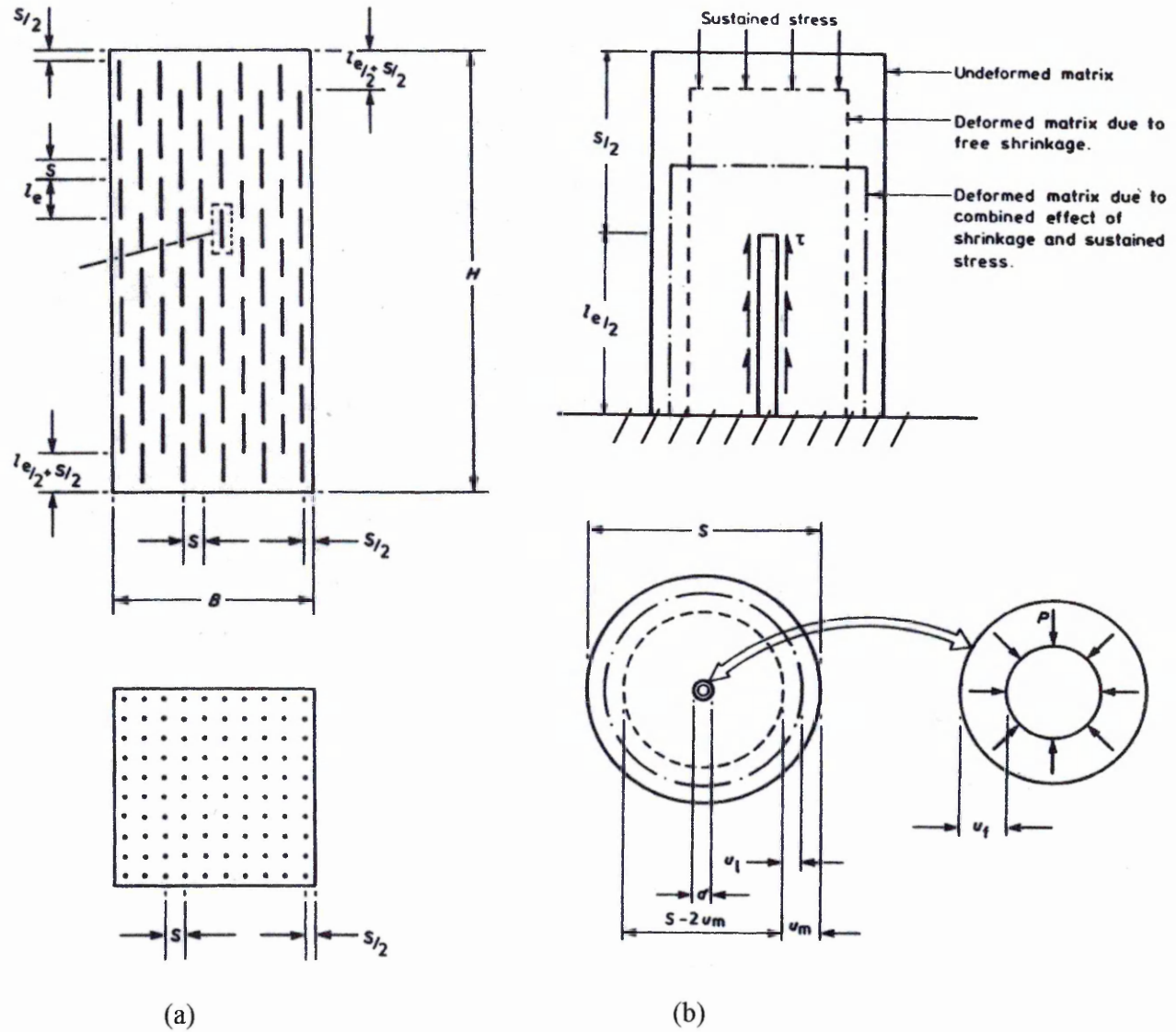

Figure 5.27 (a) Idealised fibre distribution and (b) creep model for fibre reinforced matrices[115]

Substituting equation 5.13 in equation 5.12 gives the expression for the creep strain of steel fibre reinforced matrices ε_{fc}:

$$\varepsilon_{fc} = \varepsilon_{oc} - \frac{0.6724 l^2 \alpha \mu (\varepsilon_{os} - \varepsilon_{ol})\left(\frac{s}{2} - \frac{d}{2}\right)}{s^2 \left(\left[\frac{\left(\frac{s}{2}\right)^2 + \left(\frac{d}{2}\right)^2}{\left(\frac{s}{2}\right)^2 - \left(\frac{d}{2}\right)^2} + \upsilon \right] + \frac{(1-\upsilon_f)}{\frac{E_f}{E}} \right)(0.41l + s)} \qquad \text{Equation 5.14}$$

Where:

l is the length of the randomly orientated fibres

$$\alpha = \frac{\varepsilon_{op}}{\varepsilon_{oe}}$$

$$\varepsilon_{op} = \varepsilon_{oc} - \varepsilon_{od}$$

ε_{op} is the flow component of creep of the control matrix;

ε_{oc} is the total creep strain of the unreinforced matrix;

ε_{od} is the delayed elastic strain component of the control matrix;

ε_{oe} is the instanteneous elastic strain of the control matrix;

μ is the coefficient of friction at the steel fibre and mortar matrix interface;

ε_{os} is the free shrinkage strain of the control matrix

$$\varepsilon_{ol} = \nu \cdot (\varepsilon_{oe} + \varepsilon_{oc})$$

ε_{ol} is the lateral strain of the unreinforced control matrix

ν is the Poisson's ratio of the unreinforced matrix (0.2)

ν_f is the Poisson's ratio of steel fibres

E_e is the Elastic Modulus of the matrix

E_s is the Elastic Modulus of steel fibre

5.5.3.4.2 Long term coefficient of friction

In order to determine the compressive creep of the steel fibre reinforced cement matrix ε_{fc} from equation 5.14, a knowledge of the shrinkage and creep of the control matrix is required together with a value for the coefficient of friction μ, factor α, fibre dimensions and volume. The value for the coefficient of friction of fibres in alkali activated materials is not available in current literature and, therefore, it is difficult to check directly the validity of equation 5.14. Equation 5.14 is, therefore, used to determine μ using the experimental data on compressive creep of the control and fibre reinforced matrices investigated in this research. Equation 5.14 is rearranged in terms of μ giving:

$$\mu = \frac{(\varepsilon_{oc} - \varepsilon_{fc}) \cdot s^2 \cdot (0.41l + s)}{0.6724l^2 \cdot \alpha \cdot (\varepsilon_{os} - \varepsilon_{ol}) \left(\frac{s}{2} - \frac{d}{2}\right)} \left\{ \left[\frac{\left(\frac{s}{2}\right)^2 + \left(\frac{d}{2}\right)^2}{\left(\frac{s}{2}\right)^2 - \left(\frac{d}{2}\right)^2} + \upsilon \right] + \frac{(1 - \upsilon_f)}{\frac{E_f}{E}} \right\} \qquad \text{Equation 5.15}$$

The spacing between fibres was determined using equation 5.2 as detailed in section 5.5.2.3. The values of the long term coefficients of friction, calculated from equation 5.15, for the materials tested in this investigation are presented in Table 5.23. Table 5.23 shows that the fibre volume fraction has no significant effect on the values of coefficient of friction. For example a comparison of batch code SA1 (V_f = 1.5%) and SA2 (V_f = 3%) shows similar values of μ (0.088 and 0.098 respectivelly). Similarly the values of μ for batch codes GA1 and GA2 are similar (0.028). The primary parameter which influences μ is the type of fibre. The average value of μ for glass fibres (batch codes GA1 and GA2) is 0.028 and melt extract steel fibres (batch codes SA1 and SA2) is 0.09.

There has been no previous work on the long term coefficients of friction of fibres in alkali activated materials but other researchers[114, 145, 146] have investigated the long term coefficient of friction in PC mortar. The values of the coefficient of friction μ_{ls}, determined by Mangat et al[114] using long term drying shrinkage (up to 600 days) data for PC mortar are presented in Table 5.23. The μ values or fibre reinforced

Portland cement mortars are similar to those obtained in the present investigation for fibre reinforced alkali activated materials.

Table 5.23 Coefficients of friction for fibre reinforced alkali activated materials and Portland cement mortar

Batch Code	ε_{fs} [microstrain]	V_f [%]	d [mm]	l [mm]	s [mm]	μ* (aam)	μ_{ls}** (PC)
SwA1	2250.6	1.5	0.15	7	1.389	0.045	0.04
SA1	2383.4	1.5	0.5	12	4.145	0.0879	0.09
SA2	1752.5	3	0.5	12	3.115	0.098	0.09
GA1	2345.9	1.5	0.17	12	1.655	0.028	na
GA2	1908.2	3	0.17	12	1.212	0.028	na

Note:

ε_{fs} is the 90 day compressive creep

ε_{os} = 6138.22 [microstrain]

ε_{oc} = 3489.07 [microstrain]

*values determined from the author's data for alkali activated materials (aam).

**values determined by Mangat et al[114] for PC mortar, using long term drying shrinkage data (up to 600 days)

5.5.3.5 Discussion

5.5.3.5.1 90 days compressive creep

Alkali activated materials exhibit much higher creep than Portland cement mortar and concrete. For example, Portland cement mortar has a 70 day creep strain of 938 microstrain[144] whereas alkali activated materials have a corresponding creep strain of 3256.2 microstrain (Table 5.21). One reason for this difference is the fact that ordinary Portland cement mortar contains zone M sand whereas the alkali activated materials developed in this project have a much finer sand with an average grain size of 175μm as shown in Figure 5.11. Alkali activated materials also have a lower proportion of sand. The pozzolanic materials /sand ratio is approximately 0.5

compared with 0.33 for ordinary Portland cement mortar. The quantity and type of aggregate used in a cementitious material greatly affects its creep strain[98]. Neville et al[98] explained the effect of aggregates on creep of concrete concluding that the most important factors relating to aggregate which affect creep are the quantity in the mix and the modulus of elasticity of the aggregates. Both factors contribute to resisting the creep of cement paste.

The average compressive creep of fibre reinforced alkali activated materials initially cured under 20°C, 65%RH, is 39% lower than the control unreinforced alkali activated matrix, see Table 5.21. The fibres can be considered as additional aggregates of a special shape which provide restraint to the matrix through the bond between the fibre-matrix bond.

Figure 5.28 shows the relationship between the 90 days creep of alkali activated materials initially thermal cured ε_t and the corresponding creep ε_a of materials initially cured under 20°C and 65%RH. A linear relationship between ε_t and ε_a is observed. A regression analysis of data in Figure 5.28 gives the following relationship:

$$\varepsilon_t = k\,\varepsilon_a \qquad \text{Equation 5.16}$$

where k is the slope of the ε_t versus ε_a graph.

The slope k of the graph is 0.475 (see Figure 5.28). Therefore, the compressive creep of initial thermally cured materials is 47.5% of the creep of alkali activated materials initially cured under 20°C and 65%RH. This is due to the drying out of the material by thermal curing so that creep, which is associated with the loss of bound water in the hydration products[81], is reduced.

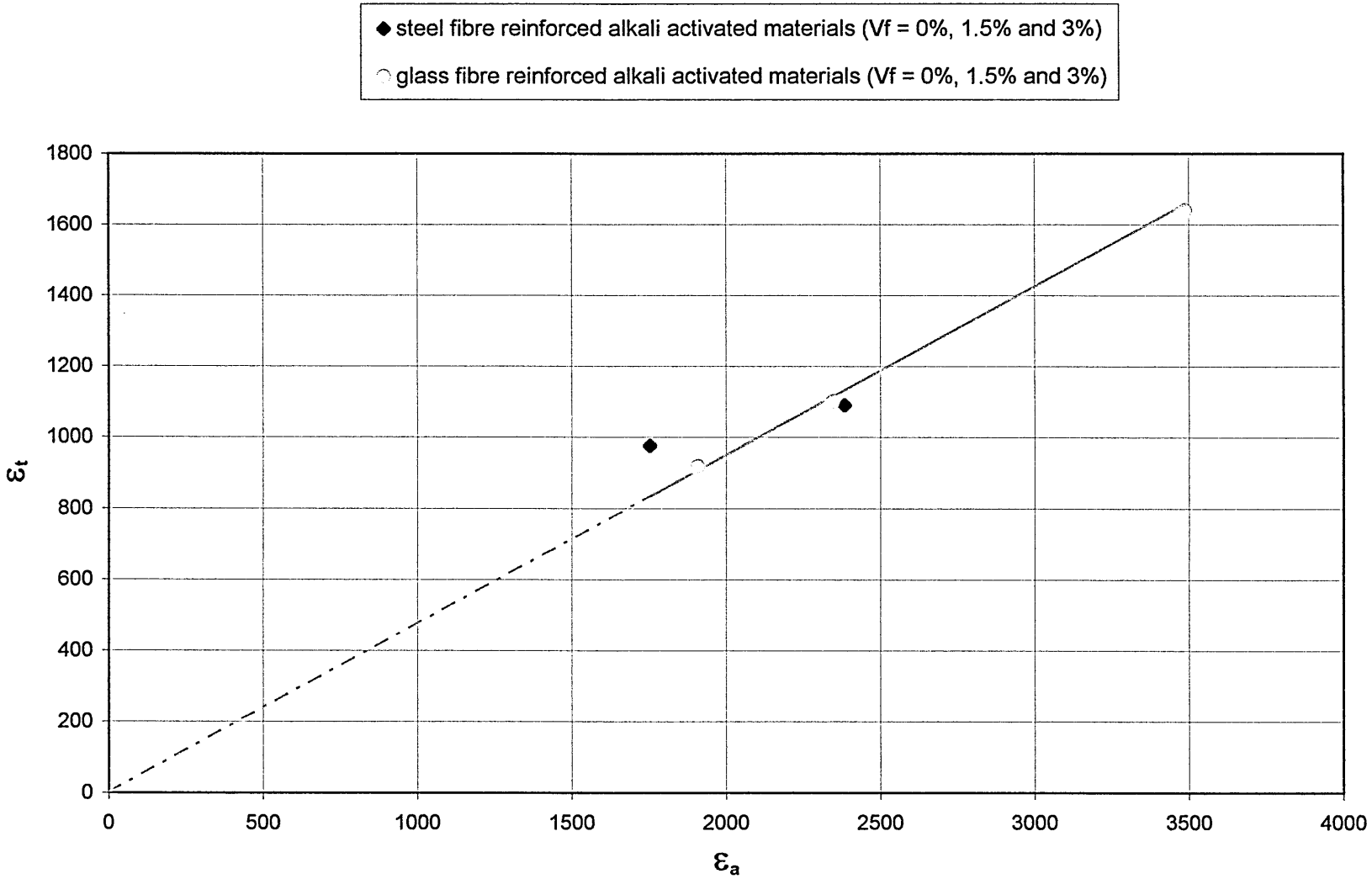

Figure 5.28 Relationship between the 90 days creep of alkali activated materials initially cured under 20°C and 65% RH and thermally treated

5.5.3.5.2 Relationship between compressive creep and V_fl/d

The relationship between the 90 day compressive creep and V_fl/d for fibre reinforced alkali activated materials initially cured under 20°C and 65%RH is given in Figure 5.29. The corresponding relationship for fibre reinforced alkali activated materials initially thermally cured is presented in Figure 5.30. The V_fl/d used ranged from 0.36 to 2.12.The experimental data of steel and glass fibre reinforced alklai activated materials are considered.

The clear trend is that creep of fibre reinforced materials decreases with increasing V_fl/d ratio (Figures 5.29 and Figure 5.30). This relationship follows the same trend free shrinkage of fibre reinforced alkali activated materials (Figure 5.19). The V_f l/d and creep strain have a very strong linear relationship for both initial curing conditions, with V_f l/d being inversely proportional to the compressive creep. This is primarily due to the decrease in fibre spacing caused by increasing V_f l/d which leads to greater restraint of the fibres to the flow component of creep[115]. Mangat and Azari[115] have concluded from their previous research that the relationship between compressive creep and fibre volume fraction of Portland cement mortars reinforced with steel fibres is linear and inversely proportional.

5.5.3.5.3 Relationship between the 90 day compressive creep and modulus of elasticity

The relationship between the 90 days compressive creep and modulus of elasticity of fibres for alkali activated materials cured at 20°C and 65% RH is presented in Figure 5.31. The corresponding relationship for materials initially thermal cured is plotted in Figure 5.32. These graphs were plotted using the 90 day creep values, obtained from Figures 5.29 and 5.30, for selected V_f l/d of 0.36, 0.70, 0.72 and 1.06. The modulus of elasticity of steel fibres (215.3 GPa) is much higher than of glass fibre (72 GPa). The relationship between the 90 days compressive creep and modulus of elasticity of fibre reinforcements is inversely proportional, following the same trend as the free shrinkage results (Figure 5.19).

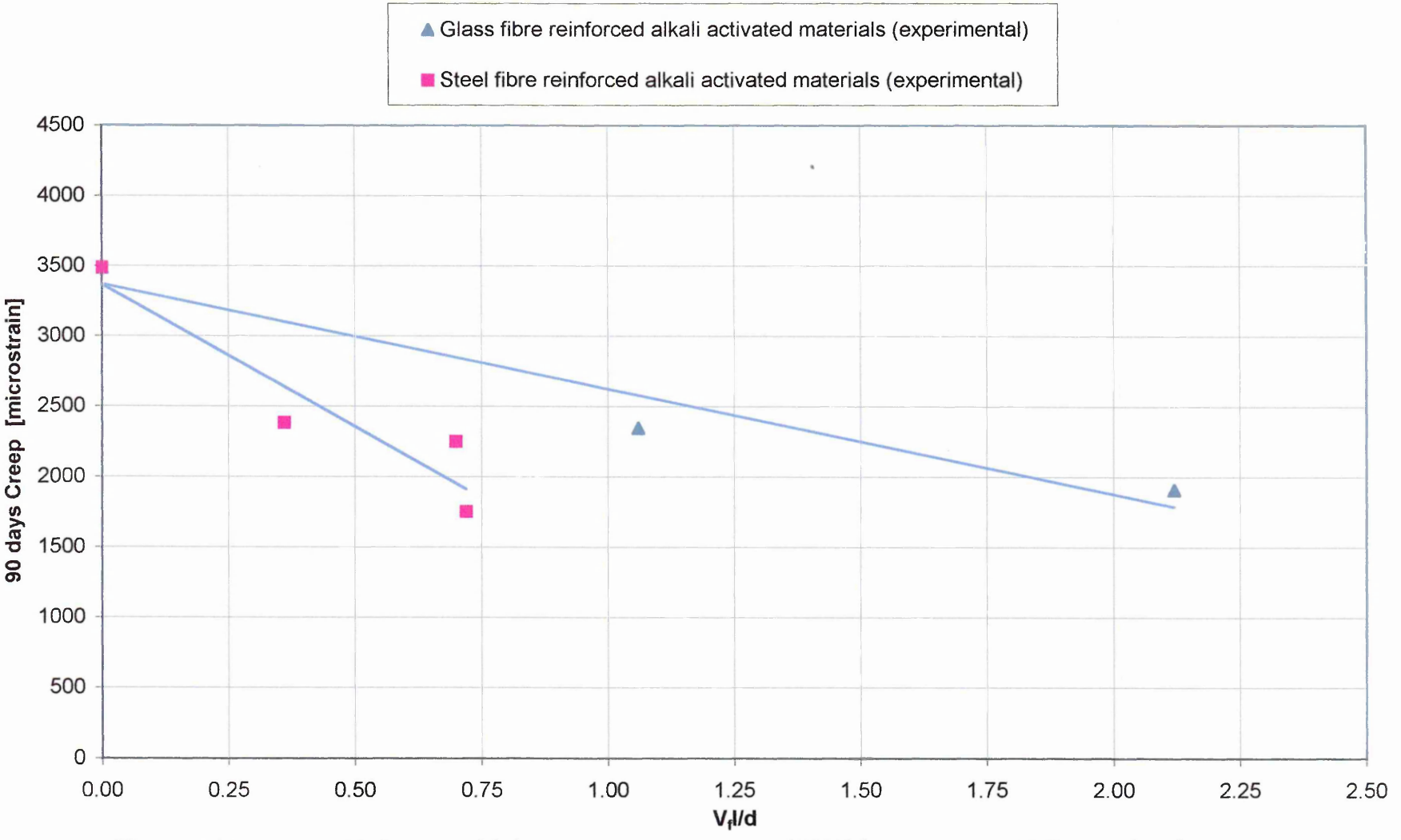

Figure 5.29 Relationship between 90 days compressive creep and $V_f l/d$ for materials initially cured under 20°C and 65%RH

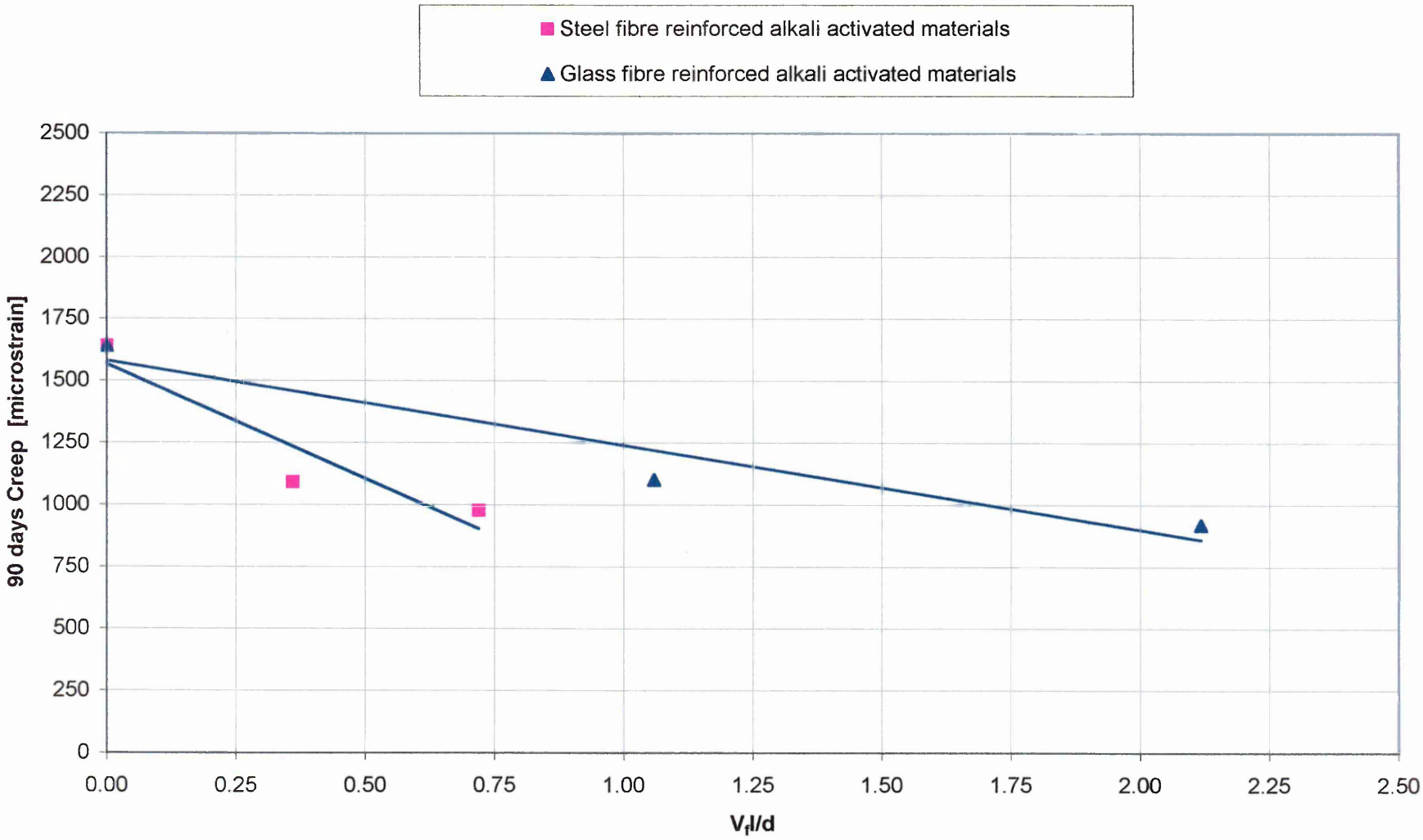

Figure 5.30 Relationship between 90 days compressive creep strains and and $V_f l/d$ for initially thermally cured materials

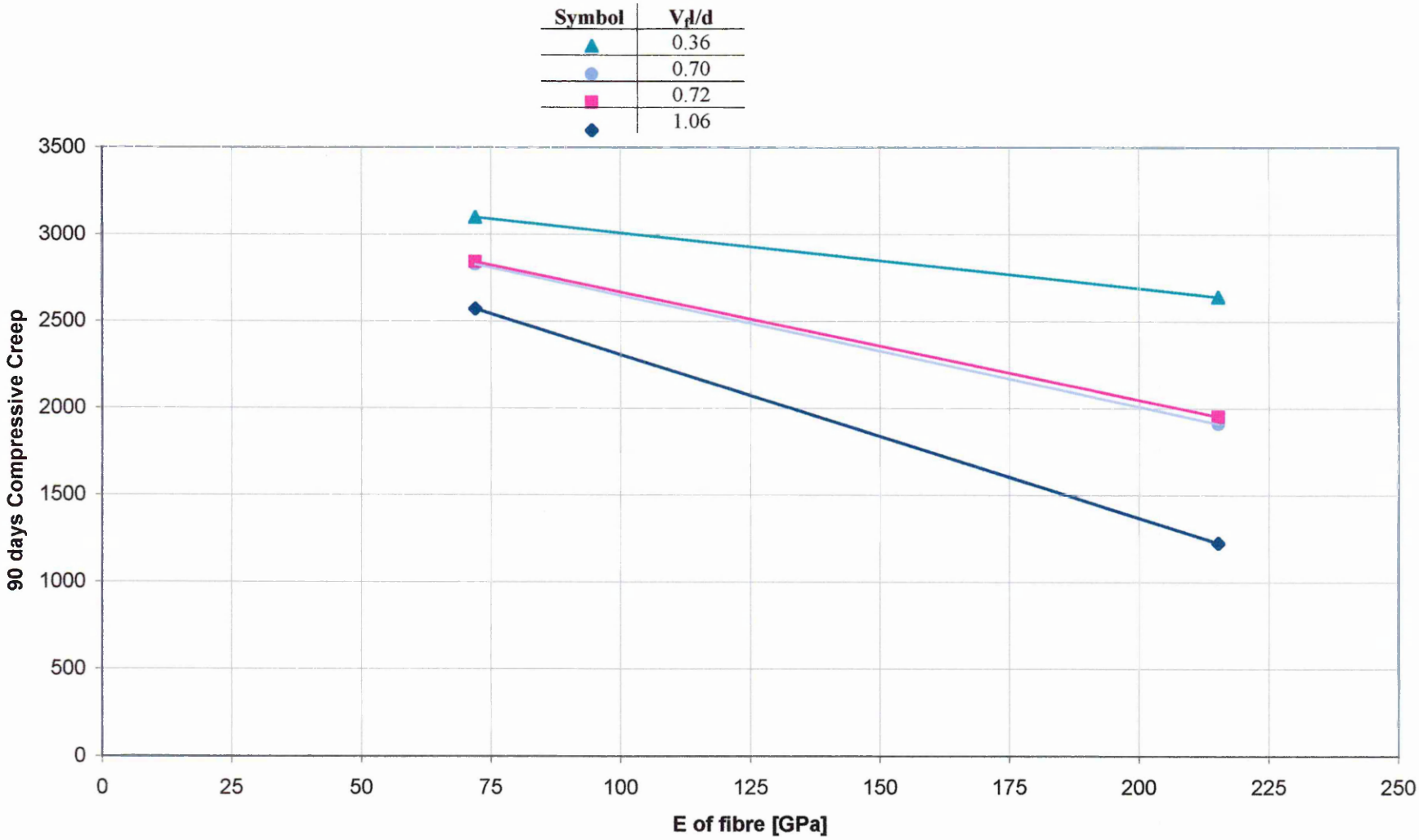

Figure 5.31 Relationship between 90 days compressive creep and E of fibre materials initially cured under 20°C and 65%RH

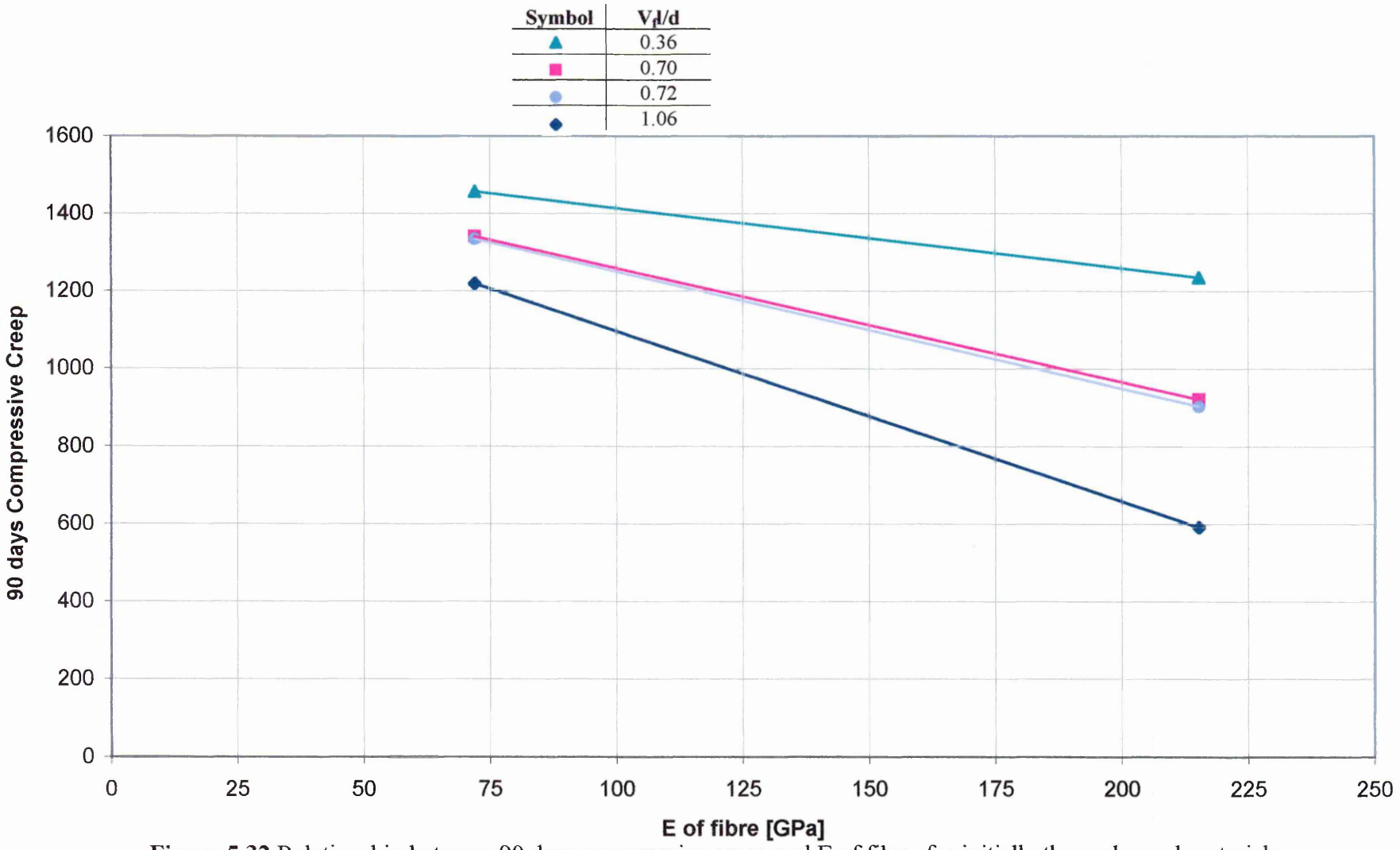

Figure 5.32 Relationship between 90 days compressive creep and E of fibre, for initially thermal cured materials

The slope of the creep strain versus modulus of elasticity of fibre graph becomes visibly higher as the V_f l/d increases, indicating that the reduction in creep due to fibre reinforcements is a function of both E and V_f l/d.

5.5.3.5.4 Design expression for compressive creep of fibre reinforced matrices

Figure 5.33 shows the relationship between the $\varepsilon_{fc}/\varepsilon_{oc}$ and fibre V_f l/d for fibre reinforced alkali activated materials. Data for two V_fl/d ratios are available for each type of fibre. Experimental data at different ages is plotted for two groups. The first group combines both glass and plain steel fibres since they show similar coefficients of friction (see Table 5.23) which gives μ values of 0.045 and 0.028 for SwA1, GA1 and GA2 respectively. The second group is melt extract steel fibres which have a much greater coefficient of friction (0.088 and 0.098 for SA1 and SA2, see Table 5.20). The data for each group of fibres falls in narrow bands, which have a close correlation with the, V_f l/d, with an average coefficient of correlation R^2 of 0.86. A regression analysis of the data in Figure 5.33 gives the following linear relationship:

$$\frac{\varepsilon_{fs}}{\varepsilon_{os}} = -z \cdot \frac{V_f \cdot l}{d} + u \qquad \text{Equation 5.17}$$

Rearranging equation 5.17 gives :

$$\varepsilon_{fs} = u \cdot \varepsilon_{os} - z \cdot \varepsilon_{os} \cdot \frac{V_f \cdot l}{d} \qquad \text{Equation 5.18}$$

The regression analysis gives the following values for the empirical coefficients z and u for the two groups of fibres glass/plain steel and melt extract.

- For glass/plain steel fibres:
  the average value of z is 0.159
  and the average value of u is 0.932
- For melt extract steel fibres:
  the average value of z is 0.607
  and the average value of u is 0.944

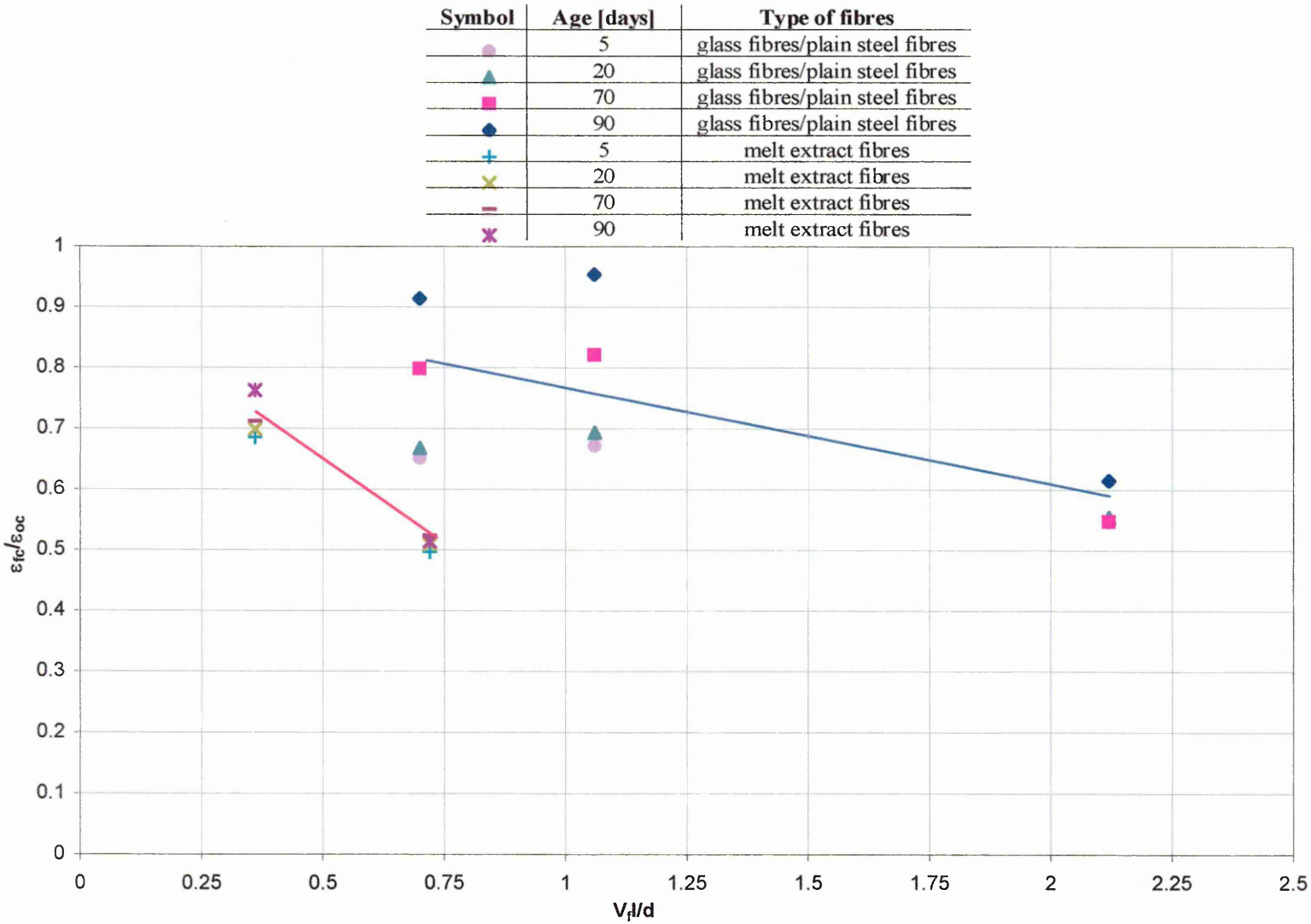

Figure 5.33 Relationship between $\varepsilon_{fc}/\varepsilon_{oc}$ and $V_f l/d$ for fibre reinforced alkali activated materials

Note that the values of empirical coefficient, u are similar for the two groups of fibres. The value of coefficient z is much grater for the melts extract fibres, indicating a greater restraint to the shrinkage provided by this group of fibres. This is due to the greater coefficient of friction, μ, of melt extract fibres.

Thus the compressive creep of fibre reinforced alkali activated materials can be obtained using equation 5.18 based on the knowledge of shrinkage and creep characteristics of the matrix and details of fibres. Equation 5.18 is valid within the range of the experimental data. It is expected that at very low, V_f l/d ratios, the slope of the linear relationship between $\varepsilon_{fc}/\varepsilon_{oc}$ and V_f l/d would increase (coefficient a will increase) to meet the boundary condition of $\varepsilon_{fc}/\varepsilon_{oc} = 1$ when V_f l/d = 0.

5.6 CONCLUSIONS

The following conclusions are based on the results of the experimental and theoretical investigations reported in this chapter.

1. Alkali activated materials exhibit much higher free shrinkage and compressive creep than normal Portland cement mortars.

2. Most of the shrinkage of alkali activated fly ash materials occurs in the first 72 hours.

3. Alkali activated materials with a lower water/ binder ratio (0.20) exhibit lower free shrinkage than those with a higher water/ binder ratio (0.25), regardless of the curing conditions.

4. The free shrinkage of alkali activated materials is considerably reduced when cured under 20°C and 95% relative humidity or in water at 20°C, as opposed to curing at 20°C, 65%RH, i.e. a reduction in relative humidity of the curing environment results in higher shrinkage.

5. The addition of fibre reinforcement greatly reduces the free shrinkage. Reductions of up to 55% at V_fl/d = 2.12 for glass fibre reinforced materials and 44% at V_fl/d = 0.76 for steel fibre reinforced materials, cured under 20°C, 65% RH, were achieved.

6. Shrinkage restraint increases with increasing fibre volume and fibre $V_f l/d$.

7. The free shrinkage of alkali activated fibre reinforced materials agrees with the theoretical model developed by Mangat and Azari[114] for steel fibre reinforced Portland cement mortars.

8. The values for the early age coefficient of friction of fibre reinforced alkali activated materials determined using the shrinkage model developed by Mangat and Azari[114,146] are comparable with those of fibre reinforced Portland cement mortars.

9. The compressive creep of alkali activated materials is reduced by approximately 50% when they are thermally cured compared with curing under 20°C, 65% RH.

10. The addition of short fibre reinforcement greatly reduces the compressive creep of alkali activated materials. Reductions of up to 45% for glass fibre reinforced materials and 50% for steel fibre reinforced materials, cured under 20°C, 65% RH were achieved.

11. Creep recovery (delayed elastic strain) increases markedly with increasing fibre volume for materials initially cured under 20°C, 65%RH.

12. Flow creep decreases sharply with increasing fibre volume for materials initially cured under 20°C, 65%RH.

13. Fibre reinforced materials initially thermally cured show no significant changes in the creep recovery or flow creep with an increase in the fibre volume.

14. The compressive creep of alkali activated fibre reinforced materials agrees with the theoretical model developed by Mangat and Azari[115] for steel fibre reinforced Portland cement mortars.

15. The values for the long term coefficient of friction of fibre reinforced alkali activated materials determined using the creep model developed by Mangat and Azari[115] are comparable with those of fibre reinforced Portland cement mortars.

"The improvement of understanding is for two ends: first, our own increase of knowledge, secondly, to enable us to deliver that knowledge to others."

John Locke

6 Mechanical properties of alkali activated materials

6.1 INTRODUCTION

The selection of a cementitious material when employed as a structural material depends primarily on its mechanical properties. Mechanical tests, therefore, play a very important role in determining the performance of a material and every specification requires a certain minimum strength that must be attained under given conditions[34]. The development of mechanical strength in cementitious composites depends on many factors such as grading of sand, aggregates and fineness of binding materials; amount of water used; time and method of mixing and temperature and humidity under which is conducted; moulding and compacting methods; storing and curing conditions; method of testing and testing age.

6.2 OBJECTIVES

A comprehensive experimental programme was undertaken to determine the mechanical properties of alkali activated materials. The mechanical properties investigated were modulus of rupture; compressive strength; tensile splitting strength; dynamic modulus of elasticity. The objectives were:

- To determine the influence of the following parameters on the mechanical properties: constituent materials and mix design, mixing casting and curing procedure.

- To determine the relationship between modulus of rupture and tensile splitting strength of fibre reinforced composites.

- To determine a relationship between dynamic modulus of elasticity and compressive strength of alkali activated materials and their fibre reinforced composites.

- To derive a theoretical prediction model for the modulus of rupture of steel and glass fibre reinforced alkali activated materials.

- To determine the fibre-matrix interfacial bond strength for fibre reinforced alkali activated materials.

6.3 EXPERIMENTAL PROGRAMME

6.3.1 Constituent Materials

The constituent materials are detailed in Chapter III (Experimental Programme) and are also summarised below.

The main pozzolanic material used was **pulverised fuel ash** (pfa) from the power plant at Ratcliffe. Its chemical composition (by weight) is given in Table 6.1.

Table 6.1 Chemical composition of the fly ash from Ratcliffe.

Element	Content [%]
Silicon dioxide (SiO_2)	47.4
Aluminium oxide (AlO_3)	25.6
Iron oxide (Fe_2O_3)	10.4
Magnesium oxide (MgO)	1.7
Calcium oxide (CaO)	3.3
Sulphate (SO_3)	1.0
Potassium oxide (K_2O)	3.1
Sodium oxide (Na_2O)	1.4
$Na_2O_e = 0.658 \cdot K_2O + Na_2O$	3.4
Titanium oxide (TiO_2)	1.0
Chlorite (Cl)	0.01
Loss of Ignition	4.54
Density (kg/m^3)	2290
Sieve Residue Retained 45μm	
$\frac{CaO + MgO + Al_2O_3}{SiO_2}$	**0.645**

The slag used in this investigation was **ground granulated blast furnace slag** from the plant located in Teesside. Its chemical composition (by weight) is given in Table 6.2.

Table 6.2 Chemical composition of ground granulated blast furnace slag from Teesside

Element	Content [%]
Silicon dioxide (SiO_2)	35.67
Aluminium oxide (AlO_3)	13.47
Iron oxide (Fe_2O_3)	0.55
Magnesium oxide (MgO)	7.45
Calcium oxide (CaO)	40.90
Sulphate (SO_3)	0.05
Sulphide (S^{2-})	0.91
Potassium oxide (K_2O)	0.26
Sodium oxide (Na_2O)	0.19
$Na_2O_e = 0.658\ K_2O + Na_2O$	0.36
Titanium oxide (TiO_2)	0.69
Chlorite (Cl)	0.013
Manganese (MnO)	0.27
Loss of Ignition	0.48
Insoluble Residue	0.14
Particle size analysis	**466**[kg/m^2]
$\frac{\underline{CaO + MgO + Al_2O_3}}{SiO_2}$	**1.733**

Microsilica (silica fume) used in this investigation was a dry densified silica fume with the chemical composition (by weight) given in Table 6.3.

Table 6.3 Chemical composition of the densified silica fume

Element	Content [%]
Silicon dioxide (SiO_2) amorphous	85 to 98
Iron oxide (Fe_2O_3)	≤ 3.0
Aluminium oxide (Al_2O_3)	≤ 1.5
Calcium oxide (CaO)	≤ 0.7
Magnesium oxide (MgO)	≤ 2.0
Sodium oxide Na_2O)	≤ 1.0
Potassium oxide (K_2O)	≤ 3.0
$Na_2O_e = 0.658 \cdot K_2O + Na_2O$	≤ 2.97
Carbon (C)	≤ 3.0
$\frac{\underline{CaO + MgO + Al_2O_3}}{SiO_2}$	**0.0494 to 0.0428**

Washed and graded **high silica fine sand** from Congleton quarry was used. Its chemical composition (by weight) is given in Table 6.4.

Table 6.4 Chemical composition of silica sand from Congleton quarry

Element	Content [%]
Silica (SiO_2)	95.13
Aluminia (Al_2O_3)	2.34
Iron oxide (Fe_2O_3)	0.24
Sodium oxide (Na_2O)	-
Potassium oxide (K_2O)	1.61
$Na_2O_e = 0.658\ K_2O + Na_2O$	1.06
L.O.I.	0.25
Average grain size [μm]	175
Bulk density [kg/m^3]	1450

Sodium silicate solution (water glass Crystal 112) with a mean molar ratio (silica modulus) SiO_2/NaO_2 =2.06 was used. Its chemical composition (by weight) is given in Table 6.5.

Table 6.5 Chemical composition of the sodium silicate solution

Element	Content [%]
Silicon dioxide (SiO_2)	30.55
Sodium oxide (Na_2O)	15.27
Water (H_2O)	54.18

Water glass hardener: An aluminium methaphosphate compound, K-Bond # 90, was used to accelerate the curing process. The general properties of the hardener are given in Table 6.6.

Table 6.6 Properties of the water glass hardener (K-Bond # 90)

Property	Description
Appearance	Fine white powder
Acidity [meq/g]	1.2 ± 0.5
Moisture [%]	≤ 1.5
Solubility in water [%]	≤ 3.0
pH	3.2 ± 0.5
Sieve residue > 44 micron [%]	≤ 1.0

Fibre Reinforcement: Three types of fibres were investigated.

a) Stainless steel fibres of straight shape and undeformed, smooth surface. The fibres were of length 7mm and diameter 0.15 mm. The aspect ratio (length/diameter) was 46.67. The specific gravity and Young's modulus of elasticity were 7.8 kg/m^3 and 215.3 GPa, respectively.

b) Melt extract steel fibres of non-uniform surface. The fibres were of length 12 mm and equivalent diameter 0.5 mm. The aspect ratio was 24. The specific gravity and Young's modulus of elasticity were 7.8 kg/m^3 and 215.3 GPa, respectively.

c) Alkali resistant integral chopped strand glass fibres (Cem-FIL 62/2) consisting of 100 filaments bound together. These fibres were resistant to breakdown of the strands during mixing. The individual filaments were of length 12 mm and diameter 14μm. The aspect ratio of the fibre strand was 70.6. The specific gravity and Young's modulus of elasticity were 2.68 kg/m^3 and 72 GPa, respectively.

6.3.2 Sample Preparation

Specimens of acceptably large dimensions, to produce reliably accurate information, were used in the investigations reported in this chapter. These were prisms of dimensions 75x75x300 mm, cylinders of 100mm diameter 200mm height and 75 mm cubes. These sizes were selected to strike an optimal balance between limiting excessive volumes of materials required and ensuring that meaningful data could be obtained on the properties of the alkali activated materials.

A detailed description of the mixing, casting and curing procedures is given in section 5.3 of Chapter V. Mixes with two different water/binder ratios (0.25 and 0.20) were investigated. The water and solids in the sodium silicate solution (water glass) were included in determining the water/binder ratio. Mixing was carried out in a forced action pan Hobart mixer. The dry component materials (fly ash, silica fume, ggbs and sand) were mixed thoroughly after which the fibre reinforcements (in fibre reinforced mixes only; see section 6.3.3), were added. Following this, sodium silicate

solution (water glass) was added and mixed with the dry components until the mixture became homogenous. The hardener was added near the end of the mixing process, in the form of a slurry to aid its dispersion in the mix. The mixes were cast in stainless steel moulds which were suitable for placing in a fan assisted oven at high temperature (up to 120°C). The internal surfaces of the moulds were coated with a relief agent (silicon oil) to prevent adherence of the cast material to the mould. Two compacting methods were employed, depending of the workability of the mix. The stiffer mixes (w/b = 0.20) were cast in two layers and compacted by applying 25 strokes of a tamping rod. The workable mixes (w/b=0.25) were cast in two layers, each layer being compacted using a vibrating table until the surface of the sample was smooth and had a glassy appearance. The test specimens were subjected to one of the following four curing conditions immediately after casting:

i. controlled conditions at 20°C and 65% relative humidity - the specimens were kept in the moulds for 7 hours then demoulded and curing maintained at 20°C and 65% RH until testing.

ii. mist conditions at 20°C and 95% relative humidity - the specimens were kept in the moulds for 7 hours then demoulded and curing maintained at 20°C and 95% RH until testing. The specimens were placed in the mist curing room and covered with polythene sheeting to prevent condensation.

iii. mist conditions at 20°C and 95% relative humidity for the first seven hours before demoulding. After demoulding the samples were stored in a water tank at 20°C until testing.

The strength development under curing conditions (i to iii) was sufficiently rapid to allow demoulding of the samples after seven hours from casting.

iv. high temperature curing - the specimens were subjected to a curing temperature programme which is presented in Figure 5.4. After casting, the samples (within the moulds) were placed in an oven and the temperature was raised from room temperature (≈20.6°C) to 30°C in 60 minutes and held at 30°C for a further 240 minutes. The temperature was then progressively increased in steps up to 120°C

as shown in Figure 5.1. Finally the temperature was gradually reduced to 20.6°C in 420 minutes (see Figure 5.1). The total duration of the curing period was 1620 minutes (27 hours). The samples were then stored at 20°C and 65% RH until testing.

6.3.3 Details of batches

The mix proportion of the dry constituent materials used were 1/ 0.5/ 0.25/ 3.25 by weight (fly ash/ ground granulated blast furnace slag/ silica fume/ sand). Water glass Crystal 112 content was 11.46% by weight of the mix, as detailed in section 5.3 (Experimental Programme) of Chapter V. The hardener content was 1.5% by weight of the sodium silicate solution (water glass), in the form of a slurry with water. The water/binder ratios and curing conditions used for the alkali activated cementitious materials and alkali activated fibre reinforced composite materials investigated in this chapter are given in Tables 6.7 and 6.8, respectively. The water content (% by weight) given in Tables 6.7 and 6.8 includes the water and solid contents of the sodium silicate solution.

Table 6.7 Composition of alkali activated fly ash materials

Batch Code	Water/Binder	Total Water [%]	Hardener [%]	Curing Conditions
A1	0.25	10.28	-	20°C and 65% RH
M1	0.25	10.28	-	20°C and 95% RH
W1	0.25	10.28	-	water curing at 20°C after 7 h
H1	0.25	10.28	-	thermal treatment
KA1	0.25	10.28	1.5	20°C and 65% RH
KM1	0.25	10.28	1.5	20°C and 95% RH
A2	0.20	6.20	-	20°C and 65% RH
M2	0.20	6.20	-	20°C and 95% RH
H2	0.20	6.20	-	thermal treatment
KA2	020	6.20	1.5	20°C and 65% RH
KM2	0.20	6.20	1.5	20°C and 95% RH

Table 6.8 Composition of fibre reinforced alkali activated materials

Batch Code	Water/ Binder	Total Water [%]	Fibres		Curing Conditions
			Type	V_f [%]	
GA1	0.25	10.28	glass	1.5	20°C and 65% RH
GH1	0.25	10.28	glass	1.5	thermal treatment
GA2	0.25	10.28	glass	3.0	20°C and 65% RH
GH2	0.25	10.28	glass	3.0	thermal treatment
SwA1	0.25	10.28	straight steel	1.5	20°C and 65% RH
SA1	0.25	10.28	melt extract	1.5	20°C and 65% RH
SH1	0.25	10.28	melt extract	1.5	thermal treatment
SA2	0.25	10.28	melt extract	3.0	20°C and 65% RH
SH2	0.25	10.28	melt extract	3.0	thermal treatment

The batch code symbols represent:

A - air cured at 20°C and 65% relative humidity;

M - mist cured at 20°C and 95% relative humidity;

W - water cured at 20°C;

H - heat (thermally) cured;

K - mix containing water glass hardener, aluminium methaphosphate compound, K-Bond # 90;

Sw - mix reinforced with stainless steel fibres (wire) of straight shape and undeformed, smooth surface;

S - mix reinforced with melt extract steel fibres of non-uniform surface;

G - mix reinforced with alkali resistant integral chopped strand glass fibres.

6.4 TESTING PROGRAMME

6.4.1 Modulus of Rupture

The modulus of rupture was determined by a three point bending test according to BS 1881: Part 118:1983 as shown in Figure 5.3. The load was increased steadily at a rate of 85 N/s in accordance with BS 1881: Part 118[136].

Three prism specimens from each mix listed in Table 6.7 and 6.8 were tested in an Avery Dennison Transverse Testing Machine (model 7123-100 kN capacity). Consequently each modulus of rupture value presented in this investigation is an

average of three measurements. The specimens were placed in the testing machine, centred with the longitudinal axis of the specimens at the right angles to the rollers. The mould filling direction was normal to the direction of loading.

The modulus of rupture was calculated using the following equation:

$$R_f = \frac{3F_f L}{2bw^2} \text{ [N/mm}^2\text{]} \qquad \text{Equation 6.1}$$

where:

F_f is the maximum transverse load at which the material fractures [N]

L is the span, [mm]

b is the width of the specimen, [mm]

w is the depth of the specimen, [mm]

6.4.2 Tensile Splitting Strength

Two100 mm diameter and 200 mm length cylinders were tested in the Avery Dennison Compression Testing Machine (model 7123-100 kN) in accordance with BS 1881: Part 117: 1983[147]. Consequently each tensile splitting strength value presented in this investigation is an average of two measurements. The specimens were positioned in the centre of a jig with packing hardboard strips carefully positioned along the top and the sofit of the plane of loading of the specimen. Then the jig was placed in the machine so that the specimen was positioned centrally, as shown in Figure 6.1. The load was applied and increased steadily at a rate of 550 N/s.

Tensile Splitting Strength was determined using the following equation:

$$R_{ts} = \frac{2F_{ts}}{\pi \cdot L \cdot d} \text{ [N/mm}^2\text{]} \qquad \text{Equation 6.2}$$

where:

F_{ts} is the maximum compressive load at which the material fractures, [N]

d is the specimen diameter

L is the length of the specimen

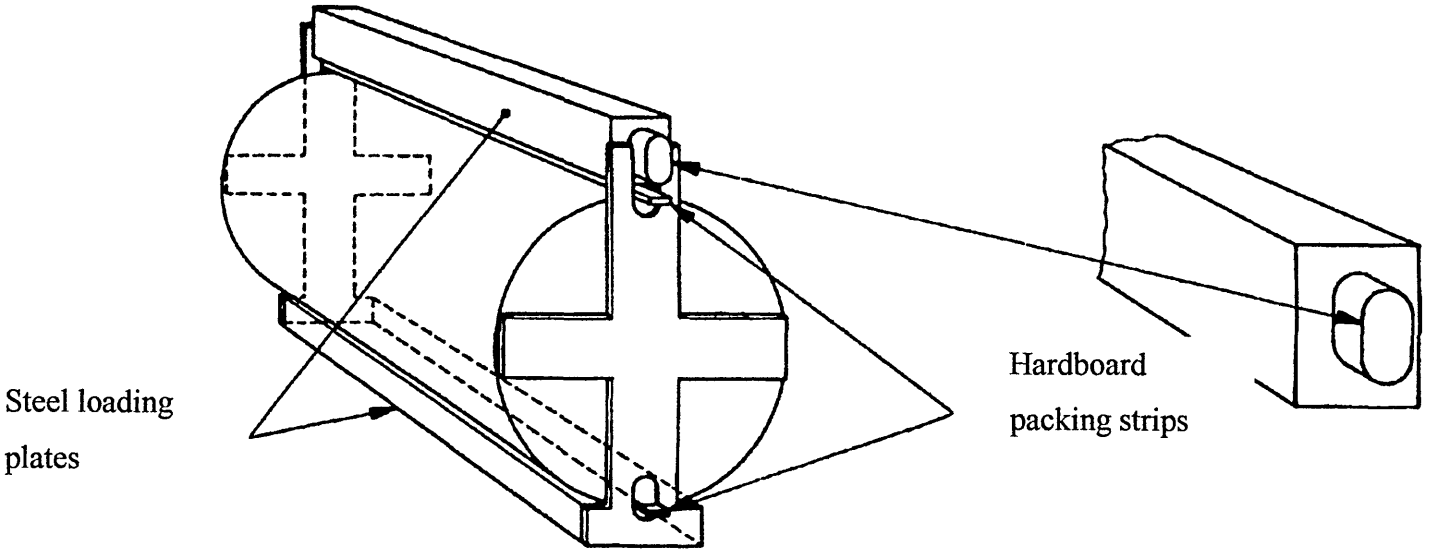

Figure 6.1 Arrangement of loading of tensile splitting test specimen

6.4.3 Compressive Strength

The halves of fractured prisms resulting from the flexural tests were cut using a water-cooled masonry saw to produce 75 mm cubes. The specimens were visually inspected to ensure that they were free from cracks, chipped surfaces and or any other defects within the volume to be tested. The resulting six cubes for each batch mix plus one 75x75x75mm originally cast cube were tested in an Avery Dennison Compressive Testing Machine (model 7123-100 kN) in accordance with BS1881: Part 116: 1986[137]. Consequently each compressive strength was an average of seven measurements.

The cubes were immersed in water for 5 minutes prior to testing to overcome the frictional forces between the surface of the test cube and the platen of the testing machine. Each test cube was centred on the lower platen of the compression machine ensuring that the load was applied on two opposite cast faces (to ensure parallelism). The load was applied and increased steadily at a nominal rate of 1250N/s.

Compressive Strength was determined using the following equation:

$$R_c = \frac{F_c}{A} \text{ [N/mm}^2\text{]} \qquad \text{Equation 6.3}$$

where:

F_c is the maximum compressive load, at which the material fractures, [N]

A is the cross-sectional area of the specimen, [mm^2]

6.4.4 Dynamic Modulus of Elasticity

The dynamic modulus of elasticity was determined using an ERUDITE (resonant frequency ultrasonic non-destructive digital indicating system) in accordance with BS 1881: Part 206 (Figure 6.2). Three prism specimens from each material were tested and the fundamental resonant frequency 'f' recorded. Consequently each dynamic modulus of elasticity value presented in this investigation is an average of three measurements.

Each 300 mm long by 75 mm square cross-section prism specimen was balanced at its mid-point and excited by a variable frequency electromagnetic exciter in contact with one end as shown in Figure 6.6. A piezoelectric accelerometer contact pick-up positioned at the other end detected the induced vibrations and the signal from this was amplified and displayed on the oscilloscope as shown in Figure 6.2. The frequency was varied until the fundamental resonant frequency, f, was obtained, indicated by maximum amplitude of the pick up signal at the same frequency as the input signal.

Figure 6.2 Dynamic modulus of elasticity test method

The dynamic modulus of elasticity E_d was then calculated from the following formula:

$$E_d = 4 \cdot f^2 \cdot l^2 \cdot \rho \qquad \text{Equation 6.4}$$

where :

f is the resonant frequency of the fundamental mode of longitudinal vibrations, [Hz]

l is the length of the specimen, [mm]

ρ is the density of the material, [kg/m^3]

The density was calculated using:

$$\rho = \frac{m_A}{V} \qquad \text{Equation 6.5}$$

where :

V is the volume of the sample determined by water displacement method using the following equation :

$$V = \frac{m_A - m_W}{m_A}$$

m_A is the mass of the specimen weighed in air

m_W is the mass of the completely immersed specimen

The dynamic modulus test is known to give reproducible results. The force applied to the material is negligible, therefore, the problems of non-linearity that occur in the static test do not arise. The dynamic modulus of elasticity approximates the tangent modulus at the origin of the stress-strain curve and, therefore, is higher than the static modulus[81].

6.4.5 Choice of test specimens

A detailed description of the choice of specimens is given in section 5.4.3 of Chapter V. Specimens of acceptably large dimensions (75mmx 75mmx 300mm prisms, 75mm cubes and 100mm diameter, 200mm height cylinders) were used in the investigations on mechanical properties of alkali activated materials. Three prisms were used for each of the modulus of rupture tests. Three cylinders were used for tensile splitting tests. One cube together with the prism halves obtained after flexural testing were used for compression testing.

6.5 RESULTS AND DISCUSSION

6.5.1 Influence of water/binder ratio on mechanical properties of alkali activated materials

6.5.1.1 Compressive Strength

A summary of the compressive strength results together with the percentage differences resulting from changes in water /binder ratio (equation 6.6) are presented in Table 6.9. The compressive strength of alkali activated materials σ_{cm} is within the range 52 N/mm^2 to 104 N/mm^2.

Table 6.9 Influence of water/binder ratio on compressive strength σ_{cm}

Batch Code	Curing conditions	Water/Binder	Compressive strength σ_{cm} [N/mm^2]	Difference in σ_{cm}
A1	20°C and 65% RH	0.25	55.0	45%
A2	20°C and 65% RH	0.20	103.7	
KA1	20°C and 65% RH	0.25	64.0	29%
KA2	20°C and 65% RH	0.20	90.5	
M1	20°C and 95% RH	0.25	52.2	15%
M2	20°C and 95% RH	0.20	70.1	
KM1	20°C and 95% RH	0.25	51.8	26%
KM2	20°C and 95% RH	0.20	61.2	
H1	thermal treatment	0.25	80.3	15%
H2	thermal treatment	0.20	94.2	

$$Difference\ in\ \sigma_{cm} = \frac{\sigma_{cm}\ (w/b = 0.20) - \sigma_{cm}\ (w/b = 0.25)}{\sigma_{cm}\ (w/b = 0.20)} \qquad \text{Equation 6.6}$$

A significant decrease in compressive strength is consistently observed with changing water binder ratio from 0.20 to 0.25 for all curing conditions. For example, under 20°C and 65% RH curing the compressive strength of material with w/b of 0.25 (batch code A1) is 45% lower than that of corresponding material with w/b of 0.20 (batch code A2).

Similarly, the thermally cured material of w/b=0.25 (batch code H1) has a compressive strength 15% lower than the corresponding material with w/b of 0.20 (batch code H2). These results will be discussed further in section 6.5.1.5.

At failure all four faces of the cubes cracked uniformly, generally with little damage to the faces in contact with the platens. The failure mode is illustrated in Figure 6.3; the unreinforced specimens showed an "explosive failure".

Unreinforced material Fibre reinforced material

Figure 6.3 Compressive test specimen failure of alkali activated fly ash materials

6.5.1.2 Modulus of Rupture

A summary of the modulus of rupture results together with the percentage differences resulting from changing the water /binder ratio from 0.20 to 0.25 (equation 6.7) are presented in Table 6.10. The modulus of rupture of alkali activated materials σ_{fm} is within the range 3.1 N/mm^2 to 10.5 N/mm^2. Modulus of rupture results follow the same trends as those for compressive strength. The materials with a lower water/binder ratio (0.20) exhibit higher modulus of rupture compared with materials with a higher water/binder ratio (0.25) for all curing conditions. For example, under 20°C and 65% RH curing, the modulus of rupture of the material with w/b of 0.25 (batch code A2) is 35% lower than that of corresponding material of w/b of 0.20 (batch code A1).

Table 6.10 Effect of water/binder ratio on modulus of rupture σ_{fm}

Batch Code	Curing conditions	Water/Binder	Modulus of Rupture σ_{fm} [N/mm^2]	Difference in σ_{fm}
A1	20°C and 65% RH	0.25	3.6	35%
A2	20°C and 65% RH	0.20	5.6	
KA1	20°C and 65% RH	0.25	3.8	16%
KA2	20°C and 65% RH	0.20	4.5	
M1	20°C and 95% RH	0.25	3.1	46%
M2	20°C and 95% RH	0.20	5.7	
KM1	20°C and 95% RH	0.25	4.3	6%
KM2	20°C and 95% RH	0.20	4.5	
H1	thermal treatment	0.25	9.3	12%
H2	thermal treatment	0.20	10.5	

$$Difference\ in\ \sigma_{fm} = \frac{\sigma_{fm}\ (w/b = 0.20) - \sigma_{fm}\ (w/b = 0.25)}{\sigma_{fm}\ (w/b = 0.20)} \qquad \text{Equation 6.7}$$

Similarly, thermally cured material of water/binder=0.25 (batch code H1) has a modulus of rupture 12% lower than the corresponding material of water/binder =0.20 (batch code H2). These results will be discussed further in section 6.5.1.5.

The decrease in modulus of rupture with increasing water/binder ratio (from 0.20 to 0.25) is greater for alkali activated materials without hardener compared with materials with hardener. The average reduction in materials without hardener is 40% compared with 11% for the corresponding materials with hardener addition.

6.5.1.3 Tensile splitting strength

A summary of the tensile splitting strength results together with their percentage differences resulting from changes in water /binder ratio (equation 6.8) are presented in Table 6.11. The tensile splitting strength of alkali activated materials σ_{fm} is within the range 4.9 N/mm^2 to 5.4 N/mm^2.

Table 6.11 Influence of water/binder ratio on tensile splitting strength σ_{tm}

Batch Code	Curing Conditions	W/B	Tensile Strength σ_{tm} [N/mm^2]	Difference in σ_{tm}
A1	20°C and 65% RH	0.25	4.9	4%
A2	20°C and 65% RH	0.20	5.1	
H1	thermally treated	0.25	5.0	6%
H2	thermally treated	0.20	5.4	

$$Difference\ in\ \sigma_{tm} = \frac{\sigma_{tm}\ (w/b = 0.20) - \sigma_{tm}\ (w/b = 0.25)}{\sigma_{tm}\ (w/b = 0.20)} \qquad \text{Equation 6.8}$$

A small decrease in tensile splitting strength is observed with changing the water/ binder ratio from 0.20 to 0.25 for both curing conditions: 20°C and 65% RH, (i) and thermal curing (iv). For example, under 20°C and 65% RH curing, the tensile splitting strength of the material with w/b of 0.25 (batch code A2) is 4% lower that of corresponding material with a w/b of 0.20 (batch code A1). Similarly, thermally cured material of water/binder=0.25 (batch code H1) has a tensile splitting strength 6% lower than the corresponding material of water/binder =0.20 (batch code H2).

6.5.1.4 Dynamic modulus of elasticity

A summary of the dynamic modulus of elasticity results together with their percentage differences resulting from changes in water /binder ratio (equation 6.9) are presented in Table 6.12. The dynamic modulus of elasticity of the alkali activated materials is within the range 16 kN/mm^2 to 29 kN/mm^2.

The results presented in Table 6.12 show that the dynamic modulus of elasticity decreases with increasing water /binder ratio from 0.20 to 0.25 for all curing conditions. For example, under 20°C and 65% RH curing, the dynamic modulus of elasticity of the material with w/b of 0.25 (batch code A2) is 38% lower than that of corresponding material of w/b=0.20 (batch code A1). Similarly, thermally cured material of water/binder=0.25 (batch code H1) has a dynamic modulus 12% lower than the corresponding material of water/binder =0.20 (batch code H2).
These results will be discussed further in section 6.5.1.5.

Table 6.12 Influence of water/binder ratio on dynamic modulus of elasticity E_D

Batch Code	Curing conditions	Water/Binder	E_D [kN/mm^2]	Difference in E_D
A1	20°C and 65% RH	0.25	17	38%
A2	20°C and 65% RH	0.20	28	
KA1	20°C and 65% RH	0.25	20	16%
KA2	20°C and 65% RH	0.20	23	
M1	20°C and 95% RH	0.25	16	26%
M2	20°C and 95% RH	0.20	22	
KM1	20°C and 95% RH	0.25	20	4%
KM2	20°C and 95% RH	0.20	21	
H1	thermal treatment	0.25	27	8%
H2	thermal treatment	0.20	29	

$$Difference\ in\ E_D = \frac{E_D\ (w/b = 0.20) - E_D\ (w/b = 0.25)}{E_D\ (w/b = 0.20)} \qquad \text{Equation 6.9}$$

6.5.1.5 Discussion

Strength of normal concrete and mortar can be improved by keeping its water/ binder ratio and binder (cement) content as low as possible[149]. The results from this investigation confirm that alkali activated materials with higher water/binder ratio (0.25) exhibit lower strength than materials with a lower water/binder content (0.20), see Tables 6.9 - 6.12. Data given in section 7.4.6 of Chapter 7 show that alkali activated materials with a higher water/binder ratio of 0.25 have a lower volume of unhydrated pozzolanic material than for the material with lower water/binder of 0.20 when cured under conditions (i) and (ii) i.e. 20°C and 65% RH or 95% RH respectively. Therefore, the layers of hydrated paste surrounding the unhydrated cement grains will be thicker for alkali activated materials with the higher water/binder ratio of 0.25. The unhydrated material is not detrimental to strength. Studies on pastes with a gel/space ratio of 1.0 show that those with a higher proportion of unhydrated cement (i.e. lower water/binder ratio) have higher strength possibly because the layers of hydrated paste surrounding the unhydrated cement grains are thinner[149].

The general trend of decreasing mechanical properties (modulus of rupture, compressive strength, tensile splitting strength and dynamic modulus of elasticity) with increasing water/binder ratio is common to hydraulic cementitious materials[81]. Neville[81] explained this as being due to pore structure and pore distribution. The presence of voids in concrete decreases its density. Voids in concrete are of entrapped air bubbles or spaces left after the water has been removed. The volume of the latter depends mainly on the water/binder ratio of the mix. Therefore, for any given method of compaction there is an optimum water content of the mix at which the sum of the volumes of air the bubbles and void space will be minimum. At this optimum water content the lowest porosity of the concrete would be obtained and, therefore, the highest strength. Increasing the workability of the mix requires an increase in the water content which will increase the porosity and, therefore, lower the strength.

6.5.2 Influence of relative humidity on mechanical properties of alkali activated materials

6.5.2.1 Compressive Strength

A summary of the compressive strength results together with the percentage differences in compressive strength resulting from changes in relative humidity of curing (equation 6.10) are presented in Table 6.13. The curing temperature was 20°C in all cases.

Alkali activated materials cured at 65% relative humidity (batch code A1, KA1, A2, and KA2) exhibit higher compressive strength then corresponding materials cured at the higher relative humidity of 95% (batch code M1, KM1 M2 and KM2), as shown in Table 6.13. For example, at a water/binder of 0.20, the compressive strength of the material cured at 95% RH (batch code M2) is 41% lower than that of the material cured at 65% RH (batch code A2).

The material with a water/binder of 0.25 cured at 95% RH (batch code M1) has a compressive strength 5% lower than the corresponding material cured at 65% RH (batch code A1). This decrease in compressive strength with increasing RH of curing (from 65% to 95%) is greater at a water/binder ratio of 0.20 compared with water/binder of 0.25. These results will be discussed further in section 6.5.2.4.

Table 6.13 Effect of relative humidity of curing on compressive strength σ_{cm}

Batch Code	Curing conditions	Water/Binder	Compressive strength σ_{cm} [N/mm^2]	Difference in σ_{cm}
A1	20°C and 65% RH	0.25	57.02	-
M1	20°C and 95% RH	0.25	54.21	5%
W1	water at 20°C	0.25	54.43	5%
KA1	20°C and 65% RH	0.25	63.97	-
KM1	20°C and 95% RH	0.25	51.78	19%
A2	20°C and 65% RH	0.20	103.74	-
M2	20°C and 95% RH	0.20	70.11	41%
KA2	20°C and 65% RH	0.20	90.52	-
KM2	20°C and 95% RH	0.20	61.16	23%

$$Difference\ in\ \sigma_{cm} = \frac{\sigma_{cm}\ (RH = 65\%) - \sigma_{cm}\ (RH \geq 95\%)}{\sigma_{cm}\ (65\%)} \qquad \text{Equation 6.10}$$

6.5.2.2 Modulus of rupture

A summary of the modulus of rupture results together with the percentage differences in modulus of rupture resulting from changing the relative humidity of curing from 65% to 95% (equation 6.11) are presented in Table 6.14. The curing temperature was 20°C.

The results presented in Table 6.14 show that the modulus of rupture of alkali activated materials is not greatly affected by the relative humidity of curing. A small increase in the modulus of rupture is generally observed with increasing relative humidity of curing from 65% to 95% with the exception of material batch code M1.

For example, at a water/binder of 0.20, the modulus of rupture of the material cured at 95% RH (batch code M2) is 12% higher than the corresponding material cured at 65% RH (batch code A2). Considering all data in Table 6.14, the average increase in the modulus of rupture under high RH curing is under 1%.

Table 6.14 Influence of relative humidity of curing on modulus of rupture σ_{fm}

Batch Code	Curing conditions	Water/Binder	Modulus of Rupture σ_{fm} [N/mm^2]	Difference in σ_{fm}
A1	20°C and 65% RH	0.25	3.6	-
M1	20°C and 95% RH	0.25	3.1	15%
W1	water curing at 20°C	0.25	3.8	-6%
KA1	20°C and 65% RH	0.25	3.8	-
KM1	20°C and 95% RH	0.25	4.3	-12%
A2	20°C and 65% RH	0.20	5.6	-
M2	20°C and 95% RH	0.20	5.7	-1%
KA2	20°C and 65% RH	0.20	4.5	-
KM2	20°C and 95% RH	0.20	4.5	0%

$$Difference\ in\ \sigma_{fm} = \frac{\sigma_{fm}\ (RH = 65\%) - \sigma_{fm}\ (RH \geq 95\%)}{\sigma_{fm}\ (RH = 65\%)} \qquad \text{Equation 6.11}$$

6.5.2.3 Dynamic Modulus of Elasticity

A summary of the dynamic modulus of elasticity results together with the percentage differences in dynamic modulus of elasticity resulting from changes in relative humidity of curing (equation 6.12) are presented in Table 6.15. The curing temperature was 20°C.

Materials with a water/binder of 0.20 show a decrease in the dynamic modulus of elasticity with increasing relative humidity of curing from 65% to 95%, following the same trends as the compressive strength results. For example at a water/binder of 0.20, the dynamic modulus of elasticity of the material cured at 95% RH (batch code M2) is 21% lower than the material cured at 65% RH (batch code A2).

Table 6.75 Effect of relative humidity of curing on dynamic modulus of elasticity

Batch Code	Curing conditions	Water/Binder	E_D [kN/mm^2]	Difference in E_D
A1	20°C and 65% RH	0.25	17.2	
M1	20°C and 95% RH	0.25	16.0	7%
W1	water curing at 20°C	0.25	18.3	-6%
KA1	20°C and 65% RH	0.25	19.6	
KM1	20°C and 95% RH	0.25	20.0	-2%
A2	20°C and 65% RH	0.20	27.7	
M2	20°C and 95% RH	0.20	21.8	21%
KA2	20°C and 65% RH	0.20	23.3	
KM2	20°C and 95% RH	0.20	20.9	10%

$$Difference\ in\ E_D = \frac{E_D\ (RH = 65\%) - E_D\ (RH \geq 65\%)}{E_D\ (RH = 65\%)} \qquad \text{Equation 6.12}$$

The materials with a water/binder ratio of 0.25 show less significant changes in the dynamic modulus of elasticity. For example, the material with a water/binder of 0.20 cured at 95% relative humidity (batch code M1) has a dynamic modulus of elasticity only 7% lower than that of corresponding material cured at 65% RH (batch code A1).

6.5.2.4 Discussion

Powers[149] concluded that hydration of hydraulic cement is greatly reduced when the relative humidity within the capillary pores drops below 80%. Therefore, for hydration to continue the relative humidity inside concrete has to be maintained at a minimum 80%. Curing at external relative humidity less than 80% was shown to result in an increase in volume of pores larger than 37nm[150]. The effect of inadequate relative humidity of curing on strength is greater at higher water/cement ratio. It is also greater in concrete with a lower rate of strength development such as concrete containing fly ash. It is not necessary for all the cement to hydrate for a satisfactory development of strength. Indeed, this is only very rarely achieved in practice. The results from the present investigation (Tables 6.13-6.15) show opposite trends to those for ordinary Portland cement mortar and concrete as they exhibit lower

compressive strength and dynamic modulus of elasticity when cured at 95% RH compared with materials cured at 65% RH. The quality of alkali activated materials seems to depend primarily on the gel/space ratio of the paste, as shown in section 7.4.6 of Chapter 7. If, however the water-filled spaces in fresh concrete are greater than the volume of the hydration products, greater hydration will lead to a higher strength and a low permeability.

6.5.3 Effect of hardener on mechanical properties of alkali activated materials

6.5.3.1 Compressive Strength

A summary of the compressive strength results together with the percentage differences in compressive strength resulting from addition of water glass hardener, aluminium methaphosphate KB # 90, (equation 6.13) are presented in Table 6.16.

Table 6.16 Effect of water glass hardener on compressive strength σ_{cm}

Batch Code	Curing conditions	Water/ Binder	Hardener [%]	Compressive strength σ_{cm} [N/mm^2]	Difference in σ_{cm}
A1	20°C and 65% RH	0.25	0	55.0	
KA1	20°C and 65% RH	0.25	1.5	63.9	-16%
M1	20°C and 95% RH	0.25	0	54.2	
KM1	20°C and 95% RH	0.25	1.5	51.8	4%
A2	20°C and 65% RH	0.20	0	103.7	
KA2	20°C and 65% RH	0.20	1.5	90.5	13%
M2	20°C and 95% RH	0.20	0	70.1	
KM2	20°C and 95% RH	0.20	1.5	61.2	13%

$$Difference\ in\ \sigma_{cm} = \frac{\sigma_{cm}\ (0\%hardener) - \sigma_{cm}\ (1.5\%hardener)}{\sigma_{cm}\ (0\%hardener)} \qquad \text{Equation 6.13}$$

The results presented in Table 6.16 show no clear influence of the hardener on the compressive strength of alkali activated materials with a water /binder of 0.25. The material with hardener addition (batch code KA1), cured under 20°C and 65% RH,

shows an increases in compressive strength (16%) when compared with the control material without hardener (batch code A1).

A comparison of materials cured under 20°C and 95% RH (batch code M1 and KM1), on the other hand, shows that the addition of hardener slightly decreases the compressive strength.

Compressive strength of alkali activated materials with hardener addition and water/binder addition of 0.20 (batch code KA2 and KM2) shows a decrease in strength compared with corresponding materials without hardener (batch code A2 and M2). For example, at 1.5% hardener addition the material cured under 20°C and 65% RH (batch code KA2) exhibits a compressive strength 13% lower than the control material without hardener (batch code A2).

6.5.3.2 Modulus of Rupture

A summary of the modulus of rupture results together with the percentage differences in modulus of rupture resulting from addition of water glass hardener, (equation 6.14) are presented in Table 6.17.

Table 6.17 Effect of water glass hardener on modulus of rupture σ_{fm}

Batch Code	Curing conditions	Water/ Binder	Hardener [%]	Modulus of Rupture σ_{fm} [N/mm^2]	Difference in σ_{fm}
A1	20°C and 65% RH	0.25	0	3.6	
KA1	20°C and 65% RH	0.25	1.5	3.8	-5%
M1	20°C and 95% RH	0.25	0	3.1	
KM1	20°C and 95% RH	0.25	1.5	4.3	-39%
A2	20°C and 65% RH	0.20	0	5.6	
KA2	20°C and 65% RH	0.20	1.5	4.5	19%
M2	20°C and 95% RH	0.20	0	5.7	
KM2	20°C and 95% RH	0.20	1.5	4.5	20%

$$Difference\ in\ \sigma_{fm} = \frac{\sigma_{fm}\ (0\%hardener) - \sigma_{fm}\ (1.5\%hardener)}{\sigma_{fm}\ (0\%hardener)} \qquad \text{Equation 6.14}$$

Materials with hardener addition and water/binder of 0.20 (batch code KA2 and KM2) show a decrease in the modulus of rupture compared with corresponding materials without hardener (batch code A2 and M2). For example, at 1.5% hardener addition the material cured under 20°C and 65% RH (batch code KA2) exhibits a modulus of rupture 19% lower than the control material without hardener (batch code A2).

Materials with hardener addition and a water/binder of 0.25 (batch code KA1 and KM1), on the other hand, show opposite trends to those with water/binder of 0.20 as they exhibit higher modulus of rupture compared with corresponding materials without hardener (A1 and M1). For example, at 1.5% hardener addition the material cured under 20°C and 95% RH (batch code KM1) shows a modulus of rupture 39% higher than the control material without hardener (batch code M1).

6.5.3.3 Dynamic modulus of elasticity

A summary of the dynamic modulus of elasticity results together with the percentage differences in dynamic modulus of elasticity resulting from addition of water glass hardener, (equation 6.14) are presented in Table 6.18.

Table 6.18 Effect of water glass hardener on dynamic modulus of elasticity E_D

Batch Code	Curing conditions	Water/ Binder	Hardener [%]	E_D [kN/mm^2]	Difference in E_D
A1	20°C and 65% RH	0.25	0	17.2	
KA1	20°C and 65% RH	0.25	1.5	19.6	-14%
M1	20°C and 95% RH	0.25	0	16.0	
KM1	20°C and 95% RH	0.25	1.5	20.0	-25%
A2	20°C and 65% RH	0.20	0	27.7	
KA2	20°C and 65% RH	0.20	1.5	23.3	16%
M2	20°C and 95% RH	0.20	0	21.8	
KM2	20°C and 95% RH	0.20	1.5	20.9	4%

$$Difference\ in\ E_D = \frac{E_D\ (0\%hardener) - E_D\ (1.5\%hardener)}{E_D\ (0\%hardener)} \qquad \text{Equation 6.14}$$

The results follow the same trend as those for modulus of rupture, for both water/ binder ratios (0.20 and 0.25). These results will be discussed further in section 6.5.5. Materials with hardener addition and water/binder addition of 0.20 (batch code KA2 and KM2) show a decrease in the dynamic modulus of elasticity compared with corresponding materials without hardener (batch code A2 and M2). For example, at 1.5% hardener addition the material cured under 20°C and 65% RH (batch code KA2) exhibits a dynamic modulus of elasticity 16% lower than the control material without hardener (batch code A2).

Materials with hardener and a water/binder of 0.25 (batch code KA1 and KM1), on the other hand, show opposite trends to those with water/binder of 0.20 as they exhibit higher dynamic modulus of elasticity compared with corresponding materials without hardener (A1 and M1). For example, at 1.5% hardener addition the material cured under 20°C and 95% RH (batch code KM1) shows a dynamic modulus of elasticity 25% higher than the control material without hardener (batch code M1).

6.5.4 Effect of thermal curing on mechanical properties of alkali activated materials

6.5.4.1 Compressive Strength

A summary of the compressive strength is presented in Table 6.19. At water/binder of 0.25, thermally cured material (batch code H1) exhibits a modulus of rupture 46% higher than the material cured under 20°C and 65% RH (batch code A1).
Thermally cured material with a water/binder of 0.20 (batch code H2), on the other hand, shows the opposite trends with the compressive strength of the thermally cured material (batch code H2) decreasing by 9% relative to the curing at 20°C and 65% RH (batch code A2). These results will be discussed further in section 6.5.4.5.

Table 6.19 Effect of thermal curing on compressive strength σ_{cm}

Batch Code	Curing conditions	Water/Binder	Compressive strength σ_{cm} [N/mm^2]	Difference in σ_{cm}
A1	20°C and 65% RH	0.25	55.0	
H1	thermal treatment	0.25	80.3	-46%
A2	20°C and 65% RH	0.20	103.7	
H2	thermal treatment	0.20	94.2	9%

$$Difference\ in\ \sigma_{cm} = \frac{\sigma_{cm}\ (20^{\circ}C\ and\ 65\%RH) - \sigma_{cm}\ (thermal\ treatment)}{\sigma_{cm}\ (20^{\circ}C\ and\ 65\%RH)} \qquad \text{Equation 6.15}$$

6.5.4.2 Modulus of Rupture

A summary of the modulus of rupture are presented in Table 6.20. Thermal curing has a great effect on the modulus of rupture of alkali activated materials. The materials exhibit higher modulus of rupture when thermally cured compared with corresponding materials cured under 20°C and 65% RH, for both water /binder ratios (0.20 and 0.25). For example, at water/binder of 0.25, the thermally treated material (batch code H1) exhibits a modulus of rupture 156% higher than the material cured under 20°C and 65% RH (batch code A1). These results will be discussed further in section 6.5.4.5.

Table 6.20 Effect of thermal curing on modulus of rupture

Batch Code	Curing conditions	Water/Binder	Modulus of Rupture σ_{fm} [N/mm^2]	Difference in 'σ_{fm}'
A1	20°C and 65% RH	0.25	3.6	-
H1	thermal treatment	0.25	9.9	-156
A2	20°C and 65% RH	0.20	5.6	-
H2	thermal treatment	0.20	10.1	-87

$$Difference\ in\ '\sigma_{fm}' = \frac{\sigma_{cm}\ (20^{\circ}C\ and\ 65\%RH) - \sigma_{fm}\ (thermal\ treatment)}{\sigma_{fm}\ (20^{\circ}C\ and\ 65\%RH)} \qquad \text{Equation 6.16}$$

6.5.4.3 Tensile splitting strength

A summary of the tensile splitting strength results is presented in Table 6.21. Thermally cured materials do not show any significant differences in their tensile splitting strength compared with corresponding materials subjected to curing under 20°C and 65% RH. For example, at water/binder of 0.25, thermal treated material (batch code H1) exhibits a tensile splitting strength only 2% higher than corresponding material cured under 20°C and 65% RH (batch code A1).

Table 6.21 Effect of thermal curing on tensile splitting strength σ_{tm}

Batch Code	Curing Conditions	Water/Binder	Tensile Strength σ_{tm} [N/mm^2]	Difference in σ_{tm}
A1	20°C and 65% RH	0.25	4.9	
H1	thermal treatment	0.25	5.0	-2
A2	20°C and 65% RH	0.20	5.1	
H2	thermal treatment	0.20	5.4	-4

$$Difference\ in\ \sigma_{tm} = \frac{\sigma_{tm}\ (20°C\ and\ 65\%RH) - \sigma_{tm}\ (thermal\ treatment)}{\sigma_{tm}\ (20°C\ and\ 65\%RH)} \qquad \text{Equation 6.17}$$

6.5.4.4 Dynamic modulus of elasticity

A summary of the dynamic modulus of elasticity results is presented in Table 6.22. The results follow the same trends as those for compressive strength results. The materials with a water/binder of 0.25 exhibit higher dynamic modulus under thermal curing compared with the materials cured at 20°C and 65% RH. For example, at a water/binder of 0.25, the thermal cured material (batch code H1) exhibits a dynamic modulus of elasticity 57% higher than the material cured under 20°C and 65% RH (batch code A1)

Materials with a water/binder ratio of 0.20 (batch code H2) show a small difference in the dynamic modulus of 6% compared with the material cured at 20°C and 65% RH (batch code A2).

Table 6.22 Dynamic modulus of elasticity of alkali activated materials

Batch Code	Curing conditions	Water/Binder	E_D [kN/mm^2]	Difference in E_D
A1	20°C and 65% RH	0.25	17.2	
H1	thermal treatment	0.25	27.0	57%
A2	20°C and 65% RH	0.20	27.7	
H2	thermal treatment	0.20	29.4	6%

$$Difference\ in\ E_D = \frac{E_D\ (20^\circ C\ and\ 65\%RH) - E_D\ (thermal\ treatment)}{E_D\ (20^\circ C\ and\ 65\%RH)} \qquad \text{Equation 6.18}$$

6.5.4.5 Discussion

Research on the effect of curing conditions on Portland cement mortar and concrete has found that a higher temperature during and following the initial contact between cement and water reduces the length of the dormant period so that the overall structure of the hydrated cement paste becomes established very early[81]. This will increase the early age strength, while it may adversely affect the strength after 7 days. The explanation is that a rapid initial hydration forms products of a poorer physical structure probably more porous, so that a proportion of the pores will always remain unfilled by the products of hydration under continuous long term hydration. It follows from the gel/space rule[81] that this will lead to lower strength compared with a less porous material at early age through slowly hydrating cement paste in which a high gel/space ratio will eventually be reached.

Research on the influence of curing temperature on concrete suggests that a rapid initial rate of hydration retards the subsequent hydration and produces a non-uniform distribution of the hydration products within the paste[151]. When the initial rate of hydration is too high (due to high temperature of curing) there is insufficient time for the diffusion of the products of hydration away from the cement particles and for their uniform precipitation in the interstitial spaces, as is the case at ambient temperatures. As a result, a high concentration of the products of hydration is built up in the vicinity of the hydrating particles and this retards the subsequent hydration

and adversely affects the long-term strength. In addition, the non-uniform distribution of the products of hydration adversely affects strength because the gel/space ratio in the interstitial space is lower than would otherwise be the case under uniform hydration.

The above findings from Portland cement mortar and concrete are opposite to the findings from the present investigation which shows that the 28 day compressive strength and modulus of rupture values of alkali activated materials cured under 20°C and 65%RH is lower than those of thermally cured materials. The porosity of materials cured at 20°C and 65% RH is lower than that of thermally cured materials, see section 7.5.6, Chapter 7. The average pore diameter, on the other hand, shows opposite trends as the material cured at 20°C had an average pore diameter much higher that that of corresponding thermally cured material (see section 7.5.6, Chapter 7).

6.5.5 Further discussion

Other researchers such as Andersson[23] and Malolepszy[10] have investigated the mechanical properties of alkali activated materials. Anderson et al used a 1:3 (binder to sand ratio) for the alkali activated mortar. Test specimens used were prisms with dimensions of 40x40x160 mm. Ground granulated blast furnace slag with a chemical composition given in Table 6.23 and fine sand with particle size between 0-2mm were used as binder and filler, respectively[23]. The alkali activator was sodium silicate solution with a silica modulus, n, of 3.35. NaOH was added to the water glass to change the silica modulus from 3.35 to 0.9 and 1.8. The alkali activator was added as a percentage of the ground granulated slag weight. The water/ binder ratio was recalculated by the author to include the proportion of solids and water from the activator in the binder and water phases. The water/ binder ratios varied as listed in Table 6.24[23].

Table 6.23 Chemical composition of the slag[23]

Elements	Content [%]
Silica (SiO_2)	35
Aluminia (Al_2O_3)	10
Iron oxide (FeO)	0.5
Magnesia (MgO)	12
Calcium oxide (CaO)	38
Sulphide (S^{2-})	1.2
Potassium oxide (K_2O)	0.8
$Na_2O_e = 0.658K_2O+Na_2O$	0.526
Manganese (MnO)	0.8
Mb/Ma	**1.11/1.68**
$\frac{CaO + MgO + Al_2O_3}{SiO_2}$	**1.714**

Note: Ma and Mb are the acidity ratio and the basicity ratio respectively and K is the coefficient of quality (detailed in section 2.3, Chapter 2)

M_b = (CaO [%] + MgO [%])/(Al2O3 [%] + SiO2 [%]) Equation 2.2

M_a= (CaO [%] + MgO [%]+Al2O3 [%])/(MnO [%]+ SiO2 [%]) Equation 2.3

K= (CaO [%] + MgO [%] + Al_2O_3 [%])/ (SiO_2 [%]) Equation 2.4

The specimens were cured under two different conditions.

1. 20°C, 80% relative humidity;
2. steam curing for8 hours with a maximum temperature of 80°C then stored at 20°C, 80% RH.

Table 6.24 shows the compressive strength, modulus of rupture and dynamic modulus of elasticity of the alkali activated mortars obtained by Andersson[23]. The compressive strength determined by Andersson[23] was in the range 14 to 48.1 N/mm^2 for air cured specimens which is much lower than 55.02 to 103.74 N/mm^2 found in the current investigation. Andersson[23] found the modulus of rupture to be in the range 3.1 to 8 N/mm^2 for air cured specimens (see Table 6.24) compared with 3.63 to 5.62 N/mm^2 determined in the current investigation.

Table 6.24 Strength of alkali activated slag mortars and reference PC mortar[23]

				Air curing (20°C and 80%RH)			Steam curing		
Activator Type	**Activator [%]of the slag weight**	**W/B**	**Slag Fineness Blaine [m^2/Kg]**	**28 days Compressive Strength**	**28 days Modulus of Rupture**	**28 days E_D [kN/mm^2]**	**28 days Compressive Strength**	**28 days Modulus of Rupture**	**28 days E_D [kN/mm^2]**
WG, n=3.35	4.0	0.45	530	14.5	3.5	16	6.6	2.2	10
WG, n=3.35	6.0	0.40	530	14.5	4.1	16	37.3	4.1	15
WG, n=3.35	6.0	0.46	530	14.6	3.4	13	45.2	5.2	17
WG, n=3.35	8.0	0.47	530	14	3.6	12	62.4	6.6	21
WG, n=1.80	4.0	0.44	530	40.8	7.7	27	36.5	6.1	23
WG, n=1.80	6.0	0.39	530	19.6	3.1	14	46.9	5.4	25
WG, n=1.80	6.0	0.45	530	40.4	5.9	24	53.6	7.1	29
WG, n=1.80	8.0	0.46	530	48.1	6.6	28	58.8	7.2	29
WG, n=0.90	4.0	0.44	530	41.8	6.8	24	24.1	4.4	30
WG, n=0.90	6.0	0.39	530	45.6	7.8	29	49.5	8.7	24
WG, n=0.90	6.0	0.45	350	29.2	4.9	17	30.5	4.9	18
WG, n=0.90	6.0	0.45	530	55.2	7.5	33	41.5	6.7	24
WG, n=0.90	6.0	0.45	670	50.4	8.8	29	38.1	6.4	24
WG, n=0.90	8.0	0.46	670	55.5	7.6	33	57.1	8.6	30
WG, n=0.90	11.0	0.49	530	47.9	8	30	59.1	8.3	31
PC		0.50	530	39.6	6.2	32	32	5.3	32

Note: PC represents reference ordinary Portland cement mortar (1:3 sand to cement ratio)

WG water glass

E_D dynamic modulus of elasticity

The test specimens used by Malolepszy[10] were prisms of dimensions 25x25x120mm. The binder was ground granulated blast furnace slag and the fine sand was of particle size distribution between 0-2mm. Three types of ground granulated slag were used. Their chemical composition is given in Table 6.25. The coefficient of quality (K) as well as basicity and acidity ratio (Mb and Ma) are shown in Table 6.25. The alkali activator was sodium silicate solution with a silica modulus, n, of 1. The mix proportions of the alkali activated mortar used by Malolepszy were 1:3 binder to sand ratio with the exception of specimens i and v which had a ratio of 1:3.86. The alkali activator dosage was 15% of the ground granulated slag weight. The water/ binder ratio was 0.42 for the alkali activated slag mortars and 0.5 for the reference Portland cement mortar.

Two conditions were applied for the first **24 hours of curing**:

1. 20°C and 95% relative humidity;
2. thermal treatment following the cycle 2-2-4-2 hours (total 10 hours), attaining a maximum temperature of 85°C. The temperature was kept constant at 20°C for 2 hours after casting, then progressively increased to 85°C in 2 hours and held at 85°C for a further 4 hours. Finally the temperature was gradually reduced to 20°C in 2 hours.

After 24 hours of initial curing in the mould as outlined above, the mortar bars were immersed in water at 20°C for 24 hours. Then the specimens were subjected to alternative cycles of storage in water and air (20°C and 65% RH) as shown in Table 6.26. The control samples where cured in water for the period 2-28 days.

The compressive strength[10] was between 51.1 and 82.2 N /mm^2 for the variable curing regime, see Table 6.27. The corresponding values for the water curing specimens[10] were 42.2 to 56.5 N/mm^2, similar to 54.4 N/mm^2 found in the current investigation, see Table 6.27. The modulus of rupture[10] was between 6.3 and 10.7 N/mm^2 for the variable curing regime shown in Table 6.26. The corresponding values for the water cured specimens were 8.2 to 10.4 N/mm^2, which are higher than 4.0 N/mm^2 found in the current investigation, see Table 6.27.

Table 6.25 Chemical composition of the slag[10]

Elements	Slag 1 [%]	Slag 2 [%]	Slag 3 [%]
Silica (SiO_2)	38.4	34.7	34.9
Aluminia (Al_2O_3)	7.3	10.0	10.1
Iron oxide (FeO)	1.4	0.37	0.32
Magnesia (MgO)	6.7	12.2	12.3
Calcium oxide (CaO)	42.5	37.4	37.4
Sulphide (S^{2-})	2.7	1.19	1.19
Manganese (MnO)	0.7	1.05	1.05
Glassy content	78.9	98.6	98.2
Mb/Ma	1.08/1.45	1.11/1.67	1.10/1.66
Specific surface area [m^2/kg]	360	350	500
$\frac{CaO + MgO + Al_2O_3}{SiO_2}$	1.471	1.718	1.713

Note: Ma and Mb are the acidity ratio and the basicity ratio respectively and K is the coefficient of quality

Table 6.26 Curing conditions[10]

Age	Curing Conditions
2 to 7 days	water at 20°C
7 to 14 days	air at 20°C and 65% RH
14 to 21 days	water at 20°C
21 to 28 days	air at 20°C and 65% RH

Table 6.27 Strength of alkali activated slag mortars and reference Portland cement mortar[10]

No.	Mb/Ma	Initial 24 h curing	28 days Modulus of Rupture	28 days Modulus of Rupture (control*)	28 days Compressive Strength	28 days Compressive Strength (control*)
i	1.08/1.45	thermal treatment	6.3	10.7	51.1	42.2
ii	1.08/1.45	20°C and 95%RH	10.7	11.8	64.1	53.4
iii	1.11/1.67	thermal treatment	10.3	11.5	59.8	49.5
iv	1.11/1.67	20°C and 95%RH	9.0	11.2	64.7	56.5
v	1.10/1.66	20°C and 95%RH	7.7	10.4	82.2	56.4
vi	1.10/1.66	20°C and 95%RH	7.8	8.2	56.6	42.7
PC		20°C and 95%RH	6.6	7.7	23.8	35.6

Note:

PC represents reference ordinary Portland cement mortar (1:3 cement to sand ratio)

Ma and Mb are the acidity ratio and the basicity ratio respectively

*cured in water during the period 2-28 days.

The measured strength of a specimen of concrete decreases with an increase in its size, and so does the variability in strength of geometrically similar specimens[81]. The influence of size on strength depends on the standard deviation of strength, therefore, the size effect decreases with increasing homogeneity of concrete. The use of larger specimens significantly reduces the size effect on mechanical properties. The cross sectional area of the compression test specimens used in this investigation was 5625 mm^2 (75mmx75mm). This is much higher than those used by Malolepszy[10], 625 mm^2 (25mmx25mm) or Andersson[23], 1600 mm^2 (40mmx40mm). Therefore, the accuracy of the results from present study is higher then those obtained by other researchers[10, 23]. A direct comparison of the results of different investigators is also not possible due to the use of different specimen sizes.

6.5.6 Compressive strength of fibre reinforced alkali activated materials

6.5.6.1 Materials cured at 20°C, 65%RH

The compressive strength of the glass and steel fibre reinforced alkali activated materials cured under 20°C and 65% relative humidity, condition (i), are presented in Table 6.28. All mixes had a water/binder of 0.25. A detailed description of the mixes is given in section 6.3.3.

Table 6.28 Compressive strength of fibre reinforced alkali activated materials σ_{cc} .

Batch Code	Fibre type	V_f [%]	V_f l/d	Compressive Strength σ_{cc} [N/mm^2]	% increase in σ_{cc}
A1 (control)	-	0	0	55.0	-
GA1	alkali resistant glass fibres (CEM-FIL 62/2)	1.5	1.06	59.5	8%
GA2	alkali resistant glass fibres (CEM-FIL 62/2)	3.0	2.12	58.9	7%
SwA1	stainless steel straight fibres	1.5	0.70	56.6	3%
SA1.	melt extract fibres	1.5	0.36	57.6	5%
SA2	melt extract fibres	3.0	0.72	58.4	6%

The results in Table 6.28 show that fibre reinforcement does not have a great effect on the compressive strength of alkali activated materials cured at 20°C and 65% RH. For example, the compressive strength of materials with 1.5% and 3% volume of glass fibre (batch code GA1 and GA2, respectively) was only 8% and 7% higher, respectively, than the control mix. Similarly, the compressive strength for steel fibre reinforced materials with a fibre volume of 1.5% and 3% (batch code SA1 and SA2, respectively) was 5% and 6% higher than the control matrix, respectively. These results will be discussed further in section 6.5.6.3.

6.5.6.2 Thermally cured materials

The compressive strength of the glass and steel fibre reinforced alkali activated materials cured thermally, condition (iv), are presented in Table 6.29. All mixes had a water/binder of 0.25. A detailed description of the mixes is given in section 6.3.3.

Table 6.29 Compressive strength of reinforced alkali activated materials σ_{cc}.

Batch Code	Fibre type	V_f [%]	V_f l/d	Compressive Strength σ_{cc} [N/mm^2]	% increase in σ_{cc}
H1 (control)	-	0	0	80.3	
GH1	alkali resistant glass fibres (CEM-FIL 62/2)	1.5	1.06	68.5	-15%
GH2	alkali resistant glass fibres (CEM-FIL 62/2)	3.0	2.12	62.1	-23%
SH1	melt extract fibres	1.5	0.70	75.3	-6%
SH2	melt extract fibres	3.0	0.36	77.2	-4%

Thermally cured glass fibre reinforced alkali activated materials (batch code GH1 and GH2) exhibit a reduction in the compressive strength compared with the corresponding control material (batch code H1). For example the compressive strength of materials with 1.5% and 3% volume of glass fibre (batch code GH1 and GH2) was 15% and 23% lower, respectively, than the control matrix.

6.5.6.3 Discussion

Figure 6.4 shows the relationship between σ_{cc}/σ_{cm} and fibre V_f l/d ratio for fibre reinforced alkali activated materials. σ_{cc} is the cube strength of the fibre reinforced composites and σ_{cm} is the strength of the control unreiforced matrix. The fibre V_f l/d ratio does not influence the compressive strength of fibre reinforced materials for both curing conditions, 20°C, 65% RH and thermal curing.

Materials reinforced with glass fibres and thermally cured maintain a constant σ_{cc}/σ_{cm} of 0.75 with varying V_f l/d. The remaining materials, steel and glass fibre reinforced cured under 20°C, 65% RH and steel fibre reinforced thermally cured maintain a constant σ_{cc}/σ_{cm} of unity with varying V_f l/d.

Under a compressive load, cracks will not act as stress raisers. Small volumes of fibres added to a mix do not produce a great change in the compressive strength of these materials. A small effect may be observed due to the formation of tensile cracks by the bowing of the surface of the specimen during the application of the compressive load. This allows some load transfer by the fibres, which will have a small effect on the compressive strength. This effect will be more noticeable in specimens with a large height/base ratio since these specimens tend to exhibit a more pronounced bowing during testing. In the present investigation the specimens used were 75 mm cubes and the effect of bowing was negligible. Consequently the effect of fibres on compressive strength was small.

Other researchers[152] have investigated the influence of W l/d (W is the fibre weight fraction) on compressive strength, as shown in Figure 6.5. They concluded that the compressive strength of concrete and mortar increases with the fibre weight ratio. The increase, however, is quite modest and the scatter of the experimental data (Figure 6.5) is high.

Symbol	Batch	Curing	Type of fibres	Volume of fibres
◆	GA1/GA2	20°C and 65% RH	glass fibres	1.5%/3.0%
■	GH1/GH2	thermal treatment	glass fibres	1.5%/3.0%
▲	SA1/SA2	20°C and 65% RH	melt extract fibres	1.5%/3.0%
●	SH1/SH2	thermal treatment	melt extract fibres	1.5%/3.0%

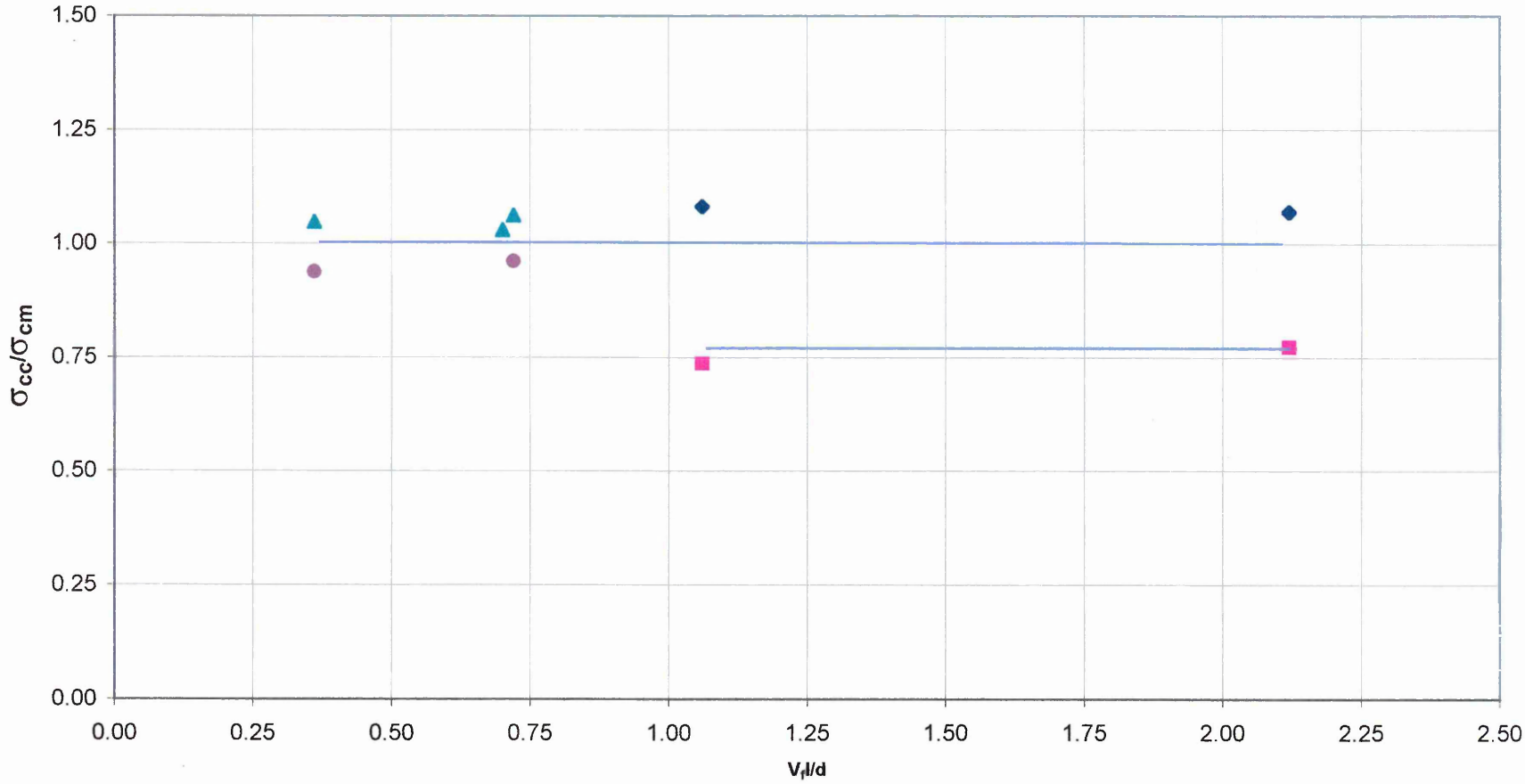

Figure 6.4 Relationship between σ_{cc}/σ_{cm} and fibre $V_f l/d$

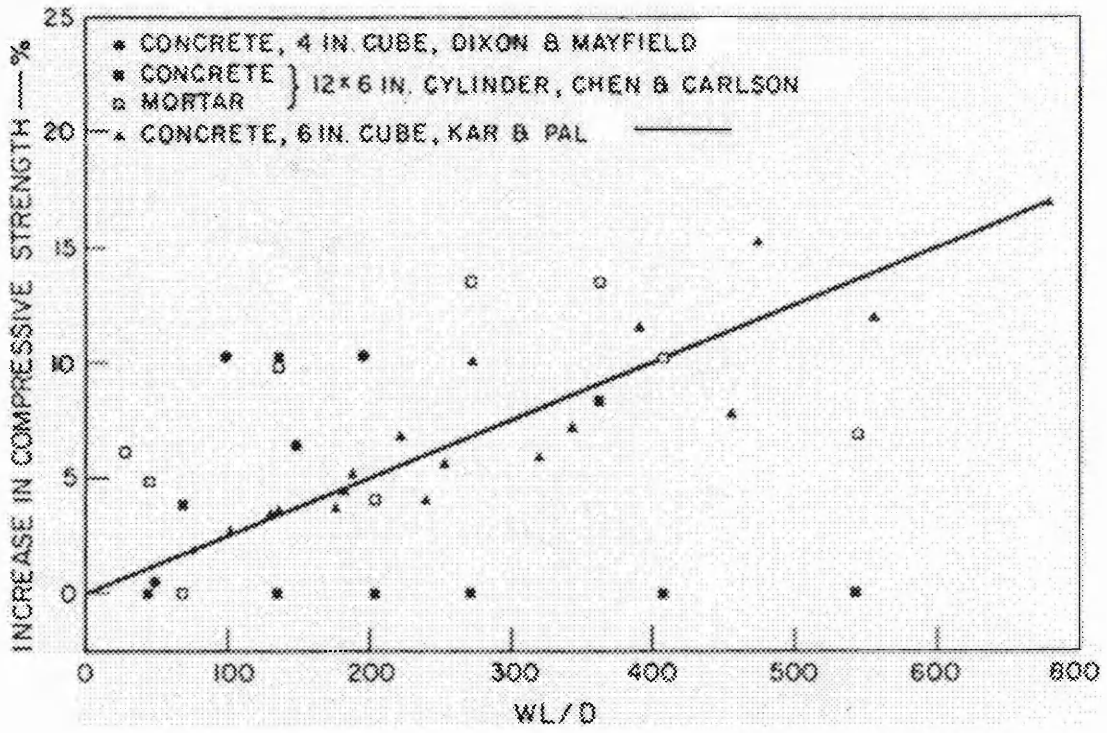

Figure 6.5 Influence of W l/d on compressive strength[152]

There is no available data on the compressive strength of short fibre reinforced alkali activated materials in literature. Researchers[124] investigated the properties of glass fibre reinforced Portland cement mortars. Takaji[124] used a 1/2 proportion mortar and a water/cement ratio of 0.63. High alumina cement and river sand were used. The specimens were cured in water at 21°C. Glass fibres of length 13mm were incorporated at0.25 to 1 percent by weight of the mix. This represents a percentage by volume of 0.12 to 0.49%, see Table 6.30.

Table 6.30 Compressive strength of fibre reinforced high alumina cement mortar[124]

Fibre Content % by weight	Fibre Content % by volume	Compressive Strength [N/mm^2]
0	0	40.8
0.25	0.12	48.5
0.50	0.24	51.9
0.75	0.36	49.6
1.00	0.49	48.4

The compressive strength of the fibre reinforced materials was between 48.35 and 51.88 N/mm^2 compared with 40.8 N/mm^2 for the control unreinforced matrix (Table 6.30). The average increase in the compressive strength of composite materials was 22% of the control matrix[124].

Sustersic et al[123] used oval steel fibres of length approximately 3mm and equivalent diameter 64μm. The binder was Portland cement with 30% ground granulated blast furnace slag replacement and 8mm size aggregates were used. The water/cement ratio was 0.50. The results are presented in Table 6.31 The average increase in compressive strength was 11.78%.

Table 6.31 Compressive Strength relative to control concrete[123]

V_f [%]	Increase in Compressive Strength [%]
1.3	20
2.6	3.57
5.1	-

6.5.7 Modulus of Rupture of fibre reinforced alkali activated materials

6.5.7.1 Materials cured at 20°C and 65%RH

The modulus of rupture of glass and steel fibre reinforced alkali activated materials cured at 20°C and 65% relative humidity is presented in Table 6.32. All mixes had a water/binder of 0.25. A detailed description of the mixes is given in section 6.3.3.

The results in Table 6.32 show that fibre reinforcement provides a considerable strengthening of the matrix. For example, the modulus of rupture of materials with 1.5% and 3% volume of glass fibre (batch code GA1 and GA2, respectively) was 96% and 177% higher, respectively, than the control matrix. Similarly, the modulus of rupture for steel fibre reinforced materials with a fibre volume of 1.5% and 3%

(batch code SA1 and SA2, respectively) was 20% and 74% higher than the control matrix, respectively.

Table 6.32 Modulus of rupture of alkali activated fibre reinforced materials

Batch Code	Fibre type	V_f [%]	V_fl/d	Modulus of Rupture σ_{fc} [N/mm^2]	% increase in σ_f
A1 (control)	-	0	0	3.6	-
GA1	alkali resistant glass fibres (CEM-FIL 62/2)	1.5	1.06	7.1	96
GA2	alkali resistant glass fibres (CEM-FIL 62/2)	3.0	2.12	10.0	177
SwA1	stainless steel straight fibres	1.5	0.70	6.1	68
SA1.	melt extract fibres	1.5	0.36	4.4	20
SA2	melt extract fibres	3.0	0.72	6.3	74

6.5.7.2 Thermally cured materials

The modulus of rupture results of glass and steel fibre reinforced alkali activated materials cured thermally are presented in Table 6.33. All mixes had a water/binder of 0.25.

Table 6.33 Modulus of rupture of alkali activated fibre reinforced materials thermally cured

Batch Code	Fibre type	V_f [%]	V_fl/d	Modulus of Rupture σ_{fc} [N/mm^2]	% increase in σ_{fc}
H1 (control)	-	0	0	9.9	
GH1	alkali resistant glass fibres (CEM-FIL 62/2)	1.5	1.06	10.5	5
GH2	alkali resistant glass fibres (CEM-FIL 62/2)	3.0	2.12	14.3	43
SH1	melt extract fibres	1.5	0.36	7.7	-23
SH2	melt extract fibres	3.0	0.72	11.2	12.5

The results presented in Table 6.33 show that fibre reinforcement is not as effective in increasing the modulus of rupture of thermally cured alkali activated materials as it is for materials cured at 20°C, 65% RH.

6.5.7.3 Discussion

Figure 6.6 presents the relationship between modulus of rupture of fibre reinforced alkali activated materials and fibre V_f l/d ratio. There is a clear trend of modulus of rupture increasing with the increase in V_f l/d for both types of fibres. This was explained by Neville[81], for fibre reinforced mortar and concrete, to be due to additional restraint on the matrix provided by the fibres. The fibres can be considered as additional fine aggregates of special shape which stiffen the cement paste matrix and increase the bond between the fine aggregates and cement paste. Other researchers[152] have concluded that the flexural strength of the fibre reinforced mortar and concrete increases proportionally with fibre concentration as shown in Figure 6.7.

Figure 6.8 shows the relationship between the non-dimensional parameter σ_{fc}/σ_{fm} and fibre V_f l/d ratio for fibre reinforced alkali activated materials. The fibre V_f l/d ratio clearly influences the modulus of rupture of both steel and glass fibre reinforced materials. A regression analysis of data in Figure 6.8 gives the following equations:

- for fibre reinforced alkali activated material cured under 20°C and 65%RH

$\sigma_{fc}/\sigma_{fm}=0.86\ V_f\ l/d + 1.00$

with a coefficient of correlation, $R^2 = 0.97$.

Hence:

$$\sigma_{fc} = \sigma_{fm} + \sigma_{fm}\ 0.86\ V_f\ l/d \qquad \text{Equation 6.19}$$

- for thermally cured fibre reinforced alkali activated material

$\sigma_{fc}/\sigma_{fm}=0.16\ V_f\ l/d + 1.00$

with a coefficient of correlation, $R^2 = 0.60$.

Hence:

$$\sigma_{fc} = \sigma_{fm} + \sigma_{fm}\ 0.16\ V_f\ l/d \qquad \text{Equation 6.20}$$

Where:

σ_{fc} is the modulus of rupture of the fibre reinforced composite,

σ_{fm} is the modulus of rupture of the control unreinforced matrix.

Symbol	Batch	Curing	Type of fibres	Volume of fibres
◆	**A1/GA1/GA2**	20°C and 65% RH	glass fibres	0%/1.5%/3.0%
■	**H1/GH1/GH2**	thermal treatment	glass fibres	0%/1.5%/3.0%
▲	**A1/SA1/SA2**	20°C and 65% RH	melt extract fibres	0%/1.5%/3.0%
●	**H1/SH1/SH2**	thermal treatment	melt extract fibres	0%/1.5%/3.0%

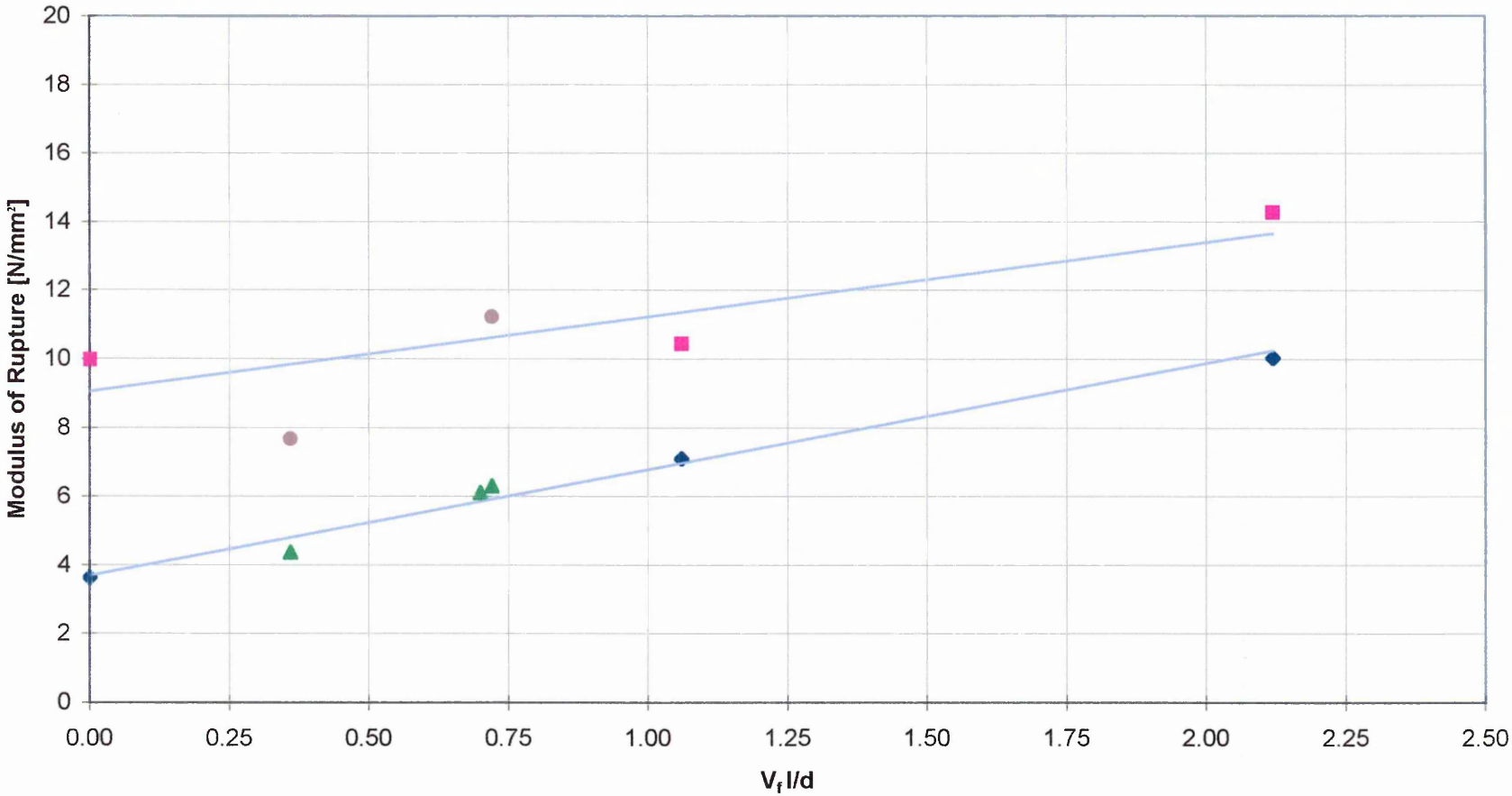

Figure 6.6 Relationship between modulus of rupture and V_f l/d

Thus the modulus of rupture of fibre reinforced alkali activated materials can be obtained using equations (6.19 and 6.20) based on the knowledge of modulus of rupture of the plain matrix and details of fibre reinforcement.

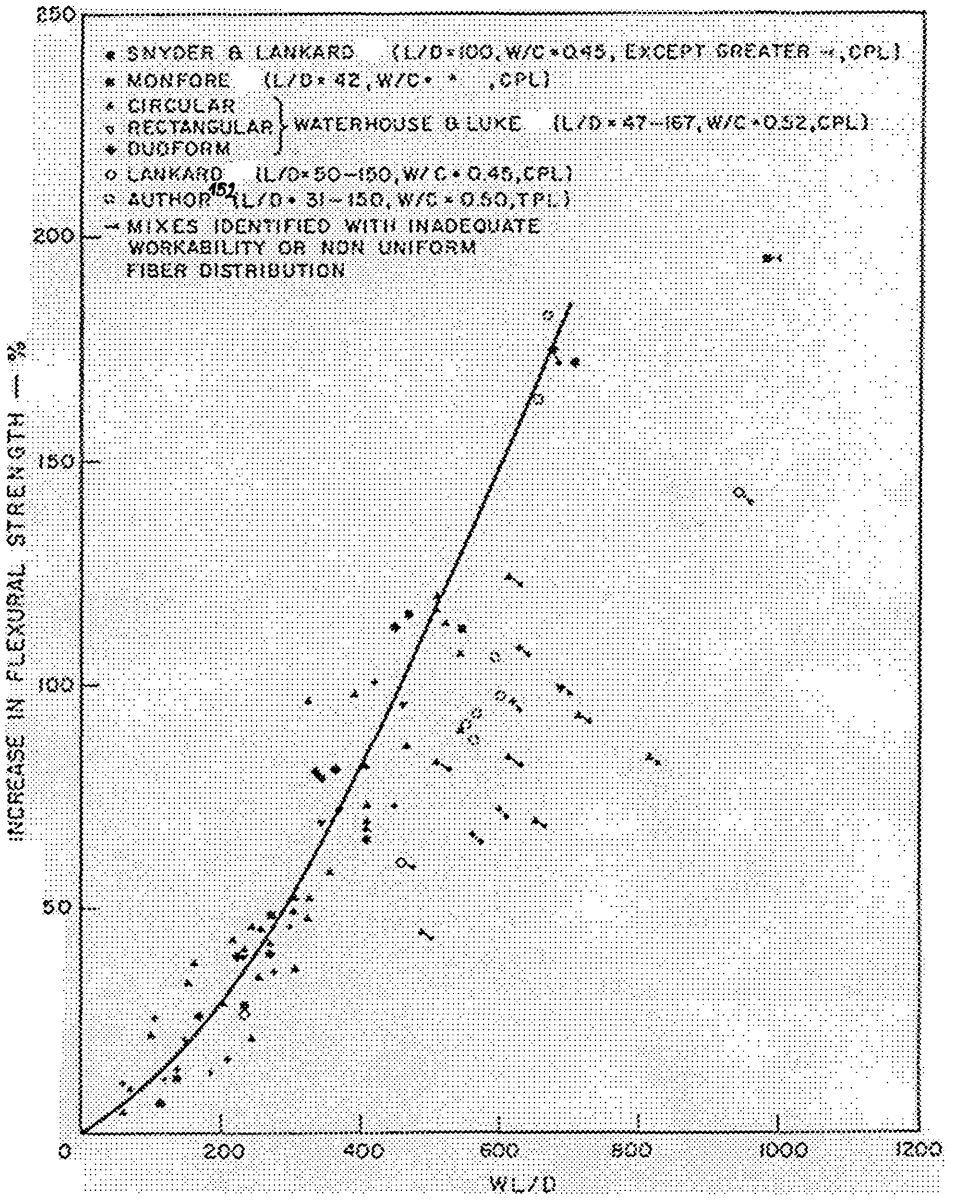

Figure 6.7 Relationship between modulus of rupture and W l/d, W is weight of fibres [% by mass][152]

Symbol	Batch	Curing	Type of fibres	Volume of fibres
◆	GA1/GA2	20°C and 65% RH	glass fibres	1.5%/3.0%
■	GH1/GH2	thermal treatment	glass fibres	1.5%/3.0%
▲	SA1/SA2	20°C and 65% RH	melt extract fibres	1.5%/3.0%
●	SH1/SH2	thermal treatment	melt extract fibres	1.5%/3.0%

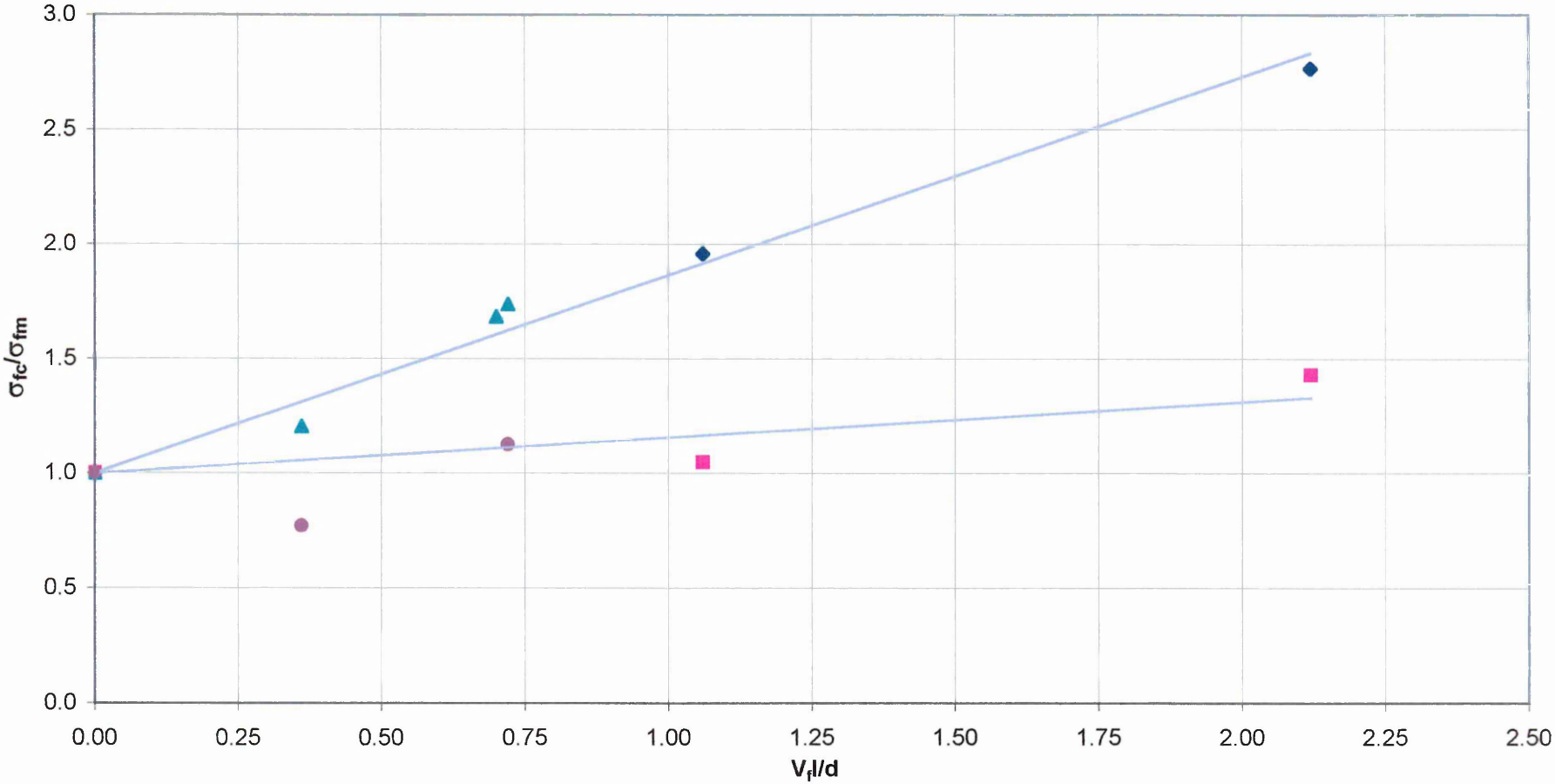

Figure 6.8 Relationship between σ_{fc}/σ_{fm} and fibre V_f l/d

There is no available data in current literature on the modulus of rupture of short fibre reinforced alkali activated materials but other researchers such as Takaji[124], Romualdi and Mandel[118] and Sustersic et al[123] have investigated the properties of glass and steel fibre reinforced Portland cement mortars. These represent some typical examples of a very comprehensive range of research conducted on the flexural properties of fibre (steel and glass) reinforced cement composites carried out by many researchers[118,119, 152,153].

Takaji[124] used a 1/2 proportion mortar and a water/cement ratio of 0.63. High alumina cement and river sand were used. The specimens were cured in water at 21°C. Glass fibres of length 13mm were incorporated at 0.25 to 1 percent by weight of the mix. This represents a percentage by volume of 0.12 to 0.49%, see Table 6.34.

Table 6.34 Modulus of Rupture of high alumina cement mortars reinforced with glass fibre[125]

Fibre length	Fibre Content % by weight	Modulus of rupture [N/mm^2]	% increase in Modulus of rupture
-	0	6.1	
13	0.25	6.2	2%
13	0.50	7.2	18%
13	0.75	6.8	11%
13	1.00	6.3	3%

Romualdi and Mandel[118] have investigated the modulus of rupture of steel fibre reinforced concrete. The fibres used in their investigations and the fibre volume ratios are presented in Table 6.35. The modulus of rupture steel fibre reinforced concrete varied between 4 and 9.1 N/mm^2, see Table 6.35, compared with 4.37 to 11.22 N/mm^2 for steel fibre reinforced alkali activated materials of the present investigations.

Sustersic et al[123] used oval steel fibres. The fibres were of length approximately 3mm and equivalent diameter 64μm. The binder used was Portland cement with 30% ground granulated blast furnace slag replacement and the maximum aggregates size was 8mm. The water/cement ratio was 0.50. The modulus of rupture results obtained in their investigations are presented in Table 6.36.

Table 6.35 Specimen size and flexural strength results of steel fibre reinforced concrete[118]

Specimen length [mm]	Specimen depth [mm]	Specimen width [mm]	Fibre diam [mm]	Fibre length [mm]	V_f (%)	V l/d	Modulus of rupture [N/mm^2]	% increase in Modulus of rupture
965.2	76.2	44.5	-	-	-	-	4.0	-
965.2	76.2	44.5	0.152	25.4	2.1	3.509	7.0	75%
965.2	76.2	44.5	0.787	19.1	2.1	0.510	4.0	0%
965.2	76.2	44.5	0.787	25.4	3.75	1.210	5.85	46%
965.2	76.2	44.5	0.787	25.4	2.1	0.678	5.6	40%
965.2	76.2	44.5	0.787	38.1	2.1	1.017	6.7	68%
965.2	76.2	50.8	-	-	-	-	2.5	-
965.2	76.2	50.8	0.177	15.7	4.3	3.814	9.1	264%
965.2	76.2	50.8	1.27	50.8	2.1	0.840	4.9	96%
965.2	76.2	50.8	1.27	50.8	1.2	0.480	5.15	106%

Table 6.36 Modulus of rupture results[123]

V_f [%]	% increase in modulus of rupture
1.3	28.57
2.6	24.28
5.1	13.57

6.5.7.4 A theoretical expression for composite flexural strength

Swamy and Mangat[153] developed a model for the flexural strength of concrete reinforced with randomly orientated and uniformly dispersed steel fibres of length, l, and diameter, d, in a cement base matrix. For the condition of strain compatibility in fibres and matrix, the tensile strength of a composite, σ_c, containing uniaxial continuous fibres can be expressed by the law of mixtures[153] as:

$$\sigma_{fc} = \sigma_{fm} V_m + \sigma_f V_f \qquad \text{Equation 6.21}$$

The average tensile stress in the fibre is :

$$\sigma_{fc} = 2 \cdot \tau \cdot \frac{l}{d} \qquad \text{Equation 6.22}$$

Where:

σ_{fc} is the composite modulus of rupture

σ_{fm} is the cement matrix modulus of rupture

τ is the fibre-matrix interfacial bond strength

V_m is the matrix volume

V_f is the volume of fibres

The effective length of N number of fibres in the direction of uniaxial stress is $0.41N \cdot l$.

Therefore, the effective volume of fibres in the direction of stress is :

$$V_{fe} = \frac{\pi \cdot d^2}{4} \cdot 0.41N \cdot l \qquad \text{Equation 6.23}$$

The total volume of fibres is :

$$V_f = \frac{\pi \cdot d^2}{4} \cdot N \cdot l$$

$$\therefore V_{fe} = 0.41 \cdot V_f \qquad \text{Equation 6.24}$$

Substituting equations 6.22 and 6.24 in equation 6.21 and introducing empirical coefficient A from experimental data[153] gives the following expression for flexural strength of a composite material containing randomly orientated fibres which fail by pull-out:

$$\sigma_{fc} = A \cdot \sigma_{fm}(1 - V_f) + 0.82 \cdot \tau \cdot V_f \cdot \frac{l}{d}$$ Equation 6.25

Dividing equation 6.25 by V_f l/d gives:

$$\frac{\sigma_{fc}}{V_f \cdot \frac{l}{d}} = \frac{A \cdot \sigma_{fm}(1 - V_f)}{V_f \cdot \frac{l}{d}} + 0.82 \cdot \tau$$ Equation 6.26

Figure 6.9 shows the relationship between $\sigma_{fc}/(V_f\, l/d)$ and $\sigma_{fm}(1\text{-}V_f)/(V_f\, l/d)$ for glass fibre reinforced alkali activated materials. The corresponding for steel fibre reinforced alkali activated materials is presented in Figure 6.10. The results presented in Figures 6.9 and 6.10 show a consistent pattern for the modulus of rupture of the fibre reinforced alkali activated materials. The equations to the best fit lines obtained by regression analysis of data shown in Figure 6.9 and 6.10 are:

- For glass fibre reinforced alkali activate materials

$$\frac{\sigma_{fc}}{V_f \cdot \frac{l}{d}} = 0.639 \cdot \frac{\sigma_{fm}(1 - V_f)}{V_f \cdot \frac{l}{d}} + 4.001$$

Rearrangin g the above equation gives :

$$\sigma_{fc} = 0.639\sigma_{fm}(1 - V_f) + 4.001 \cdot V_f \cdot \frac{l}{d}$$ Equation 6.27

Comparing equation 6.27 with 6.25 gives the ultimate fibre-matrix bond strength for glass fibres:

$0.82 \cdot \tau = 4.001$

$\tau = 4.88\ \text{N/mm}^2$

- For steel fibre reinforced alkali activated materials

$$\frac{\sigma_{fc}}{V_f \cdot \frac{l}{d}} = 0.569 \cdot \frac{\sigma_{fm}(1 - V_f)}{V_f \cdot \frac{l}{d}} + 6.409$$

Hence,

$$\sigma_{fc} = 0.569\sigma_{fm}(1 - V_f) + 6.409 \cdot V_f \cdot \frac{l}{d}$$ Equation 6.28

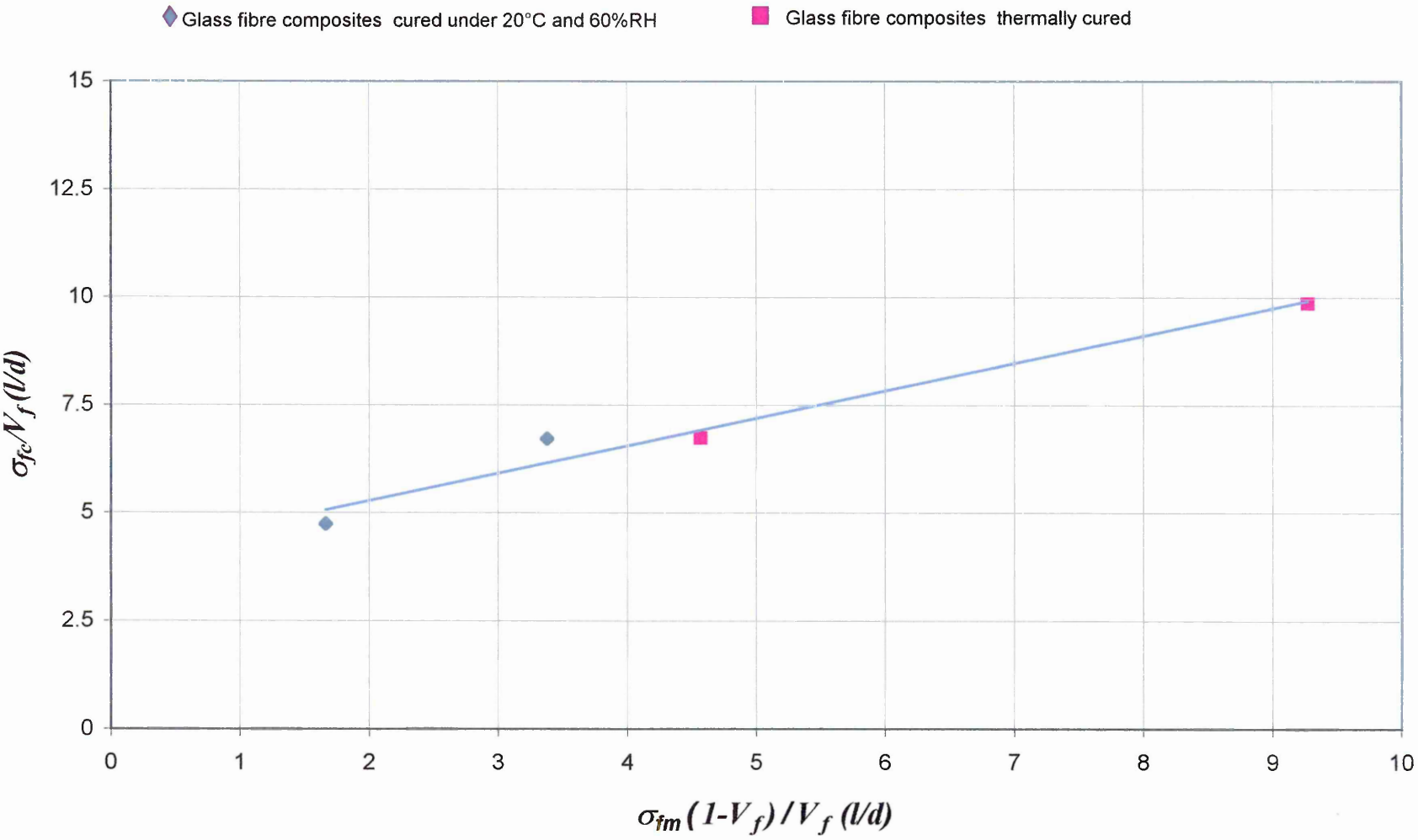

Figure 6.9 Modulus of rupture relationship for glass fibre reinforced alkali activated material

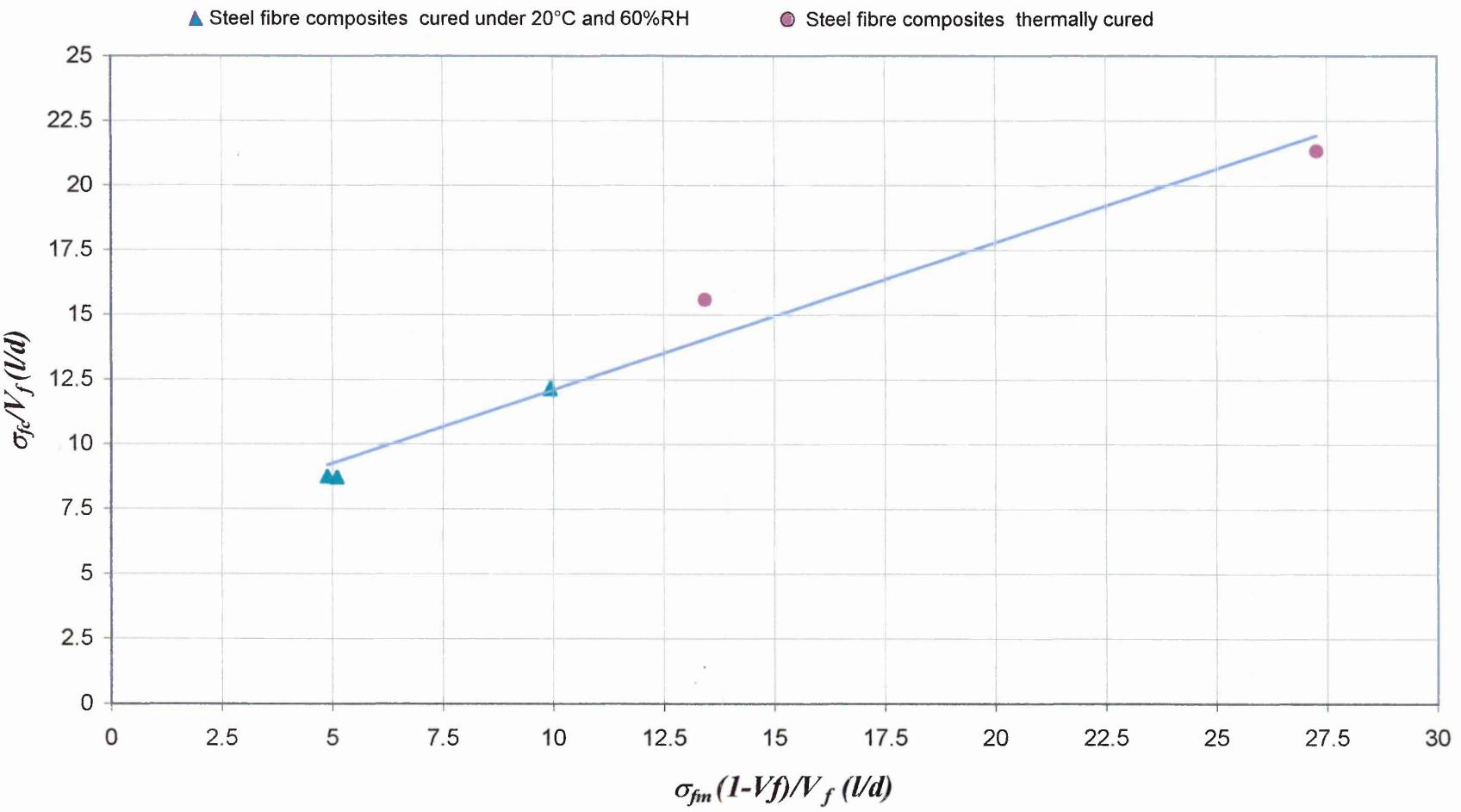

Figure 6.10 Modulus of rupture relationship for steel fibre reinforced alkali activated material

Comparing equation 6.28 with 6.25 gives the ultimate fibre-matrix bond strength for steel fibres:

$0.82 \cdot \tau = 6.409$

$\tau = 7.82\ \text{N/mm}^2$

The corresponding τ value for steel fibre reinforced Portland cement mortar and concrete[153] is 4.15 N/mm^2 which is much lower than the 7.82 N/mm^2 for steel fibre reinforced alkali activated materials.

6.5.8 Tensile splitting strength of fibre reinforced alkali activated materials

6.5.8.1 Materials cured under 20°C and 65%RH

The tensile splitting strength results of the glass and steel fibre reinforced alkali activated materials cured under 20°C and 65% relative humidity are summarised in Table 6.37. All mixes had a water/binder of 0.25.

Table 6.37 Tensile splitting strength of fibre reinforced alkali activated materials

Batch Code	Fibre type	V_f [%]	$V_f l/d$	Tensile Strength σ_{tc} [N/mm^2]	% increase in σ_t
A1 (control)	-	0	0	4.8	-
GA1	alkali resistant glass fibres (CEM-FIL 62/2)	1.5	1.06	4.9	2%
GA2	alkali resistant glass fibres (CEM-FIL 62/2)	3.0	2.12	6.4	33%
SwA1	stainless steel straight fibres	1.5	0.70	4.3	-11%
SA1	melt extract fibres	1.5	0.36	4.8	-1%
SA2	melt extract fibres	3.0	0.72	5.2	8%

The results presented in Table 6.37 show no clear influence of the fibre reinforcements on the tensile splitting strength of alkali activated materials with the exception of material with a glass fibre volume ratio of 3% (batch code GA2) for which the tensile splitting strength is 33% higher than the control material (batch code A1).

6.5.8.2 Thermally cured materials

The tensile splitting strength of the glass and steel fibre reinforced alkali activated materials cured thermally are presented in Table 6.38. All mixes had a water/binder of 0.25.

The results presented in Table 6.38 show that fibre reinforcement provides a restraint to the matrix, which increases with the increasing of fibre volume. For example, the tensile splitting strength of materials with 1.5% and 3% volume of glass fibre (batch code GH1 and GH2, respectively) was 11% and 26% higher, respectively, than the control matrix. Similarly, the tensile splitting strength for steel fibre reinforced materials with a fibre volume of 1.5% and 3% (batch code SH1 and SH2, respectively) was 5% and 40% higher than the control matrix, respectively.

Table 6.38 Tensile splitting strength of fibre reinforced alkali activated materials

Batch Code	Fibre type	V_f [%]	$V_f l/d$	Tensile Strength σ_{tc} [N/mm^2]	% increase in σ_t
H1 (control)	-	0	0	5.0	-
GH1	alkali resistant glass fibres (CEM-FIL 62/2)	1.5	1.06	5.6	11%
GH2	alkali resistant glass fibres (CEM-FIL 62/2)	3.0	2.12	6.3	26%
SH1	melt extract fibres	1.5	0.70	5.3	5%
SH2	melt extract fibres	3.0	0.36	7.1	40%

6.5.8.3 Discussion

Figure 6.11 shows the relationship between tensile splitting strength and fibre $V_f l/d$ ratio. The tensile splitting strength increases with increasing the $V_f l/d$ for both, steel and glass fibres, showing the same trend as the modulus of rupture.

Figure 6.12 shows the relationship between the non-dimensional σ_{tc}/σ_{tm} and fibre V_f l/d ratio for fibre reinforced alkali activated materials. σ_{tm} is the tensile splitting strength of the control unreinforced matrix and σ_{tc} is the tensile splitting strength of the fibre reinforced composite. There is a clear trend of σ_{tc}/σ_{tm} increasing with increasing V_f l/d, for glass and steel fibres, and for both curing conditions.

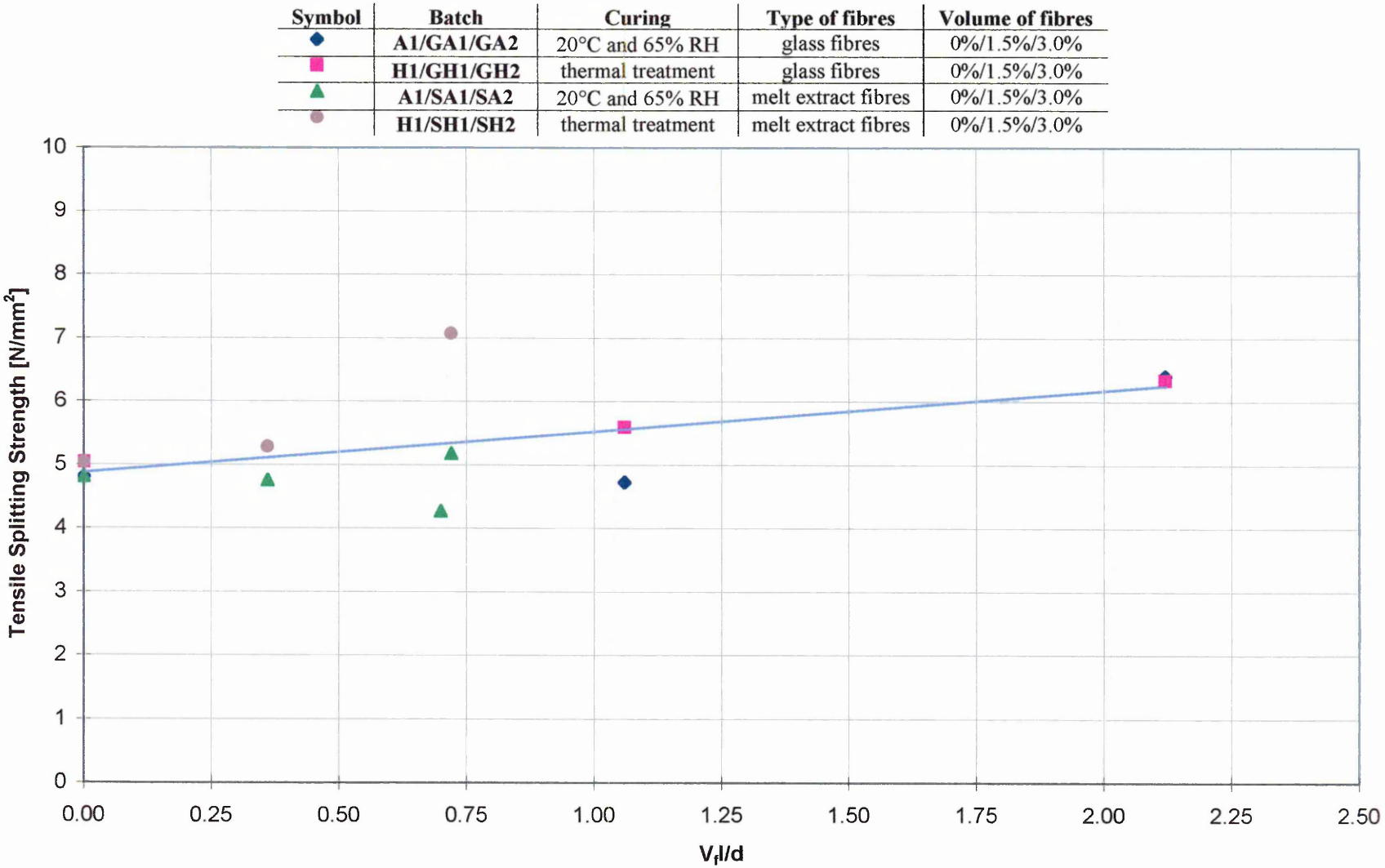

Figure 6.11 Relationship between tensile splitting strength and fibre $V_f l/d$

Symbol	Batch	Curing	Type of fibres	Volume of fibres
◆	GA1/GA2	20°C and 65% RH	glass fibres	1.5%/3.0%
■	GH1/GH2	thermal treatment	glass fibres	1.5%/3.0%
▲	SA1/SA2	20°C and 65% RH	melt extract fibres	1.5%/3.0%
●	SH1/SH2	thermal treatment	melt extract fibres	1.5%/3.0%

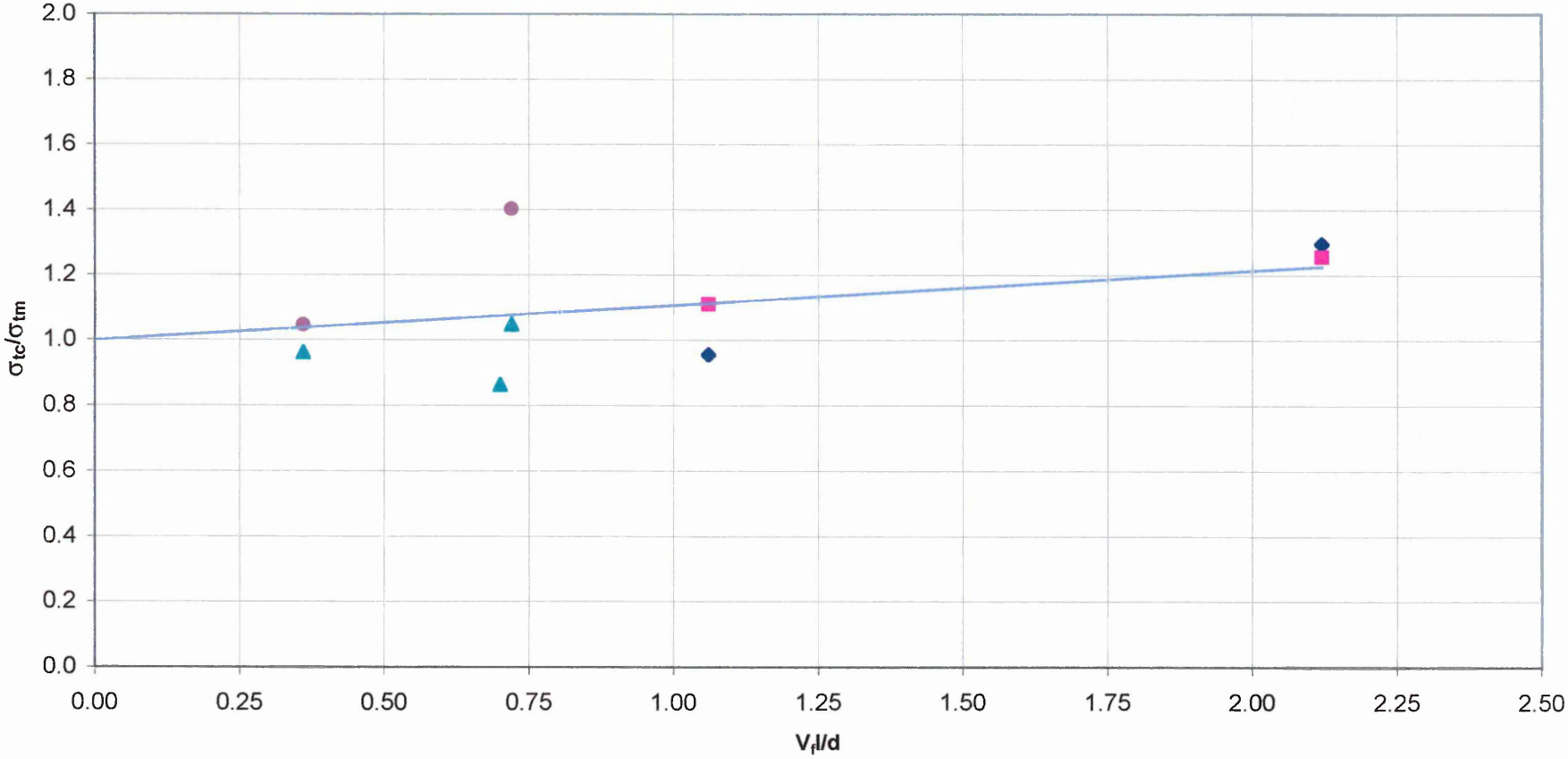

Figure 6.12 Relationship between σ_{tc}/σ_{tm} and fibre $V_f l/d$ ratio

A regression analysis of the data in Figure 6.15 gives the following equations:

$\sigma_{tc}/\sigma_{tm}=0.11\ V_f\ l/d + 1.00$

with a coefficient of correlation, R^2 of 0.65

Hence,

$\sigma_{tc} = \sigma_{tm} + \sigma_{tm}\ 0.11\ V_f\ l/d$ Equation 6.29

Thus the tensile splitting strength of fibre reinforced alkali activated materials can be obtained using equation 6.29 based on a knowledge of the tensile splitting strength of the plain matrix and details of fibre reinforcement.

There is no available data on the tensile splitting strength of alkali activated composite materials but other researchers[124] have studied the tensile strength of glass fibre reinforced high alumina cement mortar. The tensile strength of glass fibre reinforced high alumina cement mortar varied between 2.55 and 3.63 N/mm^2, see Table 6.39 compared with 4.81 to 6.41 N/mm^2 for glass fibre alkali activated materials from the present investigations.

Table 6.39 Tensile splitting strength[124]

Fibre length	Fibre Content % by weight	Fibre Content % by volume	Tensile Splitting Strength
0	0	0.00	2.55
13	0.25	0.12	3.33
13	0.50	0.25	3.4
13	0.75	0.36	3.43
13	1.00	0.49	3.63

Other researchers[152] have concluded that tensile splitting strength increases proportionally with the steel fibre concentration as shown in Figure 6.13.

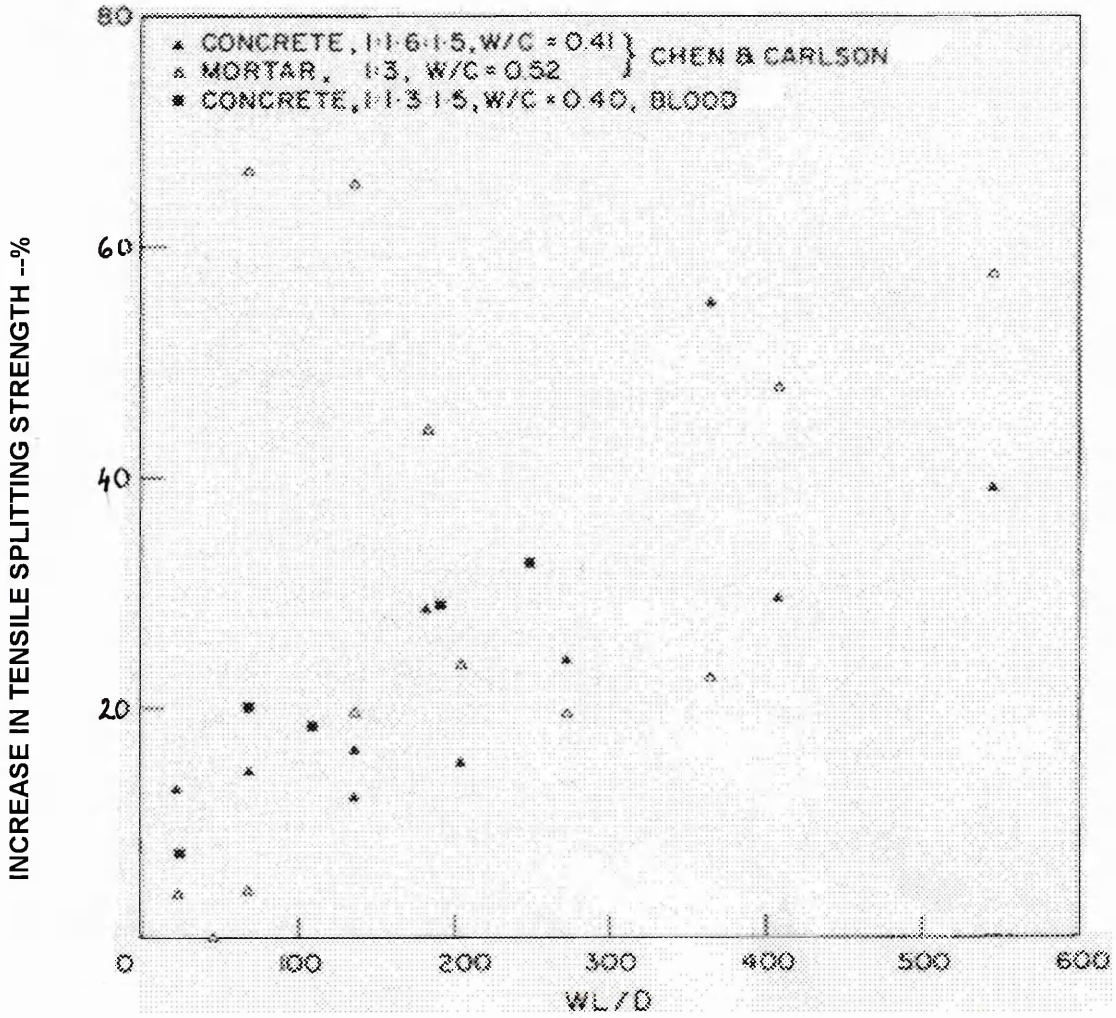

Figure 6.13 Influence of W l/d on tensile splitting strength[152]

6.5.9 Dynamic modulus of elasticity of fibre reinforced alkali activated materials

The dynamic modulus of elasticity values of the glass and steel fibre reinforced alkali activated materials cured under 20°C and 65% relative humidity are presented in Table 6.40. All mixes had a water/binder of 0.25. The dynamic modulus of elasticity results exhibit the same trends as the modulus of rupture. Both glass and steel fibres, increase the dynamic modulus of elasticity. For example, the dynamic modulus of elasticity of materials with 1.5% and 3% volume of glass fibre (batch code GA1 and GA2, respectively) was 15% higher than the control matrix.

Table 6.40 Dynamic modulus of elasticity of alkali activated fibre reinforced materials cured at 20°C and 65% RH

Batch Code	Fibre type	V_f [%]	V_f l/d	E_D [kN/mm^2]	% increase in E_D
A1 (control)	-	0	0	16	-
GA1	alkali resistant glass fibres (CEM-FIL 62/2)	1.5	1.06	19.7	15%
GA2	alkali resistant glass fibres (CEM-FIL 62/2)	3.0	2.12	19.6	14%
SwA1	stainless steel straight fibres	1.5	0.70	20.3	18%
SA1	melt extract fibres	1.5	0.36	19.6	14%
SA2	melt extract fibres	3.0	0.72	20.9	21%

The dynamic modulus of elasticity of the glass and steel fibre reinforced alkali activated materials cured thermally are presented in Table 6.41. All mixes had a water/binder of 0.25.

Table 6.42 Dynamic modulus of elasticity of alkali activated fibre reinforced materials, thermally cured

Batch Code	Fibre type	V_f [%]	V_f l/d	E_D [kN/mm^2]	% increase in E_D
H1 (control)	-	0	0	27.0	
GH1	alkali resistant glass fibres (CEM-FIL 62/2)	1.5	1.06	22.8	-16%
GH2	alkali resistant glass fibres (CEM-FIL 62/2)	3.0	2.12	21.3	-21%
SH1	melt extract fibres	1.5	0.36	21.7	-20%
SH2	melt extract fibres	3.0	0.72	25.3	-6%

Thermally cured fibre reinforced alkali activated exhibit a reduction in the dynamic modulus of elasticity compared with the control material (batch code H1). For example the dynamic modulus of materials with 1.5% and 3% volume of glass fibre (batch code GH1 and GH2) was 16% and 21% lower, respectively, than the control matrix.

6.5.9.1 Discussion

Figure 6.14 shows the relationship between E_c/E_m and fibre V_f l/d ratio for fibre reinforced alkali activated materials. E_m is the dynamic modulus of elasticity of the control unreinforced matrix and E_c is the dynamic modulus of elasticity of the fibre reinforced composite. The fibre V_f l/d ratio does not influence the dynamic modulus of elasticity of the materials as shown in Figure 6.17. E_c/E_m remains constant at about 1.2 at all V_f l/d values for curing conditions 20°C and 65%RH, whereas the constant E_c/E_m ratio is 0.85 under thermal curing.

The relationship between dynamic modulus of elasticity and compressive strength of alkali activated materials and fibre reinforced alkali activated materials is plotted in Figure 6.15. The dynamic modulus of elasticity E_D and compressive strength σ_c have a linear relationship. A regression analysis of the data in Figure 6.15 gives the following equation:

$E_D = 0.865\sigma_c^{0.76}$ Equation 6.30

with a coefficient of correlation R^2 of 0.71

There is no available data on dynamic modulus of fibre reinforced alkali activated materials but other researchers[124] investigated the properties of glass fibre reinforced high alumina cement mortar. The dynamic modulus for glass fibre reinforced high alumina cement mortar varied between 21.28 and 26.18 kN/mm^2, see Table 6.42, compared with 15.99 to 19.74 kN/mm^2 for glass fibre reinforced alkali activated materials from the present investigations (see Table 6.42).

Table 6.42 Dynamic modulus of elasticity of high alumina cement mortar[124]

Fibre length	V_f [%]	E_d [kN/mm^2]
0	0.00	26.18
13	0.12	23.73
13	0.25	-
13	0.36	-
13	0.49	21.28

Symbol	Batch	Curing	Type of fibres	Volume of fibres
◆	**GA1/GA2**	20°C and 65% RH	glass fibres	1.5%/3.0%
■	**GH1/GH2**	thermal treatment	glass fibres	1.5%/3.0%
▲	**SA1/SA2**	20°C and 65% RH	melt extract fibres	1.5%/3.0%
●	**SH1/SH2**	thermal treatment	melt extract fibres	1.5%/3.0%

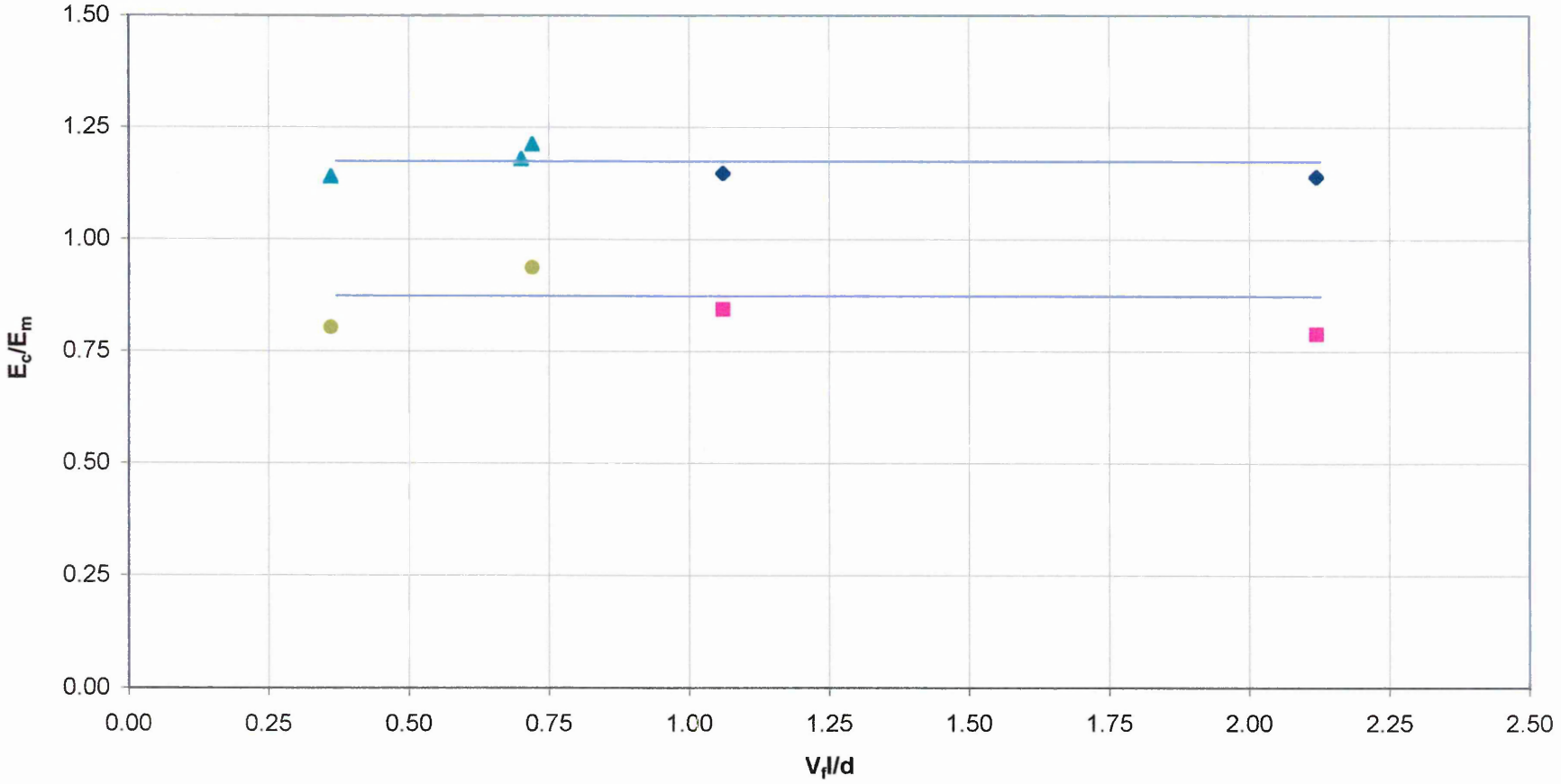

Figure 6.14 Relationship between E_c/E_m and fibre V_f l/d

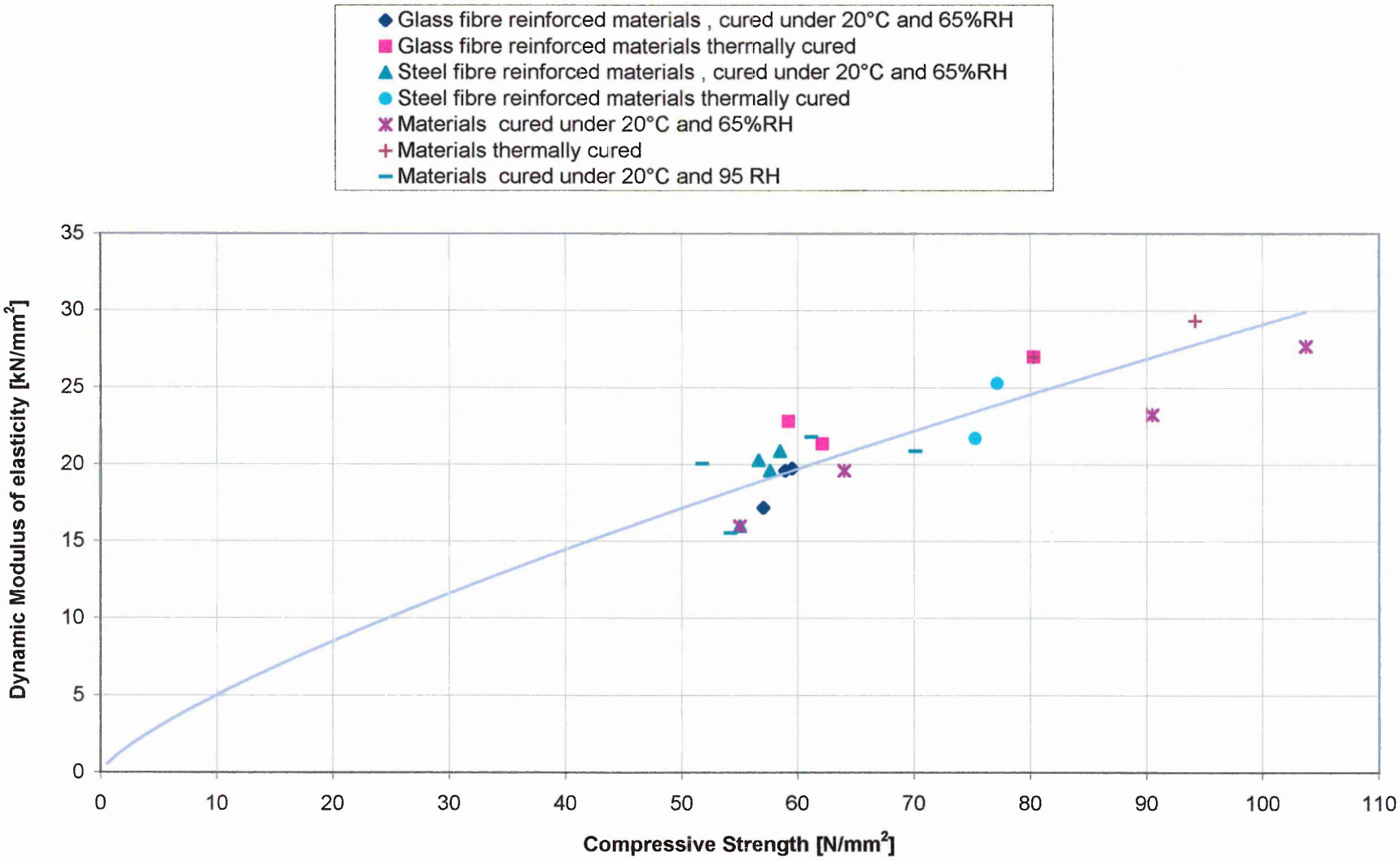

Figure 6.15 Relationship between compressive strength and dynamic modulus of elasticity

6.6 CONCLUSIONS

The following conclusions are based on the results of this investigation on the alkali activated materials derived from fly ash, microsilica, slag fillers and water glass binder:

1. The compressive strength of alkali activated fibre reinforced materials is within the range 51.78 N/mm^2 to 103.74 N/mm^2.

2. The modulus of rupture of alkali activated fibre reinforced materials is within the range 3.08 N/mm^2 to 10.5 N/mm^2.

3. The tensile splitting strength of the alkali activated fibre reinforced materials is within the range 4.94 N/mm^2 to 5.36N/mm^2.

4. The dynamic modulus of elasticity of the alkali activated reinforced materials is within the range 16.04 kN/mm^2 to 29.36 kN/mm^2.

5. Increasing the water/binder ratio from 0.20 to 0.25 decreases the compressive strength, modulus of rupture, tensile splitting strength and dynamic modulus of alkali activated materials.

6. Increasing the relative humidity of curing from 65% to 95% decreases the compressive strength and dynamic modulus of elasticity but does not significantly affect the modulus of rupture.

7. Thermal curing increases the compressive strength, modulus of rupture and dynamic modulus of elasticity of alkali activated materials.

8. Glass and steel fibre reinforcement increase the modulus of rupture, tensile splitting strength and dynamic modulus of elasticity of alkali activated materials.

9. The modulus of rupture of fibre reinforced alkali activated materials can be obtained using the following equations:

   For glass fibre reinforced alkali activated materials:

   $$\sigma_{fc} = 0.57\sigma_{fm}(1-V_f)+6.41\cdot V_f\cdot\frac{l}{d}$$

   For steel fibre reinforced alkali activated materials:

   $$\sigma_{fc} = 0.64\sigma_{fm}(1-V_f)+4.00\cdot V_f\cdot\frac{l}{d}$$

10. The fibre-matrix bond strength for glass fibre reinforced matrices is 4.88 N/mm^2 and for steel fibre reinforced matrices is 7.82 N/mm^2. This compares with a value of 4.15 N/mm^2 for steel fibres in a Portland cement mortar.

11. The dynamic modulus of elasticity and compressive strength of fibre reinforced alkali activated materials have the following relationship:

    $$E_D = 0.865\sigma_c^{0.76}$$

"To know that, we know what we know and that, we do not know what we do not know, that is true knowledge."

Henry David Theoreanu

7 Physical Properties and Durability of alkali activated fly ash materials

7.1 INTRODUCTION

ASTM C666-92[105] defines durability as "the measure of the ability of a material to endure and maintain its essential and distinctive characteristics of strength, resistance to decay and appearance. Durability is based on the time that a material can maintain its innate characteristics with use. This time will depend on the environment and the use of the material in question". The durability of cementitious materials is governed by their basic physical characteristics such as porosity and pore structure. The total volume of pores or voids in concrete comprises of pores in the hardened cement paste, entrained or entrapped air voids and pores in the aggregate. The first two categories are formed during mixing and initial hydration of the cement paste and are further refined by the setting and continued hydration of the cement matrix with time. Other void spaces can be created as a result of poor practice such as bleeding, honeycombing and air pockets.

Most of the important physical properties (i.e. density, apparent porosity, water absorption and coefficient of sorption) of hardened concrete can be related to the different characteristics of its pores, such as the size, volume, distribution and shape. The mechanical properties such as strength, elastic modulus and creep are primarily affected by the total pore volume, not their size or continuity[81]. The durability properties of cementitious materials are governed by the mass transport phenomenon of deleterious substances and are concerned with the permeability and ionic movement in the material[81]. The volume, size and continuity of the pores have been found to influence these types of properties.

7.2 OBJECTIVES

A comprehensive experimental study has been undertaken to determine the physical properties which govern the durability of alkali activated fly ash materials under investigation in this project. The properties investigated were bulk and apparent solid

density, water absorption, apparent porosity and coefficient of sorption. Direct durability tests were also carried out on the alkali activated fly ash materials to determine their freeze - thaw resistance and fire resistance.

7.3 EXPERIMENTAL DETAILS

7.3.1 Constituent Materials

The constituent materials used for the investigations presented in this chapter are detailed in Chapter III (Experimental Programme) and are also summarised in the following section.

The main pozzolanic material used was **pulverised fuel ash** (pfa) from the power plant at Ratcliffe. Its chemical composition (by weight) is given in Table 7.1.

Table 7.1 Chemical composition of the fly ash from Ratcliffe.

Element	Content [%]
Silicon dioxide (SiO_2)	47.4
Aluminium oxide (AlO_3)	25.6
Iron oxide (Fe_2O_3)	10.4
Magnesium oxide (MgO)	1.7
Calcium oxide (CaO)	3.3
Sulphate (SO_3)	1.0
Potassium oxide (K_2O)	3.1
Sodium oxide (Na_2O)	1.4
$Na_2O_e = 0.658 \cdot K_2O + Na_2O$	3.4
Titanium oxide (TiO_2)	1.0
Chlorite (Cl)	0.01
Loss of Ignition	4.54
Density (kg/m^3)	2290
Sieve Residue Retained 45μm	
$\frac{CaO + MgO + Al_2O_3}{SiO_2}$	**0.645**

The slag used in this investigation was **ground granulated blast furnace slag** from the plant located in Teesside. Its chemical composition (by weight) is given in Table 7.2.

Table 7.2 Chemical composition of ground granulated blast furnace slag from Teesside

Element	Content [%]
Silicon dioxide (SiO_2)	35.67
Aluminium oxide (AlO_3)	13.47
Iron oxide (Fe_2O_3)	0.55
Magnesium oxide (MgO)	7.45
Calcium oxide (CaO)	40.90
Sulphate (SO_3)	0.05
Sulphide (S^{2-})	0.91
Potassium oxide (K_2O)	0.26
Sodium oxide (Na_2O)	0.19
$Na_2O_e = 0.658 \cdot K_2O + Na_2O$	0.36
Titanium oxide (TiO_2)	0.69
Chlorite (Cl)	0.013
Manganese (MnO)	0.27
Loss of Ignition	0.48
Insoluble Residue	0.14
Particle size analysis	**466**[kg/m^2]
$\frac{CaO + MgO + Al_2O_3}{SiO_2}$	**1.733**

Microsilica (silica fume) used in this investigation was a dry densified silica fume with the chemical composition (by weight) given in Table 7.3.

Table 7.3 Chemical composition of the densified silica fume

Element	Content [%]
Silicon dioxide (SiO_2) amorphous	85 to 98
Iron oxide (Fe_2O_3)	≤ 3.0
Aluminium oxide (Al_2O_3)	≤ 1.5
Calcium oxide (CaO)	≤ 0.7
Magnesium oxide (MgO)	≤ 2.0
Sodium oxide Na_2O)	≤ 1.0
Potassium oxide (K_2O)	≤ 3.0
$Na_2O_e = 0.658 \cdot K_2O + Na_2O$	≤ 2.97
Carbon (C)	≤ 3.0
$\frac{CaO + MgO + Al_2O_3}{SiO_2}$	**0.0494 to 0.0428**

Washed and graded **high silica fine sand** from Congleton quarry was used. Its chemical composition (by weight) is given in Table 7.4.

Table 7.4 Chemical composition of silica sand from Congleton quarry

Element	Content [%]
Silica (SiO_2)	95.13
Aluminia (Al_2O_3)	2.34
Iron oxide (Fe_2O_3)	0.24
Sodium oxide (Na_2O)	-
Potassium oxide (K_2O)	1.61
$Na_2O_e = 0.658 \cdot K_2O + Na_2O$	1.06
L.O.I.	0.25
Average grain size [μm]	175
Bulk density [kg/m^3]	1450

Sodium silicate solution (water glass Crystal 112) with a mean molar ratio (silica modulus) SiO_2/NaO_2 =2.06 was used. Its chemical composition (by weight) is given in Table 7.5.

Table 7.5 Chemical composition of the sodium silicate solution

Element	Content [%]
Silicon dioxide (SiO_2)	30.55
Sodium oxide (Na_2O)	15.27
Water (H_2O)	54.18

Water glass hardener: An aluminium methaphosphate compound, K-Bond # 90, was selected as water glass hardener in order to accelerate the curing process. The general properties of the hardener are given in Table 7.6.

Table 7.6 Properties of the water glass hardener (K-Bond # 90)

Property	Description
Appearance	Fine white powder
Acidity [meq/g]	1.2 ± 0.5
Moisture [%]	≤ 1.5
Solubility in water [%]	≤ 3.0
pH	3.2 ± 0.5
Sieve residue > 44 micron [%]	≤ 1.0

Fibre Reinforcement: Three types of fibres were selected for the investigation.

a) Stainless steel fibres of undeformed (straight) shape, smooth surface of length 7mm and diameter 0.15 mm, were used. The aspect ratio (length/diameter) was 46.67. The specific gravity and Young's modulus of elasticity were 7.8 Kg/m^3 and 215.3 GPa, respectively.

b) Melt extract steel fibres of non-uniform surface, length 12 mm and equivalent diameter 0.5 mm were used. The aspect ratio was 24. The specific gravity and Young's modulus of elasticity were 7.8 kg/m^3 and 215.3 GPa, respectively.

c) Alkali resistant integral chopped strand glass fibres (Cem-FIL 62/2) consisting of 100 filaments bound together. These fibres were resistant to the breakdown of the strands during mixing. The individual filaments were of length 12 mm and diameter 14μm. The aspect ratio of the fibre strand was 70.6. The specific gravity and Young's modulus of elasticity were 2.68 kg/m^3 and 72 GPa, respectively.

7.3.2 Sample Preparation

Specimens of acceptably large dimensions, to produce reliably accurate information, were used in the investigations reported in this chapter. These were cylinders of 100mm diameter 200mm height and 75 mm cubes. These sizes were selected to strike an optimal balance between limiting excessive volumes of materials required and ensuring that meaningful data could be obtained on the properties of alkali activated materials.

A detailed description of the mixing, casting and curing procedures is given in section 5.3 of Chapter V (Shrinkage and creep of alkali activated fly ash materials). Mixes with two different water/binder ratios (0.25 and 0.20) were investigated. The water and solids in the sodium silicate solution (water glass) were included in the determination of water/binder ratio. Mixing was carried out using a forced action pan Hobart mixer. The dry component materials (fly ash, silica fume, ggbs and sand)

were mixed thoroughly after which the fibre reinforcements (in fibre reinforced mixes only, see section 7.3.3) were added. Following this, the required amount of sodium silicate solution (water glass) was added and mixed with the dry components (and fibres) until the mixture became homogenous. The hardener was added near to the end of the mixing process, in the form of a slurry to aid its dispersion in the mix. The mixes were cast in specially manufactured stainless steel moulds which were suitable for placing in a fan assisted oven to provide high temperature curing (up to 120°C). Two compacting methods were employed depending of the workability of the mix. The stiffer mixes (w/b = 0.20) were cast in two layers and compacted by applying 25 strokes of a tamping rod. The workable mixes (w/b=0.25) were cast in two layers, each layer being compacted using a vibrating table until the surface of the sample was smooth and had a glassy appearance. The test specimens were subjected to one of the following four different curing conditions immediately after casting:

i. controlled conditions at 20°C and 65% relative humidity - the specimens were kept in the moulds for 7 hours then demoulded and curing maintained at 20°C and 65% RH until testing.

ii. mist conditions at 20°C and 95% relative humidity - the specimens were kept in the moulds for 7 hours then demoulded and curing maintained at 20°C and 95% RH until testing. The specimens were placed in the mist curing room and covered with polythene sheeting to prevent condensation.

iii. mist conditions at 20°C and 95% relative humidity for the first seven hours before demoulding. After demoulding the samples were stored in a water tank at 20°C until testing.

The strength development under these curing conditions (i to iii) was sufficiently rapid to allow demoulding of the samples after seven hours from casting.

iv. high temperature curing - the specimens were subjected to a curing temperature programme, which is presented in Figure 5.1. After casting, the samples (within the moulds) were placed in an oven and the temperature was raised from room

temperature (≈20.6°C) to 30°C in 60 minutes and held at 30°C for a further 240 minutes. The temperature was then progressively increased in steps up to 120°C as shown in Figure 5.1. Finally the temperature was gradually reduced to 20.6°C in 420 minutes (see Figure 5.1). The total duration of the curing period was 1620 minutes (27 hours). The samples were then stored under conditions 20°C and 65% RH until testing.

7.3.3 Details of investigated batches

The proportions of dry constituent materials used were 1: 0.5: 0.25: 3.25 by weight (fly ash: ground granulated blast furnace slag: silica fume: sand). Water glass Crystal 112 content was 11.46% (by weight of the mix) as detailed in section 5.3 (Experimental Programme) of Chapter V. The hardener content was 1.5% by weight of the sodium silicate solution (water glass), in the form of a slurry with water. The water/binder ratios and curing conditions used for the alkali activated cementitious materials and alkali activated fibre reinforced composite materials investigated in this chapter are given in Table 7.7 and Table 7.8, respectively.

Table 7.7 Composition of alkali activated fly ash materials

Batch Code	Water/Binder	Total Water [%]	Hardener [%]	Curing Conditions
A1	0.25	10.28	-	20°C and 65% RH
M1	0.25	10.28	-	20°C and 95% RH)
W1	0.25	10.28	-	water curing at 20°C after 7 h
H1	0.25	10.28	-	thermal treatment
KA1	0.25	10.28	1.5	20°C and 65% RH
KM1	0.25	10.28	1.5	20°C and 95% RH
A2	0.20	6.20	-	20°C and 65% RH
M2	0.20	6.20	-	20°C and 95% RH
H2	0.20	6.20	-	thermal treatment
KA2	020	6.20	1.5	20°C and 65% RH
KM2	0.20	6.20	1.5	20°C and 95% RH

Table 7.8 Composition of fibre reinforced alkali activated materials

Batch Code	Water/Binder	Water [%]	Fibres		Curing Conditions
			Type	V_f [%]	
GA1	10.28	10.28	glass	1.5	20°C and 65% RH
GH1	10.28	10.28	glass	1.5	thermal treatment
GA2	10.28	10.28	glass	3.0	20°C and 65% RH
GH2	10.28	10.28	glass	3.0	thermal treatment
SwA1	10.28	10.28	straight steel	1.5	20°C and 65% RH
SA1	10.28	10.28	melt extract	1.5	20°C and 65% RH
SH1	10.28	10.28	melt extract	1.5	thermal treatment
SA2	10.28	10.28	melt extract	3.0	20°C and 65% RH, (i)
SH2	10.28	10.28	melt extract	3.0	thermal treatment, (iv)

Batch code symbols represent:

A - air cured at 20°C and 65% relative humidity;

M - mist cured at 20°C and 95% relative humidity;

W - water cured at 20°C;

H - heat (thermally) cured;

K - mix containing water glass hardener, (aluminium methaphosphate) K-Bond # 90;

Sw - mix reinforced with stainless steel fibres of straight shape and undeformed, smooth surface;

S - mix reinforced with melt extract steel fibres of non-uniform surface;

G - mix reinforced with alkali resistant integral chopped strand glass fibres.

7.4 TESTING PROGRAMME

7.4.1 Density and Pore structure

Density (bulk and apparent solid), water absorption, apparent porosity, coefficient of saturation and permeability of the alkali activated fly ash materials listed in Table 7.7 and Table 7.8. were determined. The top pan method was used to calculate the porosity, density (bulk and apparent solid) and percentage water absorption

according to BS 3921, 1974[133]. The standard procedure was to first dry the cube specimens at age 28-35 days in a fan assisted oven at 103 ± 2°C for 24 hours or until they showed constant mass. The specimens were then taken out of the oven and left to cool in the laboratory environment (20°C62°C). This process took approximately 12 hours. After cooling to (20°C62°C), the specimens were weighed to give the dry mass, m_D [grams], then placed in a vacuum chamber on a wire mesh base. Following this, the specimens were vacuum saturated according to BS 3921, 1974[133]. The pump of the vacuum chamber was started at 101 MPa pressure. When the pressure of 5 x 10^{-4} MPa was reached in the vacuum chamber, air-free water was allowed to cover the specimens and the samples were left submerged for a period of 10 minutes according to (BS 3921, 1974). The mass of the saturated samples, m_S [grams], was then measured, followed by the buoyed mass of the sample suspended in water, m_B [grams]. A weighting balance, Mettler PL 1200, was used which was calibrated every 6 months against accurate standards.

The temperature of the water introduced in the vacuum chamber was recorded in order to make the necessary correction for the true density of water, which is temperature dependent. Table 7.9[134] presents the values for the density of air free water under normal atmospheric pressure (1atm). Linear interpolation is permitted between the values given in Table 7.9[134]. For the present investigations the temperature of water in tests was 18.5°C, therefore, the corresponding true density ρ_w was 998.5025 [kg/m^3].

In order to determine the saturation and sorption coefficients, the test specimens were first dried in a fan assisted oven at 103 ± 2°C and then cooled to 20°C as detailed above. The dry mass of the samples was recorded m_D [grams]. The specimens were subsequently submerged in water for 24 hours under normal atmospheric pressure at 20°C. After 24 hours the samples were removed from the water, wiped with a damp cloth to remove excess water and then weighed in air to give the wet mass after 24 hours of water intake, m_{24}.

Table 7.9 Density of air free water [kg/m^3] at 1 atm pressure[134]

Temperature [°C]	Density [kg/m^3]
0	999.84
2	999.94
4	999.97
6	999.94
8	999.85
10	999.7
12	999.5
14	999.25
16	998.94
18	998.6
20	998.21
22	997.77
24	997.29
26	996.79
28	996.24
30	995.65

In order to determine the saturation coefficient, the test specimens were first dried in a fan assisted oven at 103 ± 2°C and then cooled to 20°C as detailed above. The dry mass of the samples was recorded m_D [grams]. The specimens were subsequently submerged in water for 24 hours under normal atmospheric pressure at 20°C. After 24 hours the samples were removed from the water, wiped with a damp cloth to remove excess water and then weighed in air to give the wet mass after 24 hours of water intake, m_{24}.

Total Volume

Total volume of solids and voids, V_T, is equal to the buoyed mass of the test specimen suspended in water, m_B, after correction for the true density of water.

$$V_T = \frac{m_B}{\rho_W} \quad [\text{cm}^3] \qquad \text{Equation 7.1}$$

Volume of Voids

Total volume of voids in the specimen, V_V, is calculated by subtracting the dry mass of the sample, m_D, (solids plus voids filled with air) from the saturated mass, m_S, (solids plus voids filled with water).

$$m_V = m_S - m_D \quad [\text{kg}]$$

Where : $V_V = \frac{m_v}{\rho_w}$

$$\therefore V_V = \frac{m_S - m_D}{\rho_w} \quad [\text{cm}^3] \qquad \text{Equation 7.2}$$

Volume of solids

Volume of solids in the specimen, V_S, is calculated by subtracting the volume of voids, V_V, from the total volume, V_T.

$$V_S = V_T - V_V \quad [\text{cm}^3] \qquad \text{Equation 7.3}$$

Bulk Density

Bulk density, ρ_{Bulk} is the mass of the whole material per unit volume, reflecting the density of the mineralogical content of the material and the amount of pore spaces. It is usually specified as mass per unit volume e.g. g/cm^3 or kg/m^3.

$$\rho_{Bulk} = \frac{m_D}{V_T}$$

Substituting for V_T from equation 7.1 gives : Equation 7.4

$$\rho_{Bulk} = \frac{m_D}{m_B / \rho_W} \quad [\text{g/cm}^3]$$

Apparent Solid Density

Apparent solid density $\rho_{Apparent\ Solid}$ is the density of the solids in a material, which is due purely to the mineralogical components of the material. It is usually specified as mass per unit volume e.g. g/cm^3 or kg/m^3. However, using the vacuum saturation method, the measurement of the volume of the sealed pores is impossible. Picnometry is the only method which can calculate the true solid density of the material. Therefore, the solid density determined in this investigation is not the true solid density of the material but the apparent solid density.

$$\rho_{Apparent\ Solid} = \frac{m_D}{V_S}$$

Substituting for V_s from equation 7.4 gives : Equation 7.5

$$\rho_{Apparent\ Solid} = \frac{m_D}{V_T - V_V} \quad [\text{g/cm}^3]$$

where:

m_D is the dry mass of the sample [g]

V_S is the total volume of solids [cm^3]

Apparent Porosity

Apparent porosity, p [%], is the amount of voids expressed as a percentage of the total volume V_T and is given by the expression.

$$p[\%] = \frac{V_V}{V_T} \cdot 100 \qquad \text{Equation 7.6}$$

Substituting for V_V from equation 7.3 gives :

$$p[\%] = \frac{V_T - V_S}{V_T} \cdot 100$$

Multiplying the top and bottom of above fraction by m_D, gives :

$$p[\%] = \frac{m_D(V_T - V_S)}{m_D \cdot V_T} \cdot 100$$

Simplfying the above equation gives :

$$p = \left[1 - \frac{m_D \cdot V_S}{m_D \cdot V_T}\right] \cdot 100 \qquad \text{Equation 7.7}$$

Substituting ρ_{bulk} from equation 7.4 and $\rho_{ApparentSolid}$ from equation 7.5 into equation 7.7 gives the relationship between apparent porosity and density (bulk and solid) :

$$p = \left[1 - \frac{\rho_{bulk}}{\rho_{ApparentSolid}}\right] \cdot 100 \qquad \text{Equation 7.8}$$

The porosity determined in the laboratory by vacuum saturation does not give any indication of the size and spatial distribution of the pores or the volume of sealed pores. Owing to these factors it is called the apparent porosity. The true porosity and pore structure can be determined by mercury intrusion porosimetry or scanning electron microscopy. Porosity has been used as the main parameter in determining the durability of materials in previous studies[102] owing to the fact that it is responsible for the intake and transport of deleterious substances. Porosity is also the

main indicator of the physical properties of a particular material, as apparent porosity, bulk density and solid density are linked together as seen in equation 7.8.

Water Absorption

Water absorption is the amount of water taken in by the material under normal temperature and pressure. Water absorption of each specimen was calculated as the increase in mass resulting from submersion, expressed as a percentage of the mass of the dry specimen.

$$w_a = \frac{(m_S - m_D)}{m_D} \times 100 \ [\%] \qquad \text{Equation 7.9}$$

where:

w_a is the water absorption of the specimen [%]

m_S is the mass of the samples submerged in water [g]

m_D is the dry mass of the sample [g]

In equation 7.9 the term $(m_S - m_D)$ is the weight of the volume of water filling the void space available (i.e. the open porosity).

$$(m_S - m_D) = V_V \cdot \rho_w \qquad \text{Equation 7.10}$$

Equation 7.6 is rearraged in terms of V_V giving :

$$V_V = V_T \cdot \frac{p}{100} \qquad \text{Equation 7.11}$$

Substituting V_V from equation 7.11 into equation 7.10 gives :

$$(m_S - m_D) = V_T \cdot \frac{p}{100} \cdot \rho_w \qquad \text{Equation 7.12}$$

Dividing equation 7.12 by m_D gives :

$$\frac{(m_S - m_D)}{m_D} = \frac{V_T \cdot p \cdot \rho_w}{m_D \cdot 100} \qquad \text{Equation 7.13}$$

Substituting ρ_{Bulk} from equation 7.4 and w_a from equation 7.9 into equation 7.13 gives the relationship between water absorption, bulk density and apparent porosity :

$$w_a(\%) = \frac{p \cdot \rho_w}{\rho_{Bulk}} \qquad \text{Equation 7.14}$$

Coefficient of Saturation

Coefficient of saturation is the ratio of water taken into a material in 24 hours under normal atmospheric pressure at 20°C to the potential total amount which can be absorbed, based on percentage porosity. A ratio of 1 indicates that all the available pore spaces are filled with water under atmospheric pressure. The coefficient of saturation was determined using the following equation according to BS 3921, 1974[133].

$$C_{saturation} = \frac{(m_{24} - m_D)}{(m_s - m_D)} \ [\%] \qquad \text{Equation 7.15}$$

where:

$C_{saturation}$ is the coefficient of saturation of the specimen [%]

m_{24} is the mass of the sample after 24 hours in water [g]

m_D is the dry mass of the specimen [g]

Coefficient of saturation is purely a measurement of the natural water intake into the material over a given (24 hours) period of time. Traditionally the saturation coefficient has been used by researchers to establish the likely performance of materials.

7.4.2 Permeability

7.4.2.1 Introduction

Permeability of a porous material is a measure of its resistance to flow of water or gases. It represents the mass transport properties of the material. This is an important parameter when considering the durability of cementitious materials since deterioration processes such as corrosion and carbonation will be under mass transport control. Permeability can, therefore, provide a method of indirectly assessing the durability of cementitious materials and for distinguishing the performance of different materials.

In this study a custom made permeater was used to measure the Darcian coefficient of permeability for the materials under investigation. A photograph of the permeameter is given in Figure 7.1. The apparatus applies a constant "head" of water pressure to one surface of a specimen and measures the flow of water through the specimen.

7.4.2.2 Permeameter Apparatus

The permeameter used in this study was a custom made LPM2 permeability apparatus manufactured by SPT limited. A schematic representation of the permeameter is given in Figure 7.2[154]. The isostatic sample holder is mounted on the front of a rugged steel housing.

The cabinet also contains the necessary equipment for generating the confining pressure and the oil reservoir, as well as the transducer to measure the sample pressure, and the necessary safety and control devices. The cabinet is mounted on a steel frame to provide stability, see Figure 7.1. Access to the interior of the cabinet is gained by opening the door on the back.

Figure 7.1 LPM2 permeability apparatus

The sample holder is machined from stainless steel, and rated for use with pressures up to a maximum of 150 bar. The cell consists of a cylindrical shell and two end plates. The sample is contained between a 'fixed' platen, and a 'floating' platen of the same diameter. Isolation from the hydraulic oil in the cell is provided by a sleeve of neoprene rubber, which slides over the platens and the sample, as shown in Figure 7.2. The floating platen has a 'platen pipe' attached to it, which passes through the central opening in the bottom flange. It is sealed in this opening by two 'O' rings and two bushes, but can move freely in the axial direction.

The face of the platens in contact with the sample is manufactured from a porous material (sintered stainless steel) to allow free fluid distribution over the sample face. The top plate has two ports connected with the sample face. One is connected to the syringe pump, the other to the 'upstream' pressure transducer. The use of two ports ensures proper pressure measurement, and facilitates the removal of trapped air. The floating platen has one central port, which is open to the atmosphere via the platen pipe. Since the platen pipe is insulated from the bottom flange, it is possible to perform electrical measurements on the sample.

The large size and weight of the cell components made it impracticable to load samples through the top, as is common practice with this type of cell. The top plate can move down inside the cell and is prevented from dropping out of the cell by a ridge machined in the cell body. The sample is mounted onto the top plate and then pushed upwards when screwing in the bottom flange. The assembly is moved to its final position by the filling of the cell with hydraulic oil.

7.4.2.3 Operating Parameters

A number of review documents exist in literature which provide information on experimental techniques and which can be used to define the operating parameters for permeability tests[155, 156]. Concrete Society Technical Report No. 31, 'Permeability testing of site concrete[155] provides recommendations on good practice for the measurement of permeability by flow. These guidelines have been adopted from the work of Jefferis at King's College London[155] and provide a basis for defining the test parameters used in present investigation.

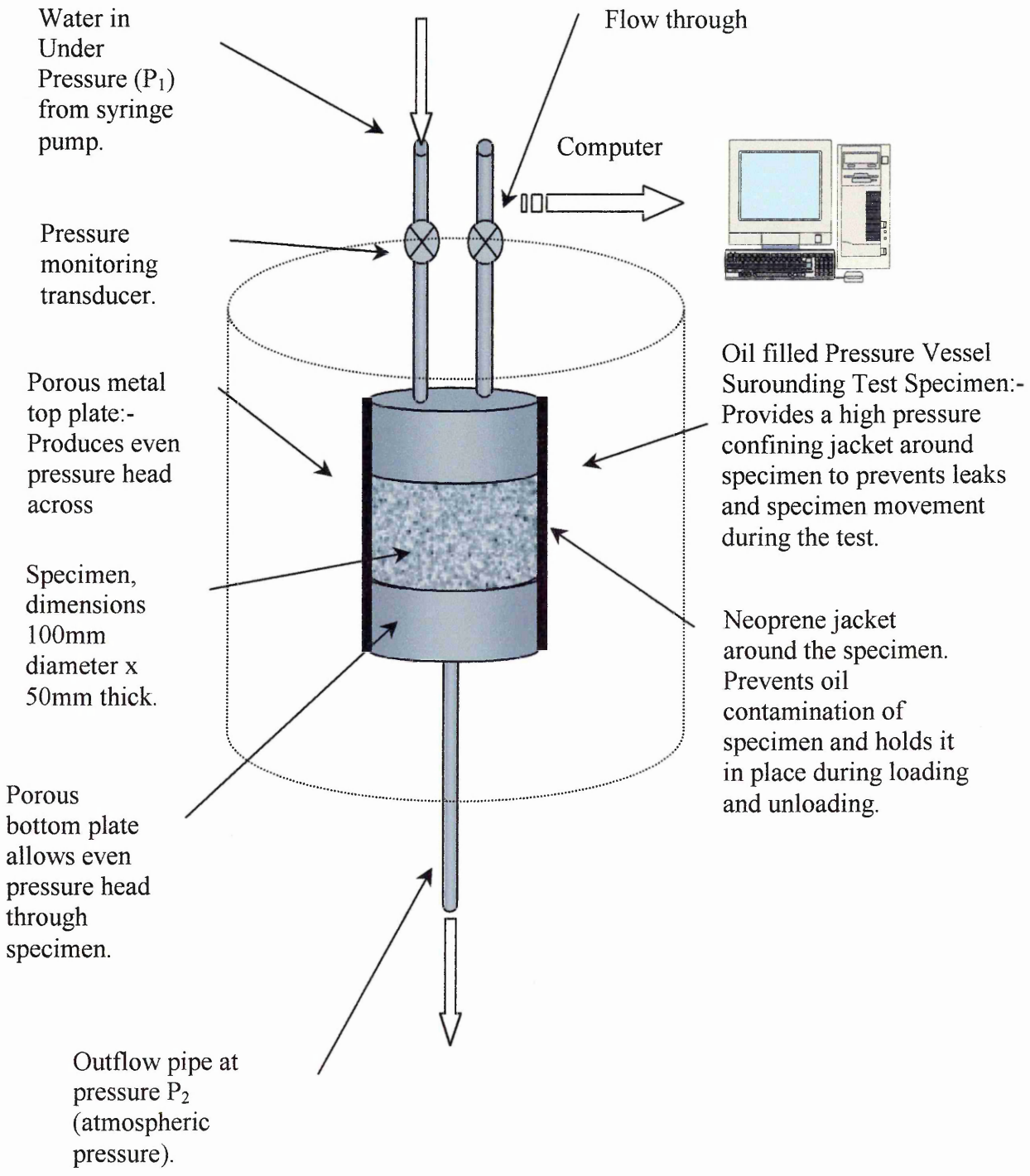

Figure 7.2 Schematic representation of permeater[154]

i. **Specimen Saturation**; The flow of water into the specimen is controlled initially by capillary forces in the material. These forces continue to act until water has passed through the full length of the specimen and wetted the under surface. Until this happens flow is not governed by Darcian flow. This means that true permeability can only be measured on specimens which are saturated. All the specimens used in this study were kept in a saturated condition in a water bath at 20°C until testing. Vacuum saturation was also tried but did not produce substantially different results from the saturated specimens.

ii. **Leak Compensation**; as the permeabilities of the repair materials used are likely to be below 10^{-13}m/s, any leaks in the system can have a large impact on the accuracy of flow rates being measured. It is recomended[156] that both the inflow and outflow should be monitored to allow compensation to be made for leaks in the system.

iii. The presence of air in the sample will act as water free voids that will disrupt the movement of water through the specimen. Applying a backpressure of 2 bar will dissolve any entrapped air in the specimen or apparatus.

iv. **Temperature changes** in the apparatus may effect the flow rate measurements; therefore temperature of the apparatus must be kept constant.

v. **Water flow rate** can be expected to vary in a non-Darcian fashion with applied pressure. At low pressure gradients chemical interactions may result in the generation of osmotic pressures between the concrete and the pore water. High pressures can result in the compression of the pore structure resulting in a lower calculated permeability and may damage the specimen. Test pressure should be chosen as near as possible to the practical situation and quoted along with the calculations. A constant test pressure should also be used during the test; changes in pressure could result in movement of the specimen which may be recorded as apparent flow.

7.4.2.4 Test Procedure

It is clear from examining the state of the art recommendations[156] that care needs to be taken in defining the experimental parameters of the permeability test, in order to be able to produce reproducible results. The test apparatus used in this study keeps the specimen under pressure in an oil filled jacket. The confining pressure applied by the oil filled jacket minimises the risk of interference from entrapped air at the surface of the specimen. Dry specimens were used for measurement of Darcian flow parameters. The apparatus was kept in a temperature-controlled environment (20°C) to minimise the effect of temperature changes on flow measurement. Distilled water was used as the permeating fluid. The effect of leaching on the low permeability specimens used in this study was considered to be negligible for the relatively short test period adopted.

The risk of water leakage in the permeater was negligible due to the high confining pressure provided by the oil jacket surrounding the specimen. This confining oil pressure was always kept at 10 bar above the water pressure head across the specimen.

A risk of contamination of the specimen from the confining oil and water leaks was likely only if the water pressure head exceeded the confining oil pressure. The permeameter had the facility to only measure inflow. Collecting the water passing through the specimen provided a check on the outflow. Periodically a check was made with an impermeable calibration specimen to detect for leaks in the system. These tests did not detect the presence of any leaks during this study.

The two major experimental parameters for this permeability study were the selection of the inflow pressure water head and the time over which the permeability measurements were conducted.

Pressure Head

The pressure head of water effectively controlled the confining oil pressure used during the test. It can be expected that flow in the specimen will vary in a non-Darcian fashion with applied pressure. As the water pressure head increases so will the confining oil pressure used, leading to the compression of the pore structure and,

therefore, lower calculated permeabilities. The lower the water pressure head the greater the scatter in the results, thereby, lowering the confidence limits of the calculated permeability [155]. This implies that with this permeameter there is a trade off between less scatter in the measured flow in the specimen as pressure head increases and the effect of high pressure head on constriction of pores. Higher head pressure also produces more measurable flow rates in low permeability materials and, therefore, reduces the time taken to produce a steady state flow, thus reducing the duration of each test. In this study, it was important to compare the permeability values of the different materials investigated. It was decided to use a constant water pressure head of 500 kPa with a confining pressure of 1500 kPa. This was a compromise value to give results with reasonable scatter and measurable flows for low permeability materials, while providing a pressure head near to a real life situation to maintain the practical relevance for the value.

Duration of test

The second important experimental parameter was the duration of the permeability test. It has been found in literature[155] that flow rate in the specimen varies with time during a permeability test. Constant flow is only achieved under special conditions. It is normally observed that flow rate reduces with time. The self-sealing property of concrete means that the period of time over which permeability measurements are taken will influence the value of permeability calculated. The effect of the self-sealing phenomenon usually occurs in the first 20 hours of the test. After this a constant value is generally reached. In this study it was decided to run all permeability tests over a period of 3 days (72 hours) and use the readings of the last 24 hours of the test to calculate the permeability.

Darcy Coefficient of Permeability

The permeability of the specimens was measured using the saturated flow technique. One side of the water-saturated specimen was subjected to a water pressure head and the rate of flow through the sample was measured. Darcy's law could then be used to determine the permeability coefficient k as follows:

$$k = \frac{dq}{dt}\frac{L}{\Delta hA}$$ Equation 7.16

where :

$\frac{dq}{dt}$ = rate of flow (m^3/s)

A = cross sectional area (m^2)

Δh = pressure head accross the sample (m)

L = thickness of sample (m)

k = coefficient of permeability (m/s)

Test Specimens

The manufacture and curing of test specimens of the selected batches of materials (Table 7.7) is detailed in section 7.3.3 of this chapter. At the age of 28 days, one 100mm diameter 200mm long cylinder, for each test batch (Table 7.7), was sectioned using a masonry saw. The specimens were first cut to remove 25mm thick discs from the top and bottom of each cylinder. The remaining length of each cylinder was then cut into discs of 100mm diameter and 5065mm thickness to provide test specimens for the permeameter. Test specimens with large voids on the circumference, which could cause sealing problems in the permeameter, were discarded. Two cylindrical discs were tested for each material (batch code) and consequently the coefficient of permeability value presented is an average of two measurements.

7.4.3 Mercury Intrusion Porisimetry

Two mercury intrusion porosimeters were used in the pore measurement analysis, which measured both macropore (Pascal 140) and mesopore regions (Pascal 240), shown in Figure 7.3. Pascal 140 apparatus is used to prepare the sample for the porosimetric analysis and secondly to measure the porosity of solids in the macropore region (1900-300,000 nm). Pascal 240 apparatus is used to determine the pore size and volume in the mesopore range, between 3.7 and 7500 nm of radius, by means of mercury intrusion at high pressures. The results obtained from the analysis are the same as that obtained by the Pascal 140, and can be combined to form a full macro and mesopore analysis.

Both apparatus apply pressure to a sample confined in mercury. The apparatus then record both the intrusion pressure and the amount of mercury intruded into the sample, to enable the PASCAL software provided to calculate the results of the porosimetric analysis.

Figure.7.3 Porosimetry apparatus

The specimens were tested at 6 months after casting. Specimens used in the porosity analysis are taken from cubes used in compressive strength tests. The samples used are taken from the centre of the cube rather than from the edge so there are no trowled or flat surfaces present, which may give a false representation of the porosity. Prior to testing, samples were dried in a fan assisted oven for 48 hrs at 70°C in order to remove as much moisture as possible without disturbing the pore structure. Specimens were then removed from the oven and stored in airtight bottles with silica gel crystals to absorb any moisture present until testing.

Mercury intrusion porosimerty is based on the capillary law governing liquid penetration into small pores. This law in the case of non-wetting liquids like mercury and pores of cylindrical shape, is expressed by Washburn equation:

$$pr = -2y\cos\theta \qquad \text{Equation 7.17}$$

Where:

p = absolute applied pressure

r = pore radius

y = mercury surface tension

θ = contact angle

Therefore when expressed in terms of pore radius equation 7.17 becomes:

$$r = \frac{-2y\cos\Theta}{p} \qquad \text{Equation 7.18}$$

It can be seen that pore radius is inversely proportional to the applied pressure. By using the average values of 141.3° for contact angle and 480dynes/cm for surface tension the relationship 7.18 can be expressed as:

$$r = \frac{750000}{p} \qquad \text{Equation 7.19}$$

Where:

r = pore radius expressed in nanometers (nm)

p = absolute applied pressure expressed in kPa

Note: 1kPa = 10^4 dyne/cm^2

Equation 7.19 is used for the approximation of pore radius by the porosimetry equipment, however it must be stated that in reality cylindrical pores almost do not exist and are more irregular in shape.

7.4.4 Freeze-Thaw Testing

A detailed description of the free-thaw testing procedure procedures is given in section 4.4.5 of Chapter IV.

The freeze - thaw test apparatus used in the present investigation consists of a chamber together with the necessary refrigerating and heating equipment and controls as shown in Figures 4.4 and 4.5. It produces continuously and automatically reproducible freeze-thaw cycles within the specified temperature ranged. One of the limitations of the equipment used in this investigation is that there is no control over the rate of freezing or thawing. The feedback from the computer controls is related to the final pre-set temperatures, which control the inputs to the system.

The duration of the freezing cycle was 100 minutes and for thawing was 24 minutes, followed by 10 minutes rain and 10 minutes to allow excess water to drain away. Rain water was chilled to 4°C before being allowed to come in contact with the frozen specimen surfaces in order to prevent thermal shock. The specimens were subjected to a total of 100 freeze-thaw cycles in 240 hours. The nominal freeze-thaw cycle used in this investigation consisted of alternatively lowering the temperature of specimens from +25°C to -15°C and raising it from -15°C up to +25°C. Temperature and humidity were monitored using a Solatron data logger. The cycles selected provided complete freezing and thawing of the test specimen due to the small specimen size and moderate freezing ad thawing rates. A typical freeze-thaw temperature profile is shown in Figure 7.4. The salient features of the profile are a steady rate of change of temperature on the freeze down cycle and maintenance of a constant temperature for a pre-set length of time; a steady thaw rate to a pre-set temperature and the maintenance of that temperature.

The test specimens were immersed in water (at 20°C) 48 hours prior to being subjected freeze-thaw cycles. Omnidirectional freezing was carried out by placing the specimens on a wire tray which was elevated from the metal floor of the chamber to allow drainage and to prevent thermal bridging. Samples were removed from the chamber after every ten freeze-thaw cycles, at the end of the thawing cycle, transferred to the laboratory and held under water (18°-20°C) for half hour, before being weighed. It was thus ensured that in each case the saturated mass was recorded, with no ice remaining inside the pores.

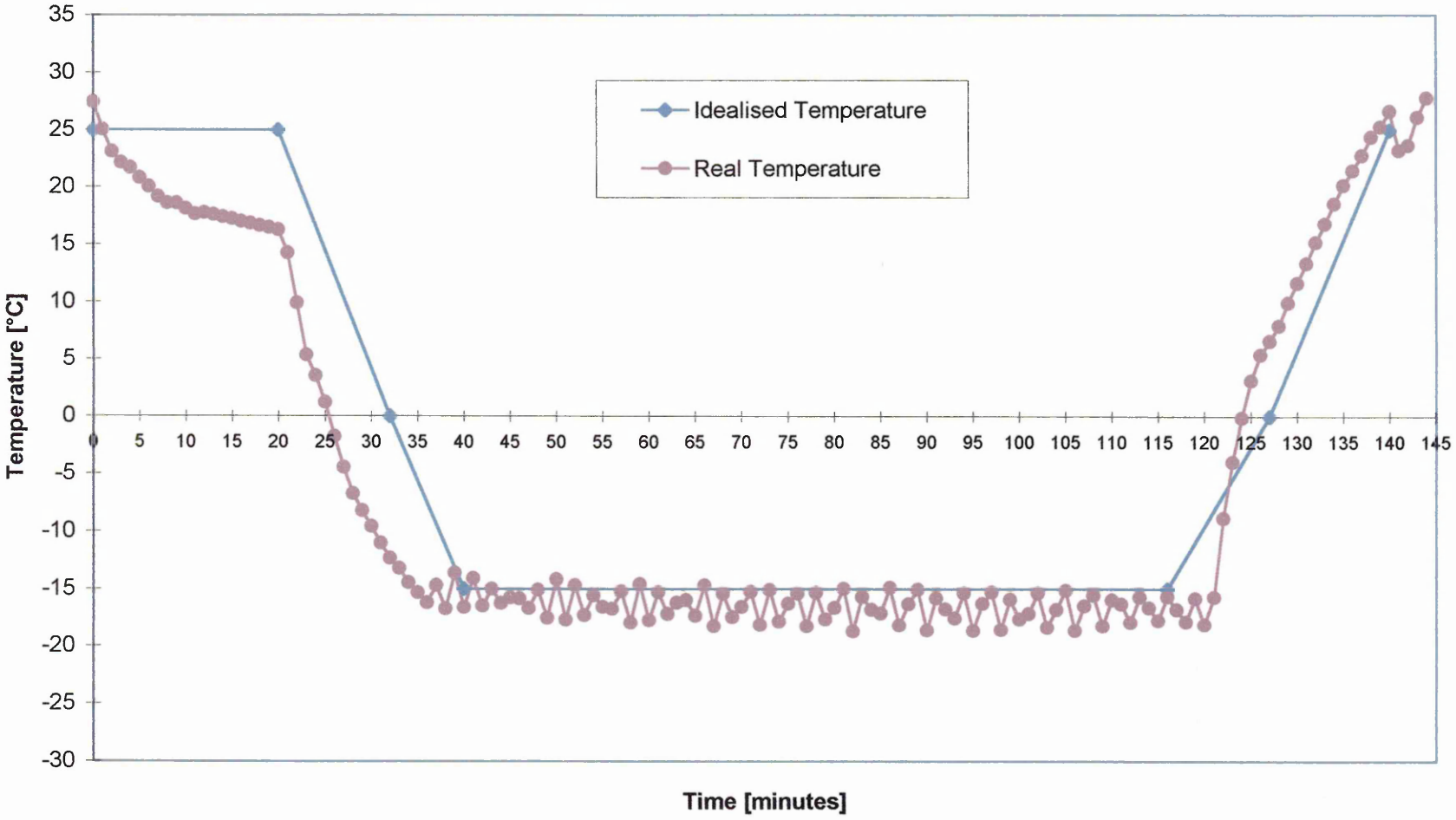

Figure 7.4 Comparison between idealised temperature profile and real test temperature

Changes in weight were recorded as well as making a visual inspection of the specimens during the test. At the end of 100 freeze-thaw cycles the specimens were removed from the chamber and left to dry out at ambient temperature until their mass was constant. Two cubes from each mix (batch code) listed in Table 7.7 and 7.8 were used to determine the residual compressive strength after 100 freeze –thaw cycles, according to BS 1881 Part: 116[137]. Consequently each residual compressive strength value is an average of two measurements. The residual compressive strength was expressed as a percentage of the compressive strength of the corresponding cube specimens which were not subjected to freeze-thaw cycling.

7.4.5 Fire Resistance Tests

7.4.5.1 Test Equipment

The equipment used for determining the fire resistance of alkali activated fly ash materials consisted of a furnace and a control module. The furnace is type GPC 1200/4, manufactured by Carbolite Company Limited as shown in Figure 7.5.

Figure 7.5 Furnace chamber of the fire testing equipment

The furnace is 730 mm high, 540 wide and 775 mm deep (external dimensions) with usable internal dimensions of 150x200x400 mm. The furnace door which is insulated with low thermal mass insulation, opens outwards and upwards and has safety weights on both sides. The control module is type West Gardian QG series programme controller as shown in Figure 7.6.

One complete revolution of the control module cam represents the pre-set time for one cycle of operation. The radial distance from the centre of the cam represents the desired set temperature. By marking the desired temperature on each line of the cam a time -temperature relation is plotted. Each mark is then connected with a line and the cam is cut to give the exact programme desired as shown in Figure 7.7. The cam follower is geared directly to a set point indicator so that the temperature setting at any time during the cycle can be observed.

Figure 7.6 Control module of the fire testing equipment

7.4.5.2 Temperature profile

Although the maximum temperatures reached during building fires are of the order of 1000-1200°C, such high temperatures occur only at the surface of the exposed structural members[111].

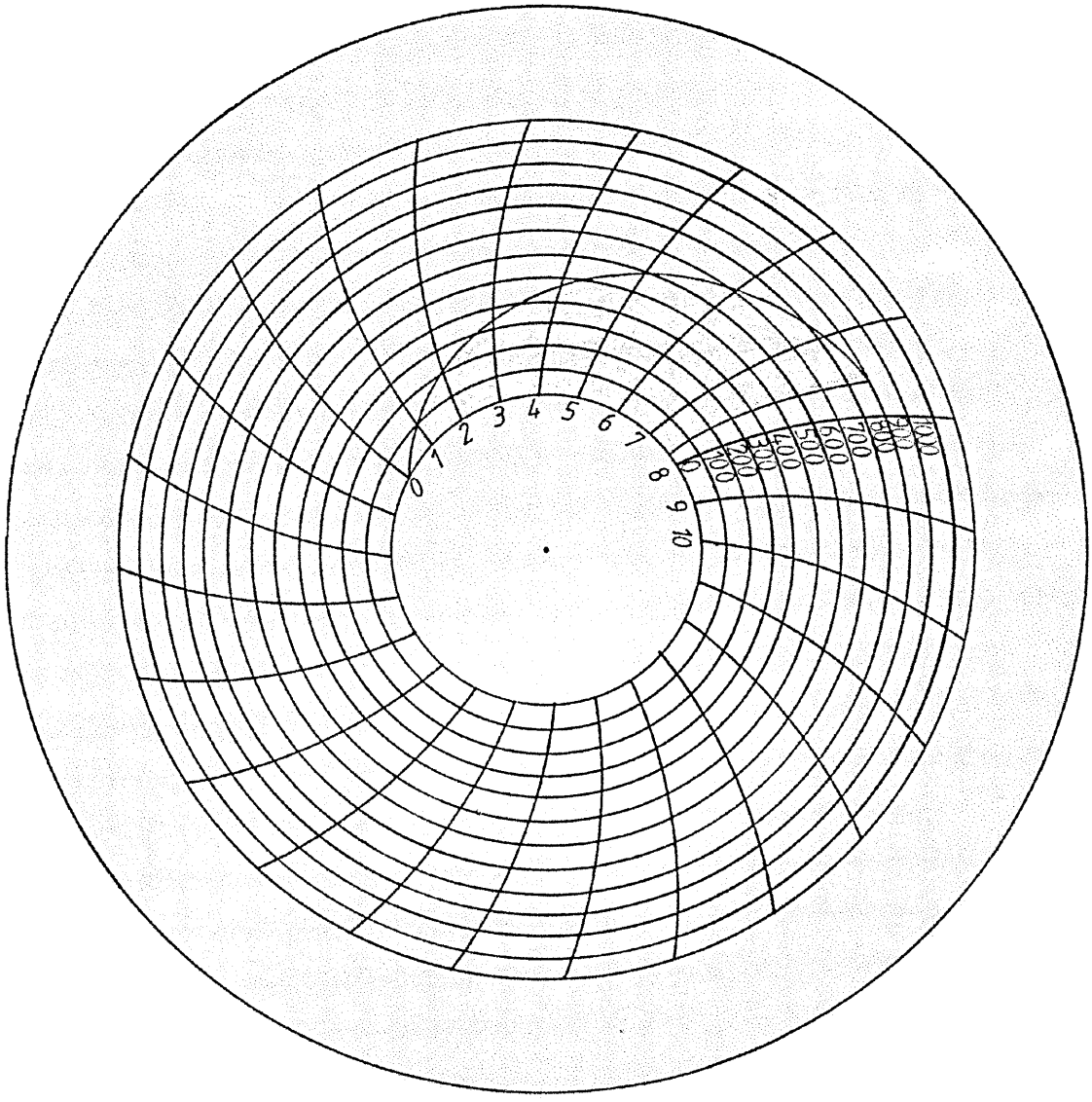

Figure 7.7 Time-temperature profile used in the fire tests.

Taking into account the relatively small size of the test specimens and the fact that the cubes were exposed on all six faces, it was decided to limit the maximum temperature to 600°C. The specimens were heated at a rate of 2°C per minute to the maximum temperature 600°C. After 600°C was reached, it was maintained constant for a further 60 minutes. The specimens were then cooled inside of the furnace. Each specimen was placed on a thermal insulation supporter in order to ensure that the overall surface of the specimen was heated uniformly. Figures 7.8 and 7.9 present the typical heating and cooling profiles for the alkali activated materials and the alkali activated fibre reinforced materials, respectively. The heating and cooling profiles were recorded for each run using a Solatron data logger, as seen in Figure 7.10, and mineral insulated thermocouples type K, as seen in Figure 7.11. The thermocouples consisted of two wires (Ni-Cr and Ni-Al) encapsulated in a mineral metal sheet resistant to temperatures up to 1100°C. Before and after exposure to high temperatures the test specimens were weighed and measured on all six faces.

7.4.5.3 Test Measurements

Damage caused by high temperature was assessed by measuring the pulse velocity and residual compressive strength of the alkali activated material. The pulse velocity measurements were conducted before and after fire testing, according to BS 1881 Part 203[157]. The apparatus used was a PRUNDITE (Portable Ultrasonic non-destructive Digital Indicating Tester) as shown in Figure 7.12.

A pulse of longitudinal vibration is produced by an electro-acoustical transducer, which is held in contact with the surface of the material under test. After traversing a known path length L in the material the pulse of the vibration is converted into an electrical signal by a second transducer. Electronic timing circuits enable the transit time T of the pulse to be measured (BS 1881, 203[157]).

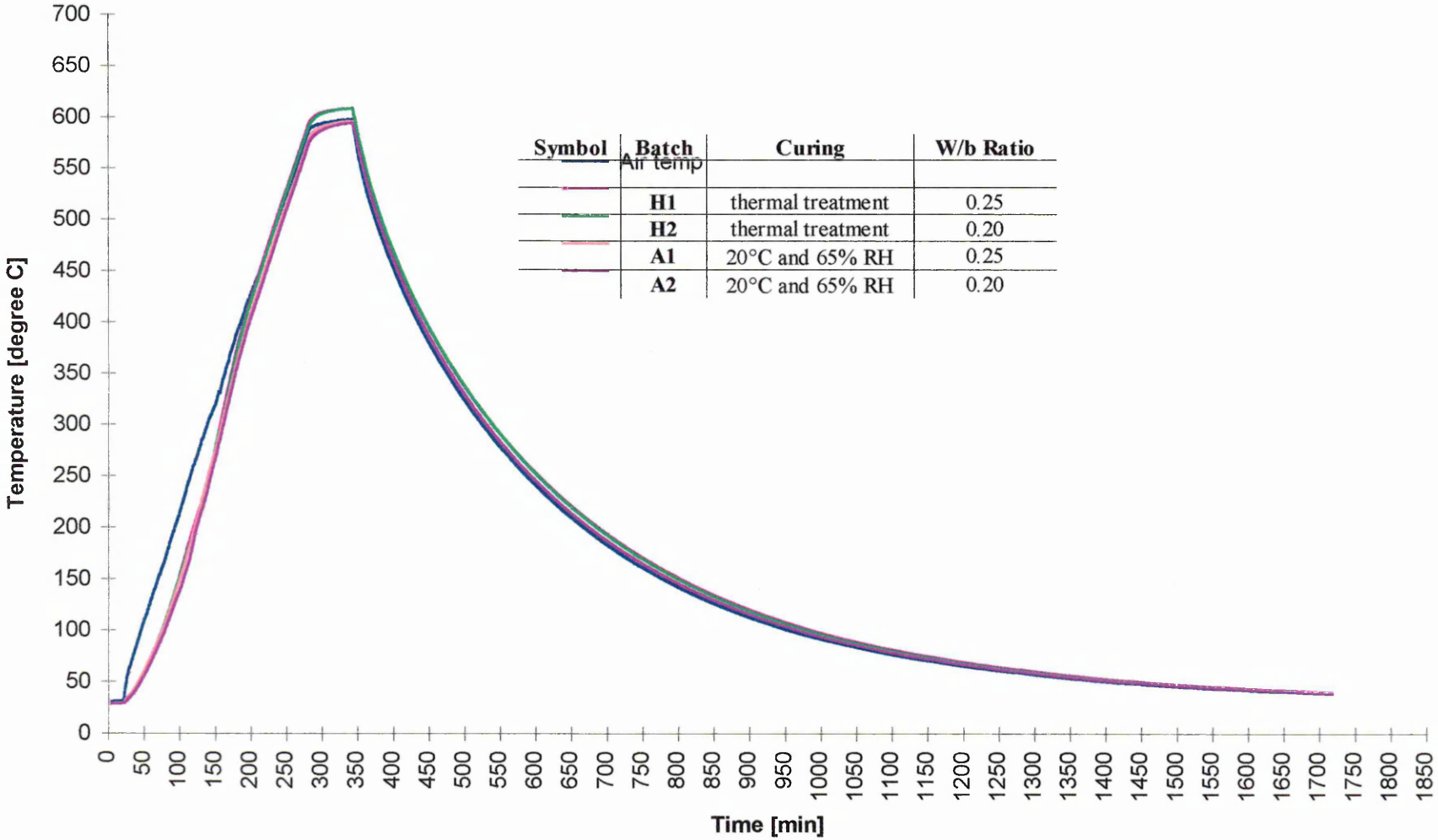

Figure 7.8 Temperature profile of alkali activated mortar specimens subjected to high temperatures

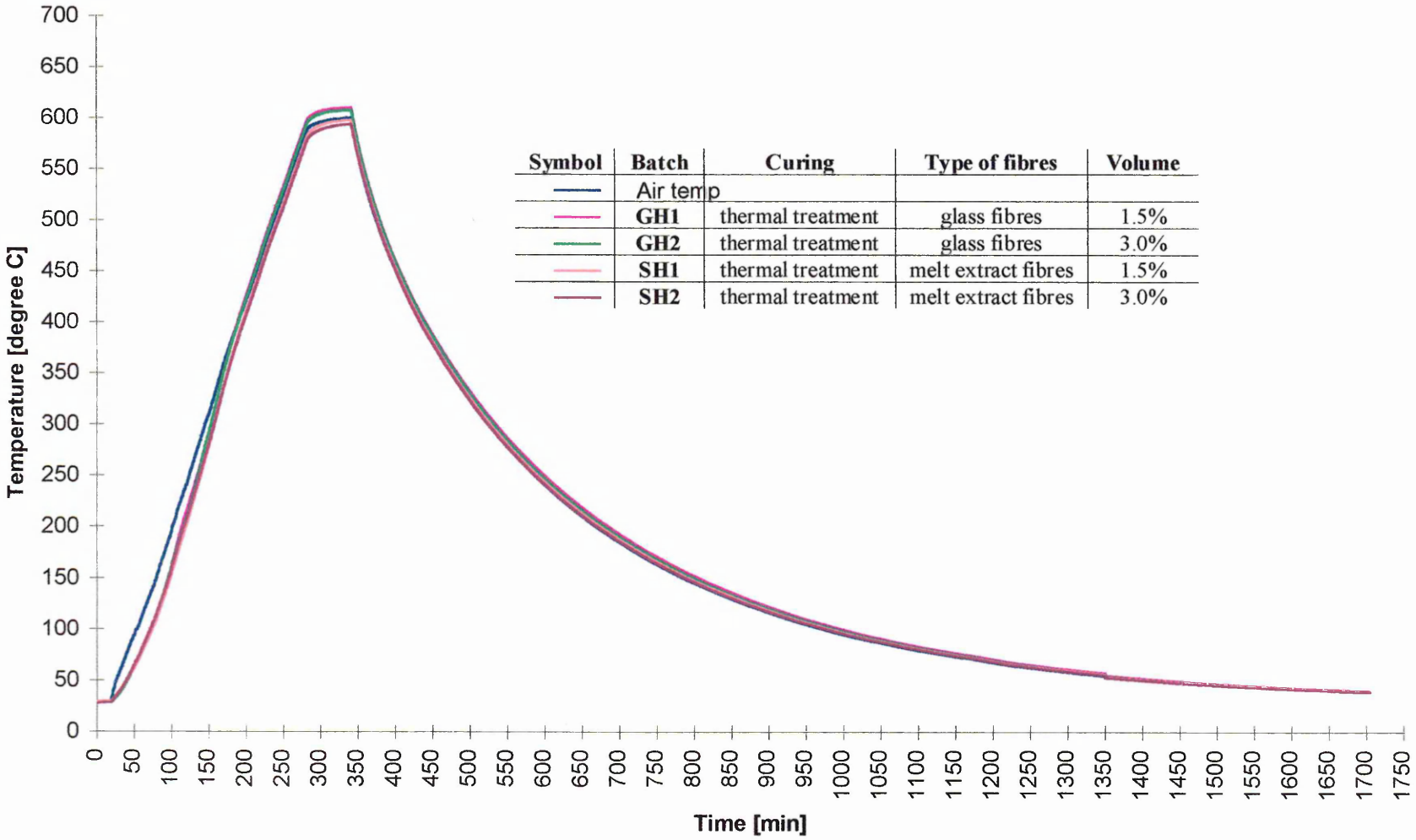

Figure 7.9 Temperature profile for fibre reinforced specimens subjected to high temperatures

Figure 7.10 Data logger used to record the heating and cooling profile

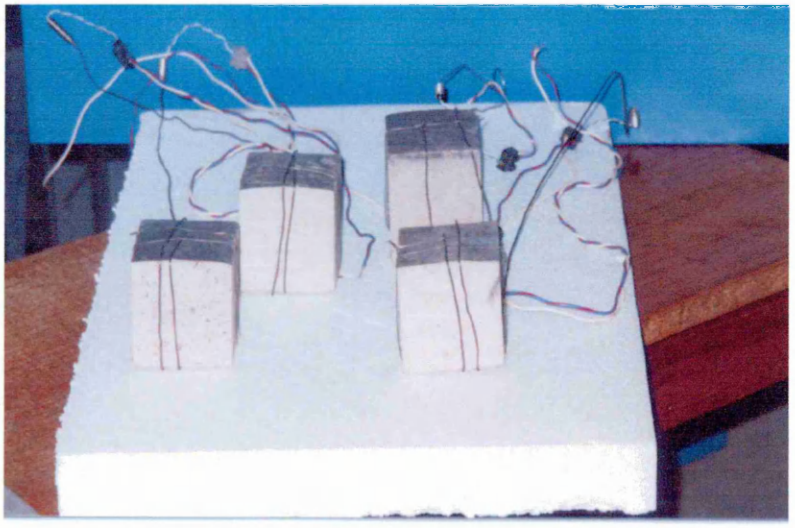

Figure 7.11 Test specimens and mineral insulated thermocouples

The pulse velocity measurements were taken by placing the two traducers on opposite faces (direct transmission) as seen in Figure 7.12. The pulse velocity measurements were within an accuracy of ± 2% which allows a tolerance in the separate measurements of path length and transit time of ± 2%. The path length was

measured using a pair of vernier callipers which were calibrated regularly against accurate standards.

Figure 7.12 Portable Ultrasonic non-destructive digital indicating tester under direct transmission of ultrasonic pulse

The pulse velocity was calculated using the following formula

$v = L/T$ [m/s] Equation 7.17

where:

L- is the path length [m]

T- is the time required by the pulse to transverse the path length [s]

Two cube specimens from each mix (batch code) listed in Table 7.7 and 7.8 were used. The pulse velocity was measured on two pairs of opposite faces of the two cubes as shown in Figure 7.14. Each pulse velocity value is the average of four measurements.

Residual compressive strength of the specimens was then determined after exposure to high temperatures (up to 600°C). The residual compressive strength for each batch of material was the average of two cube specimens. The residual compressive strength was expressed as percentage of the compressive strength of the corresponding cube specimens which were not subjected to fire testing.

4.1.1.1 Choice of test specimens

A detailed description of the choice of specimens is given in section 5.4.3 of Chapter V. Specimens of acceptably large dimensions (75mm cubes and 100mm diameter, 200mm height cylinders) were used in the investigations on physical properties and durability properties of alkali activated materials. Three cubes per mix (batch code) were used for the density and pore structure investigation. Two cubes were subjected to freeze - thaw cycling and another two were used for the fire resistance tests. Two discs (100mm diameter, 50mm height) per mix (cut from the cylinder specimen as described in section 7.4.2) were used for the permeability tests.

7.5 RESULTS AND DISCUSSION

7.5.1 Influence of water/binder ratio on physical properties

7.5.1.1 Density

The bulk and solid densities of the alkali activated fly ash materials together with the percentage differences in density resulting from changes in the water binder ratio (equations 7.21 and 7.22) are presented in Table 7.10. The results are also presented in Figures 7.13 and 7.14. The bulk density results are within the range 2001 to 2063 kg/m^3. A small decrease (less than 5%) in bulk density is consistently observed with changing water binder ratios from 0.20 to 0.25, for all curing conditions. For example, under 20°C and 65% RH curing, the bulk density of materials with w/b=0.25 (batch code A1) is 1.7% lower than the bulk density of corresponding materials of w/b=0.20 (batch code A2).

Solid density results follow similar trends as bulk density results. The decrease in solid density with the increase in the water/binder ratio from 0.20 to 0.25 is small (less than 10%), for all curing conditions, see Figure 7.14. For example, thermal cured material of water/binder=0.25 (batch code H1) shows a reduction of 6.4% in solid density compared with corresponding material with water/binder ratio of 0.20. (batch code H2).

Symbol	Batch	Curing	W/b Ratio	Hardener
	A1/A2	20°C and 65% RH	0.25/0.20	0%
	KA1/KA2	20°C and 65% RH	0.25/0.20	20%
	M1/M2	20°C and 95% RH	0.25/0.20	0%
	KM1/KM2	20°C and 95% RH	0.25/0.20	20%
	H1/H2	thermal treatment	0.25/0.20	0%

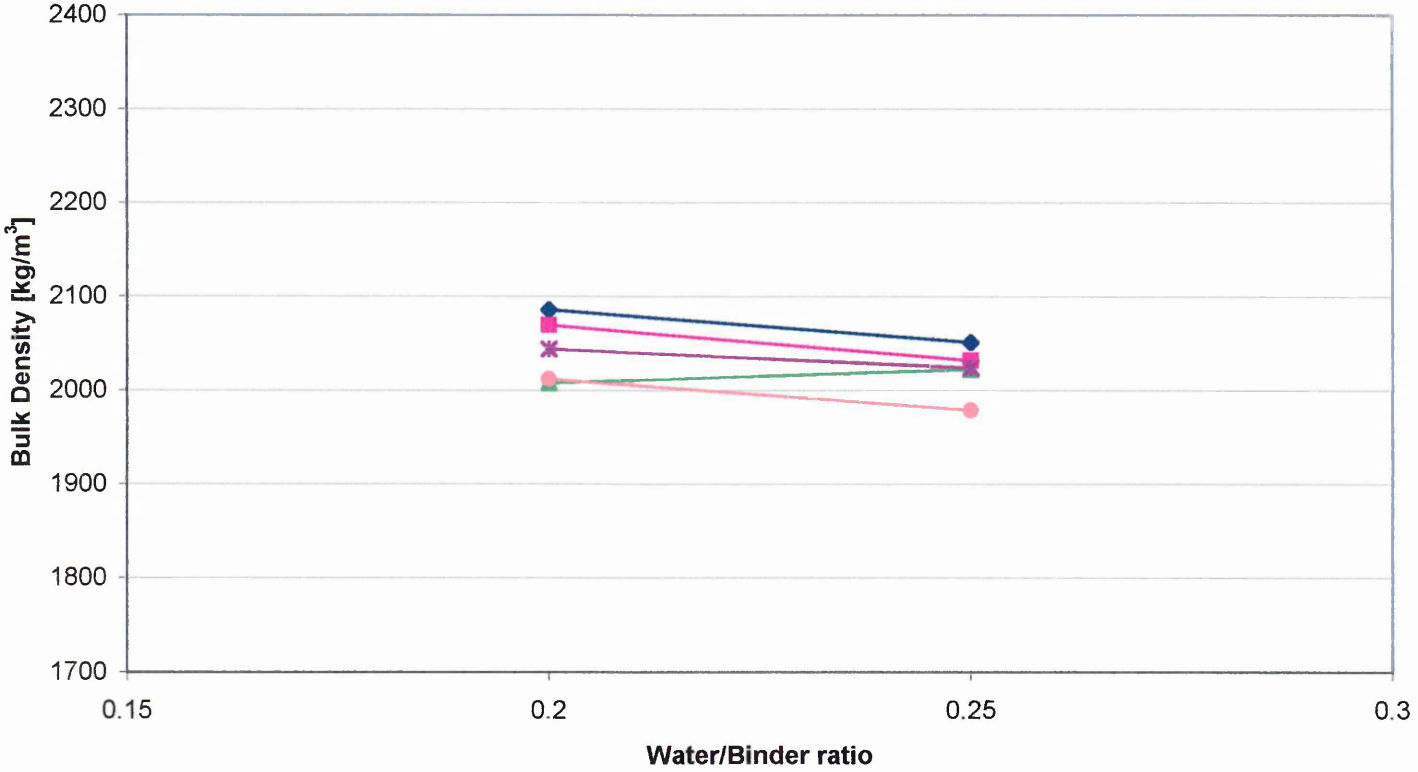

Figure 7.13 Relationship between bulk density and water/binder ratio for different curing conditions

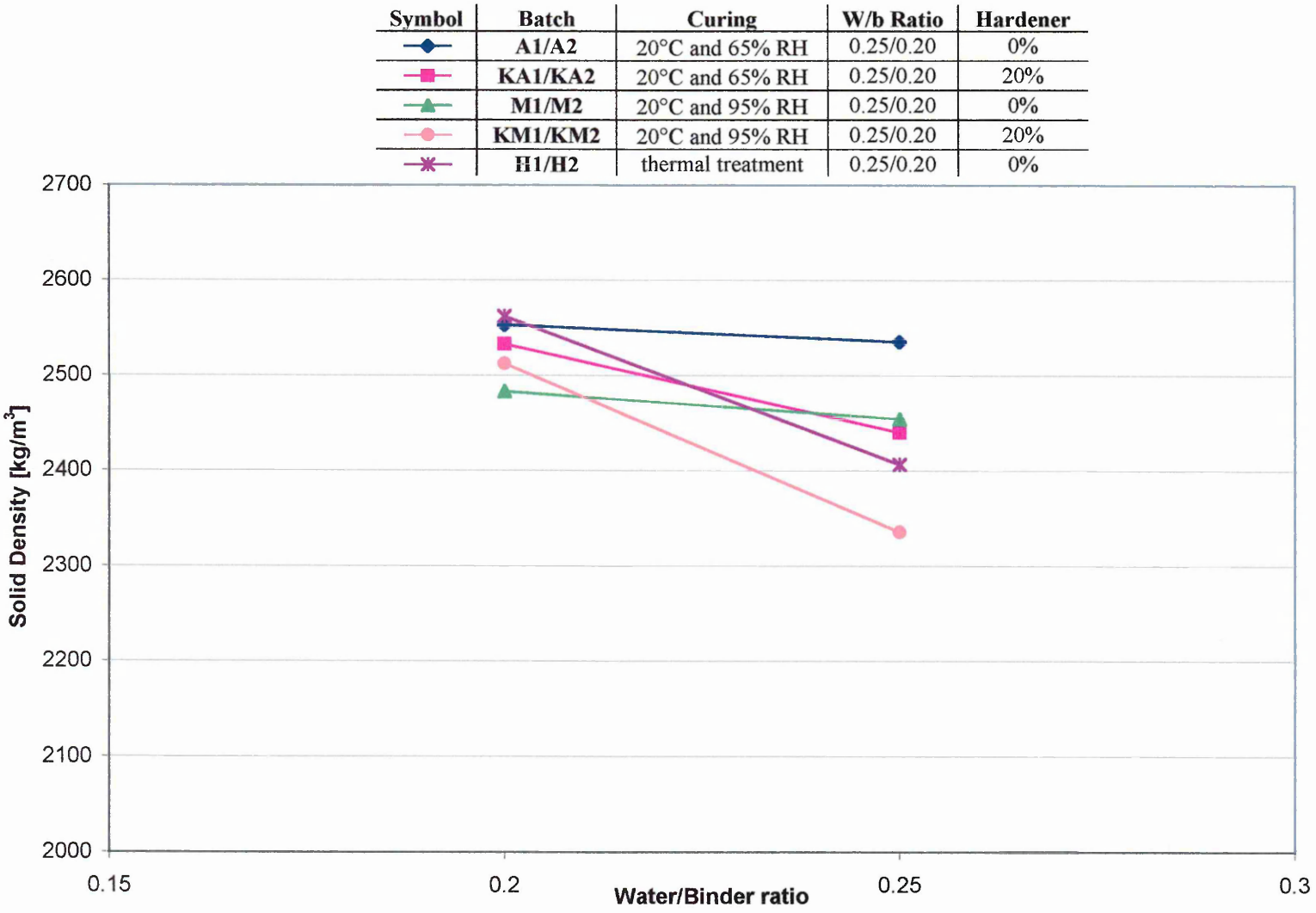

Figure 7.14 Relationship between solid density and water/binder ratio for different curing conditions

Table 7.10 Effect of water/binder ratio a density

Batch Code	Curing conditions	Water/ Binder	Bulk Density [kg/m^3]	Difference in ρ_{bulk}	Solid Density [kg/m^3]	Difference in ρ_{solid}
A1	20°C and 65% RH	0.25	2045	-	2541	-
A2	20°C and 65% RH	0.2	2080	-1.7%	2559	-0.7%
KA1	20°C and 65% RH	0.25	2026	-	2446	-
KA2	20°C and 65% RH	0.2	2063	-1.8%	2539	-3.8%
M1	20°C and 95% RH	0.25	2016	-	2460	-
M2	20°C and 95% RH	0.2	2001	0.7%	2471	-1.1%
KM1	20°C and 95% RH	0.25	1973	-	2340	-
KM2	20°C and 95% RH	0.2	2006	-1.7%	2518	-7.6%
H1	thermal treatment	0.25	2018	-	2412	-
H2	thermal treatment	0.2	2038	-1.0%	2568	-6.4%

$$Difference\ in\ \rho_{bulk} = \frac{Apparent\ Bulk\ Density\ (w/b = 0.25) - Apparent\ Bulk\ Density\ (w/b = 0.20)}{Apparent\ Bulk\ Density\ (w/b = 0.25)} \quad \text{Equation 7.21}$$

$$Difference\ in\ \rho_{solid} = \frac{Solid\ Density\ (w/b = 0.25) - Solid\ Density\ (w/b = 0.20)}{Solid\ Density\ (w/b = 0.25)} \quad \text{Equation 7.22}$$

The general trend of decreasing density (bulk and solid) with increasing water/binder ratio is common to hydraulic cementitious materials[81]. The presence of voids in concrete greatly decreases its density. Voids in concrete are in fact air bubbles of entrapped air or spaces left after the water has been removed. The volume of the latter depends mainly on the water/binder ratio of the mix. Therefore, for any given method of compaction there is an optimum water content of the mix at which the sum of the volumes of air bubbles and water space will be minimum[81]. At this optimum water content the highest density ratio of the concrete would be obtained. Increasing the workability of the mix requires an increase in the water content and since this is the lightest constituent of the mix there is a significant reduction in the density of the concrete when water content is increased.

The results from the present investigation show that the decrease in the density of alkali activated materials with an increase in the water/binder ratio (from 0.20 to 0.25) is consistent but not large. This is due to the fact that the total water content of the mix increases from 8.20% to 10.28% (with increasing the water/binder ratio from 0.20 to 0.25) which probably is not large enough to produce significant changes in the pore size and volume. Consequently the change in density is small.

7.5.1.2 Water absorption and apparent porosity

A summary of the water absorption and apparent porosity results together with the percentage differences in apparent porosity (equation 7.23) and water absorption (equation 7.24) resulting from changes in the water binder ratio are presented in Table 7.11. The results are also plotted in Figures 7.15 and 7.16. The water absorption and apparent porosity results for the alkali activated fly ash materials are within the range 7.79% to 9.98% and 15.69% to 20.75% respectively.

Table 7.11 Influence of water/binder ratio on water absorption and apparent porosity

Batch Code	Curing conditions	Water/ Binder	Wa [%]	Reduction in w_a	Apparent Porosity(p) [%]	Reduction in p
A1	20°C and 65% RH	0.25	9.38	-	19.2	-
A2	20°C and 65% RH	0.20	8.84	5.8%	18.73	4.0%
KA1	20°C and 65% RH	0.25	8.3		17.15	
KA2	20°C and 65% RH	0.20	8.91	-7.3%	18.73	-9.2%
M1	20°C and 95% RH	0.25	8.77		18.02	
M2	20°C and 95% RH	0.20	9.35	-6.6%	19.03	-5.6%
KM1	20°C and 95% RH	0.25	7.79		15.69	
KM2	20°C and 95% RH	0.20	9.98	-28.1%	20.34	-29.6%
H1	thermal treatment	0.25	7.93		16.33	
H2	thermal treatment	0.20	9.98	-25.9%	20.75	-27.1%

$$Difference\ in\ p = \frac{Apparent\ Porosity\ (w/b = 0.25) - Apparent\ Porosity\ (w/b = 0.20)}{Apparent\ Porosity\ (w/b = 0.25)} \qquad \text{Equation 7.23}$$

$$Difference\ in\ w_a = \frac{Water\ Absorption\ (w/b = 0.25) - Water\ Absorption\ (w/b = 0.20)}{Water\ Absorption\ (w/b = 0.25)} \qquad \text{Equation 7.24}$$

The apparent porosity p is related to the bulk and apparent solid density by the following expression as detailed in section 7.4.1.

$$p = \left[1 - \frac{\rho_{bulk}}{\rho_{ApparentSolid}}\right] \cdot 100 \qquad \text{Equation 7.8}$$

Therefore, for any pair of alkali activated materials, when the difference in their bulk density is smaller than the corresponding difference in their apparent solid density, then the apparent porosity differences will increase and vice-versa. Since apparent porosity p is directly related to water absorption, therefore, water absorption will be similarly affected.

Symbol	Batch	Curing	W/b Ratio	Hardener
◆	A1/A2	20°C and 65% RH	0.25/0.20	0%
■	KA1/KA2	20°C and 65% RH	0.25/0.20	20%
▲	M1/M2	20°C and 95% RH	0.25/0.20	0%
●	KM1/KM2	20°C and 95% RH	0.25/0.20	20%
✱	H1/H2	thermal treatment	0.25/0.20	0%

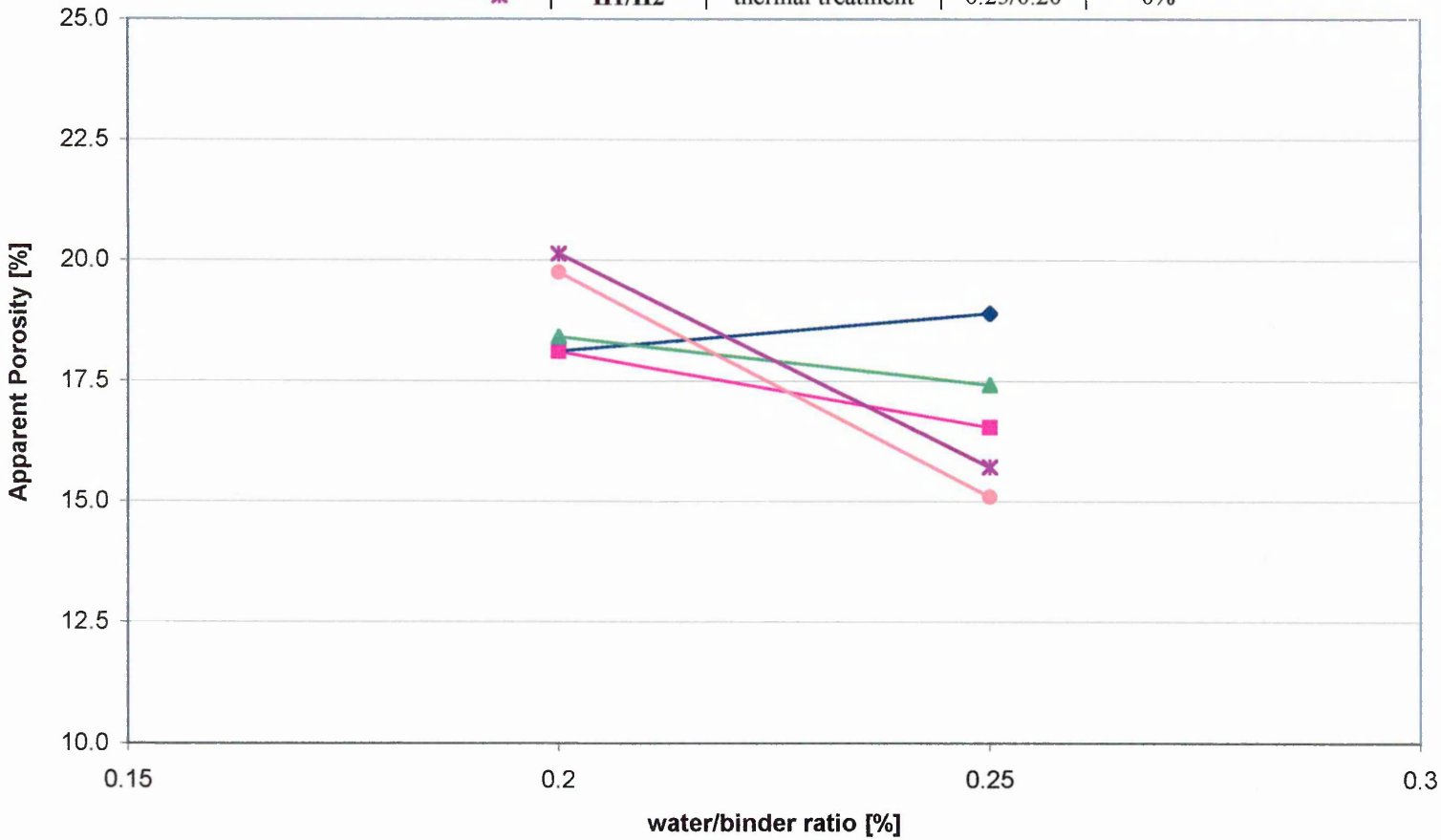

Figure 7.15 Relationship between apparent porosity and water/binder ratio for different curing conditions

Symbol	Batch	Curing	W/b Ratio	Hardener
◆	A1/A2	20°C and 65% RH	0.25/0.20	0%
■	KA1/KA2	20°C and 65% RH	0.25/0.20	20%
▲	M1/M2	20°C and 95% RH	0.25/0.20	0%
●	KM1/KM2	20°C and 95% RH	0.25/0.20	20%
✱	H1/H2	thermal treatment	0.25/0.20	0%

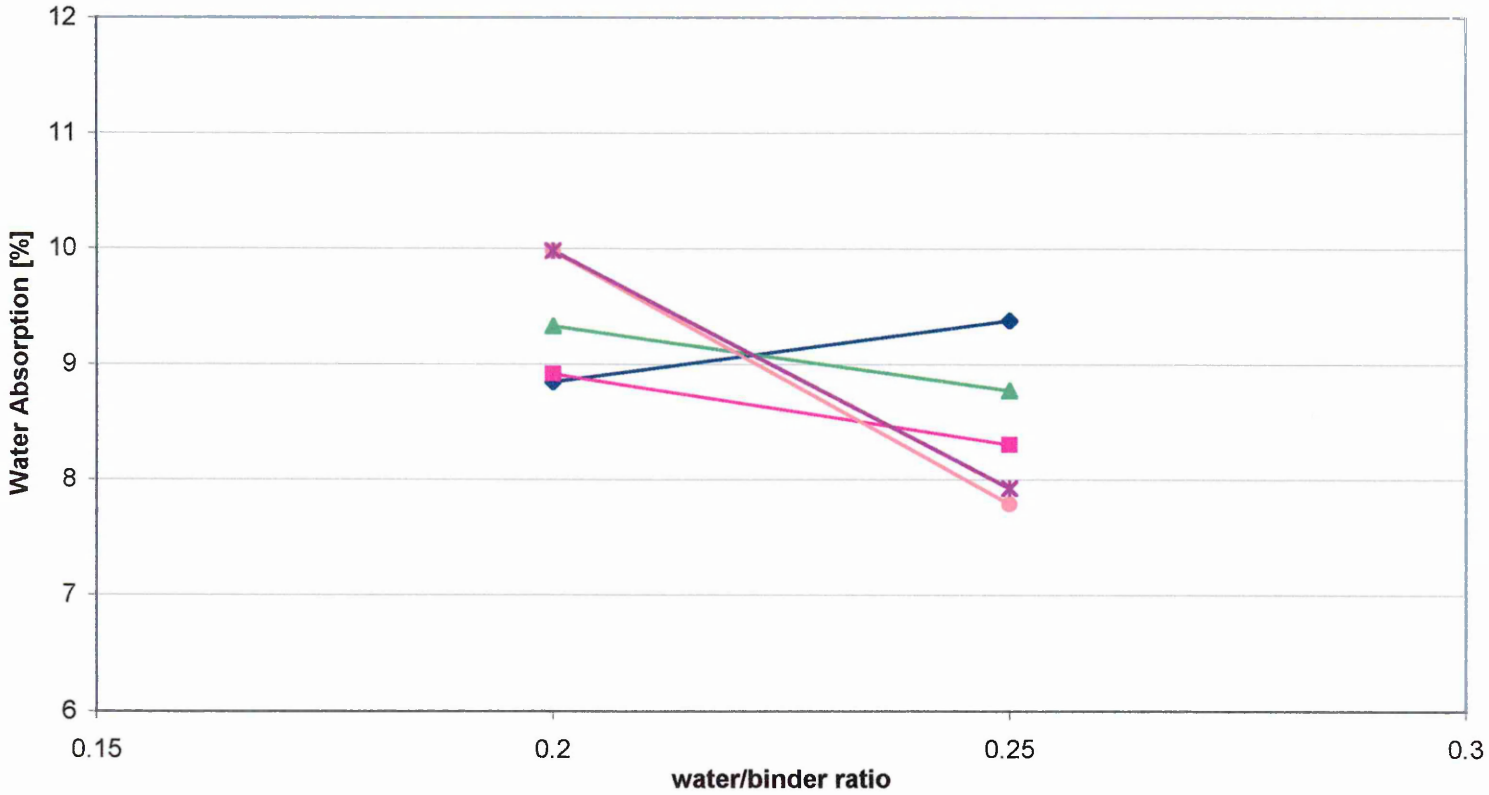

Figure 7.16 Relationship between water absorption and water/binder ratio for different curing conditions

The results presented in Table 7.10 show smaller differences in bulk density than the corresponding differences in solid density with the change in water /binder ratio from 0.20 to 0.25. Therefore, their water absorption and porosity values are decreasing with the increase in water/binder ratio from 0.20 to 0.25 with the exception of materials (batch code A1 and A2) cured under 20°C and 65% RH.

Figure 7.15 shows the relationship between the apparent porosity (p%), and the water/binder ratio for alkali activated fly ash materials subjected to different curing conditions. The corresponding relationship between water absorption (w_a%) and water/binder ratio is shown in Figure 7.16. Figure 7.15 shows that materials with a water/binder ratio of 0.25 (batch code M1, KA1, KM1 and H1) have a lower apparent porosity than materials with a lower (0.20) water /binder ratio (batch code M2, KA2, KM2 and H2). For example, at w/b=0.25 the material cured under 20°C and 95% RH (batch code M1) has an apparent porosity 5.6% lower than the corresponding material of w/b=0.20 (batch code M2). Similarly, the thermally cured material of w/b=0.25 (batch code H1) has an apparent porosity 29.6% lower than the corresponding material with w/b=0.20 (batch code H2). Materials cured under 20°C and 65% RH, on the other hand show a different trend as they have a slightly higher apparent porosity of 19.2% for w/b=0.25 (batch code A1) compared with 18.73% for corresponding material with w/b of 0.20 (batch code A2).

The results for water absorption follow the same trends as those for apparent porosity as the materials with a water/binder ratio (0.25) exhibit a lower water absorption than materials with a lower water/binder ratio of (0.20). For example, at w/b=0.25 the material cured under 20°C and 95% RH (batch code M1) has a water absorption 6.6% lower than the corresponding material (batch code M2) of water/binder = 0.20. Similarly, material of w/b=0.25, thermally treated, (batch code H1) has a water absorption 25.9% lower than the corresponding material with w/b=0.20 (batch code H2). Materials cured under 20°C and 65% RH on the other hand show an opposite trend as they exhibit a 5.8% decrease in the water absorption with reducing the water/binder ratio from 0.25 to 0.20.These results will be discussed further in section 7.4.6 and 7.4.7.

Other researchers have investigated the water absorption properties of alkali activated materials[44]. Freidin and Erell[44] investigated the water absorption of pressed

bricks made of coal fly ash, slag and water glass binder (silica modulus of 2.3) cured in open air at 20-23°C. Their water absorption results were within the range 17% to 24% depending on the water glass content of the mix[44]. These values are much higher than the values obtained in the current investigation and this could be explained by the fact that Freidin and Erell failed to control the Na_2O content in the mix. If the Na_2O content of the mix is too high, unreacted alkali will cause efflorescence during curing and weaken the sample. The cementitious material formed by Freidin and Erell[44] was weak with a very porous microstructure.

7.5.1.3 Coefficient of saturation

A summary of the coefficient of saturation results together with their percentage differences (equation 7.25) resulting from changes in the water/binder ratio are presented in Table 7.12. The results are also plotted in Figure 7.17. The coefficients of saturation for alkali activated materials presented in table are within the range 0.44 %-0.94%. A high coefficient of saturation exceeding 0.8% indicates that over half the available pores would be filled with water[102].

Table 7.12 Influence of water/binder ratio on coefficient of saturation

Batch Code	Curing conditions	Water/ Binder	Coef of Saturation [%]	Change in $c_{saturation}$
A1	20°C and 65% RH	0.25	0.68	-
A2	20°C and 65% RH	0.2	0.44	35.3%
KA1	20°C and 65% RH	0.25	0.69	
KA2	20°C and 65% RH	0.2	0.53	23.2%
M1	20°C and 95% RH	0.25	0.84	
M2	20°C and 95% RH	0.2	0.59	29.8%
KM1	20°C and 95% RH	0.25	0.94	
KM2	20°C and 95% RH	0.2	0.55	41.5%
H1	thermal treatment	0.25	0.76	
H2	thermal treatment	0.2	0.47	38.2%

$$Reduction\ in\ c_{sat} = \frac{Saturation\ Coefficient\ (w/b = 0.25) - Saturation\ Coefficient\ (w/b = 0.20)}{Saturation\ Coefficient\ (w/b = 0.25)}$$ Equation 7.25

Symbol	Batch	Curing	W/b Ratio	Hardener
◆	A1/A2	20°C and 65% RH	0.25/0.20	0%
■	KA1/KA2	20°C and 65% RH	0.25/0.20	20%
▲	M1/M2	20°C and 95% RH	0.25/0.20	0%
●	KM1/KM2	20°C and 95% RH	0.25/0.20	20%
✱	H1/H2	thermal treatment	0.25/0.20	0%

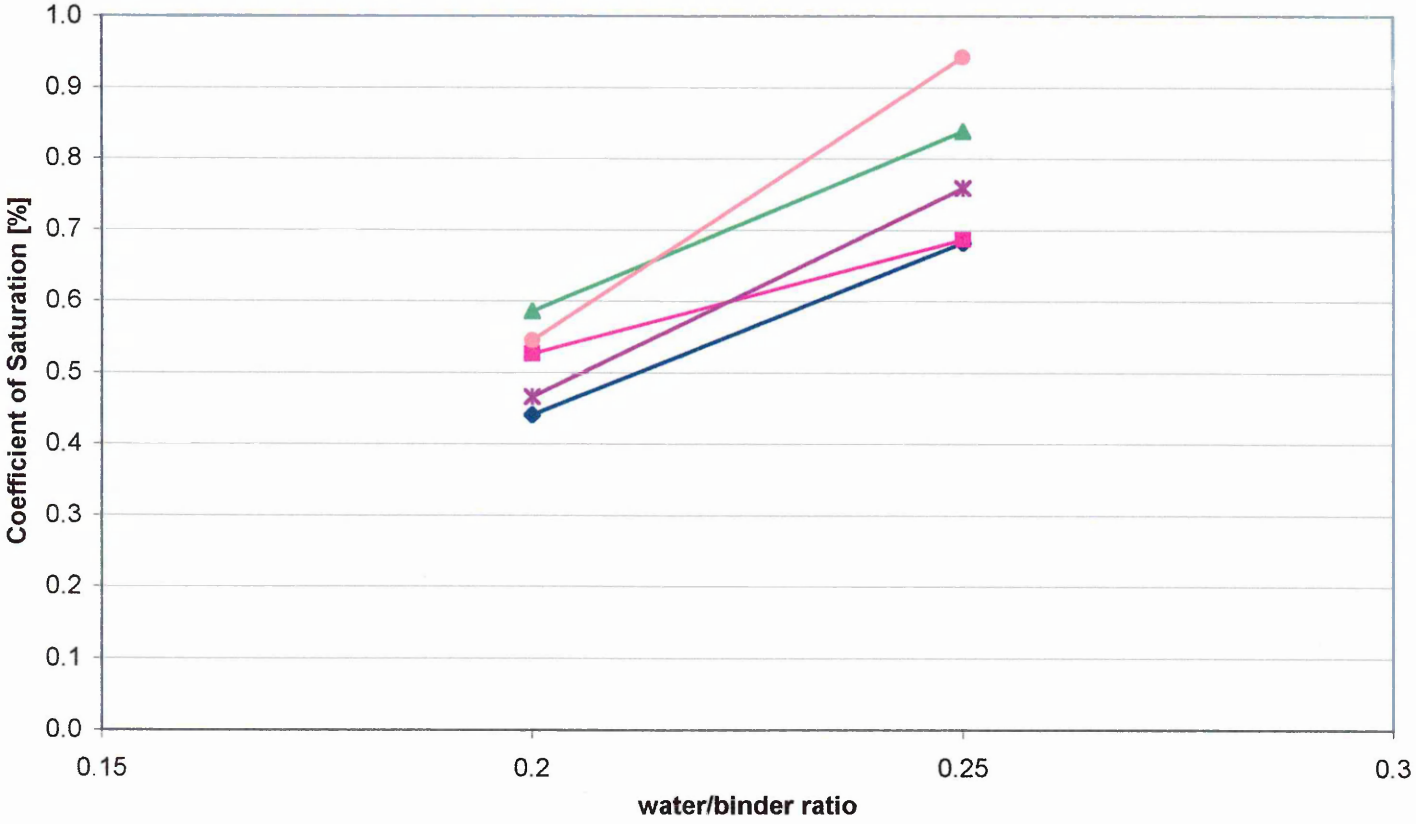

Figure 7.17 Relationship between the coefficient of saturation and water/binder ratio for different curing conditions

Figure 7.17 illustrates the relationship between coefficient of saturation and water /binder ratio for different curing conditions. Materials with a lower water/binder ratio (0.20) exhibit lower coefficient of saturation compared with materials with a higher water/binder ratio of 0.25 for all curing conditions. For example, at w/b=0.25 the material cured under 20°C and 65% RH (batch code A1) has a coefficient of saturation which is 35.3% higher than the corresponding material of w/b=0.20 (batch code A2). Similarly, material of w/b=0.25, thermal treated (batch code H1) has a coefficient of saturation 38.2% higher than the corresponding material with w/b=0.20 (batch code H2).

A comparison of Figures 7.15 and 7.16 with 7.17 shows that the coefficient of saturation results show opposite trends to the apparent porosity and water absorption results. In Figures 7.15 and 7.16 the apparent porosity and water absorption properties decrease with increasing water/binder ratio from 0.20 to 0.25 whereas in Figure 7.19 the saturation coefficient for the corresponding materials increases with increasing of water/ binder ratio. The reason for this difference is the fact that pore structure (size, shape and distribution of pores) can be different for each material. The apparent porosity does not give any indication of the pore size and shape or the volume of sealed pores. The shape and size of pores govern the rate at which the pores are filled with water and, therefore, will influence the coefficient of saturation. From the experimental data obtained in the present investigation, it was found that there is no relation between the porosity and coefficient of saturation and, therefore, knowledge of both properties is required in order to define the pore structure of the material. This agrees with the conclusions reached by other researchers[102].

7.5.2 Influence of relative humidity of curing on physical properties

7.5.2.1 Density

The density (bulk and solid) together with the percentage difference in density resulting from the changes in the humidity of curing of alkali activated fly ash materials (equations 7.26 and 7.27) are presented in Table 7.13. The results are also presented in Figures 7.18 and 7.19. The curing temperature was 20°C in all cases.

Symbol	Batch Code	Curing	W/b Ratio	Hardener
◆	A1/M1	20°C and 65%/95%RH	0.25	0%
■	KA1/KM1	20°C and 65%/95%RH	0.25	20%
▲	A2/M2	20°C and 65%/95%RH	0.20	0%
●	KA2/KM2	20°C and 65%/95%RH	0.20	20%

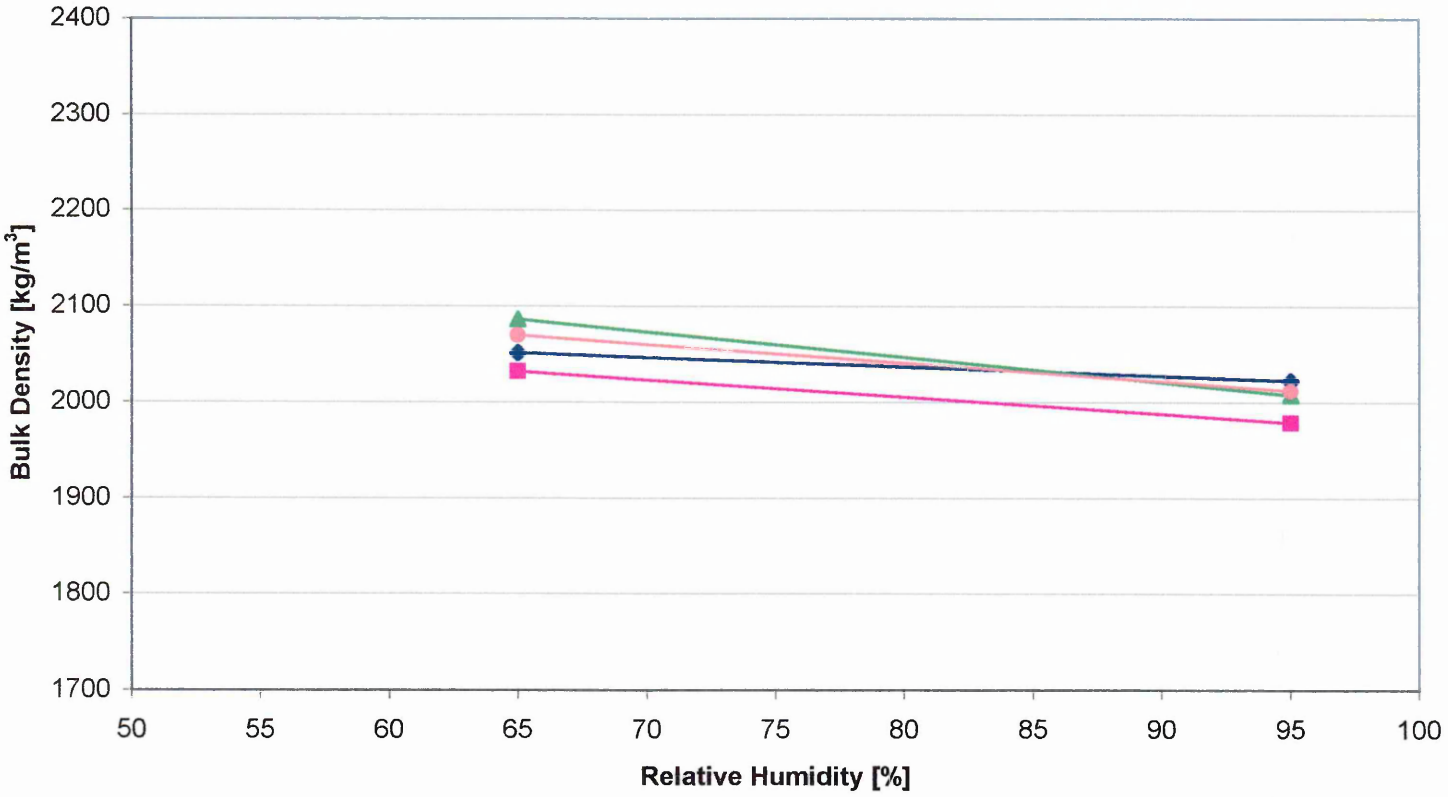

Figure 7.18 Relationship between bulk density and relative humidity of curing

Symbol	Batch Code	Curing	W/b Ratio	Hardener
◆	A1/M1	20°C and 65%/95%RH	0.25	0%
■	KA1/KM1	20°C and 65%/95%RH	0.25	20%
▲	A2/M2	20°C and 65%/95%RH	0.20	0%
●	KA2/KM2	20°C and 65%/95%RH	0.20	20%

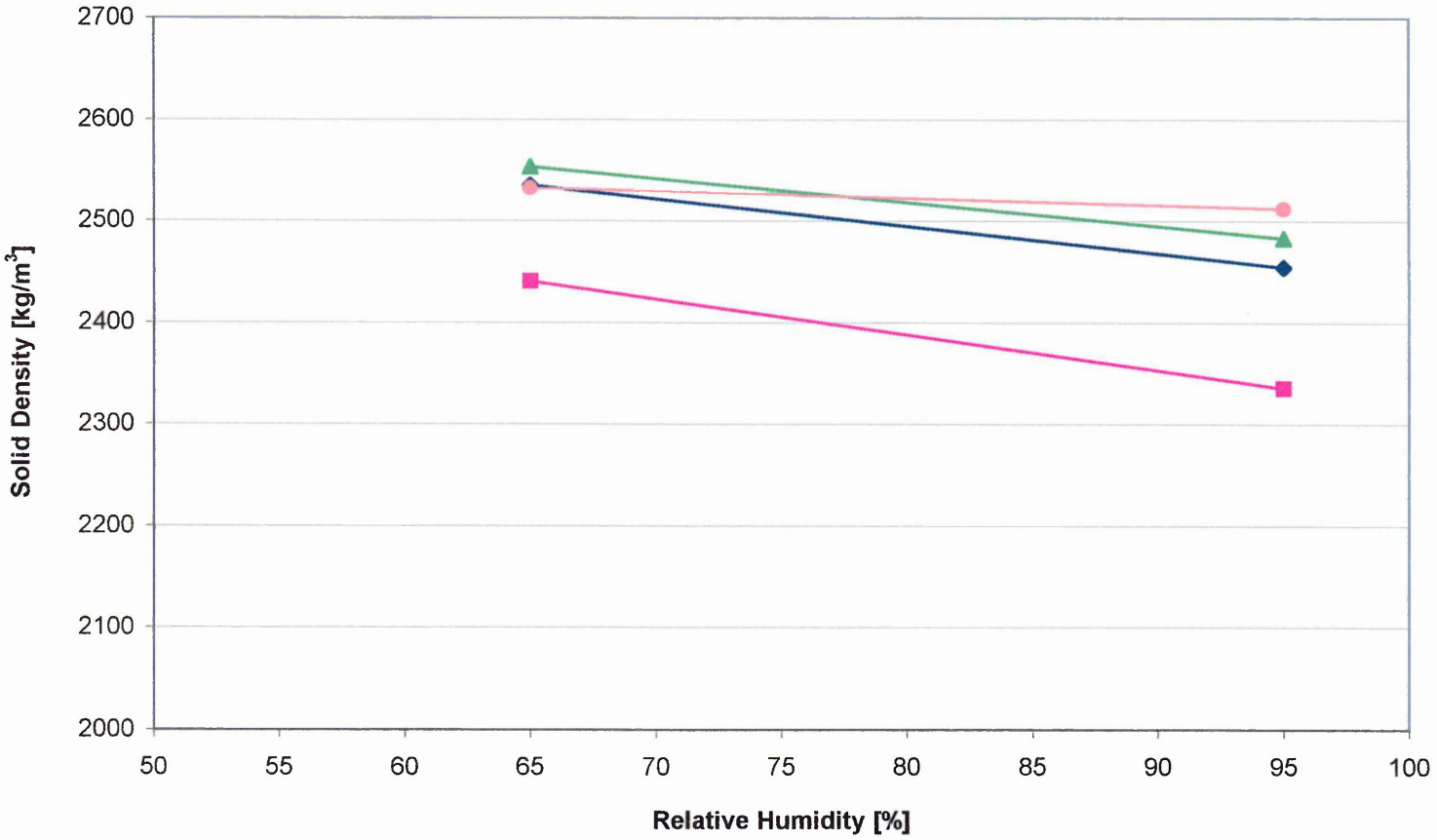

Figure 7.19 Relationship between solid density and relative humidity of curing

Table 7.13 Effect of humidity of curing on density

Batch Code	Curing conditions	Water/ Binder	Bulk Density [kg/m^3]	Difference in ρ_{bulk}	Solid Density [kg/m^3]	Difference in ρ_{solid}
A1	20°C and 65% RH	0.25	2045	-	2541	-
M1	20°C and 95% RH	0.25	2016	1.4%	2460	3.2%
KA1	20°C and 65% RH	0.25	2026	-	2446	-
KM1	20°C and 95% RH	0.25	1973	2.6%	2340	4.3%
A2	20°C and 65% RH	0.2	2080	-	2559	-
M2	20°C and 95% RH	0.2	2001	3.7%	2471	2.7%
KA2	20°C and 65% RH	0.2	2063	-	2539	-
KM2	20°C and 95% RH	0.2	2006	2.8%	2518	0.8%

$$Difference\ in\ \rho_{bulk} = \frac{Apparent\ Bulk\ Density\ (20^{\circ}C\ and\ 65\%RH) - Apparent\ Bulk\ Density\ (20^{\circ}C\ and\ 95\%RH)}{Apparent\ Bulk\ Density\ (20^{\circ}C\ and\ 65\%RH)} \quad \text{Equation 7.26}$$

$$Difference\ in\ \rho_{solid} = \frac{Solid\ Density\ (20^{\circ}C\ and\ 65\%RH) - Solid\ Density\ (20^{\circ}C\ and\ 95\%RH)}{Solid\ Density\ (20^{\circ}C\ and\ 65\%RH)} \quad \text{Equation 7.27}$$

A small decrease (less than 5%) in bulk and apparent solid density is consistently observed with increasing humidity of curing from 65% to 95%, regardless of the water/binder ratio, see Table 7.13. For example at w/b=0.25 materials cured under at 95% RH (batch code M1) exhibit bulk and solid densities 1.4% and 3.2%, respectively, lower than those of corresponding materials cured at 65% RH (batch code A1). The decrease in solid density with the increase in humidity of curing could be due to sealing of pores. When cured under higher humidity the hydration continues for longer and the capillary pores can become blocked by gel and segmented (sealed) pores. Since the products of hydration have a lower density than the solid materials, therefore the density is reduced. This phenomenon is further discussed in section 7.4.6.

7.5.2.2 Water absorption and apparent porosity

A summary of the water absorption and apparent porosity results together with the percentage differences in apparent porosity (equation 7.28) and water absorption (equation 7.29) resulting from changes in the relative humidity of curing are presented in Table 7.14. The results are also plotted in Figures 7.20 and 7.21. The curing temperature was 20°C in all cases.

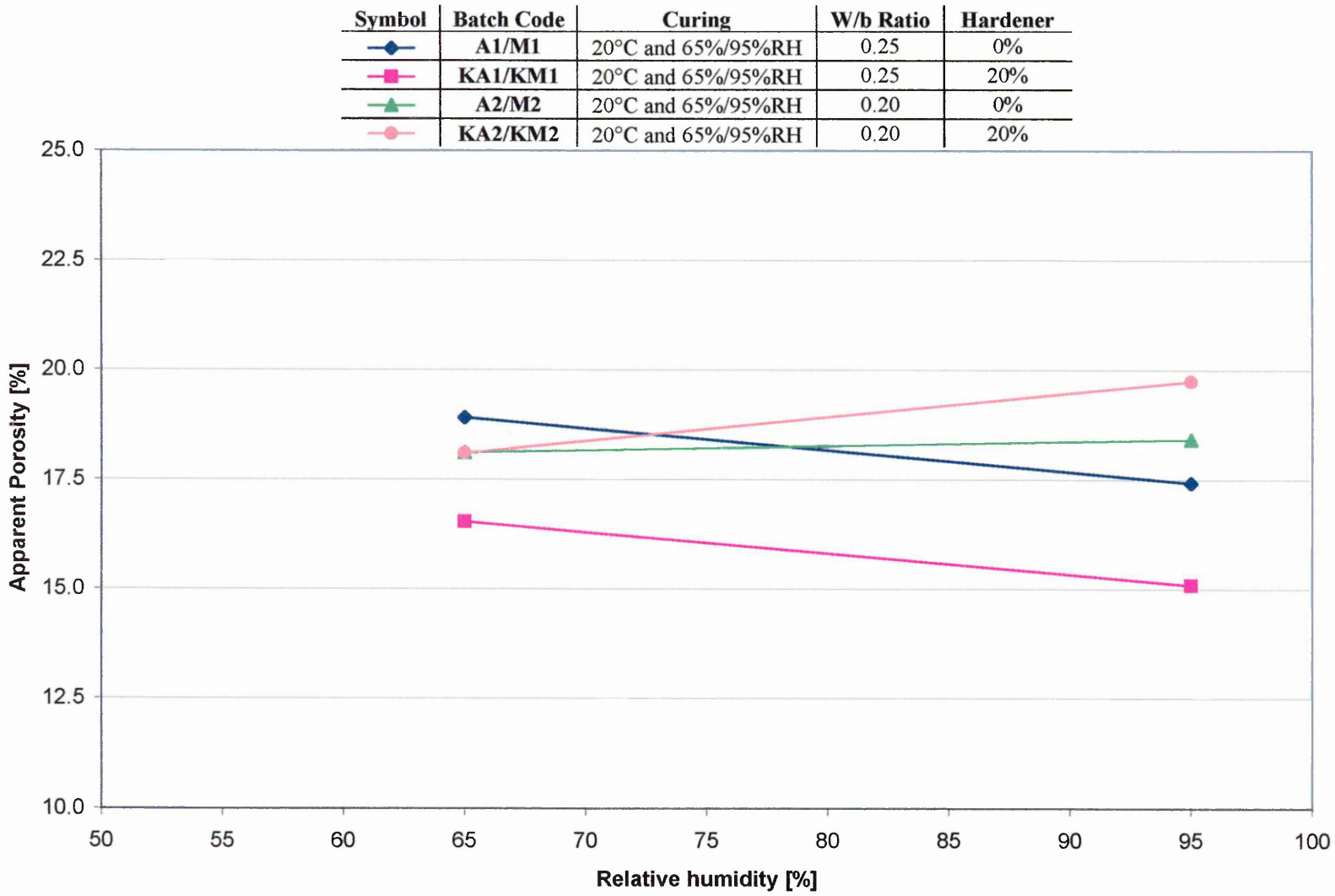

Figure 7.20 Relationship between apparent porosity and relative humidity of curing

Symbol	Batch Code	Curing	W/b Ratio	Hardener
◆	A1/M1	20°C and 65%/95%RH	0.25	0%
■	KA1/KM1	20°C and 65%/95%RH	0.25	20%
▲	A2/M2	20°C and 65%/95%RH	0.20	0%
●	KA2/KM2	20°C and 65%/95%RH	0.20	20%

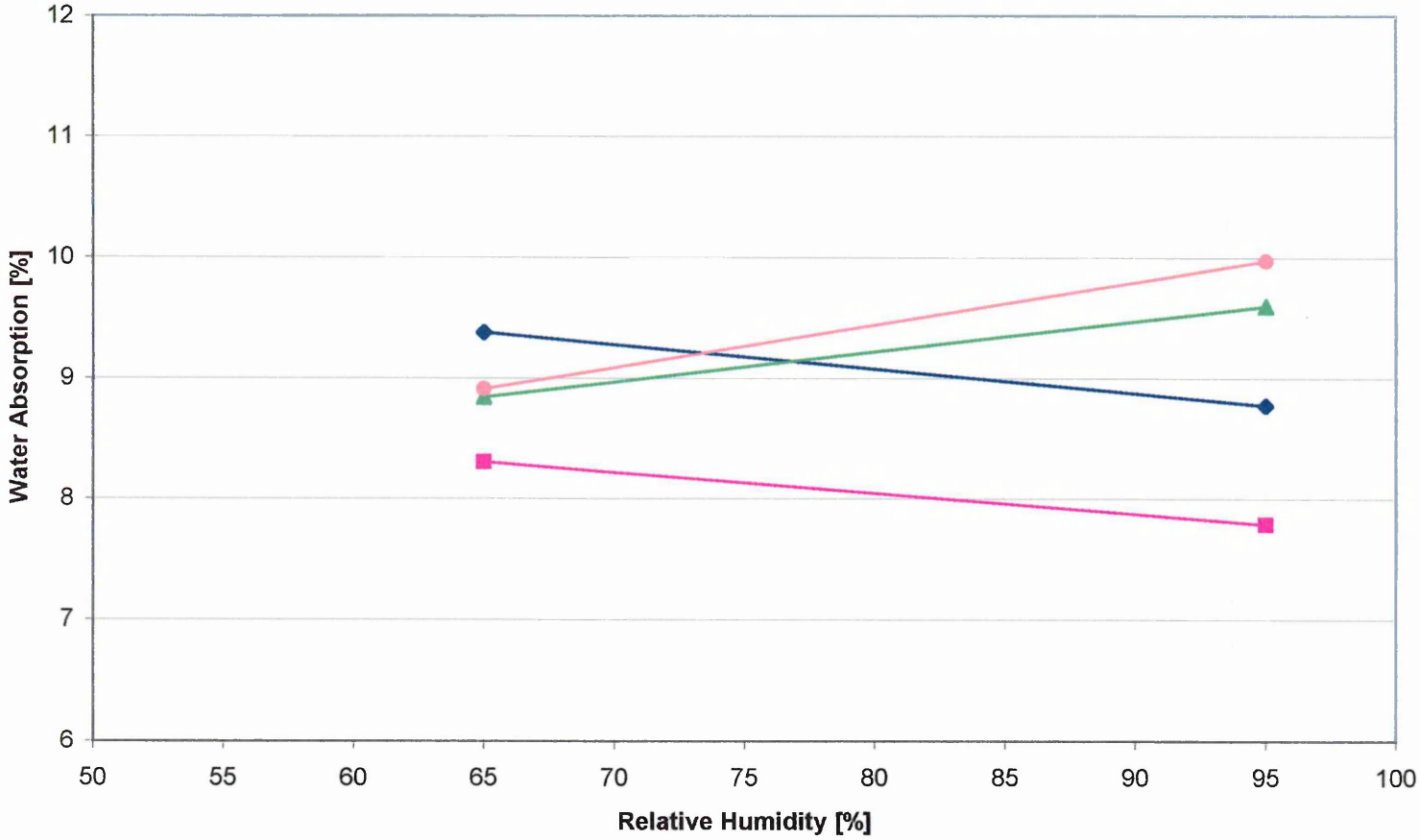

Figure 7.21 Relationship between water absorption and relative humidity of curing

Table 7.14 Influence of relative humidity of curing on water absorption and apparent porosity

Batch Code	Curing conditions	Water/ Binder	Wa [%]	Reduction in 'w_a'	Apparent Porosity [%]	Reduction in 'p'
A1	20°C and 65% RH	0.25	9.38	-	19.52	-
M1	20°C and 95% RH	0.25	8.77	6.5%	18.02	7.7%
KA1	20°C and 65% RH	0.25	8.3		17.15	
KM1	20°C and 95% RH	0.25	7.79	6.1%	15.69	8.5%
A2	20°C and 65% RH	0.2	8.84		18.73	
M2	20°C and 95% RH	0.2	9.35	-8.6%	19.03	-1.6%
KA2	20°C and 65% RH	0.2	8.91		18.73	
KM2	20°C and 95% RH	0.2	9.98	-12.0%	20.34	-8.6%

$$Re\,duction\ in\ p = \frac{Apparent\ Porosity\ (20^{\circ}C\ and\ 65\%RH) - Apparent\ Porosity\ (20^{\circ}C\ and\ 95\%RH)}{Apparent\ Porosity\ (20^{\circ}C\ and\ 65\%RH)} \qquad \text{Equation 7.28}$$

$$Re\,duction\ in\ w_a = \frac{Water\ Absorption\ (20^{\circ}C\ and\ 65\%RH) - Water\ Absorption\ (20^{\circ}C\ and\ 95\%RH)}{Water\ Absorption\ (20^{\circ}C\ and\ 65\%RH)} \qquad \text{Equation 7.29}$$

Figures 7.20 and 7.21 show that the materials with a water/binder ratio of 0.25, cured at 65% RH (batch code A1 and KA1) have a higher apparent porosity and water absorption than the corresponding materials cured at 95% RH (batch code M1 and KM1). For example at w/b=0.25, materials cured under 65% RH (batch code A1) have water absorption and apparent porosity values which are 6.5% and 7.7%, respectively higher than the corresponding material cured under 95 % RH (batch code M1). This phenomenon is further discussed in section 7.4.6.

Other researchers[158, 159] have concluded from their investigation that blended cement concrete samples cured in air at 45°C and 25% RH exhibit higher water absorption compared with samples covered with a wet burlap and plastic sheeting when cured under 20°C and 50% RH. This is due to the fact that dry curing creates larger pore volume and also larger pore size distribution owing to the cessation of hydration when water is not present[158]. Replacing 22% of cement with fly ash did not significantly influence the absorption values. The addition of 9% microsilica to Portland cement pastes yields higher water absorption values for both curing conditions (45°C, 25% RH and 20°C, 50% RH). This was attributed the larger open pores of the cementitious material when silica fume is present[159].

Materials with a water /binder ratio of 0.20, on the other hand, show opposite trends to materials of water/binder ratio of 0.25 in Figures 7.20 and 7.21. Materials with a water/binder ratio of 0.20, cured at 65% RH (batch code A2 and KA2) have a lower apparent porosity and water absorption than the corresponding materials cured at 95% RH (batch code M2 and KM2) as shown in Figures 7.20 and 7.21. For example at w/b=0.20, the materials cured under 65% RH (batch code A2) have water absorption and apparent porosity values which are 8.6% and 1.6%, respectively, lower than the corresponding material cured under 95 % RH (batch code M2).

7.5.2.3 Coefficient of saturation

The coefficient of saturation results together with the percentage differences in coefficient of saturation resulting from changes in the relative humidity of curing are presented in Table 7.15. The results are also plotted in Figure 7.22. Materials cured at 65%RH exhibit lower coefficient of saturation than those cured at 95%RH. For example, at w/b=0.25, the material cured at 65% RH (batch code A1) has a coefficient of sorption 23.5% higher than the corresponding material (batch code M1) cured under 95 % RH. Similarly for w/b=0.20, the material cured under 65% RH (batch code A2) has a coefficient of sorption 34.1% higher than the corresponding material (batch code M2) cured under 95 % RH.

Table 7.15 Influence of relative humidity of curing on coefficient of saturation

Batch Code	Curing conditions	Water/Binder	Coef of Saturation [%]	Change in $c_{saturation}$
A1	20°C and 65% RH	0.25	0.68	-
M1	20°C and 95% RH	0.25	0.84	-23.5%
KA1	20°C and 65% RH	0.25	0.69	
KM1	20°C and 95% RH	0.25	0.94	-36.2%
A2	20°C and 65% RH	0.2	0.44	
M2	20°C and 95% RH	0.2	0.59	-34.1%
KA2	20°C and 65% RH	0.2	0.53	
KM2	20°C and 95% RH	0.2	0.55	-3.8%

$$Reduction\ in\ c_{sat} = \frac{Saturation\ Coefficient\ (20^{\circ}C\ and\ 65\%RH) - Saturation\ Coefficient\ (20^{\circ}C\ and\ 95\%RH)}{Saturation\ Coefficient\ (20^{\circ}C\ and\ 65\%RH)} \quad \text{Equation 7.30}$$

Symbol	Batch Code	Curing	W/b Ratio	Hardener
◆	A1/M1	20°C and 65%/95%RH	0.25	0%
■	KA1/KM1	20°C and 65%/95%RH	0.25	20%
▲	A2/M2	20°C and 65%/95%RH	0.20	0%
●	KA2/KM2	20°C and 65%/95%RH	0.20	20%

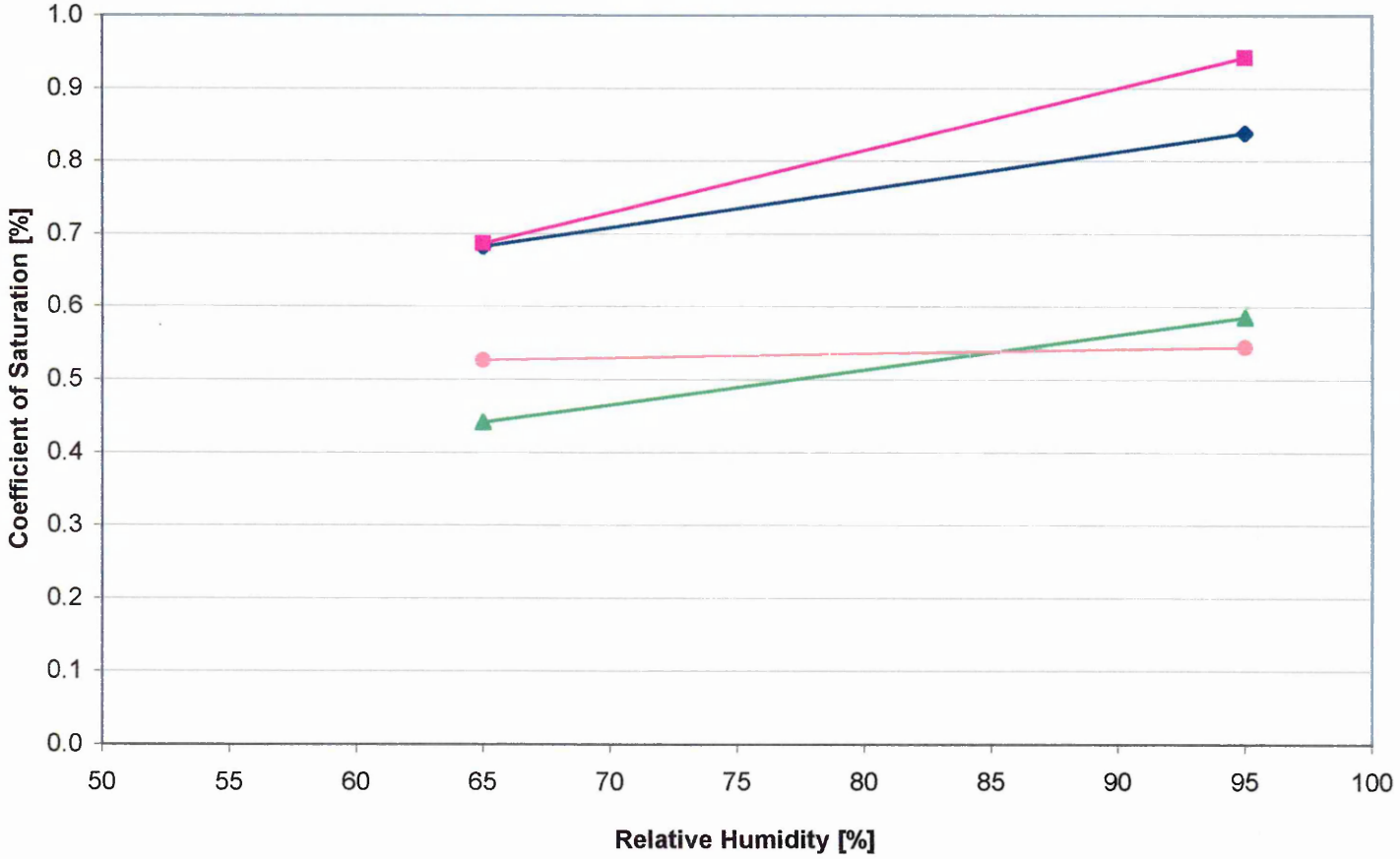

Figure 7.22 Relationship between the coefficient of saturation and relative humidity of curing

A comparison of Figure 7.22 with Figures 7.20 and 7.21 shows that the coefficient of saturation results display opposite trends to the apparent porosity and water absorption results. In Figures 7.20 and 7.21 the apparent porosity and water absorption properties decrease with increasing of relative humidity of curing whereas in Figure 7.22 the saturation coefficient increases with increasing RH of curing. This behaviour was explained in the previous section (7.4.1.3), and is due to the pore size and shape differences which influence the ease of pore filling with water.

7.5.3 Influence of hardener (aluminium methaphosphate compound) on physical properties

7.5.3.1 Density

The bulk and solid density together with the percentage difference in density (equations 7.30 and 7.31) resulting from the addition of water glass hardener (aluminium methaphosphate compound, KB #90) are presented in Table 7.16.
The batch codes KA1, KM1, KA2 and KM2 represent mixes (listed in Table 7.7) which contain 1.5% hardener. The corresponding reference mixes batch codes A1, M1, A2 and M2 contain no hardener.

Table 7.16 Effect of water glass hardener on density

Batch Code	Curing conditions	Water/ Binder	Bulk Density [kg/m^3]	Difference in 'ρ_{bulk}'	Solid Density [kg/m^3]	Difference in 'ρ_{solid}'
A1	20°C and 65% RH	0.25	2045		2541	
KA1	20°C and 65% RH	0.25	2026	0.9%	2446	3.7%
M1	20°C and 95% RH	0.25	2016		2460	
KM1	20°C and 95% RH	0.25	1973	2.1%	2340	4.9%
A2	20°C and 65% RH	0.20	2080		2559	
KA2	20°C and 65% RH	0.20	2063	0.8%	2539	0.8%
M2	20°C and 95% RH	0.20	2001		2471	
KM2	20°C and 95% RH	0.20	2006	-0.2%	2518	-1.9%

$$Difference\ in\ \rho_{bulk} = \frac{Apparent\ Bulk\ Density\ (0\%\ hardener) - Apparent\ Bulk\ Density\ (1.5\%\ hardener)}{Apparent\ Bulk\ Density\ (0\%\ hardener)} \quad \text{Equation 7.31}$$

$$Difference\ in\ \rho_{solid} = \frac{Solid\ Density\ (0\%\ hardener) - Solid\ Density\ (1.5\%\ hardener)}{Solid\ Density\ (0\%\ hardener)} \quad \text{Equation 7.32}$$

A small decrease in bulk and solid density was observed with the addition of water glass hardener, regardless of the water/binder ratio. For example, for materials cured under 20°C and 65% RH of w/b=0.25 (batch code KA1), the bulk and solid densities are 0.9% and 3.7%, respectively lower than those of corresponding control materials without hardener addition (batch code A1).

7.5.3.2 Water absorption and apparent porosity

A summary of the water absorption and apparent porosity data is presented in Table 7.17.

Materials with hardener addition, at water /binder ratio of 0.25, show lower water absorption and apparent porosity values compared with corresponding materials without hardener, for curing under 20°C, 65% RH and under 20°C, 95% RH. For example at 1.5% hardener addition, the material with w/b = 0.25, cured at 20°C and 65% RH (batch code KA1) exhibits water absorption and apparent porosity values which are 11.5% and 12%, respectively lower than the control material without hardener (batch code A1).

Table 7.17 Influence of water hardener on water absorption and apparent porosity of alkali activated materials

Batch Code	Curing conditions	Water/ Binder Ratio	Wa [%]	Reduction in w_a [%]	Apparent Porosity [%]	Reduction in p [%]
A1	20°C and 65% RH	0.25	9.38	-	19.52	-
KA1	20°C and 65% RH	0.25	8.3	11.5%	17.15	12.1%
M1	20°C and 95% RH	0.25	8.77		18.02	
KM1	20°C and 95% RH	0.25	7.79	11.2%	15.69	12.9%
A2	20°C and 65% RH	0.20	8.84		18.73	
KA2	20°C and 65% RH	0.20	8.91	-0.8%	18.73	0.0%
M2	20°C and 95% RH	0.20	9.35		19.03	
KM2	20°C and 95% RH	0.20	9.98	-6.7%	20.34	-6.9%

$$Re\,duction\ in\ p = \frac{Apparent\ Porosity\ (0\%\ hardener) - Apparent\ Porosity\ (1.5\%\ hardener)}{Apparent\ Porosity\ (0\%\ hardener)} \quad \text{Equation 7.33}$$

$$Re\,duction\ in\ W_a = \frac{Water\ Absorption\ (0\%\ hardener) - Water\ Absorption\ (1.5\%\ hardener)}{Water\ Absorption\ (0\%\ hardener)} \quad \text{Equation 7.34}$$

Materials with hardener addition, at water /binder ratio of 0.20,on the other hand, show opposite trends to corresponding materials with a water/binder ratio of 0.25, as shown in Table 7.17. For example, materials with hardener addition cured at 20°C and 65% RH (batch code KA2) show similar water absorption and apparent porosity values as the control material without hardener (batch code A1). Materials of water/binder 0.20 with 1.5% hardener addition, cured under 20°C and 95% RH (batch code KM2), exhibit water absorption and apparent porosity values which are 6.7% and 6.9%, respectively, higher than control materials without hardener (batch code M1), see Table 7.17.

A comparison of Tables 7.17 and 7.14 shows that influence of hardener follows the same trends as the influence of increasing the relative humidity of curing on alkali activated fly ash materials. The water absorption and apparent porosity of alkali activated materials, with a water/binder of 0.25, decrease with the binder addition or with increased RH of curing. On the other hand, the water absorption and apparent porosity of alkali activated materials with a water/binder of 0.20, increase slightly with the hardener addition or with increasing RH of curing.

7.5.3.3 Coefficient of saturation

A summary of the coefficient of saturation results are presented in Table 7.18.

Table 7.18 Influence of water glass hardener on coefficient of saturation

Batch Code	Curing conditions	Water/Binder Ratio	$c_{saturation}$ [%]	Change in $c_{saturation}$ [%]
A1	20°C and 65% RH	0.25	0.68	
KA1	20°C and 65% RH	0.25	0.69	-1.5%
M1	20°C and 95% RH	0.25	0.84	
KM1	20°C and 95% RH	0.25	0.94	-11.9%
A2	20°C and 65% RH	0.20	0.44	
KA2	20°C and 65% RH	0.20	0.53	-20.5%
M2	20°C and 95% RH	0.20	0.59	
KM2	20°C and 95% RH	0.20	0.55	6.8%

$$Re\,duction\ in\ c_{sat} = \frac{Saturation\ Coefficient\ (0\%\ hardener) - Saturation\ Coefficient\ (1.5\%\ hardener)}{Saturation\ Coefficient\ (0\%\ hardener)} \quad \text{Equation 7.35}$$

Materials, with hardener addition and water/binder ratio of 0.25 show an increase in the coefficient of sorption, compared with control materials (without hardener), regardless of curing condition. For example, at 1.5% hardener addition, the material with w/b = 0.20 cured at 20°C and 65% RH (batch code KA2) exhibits a coefficient of saturation 20.5% lower than control material without hardener (batch code A2), as shown in Table 7.18. Materials with w/b=0.20 cured at 20°C and 95% RH (batch code KM2) show opposite trends to the corresponding materials with a water /binder =0.25, with a 6.8% reduction in the coefficient of saturation of materials containing hardener (see Table 7.18).

7.5.4 Influence of thermal curing on physical properties

7.5.4.1 Density

The bulk and solid density of the alkali activated fly ash materials are presented in Table 7.19. A small decrease in bulk density is observed with changing the curing temperature from ambient level (20°C) to high temperatures (up to 120°C) regardless of water/binder ratio which could indicate a higher degree of hydration. For example, the bulk and solid densities of material cured at 20°C and 65% RH with a w/b=0.25 (batch code A1) are 1.3% and 5.1%, respectively higher then those of corresponding material cured at high temperatures up to 120°C (batch code H1).

Table 7.19 Effect of thermal curing on density

Batch Code	w/b	Curing	Apparent Bulk Density [kg/m^3]	Difference in ρ_{bulk}	Solid Density [kg/m^3]	Difference in ρ_{solid}
A1	0.25	20°C and 65% RH	2045	-	2541	-
H1	0.25	thermal treatment	2018	1.3%	2412	5.1%
A2	0.20	20°C and 65% RH	2080	-	2559	-
H2	0.20	thermal treatment	2038	2.0%	2568	-0.4%

$$Difference\ in\ \rho_{bulk} = \frac{Apparent\ Bulk\ Density\ (20^{\circ}C\ and\ 65\%RH) - Apparent\ Bulk\ Density\ (thermal\ treatment)}{Apparent\ Bulk\ Density\ (20^{\circ}C\ and\ 65\%RH)} \quad \text{Equation 7.36}$$

$$Difference\ in\ \rho_{solid} = \frac{Solid\ Density\ (20^{\circ}C\ and\ 65\%RH) - Solid\ Density\ (thermal\ treatment)}{Solid\ Density\ (20^{\circ}C\ and\ 65\%RH)} \quad \text{Equation 7.37}$$

7.5.4.2 Water absorption and apparent porosity

A summary of the water absorption and apparent porosity is presented in Table 7.20.

Table 7.20 Influence of thermal curing on water absorption and apparent porosity

Batch Code	Curing conditions	Water/Binder Ratio	Wa [%]	Reduction in w_a	Apparent Porosity [%]	Reduction in p
A1	20°C and 65% RH	0.25	9.38	-	19.52	-
H1	thermal treatment	0.25	7.93	15.5%	16.33	16.3%
A2	20°C and 65% RH	0.20	8.84		18.73	
H2	thermal treatment	0.20	9.98	-12.9%	20.75	-10.8%

$$Re\,duction\ in\ p = \frac{Apparent\ Porosity\ (20^{\circ}C\ and\ 65\%RH) - Apparent\ Porosity\ (thermal\ treatment)}{Apparent\ Porosity\ (20^{\circ}C\ and\ 65\%RH)} \qquad \text{Equation 7.38}$$

$$Re\,duction\ in\ w_a = \frac{Water\ Absorption\ (20^{\circ}C\ and\ 65\%RH) - Water\ Absorption\ (thermal\ treatment)}{Water\ Absorption\ (20^{\circ}C\ and\ 65\%RH)} \qquad \text{Equation 7.39}$$

Materials with a water/binder ratio of 0.25 exhibit lower water absorption and porosity when subjected to thermal curing compared with corresponding materials subjected to curing under 20°C, 65%RH. For example, thermally cured material, batch code H1 exhibits water absorption and apparent porosity values which are 15% and 16.3% respectively lower than corresponding materials cured under 20°C, 65% RH (batch code A1). This phenomenon is further discussed in section 7.4.6. Materials with a water/binder ratio of 0.20, on the other hand, show opposite trends to those with w/b=0.25, as they exhibit higher water absorption and porosity when thermal treated, compared with corresponding materials cured at 20°C and 65%RH. For example the thermally treated material (batch code H2) exhibits water absorption and apparent porosity values which are 13% and 11% respectively higher than corresponding materials cured under 20°C and 65% RH, (batch code A2). This agrees with the findings presented in Chapter IV which show clearly that the thermal curing increases the water absorption and apparent porosity.

7.5.4.3 Coefficient of saturation

The coefficient of saturation results are presented in Table 7.21.

Table 7.21 Coefficient of saturation of alkali activated fly ash materials

Batch Code	Curing conditions	Water/Binder Ratio	Coef of Saturation [%]	Change in $c_{saturation}$
A1	20°C and 65% RH	0.25	0.68	
H1	thermal treatment	0.25	0.76	-11.8%
A2	20°C and 65% RH	0.20	0.44	
H2	thermal treatment	0.20	0.47	-6.8%

$$Reduction\ in\ c_{sat} = \frac{Saturation\ Coefficient\ (20^{\circ}C\ and\ 65\%RH) - Saturation\ Coefficient\ (thermal\ treatment)}{Saturation\ Coefficient\ (20^{\circ}C\ and\ 65\%RH)} \quad \text{Equation 7.40}$$

Alkali activated fly ash materials exhibit higher coefficients of saturation when subjected to thermal curing compared with corresponding materials subjected to standard curing under 20°C and 65%RH, for both water/binder ratios (0.25 and 0.20). For example, thermally treated material of w/b = 0.25 (batch code H1) exhibits a coefficient of saturation 11.8% higher than the corresponding material cured under 20°C and 65% RH, (batch code A1). This could be due to the fact that thermal curing increases the rate of chemical reaction taking place, which will lead to high early age strength and stiffness. Due to the accompanying high shrinkage strain, the tensile stress induced by the restraint produced by the steel mould surfaces during thermal curing will be higher. Owing to these factors, microcracking occurs and, therefore, the coefficient of sorption increases. This phenomenon is further discussed in section 7.4.6.

7.5.5 Permeability coefficient

Water permeability tests on the materials with water/binder ratio of 0.25 were performed. Thermally cured materials do not exhibit a significant difference in permeability coefficient when compared with the alkali activated materials cured at 20°C and 65% RH. For example, materials cured under 20°C and 65% RH show a

permeability coefficient of 1.60 E-12 m/s compared with 3.16 E-12 m/s for the corresponding thermally cured material. It is important to recognise that the scatter of permeability test results on cementitious materials using the same apparatus is large[81]. Therefore, small differences such as between 1.60 E-12 m/s and 3.16 E-12 m/s are not significant[81]. The permeability of the alkali activated materials investigated are similar to the maximum value (5 E-12 m/s) recommended for structural concrete in the ACI 301-72[160].

Figure 7.23 shows the water permeability results for concrete obtained by other researchers [156] and for the alkali activated fly ash materials of this investigation. The results for alkali activated materials are within the limits found by other researchers[156] for Portland cement concrete, see Figure 7.23.

Other researchers[79] have investigated the water permeability of alkali activated slag materials using sodium silicate solution (Na_2SiO_3) and sodium carbonate solution (Na_2CO_3) to activate the pozzolanic materials. The dosage of alkali activator was 6% Na_2O by mass of slag. Table 7.22 presents the water permeability results of alkali activated materials obtained by Caijun[79]. The 28 day permeability coefficient for alkali activated material with a w/b=0.485 cured under 23°C and 95%RH is 7.50E-14 (determined by Caijun[79]) compared with 1.60 E-12 m/s for the alkali activated material with w/b=0.25 cured under 20°C and 65% RH (determined in the present study).

Table 7.22 Water permeability of reference PC mortar and alkali activate slag mortars[79]

Type of activator	**Curing**	**Water/Binder**	**Testing age** [days]	**Permeability coefficient** [m/s]
Na_2SiO_3	23°C and 95%RH	0.485	7	2.5E-13
Na_2SiO_3	23°C and 95%RH	0.485	28	7.50E-14
Na_2CO_3	23°C and 95%RH	0.485	7	1.00E-10
Na_2CO_3	23°C and 95%RH	0.485	28	7E-17
PC mortar	23°C and 95%RH	0.485	28	3E-10

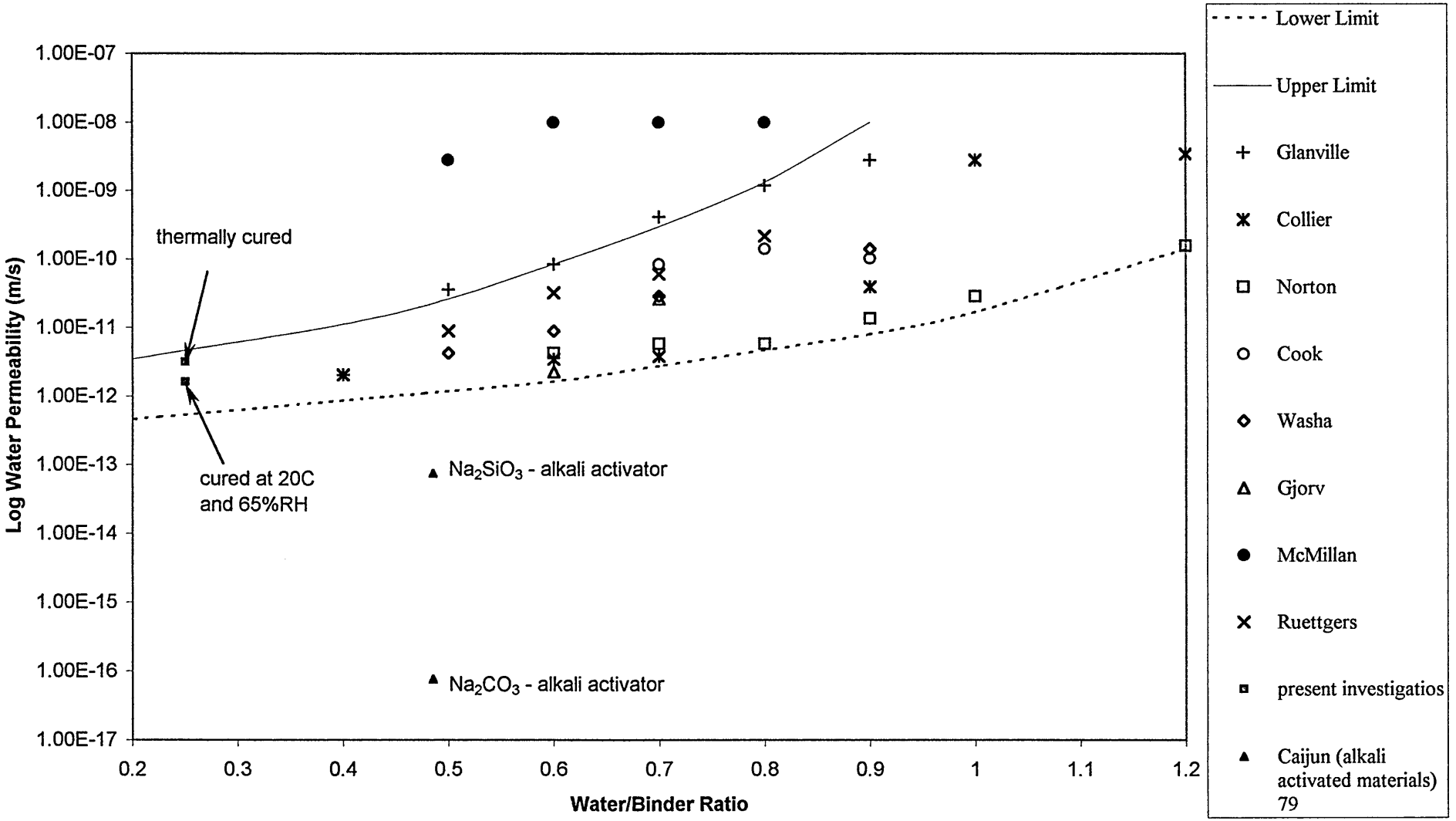

Figure 7.23 Comparison of water permeability data for concrete [156] and alkali activated fly ash materials.

7.5.6 Mercury Intrusion Porisimetry

Table 7.23provides a summary of the mercury intrusion porisimetry results for the alkali activated materials examined. Figures 7.24 to 7.29 show the actual pore size distribution for the materials. The overall conclusion from this work is that changes to the mix components or curing conditions appear to generate marked changes to the total porosity and the average pore diameters.

The results in Table 7.23show that the specimens with the lower 0.2 water/binder ratio have a higher total porosity compared to the 0.25 water/binder ratio. However, the 0.2 water/binder ratios have a smaller average pore size. This indicates that the 0.2 water binder/ratio samples have a higher number of pores than the 0.25 water/binder ratio, but of a smaller size. Specimens with hardener appear to show little effect to porosity or the average pore size from the addition of the hardener and follow the trends indicated by the other batches. The thermally cured specimens from batches H1 and H2 have the highest porosities measured, but amongst the smallest average pore sizes compared to the other alkali activated materials.

Some of the results appear contradict these findings. H1 the thermally cured specimen with a 0.2 water binder ratio has a high cumulative pore volume as would be expected from the high total porosity. However, the specific pore surface area is similar or smaller than some of the other measurements. If the material had a large number of pores with smaller diameters, it would appear logical to expect very high specific pore surface areas. It may be that while the average pore size is small a significant number of larger pores still exist.

The difference in water binder ratio does not appear to create significant difference in porosity between H1 with a 0.2 W/B and H2 with a 0.25 W/B. There may be a limit for the refinement of pore size in the specimens. The results here would tend to suggest a limit in the average pore size diameter between 0.025 and 0.05 μm. A more rigorous series of tests would be required to confirm this.

Table 7.23 Summary of Mercury Intrusion Porisimetry results

Batch	W/B Ratio	Hardener	Curing Conditions.	Cum. Pore Volume (mm^3/g)	Spec. Pore Surf. area (m^2/g)	Total Porosity (%)	Av. Pore diameter. (μm)x10^{-3}
A1	0.20	0	20°C 65%RH	69.947	5.899	14.153	25.967
KA1	0.20	20% KB#90	20°C 65%RH	65.627	3.638	14.591	77.696
H1	0.20	0	Thermal	80.035	4.792	17.673	56.445
A2	025	0	20°C 65%RH	59.582	1.829	11.173	1249.621
KA2	0.25	20% KB#90	20°C 65%RH	58.631	3.308	12.144	381.270
H2	0.25	0	Thermal	84.968	6.108	16.079	57.125

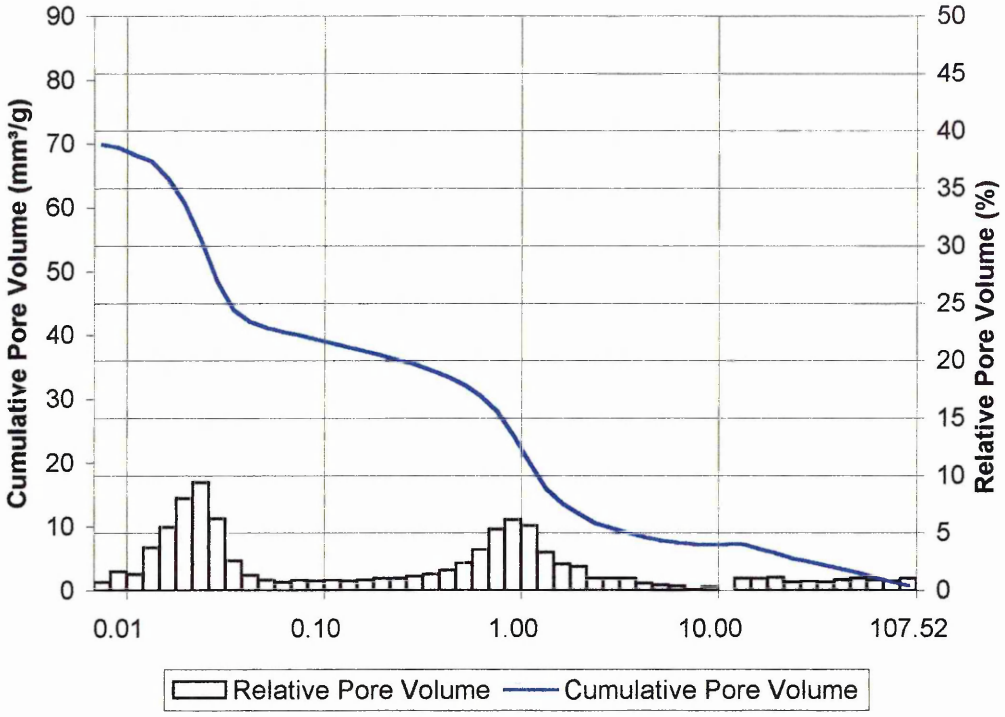

Figure 7.24 Pore Size Distribution for alkali activated material batch code A1

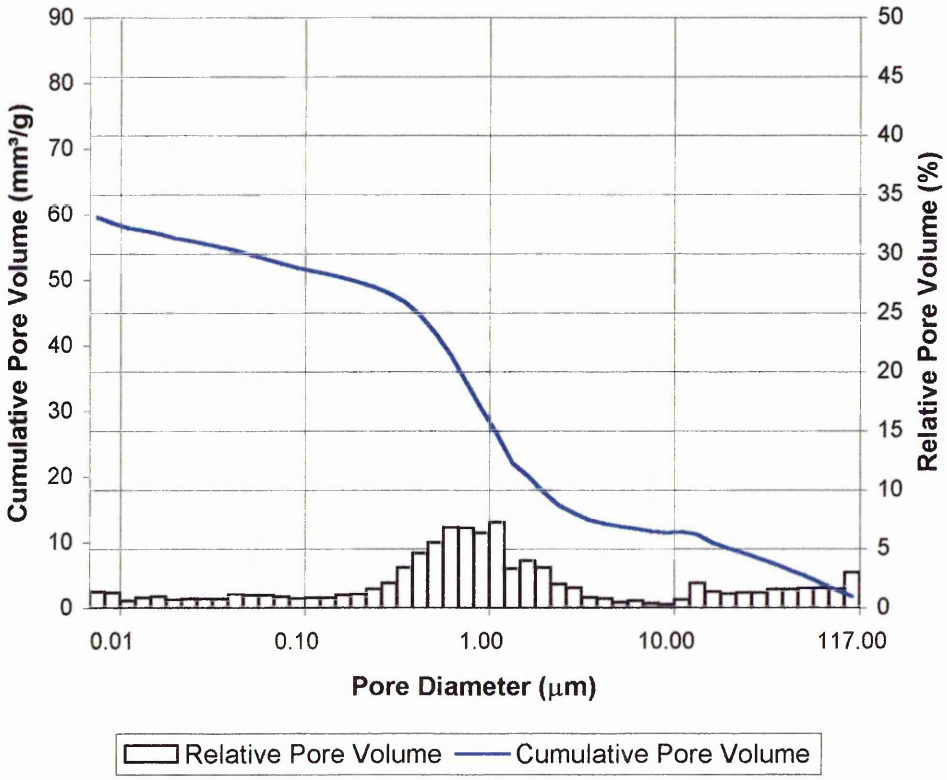

Figure 7.25 Pore Size Distribution for alkali activated material batch code A2

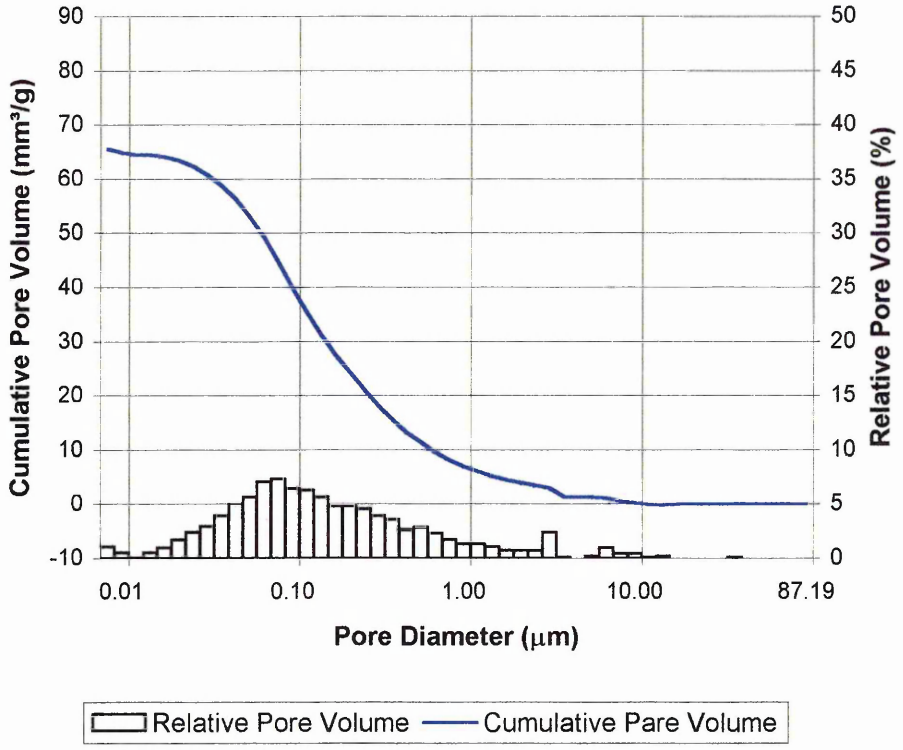

Figure 7.26 Pore Size Distribution for alkali activated material batch code KA1

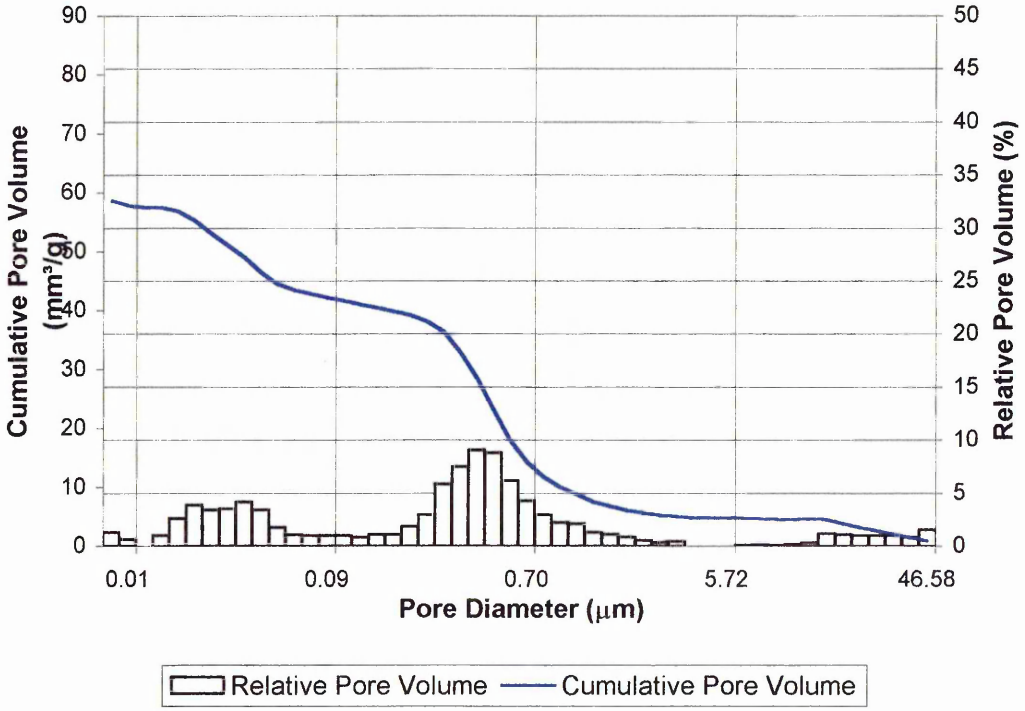

Figure 7.27 Pore Size Distribution for alkali activated material batch code KA2

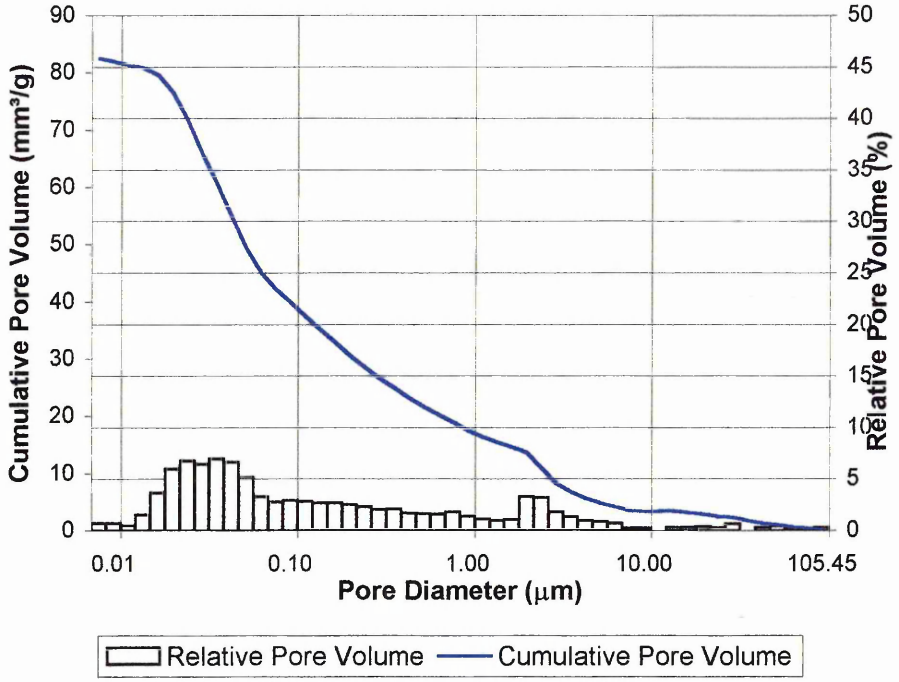

Figure 7.28 Pore Size Distribution for alkali activated material batch code H1

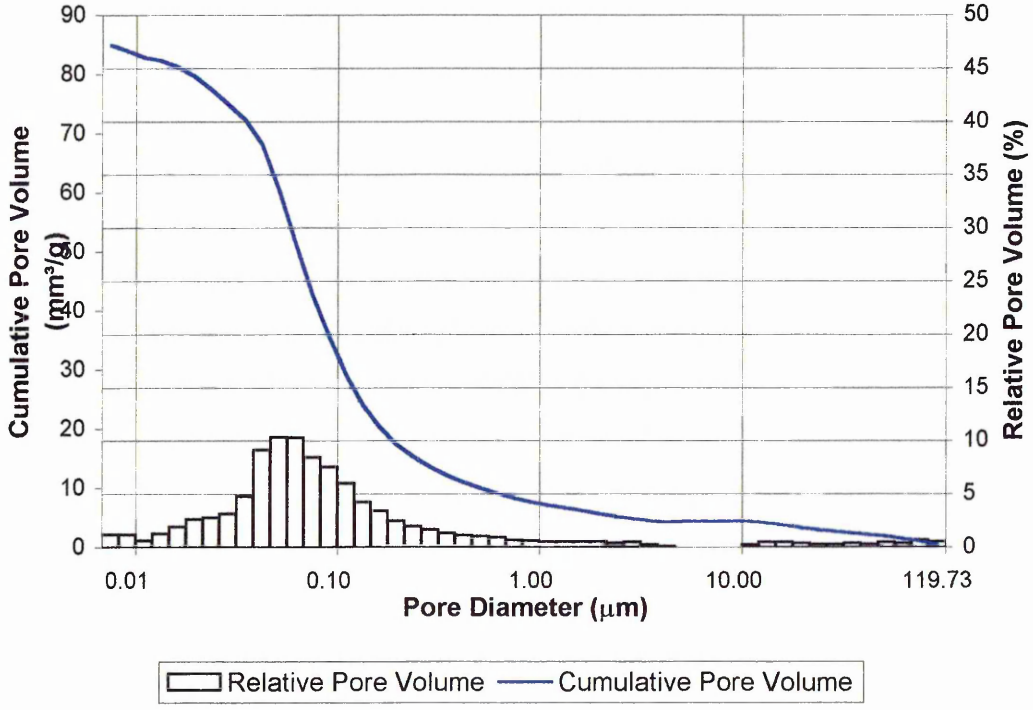

Figure 7.29 Pore Size Distribution for alkali activated material batch code H2

7.5.7 Discussion on physical properties

It is difficult to determine the precise amount of chemically combined water because of the lack of knowledge of stoichiometry of the hydration products of cement. Therefore, it is acceptable to consider that this water, determined under specified conditions[161], is taken as 23 per cent of the mass of the anhydrous cement. The specific gravity of the products of hydration is such that they occupy a greater volume (approximately 25.4%) than the absolute volume of unhydrated cement, but smaller than the sum of the volumes of dry cement and the non-evaporable water. The gel pores occupy about 28% of the total volume of gel[161]. The actual non-evaporable water content is characteristic for a given cement, but is largely independent of the water/cement ratio of the mix and of the progress of hydration. When the water/binder ratio of a mix is less than 0.38 by mass, complete hydration is not possible as the volume available is insufficient to accommodate all the products of hydration which can only be accommodated within the capillaries.

Applying these principles to alkali activated materials of this study, the volume of empty capillaries can be calculated. For example, consider a mix of 100g of pozzolanic materials (fly ash, ggbs and microslilica) and 25g of water (water/binder ratio by mass is 0.25). The water will be sufficient to hydrate x g of pozzolanic material, given by the following calculations.

Taking the average specific gravity of the dry pozzolanic material as 2.5, then the absolute volume of unhydrated cement is 100/2.5 = 40ml.

The contraction in volume of hydration is:

$0.23x \cdot 0.254 = 0.0585x$

Volume occupied by solid products of hydration product is:

$$\frac{x}{3.15} + 0.23x - 0.0585x = 0.5715x$$

Porosity is :

$$\frac{w_g}{0.5715x + w_g} = 0.28$$

where w_g is the volume of gel water

Therefore,

$w_g = 0.22x$

and the total water content by:

$0.23x + w_g = 25$

Hence, $x = 55.6$g (x could also be expressed in ml as 55.6/2.5=22.24)

and $w_g = 0.22x = 12.23$g

Thus, the volume of hydrated materials = $0.5715 \cdot 55.6 + 12.23 = 44$ml

The volume of unhydrated cement = 40 - 22.24 = 17.76ml

Therefore, the volume of empty capillaries is:

40 + 25-(44+17.76) = 3.24ml

If water is available from an outside source, the pozzolan can be hydrated further, its quantity being such that the products of hydration occupy 3.2ml more than the volume of dry pozzolan. It has been found that 22.24ml of pozzolan occupy 44ml when fully hydrated. Therefore, the products of hydration of 1ml of pozzolan occupy 44/22.24=1.98ml. The volume of empty capillaries (3.24ml) would be filled by the hydration of y ml of pozzolan such that

$$\frac{y + 3.24}{y} = 1.98$$

Hence, $y = 3.31$ml.

Therefore, the volume of still unhydrated pozzolan is 40-(22.24+3.31) = 14.45ml which has a mass of 36.125g. Thus 36% of the pozzolan has remained unhydrated and can never hydrate because the gel already occupies all the space available, the gel/space ratio of the hydrated pozzolan is 1.0. The corresponding y value for a mix with a water /binder ratio of 0.20 is 2.67ml. Therefore, the volume of still unhydrated pozzolan is 40-(17.78+2.67) = 19.55ml which has a mass of 48.875g. Thus 49% of the pozzolan has remained unhydrated.

The unhydrated material is not detrimental to strength. In fact, among cement pastes with a gel/space ratio of 1.0, those with a higher proportion of unhydrated cement (i.e. lower water/binder ratio) have a higher strength possibly because in such pastes the layers of hydrated paste surrounding the unhydrated cement grains are thinner[149].

Applying the same method to 100g of pozzolanic material mixed with different quantities of water (water/binder ratio by mass varying from 0.1 to 0.5), the volumes of capillary pore, gel water, unhydrated pozzolan and hydrated pozzolan were determined. Figure 7.30 gives a diagrammatic representation of the volume changes whcich occur on hydration of pozzolanic pastes. It shows that the water/binder determines the porosity of the hardened pozzolanic material at any stage in the hydration process. At 100% hydration, the volume of the capillaries for water/binder ratio of 0.1 is smaller than the corresponding material with w/b=0.5.

Thermally cured materials exhibit higher water absorption, apparent porosity and coefficient of saturation than the corresponding materials cured at 20°C and 65%RH. Alkali activated slag materials, cured at high temperatures are susceptible to microcracking. The microcraks are caused by the expansion of air bubbles in the paste, the thermal expansion of the air is approximately two orders of magnitude greater than that of the surrounding material. The expansion of air bubbles tends to expand the matrix which is restrained by the mould walls so that the air is put under pressure. To balance this pressure, tensile stresses are induced in the surrounding pozzolanic paste. These tensile stresses induce very fine cracks which increase the porosity, water absorption and coefficient of saturation. These disruptive effects of the expansion of the air bubbles can be reduced by a prolonged delay prior to heat curing and by a lower rate of temperature rise[81].

Rapid initial hydration appears to form hydration products with a poorer physical structure, probably more porous so that a proportion of the pores will always remain unfilled[81]. Thermal curing increases the rate of chemical reaction taking place, which will lead to high early age strength and stiffness.

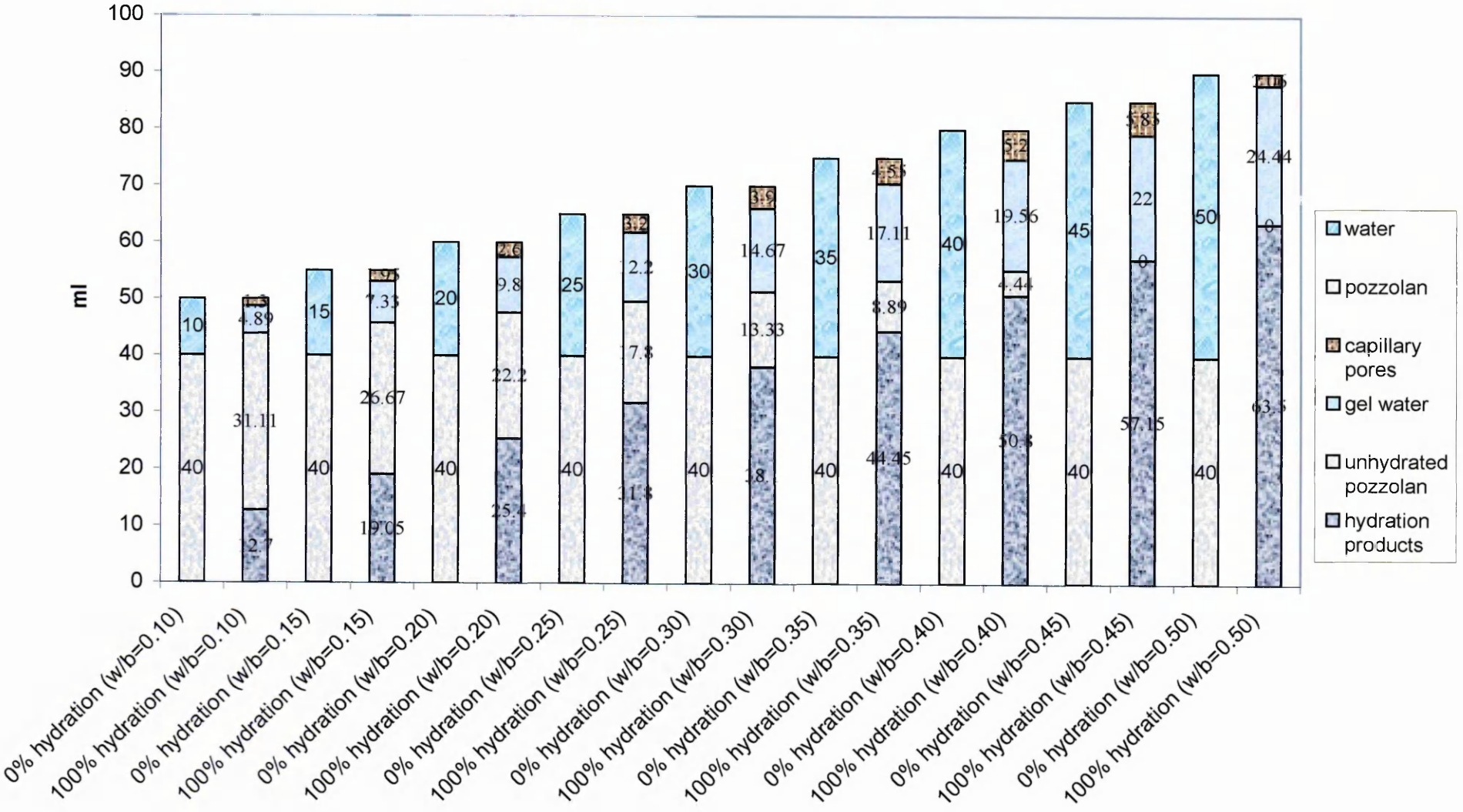

Figure 7.30 Diagrammatic representation of volume changes on hydration of pozzolanic pastes

Other researchers[151,162,163] have investigated the influence of curing temperature on concrete. Verbeck[162] suggest the rapid initial rate of hydration retards the subsequent hydration and produces a non-uniform distribution of the hydration product within the paste. When the initial rate of hydration is too high, there is insufficient time available for the diffusion of the products of hydration away from the cement particles and for a uniform precipitation in the interstitial spaces.

Goto and Roy[163] found that materials cured at 60°C have a much higher volume of pores larger than 150nm in diameter compared with corresponding materials cured at 27°C. The porosity of materials cured under 60°C, on the other hand, was lower than that of corresponding materials cured under 27°C.

7.5.8 Relationship between mechanical and physical properties

Figures 7.31 and 7.32 show the relationship between density (bulk and apparent solid) and compressive strength for alkali activated fly ash materials. The corresponding relationships between apparent porosity - compressive strength, water absorption - compressive strength and coefficient of sorption - compressive strength are shown in Figures 7.33, 7.34 and 7.35, respectively.

There clear trend is that compressive strength increases with increasing bulk density of alkali activated materials cured in different conditions, see Figure 7.31. The compressive strength and bulk density have a linear relationship given by the following equation:

$$\sigma_{cm} = 0.44\ \rho_{bulk} - 826.05 \qquad \text{Equation 7.41}$$

with a coefficient of correlation R^2 of 0.5.

where

σ_{cm} is compressive strength [N/mm^2]

ρ_{bulk} is bulk density [kg/m^3]

Symbol	Batch	Curing	W/b Ratio	Hardener
◆	A1/A2	20°C and 65% RH	0.25/0.20	0%
■	M1/M2	20°C and 95% RH	0.25/0.20	0%
▲	H1/H2	thermal treatment	0.25/0.20	0%
✱	KA1/KA2	20°C and 65% RH	0.25/0.20	20%
●	KM1/KM2	20°C and 95% RH	0.25/0.20	20%
○	W1	water curing 20°C	0.25	0%

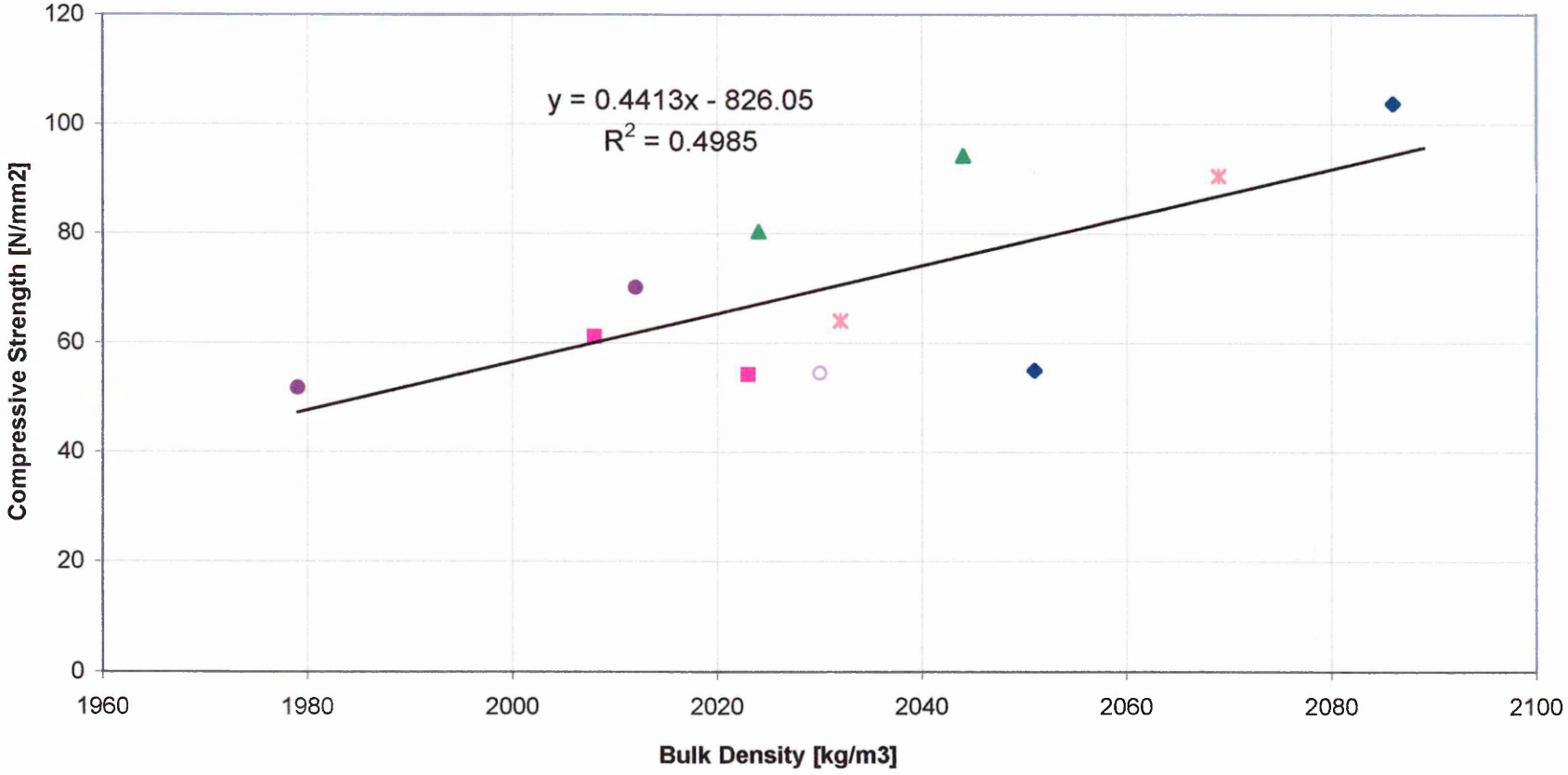

Figure 7.31 Relationship between the bulk density and compressive strength of alkali activated materials

Symbol	Batch	Curing	W/b Ratio	Hardener
◆	A1/A2	20°C and 65% RH	0.25/0.20	0%
■	M1/M2	20°C and 95% RH	0.25/0.20	0%
▲	H1/H2	thermal treatment	0.25/0.20	0%
✱	KA1/KA2	20°C and 65% RH	0.25/0.20	20%
●	KM1/KM2	20°C and 95% RH	0.25/0.20	20%
○	W1	water curing 20°C	0.25	0%

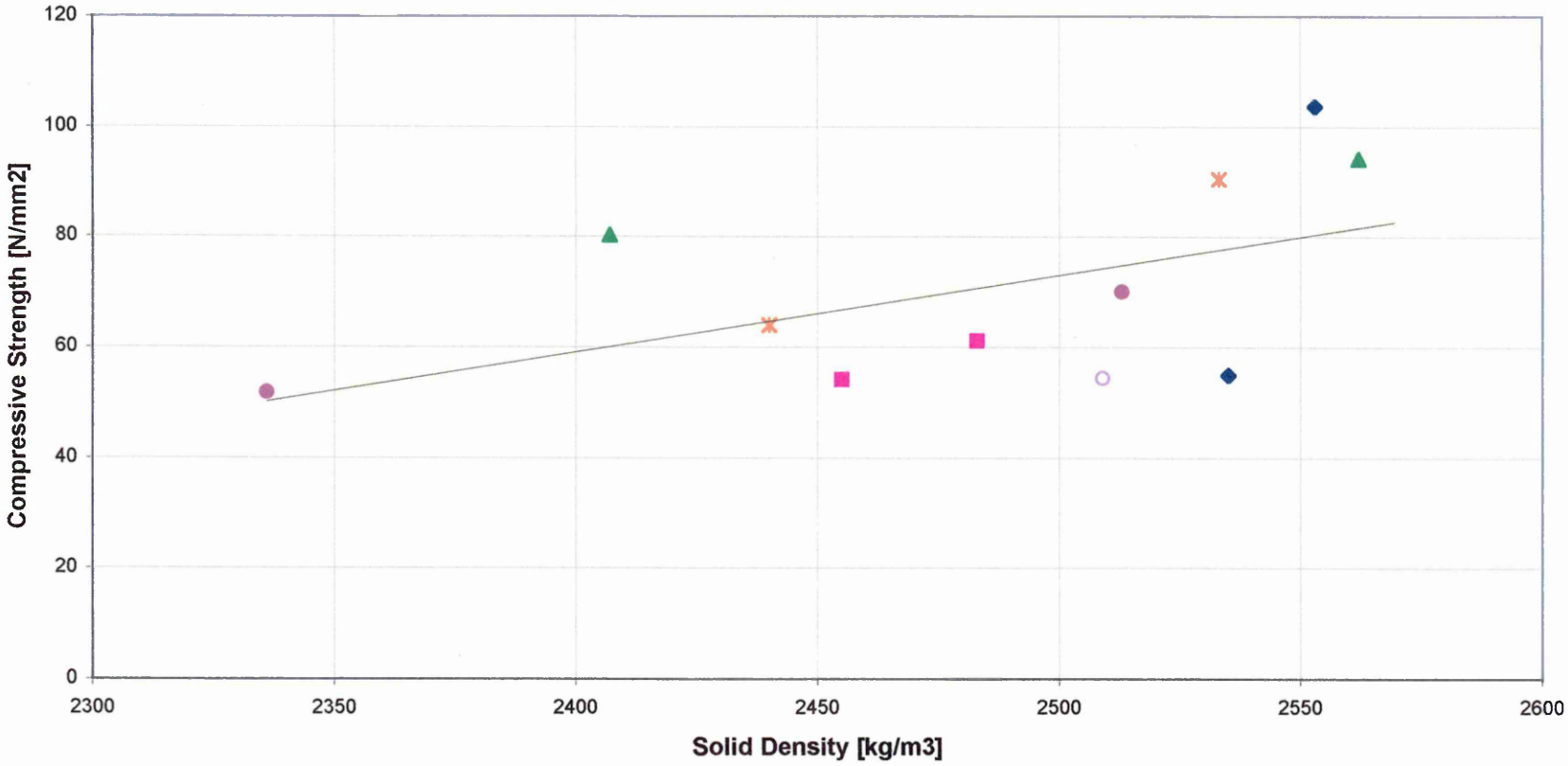

Figure 7.32 Relationship between the solid density and compressive strength of alkali activated materials

Symbol	Batch	Curing	W/b Ratio	Hardener
	W1	water curing 20°	0.25	0%
	A1/A2	20°C and 65% RH	0.25/0.20	0%
	M1/M2	20°C and 95% RH	0.25/0.20	0%
	H1/H2	thermal treatment	0.25/0.20	0%
	KA1/KA2	20°C and 65% RH	0.25/0.20	20%
	KM1/KM2	20°C and 95% RH	0.25/0.20	20%

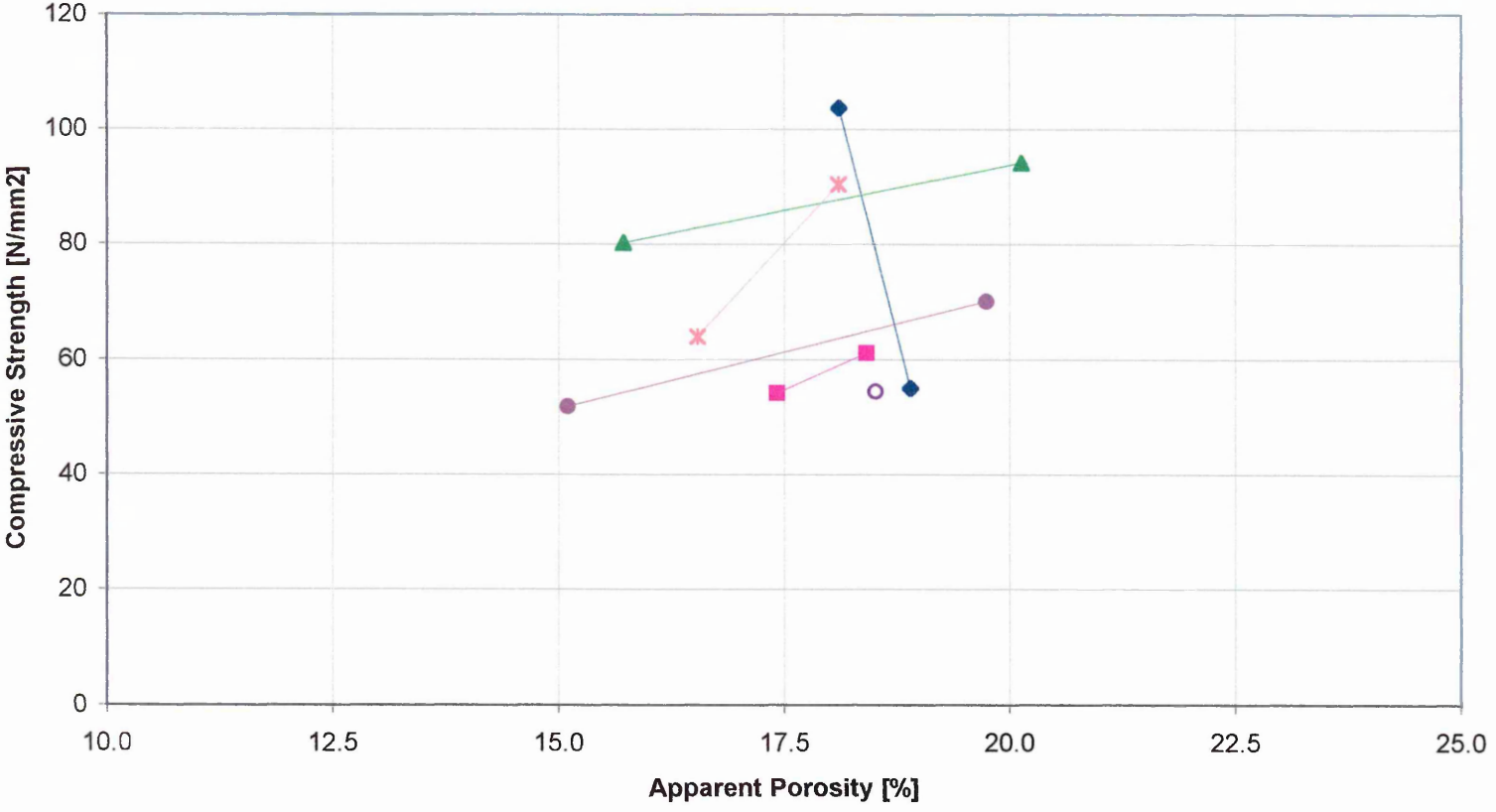

Figure 7.33 Relationship between apparent porosity and compressive strength

Symbol	Batch	Curing	W/b Ratio	Hardener
	W1	water curing 20°	0.25	0%
	A1/A2	20°C and 65% RH	0.25/0.20	0%
	M1/M2	20°C and 95% RH	0.25/0.20	0%
	H1/H2	thermal treatment	0.25/0.20	0%
	KA1/KA2	20°C and 65% RH	0.25/0.20	20%
	KM1/KM2	20°C and 95% RH	0.25/0.20	20%

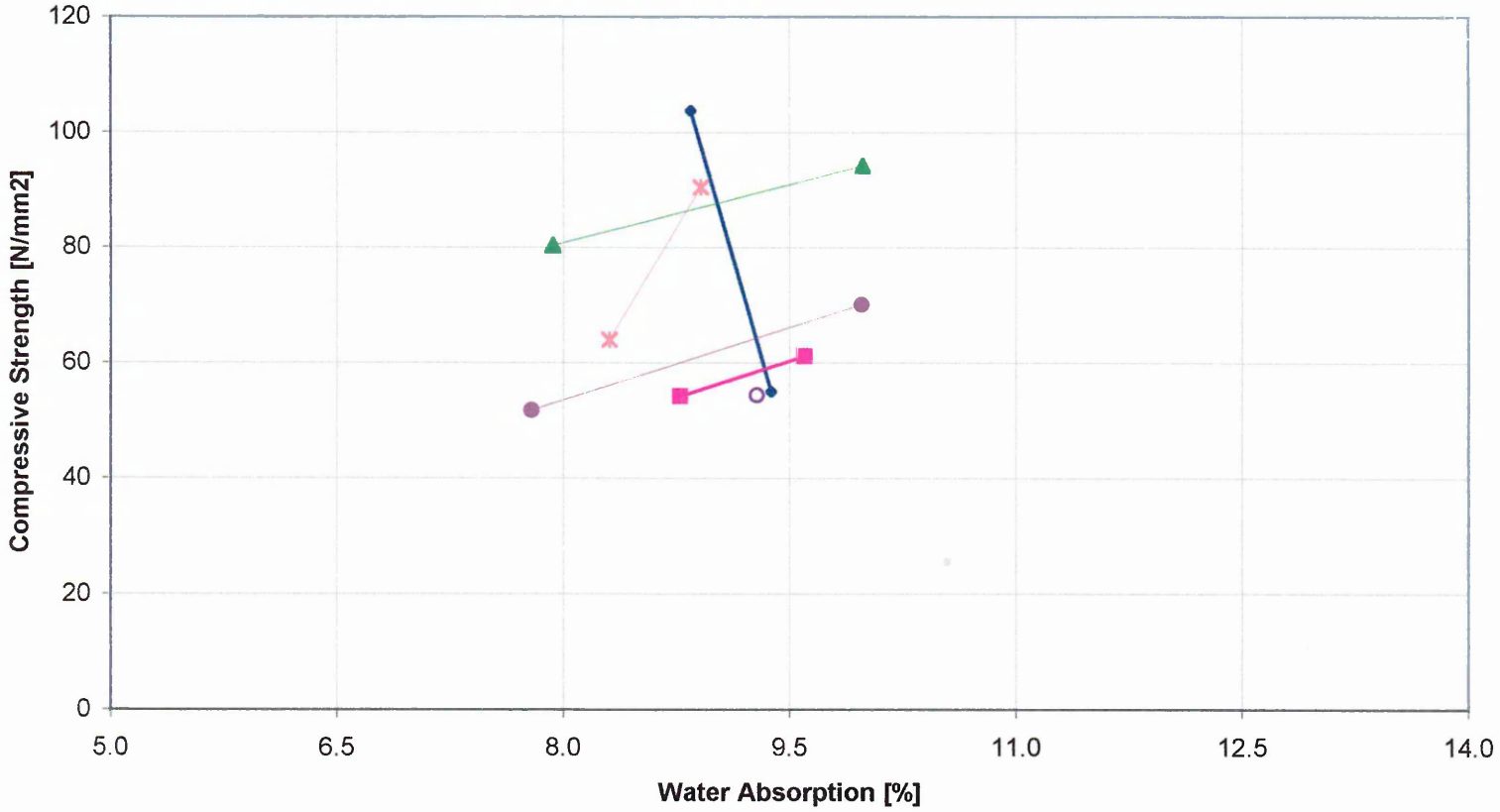

Figure 7.34 Relationship between water absorption and compressive strength

Symbol	Batch	Curing	W/b Ratio	Hardener
○	W1	water curing 20°C	0.25	0%
▲	H1/H2	thermal treatment	0.25/0.20	0%
◆	A1/A2	20°C and 65% RH	0.25/0.20	0%
■	M1/M2	20°C and 95% RH	0.25/0.20	0%
✳	KA1/KA2	20°C and 65% RH	0.25/0.20	20%
●	KM1/KM2	20°C and 95% RH	0.25/0.20	20%

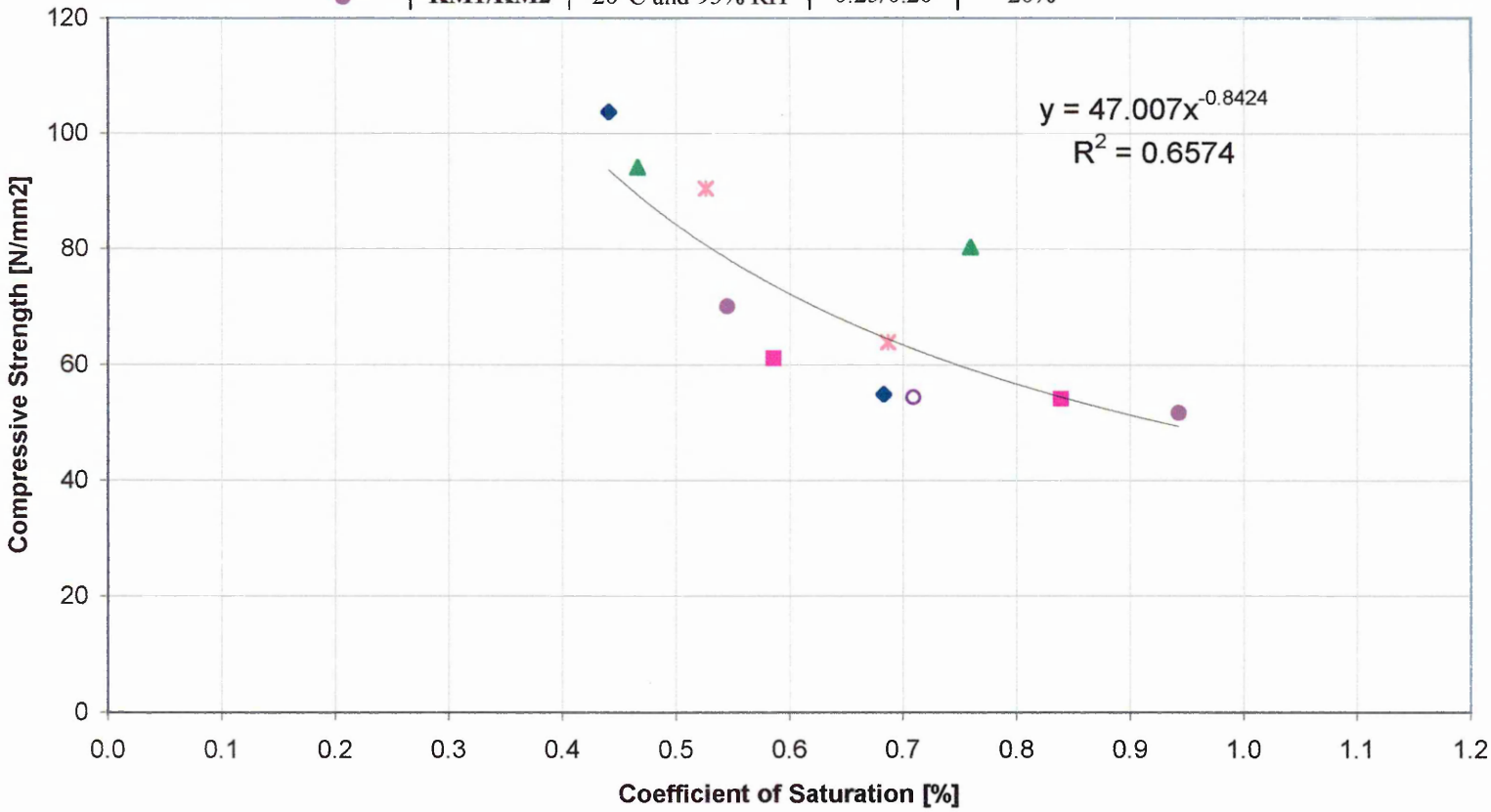

Figure 7.35 Relationship between the coefficient of saturation and compressive strength

The general trend of increasing compressive strength with increasing bulk density is common to hydraulic cementitious materials. The presence of voids in cementititous materials greatly reduce strength[81], this is in agreement with Feret's expression which relates strength to the sum of the volumes of water and air in the hardened cement paste.

There is a trend of compressive strength increasing with increasing in solid density of alkali activated materials cured in different conditions, see Figure 7.32 but a considerable scatter of data is apparent. This relationship can be expressed by the following equation:

$\sigma_{cm} = 0.14\ \rho_{bulk} - 276.66$ Equation 7.42

There is no clear trend of a relationship between compressive strength and apparent porosity or water absorption (see Figures 7.33 and 7.34) for different curing conditions.

There is a clear trend of compressive strength decreasing with increasing coefficient of saturation for all alkali activated materials cured under different conditions, see Figure 7.35. This relationship can be expressed by the following equation:

$\sigma_{cm} = 47.01\ c_{sat}^{-0.842}$ Equation 7.43

where

c_{sat} is the coefficient of saturation [%]

In cementitious materials, strength is in general a function of the pore structure, pore size distribution and the amount and type of different hydration products formed in the hardened material. Other researchers have concluded from their experimental investigations of alkali activated slag materials that the pore size distribution, pore volume and morphology of the pores are the main factors controlling strength[79]. Figure 7.33 shows the relationship between porosity and strength of alkali activated slag and Portland cement mortars[79]. Caijun[79]attributed the difference in strength between different alkali activated slag materials to difference in the pore structure of the hardened materials and not to the hydration products formed because the main

hydration products are always the same regardless of the alkali activator used, even if the minor products vary with the activator.

The results from the present investigation are contrary to those obtained by Caijun[79] as the materials with high apparent porosity generally exhibit also higher strength than the corresponding materials with lower apparent porosity, as shown in Figure 7.36. One of the reasons for this discrepancy is that the type and volume of the hydration products is the key factor governing the strength of thermally cured alkali activated fly ash materials. The hydration products and their relationship with the properties of alkali activated fly ash materials will be fully discussed in Chapter 8.

7.5.9 Durability Properties

7.5.9.1 Freeze-thaw resistance test

The accelerated weathering test was performed to compare the durability of different batches of alkali activated fly ash materials. The test monitored the variation of mass of test specimens during 100 cycles of freezing & thawing and determined the residual compressive strength after 100 cycles of freezing and thawing. The freeze-thaw resistance test was used for comparison purposes to assess the durability of the alkali activated materials.

Durability of the material can be assessed from the variation in weight of the test specimen during the exposure period. Any significant increase in the weight of samples during freeze-thaw cycling is due to a large increase in the porosity of the specimen. This is due to damage to the pore structure, the pores become bigger and can hold more water, resulting in a weight increase. If the specimens exhibit a significant reduction in weight, this will be caused by the loss of material from the surface and corners.

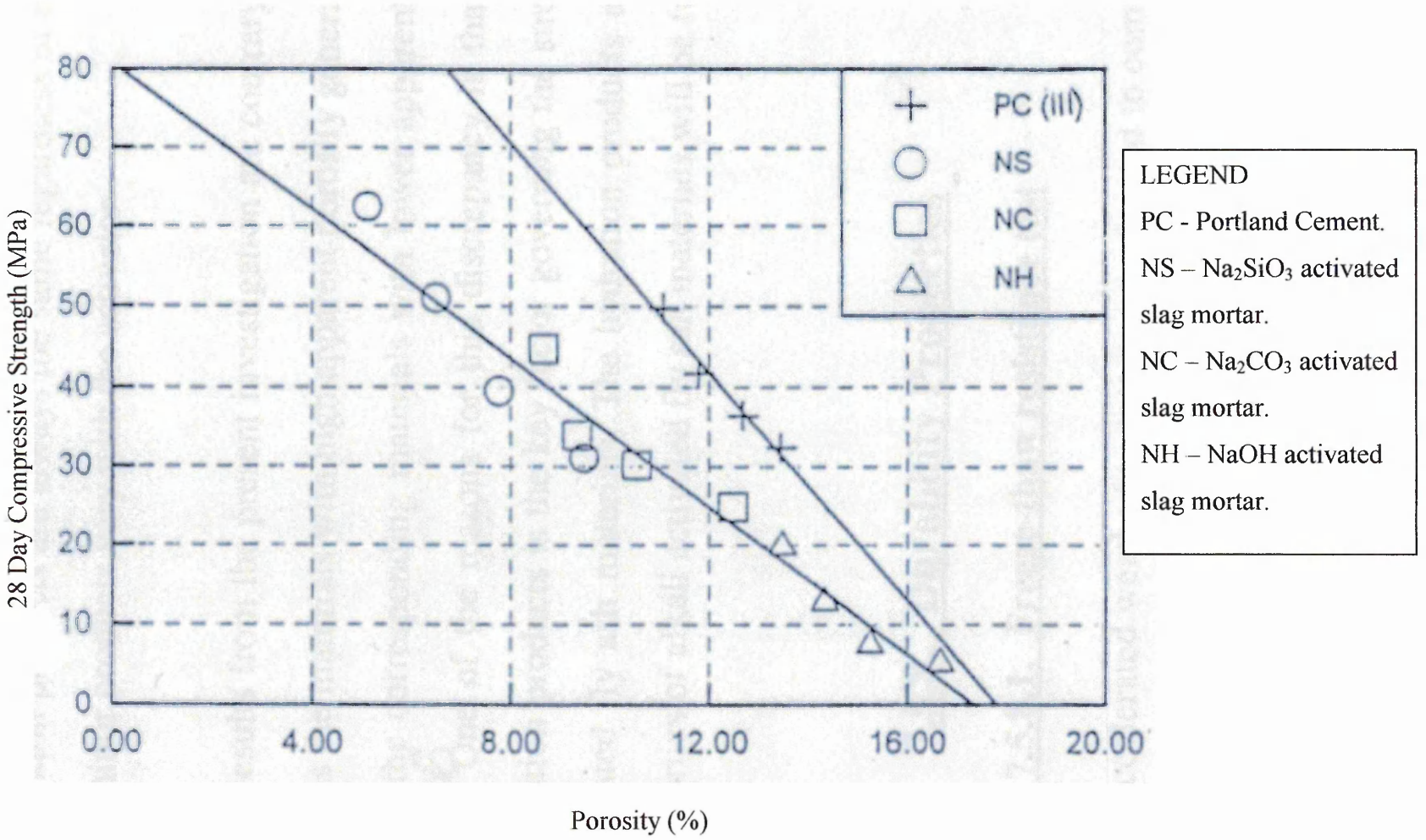

Figure 7.36 Relationship between porosity and strength of alkali-activated slag and Portland cement mortars[79].

Figure 7.37 presents the change in mass during 100 cycles of freezing and thawing for alkali activated fly ash materials. The corresponding relation between change in mass and the freeze - thaw cycles for fibre reinforced materials is shown in Figure 7.38. No significant change in mass (less than 1.5%) was observed during the 100 cycles of freezing and thawing for alkali activated fly ash materials regardless of curing conditions or water/binder ratio.

Alkali activated fibre reinforced materials also show no significant changes in mass (less than 0.5%) during 100 cycles of freezing and thawing (see Figure 7.38) following the same trends as alkali activated fly ash materials (see Figure 7.37). Monitoring the mass changes in alkali activated materials and fibre reinforced alkali activated materials proved not suitable to assess the freeze - thaw durability of the materials. A summary of the data is given in Tables 7.24 and 7.25.

A summary of the residual compressive strengths after exposure to 100 freeze-thaw cycles, is presented in Table 7.26 for alkali activated fly ash materials and Table 7.27 for fibre reinforced alkali activated materials. The residual compressive strength, *Residual* σ_c, is expressed as percentage of the compressive strength of the corresponding batch of specimens which were not subjected to freezing and thawing cycles

Figure 7.39 shows the relationship between residual compressive strength and water/binder ratio for alkali activated materials. Materials with a water/binder ratio of 0.25 exhibit higher residual compressive strength than materials with a lower water/binder ratio of 0.20 for curing conditions of 20°C, 65%RH following the same trends as the apparent porosity results (Figure 7.15). For example material A1 with a water/binder = 0.25 cured at 20°C and 65%RH has a higher residual compressive strength of 92% compared with 76% for the corresponding material batch code A2 with w/b = 0.20. The freeze - thaw resistance of alkali activated materials is governed by the mass transport phenomenon of deleterious substances and is influenced by the volume, size and continuity of the pores. Therefore, materials with higher apparent porosity will exhibit lower freeze-thaw durability hence lower residual compressive strength.

Symbol	Batch	Curing	Hardener	W/b Ratio
	A2	20°C and 65% RH	0%	0.25
	H2	thermal treatment	0%	0.25
	KM2	20°C and 95% RH	20%	0.25
	KA2	20°C and 65% RH	20%	0.25
	A1	20°C and 65% RH	0%	0.20
	H1	thermal treatment	0%	0.20
	KM1	20°C and 95% RH	20%	0.25
	KA1	20°C and 65% RH	20%	0.20
	W1	water curing at 20°C	0%	0.25

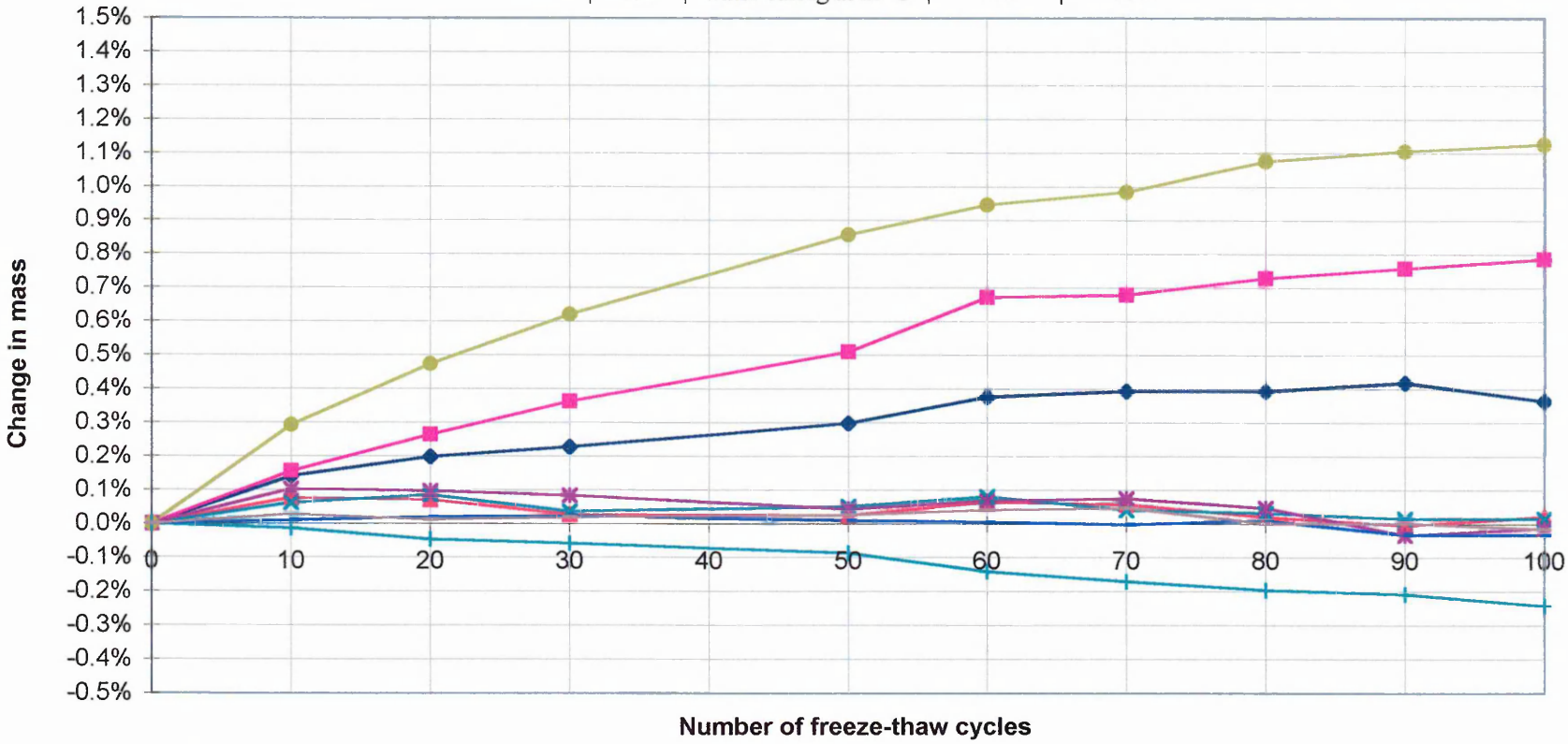

Figure 7.37 Change in mass during 100 cycles of freezing and thawing for the alkali activated fly ash materials

Symbol	Batch	Curing	Type of fibres	Volume
	GA1	20°C and 65% RH	glass fibres	1.5%
	sA1	20°C and 95% RH	straight steel fibres	1.5%
	SA1	20°C and 95% RH	melt extract fibres	1.5%
	GA2	20°C and 95% RH	glass fibres	3.0%
	SA2	20°C and 65% RH	melt extract fibres	3.0%
	GH1	thermal treatment	glass fibres	1.5%
	SH1	thermal treatment	melt extract fibres	1.5%
	GH2	thermal treatment	glass fibres	3.0%
	SH2	thermal treatment	melt extract fibres	3.0%

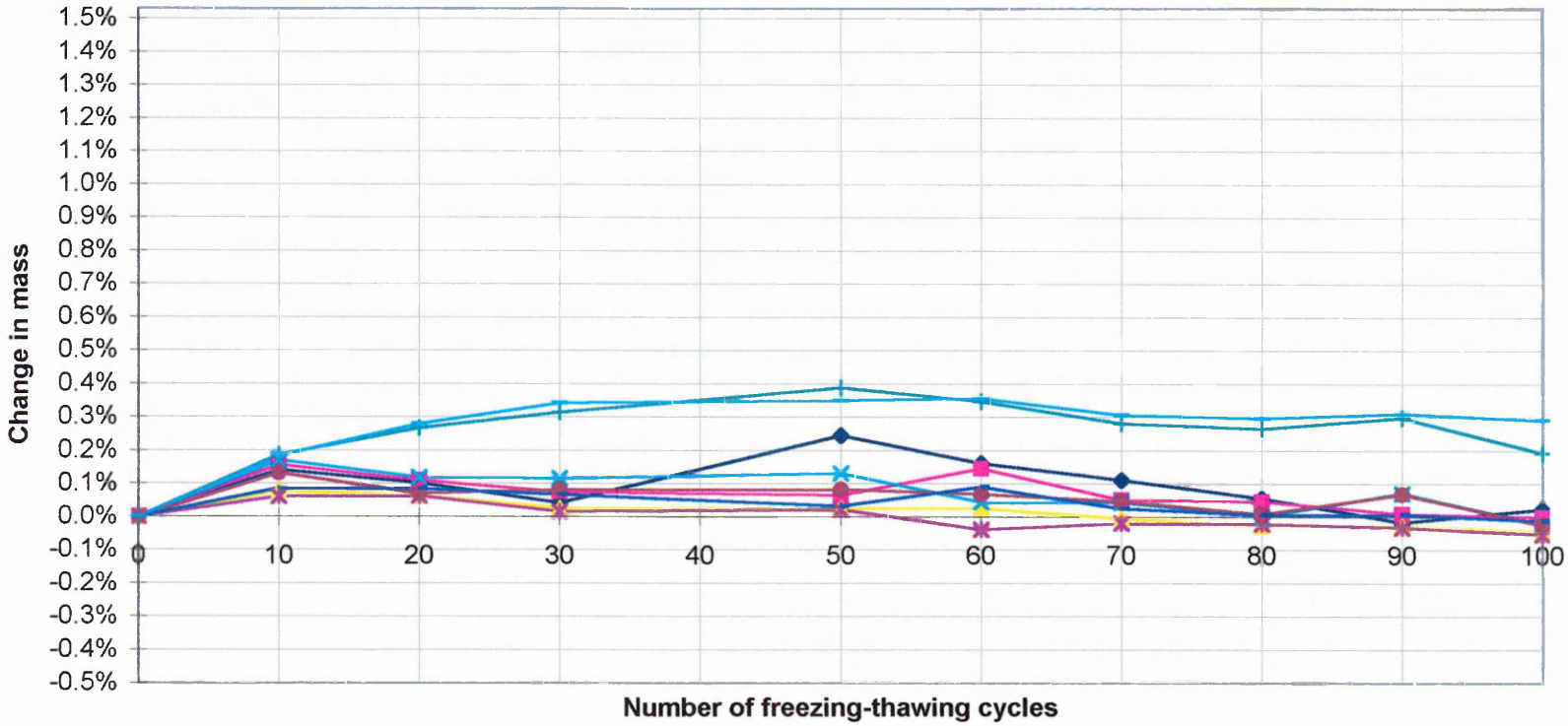

Figure 7.38 Change in mass during 100 cycles of freezing and thawing for the fibre reinforced alkali activated materials

Symbol	Batch	Curing	W/b Ratio	Hardener
—●—	A1/A2	20°C and 65% RH	0.25/0.20	0%
—△—	H1/H2	thermal treatment	0.25/0.20	0%
···※···	KA1/KA2	20°C and 65% RH	0.25/0.20	20%
—○—	KM1/KM2	20°C and 95% RH	0.25/0.20	20%

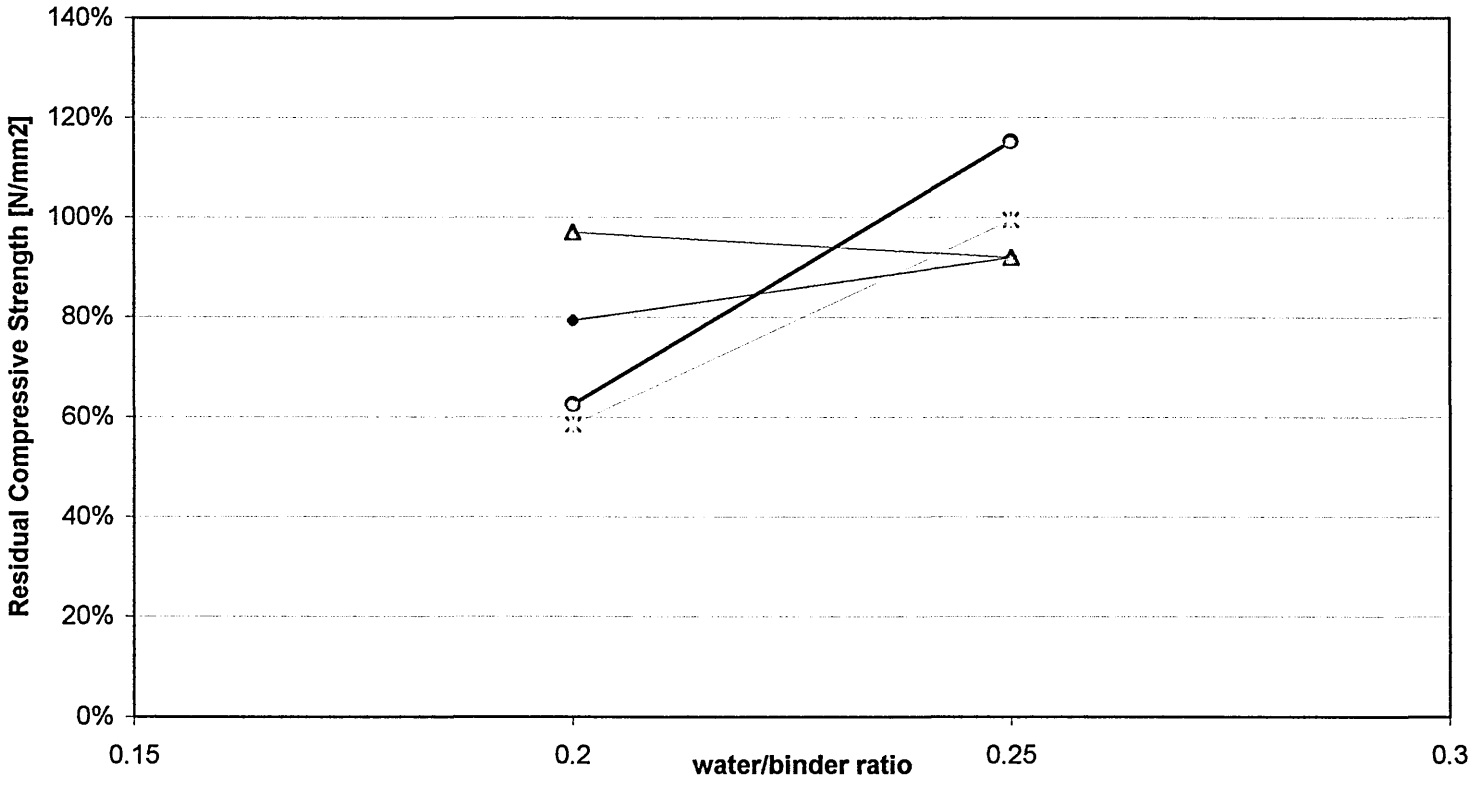

Figure 7.39 Relationship between residual compressive strength and water/binder ratio of alkali activated materials subjected to 100 freeze-thaw cycles

Table 7.24 Change in mass of alkali activated fly ash materials after exposure to 100 freeze - thaw cycles

Batch Code	Curing conditions	Water/ Binder	Mass before test [g]	Mass after test [g]	Change in mass [%]
A1	20°C and 65% RH	0.25	940.415	940.300	-0.01
W1	20°C and 95% RH	0.25	743.460	743.345	-0.02
H1	thermal treatment	0.25	922.01	932.39	+1.13
KA1	20°C and 65% RH	0.25	744.240	744.000	-0.03
KM1	20°C and 95% RH	0.25	735.555	733.780	-0.24
A2	20°C and 65% RH	0.20	955.670	959.160	+0.37
H2	thermal treatment	0.20	947.615	955.080	+0.79
KA2	20°C and 65% RH	0.20	777.265	777.380	+0.04
KM2	20°C and 95% RH	0.20	762.265	762.430	+0.02

Table 7.25 Change in mass of fibre reinforced alkali activated materials after exposure to 100 freeze – thaw cycles

Batch Code	Curing conditions	V_f l/d	Mass before test [g]	Mass after test [g]	Change in mass [%]
GA1	20°C and 65% RH	1.06	951.220	951.440	+0.02
SwA1	20°C and 95% RH	0.70	973.120	973.110	+0.01
SA1	thermal treatment	0.36	489.445	489.075	-0.08
GH1	20°C and 65% RH	1.06	932.815	932.590	-0.02
SH1	20°C and 95% RH	0.36	958.720	960.570	+0.19
GA2	20°C and 65% RH	2.12	483.055	482.935	-0.02
SA2	thermal treatment	0.72	1014.080	1013.540	-0.05
GH2	20°C and 65% RH	2.12	960.015	959.900	-0.01
SH2	20°C and 95% RH	0.72	1000.735	1003.640	+0.29

Table 7.26 Residual compressive strength of alkali activated fly ash materials after exposure to 100 freeze – thaw cycles

Batch Code	Curing conditions	Water/ Binder	$\sigma_c^{control}$ [N/mm^2]	$\sigma_c^{freeze\text{-}thaw}$ [N/mm^2]	*Residual* σ_c [%]
A1	20°C and 65% RH	0.25	63.27	58.31	92
W1	20°C and 95% RH	0.25	62.59	40.13	64
H1	thermal treatment	0.25	92.37	84.79	92
KA1	20°C and 65% RH	0.25	73.57	69.98	95
KM1	20°C and 95% RH	0.25	59.55	65.6	110
A2	20°C and 65% RH	0.20	123.19	93.48	76
H2	thermal treatment	0.20	108.34	100.49	93
KA2	20°C and 65% RH	0.20	104.10	58.26	56
KM2	20°C and 95% RH	0.20	80.63	48.22	60

Table 7.27 Residual compressive strength of fibre reinforced alkali activated materials after exposure to 100 freeze – thaw cycles

Batch Code	Curing conditions	V_f l/d	$\sigma_c^{control}$ [N/mm^2]	$\sigma_c^{freeze\text{-}thaw}$ [N/mm^2]	*Residual* σ_c [%]
GA1	20°C and 65% RH	1.06	68.42	58.38	85
SwA1	20°C and 95% RH	0.70	65.14	57.07	88
SA1	thermal treatment	0.36	66.27	58.97	89
GH1	20°C and 65% RH	1.06	68.08	65.46	96
SH1	20°C and 95% RH	0.36	86.54	69.26	80
GA2	20°C and 65% RH	2.12	67.71	53.49	79
SA2	thermal treatment	0.72	67.21	58.95	88
GH2	20°C and 65% RH	2.12	71.37	58.72	82
SH2	20°C and 95% RH	0.72	88.757	73.88	83

Note: $\sigma_c^{control}$ compressive strength before freeze-thaw exposure, [N/mm^2]

$\sigma_c^{freeze\text{-}thaw}$ compressive strength after freeze-thaw exposure, [N/mm^2]

Thermally cured materials on the other hand, show a different trend as they have similar residual compressive strengths of 92% for material with w/b=0.25 (batch code H1) compared with 93% for corresponding material with w/b = 0.20 (batch code H2), see Table 7.26.

Figure 7.40 shows the relationship between residual compressive strength and apparent porosity for alkali activated fly ash materials. There is a clear trend showing the residual compressive strength to decrease with an increase in the apparent porosity. This holds true for all curing conditions (except thermal curing) and for both water/binder ratios, see Figure 7.40. This relationship can be expressed as follows:

$$Residual\sigma_c = 77935\, p^{-2.43} \qquad \text{Equation 7.44}$$

with a coefficient of correlation R^2 of 0.82.

where, p is apparent porosity [%]

The residual compressive strengths for fibre reinforced alkali activated materials are closely grouped together in the range 79% to 96%, as shown in Table 7.27. Figure 7.41 shows the relationship between the residual compressive strength and V_fl/d; there is no clear correlation between V_fl/d and the residual compressive strength.

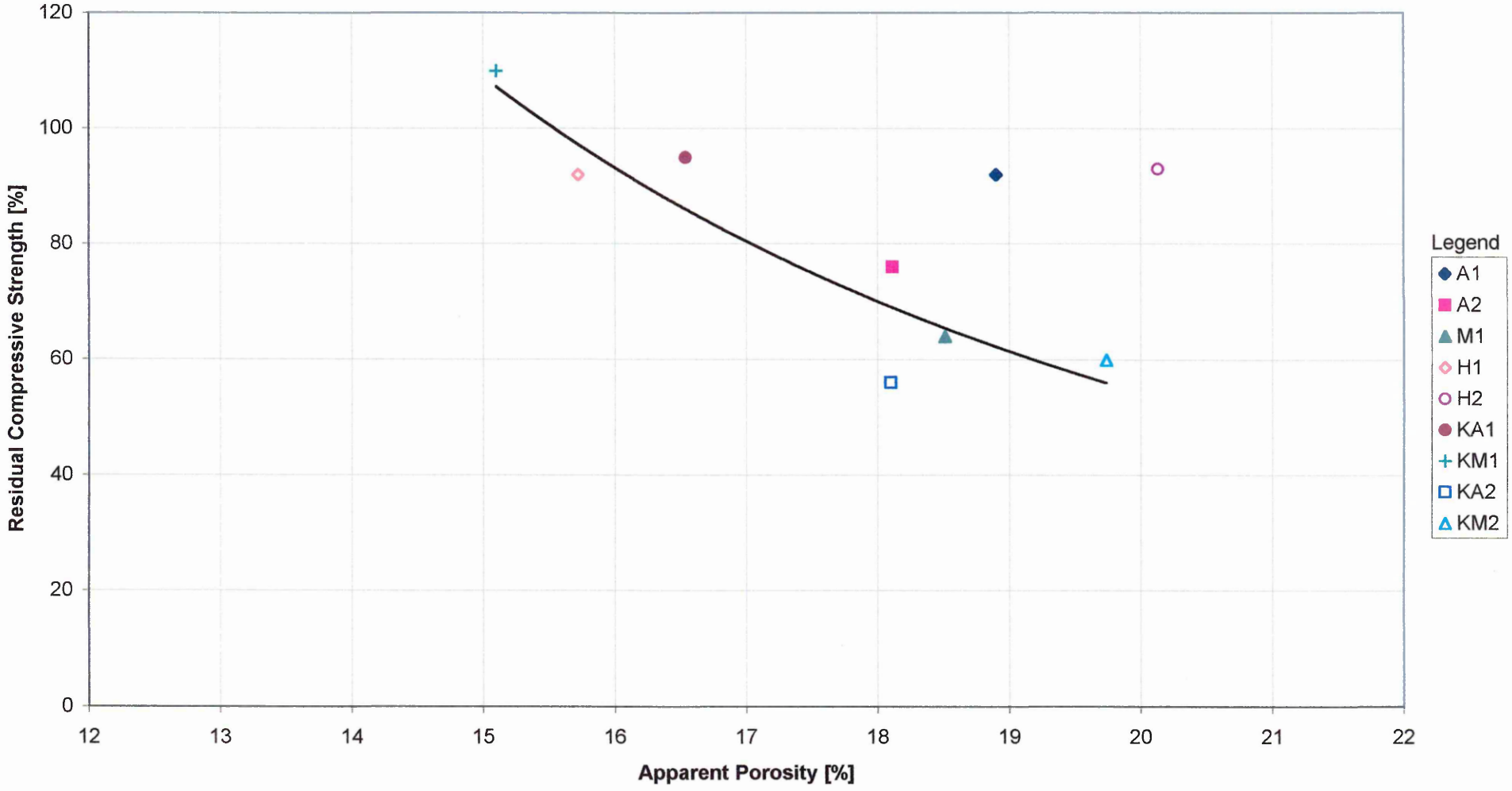

Figure 7.40 Relationship between residual compressive strength and apparent porosity of alkali activated materials subjected to 100 freeze-thaw cycles

Symbol	Batch	Curing	Type of fibres	Volume of fibres
	A1/GA1/GA2	20°C and 65% RH	glass fibres	0%/1.5%/3.0%
	H1/GH1/GH2	thermal treatment	glass fibres	0%/1.5%/3.0%
	A1/SA1/SA2	20°C and 65% RH	melt extract fibres	0%/1.5%/3.0%
	H1/SH1/SH2	thermal treatment	melt extract fibres	0%/1.5%/3.0%

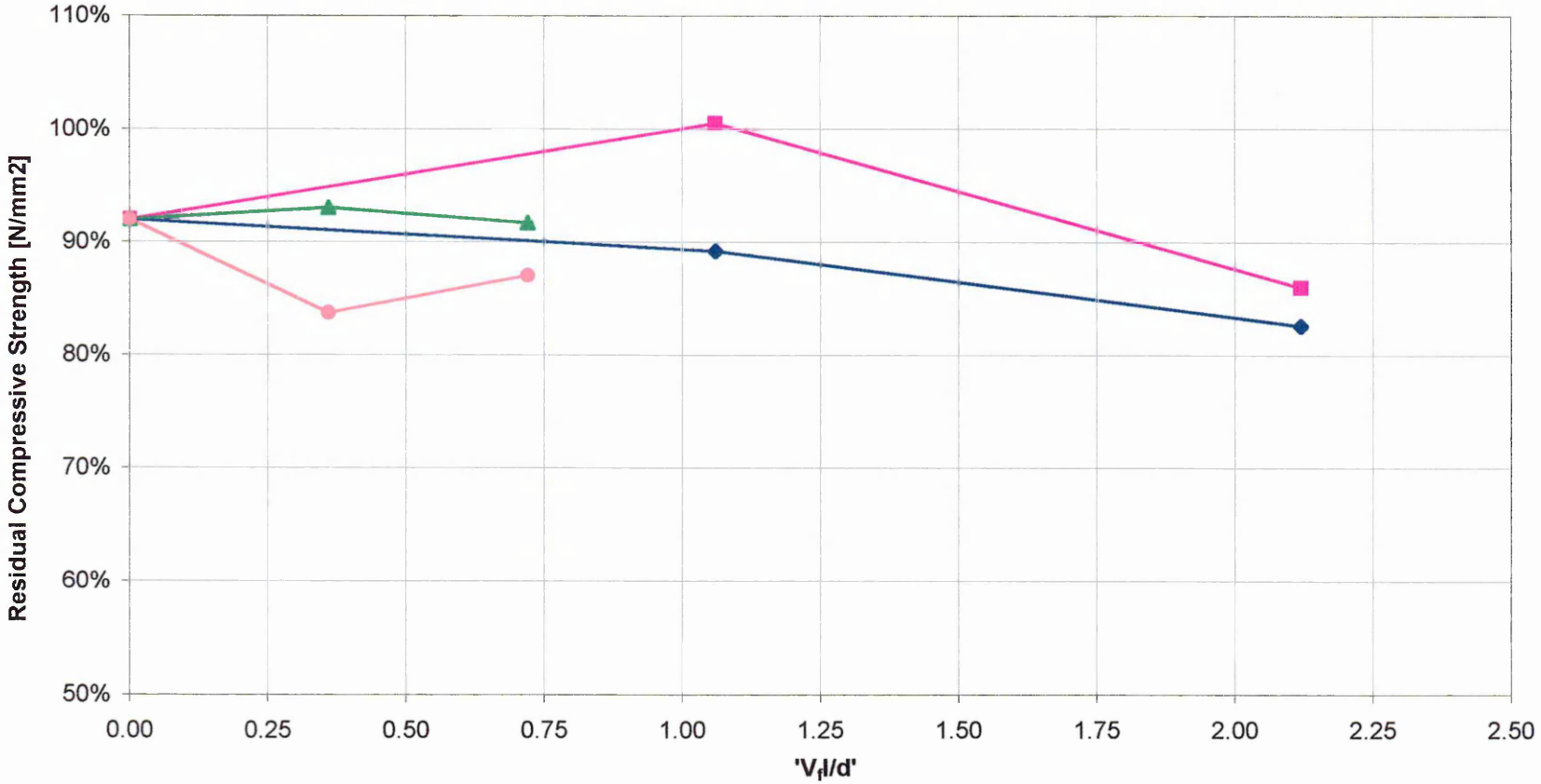

Figure 7.41 Relationship between residual compressive strength and '$V_f l/d$' of alkali activated fibre reinforced materials subjected to 100 freeze-thaw cycles

Other researchers[29] have investigated the freeze - thaw behaviour of alkali activated materials containing entrained air. The specimens were subjected to a total of 500 freeze-thaw cycles in 2000 hours. The nominal freeze-thaw cycle consisted of alternatively lowering the temperature of specimens from 4.4°C±1.7 to -17.8°C± 1.7 and raising it from -17.8°C± 1.7 to 4.4°C±1.7. The residual flexural strength after freeze - thaw cycling was between 58% and 67% and the weight loss between 0.99 and 3.70% depending on the mix design[29]. A direct comparison with the results from the present investigation is not possible since the details of the freeze-thaw cycles used in the two investigations are different.

7.5.9.2 Fire resistance

The fire resistance of alkali activated materials was assessed by means of residual pulse velocity and residual compressive strength test following exposure to temperatures up to 600°C. Change in mass was also recorded. A summary of the results is presented in Tables 7.28, 7.30 and 7.32. The corresponding results for fibre reinforced alkali activated fly ash materials are presented in Table 7.29, Table 7.31 and Table 7.33. The results are also plotted in Figures 7.42 and 7.43.

The mass loss results for alkali activated fly ash materials range between 4.5% and 4.9%, see Table 7.28. The mass losses for fibre reinforced alkali activated materials were within the range 3.9-4.3%, following similar trends as unreinforced alkali activated materials, see Table 7.29.

Figure 7.42 shows the relationship between residual compressive strength and water /binder ratio for alkali activated fly ash materials. Materials with a water/ binder ratio of 0.20 exhibit a lower residual compressive strength compared with materials with a higher water/ binder ratio of 0.25 for both curing conditions (20°C, 65% RH and 20°C, 95% RH). For example under 20°C, 65%RH curing, material batch code A1 with a w/b=0.25 has a higher residual compressive strength of 78% compared with 57% for the corresponding material with w/b=0.20, batch code A2, see Table 7.30.

Table 7.28 Change in mass of alkali activated fly ash materials after exposure to high temperatures

Batch Code	W/b	Curing Condition	Mass before test [g]	Mass after test [g]	Weight change [%]
A1	0.20	20°C and 65% RH	900.88	856.98	4.9
H1	0.20	thermal treatment	908.96	868.07	4.5
A2	0.25	20°C and 65% RH	938.87	894.15	4.8
H2	0.25	thermal treatment	918.82	876.01	4.7

Table 7.29 Change in mass of fibre reinforced alkali activated materials after exposure to high temperatures (thermal curing and w/b = 0.25 in all cases)

Batch Code	Fibre type/	V_f l/d	Mass before test [g]	Mass after test [g]	Mass loss [%]
GH1	glass fibres	1.06	891.42	855.28	4.1
SH1	melt extract fibres	0.36	891.47	853.7	4.2
GH2	glass fibres	2.12	876.55	838.9	4.3
SH2	melt extract fibres	0.72	943.41	906.37	3.9

Table 7.30 Residual compressive strength of alkali activated fly ash materials after exposure to high temperatures

Batch Code	W/b	Curing Condition	σ_{cc} [N/mm^2]	σ_{ct} [N/mm^2]	*Residual* σ_c [%]
A1	0.20	20°C and 65% RH	57.77	45.14	78
H1	0.20	thermal treatment	80.32	50.85	63
A2	0.25	20°C and 65% RH	103.74	58.97	57
H2	0.25	thermal treatment	94.21	55.96	59

Note: σ_{cc} compressive strength before exposure to high temperatures, [N/mm^2]

σ_{ct} compressive strength after exposure to high temperatures, [N/mm^2]

Table 7.31 Residual compressive strength of fibre reinforced alkali activated materials after exposure to high temperatures (thermal curing and w/b = 0.25)

Batch Code	Fibre type	V_f l/d	σ_{cc} [N/mm^2]	σ_{ct} [N/mm^2]	*Residual* σ_c [%]
GH1	glass fibres	0.55	59.19	51.34	87
SH1	melt extract fibres	0.36	75.25	53.57	71
GH2	glass fibres	1.10	62.06	39.62	64
SH2	melt extract fibres	0.72	77.18	58.21	75

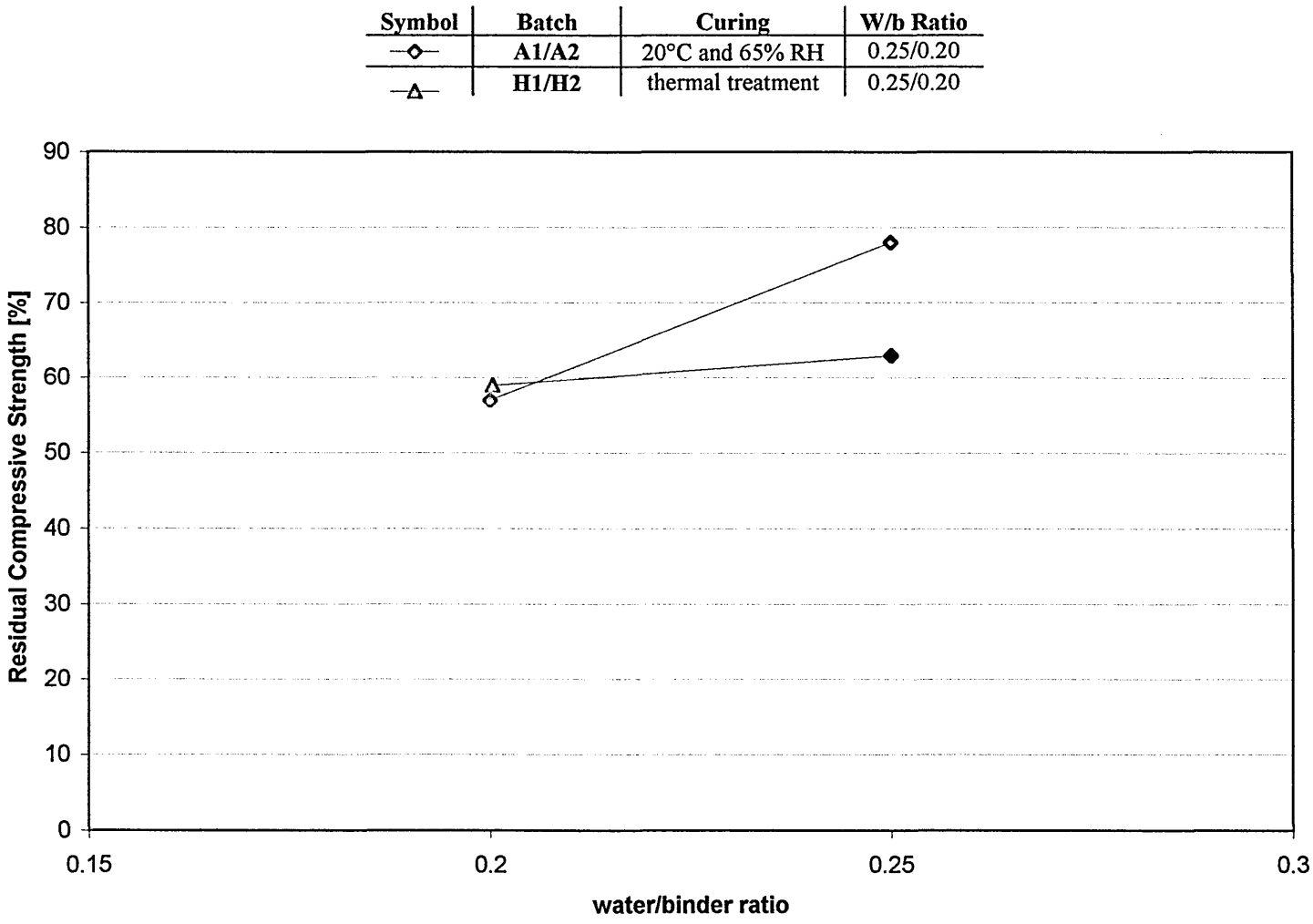

Figure 7.42 Relationship between residual compressive strength sand water/binder ratio of activated materials exposed to high temperature

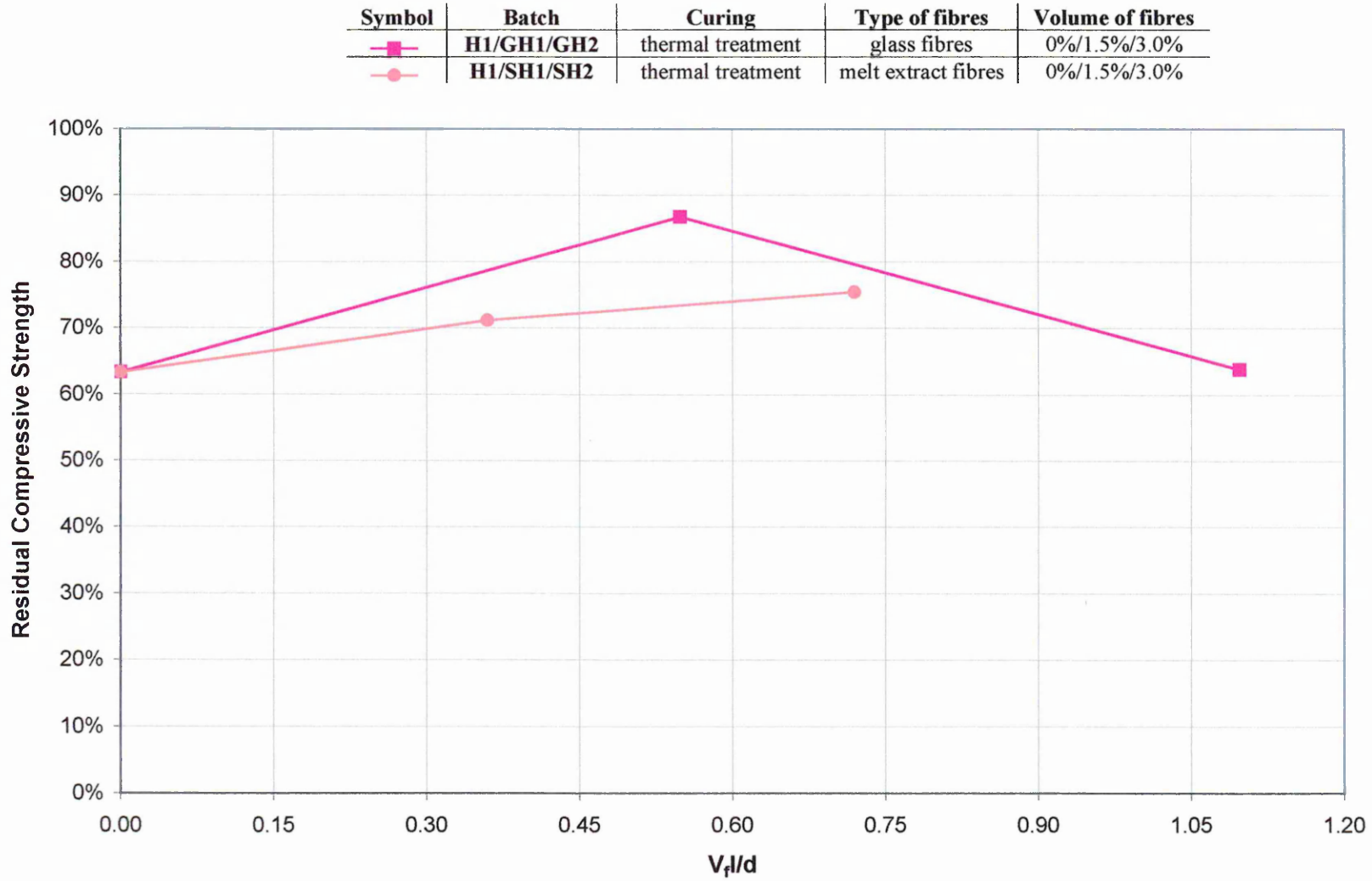

Figure 7.43 Relationship between residual compressive strength and 'V_fl/d' for fibre reiforced alkali activated materials exposed to high temperatures

A comparison of Figures 7.39 and 7.42 shows that the residual compressive strength resulting from freeze - thaw cycling exhibits the same trends as residual compressive strength caused by exposure to high temperatures (600°C). In both figures 7.35 and 7.38, materials with a water/binder ratio of 0.20 show lower residual compressive strength than corresponding materials with a higher water/binder ratio of 0.25. This was explained in the previous section 7.4.8.1 to be due to pore structure (volume, size and continuity of the pores).

The residual compressive strength results of fibre reinforced alkali activated materials range between 64% to 87% (Table 7.31). Figure 7.43 shows the relationship between the residual compressive strength and $V_f l/$. There appears to be no clear correlation between the fibre $V_f l/d$ ratio and the residual compressive strength after exposure to high temperatures (600°C). This follows the same trends as residual compressive strength after exposure to freeze-thaw cycling, see Figure 7.37.

The residual pulse velocities for alkali activated fly ash materials caused by exposure to high temperatures are in the range 40-50%, see Table 7.32. The values for the alkali activated fibre reinforced materials are approximately the same regardless of the V_f l/d and curing conditions. The minimum value is 49% and the maximum is 50% as shown in Table 7.33.

Table 7.32 Residual pulse velocity of alkali activated fly ash materials after exposure to high temperatures

Batch Code	W/b	Curing Condition	v_c [m/s]	v_t [m/s]	*Residual v* [%]
A1	0.20	20°C and 65% RH	3.63	1.83	50%
H1	0.20	thermal treatment	4.03	1.86	46%
A2	0.25	20°C and 65% RH	4.24	1.71	40%
H2	0.25	thermal treatment	4.05	1.64	40.5%

Note:

v_c pulse velocity before exposure to high temperatures, [N/mm^2]

v_t pulse velocity after exposure to high temperatures, [N/mm^2]

Table 7.33 Residual pulse velocity of fibre reinforced alkali activated materials after exposure to high temperatures (thermal curing and w/b = 0.25)

Batch Code	Fibre type	V_f l/d	v_c [m/s]	v_f [m/s]	*Residual v* [%]
GH1	glass fibres	0.55	3.65	1.78	49%
SH1	melt extract fibres	0.36	3.71	1.84	50%
GH2	glass fibres	1.10	3.49	1.72	49%
SH2	melt extract fibres	0.72	3.71	1.87	50%

The results from the present investigations are similar to those obtained by other researchers on fire resistance of cementitious materials but a direct comparison is difficult because of the difference in the testing temperature profile. However, Mohamedbhai[111] used 100 mm concrete cubes to assess the effect of high temperatures, in the range of 200-800°C (heating rate of 1°C per 10 seconds). He concluded that the residual strength of the concrete after one hour of exposure at 200, 400, 600 and 800°C can be expected to be approximately 80, 70, 60 and 30%, respectively, of the strength of the specimens not subjected to fire testing. The strength loss occurs within two hours of exposure at maximum temperature.

Mohamedbhai[111] found that the duration of exposure and cooling rate influence the pulse velocity and residual compressive strength and, consequently, the performance of concrete heated to temperatures up to 600°C. The effect of duration of exposure and cooling rate is less pronounced at high temperatures (800°C). Pulse velocity measurement seem to give a better indication of the temperature to which concrete has been exposed rather than the residual compressive strength of the concrete.

Other researchers[16] have concluded that temperatures up to 70°C have a limited effect on the compressive strength and modulus of elasticity of mass concrete containing fly ash (25% replacement of Portland cement). Specimens exposed to temperatures between 120°C-150°C show an increase in compressive strength. However, the modulus of elasticity is smaller than the corresponding value at 21°C. This is contrary to the behaviour of Portland cement concrete (without fly ash) at the same rage of temperature (120-150°C) as the strength and elasticity were both adversely affected. The increase in strength of concrete containing fly ash was attributed to the formation of tobemorite, which is 2-3 times stronger than tobemorite

gel. Tobemorite is a product of the reaction between lime and fly ash at high pressure and temperatures. At temperatures in the range 177° to 232°C, both the compressive strength and modulus of elasticity of concrete containing fly ash were reduced by 60% and 65%respectively. The deterioration in the mechanical properties of the material is thought to be due to the transformation of the tobemorite into crystalline alpha dicalcium silicate which has poor binding qualities[16].

Carette et al[112] investigated the long term effect of fire on the mechanical properties of concrete made with OPC blended with slag (35% replacement of Portland cement) and OPC blended with fly ash (25% replacement of Portland cement). Temperatures ranging from 75 to 600°C were used at a heating or cooling rate of 20°C per hour for a period of 1, 4 or 8 months[112]. The water/ binder ratio of the mixes was 0.45. The results discussed above show that the alkali activated materials of this investigation have a superior fire (high temperature exposure) resistance than normal concrete. For example, the residual compressive strength after one month of exposure at 600°C was 23% for the normal Portland cement concrete[112], 20% for concrete with slag addition[112] and 33% for the concrete with fly ash addition[112] compared with 68% for the alkali activated pozzolanic materials of the present investigation.

7.6 CONCLUSIONS

The following conclusions are based on the results of the investigation carried out in the laboratory, as detailed in section 7.5 "Results and Discussion" of this chapter:

1. The bulk and solid densities for alkali activated materials are within the range 2001 to 2063 kg/m^3 and 2340 to 2568 kg/m^3, respectively.

2. The apparent porosity and water absorption for alkali activated materials are within the range15.69 to 20.75% and 7.79 to 9.98%, respectively.

3. The coefficients of saturation for alkali activated materials are within the range 0.44 to 0.94%.

4. Raising the water/binder ratio from 0.20 to 0.25 decreases the apparent porosity and water absorption but increases the coefficient of saturation of alkali activated materials.

5. Raising the relative humidity of curing from 65% to 95% decreases the apparent porosity and water absorption of materials with a water/binder ratio of 0.25 and increases the apparent porosity and water absorption of materials with a water/binder ratio of 0.20.

6. Thermal curing increases the water absorption, apparent porosity and coefficient of saturation compared with ambient at 20°C, 65%RH

7. Materials with water /binder ratio of 0.25 show a permeability coefficient of 1.60 E-12 m/s when cured at 20°C, 65% RH and 3.16 E-12 m/s when thermally cured.

8. Compressive strength increases with an increase in bulk density of alkali activated materials cured in different conditions.

9. Compressive strength decreases with an increase in coefficient of saturation for alkali activated materials cured in different conditions.

10. No significant change in mass during the 100 freeze-thaw cycles occurred for alkali activated materials and fibre reinforced alkali activated materials.

11. The residual compressive strengths resulting from exposure to a 100 freeze - thaw cycles for alkali activated materials are within the range 56% to 95%.

12. The residual compressive strengths resulting from exposure to a 100 freeze - thaw cycles for alkali activated fibre reinforced materials are within the range 79% to 96%.

13. The residual compressive strengths resulting from exposure to high temperaturs (600°C) for alkali activated materials are within the range 57% to 78%.

14. The residual compressive strengths resulting from exposure to high temperatures (600°C) for alkali activated fibre reinforced materials are within the range 64% to 87%.

15. Residual compressive strength decreases with increasing apparent porosity for all alkali activated materials.

16. There is no correlation between the fibre V_f l/d ratio and the residual compressive strength of fibre reinforced alkali activated materials.

"All things are hidden, obscure and debatable if the cause of the phenomena be unknown, but everything is clear if this cause be known."

Louis Pasteur

8 SEM and XRD investigations of alkali activated materials

8.1 INTRODUCTION

Much of the improvement in the performance of cementitious materials has arisen from the application of physicochemical studies[70]. Mineralogical composition is one of the most important factors which decides about the physico-chemical properties of a material. Information about the mineralogical composition should always be presented beside the chemical composition and its physical characteristics of the material.

For a complete description of the chemical and mineralogical composition of a material, more than one method should be used in the investigation. Using two or three different methods of chemical and mineralogical analysis would complement each other and increase the level of confidence in the results. Microstructutral and chemical information have been gained from scanning electron microscopy (SEM) and energy dispersive X-ray microanalysis (EDAX) while other information have been gained from techniques such as feature analysis. The findings from these various techniques serve as a piece of a puzzle and are integrated to provide the current understanding of the hydration process, which has improved greatly but is still incomplete. One of the main limiting factors in the characterisation of alkali activated material's hydration has been the ability to characterise nearly amorphous solids as well as the fact that X ray analysis is very difficult to evaluate. Sand used as an ingredient in mortar causes peak ovelapping. The x-ray diffraction power method can detect only phases which are present in higher quantities than 3% (by weight).

8.2 OBJECTIVES

The current study was undertaken to characterise the microstructure and macrostructure of alkali activated calcium aluminosilicate binders. Scanning electron microscopy (SEM) together with energy dispersive X-ray microanalysis (EDAX), digital mapping and feature analysis were used to detail the microstructure and

chemical composition of hydrated phases while the development of these phases was followed using X-ray diffraction (XRD).

Integration of the results from these techniques provides characterisation of unreacted fly ash, ground granulated blast furnace slag and microsilica and identification of the crystalline hydration products. The present study is aimed mainly at determining the chemical and microstructural characterisation of alkali activated fly ash materials and exploring the relationships between:

- the structural constitution of the unreacted amorphous fly ash, ggbs and microsilica and the hydrated materials.
- the relationship between the engineering properties (strength and durability) and the microstructure of alkali activated materials.

8.3 EXPERIMENTAL DETAILS

8.3.1 Constituent Materials

The constituent materials used for the investigations presented in this chapter are detailed in Chapter III (Experimental Programme) and are also summarised in the following sections.

The main pozzolanic material used in the mixes was **pulverised fuel ash** (pfa) from Ratcliffe power plant. Chemical composition (by weight) of this ash is presented in Table 8.1.

Table 8.1 Chemical composition of the fly ash

Element	Content [%]
Silicon dioxide (SiO_2)	47.4
Aluminium oxide (Al_2O_3)	25.6
Iron oxide (Fe_2O_3)	10.4
Magnesium oxide (MgO)	1.7
Calcium oxide (CaO)	3.3
Sulphate (SO_3)	1.0
Potassium oxide (K_2O)	3.1
Sodium oxide (Na_2O)	1.4
$Na_2O_e = 0.658 \cdot K_2O + Na_2O$	3.4
Titanium oxide (TiO_2)	1.0
Chloride (Cl)	0.01
Loss on Ignition	4.54
Density (kg/m^3)	2290
Sieve Residue Retained 45μm	
$\frac{CaO + MgO + Al_2O_3}{SiO_2}$	**0.645**

The slag used in this investigation was **ground granulated blast furnace slag** (ggbs) from Scunthorpe and Purfleet steel works. Chemical composition (by weight) of this slags is presented in Table 8.2.

Table 8.2 Chemical composition of ground granulated blast furnace slags

Element	Purfleet	Scunthorpe
Silicon dioxide (SiO_2)	35.02	35.57
Aluminium oxide (Al_2O_3)	11.47	13.06
Iron oxide (Fe_2O_3)	0.72	0.66
Magnesium oxide (MgO)	8.80	9.30
Calcium oxide (CaO)	42.34	39.18
Sulphate (SO_3)	0.13	0.2
Sulphide (S^{2-})	1.00	0.43
Potassium oxide (K_2O)	0.19	0.53
Sodium oxide (Na_2O)	0.26	0.31
$Na_2O_e = 0.658 \cdot K_2O + Na_2O$	0.39	0.66
Titanium oxide (TiO_2)	0.57	0.71
Clorhidride (Cl)	0.00	0.02
Manganese (MnO)	0.23	0.48
Manganese Oxide (Mn_2O_3)	0.26	-
Loss of Ignition	0.51	1.27
Insoluble Residue	0.13	0.78
Particle size analysis	**464**[m^2/kg]	**391**[m^2/kg]
$\frac{CaO + MgO + Al_2O_3}{SiO_2}$	**1.788**	**1.730**

Microsilica (silica fume) used in this investigation was a dry densified silica fume with the chemical composition (by weight) given in **Table 8.3**.

Table 8.3 Chemical composition of the densified silica fume

Element	Content [%]
Silicon dioxide (SiO_2) amorphous	85 to 98
Iron oxide (Fe_2O_3)	max. 3.0
Aluminium oxide (Al_2O_3)	max.1.5
Calcium oxide (CaO)	max.0.7
Magnesium oxide (MgO)	max.2.0
Sodium oxide Na_2O)	max.1.0
Potassium oxide (K_2O)	max.3.0
$Na_2O_e = 0.658 \cdot K_2O + Na_2O$	max 2.97
Carbon (C)	max.3.0
$\frac{CaO + MgO + Al_2O_3}{SiO_2}$	**0.0494 to 0.0428**

Washed and graded **high silica fine sand** from Congleton quarry was used as fine aggregate in the alkali activated materials. Its chemical composition (by weight) is given in Table 8.4.

Table 8.4 Chemical composition of silica sand from Congleton

Elements [%]	Content [%]
Silica (SiO_2)	95.13
Aluminia (Al_2O_3)	2.34
Iron oxide (Fe_2O_3)	0.24
Sodium oxide (Na_2O)	1.61
Potassium oxide (K_2O)	-
$Na_2O_e = 0.658 \cdot K_2O + Na_2O$	1.06
L.O.I.	0.25
Bulk density [kg/m^3]	1450
Average grain size [μm]	175

Water glass with a mean molar ratio (silica modulus, n), SiO_2/Na_2O =2.06 was used. Its chemical composition (by weight) is given in Table 8.5.

Table 8.5 Chemical composition of water glass

Element	Content [%]
Silicon dioxide (SiO_2)	30.55
Sodium oxide (Na_2O)	15.27
Water (H_2O)	54.18

Water glass hardener: Three aluminium phosphate compounds, commercial product K-Bond were selected as water glass hardener in order to accelerate the curing process:

1. K-Bond # 80 - Aluminium Thriophosphate Compound, $AlH_2P_3O_{10}\ 2H_2O$
2. K-Bond # 90 - Aluminium Methaophosphate Compound,
3. K-Bond # 200 - Aluminium Orthophosphate Compound.

The general properties of the hardener are given in Table 8.6.

Table 8.6 General properties of the water glass hardeners

General Properties	KB#80	KB#90	KB#200
Appearance	Fine white powder	Fine white powder	Fine white powder
Acidity [meq/g]	4.3 ± 0.5	1.2 ± 0.5	1.2 ± 0.5
Moisture [%]	max 1.5	max 1.5	0.3
Solubility in water [%]	max 3.0	max 3.0	0.4
pH	2.5 ± 0.5	3.2 ± 0.5	5.3 ± 0.5
Sieve residue > 44 micron [%]	1.0	max 1.0	0.2

8.3.2 Sample Preparation

A detailed description of the mixing, casting and curing procedures is given in section 5.3 of Chapter IV. Mixing was carried out using a forced action pan Hobart mixer with a capacity of 5 kg. The dry component materials, fly ash, silica fume, ground granulated blast furnace slag and sand were mixed thoroughly. Then the water glass was added and mixed with the dry components until the mixture became homogenous. The hardener was added near the end of the mixing process in the form of a slurry, to aid its dispersion in the mix. The mixes were cast in specially manufactured stainless steel moulds which were suitable for placing in a fan assisted oven at high temperature (up to 120°C). The mixed (homogenised) material was cast in the mould in one layer and compacted by a hydraulic press using compaction pressure of a 20 N/mm^2. Immediately after casting, the test specimens were subjected to one of the following two curing conditions:

i. 20°C temperature and 65% relative humidity. The specimens were kept in the moulds for 7 hours, then demoulded and curing maintained at 20°C and 65% RH.

ii. high temperature (thermal) curing in a Forcetraft time programmable fan aided oven. After casting, the samples (within the moulds) were placed in the oven and the temperature raised from 20.6°C to 30°C and held at 30°C for 5 hours. The temperature was then progressively increased in steps up to 120°C as shown in Table 8.7. Finally the temperature was gradually reduced to 20.6°C. The total duration of the curing period was (21 hours). The samples were subsequently stored under 20°C and 65% RH.

Table 8.7 High temperature curing profile

Temperature T [°C]	**20.6**	**30**	**45**	**60**	**80**	**100**	**120**
Time [minutes]	30	300	300	300	180	60	60

8.3.3 Details of investigated batches

The source of ggbs, type of hardener and curing conditions used for the alkali activated materials considered in this Chapter are given in Table 8.8. The water glass (Crystal 112) content was 11% (by weight) with the exception of batch code RT for which the water glass content was 10% (by weight). The hardener content was 20% by weight of the sodium silicate solution (water glass). In order to obtain statistically viable results each batch consisted of 6 specimens made from the same mix.

Table 8.8 Source of ggbs, type of hardener and curing conditions used for the alkali activated materials

Group	Batch Code	Source of ggbs	Type of hardener	Curing Condition
na	**RT**	no slag	no hardener	thermal
I	**A**	no slag	no hardener	20°C and 65% RH
I	**H**	no slag	no hardener	thermal
I	**B3**	no slag	no hardener	20°C and 65% RH
II	**SA**	Scunthorpe	no hardener	20°C and 65% RH
II	**SH**	Scunthorpe	no hardener	thermal
II	**SAB3**	Scunthorpe	KB#200	20°C and 65% RH
II	**SHB3**	Scunthorpe	KB#200	20°C and 65% RH
na	**WG09**	Purfleet	no hardener	thermal
na	**WG15**	Purfleet	no hardener	thermal

Bach code key:

A - air cured at 20°C and 65% relative humidity (condition i),

H - thermally cured,

RT - fly ash from Ratcliffe power plant,

S - slag from Scunthorpe power plant

B3 - water glass hardener Aluminium Orthophosphate compound (K-Bond # 200),

WG - water glass (sodium silicate solution).

8.3.3.1 Series used to study the influence of slag

The proportion of the constituent materials is presented in Table 8.9. The chemical composition and the specific surface area of investigated slags are given in Table 8.2. All batches were cast with a compaction pressure of 20 N/mm^2 and cured as detailed in section 8.3.2.

Table 8.9 Mix proportions used for the alkali activated materials

Batch Code	Fly Ash [w_t %]	Microsilca [w_t %]	Slag [w_t %]	Sand [w_t %]	Water Glass [w_t %]	Curing
RT	25	-	-	65	10	thermal
IA	20	5	-	64	11	20°C and 65% RH
IH	20	5	-	64	11	thermal
IISA	20	5	10	54	11	20°C and 65% RH
IISH	20	5	10	54	11	thermal

8.3.3.2 Series used to study the influence of water glass hardeners

The proportions of the constituent materials used in this series is presented in Table 8.10. The hardeners selected for the present investigation was of the aluminium polyphosphate type (KB#200). Corresponding to each batch of mixes containing hardener another batch was made without hardener.

Table 8.10 Mix proportion used for the alkali activated materials

Batch Code	Fly Ash [w_t %]	Microsilca [w_t %]	Slag [w_t %]	Sand [w_t %]	Water Glass [w_t %]	Hardener [%]	Curing
IISA	20	5	10	54	11	-	20°C and 65% RH
IISAB3	20	5	10	54	11	20	20°C and 65% RH
IISH	20	5	10	54	11	-	thermal
IISHB3	20	5	10	54	11	20	thermal

8.3.3.3 Series used to study the influence of curing conditions

Two different curing conditions were employed in the present investigations as detailed in section 8.3.2. The proportion of the constituent materials used in this series are presented in Table 8.11.

Table 8.11 Mix proportion used for the alkali activated materials

Batch Code	Fly Ash [w_t %]	Microsilca [w_t %]	Slag [w_t %]	Sand [w_t %]	Water Glass [w_t %]	Hardener [%]	Curing
IA	20	5	-	64	11	-	20°C and 65% RH
IH	20	5	-	64	11	-	thermal
IISA	20	5	10	54	11	-	20°C and 65% RH
IISH	20	5	10	54	11	-	thermal
IISAB3	20	5	10	54	11	20	20°C and 65% RH
IISHB3	20	5	10	54	11	20	thermal

8.3.3.4 Series used to study the influence of silica modulus of water glass

In order to investigate the effect of silica modulus on the properties of alkali activated fly ash materials sodium silicate solution with different silica ratios n were used. However, sodium silica solution with silica modulus $n \leq 1$ is not commercially available. Therefore a water glass with mean molar ratio (silica modulus) SiO_2: Na_2O = 1.65 was modified by addition of 12.5 NaOH (technical grade) to produce water glass with silica modulus n of 0.9 and 1.5 as detailed in section 4.3 of Chapter IV.
The proportions of the constituent materials used in this series were fly ash/ ggbs: microsilia/ sand/ water glass of 17/ 17/ 5/ 50/ 10.

8.4 TESTING PROGRAMME

8.4.1 Scanning electron microscopy

8.4.1.1 Introduction

Scanning electron microscope (SEM) equiped with X-ray microanalyser was used to observe the microstructure and to analyse the element concentration in micro-areas. Using this method, semiquantitative analysis of the crystals and amorphous phases could be produced to identify the observed crystals and amorphous phases.

In a typical SEM, an electron gun and multiple condenser lenses produce an electron beam whose rays are deflected at various angles of the optic axis by the first set of electromagnetic scan coils[164]. The second set of electromagnetic scan coils deflect the beam back across the optical axis. Both sets of scan coils are in the bore of the final lens. From there, all the rays pass through the final aperture of the final lens and strike the specimen at various points. The scan coils and the cathode ray tubes are powered by the same scan generator, so that each scanned point on the specimen is uniquely reproduced on the displaying or recording cathode ray tube and video amplifiers[164]. To these amplifiers one or more of the resultant signals are fed: high energy back-scatter electrons, low-energy secondary and /or back-scatter electrons, x-rays and cathode-luminescent radiation in the UV, visible and infrared regions. All the results can be monitored separately or simultaneously by means of appropriate detectors.

8.4.1.2 Testing equipment

Scanning electron microscopy (SEM) together with energy dispersive X-ray microanalysis (EDAX), digital mapping and feature analysis were performed using a scanning electron microscope Philips XL-40 equipped with a completely computerised operating system. The SEM microscope was fitted with the following detectors:

- back-scatter detector PW 6843;
- cathodoluminescence detector PW 6886;
- specimen current detector PW 6844;

- energy dispersive X-ray LINK - ISIS EDS microanalyser
- a small infrared inspection camera PW 6832 which was used to facilitate the positioning of the specimen during investigations.

8.4.1.3 Secondary electron imaging (SEI) and back-scatter electron imaging (BSEI)

The SEM indirectly constructs a pattern or a map that can be interpreted as an image of the object. Interpretation of the SEM images is facilitated by many other attributes contributing to the visibility, particularly resolution, contrast, focus, depth topography and apparent illumination[164]. In the BEI mode the contrast is derived from differences in the atomic number of each constituent, because the intensity with which the electrons are back-scattered increases monotonically with average atomic number. Phases with a higher atomic number such as unreacted slag, fly ash and microsilica appear as white bright phases and those with a lower atomic number such as hydration products as light-dark grey phases and pores as dark patches. All these features are easily distinguished on the basis of their grey levels.

Magnifications from around 10-10000x were used in the present investigation. Since there is no actual image formed in the microscope's column, magnification is the ratio of the area scanned to the display area. The size of the display is generally fixed between 10-20cm magnification is increased by decreasing the area scanned. Magnification is generally calculated as the ratio of the length of the display divided by the corresponding length of the scanned area. The practical **resolution** of the SEM is limited to 20nm, for most specimens in optimum position relative to the detector for the secondary electrons.

Contrast in scanning electron microscopy is defined as the ratio of the change in signal between two points on the specimen and the average signal. In case of rough surface (fracture surface), topographic contrast is provided whether back-scatter or secondary electrons are detected[164]. When a plane specimen is tilted away from the normal incidence of the beam, electron back-scattering increases gradually approaching unity at the grazing incidence. The **radiation** used in the SEM is one or more of eight different types of signal. Figure 8.1 illustrates the most common signals and the location of the specimen volume from which they originate.

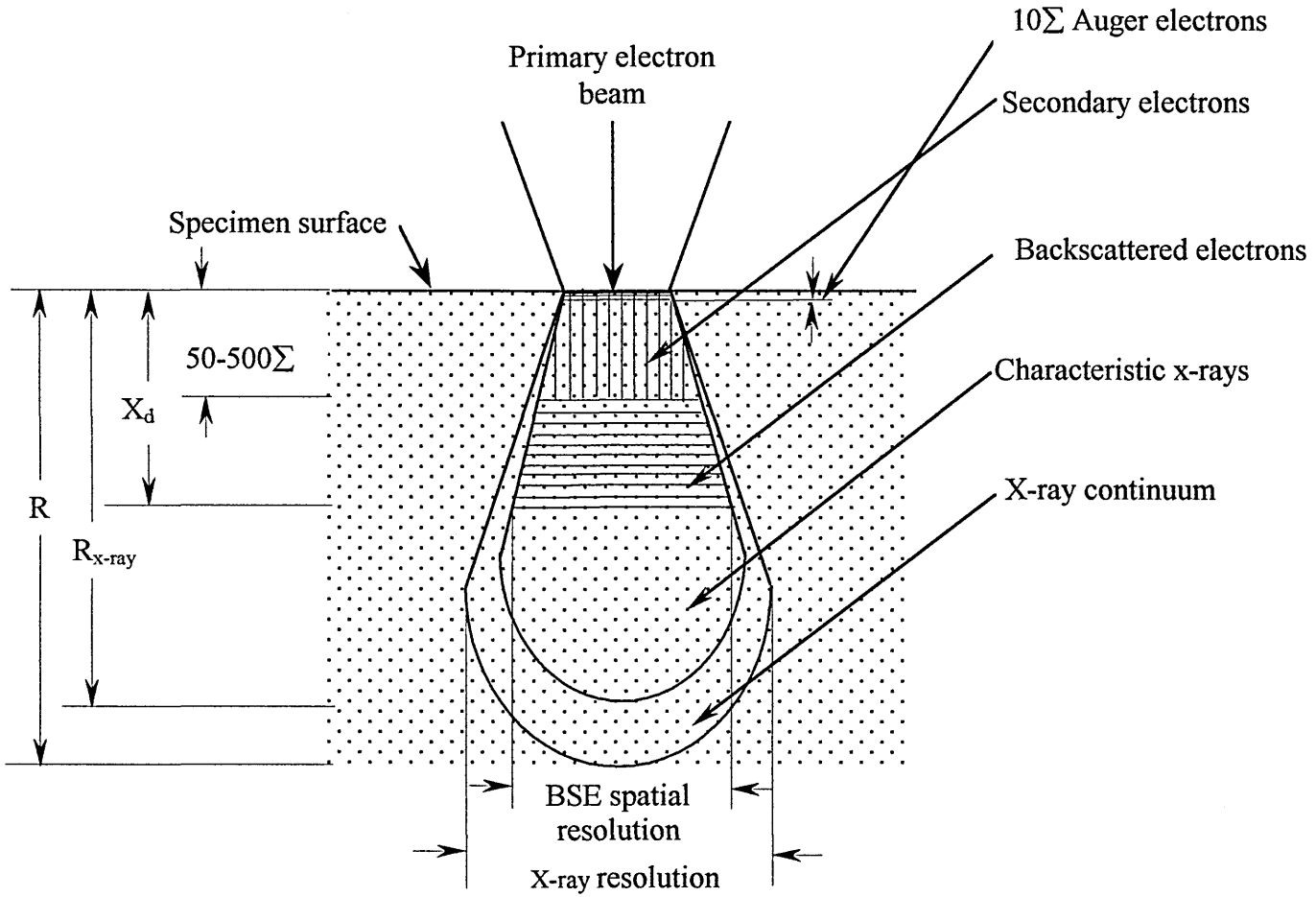

Figure 8.1 The volume within a specimen from which various types of signals originate

The scanning electron imaging in the present investigation were performed at an accelerating voltage of 25KeV. The **working distance** of the SEM is the distance between the surface of the specimen and the front surface of the objective lens. Working distance from the soffit of the pole of the objective to specimen's surface was 20mm for secondary electron imaging (SEI) and 12mm for back-scatter electron imaging (BSEI).

8.4.1.4 Energy dispersive X-ray analysis (EDAX)

The energy dispersive X-ray analysis (EDAX) method is based on the analysis of the characteristic X-ray radiation generated in the surface of the specimen by an electron beam. One of the consequences of bombarding the samples with electrons is the producing of X-rays, which, as a result of quantised transition within the element, are diagnostic of the elements present in the sample[164]. The analytical scanning electron microscope can provide a visual image of the sample under investigation together with the ability to perform a comprehensive chemical analysis of the sample or a particular region within.

This routine generates spectra of the chemical elements present under the electron beam. It allows general identifications of the elements from boron (atomic number 5) to uranium (atomic number 92). Detecting light elements (Be, B, C, N and O) is difficult because of the low energy X-rays they generate which are easily absorbed by the beryllium window of the energy dispersive X-ray microanalyser.

The limitation of this technique is that it is not possible to determine the stoichiometric composition of compounds (i.e. oxides) and the lowest detectable limit of element concentration is about 0.5%. For each of the following elements (Na, Mg, Al, Si, S, K, Ca, Fe and P for the samples containing water glass hardener) a window was painted in the current bar memory at full hight and half width of the intensity peak.

The windows from the bar memory spectrum were stored and used with the investigated specimens. The contents of these windows can then be used to obtain numerical semiquantitative information from the spectrum. Using the process spectrum option, the net and gross integrals of all windows set in the bar memory spectrum were obtained together with the window labels, start and end point (in

keV), width (in channels), efficiency factor, percentage total. Percentage total is the net integral value for each window, multiplied by the efficiency factor, expressed as percentage of the sum of the net integrals for that spectrum multiplied by their efficiency factors.

All instruments are fitted with elemental detection systems in form of Link Analyser, from Oxford Instruments. Microanalysis were carried out using the following acquisition parameters: live time 100s, accelerating voltage 20 keV, process time window Be. Checks were made to assure that the image is focused, the spot size optimised and that the X-ray count is adequate to give 7-8000 counts (24-25 dead)

8.4.1.5 Digital Mapping

An internal electron signal processing is installed on the system. Therefore it is possible to collect and store an electron image at the same time as the X-ray maps are acquired. In digital mapping the image of the sample is divided up into a number of segments (256μm x 256μm) and the chemical information obtained from the energy dispersive analyser in a particular region of the sample is stored digitally in the corresponding screen segment. Thus multilevel digital maps can be displayed concurrently with the electron image.

One map was obtained from each sample because of the amount of time required (aproximately 120 minutes) to acquire them. One square area of the map responds to one element. For each of the following elements Na, Mg, Al, Si, S, K, Ca, Fe P and for the samples containing water glass hardener a map was acquired. The higher the element concentration at a certain point on the sample surface the lighter the corresponding point on the map. EDX maps are qualitative comparative characteristics of simultaneous occurrence of the chemical elements present in the particles of the studied material.

After the selected samples were placed in the microscope chamber a suitable field of view was selected and the X-ray analyser was used to check that the detector was calibrated correctly. Microanalyses were carried out using following acquisition parameters: live time 100s, accelerating voltage 20 keV, process time 3, window Be. Checks were made to assure that the image is focused, the spot size optimised and

that the X-ray count is adequate to give 7-8000 counts (24-25 dead). Digital maps have been acquired using discrete scanning. Each point at which the scanning beam stops and the information is generated is called a pixel.

Digital maps were produced using the following X-ray image acquisition parameters:

- EM conditions: display magnification 2500x,
- Mapping parameters: x and y resolution 256x256, frames 10
- EDS: dwell time of the beam at each pixel 2ms, precision time at which the map data will be stored 16 bit, analysed window file which defines the energy ranges from which maps will be acquired
- EIM set-up: dwell time for the signal input 50ms, precision to which data will be stored 16 bit.

8.4.1.6 Image analysis (Featurescan)

Porosity is most conveniently measured in the laboratory by vacuum saturation of the pores with water as detailed in Chapter IV. Apparent porosity values obtained in this way may be of limited use in determining the durability of a as they give no indication about spatial distribution of the pores and total porosity. Apparent porosity refers to the fact that not all of the available pores are capable of being filed with water, some of them are 'blind' (closed pores) which could be open during preparation of the test specimen (cutting and polishing). Using microscopy to calculate pore size has its limitations due to the small sample size and the fact that conversions have to be applied to account for the probability that either the maximum or minimum pore size is not measured.

The feature analysis work was performed at an accelerating voltage of 25 keV and the images were obtained from backscatter electron microscopy. The image analysis is provided in form of Featuresan, a software package designed for the detection, measurement and analysis of features in an image. Images were analysed using stored data and resolution of x = 512 and y = 512. From each sample 8 fields (see Figure 8.2) were analysed, each field having a with of 3.588 mm and height of

3.518mm. Features smaller then 10 pixels were excluded, where one pixel width is 7.009 micrometers and height is 6.870 micrometer.

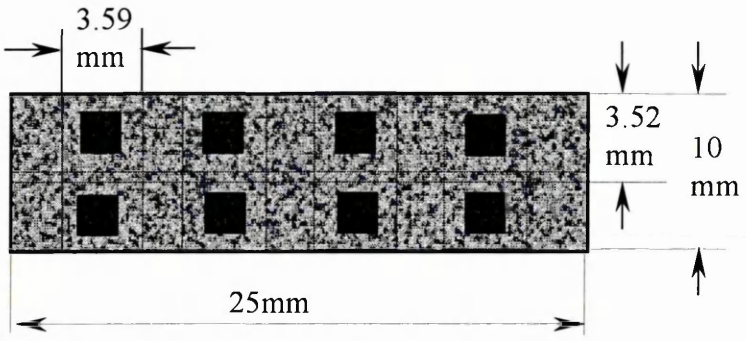

Figure 8.2 Selected fields for feature analysis(not to scale)

Nine feature measurements were performed automatically for each sample and the results were stored directly to a file for statistical analysis. These measurement were derived from ferret (see Figure 8.3) and perimeter measurements: field area, number of features detected, number of interest, field number area, number of pixels, feature length, feature breadth, mean ferret. The features touching the edges of the frame were excluded. The ferret projection used was 18 meaning that the feature breath and depth were derived from 18 measurements.

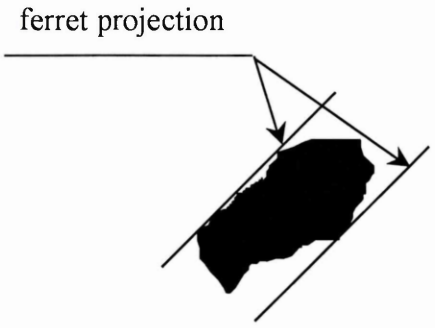

Figure 8.3 Ferret projections

8.4.1.7 Sample preparation

The manufacturing and curing of test specimens of the selected materials are detailed in section 8.3 of this chapter. At age 6 months, a prism (10 mm x 25 mm x100 mm) from each alkali activated fly ash material were sectioned using a masonry saw. From each specimen two slices were cut, normal to the trowelled (top) face of the specimen, to provide test specimens for the SEM investigations.

One slice (cross section area of 10x25mm^2) was cut from each specimen in such a way to retain the fracture surface and was used for SEI and EDAX work. Then using adhesive conductive paint it was mounted on aluminium stub, as shown in Figure 8.4.

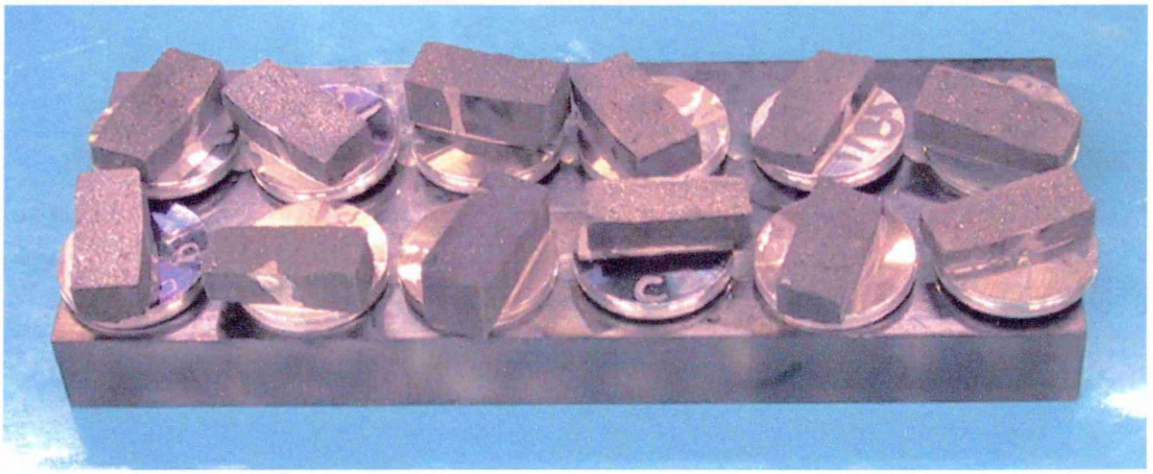

Figure 8.4 Fracture surface samples

Another 2-4 mm thick slice was cut to provide test specimens for the BSI, digital mapping and feature analysis. After cutting, the sample was polished using successively finer abrasive papers (from grade 400 to grade 1200) and then avacuum pump was used to expel the free air from the specimen. Then, an epoxy resin was allowed to fill the specimen mould almost completely. Evacuation of air and volatiles was continued under vaccum for another 15-30 min. When the resin was set the surface of the specimen was exposed and smoothed with successively finer abrasive papers and then polished with diamond paste. The specimen was washed in an ultrasonic bath, dried and permanently cemented to a aluminium stub, as shown in Figure 8.5.

The sample preparation for the powder constituent materials was slightly different from that of the hardened hydrated materials. They were glued on a special conductive tape which was stable under vacuum as seen in Figure 8.6.

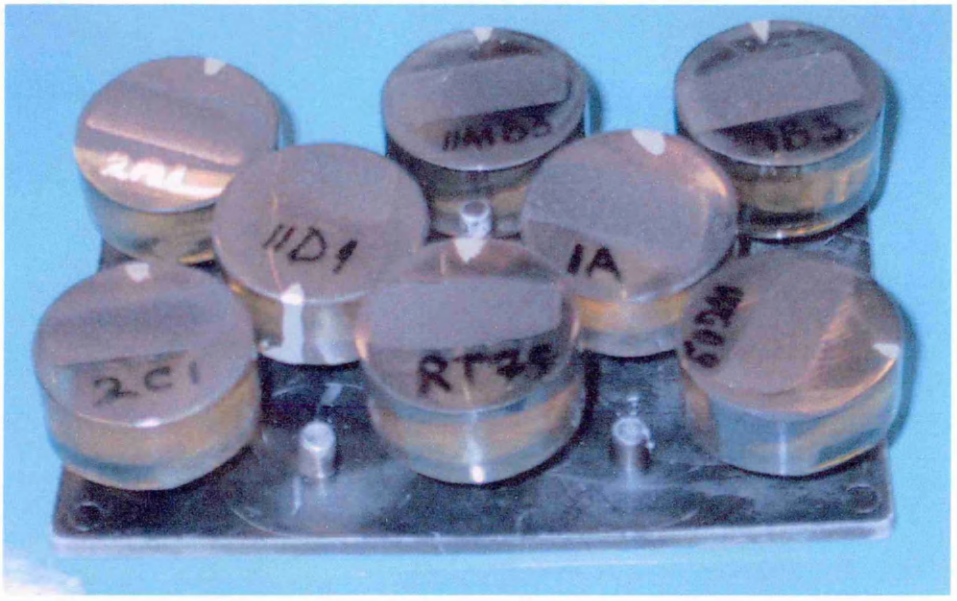

Figure 8.5 Samples cast in an epoxy resin

Figure 8.6 Powder sample

The sample preparation procedure for SEI and BSEI determinations was to coat its surface by vaporising with a thin layer (~100Å) of metal (gold) to achieve good electrical conductivity. Samples on which EDAX, digital mapping and feature analysis was performed were instead coated with carbon to avoid interference by the gold peaks in the analysis.

For samples coated with carbon, a continuous line from the base of the stud to the top of the sample was drawn using a conductive paint in order to assure good conductivity.

8.4.2 X-Ray diffraction

8.4.2.1 Introduction

Usually XRD method is used for mineralogical characterisation of the material. X-ray diffraction is a versatile, non-destructive analytical technique for identification and quantitative determination of the various crystalline compounds, known as 'phases', present in solid materials and powders. This method can only detect the crystalline phases and, therefore, is not useful for determination of amorphous phases. The limitation of this technique is that the lowest detectable limit of phase concentration is about 3% (by weight).

Identification of constituent phases of investigated materials is achieved by comparing the X-ray diffraction pattern called 'diffractogram' obtained from a sample with an internationally recognised database JCPDS containing reference patterns for more than 70,000 phases. Modern computer-controlled diffractometer systems use automatic routines to measure, record and interpret the unique diffractograms produced by individual constituents in even highly complex mixtures. Data obtained (diffraction pattern) can be interpreted by matching with standard traces or by comparing with JCPDS powder diffraction.

8.4.2.2 Theoretical background

A crystal lattice is a regular three-dimensional distribution (cubic, rhombic, etc.) of atoms in space. These are arranged so that they form a series of parallel planes separated from one another by a distance d, which varies according to the nature of the material, see Figure 8.7[165]. For any crystal, planes exist in a number of different orientations, each with its own specific d-spacing.

When a monochromatic x-ray beam with wavelength λ is projected onto a crystalline material at an angle θ, diffraction occurs only when the distance travelled by the rays reflected from successive planes differs by a complete number 'n' of wavelengths.

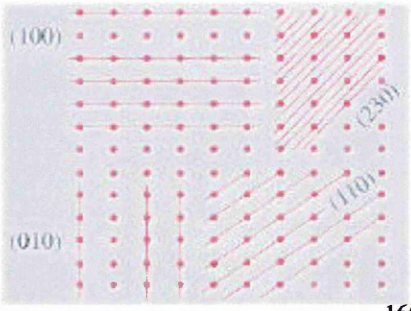

Figure 8.7 Orientation of planes in a crystal[165]

The diagram in Figure 8.8[166] shows waves 1 and 2, in phase with each other, glancing off atoms A and B of a crystal that has a separation distance d between its atomic, or lattice, planes. The reflected (glancing) angle θ, as shown by experiment, is equal to the incident angle θ. The condition for the two waves to stay in phase after both are reflected is that the path length CBD be a whole number (n) of wavelengths (λ), or nλ.

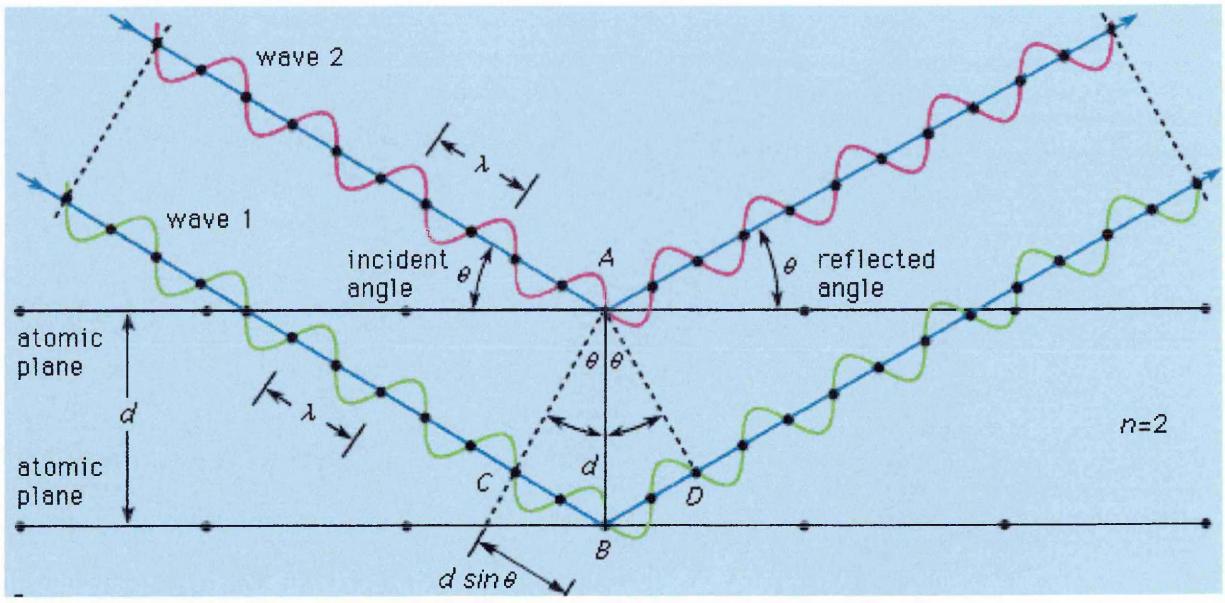

Figure 8.8 Diffraction of the X-ray beam[166]

But, from geometry, CB and BD are equal to each other and to the distance d times the sine of the reflected angle θ, or d sin θ. Thus, n = 2d sin θ, which is the Bragg law. For any other angle (corresponding to fractional n) the reflected waves will be out of phase and destructive interference will occur, annihilating them. As may be seen from the diagram, when n = 2 there is only one wavelength along path CB; also,

the reflected angle will be smaller than that for, say, n = 3. Waves reflected through an angle corresponding to n = 1 are said to be in the first order of reflection; the angle corresponding to n = 2 is the second order, and so on.

Bragg explained why the cleavage faces of crystals appear to reflect X-ray beams at certain angles of incidence (theta, θ). The variable d is the distance between atomic layers in a crystal, and the variable lambda λ is the wavelength of the incident X-ray beam ; n is an integer. Although Bragg's law was used to explain the interference pattern of X-rays scattered by crystals, diffraction has been developed to study the structure of all states of matter with any beam, e.g., ions, electrons, neutrons, and protons, with a wave length similar to the distance between the atomic or molecular structures of interest[164].

The Bragg law is useful for measuring wavelengths and for determining the lattice spacings of crystals. To measure a particular wavelength, the radiation beam and the detector are both set at some arbitrary angle θ. The angle is then modified until a strong signal is received. The Bragg angle, as it is called, then gives the wavelength directly from the Bragg law. This is the principal way to make precise energy measurements of X rays and low-energy gamma rays. The energies of neutrons, which by quantum theory have wave attributes, are frequently determined by Bragg reflection.

By varying the angle theta, the Bragg's Law conditions are satisfied by different d-spacing in polycrystalline materials. Plotting the angular positions and intensities of the resultant diffracted peaks of radiation produces a pattern which is characteristic of the sample. Where a mixture of different phases is present, the resultant diffractogram is formed by addition of the individual patterns[165].

The result of an XRD measurement is a diffractogram, showing phases present (peak positions), phase concentrations (peak heights), amorphous content (background hump) and crystallite size/strain (peak widths) as shown in Figure 8.9[165].

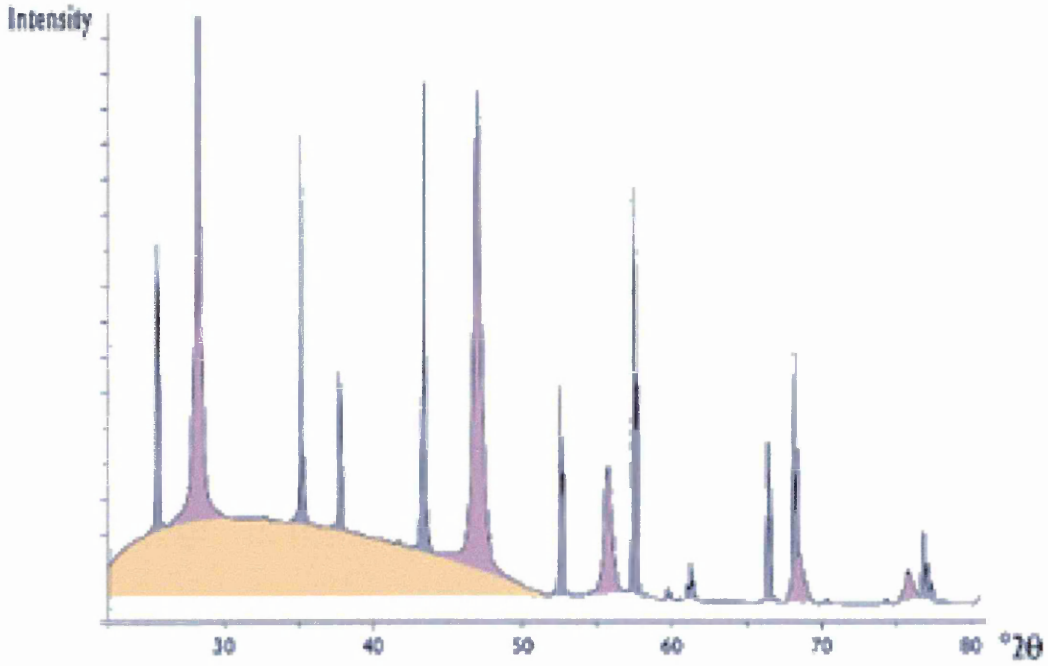

Figure 8.9 Diffractogram[165]

Figure 8.9 depicts a typical sample, comprising two crystalline phases (violet, grey), each with different average crystallite sizes, plus a proportion of amorphous material (beige). The features of the diffractogram are colour coded to indicate the relevant components. The widths of the peaks in a particular pattern provide an indication of the average crystallite size, see Figure 8.10[165]. Large crystallites give rise to sharp peaks, while the peak width increases as crystallite size reduces. Peak broadening also occurs as a result of variations in d-spacing caused by micro-strain. However, the relationship between broadening and diffraction angle 2-theta is different from that of crystallite size effects, making it possible to differentiate between the two phenomena.

8.4.2.3 Testing method

The instrument used was a A Philips PW 3710 diffractometer which has a completely computerised operating system. Software control is essential for diffractometer automation, data acquisition and storage. The system was equiped with Philips PW 1877 Automated Analytical Powder Diffraction software version 3.5B.

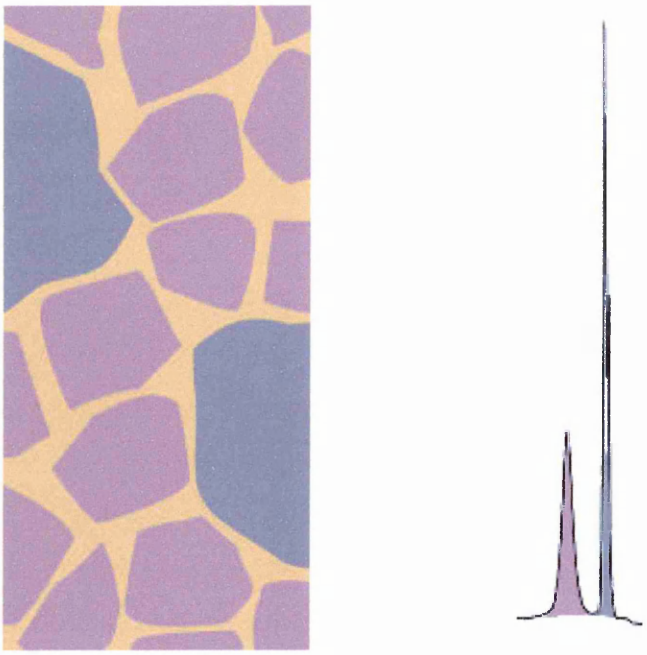

Figure 8.10 Relationship between peak with and average crystal size[165]

Cu Kα radiations were used with a voltage of 30 kV and a current of 35 mA. The samples were scanned from 3 to 70° with a step width of 0.02° and counting time of 2 second each step. The divergence slit was 1° and the recieving slit was 0.2 mm. The phase determination was performed using Philips PW1876 PC - Indentify software version 1.0. Evaluation of the X-ray records was done by comparing the identified values d_t/I_t of the investigated phases with d_m/I_m from the searching system (IDENTIFY) and set of tables JCPDS (Joint Committee on Powder Diffraction Standards, Selected Powder Diffraction Data for Minerals). The search match was done using five of the strongest lines of the reference patterns. Only lines of the analysed DI file with a relative intensity equal or larger than 3.02 were used in the search step. Reference patterns with a search score smaller than 20 were not accepted for the match step. In case of the according data dt/It satisfying the d_m/I_m values of more than one phase with similar structure, all such minerals are given. Possibilities of the priority occurrence of one of them are discussed in section 8.5.

8.4.2.4 Sample Preparation

The XRD samples were ground in an Agate mortar to a fine powder of below 80 μm in particle size. The fine powder was compacted in a aluminium mould known as the specimen counter. The specimen and the counter are configured such that the Bragg condition is always maintained. The diffracted X-rays are detected using a proportional counter from which the output is plotted against the Bragg angle, resulting in a plot of X-Ray intensity versus 2θ. In this way d (h,k,l) can be determined. The data acquired could be manipulated by a number of different options, using Philips PW 1877 APD software, such as peak searching α2 stripping, smoothing and peak synthesis. Table 8.12 gives details of the testing schedule of selected batches of mixes.

Table 8.12 Experimental programme

Group	Batch Code	SCANNING ELECTRON MICROSCOPY							X-RAY DIFFRACTION
		SEI	BSI	Fracture Surface	EDAX	Windows Integrals	Feature Scan (Macroporosity)	Digital Mapping	
na	RT	yes	yes	yes	yes	yes	yes	yes	yes
I	A	yes	yes	yes	yes	yes	yes	yes	yes
I	H	yes	yes	yes	yes	yes	yes	yes	yes
II	SA	yes	yes	yes	yes	yes	yes	yes	yes
II	SH	yes	yes	yes	yes	yes	yes	yes	yes
II	SAB3	yes	yes	yes	yes	yes	yes	yes	yes
II	SHB3	yes	yes	no	yes	yes	yes	no	yes
na	WG09	yes	yes	no	yes	yes	yes	yes	yes
na	WG15	yes	yes	yes	yes	yes	yes	yes	yes

8.5 RESULTS AND DISCUSSION

8.5.1 Constituent materials

8.5.1.1 Pulverised fuel ash (pfa)

Fly ashes constitute the fine particulate residues of the responses of individual fragments of ground coal suspended in an air stream moving rapidly through a brief exposure to high temperature conditions in a power plant boiler[167]. There is little possibility of exchange of mass between separated suspended particles. As a result, each small fragment of coal reacts individually. Therefore the chemical composition of each particle can be different depending on the proportion of clay, quartz, sulphide and other minerals that may have been present in that specific fragment of the sample. The chemical composition of each particle together with the temperature at which they are exposed during burning and cooling strongly influences the shape and fineness of the grains and also influences the reactivity of the ashes and their utilisation in building and construction materials. It means that microscopic observations of the samples can give much information about the mineralogical properties of fly ashes. The scanning electron microscopy together with X-ray microanalysis were used for microstructure observations. Figures 8.11 (a and b) presents the typical microstructure of fly ash from Ratcliffe and its X-ray microanalysis. The semi-quantitative analysis of pfa is presented in Table 8.13.

Table 8.13 Semi-quantitative analysis of the element composition of the Pfa (SEM)

ELEMENTS	Pfa [%]
Silicon (Si)	69.6
Aluminium (Al)	14.20
Iron (Fe)	6.1
Titanium (Ti)	-
Magnesium (Mg)	-
Calcium (Ca)	-
Sulphur (S)	-
Potassium (K)	10.0
Phosphor (P)	-

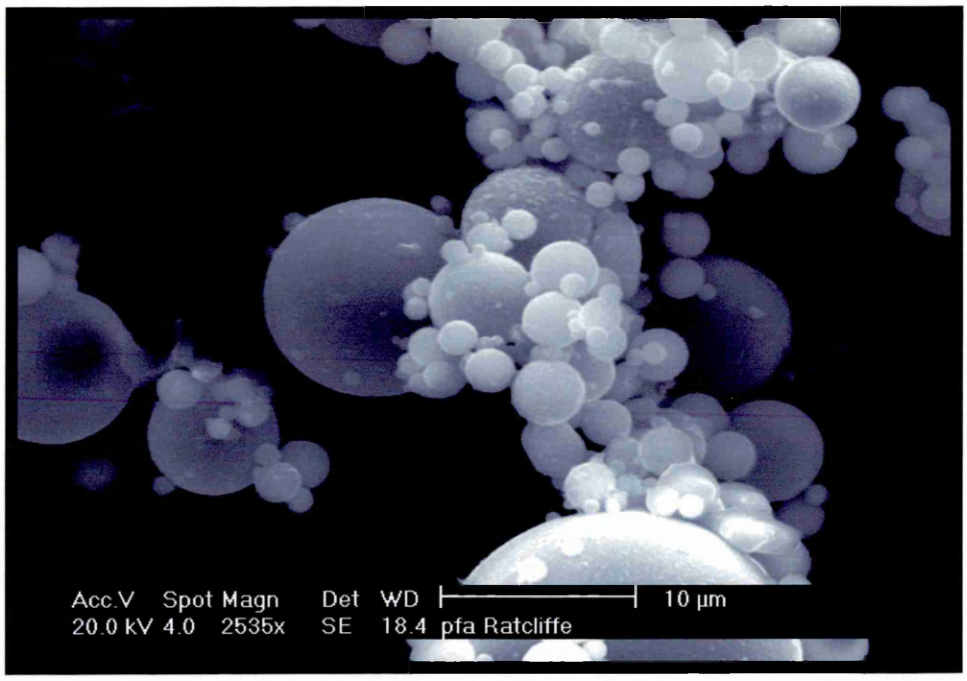

(a)

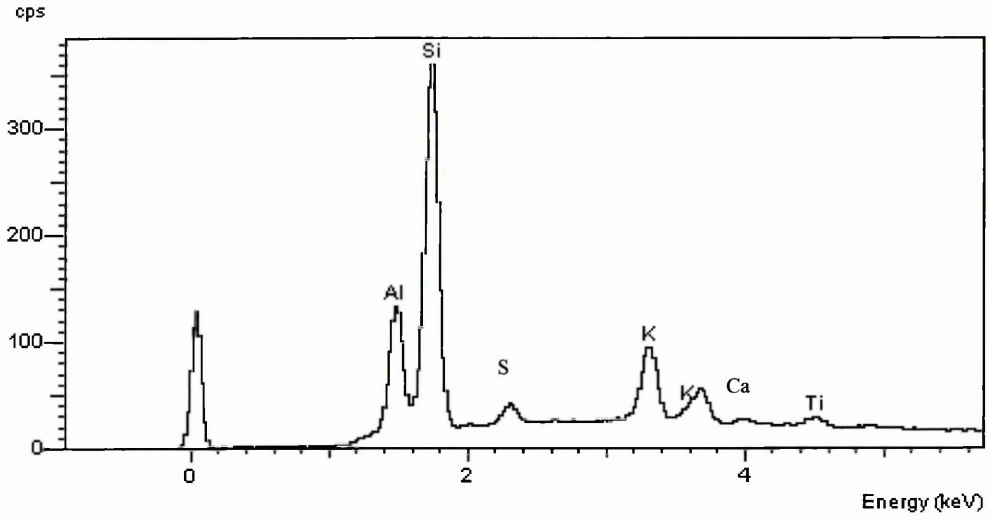

(b)

Figure 8.11 Microstructure of pulverised fuel ash (pfa) from Ratcliffe power plant

The particle shape of the fly ash from the power plant in Ratcliffe can be divided in two categories:

1. The bulk of the fly ash is composed of spherical particles of various diameters. They have a smooth surface and contain Al, Si, Ca, Fe and in some cases it is possible to find very small amounts of Mg. The concentration of these elements differs from particle to particle. On the SEM micrographs, in Figure 8.11(a), a large number of spherical particles with the surface covered with finely crystallised material can be observed. The occurrence of such fly ash morphology has been reported previously by Diamond[167].
2. Very small amounts of irregular shaped particles with a porous surface have also been observed. These particles contain sulphur and it was assumed that they are incompletely burned pieces of coal. The less regular, grey formations are mullite containing particles, quartz fragments from irregular, fissured transparent grains.

8.5.1.2 Ground granulated blast furnace slag (ggbs)

It appears from the literature[1] that the mineralogical character and properties of class C fly ash which contain high proportions of calcium is very similar to blast furnace slag. Figure 8.12 (a and b) shows the powder diffraction pattern for the unhydrated ground granulated blast furnace slag from Tesside and its X-ray microanalysis. The semi-quantitative analysis of ggbs is presented in Table 8.14.

Table 8.14 Semi-quantitative analysis of ggbs

ELEMENTS	Ggbs [%]
Silicon (Si)	21.9
Aluminium (Al)	3.2
Iron (Fe)	
Titanium (Ti)	
Magnesium (Mg)	0.3
Calcium (Ca)	73.1
Sulphur (S)	1.5
Potassium (K)	
Phosphor (P)	

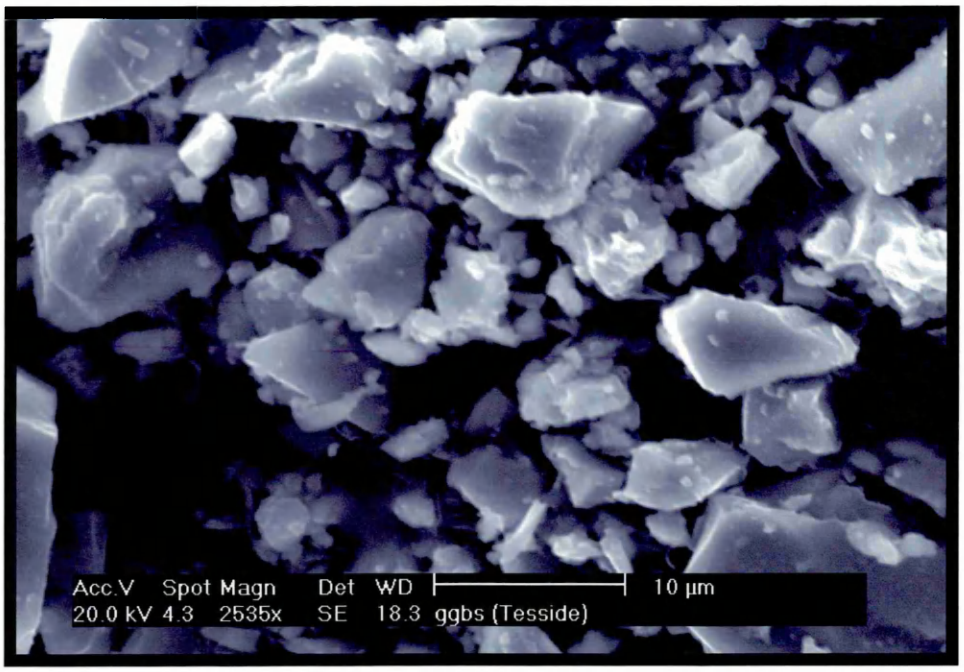

(a)

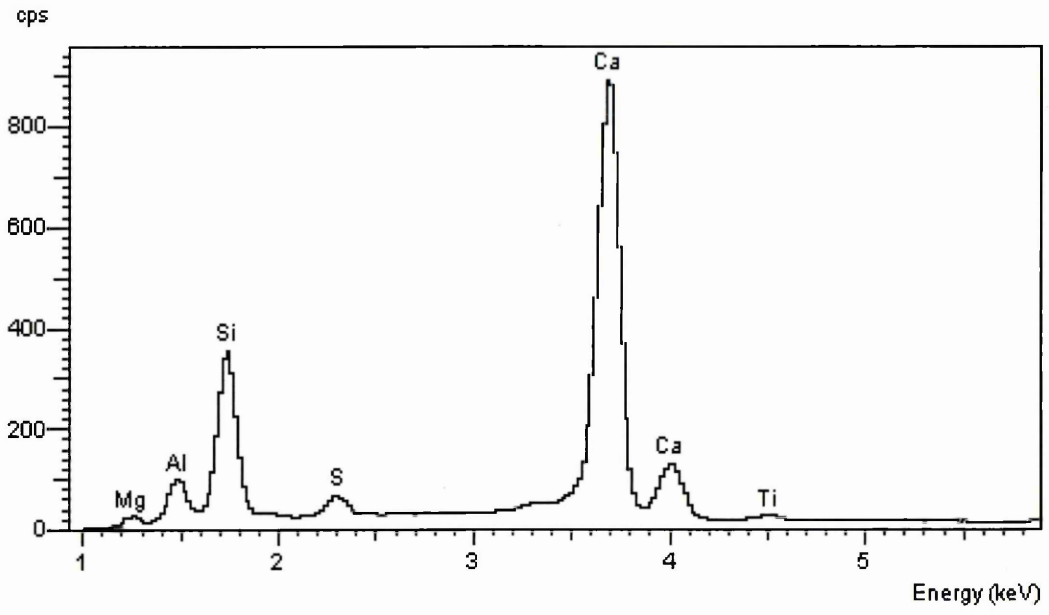

(b)

Figure 8.12 Microstructure of ground granulated blast furnace slag (ggbs) from Tesside power plant

8.5.1.3 Condensed silica fume (microsilica)

Silica fume consists mainly of amorphous (noncrystaline) silica with a very high surface area which makes it highly pozzolanic. Figure 8.13 (a and b) show the powder diffraction pattern for the unhydrated microsilica and its X-ray microanalysis. The semi-quantitative analysis of microsilica is presented in Table 8.15.

Table 8.15 Semi-quantitative analysis of microsilica

ELEMENTS	Microslilica [%]
Silicon (Si)	98.5
Aluminium (Al)	
Iron (Fe)	
Titanium (Ti)	
Magnesium (Mg)	
Calcium (Ca)	
Sulphur (S)	trace
Potassium (K)	1.5
Phosphor (P)	

8.5.1.4 Water Glass Hardener

The water glass hardeners were all of the aluminium polyphosphate type. They were selected due to their use as hardeners in water glass based paints, where they are supposed to improve flexibility and water absorption properties. Figure 8.14 (a and b) shows the powder diffraction pattern for the water glass hardener KB#200 and its X-ray microanalysis. The semi-quantitative analysis of hardener KB#200 is presented in Table 8.16.

Table 8.16 Semi-quantitative analysis of water glass hardener KB#200

ELEMENTS	KB#200[%]
Silicon (Si)	47.8
Aluminium (Al)	8.7
Iron (Fe)	0.5
Titanium (Ti)	
Magnesium (Mg)	
Calcium (Ca)	
Sulphur (S)	
Potassium (K)	43.0
Phosphor (P)	

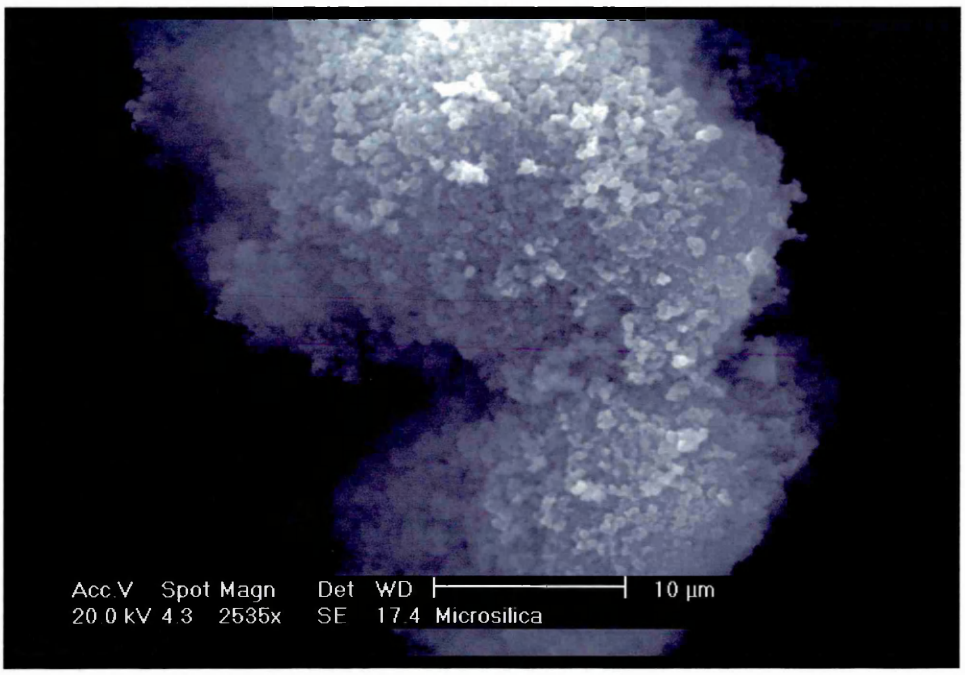

(a)

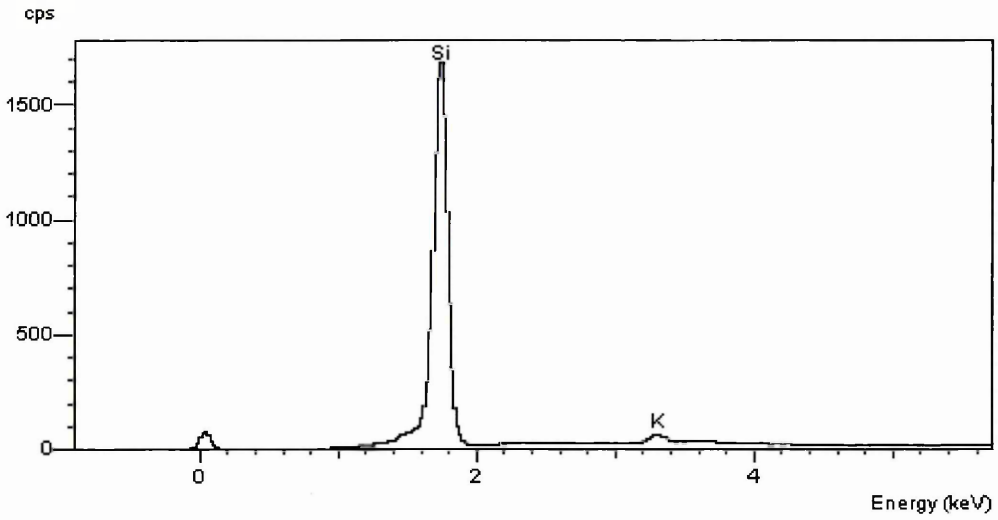

(b)

Figure 8.13 Microstructure of microsilica (silica fume)

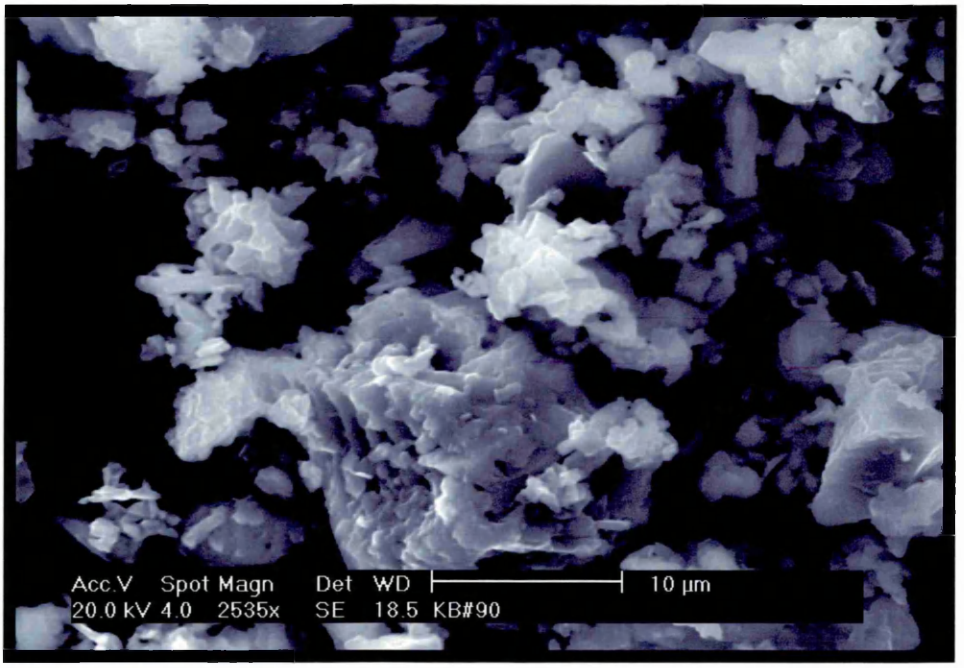

(a)

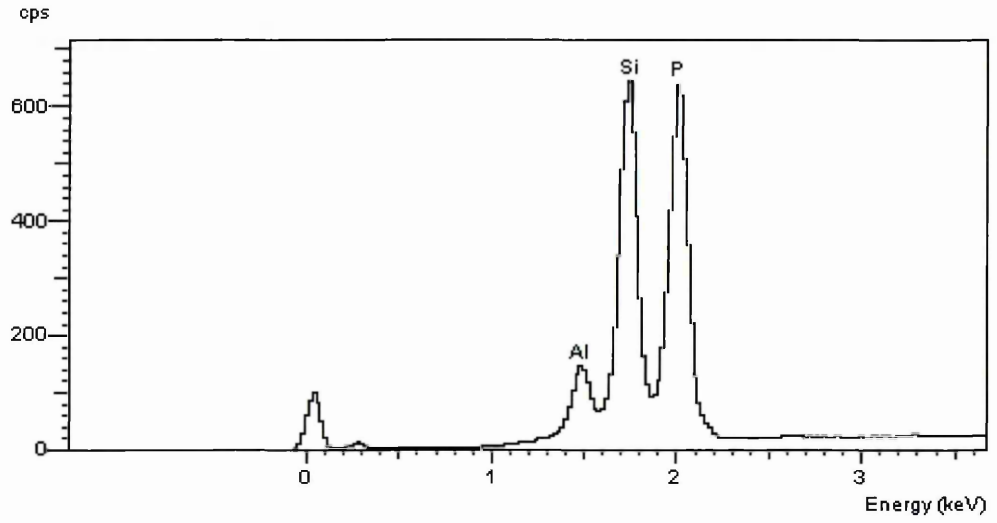

(b)

Figure 8.14 Microstructure of water glass hardener KB#90 (aluminium methaphosphate compound)

8.5.2 SEM and EDAX of alkali activated materials

The alkali activated materials have been examined under the scanning electron microscope using the EDAX facility of the microscope to undertake chemical analysis of the samples. Two different methods of sample preparation have been employed for the examination of the alkali activated materials, polished specimens and the examination of fracture surfaces as detailed in section 8.4.1.7.

The use of polished and fracture surface specimen allows the investigation of the microstructure of the sample by a variety of techniques under the SEM including, back scattered electrons, secondary electrons, EDAX and digimapping of EDAX results. The aim is to elucidate information about the chemical composition and structure of the hydration products. In addition the feature analysis technique allows the measurement of pore sizes in the sample and total porosity. It must be stressed that these values do not represent the apparent porosity. The porosity determined using the feature analysis technique only takes into account the small-medium size pores.

8.5.2.1 Thermally cured alkali activated fly ash material (batch code RT)

Material RT is an alkali activated material containing fly ash with no blast furnace slag or microsilica and has undergone thermal curing. This material has a flexural strength of 9.32 N/mm^2 and a density of 2420.4 Kg/m^3. Figure 8.15 shows the pore distribution of the material. This indicates that the largest pore area was for pore sizes between 200000 and 250000 $microns^2$. Table 8.17 presents a summary of the results from the feature analysis. The material has a total pore area of 8.1% of the material.

Figure 8.16 (a and b) show the microstructure of the thermally cured alkali activated fly ash material (batch code RT). Figures 8.17 (a and b) presents the digital mapping micrographs of material batch code RT showing the distribution of chemical elements within the structure. In the matrix of this material various sizes of circular particles can be seen, some of which appear to be hollow. This would indicate that they are particles of unreacted fly ash. In addition there are some larger irregular

shaped particles most likely crystalline material from the fly ash. The back scattered image (Figure 8.16 b) shows the fly ash grains to be lighter than the matrix indicating the presence of atoms with a higher atomic number. However, the large irregular shaped hydrated particle has the same colour as the fly ash grains, suggesting it to be of similar composition to fly ash. There are some particles in the matrix which indicate a substance with a higher atomic number than the hydrated fly ash. It is likely that these are particles of un-burnt coal from the fly ash.

These conclusions are confirmed by the digital mappings presented in Figures 8.17 (a and b) which show the calcium to be located at these sites. The matrix can be seen to be rich in aluminium and silicon with the presence of the alkali earth metals sodium and potassium and, in addition, the presence of magnesium is indicated. However, the level of calcium is low. This suggests the matrix to be composed of aluminium silicates of sodium, potassium and magnesium as opposed to a calcium silicate hydrate or related mineral. Examination of the EDAX results for material batch code RT also strongly indicates this. Table 8.18 details the results from the EDAX performed at the points shown in Figure 8.18. For example, Table 8.18 shows that the average Si/Al ratio is 2.36 compared with Ca/Al ratio of 0.13 which reinforces the hypothesis that the matrix is composed of aluminium silicates of sodium, potassium and magnesium. The matrix of hydration products and, embedded in it spheres of fly can be seen in Figure 8.18. This indicates that the fly ash has reacted to form the hydration products of the matrix. The combined levels of potassium and sodium are higher than the levels of calcium. This is confirmed by the low Ca/Si ratio and the high Si/Al ratio. According to La Rossa et al[57] this indicates that the likelihood of CSH formation is low. It also strongly indicates the possibility that aluminium silicate type zeolites have been formed as a hydration product, incorporating sodium and potassium as opposed to calcium. The appearance of the matrix at the fracture surface presented in Figure 8.19 shows an irregular surface with a smooth flat particle in the left hand side of the micrograph. This appears to be a cleaved grain of sand and suggests that both the matrix and the bond between the matrix and the sand were stronger than the sand particles.

Table 8.17 Summary of the data from feature scan measurements for material RT (Pore area 8.063%)

Measurement	No. data	Mean	Median	Min	Max
No detected	7	103.6	89.96	27	196
Area/mm ^2	725	0.0098	0.0036	0.005	1.235
Feature breadth/mm	725	0.0617	0.0326	0.0137	1.093
Feature length/mm	725	0.0904	0.0534	0.0308	1.833
Field area/mm ^2	7	12.62	0	12.62	12.62
Field number	7	4	3.985	1	7
Mean Feret/mm	725	0.077	0.0451	0.027	1.474

Table 8.18 Semi-quantitative chemical analysis of thermally cured alkali activated fly ash material (batch code RT)

Spot. No.	Na	Mg	Al	Si	S	K	Ca	Fe	Na/Al	Si/Al	Ca/Al	K/Al	Ca/Si	Al/Ca	S/Ca
1	0.57	1.01	37.6	50.7	0.24	8.34	0.2	1.35	0.02	1.35	0.01	0.22	0.00	188.00	1.20
2	3.08	1.39	17.67	63.19	1.78	5.23	5.38	2.28	0.17	3.58	0.30	0.30	0.09	3.28	0.33
3	2.52	1.14	25.47	59.76	1.1	5.24	3.49	1.29	0.10	2.35	0.14	0.21	0.06	7.30	0.32
4	1.88	1.27	20.9	57.79	2.3	5.9	3.53	6.43	0.09	2.77	0.17	0.28	0.06	5.92	0.65
Average	*1.986*	*1.216*	*24.508*	*57.846*	*1.544*	*6.122*	*3.226*	*3.556*	*0.08*	*2.36*	*0.13*	*0.25*	*0.06*	*7.60*	*0.4786*

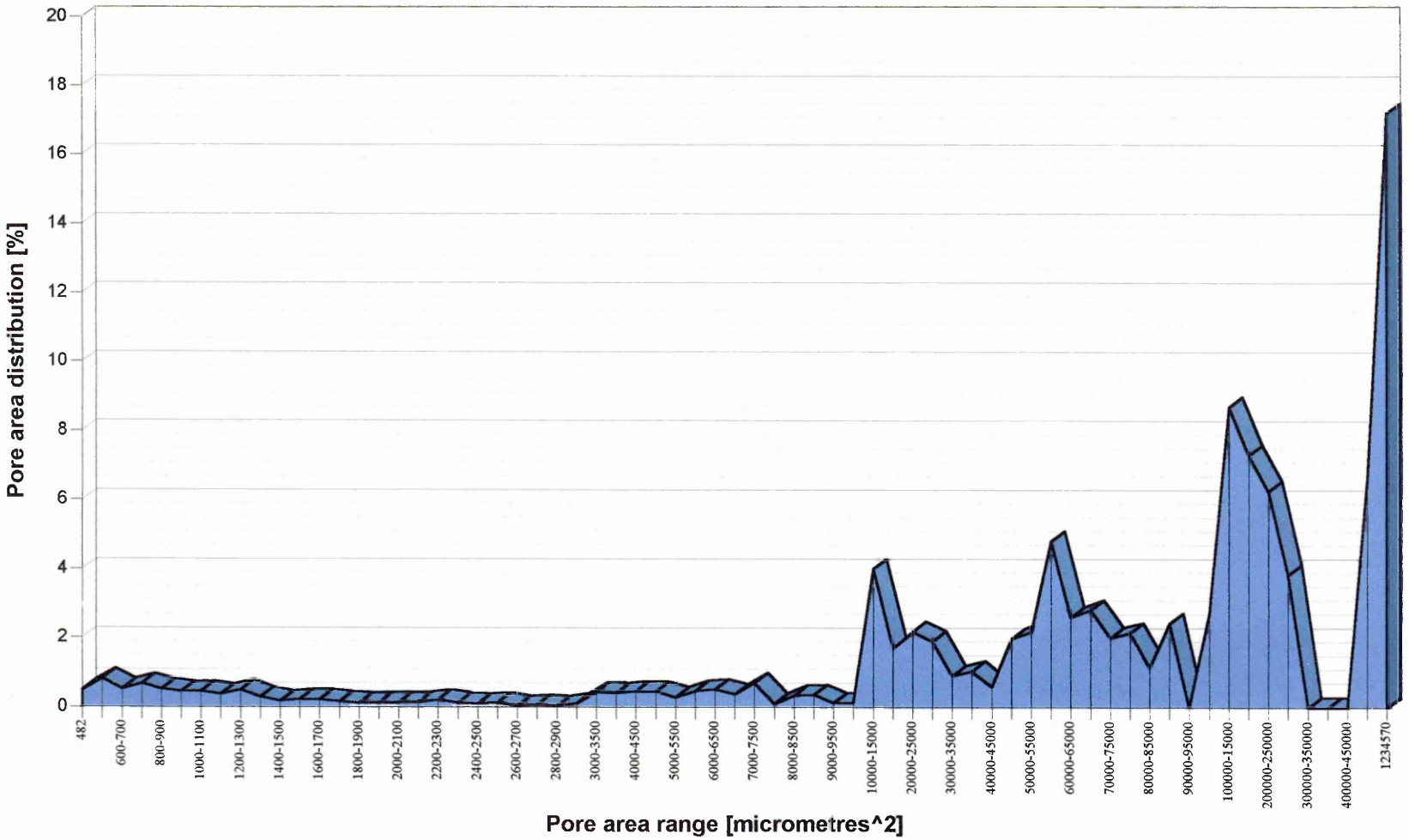

Figure 8.15 Pore area distribuion of thermally cured alkali activated fly ash material (batch code RT)

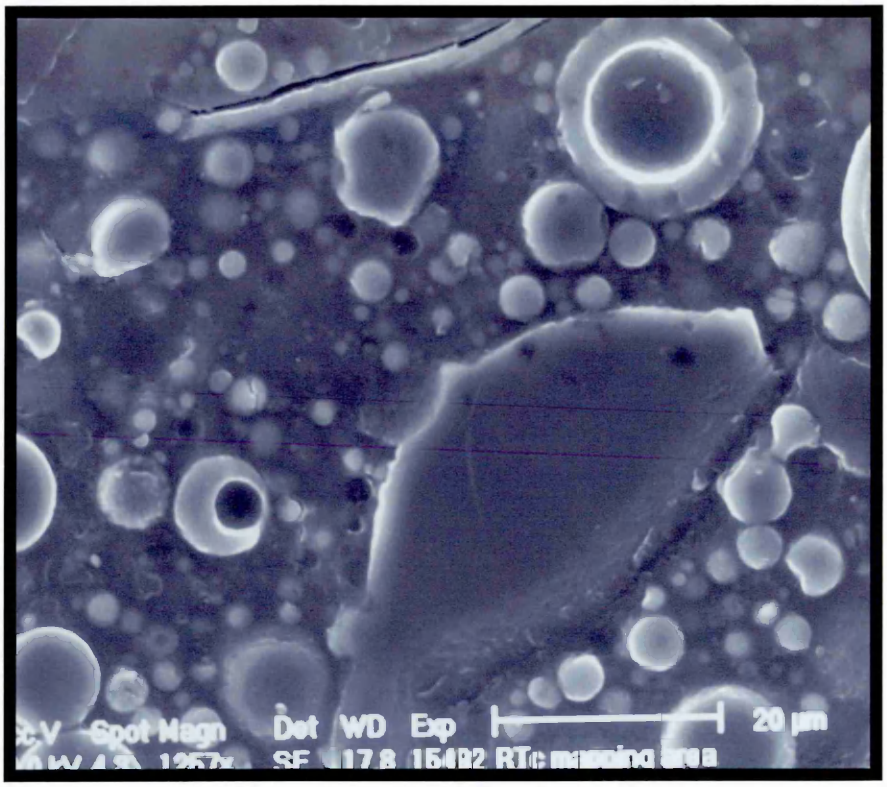

(a)

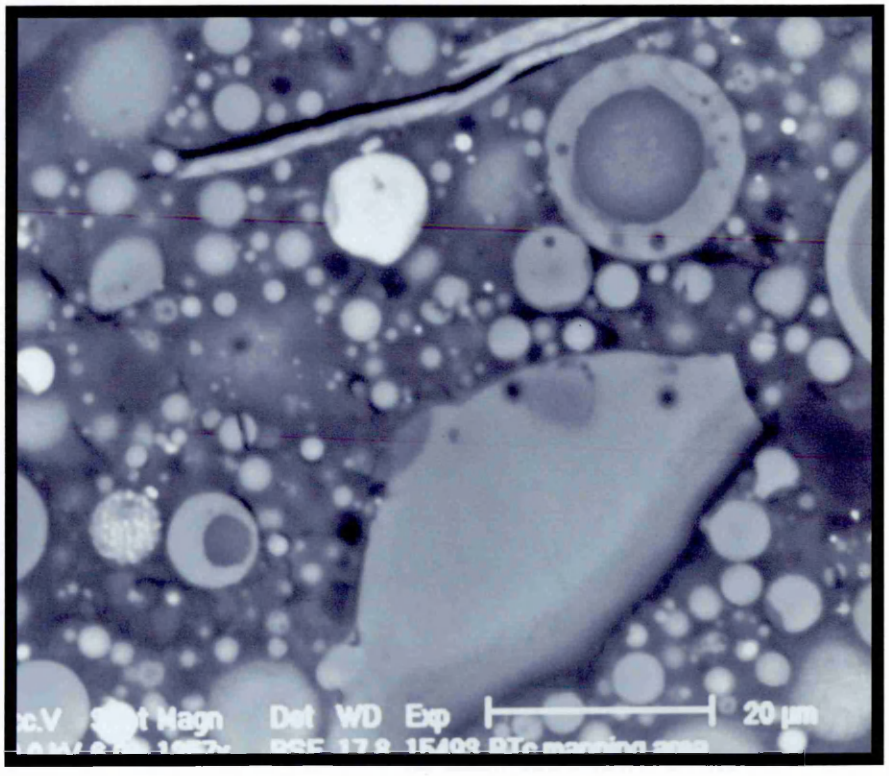

(b)

Figure 8.16 (a and b) Secondary electron image and backscattered electron image of thermally cured alkali activated fly ash material (batch code RT).

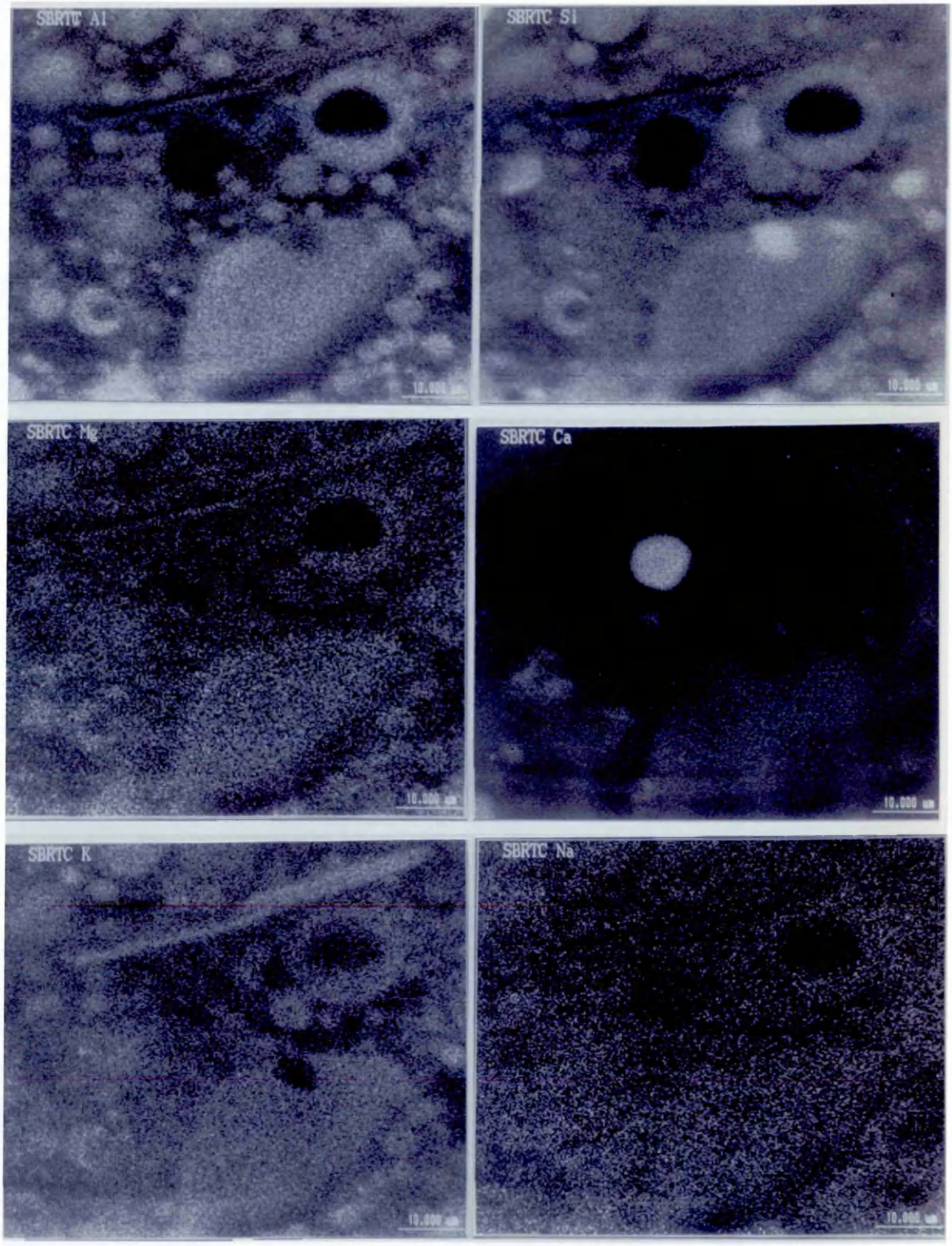

Figure 8.17 (a) Mapping of the Al, Si, Mg, Ca, K and Na elements in the thermally cured alkali activated fly ash material (batch code RT).

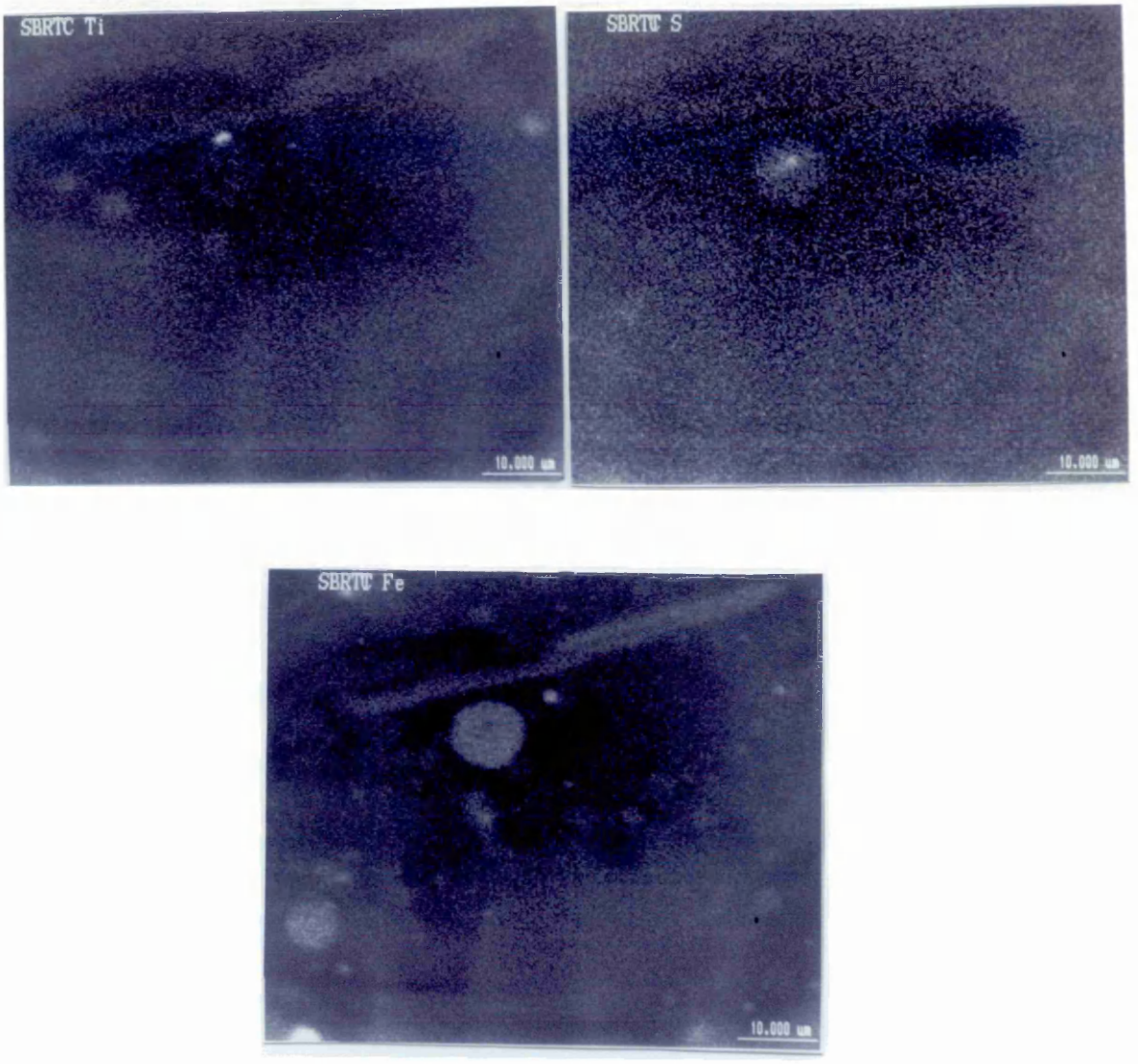

Figure 8.17 (b) Mapping of Ti, S and Fe elements in the thermally cured alkali activated material (batch code RT).

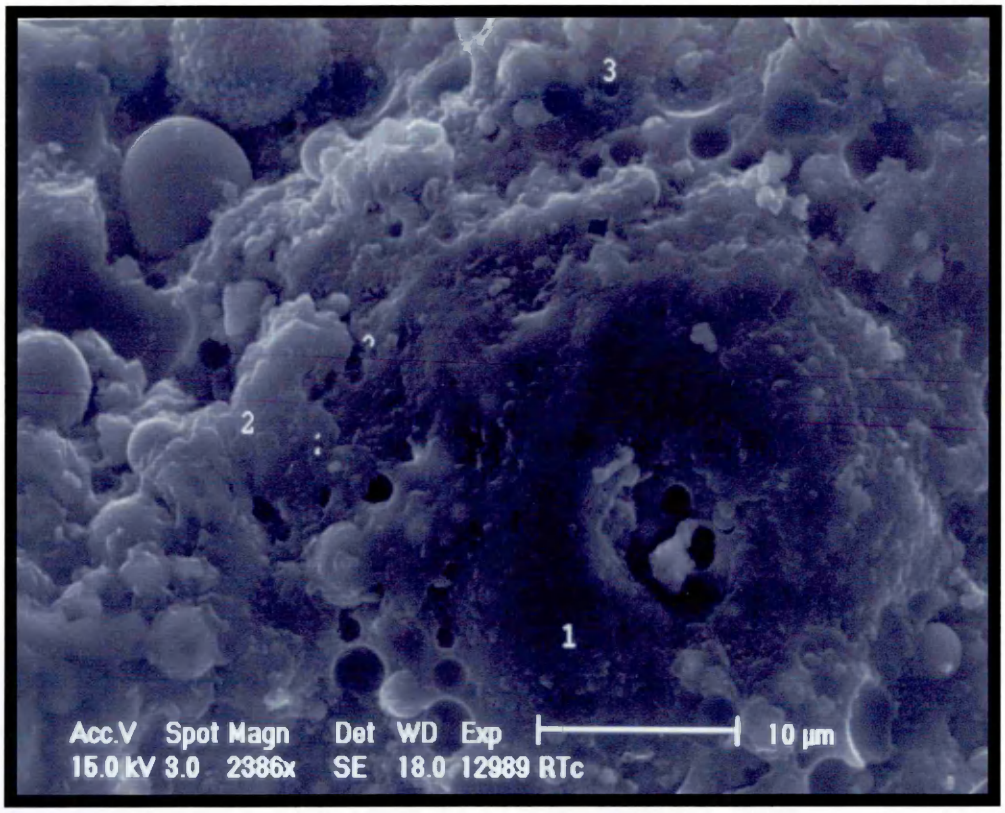

Figure 8.18 SEI of the fracture surface of alkali activated material (batch code RT).

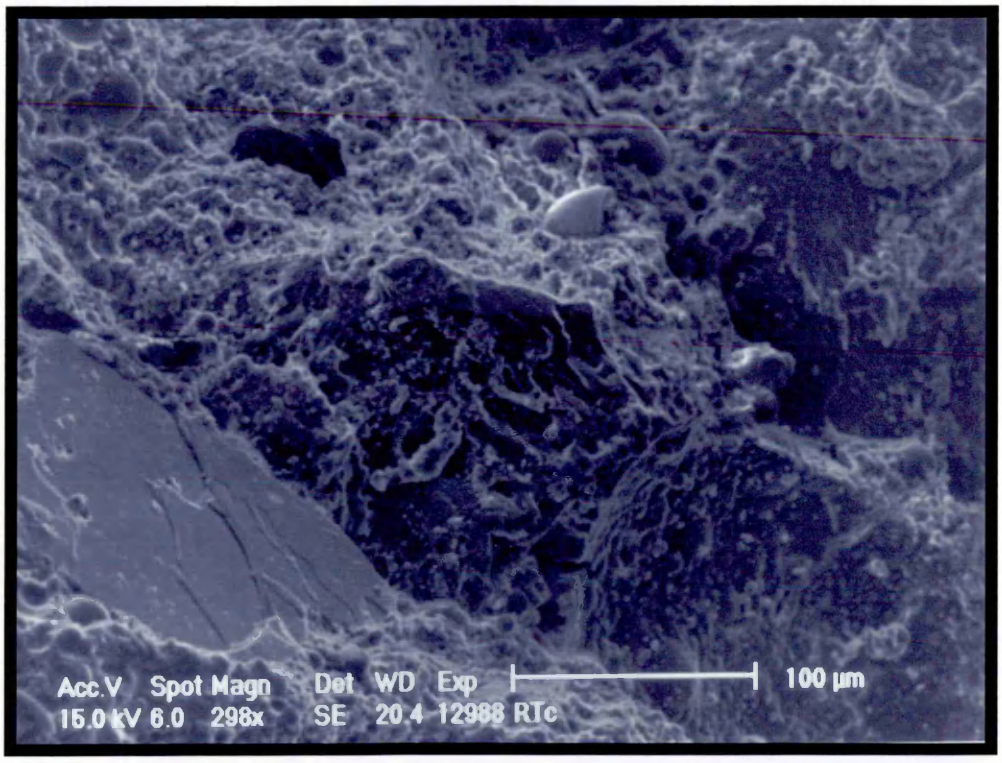

Figure 8.19 Bond between the sand grain and the matrix for material (batch code RT).

8.5.2.2 Alkali activated fly ash material with microsilica

8.5.2.2.1 Materials cured under 20°C and 65% RH (batch code IA)

Material batch code IA (Table 8.8) has a similar composition to material RT except for the addition of microsilica into the mix. The flexural strength increases with the addition of microsilica up to 20.06 N/mm^2. However the pore area is similar at 8.5%, Table 8.22 presents a summary of the results from the feature analysis. The pore distribution in Figure 8.19 shows that the pore structure has been refined with the largest frequency of pore area being in the range 100000 to 150000 microns^2.

A comparison of Figures 8.15 and 8.20 suggests that there is a larger quantity of smaller pores in the material with microsilica (batch code IA) compared with thermally cured material (batch code RT) compared with material with microsilica. It also suggests that the refinement of the pore size has increased the strength of the material by reducing the stress raisers (i.e. pores and microcracks) in the microstructure.

Figure 8.21 (a and b) presents the secondary electron image and the backscattered electron image, respectively, of the alkali activated material cured under 20°C and 65% RH (batch code IA). The micrographs show a matrix containing a number of irregular shaped particles of various sizes. The backscattered image shows a variation in contrast between different shaped particles (Figure 8.21 b). The variation in contrast indicates differences in the chemical composition of constituent particles. By comparison the matrix appears to be relatively uniform in composition. Figures 8.22 (a and b) show the mapping of the main chemical elements which provide further evidence of the composition of the sample. A number of irregular shaped particles are very rich in silicon and comparatively low in aluminium and calcium. It is, therefore, likely that these irregular shaped particles are grains of sand embedded the matrix. The material (batch code IA) contains no ground granulated blast furnace slag, therefore fly ash is the only source of calcium in the material. By examining the distribution of elements it can also be seen that silicon is distributed across the sample while low levels of sodium and magnesium can be found, see Figure 8.22 (a). However, calcium and aluminium are almost entirely located in the discrete areas suspected of being unreacted particles of fly ash. The conclusion from this is that the

matrix is a silicate hydrate, but not a calcium silicate hydrate. It is likely that it forms a similar hydrate to calcium silicate hydrate (CSH) as proposed in literature[11, 19, 20, 70], but aluminium, sodium and magnesium have replaced some of the calcium in the structure of the hydration product.

These findings are consistent with the information obtained from the investigations of the fracture surface. Figures 8.23 (a and b) presents the secondary electron images obtained from a specimen of batch code IA. These show a rough undulating surface embedded with irregular sized and shaped particles. The surface has a fibrous needle like crystalline growth from the specimen surface. Comparing with Figure 8.18, Figure 8.23 shows that materials with microsilica have a more fibrous microstructure.

Table 8.20 details the results from the EDAX performed at the points shown in Figure 8.23 (a and b). The analysis shows the aluminium content to be relatively low with only two sites with concentrations above 5%. The level of sodium shows considerable variation between 6% and 33%, however the calcium content shows only three sites were it was higher than the sodium level. Of these sites only two have Ca/Si ratio which would indicate the formation of CSH. The sodium and silicon levels suggest a CSH type of hydration phase with sodium replacing the calcium in the hydration product.

Table 8.19 Summary of data from the feature scan measurements for material IA (Pore area 8.496%)

Measurement	No. data	Mean	Median	Min	Max
No detected	7	123.3	129	82	172
Area/mm ^2	863	0.0087	0.0014	0.0005	0.3586
Feature breadth/mm	863	0.0671	0.0369	0.0137	0.5015
Feature length/mm	863	0.1134	0.0647	0.0308	1.072
Field area/mm ^2	7	12.62	0	12.62	12.62
Field number	7	4	3.985	1	7
Mean Feret/mm	863	0.0923	0.0527	0.027	0.8163

Table 8.20 Semi-quantitative chemical analysis of thermally cured alkali activated material cured under 20°C and 65% RH (batch code IA)

Spot No.	Na	Mg	Al	Si	S	K	Ca	Fe	Na/Al	Si/Al	Ca/Al	K/Al	Ca/Si	Al/Ca	S/Ca
1	7.7	0.45	2.52	81.19	4.69	0.69	0.39	2.36	3.06	32.22	0.15	0.27	0.00	6.46	12.03
2	15.42	0.36	1.99	81.08	0.19	0.86	0.07	0.04	7.75	40.74	0.04	0.43	0.00	28.43	2.71
3	7.98	0.13	5.09	79.92	2.21	1.56	2.02	1.09	**1.57**	**15.70**	**0.40**	0.31	0.03	2.52	1.09
4	13.26	0.24	0.29	44.07	2.46	0.5	38.77	0.4	45.72	151.97	133.69	1.72	**0.88**	**0.01**	0.06
5	18.15	-0.17	0.35	25.31	2.9	0.65	52.68	0.12	51.86	72.31	150.51	1.86	**2.08**	**0.01**	0.06
6	32.76	0.01	5.62	52.71	1.79	6.58	-0.1	0.63	5.83	9.38	-0.02	1.17	0.00	-56.20	-17.90
7	6.11	0.22	0.62	76.47	7.27	0.92	7.87	0.52	9.85	123.34	12.69	1.48	0.10	0.08	0.92
8	7.27	0.07	2.18	82.95	2.58	1.11	3.25	0.62	3.33	38.05	1.49	0.51	0.04	0.67	0.79
Average	*13.581*	*0.1638*	*2.332*	*65.463*	*3.0113*	*1.609*	*13.119*	*0.7225*	*5.82*	*28.07*	*5.62*	*0.69*	*0.20*	*0.18*	*0.2295*

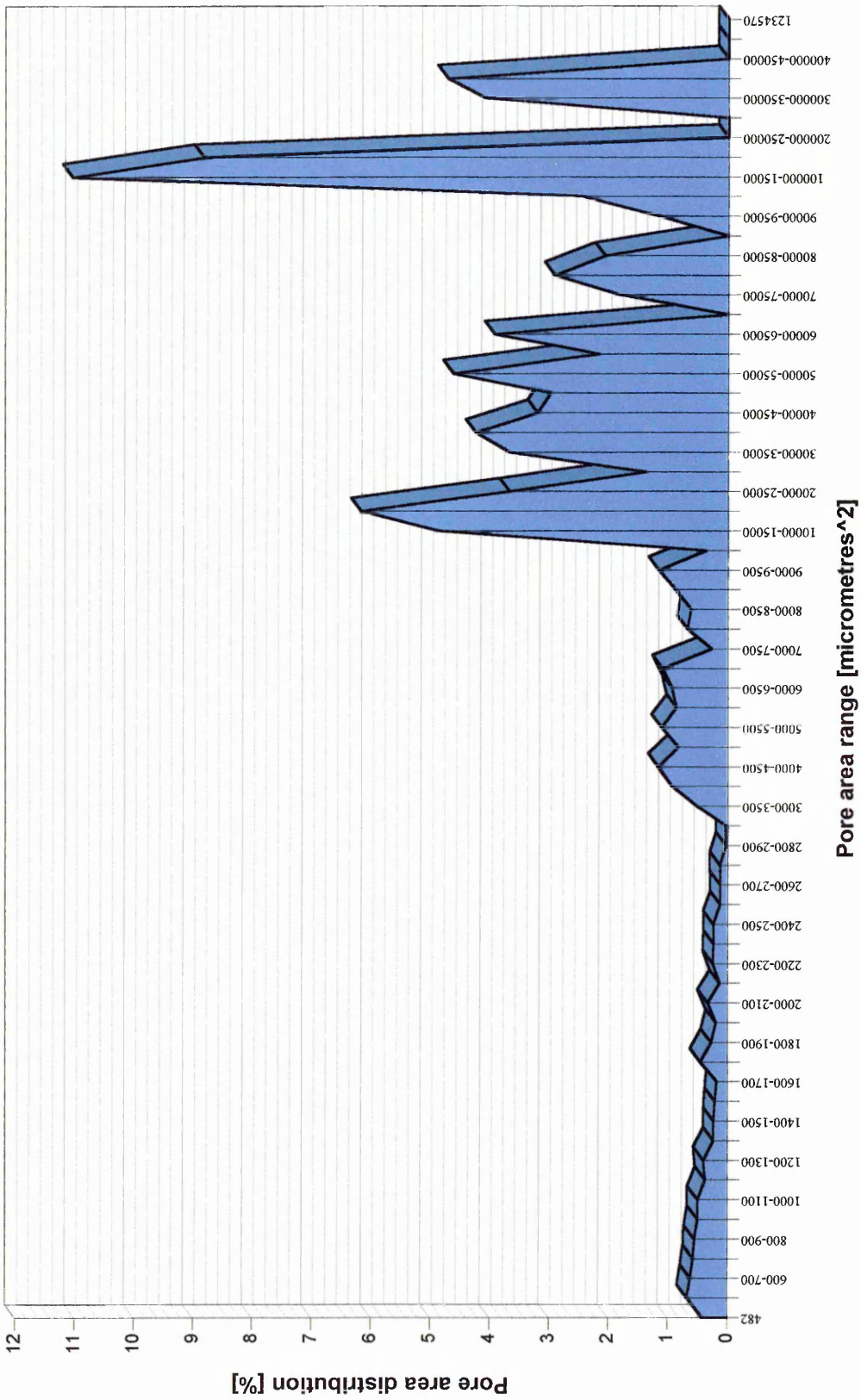

Figure 8.20 Pore area distribution of alkali activated fly ash material cured under 20°C and 65% RH (batch code IA)

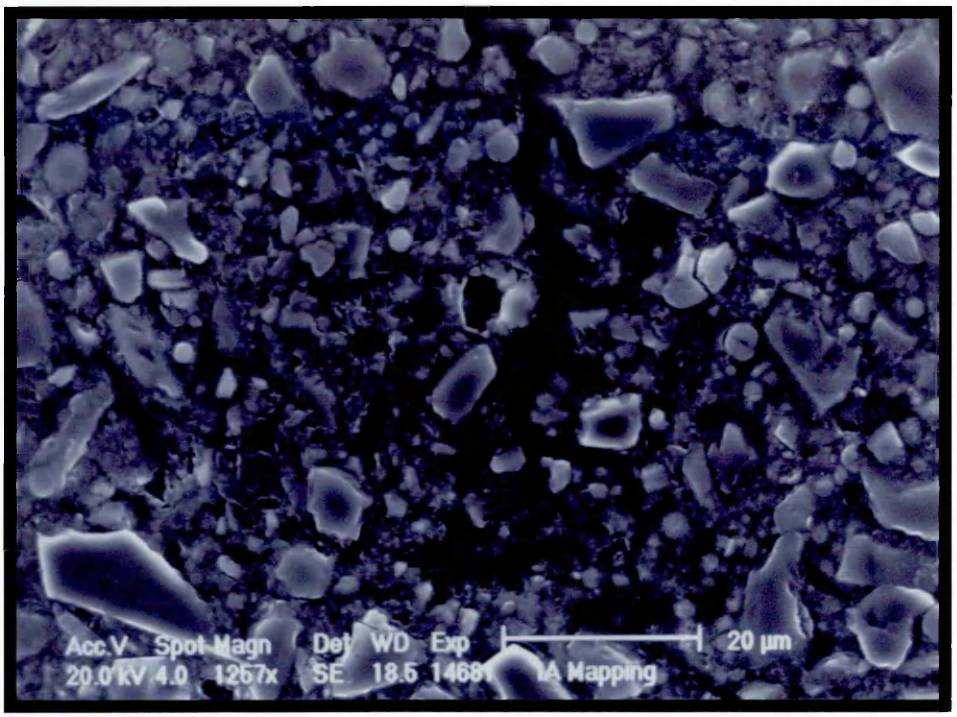

(a)

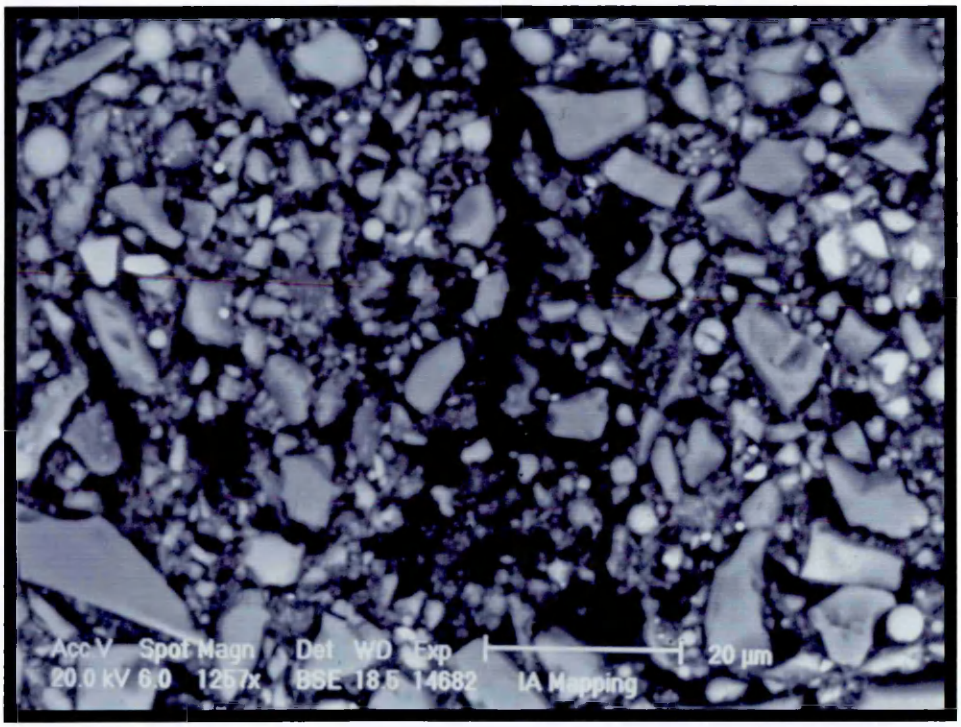

(b)

Figure 8.21 Secondary electron image and backscattered electron image of alkali activated fly ash material cured under 20°C and 65% RH (group I - batch code A).

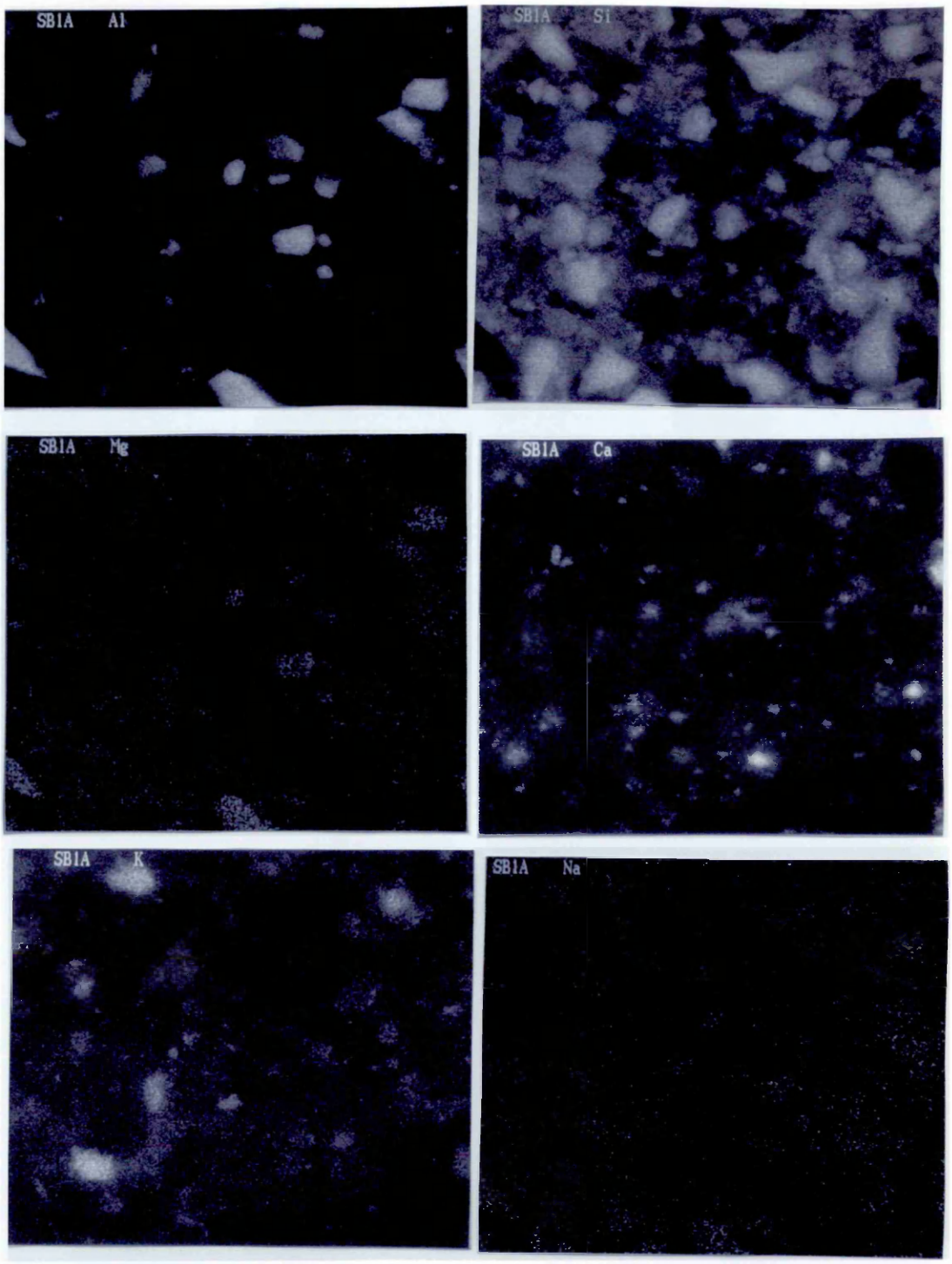

Figure 8.22 (a) Mapping of Al, Si, Mg, Ca, K and Na elements in the alkali activated fly ash material cured under 20°C and 65% RH (group I batch code A)

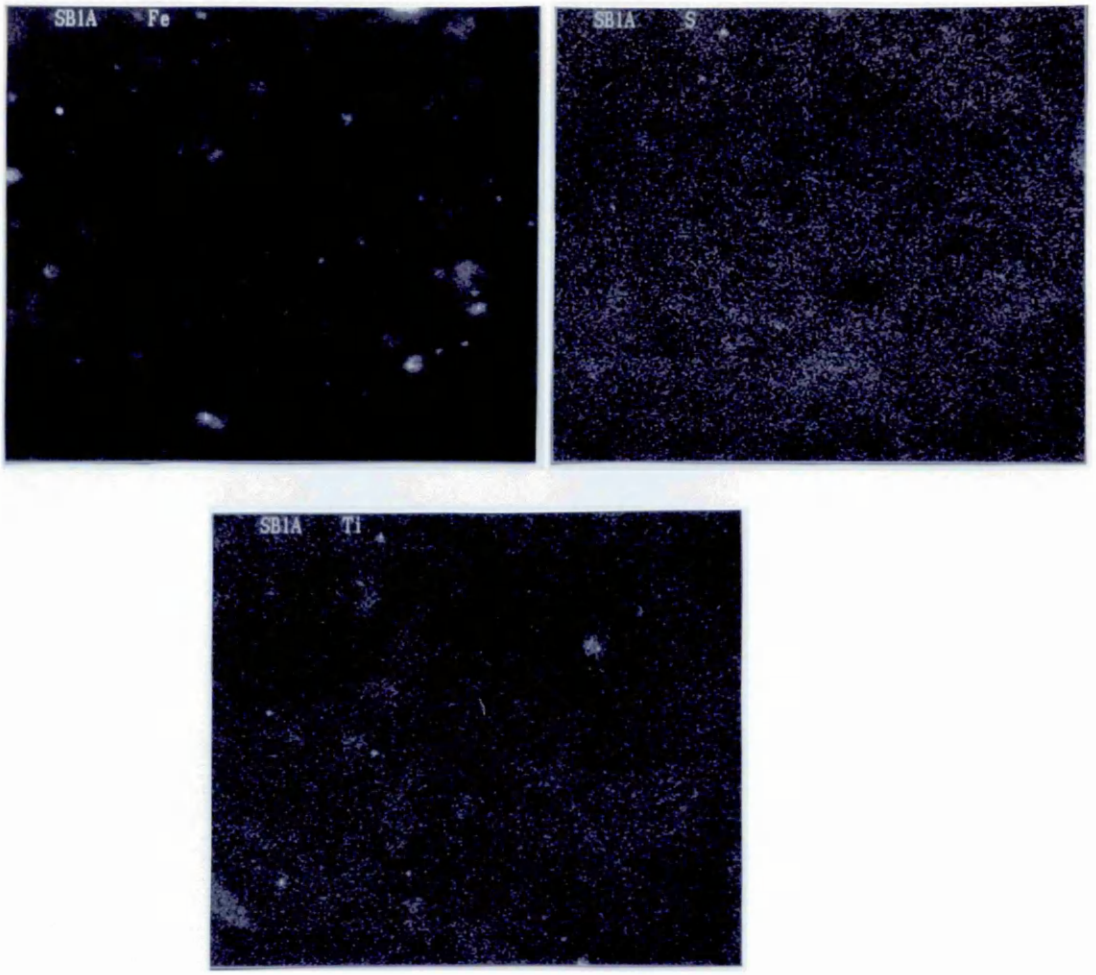

Figure 8.22 (b) Mapping of Fe, S and Ti elements in the alkali activated fly ash material cured under 20°C and 65% RH (batch code IA).

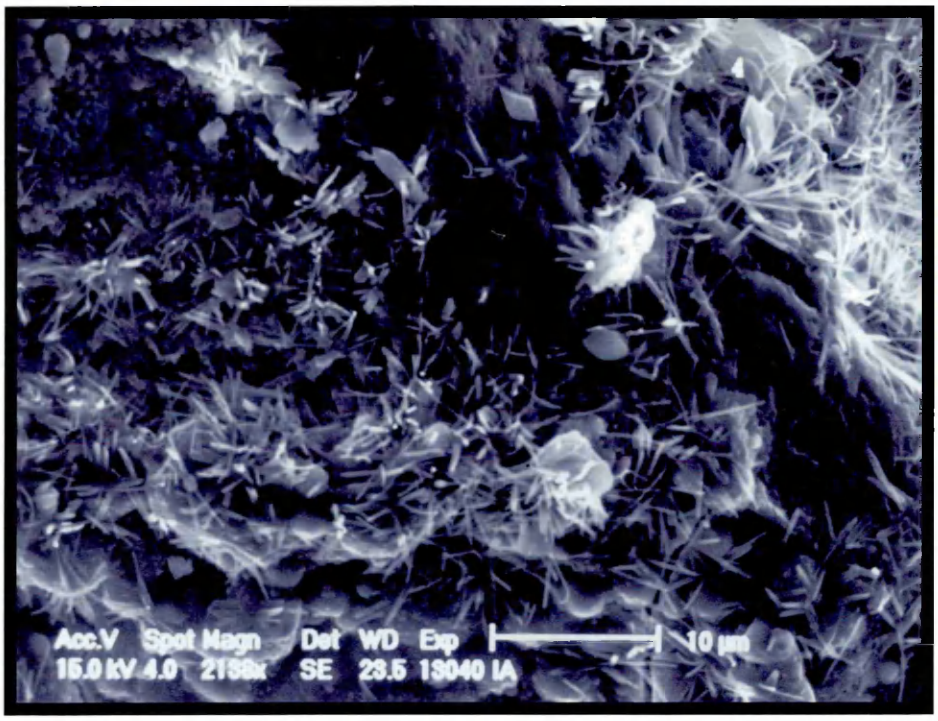

(a)

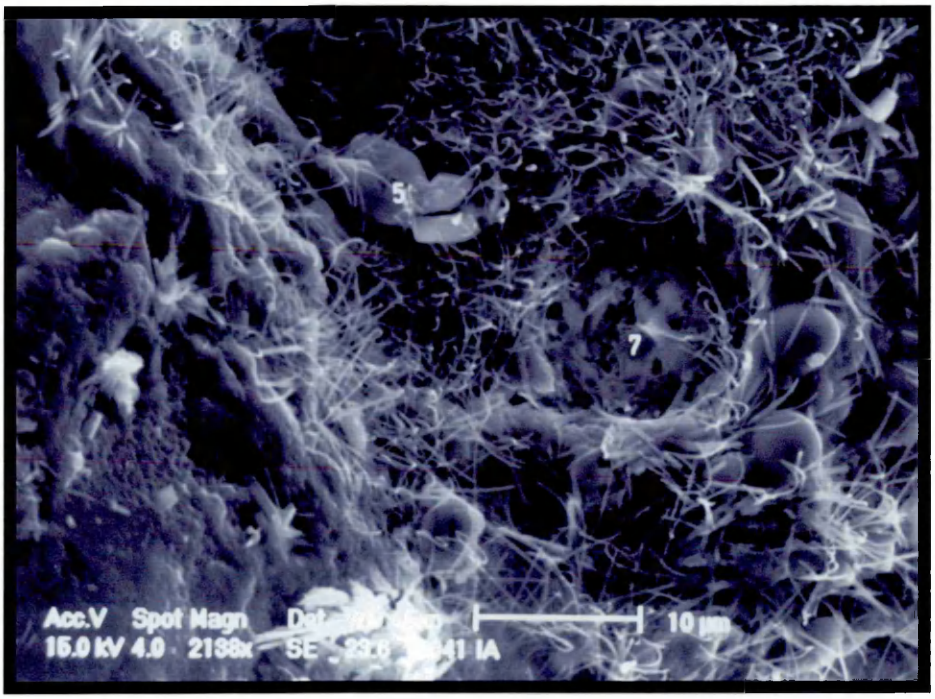

(b)

Figure 8.24 (a and b) SEI of the fracture surface of alkali activated material (group I - batch code A)

8.5.2.2.2 ***Thermally cured material (batch code IH)***

Material batch code IH has the same composition as material batch code IA. It has undergone a high temperature (up to 120°C) curing as opposed curing under 20°C and 65% RH or batch code IA. The pore distribution is presented in Figure 8.24 and Table 8.21 presents a summary of the results from the feature analysis. This indicates that the largest pore area was for pore sizes between 20000 and 25000 microns^2. Material IH did not show a significant increase in the flexural strength 21.89N/mm^2 compared with 20.06 N/mm^2 for the corresponding materials batch code IA. However, it shows an increase in the total pore area to12.8% compared with 8.5% for the corresponding material batch code IA. A comparison of Figures 8.20 and 8.24 shows that the thermally cured materials exhibit higher porosity but smaller pore sizes compared with those cured under 20°C and 65% RH.

The back scattered electron image and secondary electron image of material IH is given in Figure 8.25 (a and b). In the secondary electron image (Figure 8.25 a), it can be seen that the right hand side is covered by an amorphous layer of hydration product. On the left hand side of the image particles of fly ash can be seen embedded in the matrix. This is confirmed by the back scattered image in Figure 8.26 b, the hydration product is a darker shade of grey than the fly ash particles indicating a difference in chemical composition from the fly ash.

The mapping images in Figures 8.26 (a and b) show the distribution of chemical elements in material IH. It can be seen that the main species found in the hydration product is silicon, as with batch IA. Sodium and magnesium can also be found. However a comparison of Figures 8.22(a) and 8.26(a) shows that the aluminium content is higher in material IH. There also appears to be a limited amount of sulphur in the matrix as shown in Figure 8.26 b.

Table 8.22 details the results from the semi-quantitative chemical analysis performed at the points shown in Figure 8.27 (a, b and c). The calcium to silica ratio is too low for the formation of calcium silicate hydrate to be possible. The aluminium and sodium levels vary widely with the location where analyses were undertaken. Figures 8.28 (a, b and c) shows that aluminium and sodium is associated with two distinct types of hydration product. In Figures 8.27 (a and b) the crystalline hydration product at spots 1,3 and 5 is high in sodium. Areas 1 and 5 are also rich in sulphur. This

would suggest a silicate like phase containing sulphur. The amorphous hydration product at spots 7, 8 and 9 is high in aluminium. This would appear to be the major hydration product in the material, which is likely to be an aluminium silicate with a combination of sodium, magnesium and potassium. This is different from batch IA which was much lower in aluminium.

Table 8.21 Summary of the data from feature scan measurements for thermally cured material IH (Pore area 12.781%)

Measurement	No. data	Mean	Median	Min	Max
No detected	7	299	294.2	242	367
Area/mm ^2	2093	0.0054	0.0012	0.005	0.276
Feature breadth/mm	2093	0.0616	0.0399	0.0137	0.6302
Feature length/mm	2093	0.1039	0.72	0.0308	1.296
Field area/mm ^2	7	12.62	0	12.62	12.62
Field number	7	4	3.985	1	7
Mean Feret/mm	2093	0.0845	0.0584	0.0271	0.9904

Table 8.22 Semi-quantitative chemical analysis of thermally cured alkali activated material (batch code IH)

Spot No.	Na	Mg	Al	Si	S	K	Ca	Fe	Na/Al	Si/Al	Ca/Al	K/Al	Ca/Si	Al/Ca	S/Ca
1	29.2	0.4	0.21	54.61	10.61	1.13	3.17	0.68	139.05	260.05	15.10	5.38	0.06	0.07	3.35
2	2.2	-0.1	-0.19	95.57	1.1	-0.05	1.4	0.06	-11.58	-503.05	-7.37	0.26	0.01	-0.14	0.79
3	33.78	0.34	5.8	45.04	5.99	7.35	0.18	1.52	**5.82**	**7.77**	**0.03**	1.27	0.00	32.22	33.28
4	3.55	0.07	0.34	94.47	0.96	-0.05	0.45	0.21	10.44	277.85	1.32	-0.15	0.00	0.76	2.13
5	18.46	0.26	0.31	62.37	10.39	1.62	4.74	1.84	59.55	201.19	15.29	5.23	0.08	0.07	2.19
6	0.5	0	-0.17	97.97	0.11	-0.03	1.05	0.56	-2.94	-576.29	-6.18	0.18	0.01	-0.16	0.10
7	2.79	1.43	22.43	61.86	0.7	5.34	1.78	3.68	0.12	2.76	0.08	0.24	0.03	12.60	0.39
8	0.54	0.29	4.16	91.24	0.25	2.07	0.82	0.63	0.13	21.93	0.20	0.50	0.01	5.07	0.30
9	1.25	1.09	29.24	60.55	0.3	4.35	1.62	1.6	0.04	2.07	0.06	0.15	0.03	18.05	0.19
10	7.64	0.68	21.47	57.18	1.34	5.38	3.53	2.78	0.36	2.66	0.16	0.25	0.06	6.08	0.38
11	10.43	0.41	7.86	70.01	5.76	2.51	2.08	0.93	**1.33**	**8.91**	**0.26**	0.32	0.03	3.78	2.77
12	2.01	0.46	10.71	77.16	0.85	3.82	3.02	1.97	0.19	7.20	0.28	0.36	0.04	3.55	0.28
Average	*11.789*	*0.596*	*11.354*	*64.447*	*4.021*	*3.730*	*2.327*	*1.737*	*1.04*	*5.68*	*0.20*	*0.33*	*0.04*	*4.88*	*1.7283*

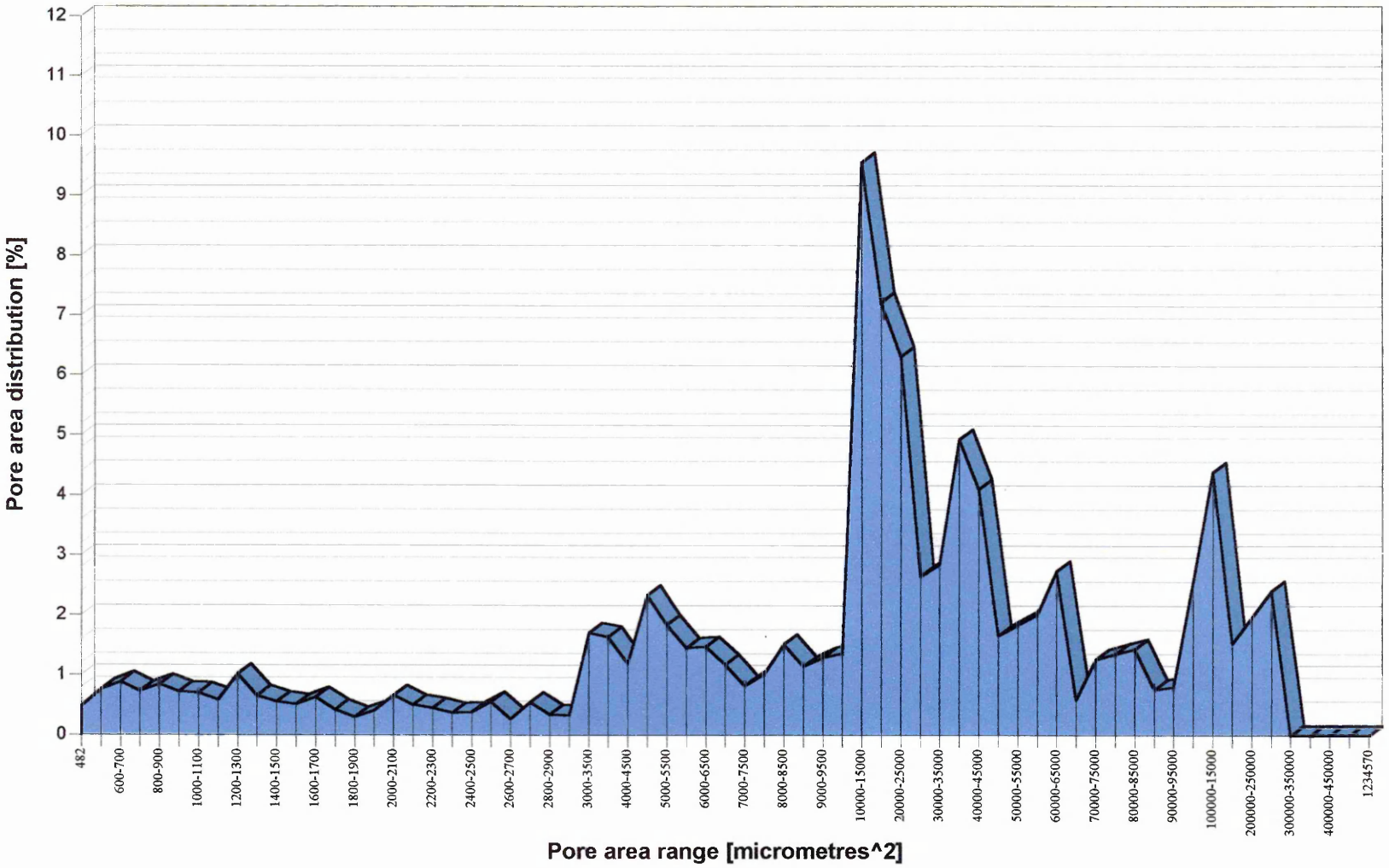

Figure 8.24 Pore area distribution of thermally cured material without slag and hardener (batch code IH)

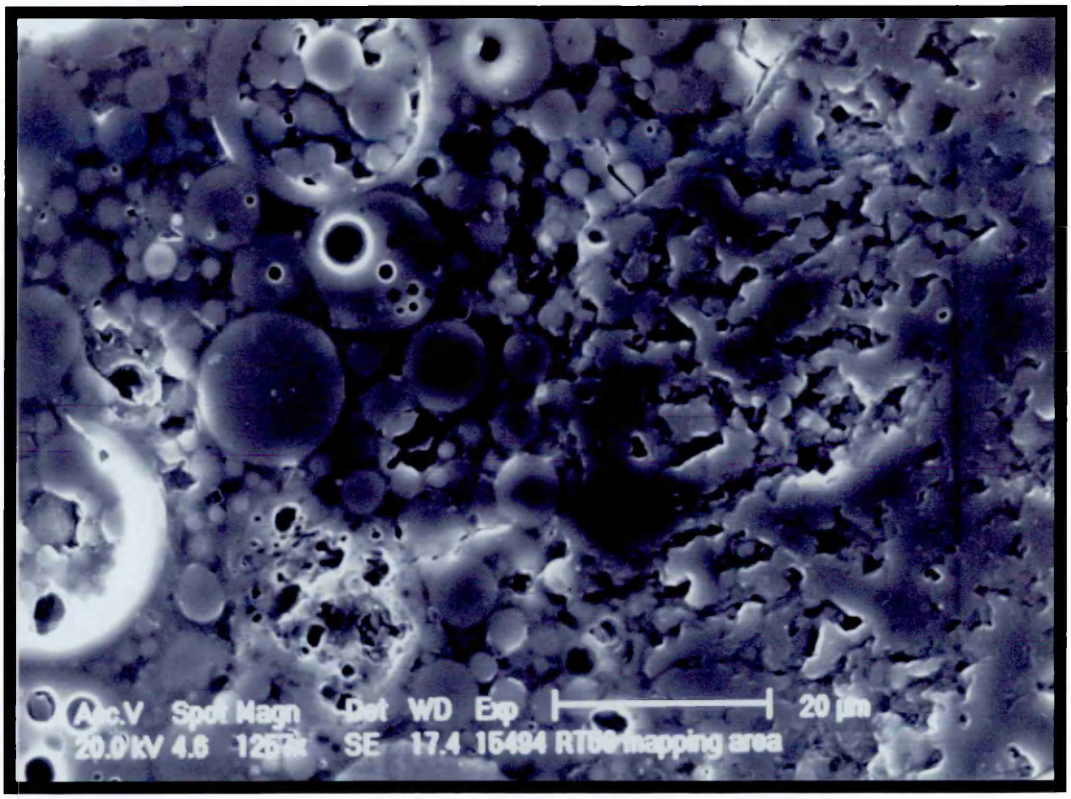

(a)

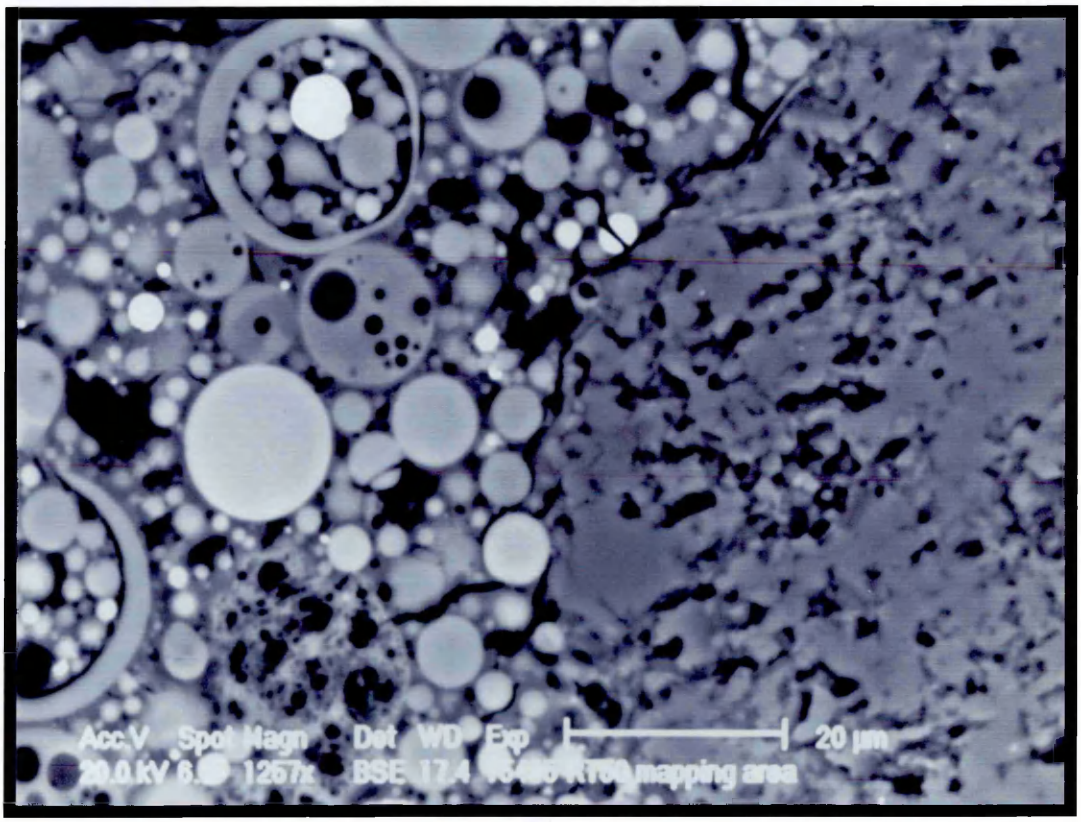

(b)

Figure 8.25 (a and b) Secondary electron image and backscattered electron image of thermally cured alkali activated fly ash material (group I batch code H)

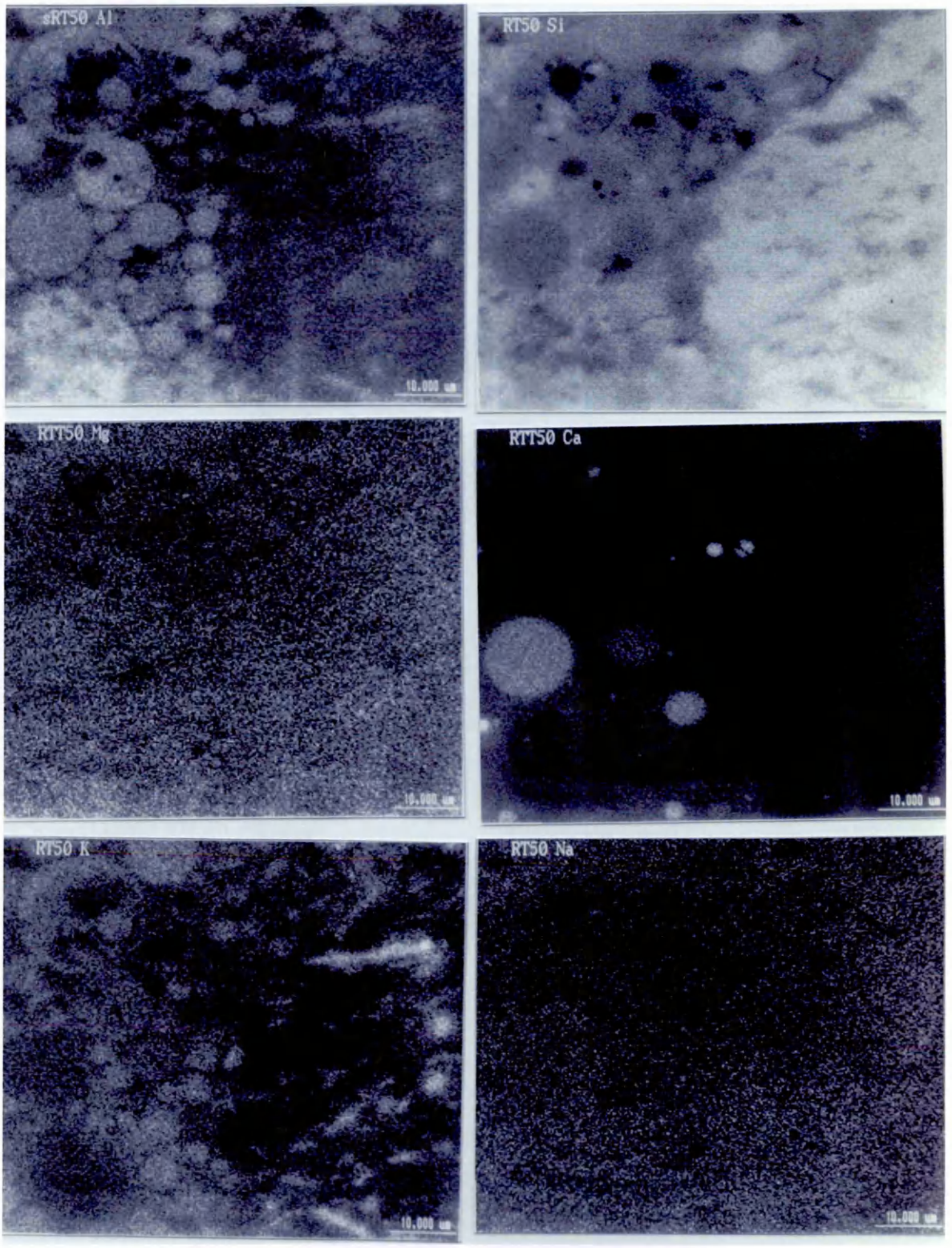

Figure 8.26 (a) Mapping of the Al, Si, Mg, Ca, K and Na elements in the thermally cured alkali activated fly ash material (group I - batch code H)

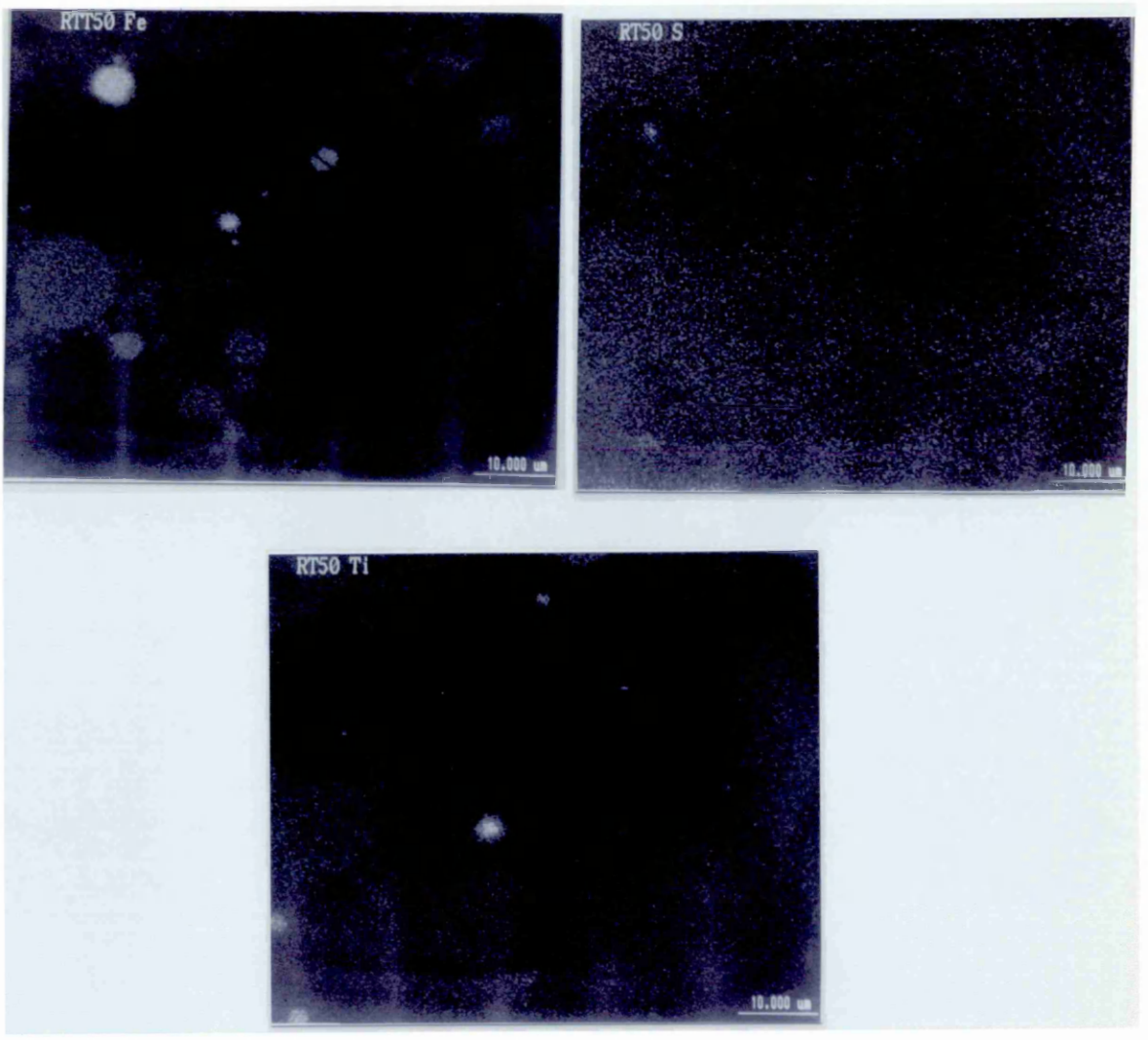

Figure 8.26 (b) Mapping of the Fe, S and Te in the thermally treated alkali activated fly ash material (group I - batch code H)

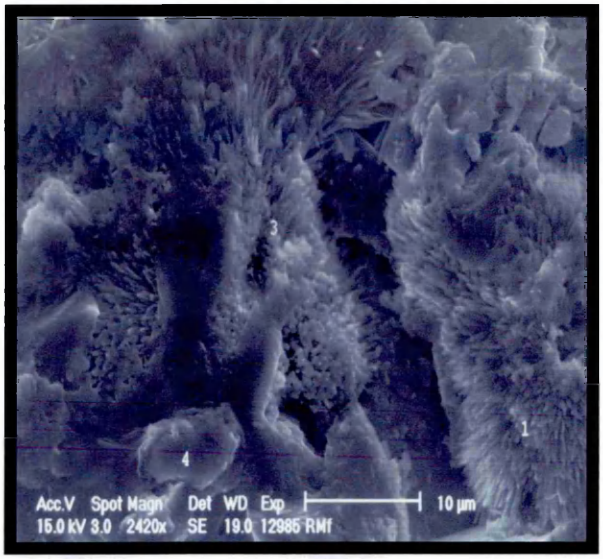

(a)

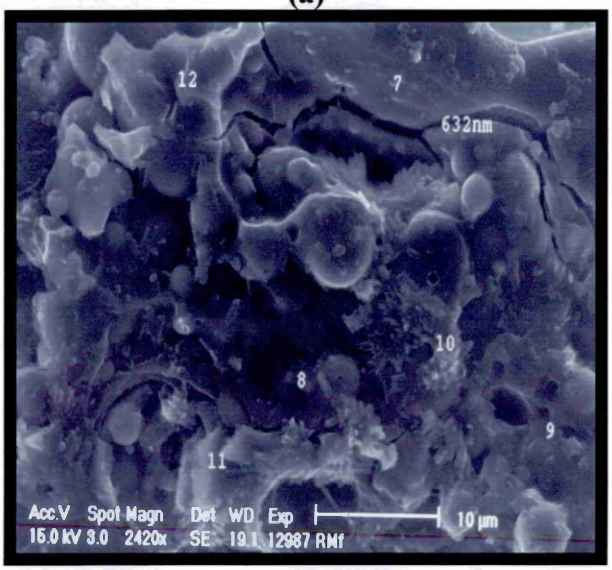

(b)

(c)

Figure 8.27 (a,b and c) SEI of the fracture surface of alkali activated materials (group I - batch code H)

8.5.2.3 Alklai activated materials containing ggbs

8.5.2.3.1 Material cured at 20°C and 65% RH batch code IISA

Material IISA contains 20% fly ash, 5% microsilica, 10% slag and 11% water glass the remaining 54% being sand (see Table 8.10). The modulus of rupture is similar to materials IA and IH at 21.87 N/mm^2. Table 8.23 presents a summary of the results from the feature analysis. The pore area is slightly lower than for IA and IH at 5.47%. However, the pore area distribution presented in Figure 8.28 shows that the pore structure has been further refined, with a greater percentage of the pores having areas within the range 10000 to15000 microns^2.

The fracture surfaces presented in Figures 8.29 and 8.30 show a material with a rough irregular surface containing fly ash particles embedded in it and a large number of micro-cracks can be seen running across. However, the matrix is dense and well consolidated. Some unreacted particles of the constituent materials can be seen embedded in the hydrated matrix in Figure 8.30. It also shows a sand grain surrounded by the hydrated matrix containing small particles. As discussed previously (section 8.5.2.2) the spherical particles are fly ash grains and the irregular shaped particles are the blast furnace slag grains.

Table 8.24 presents the EDAX results performed at the points shown in Figures 8.30 and 8.31. These results show higher levels of calcium than previous materials (batch code IA and IH). However, the overall composition still suggests that the calcium to silicon level is below that expected for calcium silicate hydrate (CSH) formation. Material IISA contains slag unlike materials IA and RT which only contained fly ash. This would result in a higher level of calcium in the material IISA as shown in Table 8.24.

Figures 8.31 (a and b) show the secondary and backscatter electron images of the polished surface of material batch code IIA1.The results of digital mapping analysis (Figure 8.32 a and b) also show the calcium to be concentrated around individual particles. This would indicate that it is only associated with the blast furnace slag particles. This makes the role of the blast furnace slag unclear. If the calcium has remained local to the areas with slag particles it may suggest that the slag particles

have been consumed in the chemical reactions. Alternatively, all the calcium may have been consumed creating small quantities of CSH hydration product around the slag particle. The matrix can be seen to be rich in silicon and aluminium with sodium potassium and magnesium distributed through the matrix. This would indicate the formation of complex hydration products such as alumino-silicates.

Table 8.23 Summary of the data from the feature scan measurements for material batch code IISA (Pore area 5.468%)

Measurement	No. data	Mean	Median	Min	Max
No detected	7	152.7	138.1	107	202
Area/mm ^2	1069	0.0045	0.0012	0.0005	0.1017
Feature breadth/mm	1069	0.055	0.0345	0.0137	0.2817
Feature length/mm	1069	0.0838	0.0551	0.0308	0.6024
Field area/mm ^2	7	12.62	0	12.62	12.62
Field number	7	4	3.985	1	7
Mean Feret/mm	1069	0.0704	0.0471	0.027	0.4496

Table 8.24 Semi-quantitative chemical analysis of alkali activated material with ggbs cured under 20°C and 65%RH (batch code IISA)

Spot No.	Na	Mg	Al	Si	S	K	Ca	Fe	Na/Al	Si/Al	Ca/Al	K/Al	Ca/Si	Al/Ca	S/Ca
1	4.33	2.41	7.68	64.5	1.52	0.89	18.44	0.23	0.56	8.40	2.40	0.12	0.29	0.42	0.08
2	-	-	-	100.17	-	-	-	-	-	-	-	-	-	-	-
3	1.56	0.4	7.84	58.54	2.19	1.81	27.23	0.43	0.20	7.47	3.47	0.23	0.47	0.29	0.08
3R	4.38	1.09	3.49	56.7	1.85	0.97	31.32	0.2	**1.26**	**16.25**	**8.97**	0.28	0.55	0.11	0.06
4	2.1	5.04	12.29	49.72	2.44	0.85	27.5	0.05	0.17	4.05	2.24	0.07	0.55	0.45	0.09
Average	*3.093*	*2.235*	*7.825*	*57.365*	*2.000*	*1.130*	*26.123*	*0.228*	*0.40*	*7.33*	*3.34*	*0.14*	*0.46*	*0.30*	*0.0766*

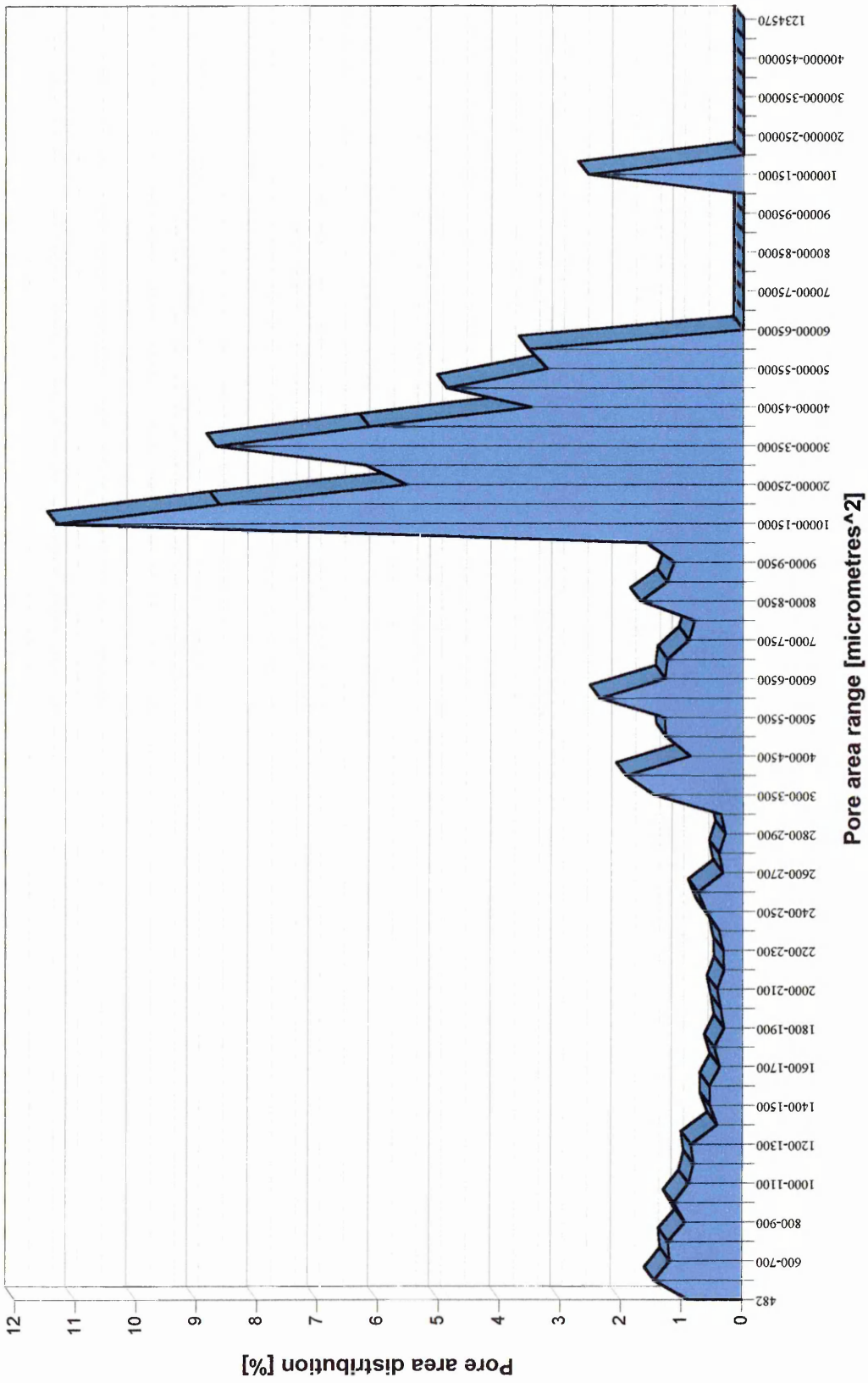

Figure 8.28 Pore area distribution of alkali activated fly ash material with slag (batch code IIA1)

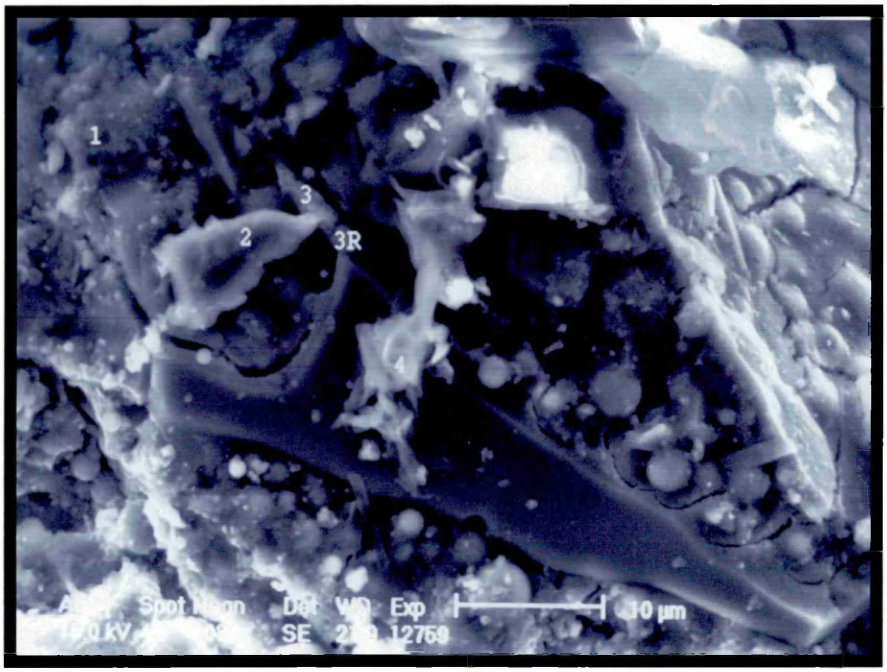

Figure 8.29 SEI on the fracture surface of alkali activated material (group II - batch code SA)

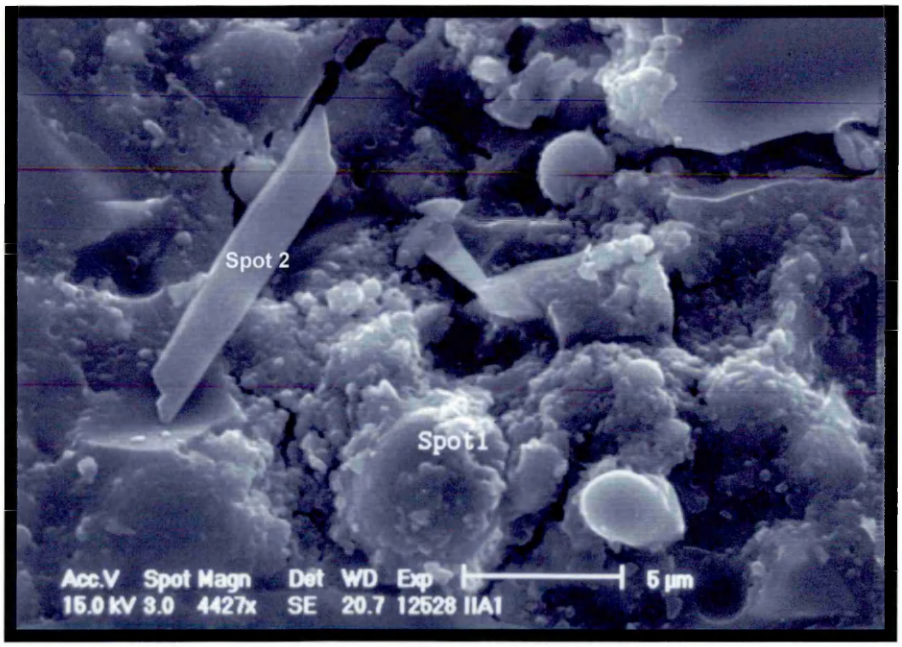

Figure 8.30 SEI on the fracture surface of alkali activated material (group II - batch code SA)

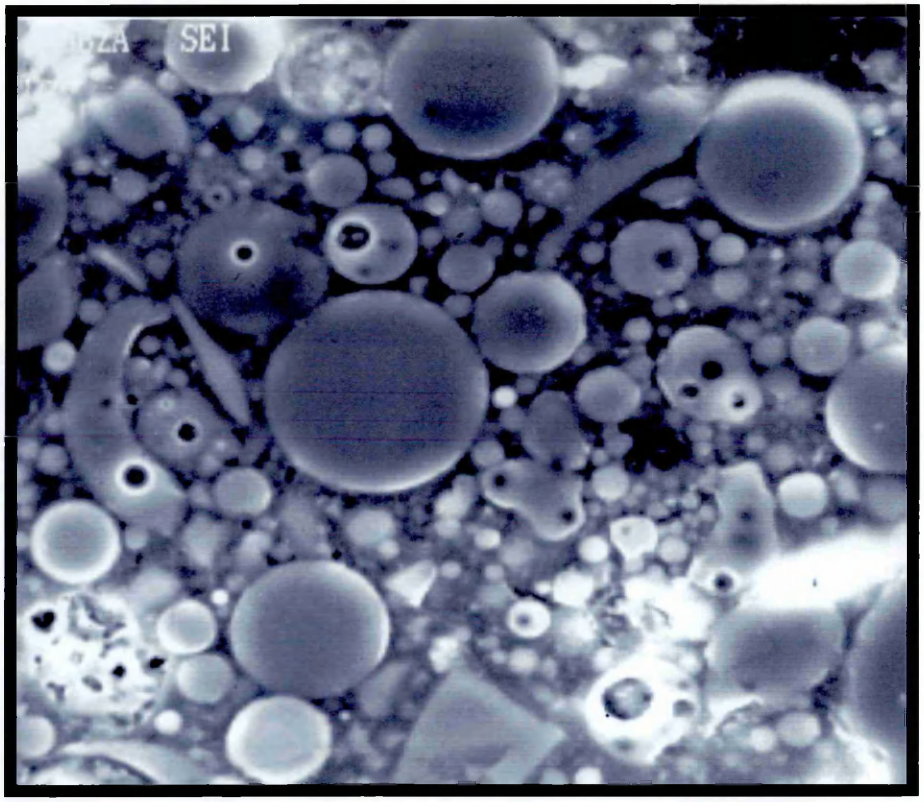

(a)

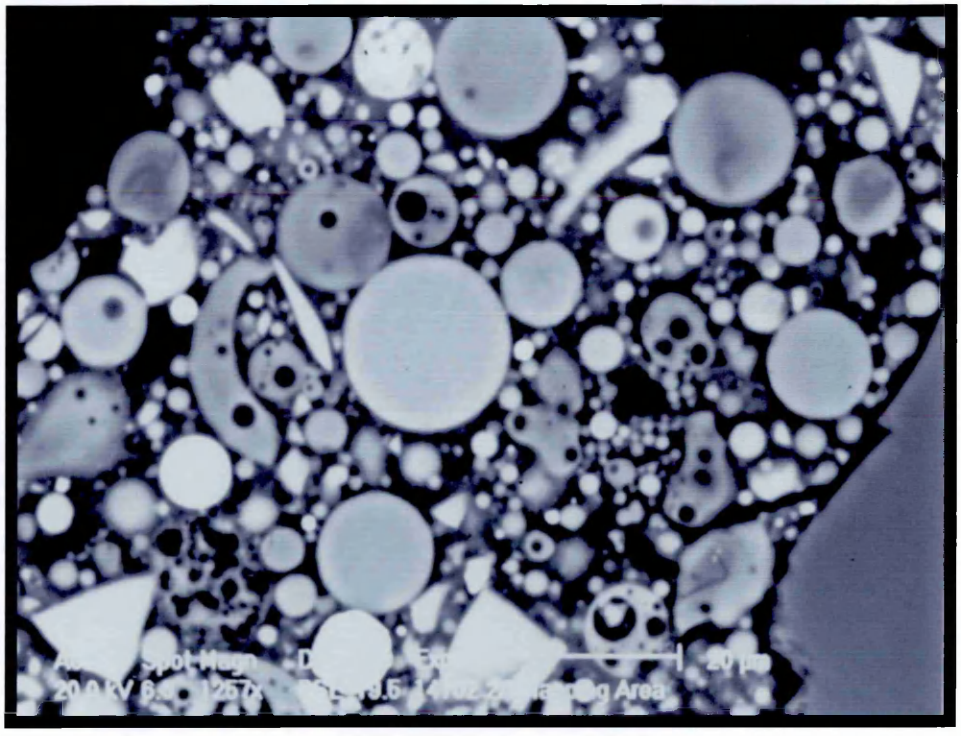

(b)

Figure 8.31 (a and b) Secondary electron image and backscattered image of alkali activated material with ggbs cured under 20°C and 65%R (group II - batch code SA)

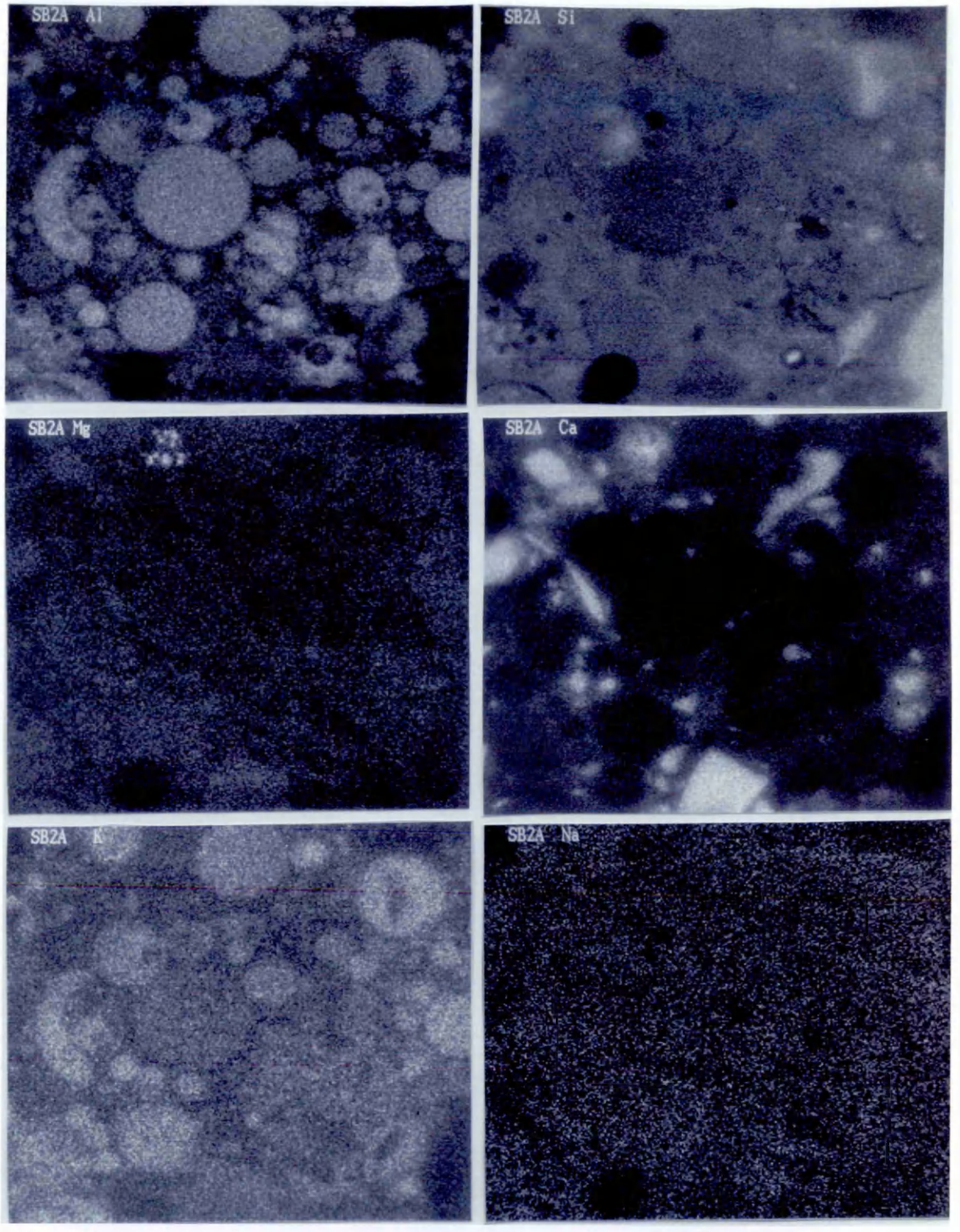

Figure 8.32 (a) Mapping of Al, Si, Mg, Ca, K and Na elements in the alkali activated material with ggbs, cured under 20C and 65% RH (group II - batch code SA)

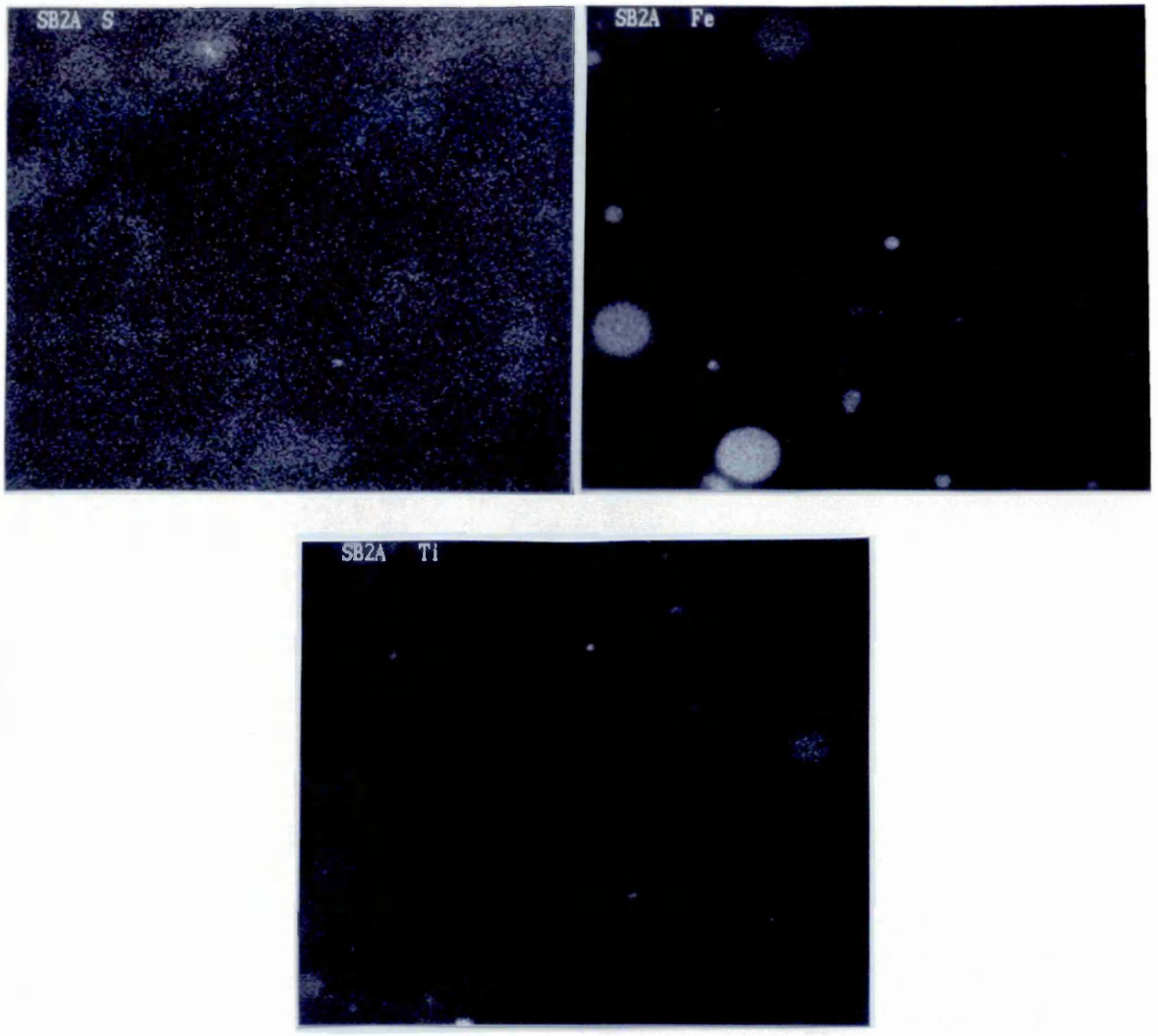

Figure 8.32 (b) Mapping of S, Fe and Ti elements in the alkali activated material with ggbs, cured under 20C and 65% RH (group II - batch code SA)

8.5.2.3.2 Thermally cured material (batch code IISH)

Material batch code IISH has the same content of fly ash, slag and microsilica as material batch code IISA. It has undergone the thermal curing instead of curing under 20°C and 65% RH. Table 8.25 presents a summary of the results from feature analysis. There is a significant difference in flexural strengths of the two materials. The modulus of rupture of material IISH is 38.84 N/mm^2 compared with 21.87 N/mm^2 for material IISA. However, the pore area distribution presented in Figure 8.33 is similar at 4.8% compared with 5.5% for material IISA. A comparison of Figures 8.28 and 8.33 also shows that the pore area distribution is similar. This suggests that the change in strength is not as a result of changes to the pore structure of the material.

The back scattered electron image and secondary electron image of material IISA can be seen in Figures 8.34 (a and b). This shows a clear matrix of hydration products. Embedded within the matrix, spheres of fly ash can be seen including particles cut into two showing the hollow interior of glassy spheres. Other areas of the structure show irregular shaped particles, all the particles appear to be coated in hydration products. The structure also shows a number of pores and cracks within the sample. The identification of individual particles can also be seen in the back scattered electron image of the sample (Figure 8.34 b). The irregular shaped particles are lighter in colour than the spherical fly ash particles. This would indicate that the irregular shaped particles contain atoms of higher atomic number such as Ca and Fe. From this it can be deduced that these particles are most likely to be unburnt coal particles and unhydrated slag grains.

Figures 8.35 (a and b) present the digital mapping micrographs of material IISA showing the distribution of chemical elements within the structure. Table 8.26 details the results from the EDAX performed at the points shown in Figure 8.36 (a). Silicon is the most abundant element as would be expected. However, the majority of the particles embedded in the matrix appear to have a similar concentration of silicon as the matrix. Areas containing pores, cracks or the hollow cross section of fly ash grains are shown as dark areas with no silicon content. Aluminium appears to be the next most abundant element and the digital map of this element (see Figure 8.35 a) reveals a greater level of variation with location, where the analysis was performed,

than for silicon. Individual particles are clearly far richer in aluminium than the hydration products of the matrix. The major source of aluminium is the fly ash grains and this would suggest that only a small proportion of the fly ash grains has reacted to form hydration products. As for other batches examined (see sections 8.5.2.1 and 8.5.2.2) calcium is also concentrated around the irregular shaped particles further suggesting that this is the site of blast furnace slag particles. Little or no calcium is found outside these areas in the microstructure. This would suggest that the blast furnace slag has not fully reacted in the structure to form hydration products. Other elements such as potassium, magnesium and sulphur also appear to be concentrated in discrete areas. However, a significant concentration exists in the matrix. Sodium appears to be distributed evenly throughout the matrix, similar to silicon but at lower concentrations. It would suggest that levels of aluminium, potassium, sulphur and magnesium come from the reaction of fly ash and blast furnace slag, while sodium and silicon come from the water glass activator reactions.

The results of materials IISA and IISH are very similar. Both materials show aluminium and silicon in the matrix at high levels, sodium, potassium and magnesium also occurring in the matrix. Calcium, in both cases, is confined to areas around blast furnace slag particles. This would suggest that the major hydration product in each case is an alumino silicate of some form. It has not been possible with SEM to detect differences in hydration products between the thermally cured IISH specimens and the ambient cured IISA specimens. The results of the EDAX traces for material IISH (see Table 8.26) show areas with much higher levels of sodium and aluminium than for material IISA (see Table 8.24). These areas can be seen in Figure 8.36 as a layer of hydration product. This may indicate differences in hydration products between materials IISA and IISH. However, it is not conclusive proof of the type or composition of the hydration product.

Table 8.25 Summary of data from the feature scan measurements for material IISH (Pore area 4.775%)

Measurement	No. data	Mean	Median	Min	Max
No detected	7	157.1	156.9	110	231
Area/mm ^2	1100	0.0038	0.0008	0.0005	0.1182
Feature breadth/mm	1100	0.0506	0.0348	0.0137	0.3801
Feature length/mm	1100	0.0788	0.0548	0.0308	0.6684
Field area/mm ^2	7	12.62	0	12.62	12.62
Field number	7	4	3.985	1	7
Mean Feret/mm	1100	0.0658	0.0462	0.0271	0.5377

Table 8.26 Semi-quantitative chemical analysis of thermally cured alkali activated material IISH

Spot No.	Na	Mg	Al	Si	S	K	Ca	Fe	Na/Al	Si/Al	Ca/Al	K/Al	Ca/Si	Al/Ca	S/Ca
1	0.76	1.2	37.7	54.43	0.16	4.71	0.18	0.86	0.02	1.44	0.00	0.12	0.00	209.44	0.8889
2	1.57	1.97	11.08	65.5	0.83	2.29	15.84	0.91	0.14	5.91	1.43	0.21	0.24	0.70	0.0524
3	0.46	1.28	29.92	58.23	0.07	5.63	0.91	3.49	0.02	1.95	0.03	0.19	0.02	32.88	0.0769
4	22.46	0.11	3.43	35.15	33.49	1.11	1.05	0.32	6.55	10.25	0.31	0.32	0.03	3.27	31.895
5	4.45	0.93	11.45	72.16	0.37	2.93	5.66	1.97	0.39	6.30	0.49	0.26	0.08	2.02	0.0654
6	12.18	1.44	8.78	54.13	17	1.65	4.05	0.59	**1.39**	**6.17**	**0.46**	0.19	0.07	2.17	4.1975
7	21.55	2.62	4.98	38.92	25.86	1.41	4.39	0.27	**4.33**	**7.82**	**0.88**	0.28	0.11	1.13	5.8907
8	17.18	0.5	3.43	27.08	47.09	0.81	3.41	0.51	**5.01**	**7.90**	**0.99**	0.24	0.13	1.01	13.809
9	1.56	13.31	2.05	66.32	3.45	1.02	11.62	0.68	0.76	32.35	5.67	0.50	0.18	0.18	0.2969
10	4.32	0.84	10.45	61.47	1.49	2.44	4.61	14.4	0.41	5.88	0.44	0.23	0.07	2.27	0.3232
Average	*8.649*	*2.42*	*12.327*	*53.339*	*12.981*	*2.4*	*5.172*	*2.4*	*0.70*	*4.33*	*0.42*	*0.19*	*0.10*	*2.38*	*2.5099*

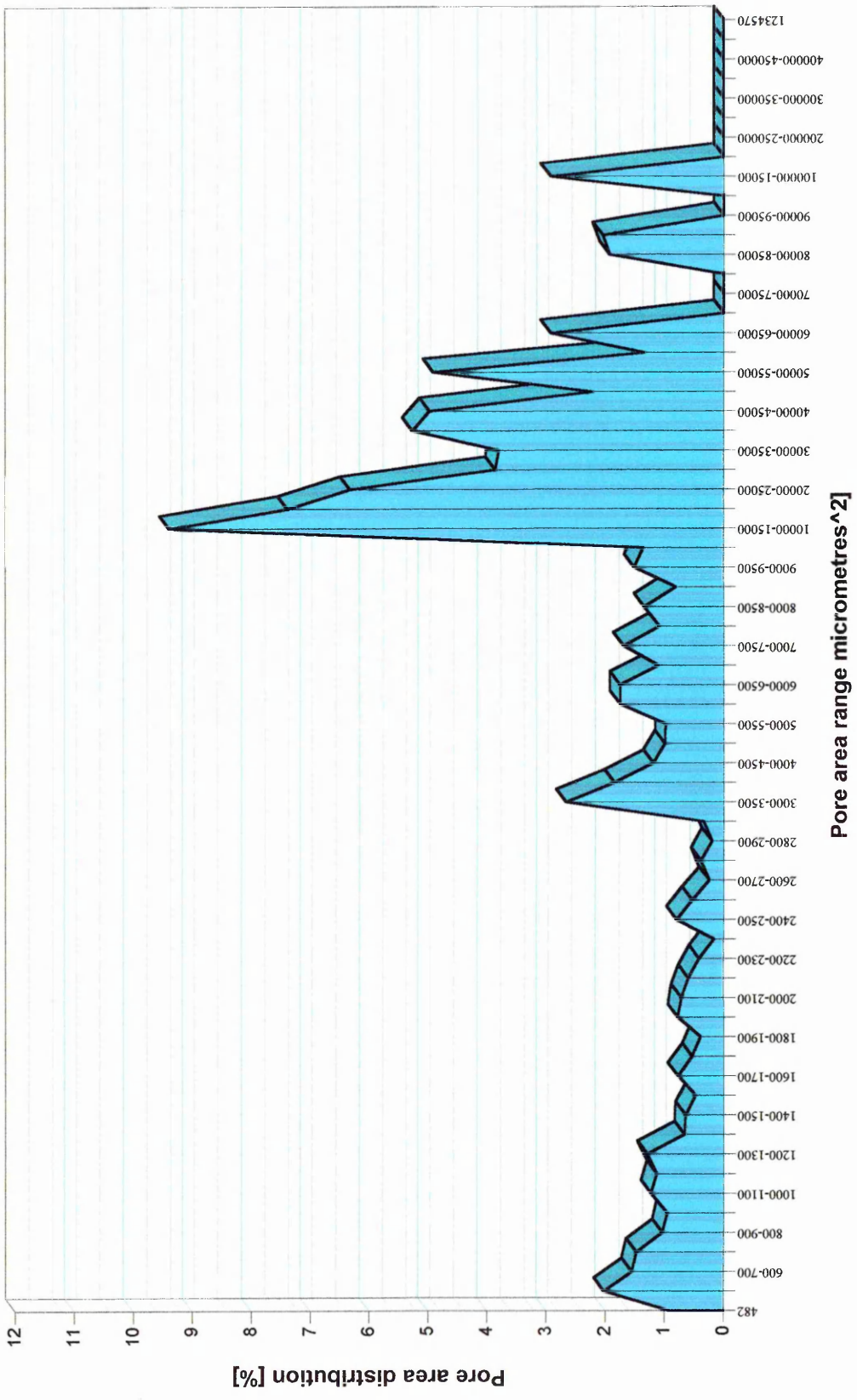

Figure 8.33 Pore area distribution of thermally cured alkali activated fly ash material containing slag (batch code IIH1)

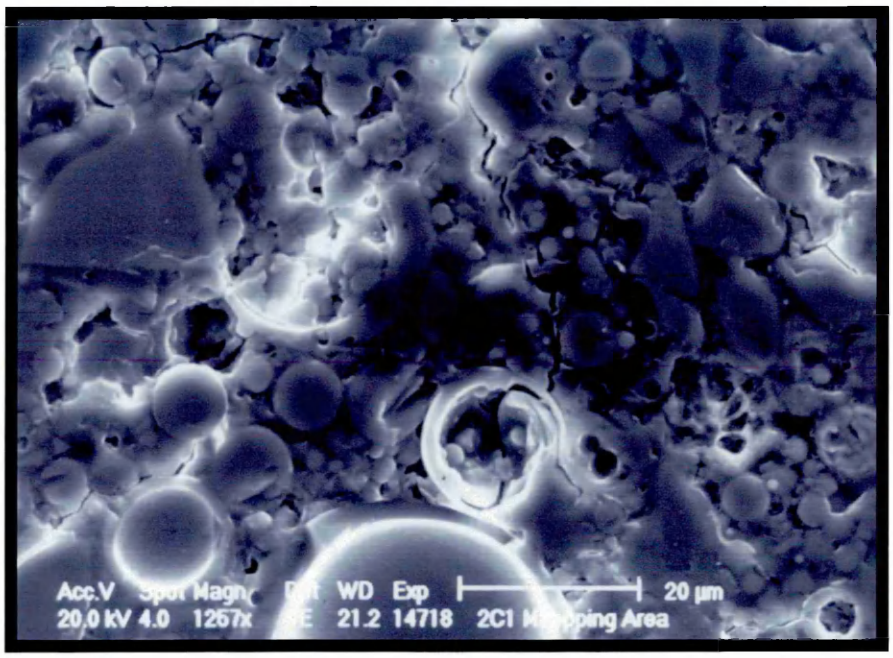

(a)

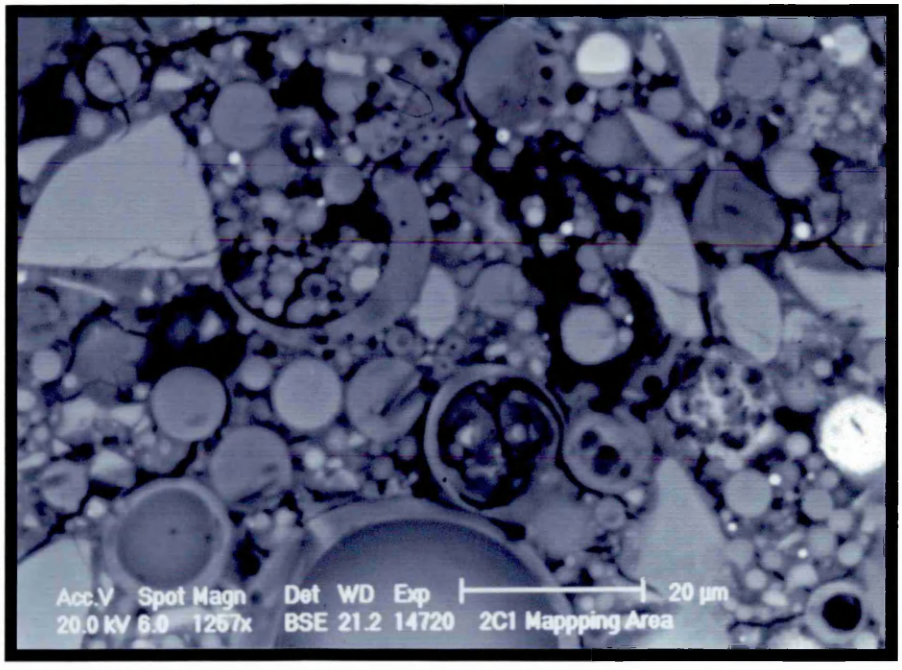

(b)

Figure 8.34 (a and b) Secondary electron image and backscattered image of alkali activated material with ggbs (group II - batch code SH).

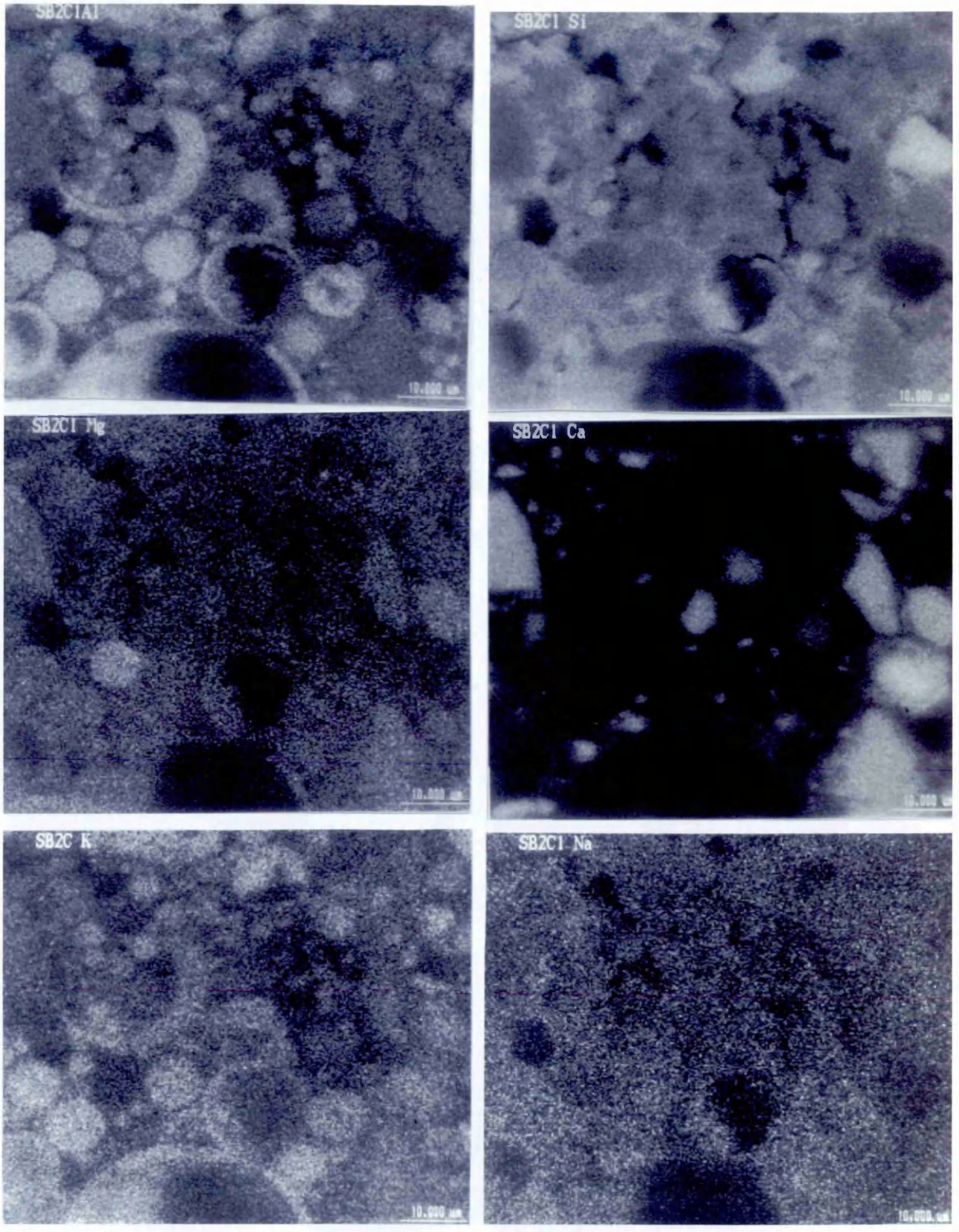

Figure 8.35 (a) Mapping of Al, Si, Mg, Ca, K and Na elements in the thermally cured alkali activated fly ash material with ggbs (group II - batch code SH).

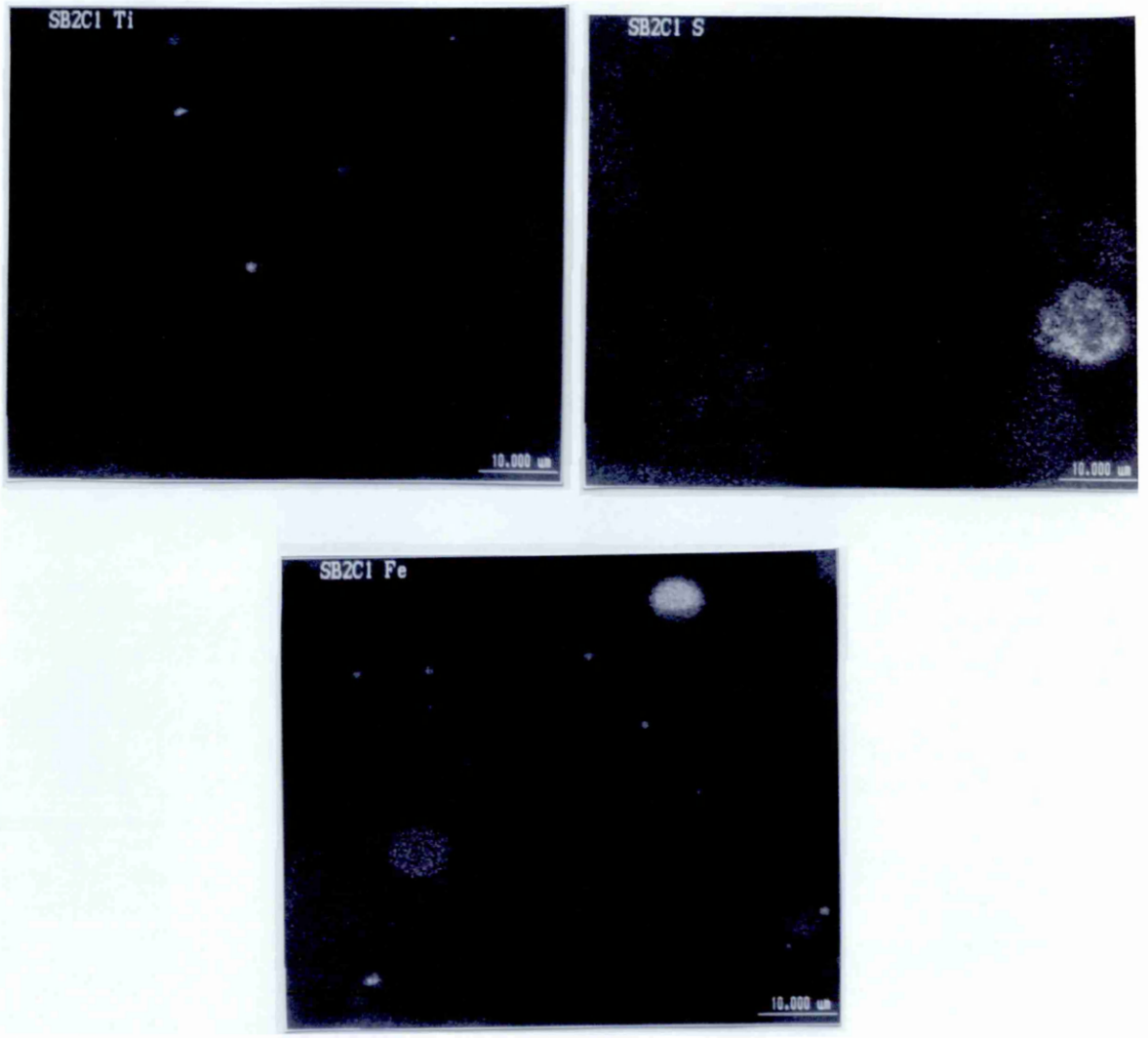

Figure 8.35 (b) Mapping of Ti, S and Fe elements in the thermally treated alkali activated fly ash material with ggbs (group II - batch code SH).

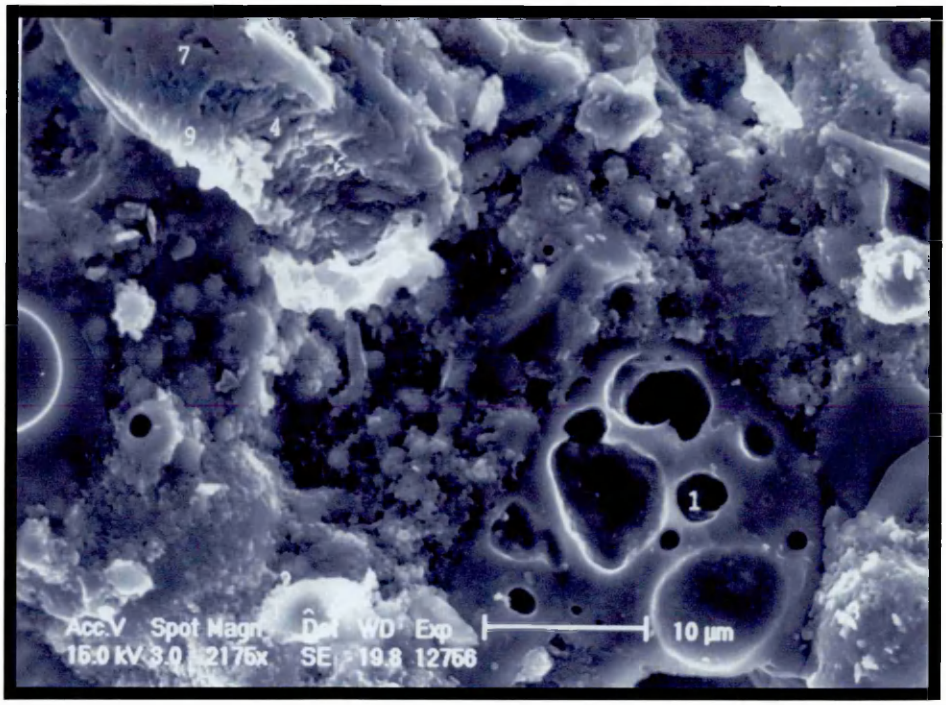

(a)

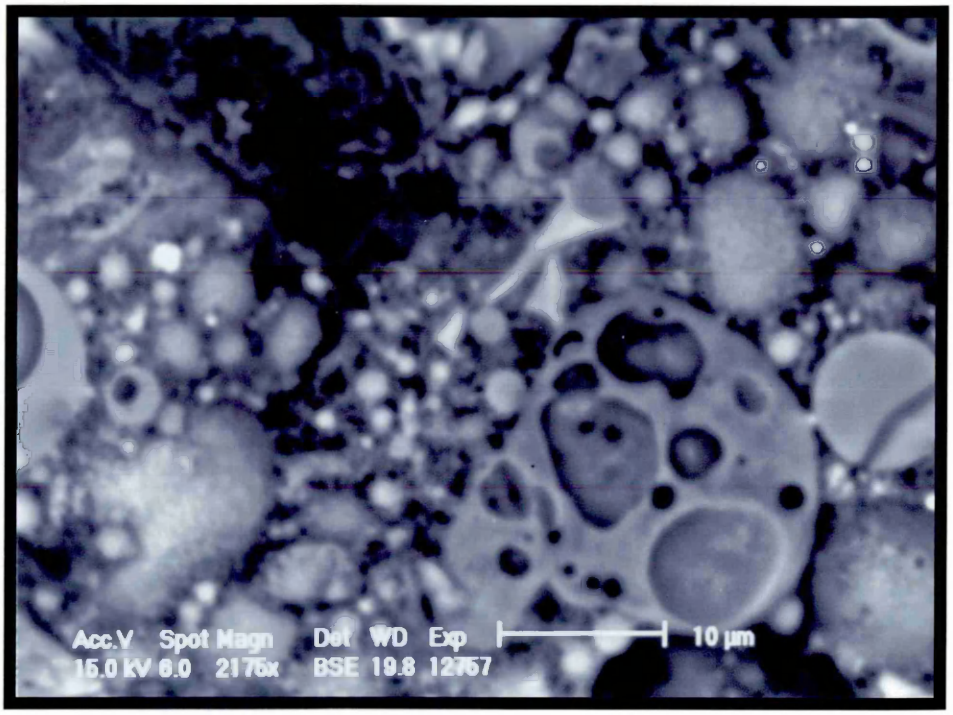

(b)

Figure 8.36 Secondary electron image and back scattered image of the fracture surface of alkali activated fly ash material with ggbs (group II - batch code SH)

8.5.2.4 Alkali activated fly ash material with microsilica,ggbs and hardener

8.5.2.4.1 Material cured under 20°C and 65%RH (batch code IISAB3)

Material IISAB3 has the same proportion of fly ash, ggbs, and microsilica and was cured in the same conditions as the material IISA except that it also contains a water glass hardener. A comparison of materials IISAB3 and IISA is intended to determine the effect of a water glass hardener on the structure of the material. There were no significant differences between modulus of rupture of these materials. Figure 8.37 shows the pore distribution of material IISAB3. Table 8.27 presents a summary of the results from the feature analysis. The pore area of material IISAB3 is slightly lower than for IISA at 5.11%.

The back scattered electron image and secondary electron image of material IISAB3 (see Figure 8.38 a and b) shows a considerable number of similarities to IISA. Figures 8.39 (a and b) present the digital mapping micrographs of material IISAB3 showing the distribution of chemical elements within the structure. Table 8.28 details the results from the EDAX performed at the points shown in Figures 8.40 and 8.41. This is confirmed by the back scattered image for IISAB3 indicating that the two materials are chemically and structurally very similar. The major difference is the presence of phosphorous from the water glass hardener. However, the digital mapping images show the phosphate to be concentrated in discrete areas of the structure. This would suggest that the hardener has not been distributed fully through the matrix. It is likely, therefore, that the effect of the hardener may also only be found in discrete areas. The composition of the hydration products appear to have some similarities with material IISA. The EDAX analysis presented in Table 8.28 show material IISAB3 to have higher levels of sodium than material IISA. Spot analyses on the surface also show high levels of phosphorous contrary to the findings of the digital mapping.

The appearance of the fracture surface of batch IISAB3 (see Figure 8.40 - 8.42) also show some similarities with previously observed phenomenon. Slender fibrous like crystal growths can be seen extending from the surface of the matrix. The analysis

show these areas to be high in sodium and sulphur. These growths may possibly be crystals of ettringite or other sulphur containing alumino silicate hydration products. Figure 8.42 presents the secondary electron image of a fly ash cenosphere with the crystalline growth from the surface. This confirms that the fly ash has reacted and produced hydration products in form of needle like crystals.

Table 8.27 Summary of data from feature scan measurements for material IISAB3 (Pore area 5.1%)

Measurement	No. data	Mean	Median	Min	Max
No detected	7	280.7	276.9	253	314
Area/mm ^2	1965	0.0023	0.001	0.0005	0.0451
Feature breadth/mm	1965	0.0429	0.0341	0.0137	0.2463
Feature length/mm	1965	0.0725	0.0567	0.0308	0.5223
Field area/mm ^2	7	12.62	0	12.62	12.62
Field number	7	4	3.985	1	7
Mean Feret/mm	1965	0.0589	0.0443	0.027	0.3908

Table 8.28 Semi-quantitative chemical analysis of alkali activated material with ggbs and hardener cured under 20°C and 65% RH (batch code IISAB3)

Spot No.	Na	Mg	Al	Si	P	S	K	Ca	Fe	Na/Al	Si/Al	Ca/Al	K/Al	Ca/Si	Al/Ca	S/Ca
1	31.16	0.42	6.46	34.62	8.73	9.4	2.92	5.62	0.97	**4.82**	**5.36**	**0.16**	0.08	0.16	1.15	1.6726
2	5.56	0.66	5.43	59.88	10.43	10.3	3.66	3.37	0.72	**1.02**	**11.03**	**0.06**	0.06	0.06	1.61	3.0564
3	19.27	0.67	6.4	33.06	9.97	22.06	2.1	5	1.46	**3.01**	**5.17**	**0.15**	0.06	0.15	1.28	4.412
4	19.66	-0.11	1.27	16	8.62	51.26	0.8	2.22	0.29	15.48	12.60	0.14	0.05	0.14	0.57	23.09
5	14.11	0.01	6.19	47.72	5.78	16.52	1.83	6.79	1.05	**2.28**	**7.71**	**0.14**	0.04	0.14	0.91	2.433
6	8.63	0.15	7	63.79	8	8.58	1.33	2.29	0.23	**1.23**	**9.11**	**0.04**	0.02	0.04	3.06	3.7467
7	7.84	-0.12	7.62	64.51	7.78	5.23	2.57	4.38	0.19	**1.03**	**8.47**	**0.07**	0.04	0.07	1.74	1.1941
8	7.2	-0.05	8.21	63.75	8.74	6.75	1.74	2.72	0.93	**0.88**	**7.76**	**0.04**	0.03	0.04	3.02	2.4816
9	8.84	0.66	9.42	62.44	8.55	3.92	1.64	3.62	0.91	**0.94**	**6.63**	**0.06**	0.03	0.06	2.60	1.0829
Average	*13.586*	*0.254*	*6.444*	*49.530*	*8.511*	*14.891*	*2.066*	*4.001*	*0.750*	*2.108*	*7.686*	*0.621*	*0.321*	*0.081*	*1.611*	*3.722*

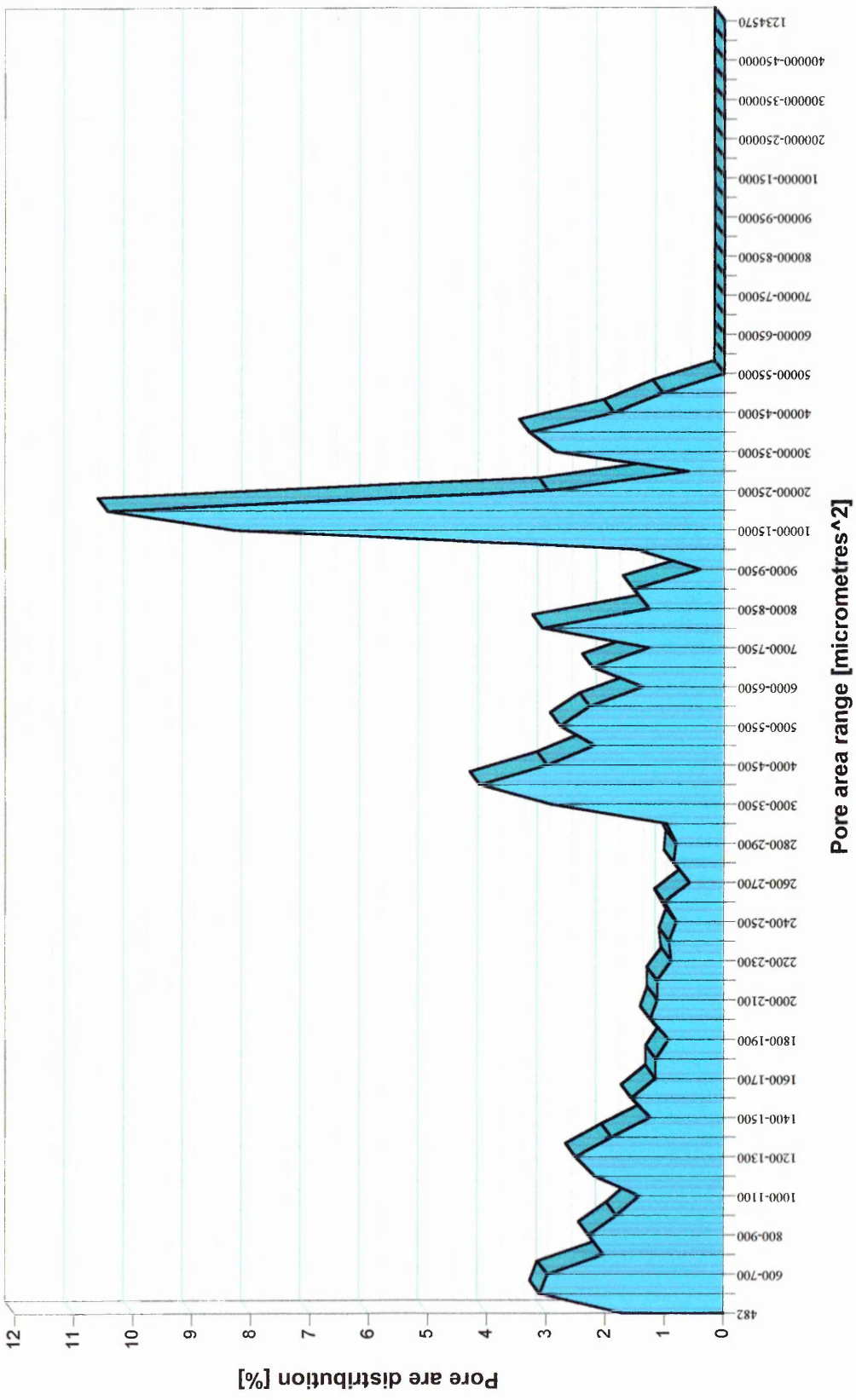

Figure 8.37 Pore area distribution for alkali activated fly ash material containing slag and KB#200 hardener (batch code IIA1B3)

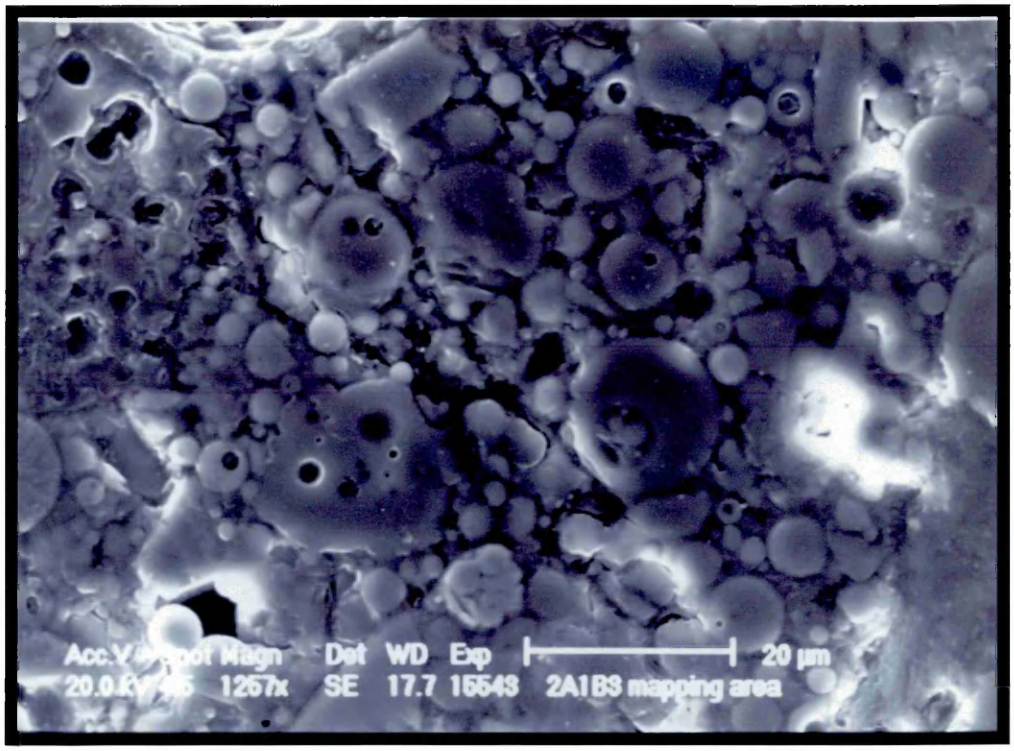

(a)

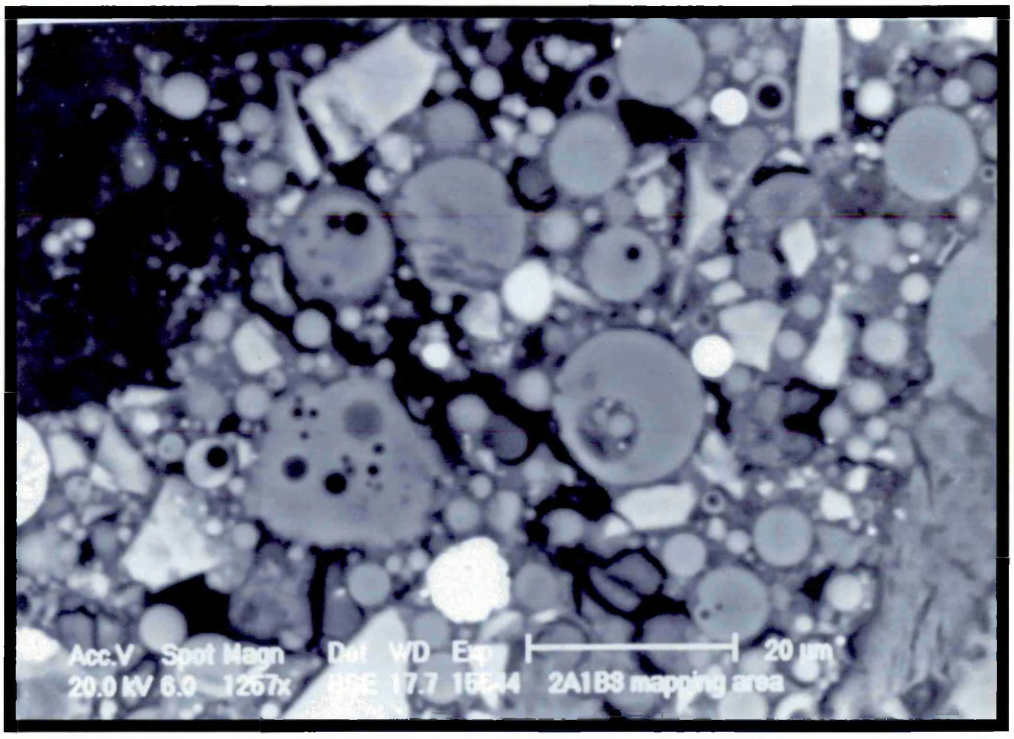

(b)

Figure 8.38 (a and b) Secondary electron image and back scattered image of alkali activated material with ggbs and hardener (group II - batch code SAB3)

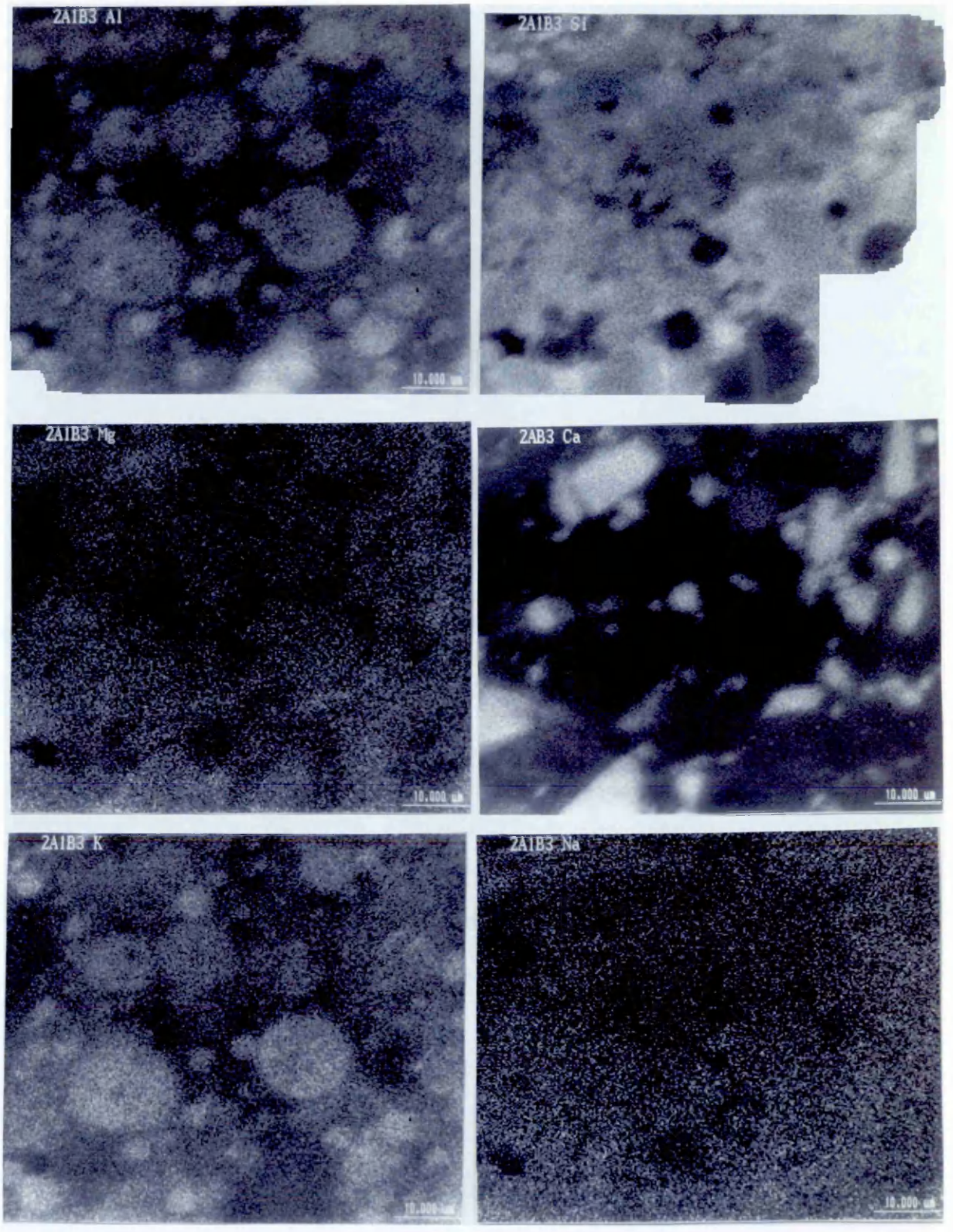

Figure 8.39 (a) Mapping of Al, Si, Mg, Ca, K, and Na elements in the alkali activated material with ggbs and hardener (group II – SAB3).

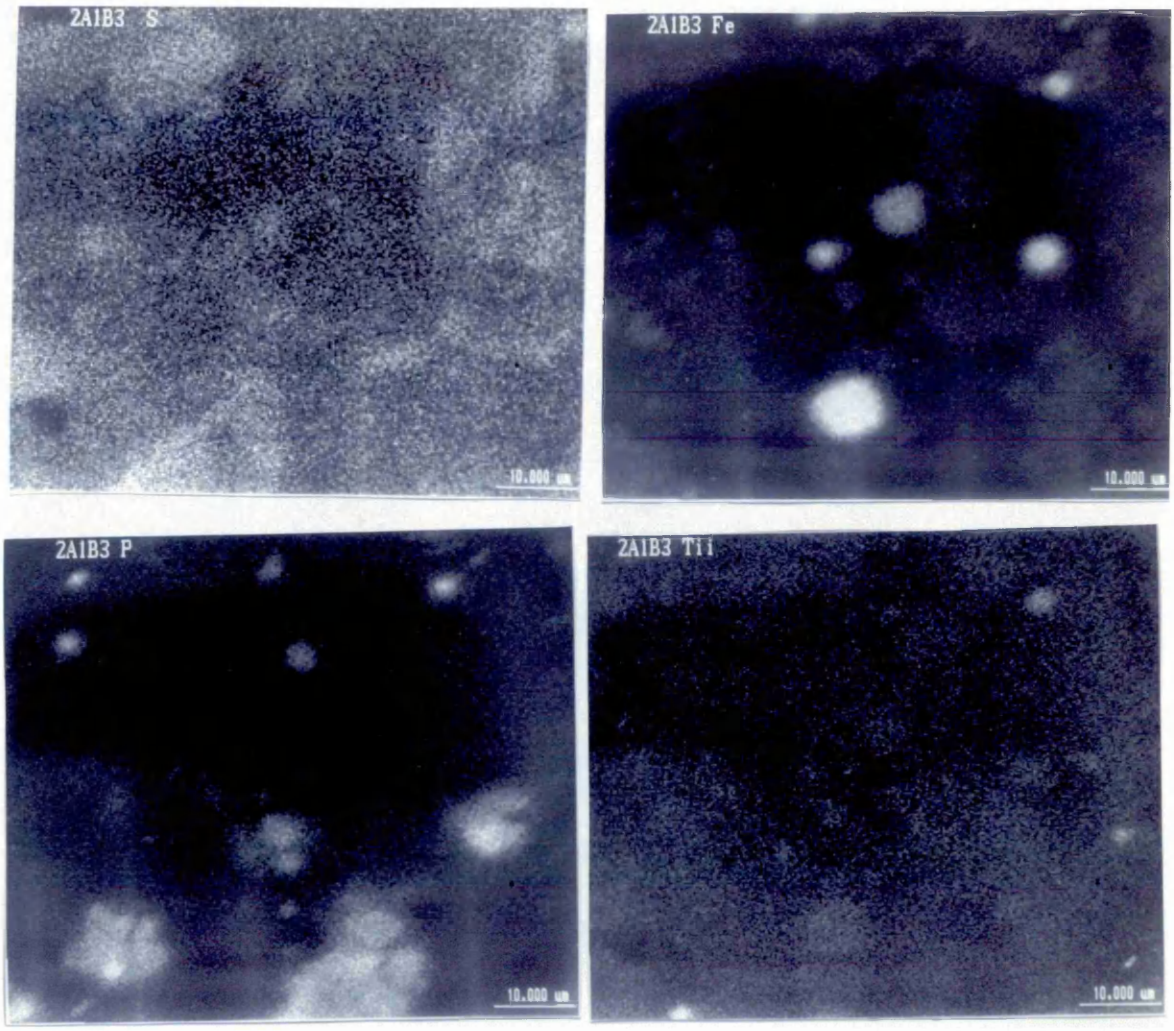

Figure 8.39 (b) Mapping of S, Fe, P and Ti elements in the alkali activated material with ggbs and hardener addition (group II - batch code SAB3)

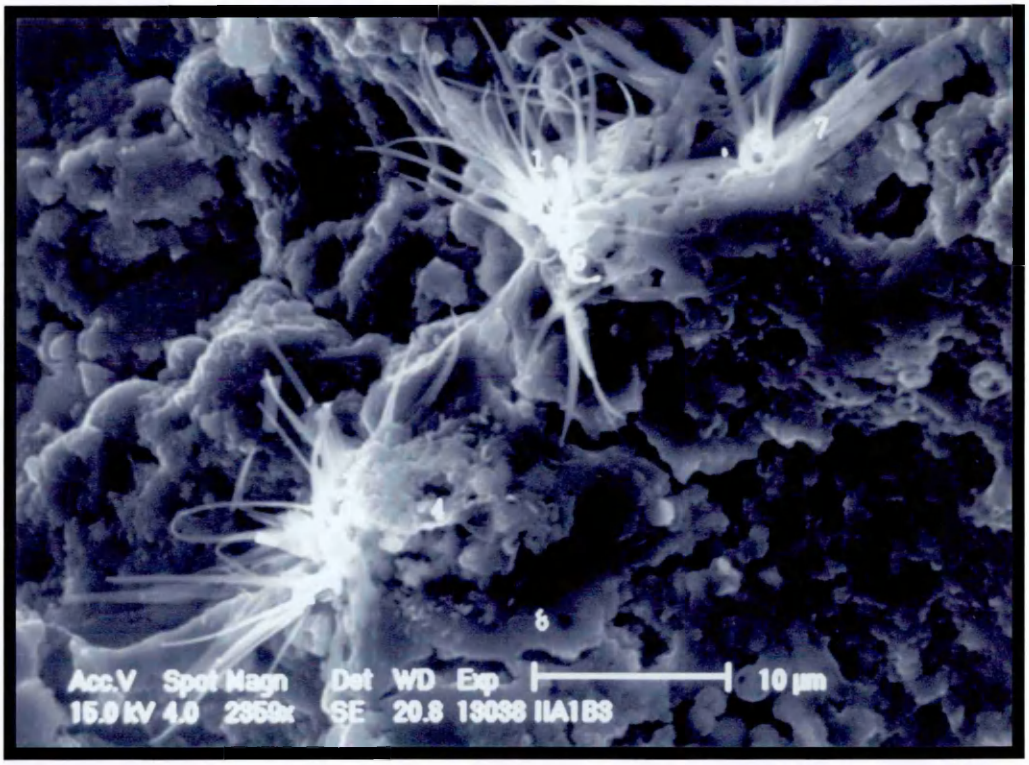

Figure 8.40 Secondary electron images of fracture surface of material with ggbs and hardener (group II - batch code SAB3).

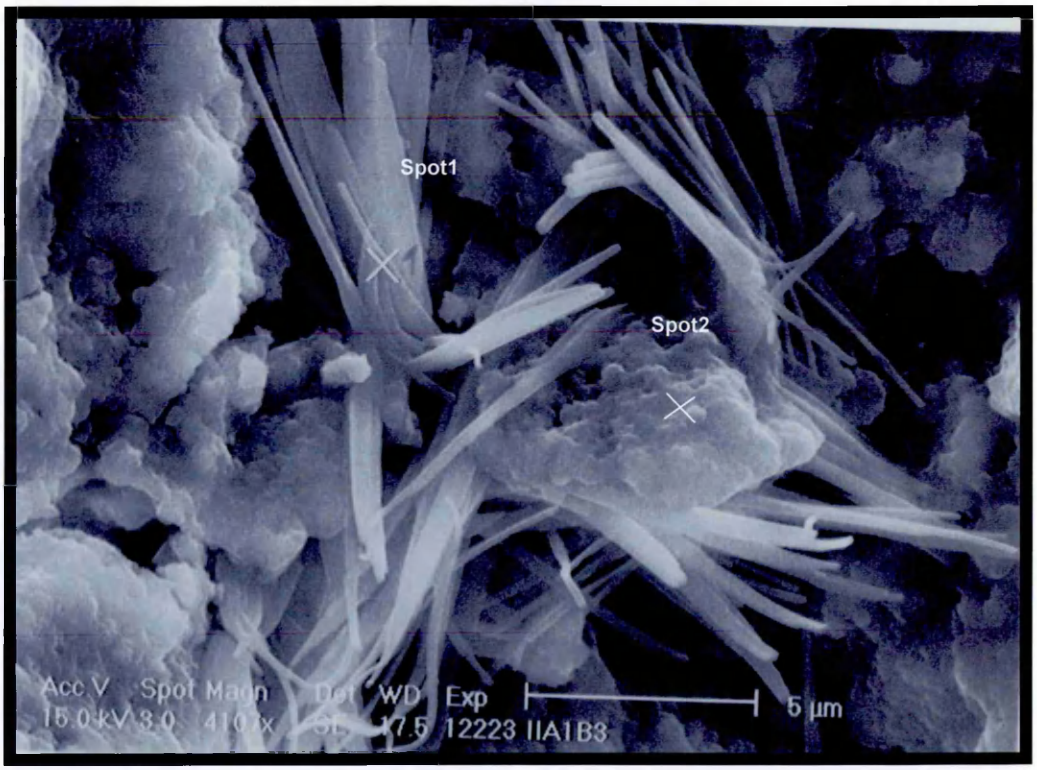

Figure 8.41 Secondary electron images of fracture surface of material with ggbs and hardener (group II - batch code SAB3)

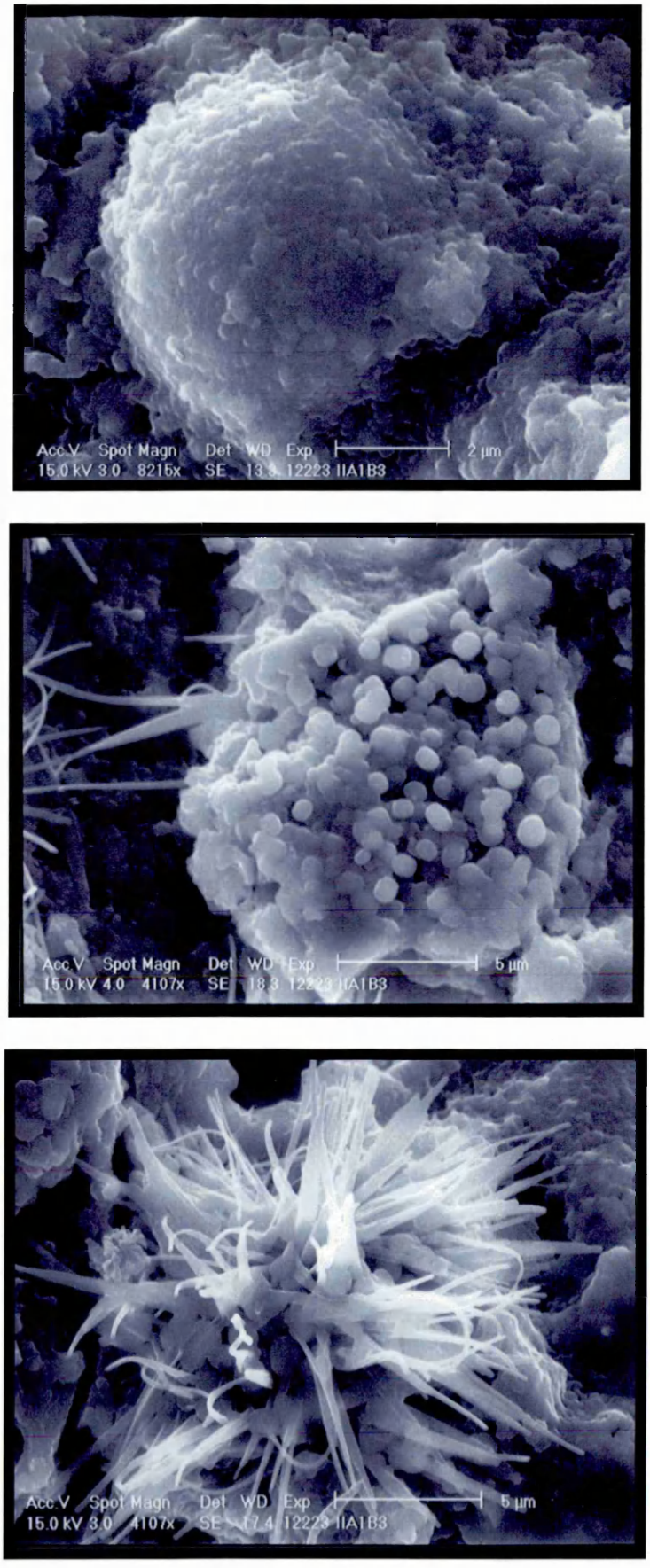

Figure 8.42 Scanning electron images of alkali activated material with ggbs and hardener (group II - batch code SAB3)

8.5.2.4.2 Thermally cured material (batch code IISHB3)

Material IISHB3 has the same proportion of fly ash, ggbs, and microsilica and was cured in the same conditions (thermal curing) as the material IISH except that it also contains a water glass hardener. There is no significant difference in the flexural strengths of the two materials (IISHB3 and IISH). The flexural strength for material batch code IISHB3 is 36.90 N/mm^2 compared with 38.84 $N/mm^2$for material batch code IISH. Table 8.29 shows a summary of the results from the feature analysis of material IISHB3. The pore area of material IISHB3 is much higher 8.1% compared with 4.8% for the corresponding material IISH and a comparison of Figures 8.33 and 8.43 shows that the pore area distribution is different.

Table 8.30 details the results from the EDAX performed at the points shown in Figure 8.44. These show an increase in the proportion of aluminium and sodium in the hydration products when compared with corresponding material batch code IISAB3.

Table 8.29 Summary of data from feature scan measurements for material IISHB3 (Pore area 8.1%)

Measurement	No. data	Mean	Median	Min	Max
No detected	5	162.6	168.1	109	217
Area/mm ^2	813	0.0045	0.003	0.0005	0.989
Feature breadth/mm	813	0.0503	0.0352	0.0137	0.9653
Feature length/mm	813	0.0763	0.0596	0.0308	2.33
Field area/mm ^2	5	12.62	0	12.62	12.62
Field number	5	3	2.99	1	5
Mean Feret/mm	813	0.0641	0.0494	0.0273	1.799

Table 8.30 Semi-quantitative chemical analysis of thermally cured alkali activated material with ggbs and hardener (batch code IISHB3)

Spot No.	Na	Mg	Al	Si	S	K	Ca	Fe	Na/Al	Si/Al	Ca/Al	K/Al	Ca/Si	Al/Ca	S/Ca
1	0.92	0.16	1.4	96.3	0.13	0.36	0.51	0.22	0.66	68.79	0.36	0.26	0.01	2.75	0.2549
2	1.75	1.2	15.64	66.51	2.57	2.62	3.68	6.03	0.11	4.25	0.24	0.17	0.06	4.25	0.6984
3	1.11	0.94	23.54	65.06	0	5.33	2.65	1.37	0.05	2.76	0.11	0.23	0.04	8.88	0
4	1.23	1.34	26.78	58.56	-0.07	4.05	3.83	2.27	0.05	2.19	0.14	0.15	0.07	6.99	-0.018
5	5.12	1.18	23.05	54.98	0.81	1.47	12.58	0.81	0.22	2.39	0.55	0.06	0.23	1.83	0.0644
6	2.15	1.37	5.07	86.08	0.27	1.67	2.59	0.8	0.42	16.98	0.51	0.33	0.03	1.96	0.1042
Average	*2.047*	*1.032*	*15.913*	*71.248*	*0.618*	*2.583*	*4.307*	*1.917*	*0.13*	*4.48*	*0.27*	*0.16*	*0.06*	*3.70*	*0.1436*

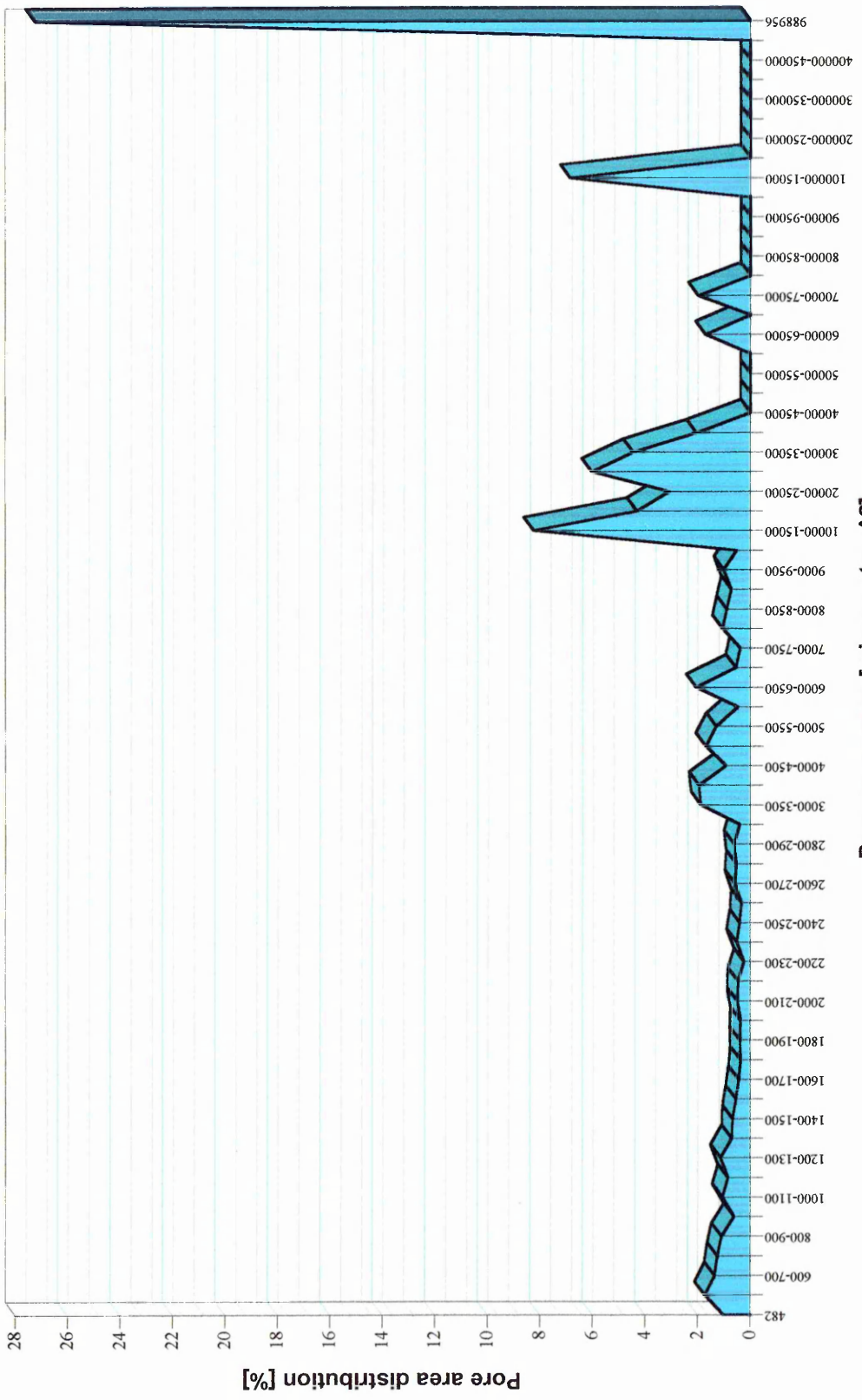

Figure 8.43 Pore area distribution of thermally cured alkali activated fly ash material containing slag and KB#200 hardener (batch code IIH1B3)

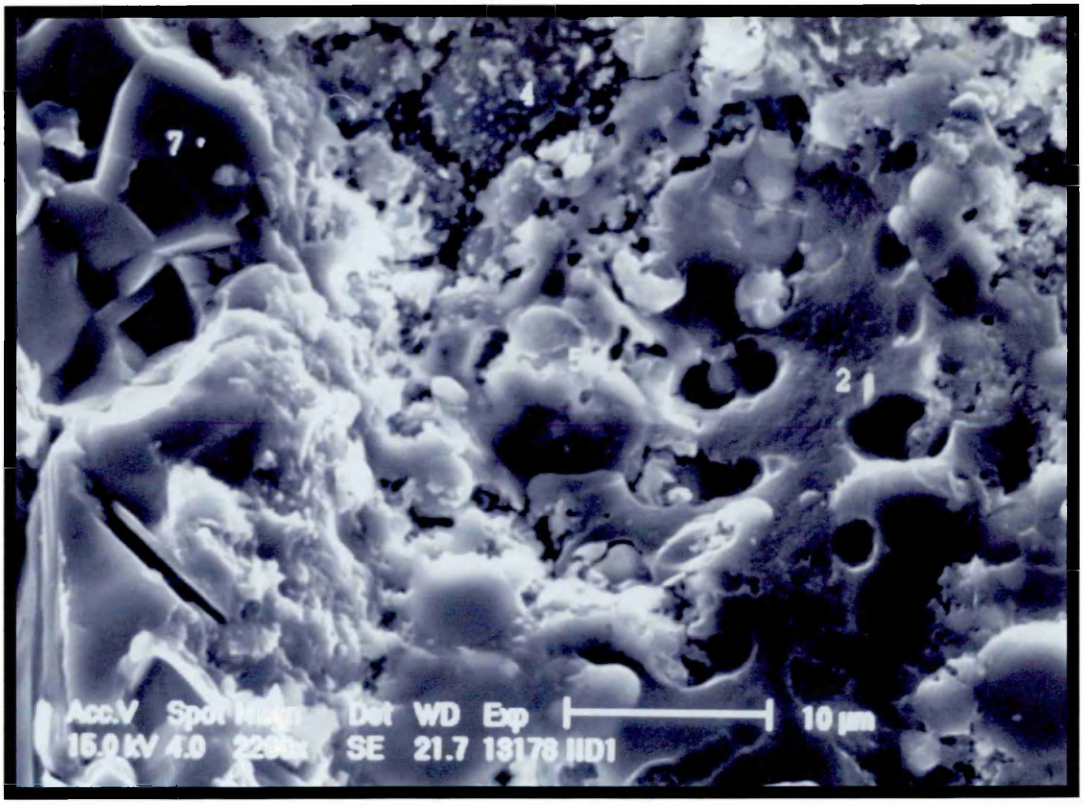

Figure 8.44 Microstructure of thermally cured material with ggbs and hardener (group II batch code SHB3).

8.5.2.5 Alkali activated materials with water glass of silica modulus of 0.9 and 1.5

Materials WG09 and WG15 contain 20% fly ash, 5% microsilica, 10% slag and 11% water glass the remaining 54% being sand (see section 8.3.3.5). Batch WG 09 and 15 are intended to investigate the effect of the silica modulus of the water glass. The silica modulus is the ratio of SiO_2 to Na_2O content of the water glass. Therefore, a water glass with a lower silica modulus will have a greater Na_2O content when compared to one with a higher modulus. As the composition of materials WG09 and WG11 is the same except for the water glass modulus, it can be expected that a mix containing a lower silica modulus water glass will have a lower calcium to silica ratio. A high silica to calcium ratio has been shown by other researchers[50, 53, 68] to form calcium silicate hydrate (CSH) hydration product. This suggests that the higher the silica modulus, the greater the chance of CSH formation.

Tables 8.31 and 8.32 present a summary of the results from the feature analysis of materials WG09 and WG15. Material WG09 has a total pore area of 4.0% comparable with 5.7% for material WG 15. Figures 8.45 and 8.46 show the pore distribution of these materials. These indicate that the largest pore area was for pore sizes between 20000 and 25000 microns^2 in both cases.

The secondary electron image and backscatter electron image for specimen WG09 are given in Figure 8.47. Material batch code WG 15 (Figure 8.48) shows very similar results to material batch code WG 0.9. Table 8.33 details the results from the EDAX performed at the points shown in Figure 8.49 for material WG 09 . Fly ash particles can be seen embedded in the matrix together with more irregular shaped particles. The digital mapping results show high silicon content with some aluminium. In addition there is also sodium, potassium, magnesium and sulphur present. There is also a high calcium content in the matrix. Much of the calcium appears to be associated with particles in the matrix, however there is also calcium in the hydration products unlike other materials examined previously in this section.
Table 8.33 details the results from the EDAX performed at the points shown in Figure 8.50 (a and b) for material WG15. However, in Table 8.35 the average levels

of sodium appear to be higher in sample WG 09 compared to WG 11 and the calcium levels are lower.

The differences are small and it does not provide conclusive evidence of CSH formation in either material. The reason for the higher Ca content of these materials is that they were produced using a slag with a higher calcium content. The apparent presence of calcium in the matrix could also be linked to the higher slag content in these two batches of samples as the slag content provides the much of the calcium found in the materials. This would appear to confirm that the calcium to silica ratio is important in predicting the formation of CSH.

The presence of sodium and aluminium still suggests that the hydration products consist of an aluminium silicate with sodium as opposed to calcium. The presence of sulphur also suggests the formation of an ettringite or other sulphur containing alumino silicate type phase.

Table 8.31 Summary of data from feature scan measurements for material batch code WG09 (Pore area 4.0%)

Measurement	No. data	Mean	Median	Min	Max
No detected	7	157	167.1	116	183
Area/mm ^2	1099	0.0033	0.0008	0.005	0.1243
Feature breadth/mm	1099	0.0461	0.0346	0.0137	0.3426
Feature length/mm	1099	0.077	0.53	0.0308	1.016
Field area/mm ^2	7	12.62	0	12.62	12.62
Field number	7	4	3.985	1	7
Mean Feret/mm	1099	0.0629	0.0424	0.0271	0.7108

Table 8.32 Summary of data from feature scan measurements for material batch code WG11 (Pore area 5.7%)

Measurement	No. data	Mean	Median	Min	Max
No detected	8	216.6	221	153	275
Area/mm ^2	1733	0.0033	0.0009	0.005	0.1839
Feature breadth/mm	1733	0.0454	0.0343	0.0137	0.4052
Feature length/mm	1733	0.0798	0.515	0.0308	1.212
Field area/mm ^2	8	12.62	0	12.62	12.62
Field number	8	4.5	4.5	1	8
Mean Feret/mm	1733	0.0643	0.0455	0.027	0.8495

Table 8.33 Semi-quantitative chemical analysis of thermally cured alkali activated materials with a water glass of silica modulus of 0.9 and 1.5 (batch code WG09 and 11)

WG 09 Spot No.	**Na**	**Mg**	**Al**	**Si**	**S**	**K**	**Ca**	**Fe**	**Na/Al**	**Si/Al**	**Ca/Al**	**K/Al**	**Ca/Si**	**Al/Ca**	**S/Ca**
1	68.54	0.68	2.02	16.06	4.46	3.19	4.29	0.77	33.93	7.95	2.12	1.58	0.27	0.47	1.04
2	0.58	0.02	-0.05	98.89	0.06	0.06	0.36	0.08	-11.60	-1978	-7.20	-1.20	0.00	-0.14	0.17
3	0.36	3.76	6.59	35.69	1.78	0.94	50.61	0.27	0.05	5.42	7.68	0.14	**1.42**	**0.13**	0.04
4	4.53	0.2	34.9	52.86	1.25	3.39	2.08	0.79	0.13	1.51	0.06	0.10	0.04	16.78	0.60
Average	*24.477*	*1.547*	*14.503*	*34.870*	*2.497*	*2.507*	*18.993*	*0.610*	*1.69*	*2.40*	*1.31*	*0.17*	*0.54*	*0.76*	*0.1314*
WG 15 Spot No.	**Na**	**Mg**	**Al**	**Si**	**S**	**K**	**Ca**	**Fe**	**Na/Al**	**Si/Al**	**Ca/Al**	**K/Al**	**Ca/Si**	**Al/Ca**	**S/Ca**
1	1.2	0.69	23.66	63.27	0.55	9.91	0.11	0.61	0.05	2.67	0.00	0.42	0.00	215.09	5.00
2	0.08	-0.03	0.05	99.16	0.02	0.37	0.27	0.08	1.60	1983	5.40	7.40	0.00	0.19	0.07
3	0.33	3.68	7.51	30.41	2.15	0.64	55.27	0.01	0.04	4.05	7.36	0.09	**1.82**	**0.14**	0.04
4	1.85	3.81	4.3	63.94	0.87	0.92	23.93	0.38	0.43	14.87	5.57	0.21	0.37	0.18	0.04
5	2.85	1.84	22.59	57.29	0.76	3.45	8.01	3.21	0.13	2.54	0.35	0.15	0.14	2.82	0.09
6	1.6	1.45	4.53	79.13	1.18	1.01	10.83	0.27	0.35	17.47	2.39	0.22	0.14	0.42	0.11
7	1.58	0.98	39.22	50.44	0.12	5.72	0.19	1.75	0.04	1.29	0.00	0.15	0.00	206.42	0.63
Average	*1.568*	*2.075*	*16.968*	*57.413*	*0.938*	*3.608*	*16.390*	*1.038*	*0.09*	*3.38*	*0.97*	*0.21*	*0.29*	*1.04*	*0.0573*

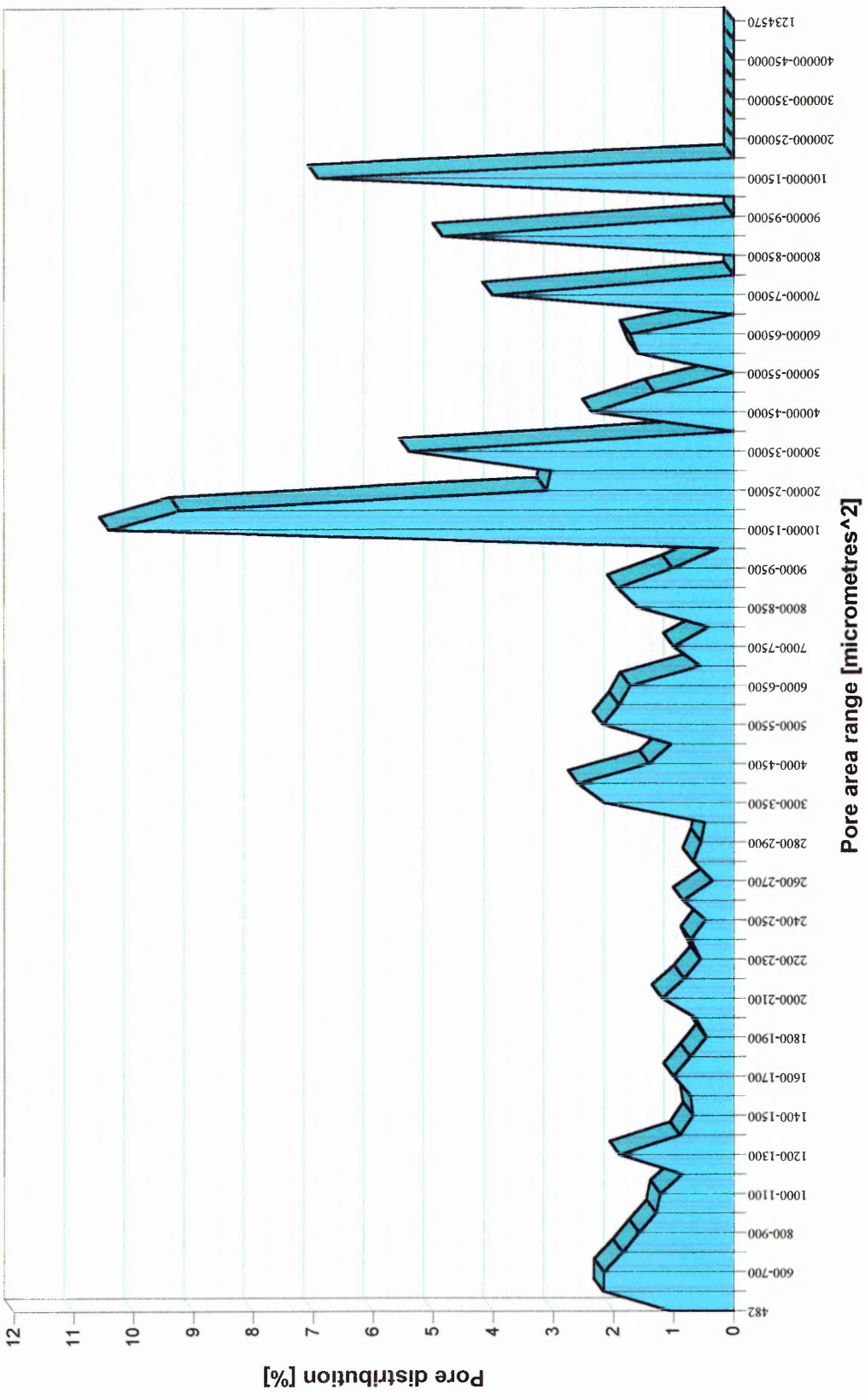

Figure 8.45 Pore area distribution of material activated by water glass with silica modulus 0.9 (batch code wg0.9)

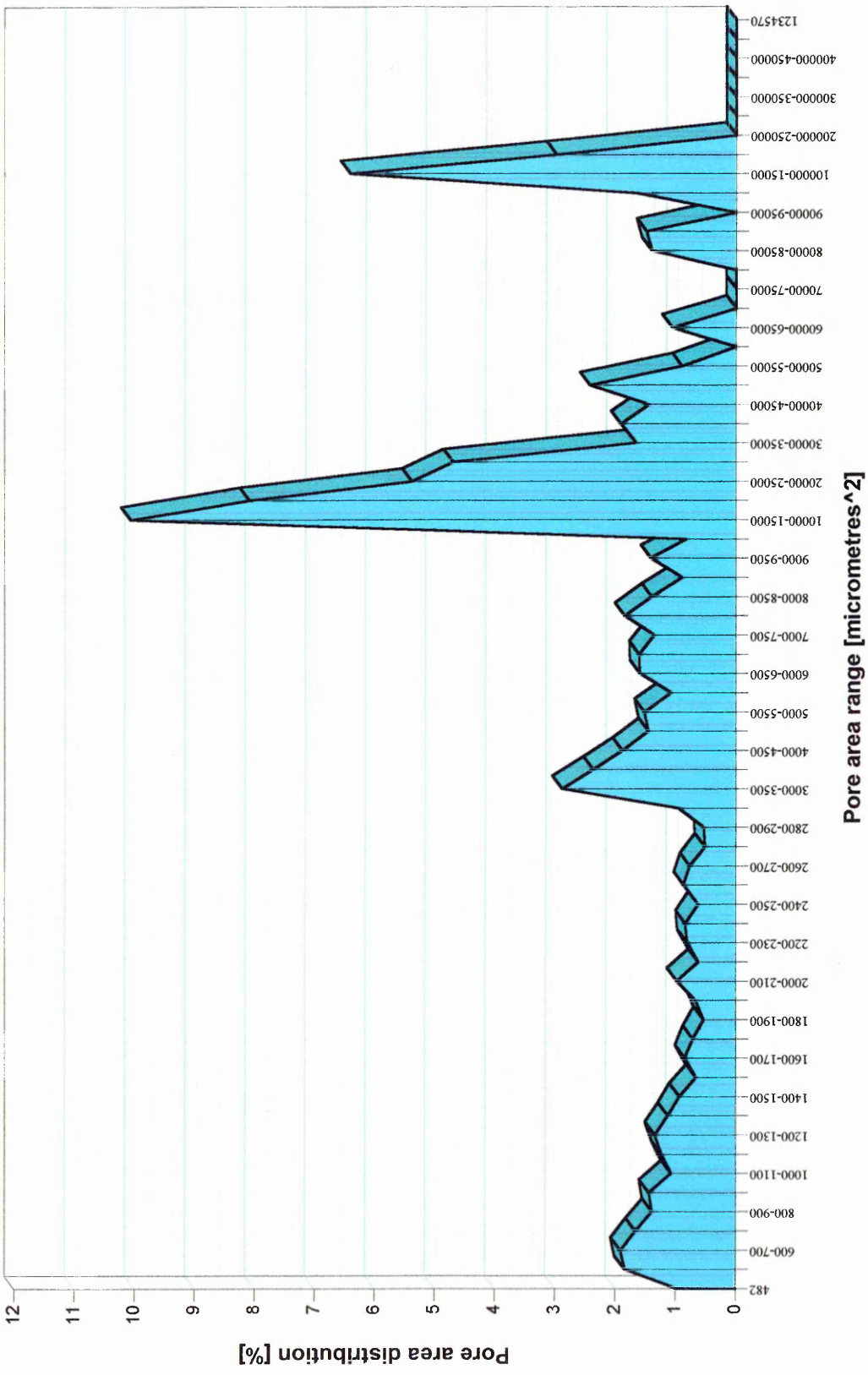

Figure 8.46 Pore area distribution of material activated by water glass with silica modulus 1.5 (batch code wg1.5)

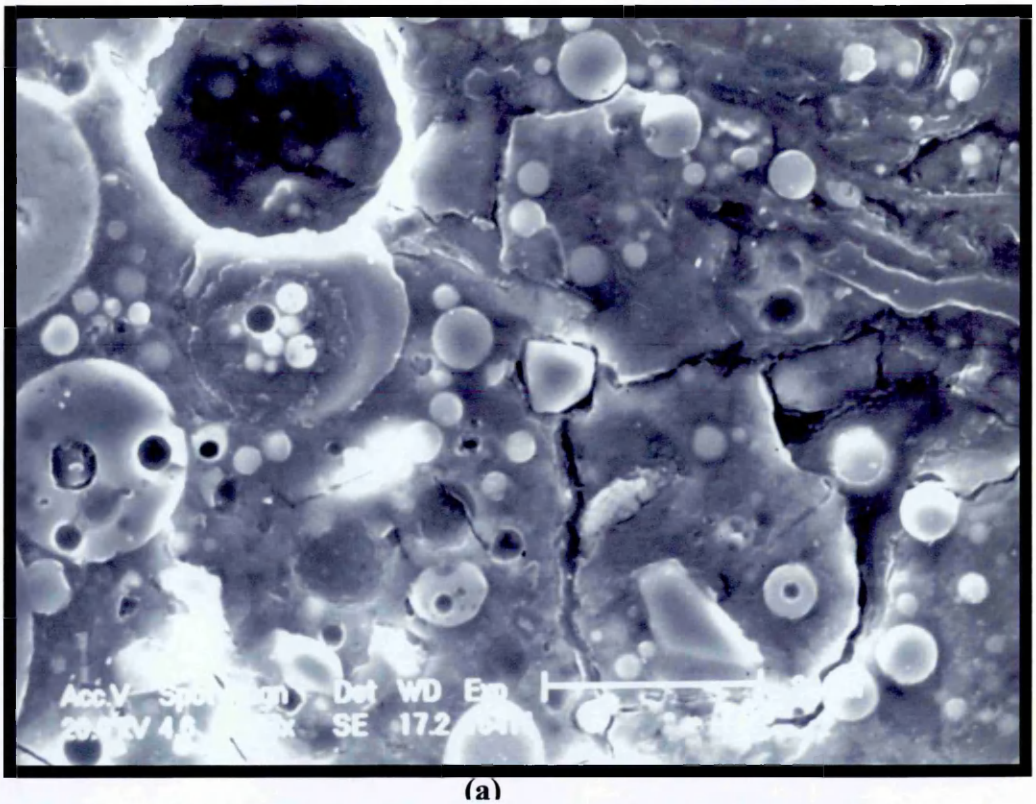

(a)

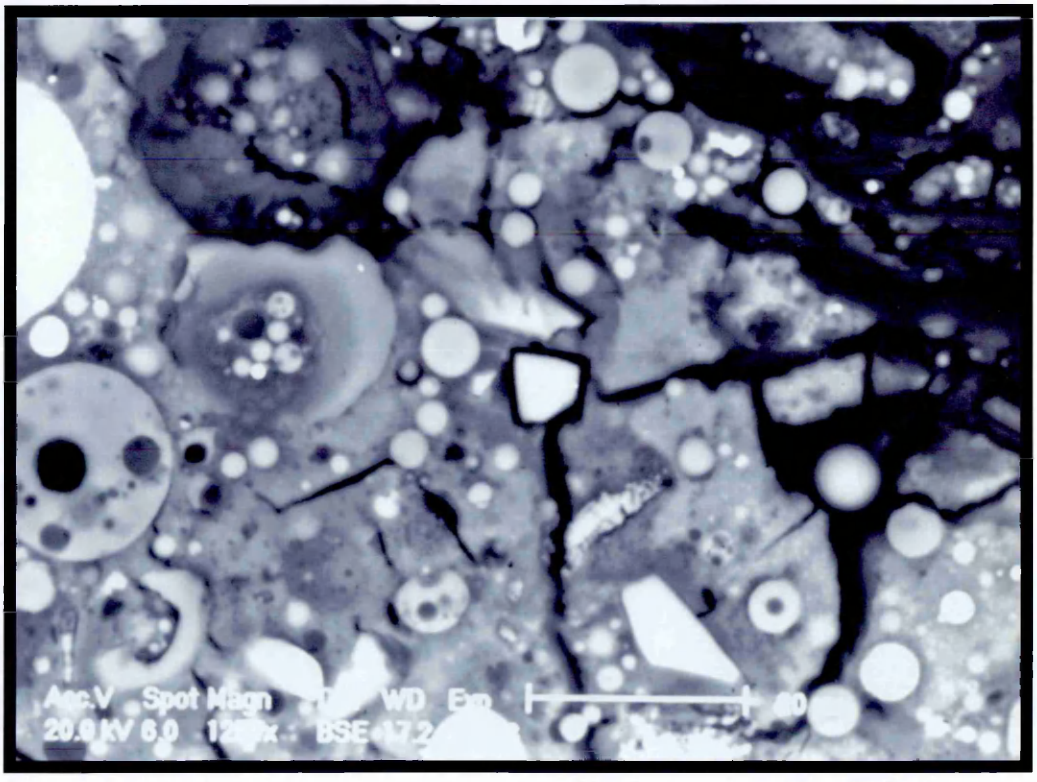

(b)

Figure 8.47 Secondary electron image and back scattered image of alkali activated material with a water glass of n=0.9 (batch code WG0.9)

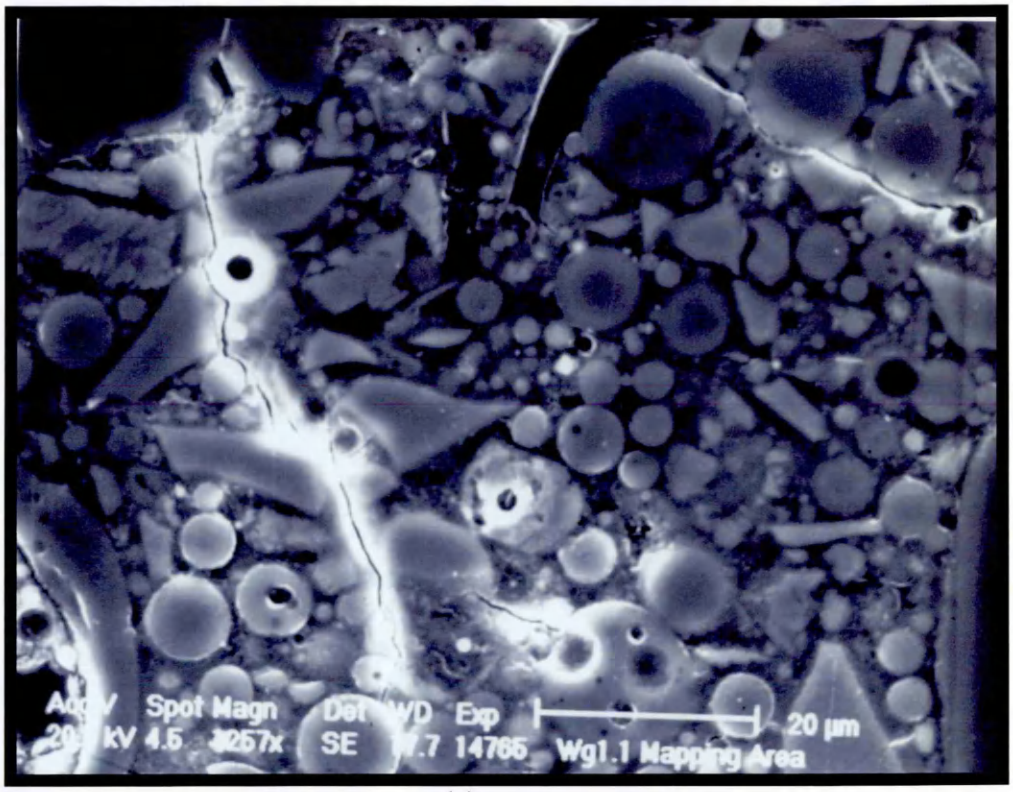

(a)

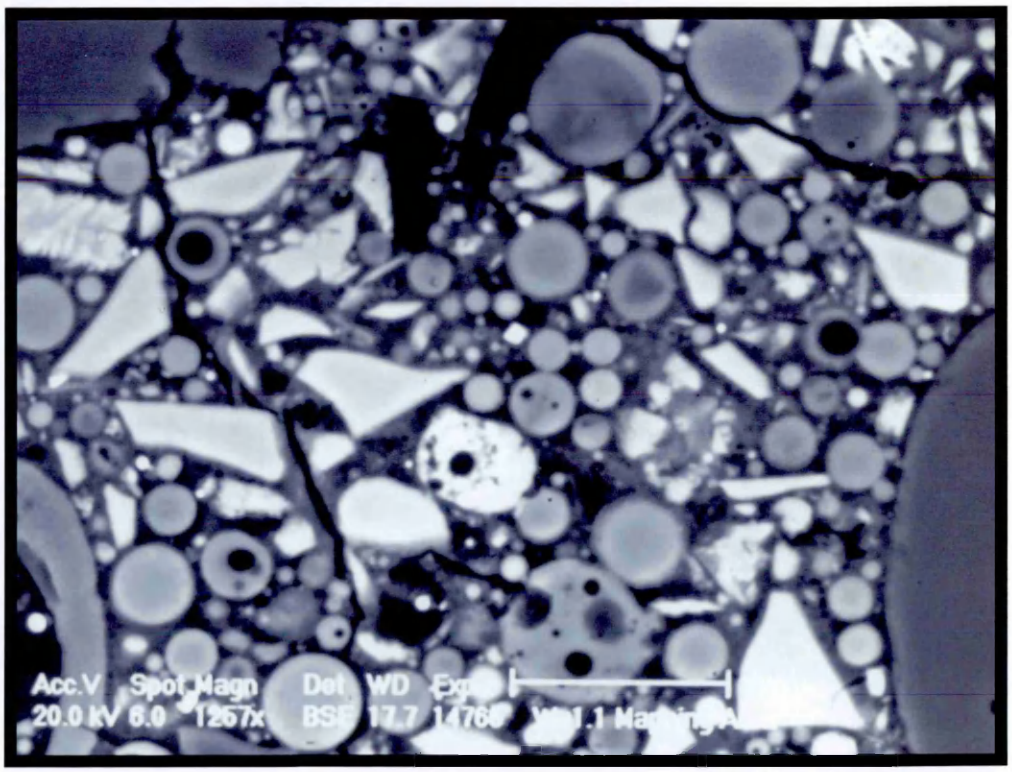

(b)

Figure 8.48 Secondary electron image and backscatter image of alkali activated material with a water glass of n=1.5 (batch code WG1.5)

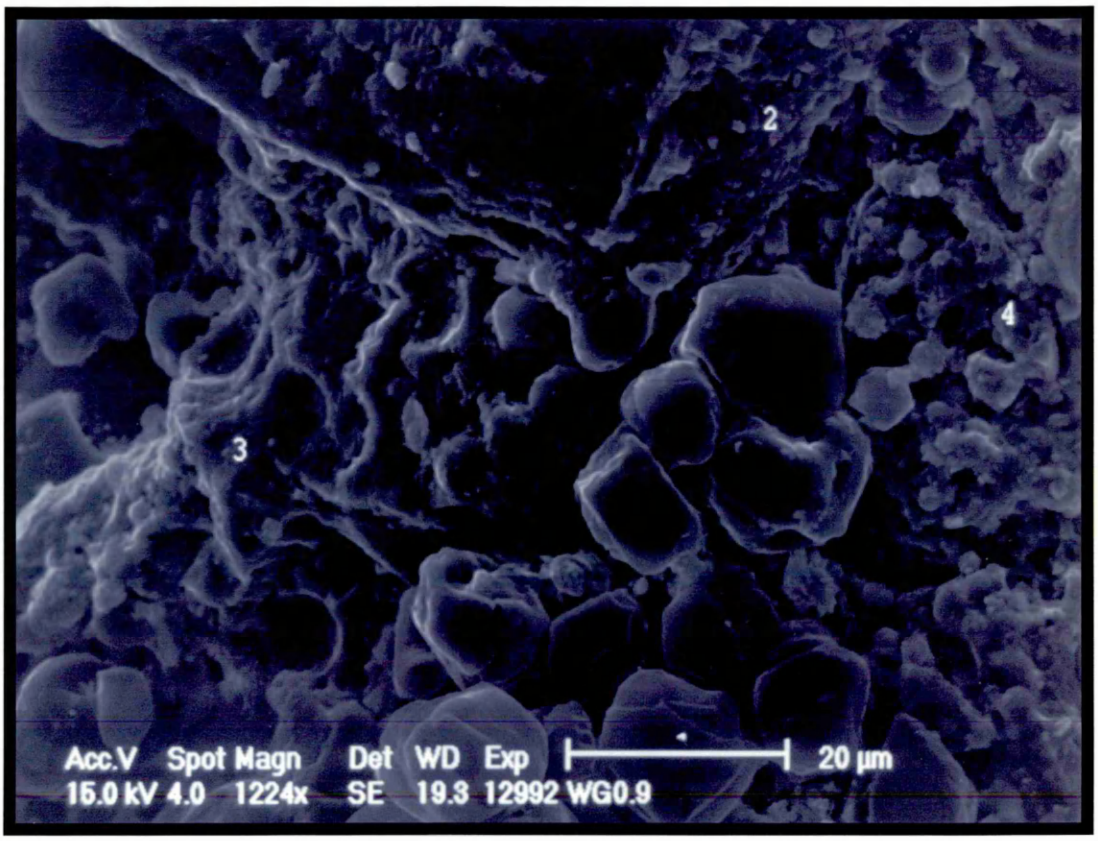

Figure 8.49 Secondary electron image of fracture surface of material (batch code WG0.9)

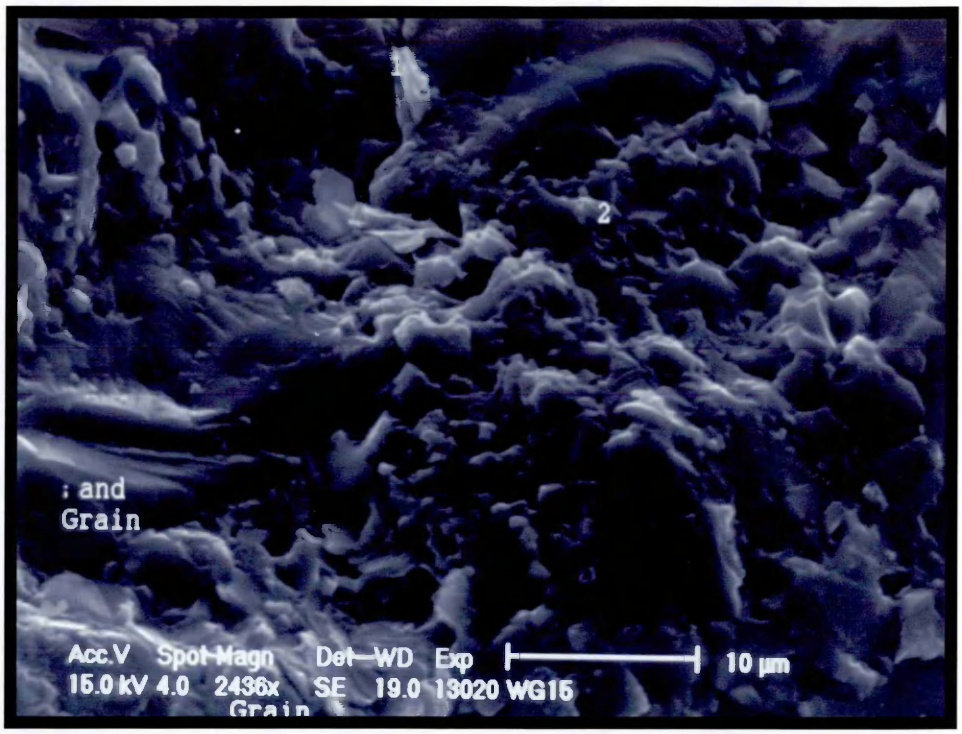

(a)

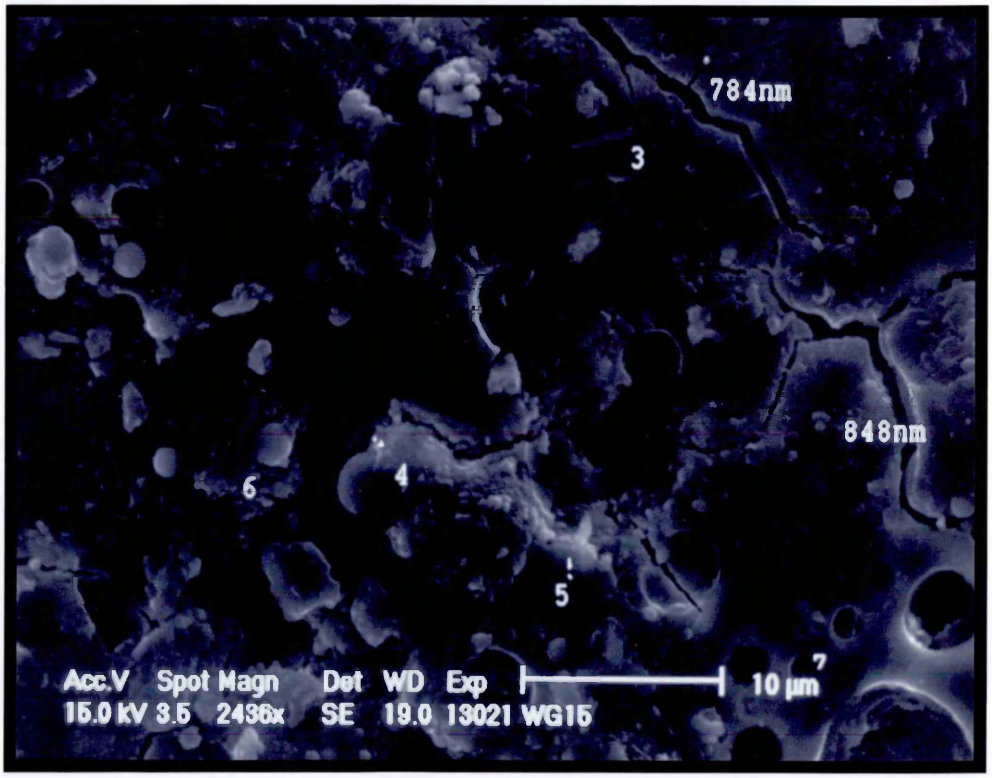

(b)

Figure 8.50 Secondary electron image of fracture surface of material (batch code WG1.5)

8.6 X-RAY DIFFRACTION CHARACTERISATION OF ALKALI ACTIVATED MATERIALS

8.6.1 Constituent materials

8.6.1.1 Pulverised fuel ash (pfa)

In this study only low-calcium UK fly ashes have been used. These fly ashes due to the high proportion of silica and aluminium, consist principally of aluminosilicate glass[1]. Figure 8.52 shows the powder diffraction pattern for the unhydrated fly ash from Ratcliffe. The dominant feature is the broad amorphous hump at a $2\theta \sim 25$.

In energetical fly ashes investigated the main component is being created by the amorphous - glassy phase which is expressed always by the lifting the background of the record curve. There are newly formed high-temperature phases of the iron oxide and silicates type. Table 8.34 shows the X-ray analysis results for the fly ash from Ratcliffe. The most intense peak at 3.392Å, along with peaks at 5.390Å, 3.425 Å, 2.542Å and 2.206Å can be attributed to mullite ($Al_6Si_2O_{13}$), a phase commonly found in pulverised fuel ash. Mullite peaks remain in the data for hydrated fly ash indicating that the crystalline phase in the unhydrated fly ash does not take part in the reactions. Diffraction lines of both rhombic Al-silicates silimanite and mullite are being overlapping, so it is difficult to distinguish between them. The silimanite is one of 3 modifications of Al_2SiO_5, stable from temperatures of 800 °C, with double co-ordinations of aluminium in the structure Al^{IV} and Al^{VI} against SiO_4/O tetrahedrons. It is formed probably at the combustion of clayey minerals of kaolinite ($2SiO_2.Al_2O_3+4OH$) halloysite, montmorillonite, - minerals creating components of claystone layers in coal. Silimanite changes at the temperature of 1550°C into mullite, so the presence of each phase can be determine from the data of temperature at the combustion. The peaks at 2.694Å, 2.518Å and 1.6943Å can be attributed to hematite (Fe_2O_3).

According to Mehta [4], Hubbart et al examined fly ashes from 26 UK sources. They were all found to be low in calcium oxide (CaO) and all contained mullite (9-43%), quartz (1-9%), hematite (3-11%), magnetite (2-9%), unburnt carbon (1-12%) and concentration of amorphous silicates ranging from 29-74%.

Table 8.34 X-ray analysis results for fly ash from Ratcliffe power plant

measured values			Reference Patterns									
			Mullite		Quartz		Aluminium		Corundum		Hematite	
Angle [°2θ]	d_m [Å]	I_m [%]	d_z [Å]	I_t [%]	d_z [Å]	I_t [%]	d_z [Å]	I_t [%]	d_z [Å]	I_t [%]	d_z [Å]	I_t [%]
16.30	5.430	3.4										
16.410	5.397	45.7	5.390	50								
20.850	4.257	31.7			4.257	22						
21.87	4.061	12.4										
25.530	3.486	26.4							3.480	70		
25.995	3.425	53.6	3.428	95								
26.250	3.392	38.4	3.390	100								
26.580	3.349	100			3.342	100						
27.010	3.298	20.3										
33.190	2.694	16.1									2.700	100
35.22	2.546	3.1							2.551	97		
33.295	2.541	5.7	2.542	50								
35.570	2.522	18.5										
35.63	2.518	12.9									2.519	70
35.77	2.508	7.9										
38.465	2.339	90.4					2.338	100				
40.835	2.208	16.7	2.206	60								
42.545	2.123	12.9							2.085	100		
44.685	2.026	49.6					2.024	47				
50.095	1.8195	13.9			1.8179	14						
54.085	1.6943	12.9									1.6941	45
57.290	1.6069	11.0							1.6014	82		
57.530	1.6007	11.9										
JCPDS Card No.			**15-0776**		**33-1161**		**04-0787**		**42-1468**		**33-0664**	

8.6.1.2 Ground granulated blast furnace slag (ggbs)

Owing to the high proportion of calcium, magnesium aluminium and silica, ggbs consists mainly of calcium aluminosilicate glasses. The chemical composition of glass in ggbs corresponds to the melilite phase which is a solid solution phase between gehlenite and akemanite. In addition to those diopsite and merwinite have been detected in the devitrified slag particles[1].

The dominant feature is the broad amorphous hump at $2\theta \sim 30$. The peaks at 2.339Å and 2.026Å are attributed to Al from the sample counter and have been excluded from the analysis. Some peaks from mineral phases appear, but only with very low intensities indicating very low crystal content. The most intense peak at 0.267 nm, along with weak peaks at 0.187Å can be attributed to merwinite (C_3MS_2), a phase commonly found in ground granulated slag. Merwinite peaks remain in the data for hydrated slag indicating that the crystalline phase in the unhydrated slag does not take part in the hydration reactions. A similar observation was made by Talling[40] in merwinite bearing slags.

8.6.1.3 Condensed silica fume (microsilica)

Silica fume consists mainly of amorphous (noncrystaline) silica with a very high surface area which makes it highly pozzolanic[1]. The dominant feature is the broad amorphous hump at a $2\theta \sim 21$. The peaks at 2.339 Å and 2.026 Å are attributed to the Al from the sample counter and have been excluded from the analysis. Some peaks from mineral phases appear, but only with very low intensities indicating very low crystal content.

8.6.1.4 Alkali Activated Materials

The X-ray diffraction of some of the alkali activated materials was used to obtain more information on the relationship between chemical composition of the hydration products and the properties of the material. The strongest peaks observed in all the x-ray diffraction traces for the alkali activated materials examined match those for

quartz. This matched the diffraction trace obtained for the sand used in the mix. The intensity of the quartz peaks was many orders of magnitude greater than for any hydration products present in the mix. This made identification of hydration products extremely difficult as the height of the relevant peaks was close to that of the background count measured from each sample.

Analyses of all the traces recorded show a similar composition. This appeared to be a mixture of aluminium silicates of various compositions. Table 8.35 shows a typical list of materials with good matches of d spacings to those observed from the x-ray diffraction traces. It was not possible to identify specific differences between the different mixes examined. While it was not possible identify specific differences between different material batches, it was possible to identify certain features across the range of material batches

None of the x-ray diffraction traces showed a peak at 3.06 Å, this is the main peak attributed to C-S-H by Schilling[70] which matches the (220) plane in tobermorite. The lack of this peak in the current study suggests that C-S-H is not present in the material batches examined. This contradicts many authors[11,19,20,70] who propose that the major hydration product observed in fly ash materials is a type C-S-H with sodium replacing the calcium in the C-S-H. This is not however conclusive proof since for materials RT, IA, IH, IISA and IISAB3 a peak exists around 3 Å. It is possible that this may represent some form of CSH[50,70]. This peak is absent in thermally treated slag containing materials IISH and IISHB3. These two batches exhibited the highest flexural strength. This may represent evidence of a change in the type hydration products to those with a high Al_2O_3/SiO_2 ratio such as zeolites of the form $[R_2OnAl_2O_3xSiO_2nH_2O]$. A more detailed quantitative x-ray diffraction analysis of these types of materials would be required to confirm this hypothesis. This was beyond the scope of the present study.

Table 8.35 Typical X-ray analysis results for alkali activated materials

Material RT

Card.	Rel match	I [%]	Displ	Chemical Formula	Mineral Name
33-1161	0.96	48	-46	SiO2	Quartz, syn
16-0440	0.41	1	-99	Ca3Al6O12!CaSO4	Ye'elimite, syn
33-0256	0.40	1	-3	Ca4Al6O12SO4	Ye'elimite, syn
27-0606	0.35	0	37	H2Si2O5	Silicon OxideHydrate
21-0167	0.33	1	-3	CaSO4!xH2O	Calcium Sulfate Hydr.
20-0452	0.29	1	-4	CaAl2Si2O8!4H2O	Gismondine
20-0452	0.29	1	-4	CaAl2Si2O8!4H2O	Gismondine
42-1378	0.29	1	73	Na10Mg3Al16Si32O96!25H2O	Analcime, magnesian
41-1382	0.27	1	12	Al(SO4)(OH)!5H2O	Rostite
10-0425	0.21	1	25	Al2O3	Aluminum Oxide
25-1500	0.28	0	8	Na8Al6Si6O24(SO4)!2H2O	Vishnevite
21-0133	0.23	1	91	CaAl2Si7O18!2H2O	Calcium Aluminum Silicate Hyd.

Material IH

33-1161	0.97	58	-46	SiO2	Quartz, syn
12-0539	0.43	1	62	Al2O3	Aluminum Oxide
33-0256	0.35	1	-59	Ca4Al6O12SO4	Ye'elimite, syn
21-0913	0.34	1	30	Ca4Fe9O17	Calcium Iron Oxide
37-1377	0.29	2	-24	Al(OH)3	Aluminum Hydroxide
41-1382	0.26	1	62	Al(SO4)(OH)!5H2O	Rostite
21-0167	0.25	1	-3	CaSO4!xH2O	Calcium Sulfate Hydrate
35-0121	0.24	1	23	Al2O3	Aluminum Oxide
15-0641	0.21	1	-22	Ca2SiO4!0.35H2O	Calcium Silicate Hydrate
31-0298	0.19	1	-3	Ca2SiO4	Calcium Silicate
39-1372	0.19	1	-4	Ca(Si6Al2)O16!4H2O	Yugawaralite

Material IISH

33-1161	0.88	69	-34	SiO2	Quartz, syn
02-0083	0.34	0	33	Ca3Al2O6!xH2O	Calcium Aluminum Oxide Hyd.
23-0125	0.3	1	-64	Ca6Si6O17(OH)2	Xonotlite, syn
37-1377	0.29	1	-3	Al(OH)3	Aluminum Hydroxide
41-0753	0.29	2	17	CaFeO3	Calcium Iron Oxide
31-0298	0.28	1	-68	Ca2SiO4	Calcium Silicate
41-1382	0.27	2	12	Al(SO4)(OH)!5H2O	Rostite
24-0006	0.27	1	-68	Al(OH)3	Nordstrandite, syn
20-0452	0.25	2	12	CaAl2Si2O8!4H2O	Gismondine
20-0452	0.25	2	12	CaAl2Si2O8!4H2O	Gismondine
10-0425	0.24	1	69	Al2O3	Aluminum Oxide
31-0579	0.24	2	-46	H2Si3O7	Hydrogen Silicate
14-0298	0.23	2	-4	Na9(AlO2)9(SiO2)15!27H2O	Sodium Aluminum Silicate Hyd.
27-0015	0.22	1	-4	Al12H12Si36O96	Aluminum Hydrogen Silicate
39-0193	0.22	1	-4	H2.04Al2Si5.8O15.62	Aluminum Hydrogen Silicate
29-0291	0.22	2	70	Ca4Al4Si4O6(OH)24!3H2O	Vertumnite
16-0339	0.21	1	17	Ca2Al(OH)7!6.5H2O	Calcium Aluminum Hydrox. Hyd.
35-0060	0.2	1	-24	H8Si8O20	Hydrogen Silicate
30-0226	0.2	1	30	Ca2(Al,Fe)2O5	Brownmillerite, syn
30-0902	0.17	1	45	K2Al2Si3O10!3H2O	Potassium Aluminum Silicate Hy

8.6.2 Discussion on Hydration Products

The comparison of material RT which contains only fly ash, with material IA containing fly ash and microsilica shows a marked increase in flexural strength. The main cause for this change is the refinement in the pore structure as well as changes in the hydration products formed caused by the addition of the microsilica.

The addition of slag to batches IA to produce batches IISA causes the calcium level to increase (as expected). There is no further refinement of the pore structure and the modulus of rupture is similar as for batches without slag (IH and IA). However, thermal curing causes a large increase in modulus of rupture of material containing slag (compare batches IISA and IISH) without any significant refinement of the pore structure. The thermal cured material IISH shows a higher proportion of aluminium and sodium in the hydration products. This can be further seen when comparing materials which contain water glass hardener (IISAB3 and IISHB3). Material IISAB3 is similar to IISA except that the former contains water glass hardener. Material IISHB3 is the thermal cured version of IISAB3. The thermally cured material containing hardener (IISHB3) shows similarly large increase in modulus of rupture compared with materials IISAB3 cured under 20°C and 65% RH as was the case in materials without hardener (IISA and IISH). The proportion of aluminium in the hydration products also increases in a similar manner.

It is clear form these observations that the macro changes in pore structure will only provide a certain level of increase to flexural strength. Further improvements in flexural strength must be from another strengthening mechanism. It has been proposed in literature that the presence of zeolites in the hydration products of a cementitious material will strengthen it. This is difficult to prove from EDAX analysis, as this only produce information about the chemical elements present and do not determine the stoichiometric composition of the hydration products. However the EDAX together with digital mapping and feature analysis indicate the important features which play an important role in the microstructure of alkali activated fly ash materials. Improvement in flexural strength requires an increase in the proportion of aluminium in the hydration products and thermal curing to activate it. The addition

slag and microsilica is the source for increased aluminium levels. Material IH was thermally cured but contained no slag and did not show a significant increase in modulus of rupture compared to material IA (cured under 20°C and 65% RH). However, both materials IISH and IISHB3 which contained slag and were thermal cured, exhibited a large increase in flexural strength compared with corresponding materials cured under 20°C and 65% RH. All the thermal cured samples showed an increase in aluminium levels.

Literature[64,168] points to temperature of curing as being important in determining the type of zeolites formed. The increased levels of aluminium suggest that more complicated aluminium silicates have been formed and these new hydration products have strengthened the materials, thereby indicating a strong possibility that zeolites have been formed. This conclusion is supported by the x-ray diffraction results. The high temperature cured materials show an increased tendency to form aluminium silicates of the form $[R_2OnAl_2O_3xSiO_2nH_2O]$.

LaRossa et al[57] found that three major factors affect the hydration reactions; temperature, composition of materials and concentration of alkaline solution. In particular the solution needed to be high in Al/Si ratio and low in the Ca/Si ratio to form zeolite hydration products. A high calcium level tends to form CSH as a hydration product. In all the mixes investigated in this study, the Ca:Si ratio is low and there is no real evidence of the formation of CSH. This was also found by Shi et al investigating the effect of alkaline activators on slags. Variations in the composition of the slags was found to affect the hydration products. Katz[169] found that different curing temperature and composition affected the microstructure of alkali activated fly ash. Further evidence of this behaviour has been shown Caijun[49,79,171,172] and Wang et al[11,19,20]. Microsilica has been found to react with sodium hydroxide to produce sodium silicate hydrate[173], but no evidence of sodium silicate hydrate was found in the present study.

This suggests that the results of the present study generally confirm previous research. The addition of slag to the fly ash increases the calcium and aluminium content of the mix. The Ca:Si ratio is not high enough to form CSH. Zeolites are

found in these materials, but it is suspected that these hydration products do not strengthen the material. The addition of slag does refine the microstructure to increase the strength of the material. The addition of microsilica further lowers the Ca:Si ratio and also the Al:Si ratio. However, there appears to be a change in the hydration products for thermally cured batches containing microsilica. This would indicate a change in the type of zeolite formed to one which strengthens the material. This suggests that the Ca:Si ratio are the key parameter controlling the type of hydration products formed.

"All science is concern with the relationship of cause and effect. Each scientific discovery increases man's ability to predict the consequences of his actions and thus his ability to control future events."

Laurence J. Peler

9 Limitation of Present Research, Conclusions and Recommendations for Further Research

9.1 LIMITATIONS OF PRESENT RESEARCH

Sodium silicate solution was selected as the alkali activator used in the investigation from an extensive list of possible activators. This selection was based on the results of the literature search of previous work carried out in this field. It was not possible, given the time constraints of the project, to investigate other alkali activators. Utilising only two water to binder ratios of 0.2 and 0.25 made further limitations of the experimental programme. A wider range of water/binder ratio needs to be investigated in future work.

No initially cured alkali activated materials were tested for compressive creep and, therefore, no empirical correlation with the fibre reinforced composites could be drawn for the initially thermally cured materials. It was only possible to carryout a limited number of permeability tests. In order to gain information about the influence of different parameters on the permeability of alkali activated materials a larger number of tests will be required.

The investigation of the relationship between chemical composition, microstructure and properties (strength, durability and porosity), was intended to examine the relationship between principal phases in the hydration products and strength development in the materials. To enable this, X-ray diffraction measurements were conducted on powdered mortar samples. However, one of the main limiting factors in the characterisation of hydration products has been the presence of the sand in the materials. The peaks generated by the sand in the x-ray diffraction traces overlap and mask those of the hydration products of the alkali activated materials. The presence of amorphous phases as well as crystalline phases in the materials has prevented a detailed analysis of hydration products.

9.2 CONCLUSIONS

The following conclusions are based on the results of this investigation on alkali activated materials derived from fly ash, microsilica, slag fillers using water glass as the activator:

1. The physical and chemical composition of fly ash strongly influences the mechanical and physical properties of the alkali activated material.

2. The addition of microsilica has a marked positive effect. The sample with 5% micro silica (by weight) exhibited a modulus of rupture approximately two times larger than the sample without microsilica.

3. Samples with 5% microsilica and no slag addition developed a convex top surface during curing at high temperatures

4. Samples compacted by pressure application give superior mechanical properties than hand compacted ones. Pressure compaction produces a more homogeneous mix than hand compaction, because of the poor workability of mix.

5. Addition of slag improves the mechanical and physical properties of the material. As with fly ash, the physical and chemical composition of slag influences strength development.

6. The addition of slag increased the modulus of rupture and compressive strength by approximately 1.8 times.

7. The addition of slag reduced water absorption by 24% and apparent porosity by 72%.

8. The addition of slag improves freeze thaw resistance of the material. Samples with fine slags, cured at ambient temperature, gave the best overall freeze thaw resistance.

9. The addition of K-Bond hardeners had little effect on flexural strength, but did effect the durability and physical properties of the material

10. Samples without slag or K-Bond hardeners did not survive the freeze thaw test. The presence of K-Bond 90 and 200 greatly improved the freeze thaw resistance.

11. Thermal curing improves the mechanical properties, but decreases the density and increases the water absorption and apparent porosity. After thermal curing the majority of materials developed a convex surface.

12. Residual modulus of rupture of thermally cured materials was lower than that of materials cured under 20°C and 65% RH.

13. The optimum Na_2O content of the mix was found to be of the order of 3%. Fly ashes are naturally higher in Na_2O and K_2O content than slags, making the optimum silica modulus of the water glass to be around 2 for fly ash activation compared with 1 to 1.5 for slag activation.

14. The silica modulus of water glass influences strength. The advantage of a higher silica modulus is that it allows the addition of more water glass to obtain a constant (3%) Na_2O content, which results in a more workable mix.

15. Alkali activated materials exhibit much higher free shrinkage and compressive creep than normal Portland cement mortars.

16. Most of the shrinkage of alkali activated fly ash materials occurs in the fist 72 hours.

17. Alkali activated materials with a lower water/ binder ratio (0.20) exhibit lower free shrinkage than those with a higher water/ binder ratio (0.25), regardless of the curing conditions.

18. The free shrinkage of alkali activated materials is considerably reduced when cured under 20°C and 95% relative humidity or in water at 20°C, as opposed to curing at 20°C, 65%RH, i.e. a reduction in relative humidity of the curing environment results in higher shrinkage.

19. The addition of fibre reinforcement greatly reduces the free shrinkage. Reductions of up to 55% at $V_f l/d = 2.12$ for glass fibre reinforced materials and 44% at $V_f l/d = 0.76$ for steel fibre reinforced materials, cured under 20°C and 65% RH, were achieved.

20. Shrinkage restraint increases with increasing fibre volume and fibre $V_f l/d$.

21. The free shrinkage of alkali activated fibre reinforced materials obeys the theoretical model developed by Mangat and Azari[114] for steel fibre reinforced Portland cement mortars.

22. The compressive creep of alkali activated materials is reduced by approximately 50% when they are thermally cured compared with curing under 20°C, 65% RH.

23. The addition of short fibre reinforcement greatly reduces the compressive creep of alkali activated materials. Reductions of up to 45% for glass fibre reinforced materials and 50% for steel fibre reinforced materials, cured under 20°C, 65% RH were achieved.

24. Compressive creep decreases with increasing fibre volume and $V_f l/d$.

25. The compressive creep of alkali activated fibre reinforced materials obeys the theoretical model developed by Mangat and Azari[115] for steel fibre reinforced Portland cement mortars.

26. The compressive strength of alkali activated fibre reinforced materials is within the range 51.78 N/mm^2 to 103.74 N/mm^2.

27. The modulus of rupture of alkali activated fibre reinforced materials is within the range 3.08 N/mm^2 to 10.5 N/mm^2.

28. Increasing the water/binder ratio from 0.20 to 0.25 decreases the compressive strength, modulus of rupture, tensile splitting strength and dynamic modulus of alkali activated materials.

29. Increasing the relative humidity of curing from 65% to 95% decreases the compressive strength and dynamic modulus of elasticity but does not significantly affect the modulus of rupture.

30. Thermal curing increases the compressive strength, modulus of rupture and dynamic modulus of elasticity of alkali activated materials.

31. The modulus of rupture of fibre reinforced alkali activated materials can be obtained using the following equations:

for glass fibre reinforced alkali activated materials

$$\sigma_{fc} = 0.57\sigma_{fm}(1-V_f)+6.41\cdot V_f\cdot\frac{l}{d}$$

for steel fibre reinforced alkali activated materials

$$\sigma_{fc} = 0.64\sigma_{fm}(1-V_f)+4.00\cdot V_f\cdot\frac{l}{d}$$

32. The fibre-matrix bond strength for glass fibre reinforced matrices is 4.88 N/mm^2 and for steel fibre reinforced matrices is 7.82 N/mm^2. This compares with a value of 4.15 N/mm^2 for steel fibres in a Portland cement mortar.

33. The bulk and solid densities of alkali activated materials are within the range 2001 to 2063 kg/m^3 and 2340 to 2568 kg/m^3, respectively.

34. The apparent porosity and water absorption for alkali activated materials are within the range15.69 to 20.75% and 7.79 to 9.98%, respectively.

35. Raising the relative humidity of curing from 65% to 95% decreases the apparent porosity and water absorption of materials with a water/binder ratio of 0.25 and increases the apparent porosity and water absorption of materials with a water/binder ratio of 0.20.

36. Thermal curing increases the water absorption, apparent porosity and coefficient of saturation compared with ambient curing at 20°C, 65%RH

37. Compressive strength decreases with an increase in coefficient of saturation for alkali activated materials cured in different conditions.

38. The residual compressive strengths resulting from exposure to 100 freeze - thaw cycles for alkali activated materials are within the range 56% to 95%.

39. The residual compressive strengths resulting from exposure to 100 freeze - thaw cycles for alkali activated fibre reinforced materials are within the range 79% to 96%.

40. The residual compressive strengths resulting from exposure to high temperatures (600°C) for alkali activated materials are within the range 57% to 78%.

41. The residual compressive strengths resulting from exposure to high temperatures (600°C) for alkali activated fibre reinforced materials are within the range 64% to 87%.

9.3 RECOMMENDATIONS FOR FURTHER RESEARCH

There are a number of diverse areas in which the present research into alkali activated materials can be extended. The current work has shown the potential for this material to be used as a construction material. The mechanical properties and durability achieved are comparable or superior to those for ordinary Portland cement. There are still areas to be examined in order to exploit the potential of this material.

The high early age shrinkage could prove problematic if this type of fly ash material was used as a castable material. In addition there is a lack of work on suitable plasticisers and additives to control setting time. These would be required in order to obtain a mix with the desired range of workability.

The durability and chemical resistance of the material has still to be completely characterised. The chemical resistance of the material towards sulphate attack, chloride ingress or carbonation have been beyond the present study. The susceptibility of the material to chloride ingress and carbonation could be important if it is to be reinforced with steel. The use of fly ash and slag also opens up the possibility of leaching of chemical contaminants such as heavy metals from the contaminated radioactive materials. The zeolitic nature of the hydration products for this type of material is known for the ability to bind heavy metals into the structure. However, with the health risks this may pose, further research may be necessary to quantify these risks.

As with any new building material, one of the major tasks will be to build up a body of evidence to generate confidence in the material in actual construction. Work with larger sized specimens and built structures will be necessary to properly access the performance of the material to allow the generation of associated building practices and standards. The performance of the material with steel reinforcement bars has not been studied nor has the construction practices necessary for the use of the material. It is also apparent from the current work that the material is coloured dark grey to black. The uptake and use of a material is also governed by the aesthetics of the

finished surface it produces. Work would also be required to investigate the public response to the material and the control of colour and surface finish.

It is clear that strength development is a function of the hydration products that develop in the mix and these are affected by the mix composition and the curing temperature. The current work found parameters such as the Si/Al ratio and the Ca/Si ratio and the Na_2O content to be important. These chemical parameters decide the principal phase in the hydration products formed, between calcium silicate hydrate (C-S-H) and zeolite (R_2O n Al_2O_3 x SiO_2 r H_2O). Further work is required to investigate the fundamental relationship between chemical composition, microstructure and properties on the composite material. This work will allow the optimisation of the alkali activated materials, using fly ashes from various sources.

Overall, the main aim of this research project was to investigate the use of waste materials such as fly ash to produce construction materials. While it is clear that the potential exists, there are still some areas to be clarified before these materials can be commercially exploited.

REFERENCES

1 MEHTA, P. K., "Cementitious By-products", pp. 3-46.

2 CABRERA, J. G. and WOOLLEY, G. R., "Fly ash utilisation in Civil Engineering", *Environmental aspects of construction with waste materials,* Vol. 60, Chapter 89, pp. 345-356, 1994.

3 KANE, J. S. and GILLS, T. E., "Certification of a new NIST fly ash standard reference material", *Fresenius Journal of Analytical Chemistry*, No. 352, pp. 193 - 196, 1995.

4 DAVIS, R. E., *ICI Mag. Proceeding,* 33, No. 5, pp.577 - 612, 1937.

5 AMERICAN SOCIETY FOR TESTING MATERIALS, "Standard specifications for coal fly ash and raw calcined natural pozzolan for use as a mineral admixture in Portland cement concrete", *ASTM C 618-94a,* 1994.

6 AMERICAN SOCIETY FOR TESTING MATERIALS "Standard specifications for blended hydraulic cements", *ASTM C 595M-95,* 1995.

7 COPPOLA, L., BEALZ, G., DINELLI, G. and COLLEPARDI, M., "Prefabricated building elements based on FGD gypsum and ashes from coal fired electric generating plants", *Materials and Structures*, Vol. 29, pp. 305-311, June 1996.

8 SARKAR, S. L., "Roles of silica fume, slag and fly ash in the development of high performance concrete microstructure", *ACI Journal*, Vol.149, pp.449-460, 1994.

9 CHUNXIANG, Q. and HONGDING, G." Mechanism of mineral admixture suppressing alkali-silica reaction, Part I", *Cement and Concrete Research*, Vol.24, No.6, pp.1111-1120, 1994.

10 MALOLEPSZY, J., and DEJA, J., "The influence of curing condition on the mechanical properties of alkali-activated slag binders", *CBI Forskning Research ,fo 1.88,* Alkali-activated slag, pp. 65-81, Stockholm, 1988.

11 WANG, S-D., "Review of recent research on alkali-activated concrete in China", *Magazine of Concrete Research,* Vol.43, No.154, pp.29-35, 1991.

12 WEI-HENG SHIH, HSIAO-LAN CHANG and ZHIJIAN SHEN, "Conversion of Class-F Fly Ash to Zeolites"; *Materials Research Society Symposium Proceedings,* Vol. 371; pp.39-44, 1995.

13 HOOTON, R. D., "The reactivity and hydration products of blast furnace slag", *Supplementary Cementing Materials for Concrete,* Editor: Malhotra, V. M., Minister of Supply and Services, Canada, 1987.

14 SHI, C. and DAY, R., "Selectivity of the alkali activators for the activation of slags", *Cement, Concrete and Aggregates,* Vol. 18, No. 1, pp. 8-14, June 1996.

15 AMERICAN SOCIETY FOR TESTING MATERIALS "Standard test method for hydraulic activity of ground slag by reaction with alkali", *ASTM C 1073-91,* May 1992.

16 NASSER, K. W. and MARZOUK, H. M., "Properties of Mass Concrete containing fly ash at high temperatures", *ACI Journal,* April 1979.

17 SASATANI, T., TORII, K. and KAWAMURA, M." Five-year exposure test on long-term properties of concrete countering fly ash, blast furnace slag and silica fume", *ACI Journal,* Vol.153, pp.283-296, 1995.

18 ISOZAKI, K., IWAMOTO, S. and NAKAGAWA, K., "Some properties of alkali-activated slag cements", *Proceedings of the 8th International Congress on the Chemistry of Cement.* Rio de Janeiro, Vol. vi, pp.395-399, 1986.

19 WANG, S-D., PU, X-C., SCRIVENER, K.L. and PRATT, P. L. "Alkali-activated slag cement and concrete: review of properties and problems", *Advanced in Cement Research*, Vol.7, No.27, pp.93-102, July 1995.

20 WANG, S-D., SCRIVENER, K .L. and PRATT, P. L., "Factors affecting the strength of alkali activated slag", Cement and Concrete Research, Vol.24, No.6, pp.1033-1043, 1994.

21 MESTO, J. AND KAJAUS, E., "Activation of blast furnace slag by some inorganic materials", *Proceeding of the 1st International Conference on the use of fly ash, silica fume slag & other minerals by-products in concrete*, pp.1059-1073, Montobello, 1983.

22 MALOLEPSZY, D., "Activation of synthetic melitite slags by alkalies", *Proceedings of the 8th International Congress on the chemistry of cement*, Brazil, Vol. 4, pp. 104-107.

23 ANDERSSON, M. A., and GRAM, H-E., "Properties of alkali-activated slag", *CBI Forskning Research, fo 1.88,* Alkali-activated slag, pp. 9-63, Stockholm, 1988.

24 PARAMESWARAN, P S and CHATTERJEE A. K., "Alkali activated of Indian blast furnace slag", *Proceedings of the 8th International Congress on the Chemistry of Cement*, Vol. 4, pp. 86-91, 1986.

25 BIN, Q., "Investigations of Alkali-Steel and BFS Slag Cements", *MSc thesis*, Nanjing Institute of Chemical Technology, Nanjing, P.R.China.

26 BIJEN, J. and WALTJE, H., "Alkali activated slag-fly ash cements", Proceedings of the 3rt International Conference on the use of Fly Ash, Silica Fume, Slag and Natural Pozzolanas in concrete", Norway, pp. 1565-1578,1989.

27 SMITH, M. A. and OSBORNE, G. J., "Slag / Fly ash cements", *World cement technology*, Vol. 8, No. 4, pp. 223-233, Nov/Dec 1977.

28 NARANG, K. C. and CHOPRA, S. K., "Studies on alkaline activation of BF, steel and alloy slags", *Silicate Industriele*, Vol. 9, pp.175-182, 1993.

29 DOUGLAS, E., BILODEAU, and MALHOTRA, V.M., "Properties and durability of alkali-activated slag concrete", *ACI Materials Journal*, Vol. 89, No. 5, pp.509-516, September-October 1992.

30 MALHOTRA, S. K. AND TEHRI, S. P., "Development of bricks from granulated blast furnace slag", *Construction and Building Materials*, Vol.10, No.3, pp.191-193, 1996.

31 DUBE, S. K. AND PALIT, A., "Studies in the development of the fly ash bricks - an approach for cleaner environment-Part 1", *Proceedings of American Power Conference putting technology to work*, 1994, Vol.56, No.1-2, pp.315-320.

32 DUBE, S. K and PALIT, A., "Studies in the development of the fly ash bricks an approach for cleaner environment-Part2", *Proceedings of American Power Conference putting technology to work*, Vol.57, No.1-3, pp. 471-476, 1994.

33 LENZ, U., MEYRAHN, H., MOHLENBRUCH, N., PAFFGEN, H. P. and REICH-WALBER, M., "Reutilization Studies for brown coal ash", *Coal Science and Technology,* Vol. 24, No. 493, pp. 1995-1998, 1995.

34 LEA, F. M., *"The chemistry of cement and concrete"*, 3^{-rd} edition, pp.454-489, E. Arnold, London, 1988.

35 KUKKO, H. and MANNONEN, R., "Chemical and mechanical properties of alkali-activated blast furnace slag (F-concrete)", *Nordic Concrete Research*, No.1, pp.16.1-16.16, Oslo, 1982.

36 SHARPE, A. G., *"Inorganic Chemistry"*, 2nd edition, Longman, London 1986.

37 CROSFIELD "Soluble silicates and their applications", Issue No. 1, July 1993.

38 TALLING, B. and BRANDSTETR, J., "Present state and future of alkali-activate slag concrete", *Proceeding of the 3 rd International Conference on the use of fly ash, silica fume, slag & natural Pozzolanas in concrete.* Trondheim, Norway, Vol.2, pp.1519-1545, 1989.

39 BUENFELD, N. R. and AHMED, Y. H., "GGBS-Based S/S of Toxic Waste", A study undertaken for the Appleby group, 1992.

40 TALLING, B., "Effect of curing conditions of alkali activated slags", *Proceeding of the 3 rd International Conference on the use of fly ash, silica fume, slag & natural Pozzolanas in concrete,* Trondheim, Norway, Vol. 2, pp.1485-1500, 1989.

41 SHI CAIJUN. and LI YINYU., "Investigation on some factors affecting the characteristics of alkali-phosphorous slag cement", *Cement and Concrete Research*, Vol. 19, No. 4, pp. 527-533, 1989.

42 BLAAKMEER, J., "Diabind: An alkali-activated slag fly ash binder for acid resistant concrete", *Advanced Cement Based Materials*, Vol. 1, pp. 275-276, 1994.

43 DOUGLAS, E., BILODEAU, A., BRANDSTETR, J. and MALHOTRA, V. M., "Alkali activated ground granulated blast furnace slag concrete: preliminary investigation", *Cement and Concrete Research*, Vol. 21, No. 5, pp. 101-108, 1991.

44 FREIDIN, K. and ERELL, E., " Bricks made of coal fly ash and slag cured in open air", *Cement and Concrete Composites*, Vol. 17, No. 4, pp. 289-300, 1995.

45 NAKANO, J. and MURAKAMI, M., "K-Bond - New type water glass hardener", *Polymers Paint Journal,* June12, 1985.

46 DUGAT, J., ROUX, N. and BERNIER, G., "Mechanical properties of reactive powder concrete", *Materials ad Structures*, Vol. 29, pp. 233-240, May 1996.

47 LAWRENCE, C. D., "The properties of cement paste compacted under high pressure", *Cement Concrete Assoc. Res,* No. 19, London, June 1969.

48 BERUBE, M. A., CHARLES-GIBERGUES, A., DUCHESENE, J. and NAPROUX, P., " Influence of Particle size distribution on the effectiveness of type-F fly ash in suppressing expansion due to alkali-silica reactivity", *ACI Special Publication,* Vol. 153, Ch.62, pp. 177-192, 1995.

49 CAIJUN SHI., WU XUEQUAN. and TANG MINGSHU "Hydration of alkali-slag cements at 150C", *Cement and Concrete Research*, Vol. 21, pp. 91-100, 1

50 991. TAYLOR, H. F. W., "Nanostructure of C-S-H: Current Status", *Advanced Cement Based Materials*, Vol. 1, pp. 38-46, 1993.

51 GLUKHOVSKY, V. D., ROSTOVSKAJA, G. S. and RUMYNA, G. V., "High Strength slag-alkaline cements"; *7th International Congress on the Chemistry of Cement*, Vol. V; pp.164-68, 1980.

52 GLUKHOVSKY, V. D., ZAITSEV, Y. and PAKHOMOV, V., "Slag-alkaline cements and concrete structures, properties, technological and economical aspects of the use", *Silicates Industriels*, Vol. 10, pp.197-200, 1983.

53 SPEARS, D. A., SHARP, J. H., THOMPSON, D. and ARGENT, B. B., "Prediction of the phases present in fly ash, their composition and the influence of these factors on its utility and disposal, Institute of Energy "and *International Conference Combustion and Emission Control*, Ch. 37, pp. 71-87, 1995.

54 ATKINS, M., BENNETT, D., DAWES, A., GLASSER, A., KIDNESS, F. and READ, D., "A thermodynamic model for blended cements"; *DoE Report*, No:DoE/HMP/RR/92/005, December 1991.

55 GLASSER, F. P., McPHEE, D. E. and LACHOWSKI, E. E., "Modelling approach to predict the equilibrium phase distribution in slag-cement blends and their solubility properties" Materials Research Society Symposium Proceedings, Vol. 112, pp. 3-12, 1988.

56 GLASSER, F. P. and JAPPY, T. G., "Phases and density changes during the conversion reaction in high alumina cement", *Materials de Construction*, Vol. 2, pp. 5-12, 1992.

57 LAROSA, J. L., KWAN, S. and GRUTZECK, M. W., "Zeolites Formation in Class F Fly Ash Blended Cement Pastes"; *Journal of American Ceramic Society*, Vol. 75, pp. 1574-80, 1992.

58 AKIRA YOSHIDA and KOUZOU INOUE, "Formation of faujasite-type zeolites from ground Shirasu volcanic ash", *Zeolites*, Vol. 6, pp. 467-73, 1986.

59 XU AIMIN and SARKAR SHONDEEP "Microstructural development in high-volume fly ash cement system", *Journal of Materials in Civil Engineering*, Vol. 6, No. 1, pp. 117-136, February 1994.

60 CHENG QING-HUA, AREZKI TAGNIT-HAMOU and SHONDEEP SARKAR "Strength and microstructural properties of water glass activated slag", *Proceeding of Materials Research Society Symposium*, Vol. 245, 1992.

61 NAIQIAN FENG, HONGWEI JIA and ENYI CHEN "Study on the suppression effect of natural zeolite on expansion of concrete due to alkali-aggregate reaction", Vol. 50, No. 1, pp. 17-24, March 1998.

62 FU YAN, DING JIAN and BEAUDOIN, J. J., "Zeolite based additives for high alumina cement products", *Advanced Cement Based Materials*, Vol. 3, pp. 37-42, 1996.

63 WEI, F., GRUTZEK, M. W. and ROY, D. M., "The retarding effect of fly ash upon the reaction of cement pastes: The first 24 hours", *Cement and Concrete Research*, Vol. 15, No. 1, pp. 174-184, 1985.

64 QULLINN, K. C., DUERDEN, S. L., MAJUMDAR, A. J., "Formation of zeolite in OPC-PFA mixes", *Cement and Concrete Research*, Vol. 23, pp. 991-992, 1993.

65 MEHTA, P. K., "Mechanism of expansion associated with ettringite formation", *Cement and Concrete Research*, Vol. 3, pp. 1-6, 1973.

66 LAFTHUMA, H., "Revue Materials Construction", *Trav. Publication*, Vol. 243, pp. 441, 1929.

67 TALERO, R., "Ettringite from Portland cement origin and ettringite from pozzolanic origin: analogies, differences and semiquantitative relations with their respective origins: interrogations", *9th International Congress on the Chemistry of Cement*, pp. 343-349.

68 RICHARDSON, I. G. and GROVES, G. W., "The composition and structure of C-S-H gels in cement pasted containing blast furnace slags", *9th International Congress on the Chemistry of Cement,* pp. 350-356.

69 AMITRAVA, R., SHILING, P. J. and HARVILL, C. E., "Activation of Ground Blast-furnace Slag by Alkali-Metal Alkaline-Earth Hydroxides", *Journal of American Ceramic Society*, Vol. 75, pp. 3233-40, 1992.

70 SHILING, P. J., "*The structure of cementitious materials produced by alkali activation of calcium aluminosilicate glasses*", PhD Thesis, Louisiana State University, May 1992.

71 KUTTI, T., "Hydration products of alkali activated slag", *9th International Congress on the Chemistry of Cement,* pp. 468-474.

72 STADE, H., "On the reaction of the C-S-H (di, poly) with alkali hydroxides", *Cement and Concrete Research*, Vol. 19, pp. 802-810, 1989.

73 HUANHAI, Z., WU, X. and MINGSHU, T., "Kinetic studies on hydration of alkali activated slag", *Cement and Concrete Research*, Vol. 23, pp. 1253-1258, 1993.

74 BELITSKY, I. V., SAKATA, A., KADO, T. and GOTO, S., "Kinetics of the hydration of slag in the slag-alkaline cements" *Proceedings of the 3rd International Symposium on the Cement and Concrete*, Beijing, China, pp. 1028-1031.

75 REGROUD, M., HORNAIN, H. and MORTUREAUX, B., Silicates Industrials, Vol. 42, pp. 19-27, 1977.

76 WU, X., ROY, M. and LANGTON, C. A. *Cement and Concrete Research*, Vol. 13, pp. 277-286, 1983.

77 KONDO, R., SONG and DIMOND, S "The latent property of granulated blast furnace slag by various activators", Tetsu to Hagans, Vol. 65, pp.1825-1829, 1977.

78 UCHIKAWA HIROSHI, OKAMURA TAKAYOSHI AND TAKEHIRO MINORU "Relationship between the structure and policondensation degree of silicate anion of C-S-H estimated by FT-NMR, GPC and SFC , and the strength of mortar", *9th International Congress on the Chemistry of Cement,* pp.195-201.

79 SHI CAIJUN "Strength, pore structure and permeability of alkali-activated slag mortars", *Cement and Concrete Research*, Vol. 26, No. 12, pp. 1789-1799, 1996.

80 ROBLER, M. and ODLER, I., "*Cement and Concrete Research*", No. 2, pp. 320-330, 1985.

81 NEVILLE, A. M., "*Properties of concrete*", Fourth and final edition, Longman Group Limited, 1995.

82 L'HERMITE, R., "Volume changes of concrete", Proceedings of the 4th International Congress on the Chemistry of Cement, Washington D C, pp. 659-694,1960.

83 ROSS, A. D., "Shape size and shrinkage", *Concrete and Constructional Engineering*, pp. 193-199, August 1944.

84 L'HERMITE, R., "Quelques problems mal connus de la technologie du beton", *Il Cemento*, Vol. 75, No. 3, pp. 231-246, 1978.

85 ALMUDAIHEEM, J. A. and HANSEN, W., "Effect of specimen size and shape of drying shrinkage", *ACI Materials Journal*, Vol. 84, No. 2, pp. 130-134, 1987.

86 HANSEN, T. C., "Effect of wing on creep and drying shrinkage of hardened cement and mortar concrete, ASTM Materials Research & Standards, Vol. 6, pp. 16-19, 1966.

87 BYFORS, K., KLINGSTEDT, G., LEHTONEN, V., PYY, H. and ROMBEN, L., "Durability of concrete made with alkali-activated slag", *Proceeding of the 3rd International Conference on the use of fly ash, silica fume, slag & natural Pozzolanas in concrete,* Trondheim, Norway, Vol. 2, pp. 1492-1466, 1989.

88 HAKKINENE, T., PYY, H. and KOSKINEN, P., "Microstructural and permeability properties of alkali activated slag concrete", *Research Reports 486,* Technical Research Centre of Finland, Espoo, 1986.

89 VESIKARI, E., "Frost resistance of F-concrete", *Research Reports 474,* Technical Research Centre of Finland, Espoo, 1987.

90 DOUGLAS, E., BILODEAU, A., MALHOTRA, V. M., "High performance concrete incorporating large volumes of ASTM class F fly ash", *Advances in Cement and Concrete,* pp. 508-523.

91 ILLSTON, J. M., "The components of strain in concrete under sustain compressive stress", *Magazine of Concrete Research,* Vol. 17, No. 50, March 1965.

92 EMBERSON, N. K. and MAYS, G. C., "Significance of property mismatch in the patch repair of structural concrete. Part 1: Properties of the repair system", *Magazine of Concrete Research,* Vol. 42, No. 152, pp. 147-160.

93 BROOKS, J. J and NEVILLE, A. M. "A comparison of creep, elasticity and strength of concrete in tension and compression", *Magazine of Concrete Research Construction*, Vol. 29, No. 100, pp. 131-141, September 1978.

94 ILLSTON, J. M. and POMEROY "*Recommendations for a standard creep test*", Concrete, pp. 24-25, December 1975.

95 NASSER, K. and Al-MANASEER, A. "Shrinkage and creep of concrete containing 50% of lignite fly ash at high temperatures", *Cement Concrete and Aggregates* Vol. 9, No. 2, pp. 95-100, 1987.

96 MARZOUK, H., "Creep of high strength and normal strength concrete", *Magazine of Concrete Research,* Vol. 43, No. 155, pp. 121-126, June1991.

97 BROOKS, J. J., WAINWRIGHT, P. J. and Al-KAISI, A. F., "Compressive and tensile creep of heat cured Portland and slag cement concrete", *Magazine of Concrete Research,* Vol. 43, No. 154, pp. 1-14, March 1991.

98 NEVILLE, A. M., DILGER, W. H. and BROOKS, J. J. *"Creep of plain and structural concrete"*, Construction Press, Longman Ltd, New York, 1983

99 THEODORAKOPOULOS, D. D., "Creep characteristics of glass reinforced cement under flexural loading", *Cement & Concrete Composites*, Vol. 17, pp. 267-279, 1995.

100 SWAMY, R. N., THEODORAKOPOULOS, D. D. and STAVRIDES, H., "Shrinkage and creep characteristics of glass fibre reinforced cement composites", *International Congress on the glass fibre reinforced cement*, Brighton, pp. 76-96, 1997.

101 WINKLER, E. M., "Damage to stone and concrete: Geological Consideration", *Engineering Geology*, Vol. 2, No. 5, Elsevier Publishing Company, Amsterdam 1968.

102 LAYCOCK, E. A., "Frost degradation and weathering of the magnesian limestone building stone of the Yorkshire province", *PhD Thesis*, Sheffield University, Sheffield, U.K, August 1997.

103 DUNN, J. R. and HUDEC, P. P., "Water, clay and rock soundness" *Ohio Journal of Science,* Vol. 66, No. 2, pp. 155-167.

104 WINKLER, E. M., "The importance of air pollution in the corrosion of stone and metals", *Engineering Journal*, Vol. 4, Elsevier Publishing Company, pp. 327-334,Amsterdam 1970.

105 AMERICAN SOCIETY FOR TESTING MATERIALS "Standard test method for resistance of concrete to rapid freezing and thawing", *ASTM C666-92,* November 1992.

106 BRITISH STANDARD INSTITUTION, "Specification for air -entraining admixtures" *BS 5075: Part 2*, 1982.

107 PEAKE, F. and FORD, R. W., "A panel freezing test for brickwork", *British Ceramic Research Association,* February 1984.

108 BOWSER, J. D., KRAUSE, G. L. and TADROS, M. K., "Freeze-Thaw durability of high performance concrete masonry units", *ACI Materials Journal,* pp. 386-394, July - August 1996.

109 GIFFORD, P. M., GILLOT, J. E., "Freeze-thaw durability of activated blast furnace slag cement concrete", *ACI Materials Journal,* pp. 242-245, May-June 1996.

110 LANKARD, D. R., BIRKIMER, D. L., FONDRIEST, F. F. and SNYDER, M. J., "Effect of moisture an the structural properties of Portland cement concrete exposed to temperatures up to 500 degrees F, *American Concrete Institute*, ACI special publication SP 25, pp. 59-102, 1971.

111 MOHAMEDBHAI, G. T. G., "Effect of exposure time and rates of heating and cooling on residual strength of heated concrete", *Magazine of Concrete Research*, Vol. 38, No. 136, pp. 151-158, September 1986.

112 CARETTE, G. G., PAINTER, K. E. and MALHOTRA, V. M., "Sustained high temperature effect on concretes made with normal Portland cement, normal Portland cement and slag and normal Portland cement and fly ash", *Concrete International, July 1982.*

113 RILEY, M. A., "Possible new method for the assessment of fire damaged concrete", *Magazine of Concrete Research*, Vol. 43, No. 155, pp 87-92, June 1991.

114 MANGAT, P. S. and AZARI, M. M., "A theory for the free shrinkage of steel fibre reinforced cement matrices", *Journal of Materials Science*, Vol. 19, pp. 2183-2194, 1984.

115 MANGAT, P. S. and AZARI, M. M., "A theory for the creep of steel reinforced cement matrices under compression ", *Journal of Materials Science*, Vol. 20, pp. 1119-1133, 1985.

116 MANGAT, P. S. and GURUSAMY, K., "Flexural strength of steel fibre reinforced cement composites", *Journal of Materials Science*, Vol. 22, pp. 3103-3110, 1987.

117 SWAMY, R. N., MANGAT, P. S. and RAO, C. V., "The mechanics of fibre reinforcement of cement matrices", *An International Symposium: Fibre reinforced concrete*, ACI Publication SP 44-1, pp. 1-29, 1974.

118 ROMUALDI, J. P. and MANDEL, J. A., "Tensile strength of concrete affected by uniformly distributed closely spaced short lengths of wire reinforcement, *ACI Journal*, Vol. 61, No.6, June 1964.

119 PATEL, J. K., DESAI, N. B. and RANA, J. C., "Properties and application of steel, polypropylene and polyester fibre reinforced concrete", *Fibre reinforced cements and concretes – Recent developments,* Elsevier Science Publishers Ltd., pp. 306-315, 1989.

120 FERRY, R., "The use of alkali resistant glass fibres in traditional concrete", *10^{th} Biennial Congress of the GRCA*, Strasbourg France, October 1995.

121 FERRY, R., "Alkali resistant glass fibres in concrete", *Sheffield University Workshop on fibre reinforced cement and concrete*, pp.1-11, July 1994.

122 PROCTOR, B. A., "The development and performance of alkali resistant glass fibres for cement reinforcement", *Proceedings of the International Symposium on Fibre Reinforced Concrete*, Madras India, pp. 3.3-3.19, December 1987.

123 SUSTERSIC, J., URBANCIC, S. and KUHAR, V., "Dynamic loading resistance of fibre reinforced concrete containing thin and short fibres", *Proceedings of the International Symposium on Fibre Reinforced Concrete*, Madras India, pp. 3.3-3.19, December 1987.

124 TAKAGI JUNJI "Some properties of glass fibre reinforced concrete", *International Symposium on the Fibre Reinforced Concrete*, ACI publication SP44-5, pp. 93-113, 1974

125 BRITISH STANDARD INSTITUTION, "Pulverized-fuel ash. Specification for pulverized-fuel ash for use with Portland Cement" *BS 3892: Part 1,* 1997.

126 BRITISH STANDARD INSTITUTION, "Specification for ground granulated blastfurnace slag for use with Portland cement" *BS 6699,* 1992.

127 BRITISH STANDARD INSTITUTION, "Methods of testing cement. Chemical analysis of cement" BS EN 196-2, 1995.

128 BRITISH STANDARD INSTITUTION, "Testing aggregates. Guide to sampling and testing aggregates" BS 812: Part 101, 1984.

129 COPERNICUS PROJECT CIPA-CT94-0178, "Recycling of fly ash for producing high performance construction materials based on a mineral binder system", Final Report, 1994.

130 BRITISH STANDARD INSTITUTION, "Methods of testing cement. Determination of strength" BS EN 196-1, 1995.

131 BRITISH STANDARD INSTITUTION, "Engineering drawing practice" *BS 308: Part 3: Geometrical Tolerancing,* 1986.

132 BRITISH STANDARD INSTITUTION, "Testing concrete. Methods for determination of density of hardened concrete" BS 1881: Part 114, 1984.

133 BRITISH STANDARD INSTITUTION, "Specification for clay bricks" BS 3921, 1974.

134 TAYLOR-FIRTH, A., Fundamental physical propertties of construction materials, *Sheffield Hallam University, School of Construction.*

135 AMERICAN SOCIETY FOR TESTING MATERIALS "Test for flexural Strength of concrete (using simple beams with centre-point loading)", *C 293-94.*

136 BRITISH STANDARD INSTITUTION, "Method for determination of flexural strength" *BS 1881: Part 118*, 1983.

137 BRITISH STANDARD INSTITUTION, "Method for determination of compressive strength of concrete cubes" *BS 1881: Part 116*, 1986.

138 British Ceramics Research Association Ltd. (BCRA), Freeze and thaw testing of a brick panel", 1984.

139 BRITISH STANDARD INSTITUTION, "Testing concrete. Method for making test cubes from fresh concrete" *BS 1881: Part 108*, 1983.

140 BRITISH STANDARD INSTITUTION, "Method for determination of static modulus of elasticity in compression" *BS 1881: Part 121,* 1983.

141 KONG, F. K. and EVANS, R. H., *"Reinforced and prestress concrete"*, Van Nonstrand Reinhold Co Ltd, Third Edition, 1987

142 MANGAT, P. S. and LIMBACHIYA, M. K., "Repair materials properties which influence the long term performance of concrete structures*"*, *Construction and Building Materials*, Vol. 9, No. 2, pp. 81-90, 1995.

143 MANGAT, P. S. and LIMBACHIYA, M. K., "Repair materials properties for effective structural applications", *Cement and Concrete Research*, Vol. 27, No. 4, pp. 601-617, 1997.

144 O'FLAHERTY, F *"PhD Thesis"*, Sheffield Hallam University, Sheffield, U.K.

145 MANGAT, P. S. and AZARI, M. M., "Plastic shrinkage of fibre reinforced concrete", *Materials and Structures, Vol. 23*, pp.186-195, 1990.

146 MANGAT, P. S., MANARAKIS, G. and AZARI, M. M., "A theory for early age free shrinkage of steel fibre reinforced cement composites", *International Conference on recent developments in fibre reinforced cement and concrete*, Cardiff, UK, pp. 188-199, Sept 1989.

147 BRITISH STANDARD INSTITUTION, "Method for determination of tensile splitting strength" *BS 1881: Part 117*, 1983.

148 BRITISH STANDARD INSTITUTION, "Recommendation for determination of strain in concrete" *BS 1881: Part 206*, 1986.

149 POWERS, T. C. and BROWNYARD, T. L., "Studies on the physical properties of harden Portland cement paste (nine parts)", *Journal of American Construction Institute*, Vol. 43, Oct. 1946- April 1947.

150 POWERS, T. C., "A discussion on the cement hydration in relation to curing of concrete", *Proceedings of the Highway Research Board*, Vol. 27, pp. 178-188, Washington DC, 1947.

151 VERBECK, G. J. and HELMUTH, R. A., "Structures and cement properties of cement pastes", *Proceedings of the 5th International symposium on the chemistry of Cement,* Tokyo, Vol. 3, pp. 1-32, 1968.

152 JOHNSTON, C. D., "Steel Fibre reinforced mortar and concrete- a review of mechanical properties", *An International Symposium: Fibre reinforced concrete*, ACI Publication SP 44-1, pp. 127-143, 1974.

153 SWAMY R, N. and MANGAT, P. S., "A theory for the flexural strength of steel fibre reinforced concrete", *Cement and Concrete Research,* Vol., pp. 313-325, 1974.

154 PEET, M. "Incipient corrosion in repair materials", PhD Thesis, Sheffield Hallam University, Sheffield, U.K to be submitted.

155 CONCRETE SOCIETY, "Permeability testing of site concrete", Technical Report No. 31.

156 LAWRENCE, C. D., "Water permeability of concrete", *Concrete Society Materials Research seminar, Serviceability of concrete,* Slough, July 1985.

157 BRITISH STANDARD INSTITUTION, "Recommendation for measurement of velocity of ultrasonic pulses in concrete" *BS 1881: Part 203*, 1986.

158 KHATIB, J. M. and MANGAT, P. S., "Absorption characteristics of concrete as a function of location relative to casting position", *Cement and Concrete Research,* Vol. 25, No. 5, pp. 999-1010, 1995

159 MANGAT, P. S and KHATIB, J. M., "Influence of initial curing on the pore structure and porosity of blended cement concretes", *Proceeding of the 4th International Conference on concrete*", Editor Malhotra V., ACI- SP 132-45, Vol. 1, pp. 813-833.

160 AMERICAN CONCRETE INSTITUTE "Specification for structural use of concrete*", ACI 301-72*

161 COPELAND, L. E. and HAYES, J. C., "The determination of non-evaporable water in hardened Portland cement paste, ASTM Bulletin No. 194, pp. 70-74, Dec. 1953.

162 HERTZ, K. D., "Danish investigations on silica fume concretes at elevated temperatures", *ACI Materials Journal*, Vol. 89, No. 4, pp.345-347, July-August 1992.

163 GOTO, S. and ROY, D. M., "The effect of w/b ratio and curing temperature on the permeability of hardened cement paste, Cement and Concrete research, Vo. 11, No. 4, pp. 575-579, 1981

164 ROCHOW, T. G. and TUCKER, P. A., *"Introduction to Microscopy by means of light, electrons, X-rays or acoustics"*, Second edition, 1995, Plenium Press1994.

165 PHILIPS, *"X-ray diffraction characterisation brochure"*.

166 ENCYCLOPEDIA BRITANNICA, 1998.

167 DIMOND, S., CCR, Vol. 16, pp. 569-579, 1986,

168 KATZ, A. "Microscopic study of alkali activated fly ash", *Cement and Concrete Research*, Vol. 28, No. 2, pp. 197-208, 1998.

169 PALOMO, A., GRUTZECK, M. W. and BLANCO, M. T., "Alkali activated fly ashes- A cement for the future", *Cement and Concrete Research*, Vol. 29, pp. 1323-1329, 1999.

170 CATALFAMO, P., DI PASQUALE, S. AND CORIGLIANO, F. "Influence of the calcium content of the fly ash features in some innovative applications", *Waste Materials in Construction: Putting Theory into Practice*, Elsevier Science, 1997.

171 SHI, C. and DAY, R. "Pozzolanic reaction in the presence of chemical activators. Part I Reaction Kinetics", *Cement and Concrete Research*, Vol. 30, pp. 51-58, 2000.

172 SHI, C. and DAY, R. "Pozzolanic reaction in the presence of chemical activators. Part II Reaction Products and Mechanism", *Cement and Concrete Research*, Vol. 30, pp. 607-613, 2000.

173 KENDRICK, D. A, PARSONAGE, J. R. and VAZIFDAR, R. "Interaction of alkali and alkali earth metal hydroxides with microsilica", *Cement and Concrete Research*, Vol. 30, pp. 51-58, 2000.